Transition metal sulfide catalysts

- A DFT study of structure and reactivity

Moses, Poul Georg

Publication date:
2008

Document Version
Early version, also known as pre-print

Poul Georg Moses

Transition metal sulfide catalysts

— A DFT study of structure and reactivity

Ph.D. Thesis
May 2008

Center for Atomic-scale Materials Design
Department of Physics
Technical University of Denmark
DK-2800 Kongens Lyngby, Denmark

Preface

This thesis is submitted in candidacy for the Ph.D. degree from the Technical University of Denmark (DTU). The work has been carried out over the last three years at the Center for Atomic-scale Materials Physics (CAMP)/Center for Atomic-scale Materials Design (CAMD), Department of Physics, DTU, with Professor Jens K. Nørskov as supervisor.

I would first of all like to thank past and present collaborators on the various projects. I would like to thank my supervisors both the official Jens Nørskov and the unofficial Henrik Topsøe for fruitful discussion, guidance and relentless optimism. Furthermore, Berit Hinnemann who has been on and off the project is thanked for being enthusiastic and helpful. Past and present office mates are thanked for discussion and fun over the years.

I thank Frank Abild-Pedersen, Jens Hummelshøj, Jan Rossmeisl, Heine A. Hansen, Carsten Rostgaard, Felix Studt, and Souheil Saadi for proof reading.

A special thanks goes to the land of Niflheim and its inhabitants Ole Holm Nielsen, Jens Jørgen Mortensen, and Marcin Dulak for producing thousands of cpu hours and thereby making this project possible.

My warmest thanks to Sara Alfort and Harald Alfort Moses for love, motivation and distraction.

Poul Georg Moses

Abstract

In this thesis, density functional theory (DFT) is applied in a study of topics related to hydrodesulfurization catalysis.
A series of calculated adsorption energies of hydrogen containing molecules on transition metals are presented. From the data set of adsorption energies linear relations between adsorption energies of the central atom and the hydrogenated central atom are derived. Insight into the underlying physics dictating the linear correlations is obtained by the development of a model based on the d-band model and effective medium theory. The study is extended to sulfides, nitrides, and oxides where similar linear relations are observed.
The structure of Ni and Co promoted MoS_2 catalysts is investigated in a combined DFT and scanning tunneling microscopy study. This study reveals that promotion with Co and Ni changes the shape and electronic structure of the nanoparticles. Two different kinds of morphology are observed, type A which is hexagons with promoters positioned at the $(\bar{1}010)$ edge, these are formed both for Ni and Co promoted particles. The second morphology termed type B is only formed by Ni promotion and has the shape of truncated hexagons, with the $(\bar{1}010)$ fully promoted with Ni and the $(10\bar{1}0)$ edge partially promoted with Ni. All structures have bright brims near and on the edge which are found to be the results of metallic edge states.
The hydrodesulfurization of thiophene is investigated over MoS_2 and Co promoted MoS_2 (CoMoS). The active sites are found to be vacancy sites at the $(\bar{1}010)$ edge of MoS_2 and so-called brim sites at the CoMoS $(\bar{1}010)$ edge and the $(10\bar{1}0)$ edge of MoS_2. The hydrogenation pathway (HYD) and the direct desulfurization (DDS) pathway are investigated on all sites. For the non promoted catalyst it is found that interaction between the $(\bar{1}010)$ and the $(10\bar{1}0)$ edge is important. The reason being that hydrogenation is facile at the $(10\bar{1}0)$ edge while the $(\bar{1}010)$ has the highest activity for SC scission. The HYD pathway is found to be more important than the DDS pathway on non promoted MoS_2. The DDS pathway is proposed to be slow since adsorption and hydrogenation of thiophene at the non promoted $(\bar{1}010)$ edge vacancy is unlikely. Co promotion increases the importance of the DDS pathway. This is because Co promotion increases the thiophene adsorption energy and at the same time the hydrogenation activity of the

catalyst is also found to increase.
A study of the inhibition by H_2S, benzene, and pyridine underpins that the Mo edge brim site is the hydrogenation site for unpromoted MoS_2. The mechanism of inhibition by the basic pyridine molecule is found to be due to the formation of a strongly bound pyridinium ion, thus the pyridinium ion blocks the $(10\bar{1}0)$ edge brim sites and furthermore use hydrogen during the protonation of pyridine. To determine the importance of van der Waals (vdW) forces in adsorption on MoS_2 a recently developed exchange correlation functional (vdW-DF) which includes (vdW) forces is implemented. The implementation have been tested and applied in a study of thiophene and butadiene adsorption on the basal plane of MoS_2. The vdW-DF functional yields adsorption energies very close to experimental findings. The contribution of vdW forces to the adsorption energy is found to be almost 0.5eV for thiophene adsorption. Thus, indicating that the inclusion of vdw forces is important in order to determining the coverage of species like thiophene accurately.
Finally a screening study for new hydrogen evolution catalysts is carried out. It is established that the free energy of H adsorption is a descriptor for the hydrogen evolution activity. The H adsorption energy is calculated for Co promoted and non-promoted MoS_2 and WS_2. It is found that all the studied catalyst should be good hydrogen evolution catalysts. Furthermore, DFT predicts that Co promotion should increase the hydrogen evolution activity. These predictions are confirmed by experiments.

Resumé

I denne afhandling bliver density functional theory (DFT) anvendt i en række studier med relation til afsvovlingskatalyse.
En serie adsorptionsenergier for molekyler, der indeholder brint, er blevet beregnet ved hjælp af DFT. Fra disse energier udledes lineære sammenhænge mellem adsorptionen energier for centralatomet og det hydrogenerede centralatom. Endeligt udledes en model som forklarer eksistensen af de observerede lineære sammenhænge. Lignende lineære sammenhænge på sulfider, nitrider og sulfider er også blevet observeret.
Strukturen af Ni og Co promoteret MoS_2 katalysatorer er blevet undersøgt i et kombineret DFT og scanning tunnelling microscopi-studie, der afslører, at Ni og Co promotering ændre formen og den elektroniske struktur af nanopartiklerne. Der er blevet fundet to forskellige strukturer. Type A, der har en heksagonal form med promoter-atomerne placeret på $(\bar{1}010)$ kanten. Disse bliver dannet ved både Ni og Co promotering. Den anden form, der bliver kaldet type B, bliver kun dannet ved Ni promotering og har en trunkeret heksagonal form. Hvor $(\bar{1}010)$ kanten er fuldt promoteret med Ni og $(10\bar{1}0)$ kanten kun delvist promoteret. Begge strukturer har en lysende rand placeret på og ved kanten, der skyldes eksistensen af metalliske kanttilstande.
Afsvovlingen af thiophen bliver undersøgt på både MoS_2 og Co promoteret MoS_2 (CoMoS). Hydrogeneringsvejen (HYD) og den direkte afsvovlingsvej (DDS) er blevet undersøgt på alle aktive sites. På den upromoverede katalysator ses det at samarbejde mellem $(\bar{1}010)$ og $(10\bar{1}0)$ kanten er vigtig, fordi hydrogenering nemt foregår på $(10\bar{1}0)$ kanten, mens brydning af svovlkarbon bånd foregår nemmest på $(\bar{1}010)$ kanten. HYD vejen ses at være den vigtigste reaktionsvej på upromoteret MoS_2. DDS vejen er langsom, fordi adsorption og hydrogenering af thiophen i vakancen på $(\bar{1}010)$ kanten er usandsynlig. Co promotering øger betydningen af DDS vejen, fordi Co promotering både øger thiophens adsorptionsenergi og hydrogeneringsaktiviteten.
Et studie af H_2S, benzene og pyridine forgiftning understøtter, at hydrogenering foregår på $(10\bar{1}0)$ kantens brim site. Forgiftning p grund af pyridine har vist sig at foregå ved, at en stærkt bunden pyridium ion dannes og derved blokeres $(10\bar{1}0)$ kantens brim site, samtidig med at brint forbruges. Betydningen af van der Waals vekselvirkning for størrelsen af adsorption-

senergier er blevet undersøgt ved at implementere et nyudviklet "exchange-correlation" funktionale (vdW-DF). Implementeringen er efterfølgende blevet testet og anvendt i et studie af thiophen og butadien adsorption på basalplanet af MoS_2. vdW-DF funktionalet giver adsorptionsenergier, der er meget tæt på de eksperimentelle adsorptionsenergier. vdW bidraget til adsorptionsenergien af thiophen er tæt på 0.5eV, hvilket viser, at vdW vekselvirkninger skal medtages for at kunne få præcise adsorptionsenergier og dermed en bedre beskrivelse af dækningen af thiophen og lignende molekyler på MoS_2. Endelig er der blevet udført et screeningsstudie for at bestemme nye og bedre hydrogenudviklingskatalysatorer. Det bliver slået fast, at en god indikator for hydrogenudviklingsaktivitet er ændringen i fri energi ved adsorption af brint på katalysatoren. Den fri bindingsenergi er blevet beregnet for promoteret og upromoteret WS_2 og MoS_2 og resultatet er, at alle disse katalysatorer er lovende til hydrogenudvikling. Desuden viser DFT, at Co promotering øge aktiviteten yderligere, hvilket bliver bekræftet af eksperimenter.

List of included papers

Paper I *Biomimetic hydrogen evolution: MoS_2 nanoparticies as catalyst for hydrogen evolution* B. Hinnemann, P.G. Moses, J. Bonde, K.P. Jørgensen, J.H. Nielsen, S. Horch, I. Chorkendorff, J.K. Nørskov, Journal Of The American Chemical Society, 127, 5308, (2005)

Paper II *A density functional of inhibition of the HDS hydrogenation pathway by pyridine, benzene, and H_2S on MoS_2-based catalysts*, Á. Logadóttir, P.G. Moses, B. Hinnemann, N-Y Topsøe, K.G. Knudsen, H. Topsøe, J.K. Nørskov, Catalysis Today, 111, 44, (2006)

Paper III *The hydrogenation and direct desulfurization reaction pathway in thiophene hydrodesulfurization over MoS_2 catalysts at realistic conditions: A density functional study*, P.G. Moses, B. Hinnemann, H. Topsøe, J.K. Nørskov, Journal Of Catalysis, 248, 188, (2007)

Paper IV *Scaling properties of adsorption energies for hydrogen-containing molecules on transition-metal surfaces*, F. Abild-Pedersen, J. Greeley, F. Studt, J. Rossmeisl, T.R. Munter, P.G. Moses, E. Skulason, T. Bligaard, J.K. Nørskov, Physical Review Letters, 99, 016105, 2007

Paper V *Location and coordination of promotor atoms in Co- and Ni-promoted MoS_2 based hydrotreating catalysts*, J.V. Lauritsen, J. Kibsgaard, G.H. Olesen, P.G. Moses, B. Hinnemann, S. Helveg, J.K. Nørskov, B.S. Clausen, H. Topsøe, E. Lægsgaard, F. Besenbacher, Journal Of Catalysis, 249, 220, (2007)

Paper VI *Recent STM, DFT and HAADF-STEM studies of sulfide-based hydrotreating catalysts: Insight into mechanistic, structural and particle size effects*, F. Besenbacher ,M. Brorson , B.S. Clausen, S. Helveg, B. Hinnemann, J. Kibsgaard, J.V. Lauritsen, P.G. Moses ,J.K. Nørskov, H. Topsøe, Catalysis Today, 130, 86, 2008

Paper VII *Recent density functional studies of hydrodesulfurization catalysts: insight into structure and mechanism*, B. Hinnemann, P.G. Moses, J.K. Nørskov, Journal Of Physics: Condensed Matter, 20, 064236, 2008

Paper VIII *Scaling Relations for Adsorption Energies on Transition Metal Oxide, Sulfide and Nitride surfaces* E.M. Fernández, P.G. Moses, A. Toftelund, H.A. Hansen, J.I. Martinez, F. Abild-Pedersen, J. Kleis, B. Hinnemann, J. Rossmeisl, T. Bligaard, J.K. Nørskov, Angewandte Chemie International Edition, In Press (2008)

Paper IX *Hydrogen Evolution on Nano-particulate Transition Metal Sulfides* J. Bonde, P. G. Moses, T. F. Jaramillo, J. K. Nørskov, I. Chorkendorff, Faraday Discussions, accepted

Paper X *Adsorption and van der Waals binding of thiophene, butane, and benzene on the basal plane of MoS_2 - a density functional study.* P.G. Moses, B.I. Lundqvist, J.K. Nørskov, to be submitted

Contents

Chapter 1

Introduction

1.1 Hydrodesulfurization catalysis

The main topic of this thesis is hydrodesulfurization (HDS) catalysis. HDS is the catalytic reactions taking place when sulfur is removed from crude oil in order to produce clean diesel fuel. HDS is an important catalytic process since the removal of sulfur from diesel fuel reduces air pollution and acid rain. The worlds increasing energy consumption and the increasing focus on the environment are compelling policy makers to enforce stricter legislations on diesel fuel. Today even the sulfur content in oil used for ship engines are being restricted [1]. Present day strict environmental legislations force refiners to produce ultra clean diesel fuel. This requirement calls for new and improved hydrodesulfurization catalysts.
HDS catalysis has been an active research field for decades, but nevertheless a detailed understanding at the atomic scale is still not fully developed, e.g there is no general agreement on the nature of the active site/sites. Such an insight is needed in order to improve the HDS catalyst and in the present thesis density functional theory will be used to investigate several important aspects of HDS catalysis.

1.2 Density functional theory and Catalysis informatics

Density functional theory (DFT) is the most successful theory for determining the electronic structure of systems relevant for heterogenous catalysis. The strength of density functional theory lies in its very favorable ratio between accuracy and demand for CPU time. The merits of density functional theory within fields such as chemistry, physics and material science is well recognized and has led to the nobel prize to the founder of modern day DFT [2].
Density functional theory and supercomputer speed are today of such qual-

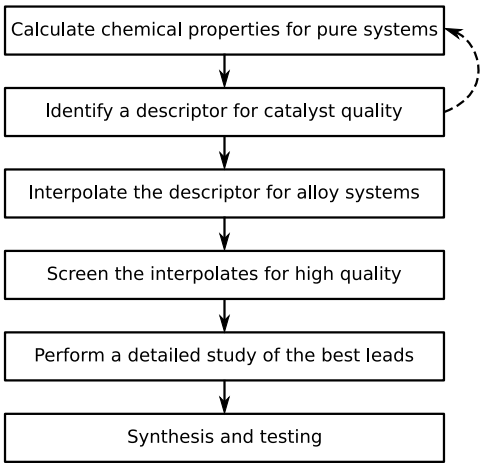

Figure 1.1: Road map to first principle catalyst design . Adapted from [6].

ity that catalyst design based on theoretical leads alone is becoming reality [3, 4, 5]. A possible route to catalyst design based on theory can be seen in Fig. 1.1. The first step is the traditional DFT study of a single catalyst, identifying the structure, the reaction mechanism, stability and other key properties. When one system is well understood less involved studies are undertaken (step 2 Fig. 1.1) in order to determine the key descriptors of activity. Then in a large scale screening study the descriptor is calculated on a huge number of systems (step 3). Such a study can with advantage use known scaling relations or simple interpolation schemes in order to save computer time. In the case where no suitable interpolation schemes exist brute force full scale DFT calculations must be carried out in order to calculate the descriptor on a series of candidates. This is at present only feasible for relatively simple descriptors such as adsorption energies of simple molecules on fairly simple surfaces such as closed packed metal surfaces. When an interpolation scheme or the full scale study has been undertaken the best candidates can be picked out on basis of the value of their activity descriptor (step 4). At this point more elaborate theoretical studies can be carried out in order to validate the accuracy of the interpolation scheme and/or the predictive power of the descriptor (step 5). The last step is experimental testing in order to validate the theoretical predictions.

1.3 Outline of the thesis

This thesis focuses on catalysis by sulfides and more specifically on HDS catalysis. In chapter 2 a brief introduction to the theory used in the rest of the thesis is given. The time needed to design new HDS catalysis may, as it is the case for transition metal based catalysis, be decreased if some of the involved quantities can be calculated by simple scaling laws and/or interpo-

lation schemes. In chapter 3 we establish scaling laws of adsorption energies on transition metal surfaces and on sulfides, nitrides and oxides. Such scaling laws could potentially be used to save CPU time in future screening projects. Even though HDS catalysis have been investigated intensely with both experimental and theoretical methods a clear picture of the reaction mechanisms of HDS does not exist. Thus, in order to establish the nature of the active site of HDS catalysts chapter 5 investigates the structure of promoted catalysts via a combined DFT and scanning tunneling microscopy study. The reaction mechanism of HDS of thiophene over MoS_2 and the effect of Co promotion are investigated in chapter 6. The demand for ultra clean diesel requires that even the most refractory sulfur containing organic compounds are desulfurized. To achieve this insight into inhibition of the HDS reaction becomes an issue. In chapter 7 the mechanism of inhibition by benzene, pyridine, and H_2S is investigated. The refractory sulfur containing organic compounds and many of the inhibitors of HDS are cyclic molecules and part of the adsorption energy is therefore expected to come from van der Waals forces. Due to lack of a better choice most studies assume that van der Waals forces are insignificant. However, in chapter 8 a recently implemented exchange correlation functional is used to calculate the adsorption energies including van der Waals forces on the basal plane of MoS_2 for the adsorption of thiophene and butadiene.
Returning to the schematic representation of the road map to first principle design (Fig. 1.1), it is recognized that the present work is focused on laying the groundwork for designing new HDS catalyst. The detailed investigation of the HDS mechanism belongs to the first and second step, while establishing scaling laws is forming the basis for proceeding to step 3.
We have not attempted a screening study for new HDS catalyst, but instead chapter 9 is presenting an initial design study of transition metal sulfides as hydrogen evolution catalyst which turn out to be a much simpler catalytic reaction than HDS. Finally, chapter 10 presents an overall conclusion and outlook.

Chapter 2

Theory

Adsorption and reactivity of molecules on surfaces depend on the electronic structure and are as such governed by quantum mechanics. It has due to the advent of density functional theory and the exponential increase in CPU speed often referred to as Moors law become possible over the last decade to numerically solve the quantum mechanical problem for realistic models of the real catalytic systems. Hence, obtaining information about the structure of the catalyst, the adsorption energies, and energy barriers for chemical reactions on the catalyst.

Understanding the obtained results requires a theoretical framework describing the chemistry and physics of adsorption and chemical reactions. Several books and reviews have been devoted to the theory of adsorption and reactivity of surfaces [7, 8, 9, 10, 11, 12]. The scope here is to give a brief introduction to some important concepts within this field with emphasis on the concepts used in the following sections and chapters.

2.1 Density functional Theory

2.1.1 The Schrödinger equation

The electronic structure of matter is governed by the time-dependent Schrödinger equation. If the problem at hand does not have any time dependence, the time-dependent Schrödinger equation can be reduced to the time-independent Schrödinger equation (TISE). When considering a system consisting of ions and electrons one can apply the Born-Oppenheimer approximation. The movement of the electrons and the movement of the ions can be decoupled, because the mass difference between electrons and ions is very large $m_e/M_{ions} << 1$. The ions are then considered to move on a potential energy surface created by the electrons. The positions of the ions $\{\boldsymbol{R_\alpha}\}$ then become a parameter, and this simplifies the calculations. Atomic units are used throughout this section, $e^2 = \hbar = m_e = 1$. The time

independent Schrödinger equation for an N-electron problem is

$$\hat{H}\Psi = E\Psi \tag{2.1}$$

With $\Psi = \Psi(\boldsymbol{r_1}, \boldsymbol{r_2}, \ldots, \boldsymbol{r_N})$ being the N particle wavefunction and E being the electronic energy of the system. The Hamiltonian $\hat{H}$ can be written as follows:

$$\hat{H} = \underbrace{\sum_{i=1}^{N} \frac{1}{2}\nabla_i^2}_{\text{Kinetic Energy}} + \underbrace{\sum_{i=1}^{N} \upsilon(\boldsymbol{r_i})}_{\text{External potential energy}} + \underbrace{\sum_{i<j}^{N} \frac{1}{|\boldsymbol{r_i} - \boldsymbol{r_j}|}}_{\text{Electron-electron interaction}} \tag{2.2}$$

In the following the kinetic energy term is denoted $\hat{T}$. The external potential energy, consists of both contributions from external fields and the electron-ion interactions. The electron-ion interactions are given by $\upsilon(r_i) = \sum_\alpha \frac{Z_\alpha}{|r_i - R_\alpha|}$ with R_α being the ion coordinates and Z_α is the charge of the ions. The electron-ion interaction term is denoted by $\hat{V}_{ext}$ and the single electron contributions, which sum up to $\hat{V}_{ext}$ are termed υ_{ext}. The electron-electron interaction term is denoted by $\hat{V}_{ee}$. The Hamiltonian in equation 2.2 is then represented by $\hat{H} = \hat{T} + \hat{V}_{ext} + \hat{V}_{ee}$. The ion-ion interaction is omitted since this is just a constant for a specific ion configuration and can be added separately according to the Born Oppenheimer approximation.
The major problem in many-body physics is to solve equation 2.1 with the Hamiltonian in equation 2.2. This can be done by different wavefunction methods [13] which give precise results, but these methods are computational extremely heavy. The success of electronic structure theory in heterogeneous catalysis is due to the development of density functional theory (DFT) which has a very favorable ratio between accuracy and CPU time. Several books have been written on DFT and for more details see [14, 15] in the following sections a brief introduction will be given. The success of DFT is based on a series of developments in both theory and algorithms. Most notable among these are the following:

Hohenberg Kohn theorems The foundation of density functional theory [16].

Kohn Sham theorems Providing a fast and consistent frame work for finding the ground state properties[17].

Generalized Gradient approximations Increasing the accuracy for adsorption energies e.g. reference [18, 19].

2.1.2 Hohenberg-Kohn theorems

In 1964, Hohenberg and Kohn [16] provided the theoretical foundation for applying the electron density $n(\boldsymbol{r})$ instead of the many-body wavefunction.

Thereby the number of variables can be reduced from 3N to 3. The first Hohenberg-Kohn theorem states the following:

Hohenberg-Kohn theorem 1 *The external potential $v_{ext}(\boldsymbol{r})$ is to within a constant a unique functional of the electron density $n(\boldsymbol{r})$.*

The theorem is proven by assuming that there exist two different external potentials v giving the same ground state density n_0 and then showing by using the variational principle that this leads to a contradicting result. The total energy functional is then

$$E[n] \quad = \quad T[n] + V_{ext}[n] + V_{ee}[n] \tag{2.3}$$

Hohenberg-Kohn theorem 2 *For a trial density $\tilde{n}(\boldsymbol{r})$ such that $\tilde{n}(\boldsymbol{r}) \geq 0$ and $\int \tilde{n}(\boldsymbol{r})d\boldsymbol{r} = N$,*

$$E_0 \leq E_v[\tilde{n}(\boldsymbol{r})]$$

where $E_v[\tilde{n}(\boldsymbol{r})]$ is the energy functional 2.3.

This theorem provides a minimization scheme for finding n_0 and can be proven using the variational principle.
Fortunately it can be shown by use of the variational principle that only the groundstate wavefunction minimizes the energy and this result leads to a minimization scheme called Levy and Lieb constrained search, see equation 2.4.

$$E_o = \underset{n}{Min} \left\{ \underset{\Psi \to n}{Min} \left[\langle \Psi | \hat{T} + \hat{V}_{ee} | \Psi \rangle + \int v(\boldsymbol{r}) n(\boldsymbol{r}) d\boldsymbol{r} \right] \right\} \tag{2.4}$$

However, the exact form of $T[n]$ $+V_{ee}[n]$ in equation 2.4 is not known and a Levy and Lieb constrained search is therefore not of practical use [14]. This problem can be overcome by following the approach of Kohn and Sham.

2.1.3 Kohn-Sham Equations

DFT does in principle reduce the quantum mechanical problem to 3 dimensions. However, the problem of finding n_o giving an external potential $v_{ext}(\boldsymbol{r})$ still involves solving the many body Schrödinger equation. So the problem of finding the ground state density without recourse to the many body Schrödinger equation still remains. A solution to this problem is given by the Kohn-Sham theorem which states

Kohn-Sham theorem 1 *Let $n_0(r)$ be the ground-state density of interacting electrons moving in the external potential $v_0(r)$. Then there exists a unique local potential $v_{eff,0}(r)$ such that non-interacting particle exposed to $v_{eff,0}(r)$ have the ground-state density $n_0(r)$.*

The Kohn-Sham theorem simplifies the problem since the energy is given as

$$E_{HK}(n) = T_{HK}(n) + F(n) \tag{2.5}$$

where $T_{HK}(n)$ is the kinetic energy of a non interacting electron gas and

$$F(n) = E_H(n) + E_{XC}(n) \tag{2.6}$$

which is the sum of the hartree energy

$$E_H(n) = \frac{1}{2}\int\int \frac{n(r)n(r')}{|r-r'|}drdr' \tag{2.7}$$

and a term called the exchange correlation energy. The strength of the Kohn-Sham approach is that in order to get T_{HK} we only need to solve the schrödinger equation for the non-interaction electron gas which is done in a self consistent loop solving the set of equations called the Kohn-Sham equations given in Eq. 2.8 and 2.9

$$\hat{h}_s\psi_i \quad = \quad [-\frac{1}{2}\nabla^2 + \upsilon_{eff}(\boldsymbol{r})]\psi_i = \varepsilon_i\psi_i \tag{2.8}$$

The density is given by equation 2.9.

$$n(\boldsymbol{r}) \quad = \quad \sum_{i_{occ}} |\psi_i|^2 \tag{2.9}$$

The effective potential $\upsilon_{eff}(\boldsymbol{r})$ is defined in equation 2.10

$$\upsilon_{eff}(\boldsymbol{r}) = \int \frac{n(\boldsymbol{r'})}{|\boldsymbol{r}-\boldsymbol{r'}|}d\boldsymbol{r'} + \upsilon(\boldsymbol{r}) + \frac{\delta E_{XC}[n(\boldsymbol{r})]}{\delta n(\boldsymbol{r})} \tag{2.10}$$

The total energy has its minimum at the ground state energy and it can be shown the the total energy is variational around the ground state with respect to small independent variation in effective potential and density [20, 8], so that

$$E(n_0 + \delta n, \nu_0 + \delta\nu) = E_0 + O^2(\delta n, \delta\nu) \tag{2.11}$$

2.1.4 Exchange-Correlation energy

The Kohn-Sham scheme is in principle exact, but the expression for the exchange-correlation functional E_{XC} is unknown. The exchange-correlation energy functional is given by:

$$E_{XC}[n] \quad = \quad \frac{1}{2}\int\int drdr' \frac{\bar{n}_{XC}(\boldsymbol{r},\boldsymbol{r'})n(\boldsymbol{r})}{|\boldsymbol{r}-\boldsymbol{r'}|}$$

$\bar{n}_{XC}(\boldsymbol{r}, \boldsymbol{r'})$ is the average exchange-correlation hole given by $\bar{n}_{XC}(\boldsymbol{r}, \boldsymbol{r'}) = \int_0^1 d\lambda n_{XC}^{\lambda}(\boldsymbol{r}, \boldsymbol{r'})$, where λ is the coupling strength: $\lambda = 1$ is the fully interacting system and $\lambda = 0$ is the non-interacting system.
$\bar{n}_{XC}(\boldsymbol{r})$ is a consequence of the depletion of electrons around a single electron, since an electron at position $\boldsymbol{r}$ reduces the probability of finding another electron near $\boldsymbol{r}$. Integrating $\bar{n}_{XC}(\boldsymbol{r}, \boldsymbol{r'})$ over all space gives -1, this is called the sum rule and it means, that the electron hole has the same charge as the electron, but the opposite sign.

Local Density Approximation, LDA

The simplest approximation to the exchange-correlation is obtained by assuming that the exchange-correlation hole resembles the hole of a uniform interacting electron gas with the same density. This is called the local density approximation.

$$E_{XC}^{LDA}[n] \quad = \quad \int n(\boldsymbol{r}) \varepsilon_{XC}(n(\boldsymbol{r})) d\boldsymbol{r}$$

The exchange-correlation hole of the interacting electron gas has been calculated by quantum Monte Carlo methods and is tabulated for different densities [21, 22]. LDA has been rather successful, even though it should only be successful for slowly varying densities. The reason for the success of LDA, is that it obeys the sum rule and that E_{XC} depends on spherical averages.

Generalized Gradient Approximation, GGA

LDA can be considered as the first term in a Taylor series. An improved exchange-correlation functional could therefore be obtained by including higher terms in the Taylor series. The Generalized Gradient Approximation (GGA) includes the gradient and takes care, that the sum rule and other requirements are fulfilled.

$$E_{XC}^{GGA}[n] \quad = \quad \int n(\boldsymbol{r}) \varepsilon_{XC}^{GGA}(n(\boldsymbol{r}), \nabla n(\boldsymbol{r})) d\boldsymbol{r}$$

There exist different GGA functionals including the PW91 [18], PBE [23], revPBE [24], and RPBE [19]. PW91 is overestimating adsorption energies by approximately 0.5eV, while RPBE has been shown to give the best results, it overestimates by approximately 0.25eV [19].

vdW-DF XC-functional

The vdW-DF functional is a recently developed functional which includes van der Waals interactions [25]. Van der Waals interactions are due to

correlation effects and is a long range effect which is not included in GGA-type XC functionals. The derivation is based on theory of the homogeneous electron gas and the interested reader is referred to appendix A for details on the derivation of the vdW-DF XC-functional. The basics of the derivation is given below:

- E_{XC} is written in terms of the adiabatic connection formula:
  $E_{XC} = \int_0^1 d\lambda \left\langle \Psi | \hat{V}_{ee} | \Psi \right\rangle_\lambda - E_H$
- The retarded correlation function is introduced via the fluctuation dissipation theorem:
  $E_{XC} = \int_0^1 \frac{d\lambda}{d\lambda} \int_0^\infty \frac{du}{2\pi} Tr[\chi_\lambda V_\lambda] - E_{self}$
- The interaction parameter integration is performed using the full potential approximation:
  $E_C^{nl} = \int_0^\infty \frac{du}{2\pi} Tr[ln(1 - \chi_\lambda V)] - ln(\epsilon)$
- The dielectric function is approximated by a plasmon pole type approximation

This leads to a simple expression for the XC-energy:

$$E_{XC} = E_c^0 + E_c^{nl} + E_x \tag{2.12}$$

Where E_c is the LDA correlation, E_x is the exchange energy, and E_c^{nl} is the non local correlation energy which is given by

$$E_c^{nl} = \int \int dr dr' n(r) \phi(r, r') n(r') \tag{2.13}$$

The interaction kernel $\phi(r, r')$ has been tabulated for two parameters δ and D which is given by the density $n(r)$ and $n(r')$ and the distance between r and r', $|r - r'|$. The interaction kernel can be seen in Fig. 2.1
We have implemented vdW-DF in the grid based projected augmented wave program GPAW [26]. The interested reader is referred to Appendix B for more details on the implementation. The current implementation is non self consistent and treated as a perturbation to the self consistent GGA density. Calculating E_c^{nl} requires approximately as much CPU time as the electronic convergence of the KS equations.

2.1.5 Spin Polarized Calculations

The Hohenberg-Kohn theorems and the Kohn-Sham equations can be extended to include spin, which makes it possible to treat magnetic system [27, 28]. It is possible to treat the spin polarized system as if it had two different densities one for spin-up and one for spin-down. This also means that spin polarized calculations require at least twice as much CPU time.

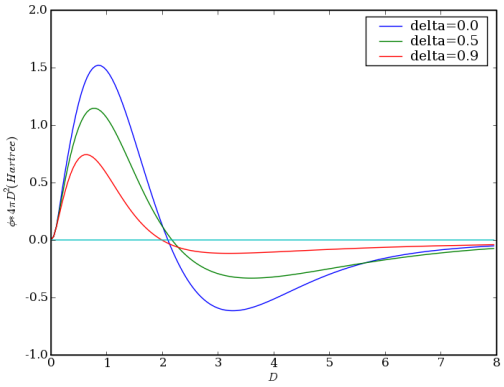

Figure 2.1: The interaction kernel phi

2.1.6 Computational approximations

Density functional theory can be implemented in several different ways and in this thesis the calculations have performed with the plane-wave code Dacapo unless otherwise noted [29, 19].

Basis

Dacapo uses a basis consisting of plane-waves. The choice of plane-waves is advantageous when considering periodic systems and it also has the advantage of being easy to test and improve the completeness/convergence. It also has some drawbacks, it is not optimal for cluster calculations, and it requires that the core electrons are represented in some other way than plane waves. Dacapo represents the core electrons with pseudopotentials. The Kohn-Sham wave functions should in principle be expanded in an infinite number of reciprocal lattice vectors, but it turns out that Fourier coefficients of high energy plane waves are very small and these can therefore be excluded. The truncation is done at a certain cutoff energy E_{cut}, which depends on the pseudopotentials used and the desired accuracy. The E_{cut} in this thesis is 25-30Rydberg.

The plane wave basis means that periodic boundary conditions (PBC) must be applied. PBC is extremely useful when modeling bulk structures but not that useful for systems like surfaces and molecules. Surfaces and molecules must be modeled using a so called supercell in order to include vacuum or distance between adsorbed species. The PBC applies to the supercell and the supercell includes the aperiodic system, an example can be seen in figure 2.2. The appropriate size of the unit cell must be tested in order to make sure that no or only insignificant interactions occur between the repeated unit cells.

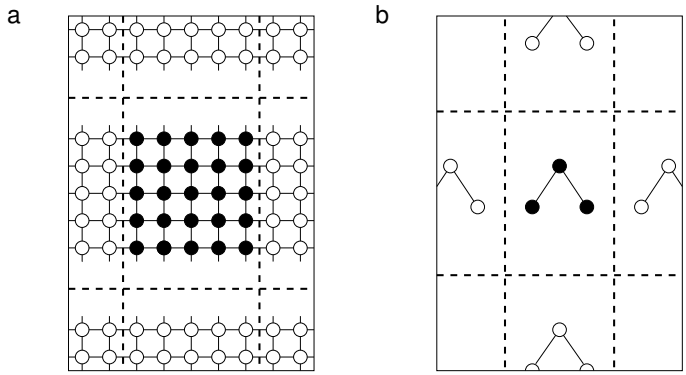

Figure 2.2: Periodic Boundary Conditions a) super cell geometry for an infinite stripe, b) super cell geometry for a molecule. Adapted from [30]

Pseudopotentials

Pseudopotentials are used because

- Chemical properties are often only determined by valence electron, while the effect of the core electrons is small.
- Core electrons have wave functions with many nodes and the valence state wave functions have to be orthogonal to these.
- The expansion of the core electrons wave functions with many nodes requires high energy plane-waves.

Therefore the all-electron potentials and the wavefunctions are replaced by pseudopotentials and pseudo-wavefunctions. In order to secure the accuracy and transferability of the pseudopotentials they should have the following properties [31, 32].

- Real and pseudo valence eigenvalues agree for a chosen prototype atomic configuration.
- Real and pseudo atomic wave functions agree beyond a chosen core radius r_c.
- The integrals from 0 to r of the real and pseudo charge densities agree for $r > r_c$ for each valence state (norm conservation).
- The logarithmic derivatives of the real and pseudo wave function and their first energy derivatives agree for $r > r_c$.

The norm conserving properties have been shown to require quite high energy cutoffs for transition metals and oxygen and therefore a scheme has been derived which relax the norm conserving condition and thereby allow the use of smaller energy cutoff while still obtaining precise results [33]. These pseudopotentials are called ultrasoft pseudopotentials.

k-point sampling

Dacapo uses periodic boundary conditions and that restricts the k-points to the first Brillouin zone. There exits a infinite but countable number of k-points, but in practice the wave functions only have to be evaluated at a few k-points. There exits methods for choosing these k-points in an intelligent way in order to obtain the highest accuracy with the smallest k-point set [34, 35]. When testing the number of k-points, it is important to remember that the variational principle does not apply to the number of k-points. This means that the energy does not continually decrease, but shows oscillations around the ground state, when increasing the number of k-points.

Fermi Temperature

The Fermi-Dirac distribution is a Heavyside function at 0K which means that the occupation number of any state is either 0 or 1. This introduces numerical problems when trying to minimize the energy. This is especially a problem for transition metals, which have complicated Fermi surfaces. The numerical problems can be overcome by introducing an artificial temperature which broadens the Fermi-Dirac distribution. When convergence is reached the finite temperature result is then extrapolated back to 0K [36]. The higher the Fermi temperature the faster convergence but a too high Fermi temperature violates the assumptions made in order to extrapolate back to 0K. In general, a higher temperature can be used for conducting systems than isolating systems. In this thesis k_BT=0.1eV is used for conducting systems and k_BT=0.01-0.001eV is used for molecules.

2.1.7 Atom dynamics

The forces between the ions are determined using the Born Oppenheim approximation and the Hellmann-Feynmann theorem which states that [37]:

$$f_I = -\langle\psi|\frac{\partial \hat{H}_I}{\partial \boldsymbol{R_I}}|\psi\rangle = \frac{-\partial E[n]}{\partial \boldsymbol{R_I}} \tag{2.14}$$

Here, $E[n]$ is the self-consistent ground state energy and $\boldsymbol{R_I}$ is the ion coordinates. The Hellmann-Feynmann theorem also means that errors in the forces are of first order with respect to errors in the wave functions, which means that higher energy cutoffs may be required in order to ensure convergence in forces. Convergence in the forces can also be improved by using a

density cutoff higher than the energy cutoff. Using a higher density cutoff mainly cost memory and not computer time. The relaxation of the ions to the minimum energy configuration is done using the quasi-Newton algorithm. Minimization algorithms converge to a local minima and it is therefore important to test different starting configurations in order to make it more probable that the relaxed structure is a global minimum.

2.1.8 Transition state searches

The main algorithm employed in the present work is the Nudged Elastic Band Method (NEB)[38] which is an algorithm to determine the minimum energy path (MEP) from one local minimum to another. The NEB algorithm must be given an initial state, a final state and N intermediate images. Image means in this context atomic configuration. These intermediate images can be constructed by simply making a linear interpolation from the initial to the final state or they can be made manually. The MEP is then found by connecting the N+2 images by springs and then relaxing the images according to the spring force parallel to the reaction coordinate and the true force perpendicular to the reaction coordinate. This ensures that the springs only determine the distances between images and the true force determines the position of the MEP. Different improvements have been made to NEB. They aim at improving the accuracy of the transition state energy, for instance the Climbing Image method [39], and decreasing the number of necessary force steps.

2.1.9 Scanning Tunnel Microscopy Simulation

In Scanning Tunnelling Microscopy (STM) a sharp metal tip is approached to a sample surface within approximately 5Å. This allows the wave function of the tip and the sample to significantly overlap and thereby it becomes possible for the electrons to tunnel between the tip and the sample. A schematic of how STM works can be seen in figure 2.3. Applying a small bias between the tip and the sample shifts the Fermi levels of the tip and the sample relative to each other making it possible for the electrons to tunnel from filled states to empty states, in either the sample or the tip depending on the bias. It is possible to measure a tunnel current. A very delicate mechanical feedback system allows the tip to be scanned across the sample surface in either constant current mode or constant height mode and thereby mapping out a complicated convolution of the local density of states (LDOS) near the Fermi level of the sample and the LDOS of the tip. The success of the STM depends heavily on the exponential dependence of the tunnelling current on the tip-sample distance which means that only the wave functions of the outermost atom of the tip interact with the sample. Therefore, it is essentially the LDOS of the sample which is mapped out.
When analyzing STM data, it is extremely important to remember that it is

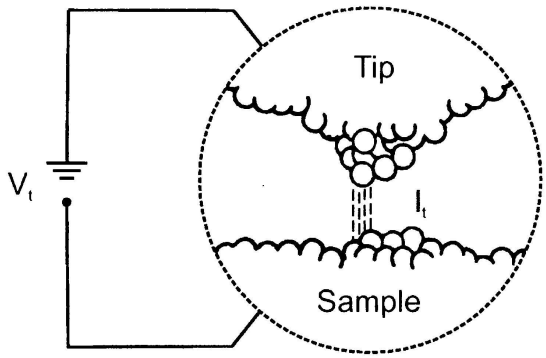

Figure 2.3: Schematic illustration of the principle of a STM. Adapted from [40]

the LDOS near the Fermi level, which is mapped. It may significantly differ from the total density of states. This means that STM images are a rather complicated convolution of geometric and electronic structure at the sample surface for instance a high LDOS, seen as protrusions in constant current mode, does not necessarily mean that an atom is located at this position. It is therefore important to combine STM with other surface science techniques and/or theoretical calculations in order to make correct interpretations of the obtained data.
A full theoretical description of the tunneling current is a very complex task, because the geometry of the tip and the sample must be known. It is fortunately possible to make some assumptions which make it possible to calculate the tunneling current as seen in equation 2.15

$$I_t(\boldsymbol{r_0}) \propto V \sum_s |\phi_s(\boldsymbol{r_0})|^2 \delta(\epsilon_s - \epsilon_F) = V n_s(\epsilon_F, \boldsymbol{r_0})) \tag{2.15}$$

Here ϵ_s is the energy of sample state $\phi_s(\boldsymbol{r_0})$, V is the bias, ϵ_F is the energy of the Fermi level and $\boldsymbol{r_0}$ is the position where the current is evaluated. This is the Tersoff-Hamann model. Within the Tersoff-Hamann model the current is only a function of the bias voltage and the LDOS at the Fermi level. Several assumptions are made in the Tersoff-Hamann model: The tip is assumed to be spherical, the voltages and temperature are assumed to be low and the two systems are assumed to be independent following Bardeens theory of tunneling [41, 42, 43]. The Tersoff-Hamann model has been generalized to make the tip wave function have any spherical symmetry [44]. Even though the Tersoff-Hamann model is very simple, it has been shown to be qualitatively successful in several studies [45, 46, 47], but it has also been shown to fail in some special cases [48]. It is difficult to obtain quantitative results with the Tersoff-Hamann model, because it tends to underestimate the corrugation of the surface at realistic tip-surface distances.

The STM simulation tool used in this thesis allows for the use of four different tips s,p_x, p_y and p_Z. The current is calculated using equation 2.16.

$$I_t(\boldsymbol{r_0}) \propto \sum_n \int \frac{d\boldsymbol{k}}{\Omega_{BZ}} |\phi_{nk}(\boldsymbol{r_0})|^2 \delta(\epsilon_{nk} - \epsilon_F) \tag{2.16}$$

The integration is over the first Brillouin zone and n is the band index. The integral over the Brilloiun zone is replaced by a summation as described in section 2.1.6. Further description of the STM-tool can be found in [49]. The important parameter to choose when applying the STM-tool is the LDOS or as it is usually referred to the contour value. The Tersoff-Hamann model is best suited for qualitative analysis and the contour value is therefore chosen by calibrating it to a reference system. This procedure of course means that meaningful STM simulations can only be done having access to experimental results.

2.2 First principle thermodynamics

Pure DFT results give the groundstate energies at 0K. Therefore in order to take pressure and temperature into account thermodynamics either directly from first principles using statistical mechanics or in combination with tabulated data are used to calculate properties such as Gibbs free energies. This has been done in a series of studies and is often used to predict the most stable surface structures at specific reaction conditions [50, 51, 52].

2.2.1 Edge free energy

A thorough derivation of the equations needed to calculated the free energy of MoS_2 are found in reference [50]. These equation can be extended to promoted structures in which case the edge free energy is given as in equation 2.17

$$\begin{aligned}\gamma^i = E^i_{stripe}(PMeS + N^i_H \cdot H) - N^i_{Me} \cdot E^{bulk}_{MeS_2} \\ - N^i_P \cdot \frac{E^{bulk}_{P_xS_y}}{x} + \mu_S \left[(2N^i_{Me} + \frac{y}{x}N^i_P - N^i_S)\right] - \mu_H \cdot N^i_H\end{aligned} \tag{2.17}$$

Where P is the promoter (e.g Co), Me is the host metal (e.g Mo), N^i_m is the number of species m on edge i. The chemical potential of H_2S and H_2

is found using equation 2.18 and 2.19.

$$\begin{aligned}\mu_S &= \mu_{H_2S} - \mu_{H_2} \\ &= [\Delta h_{H_2S}(T, p^{\ominus}) - \Delta h_{H_2}(T, p^{\ominus})] \\ &+ [E^{vib}_{H_2S}(T = 0K) - E^{vib}_{H_2}(T = 0K)] - (E_{H_2S} - E_{H_2}) \\ &- T[s_{H_2S}(T, p^{\ominus}) - s_{H_2}(T, p^{\ominus})] + k_B T ln\left(\frac{p_{H_2S}}{p_{H_2}}\right)\end{aligned} \tag{2.18}$$

$$\begin{aligned}\mu_H &= \frac{1}{2}\mu_{H_2} \\ &= \frac{1}{2}\left[\Delta h_{H_2}(T, p^{\ominus}) + E^{vib}_{H_2}(T = 0K) + E_{H_2} - T s_{H_2}(T, p^{\ominus}) + k_B T ln\left(\frac{p_{H_2}}{p^{\ominus}}\right)\right]\end{aligned} \tag{2.19}$$

$\Delta h_i(T, p^{\ominus}) = h_i(T, p^{\ominus}) - h_i(T = 0K, p^{\ominus})$ and $h_i(T, P)$ is the enthalpy of component i at temperatur=T and pressure= P. $E^{vib}_i(T = 0K)$ is the sum of the vibrational ground state energies of component i. $s_i(T, P)$ is the entropy of component i, p_i is the partial pressures of component i.
For practical purposes it useful to choose a reference edge and calculate the i edge energy with relative to the reference edge 0

$$\begin{aligned}\gamma^i - \gamma^0 = E^i_{stripe}(PMS + N^i_H \cdot H) - E^0_{stripe}(PMS + N^0_H \cdot H) \\ + (N^0_{Me} - N^i_{Me})E^{bulk}_{MeS_2} \\ + (N^0_P - N^i_P)\frac{E^{bulk}_{P_xS_y}}{x} \\ + \mu_S\left[(2N^i_{Me} + \frac{y}{x}N^i_P - N^i_S) - (2N^0_{Me} + \frac{y}{x}N^0_P - N^0_S)\right] \\ + \mu_H(N^0_H - N^i_H)\end{aligned} \tag{2.20}$$

This can be further simplified in the situation where $N^i_{Me} = N^0_{Me}$ and $N^i_P = N^0_P$.

$$\begin{aligned}\gamma^i - \gamma^0 = E^i_{stripe}(PMS + N^i_H \cdot H) - E^0_{stripe}(PMS + N^0_H \cdot H) \\ + \mu_S(N^0_S - N^i_S) \\ + \mu_H(N^0_H - N^i_H)\end{aligned} \tag{2.21}$$

Eq. 2.17 and 2.21 are used in this thesis to predict the equilibrium edge structures.

2.3 Models of chemisorption

The present section is meant to give an overview of the theories of adsorption which will be referred to in later chapters. This section is not meant to be a thorough review, which can be found in several books and reviews [7, 8, 9, 10, 11, 12].

2.3.1 Geometric and electronic effects

The chemistry of surfaces is often divided into a geometric and an electronic part, this is to a certain degree superficial since both parts originates from differences in the electronic structure, but it is nevertheless still useful when investigating trends and correlations in heterogeneous catalysis to make a distinction. In the present thesis the electronic effect is defined as the change in energies for a fixed local geometry and the geometric effect is the difference in energies between different local geometries.

2.3.2 One electron energies

In equation 2.11 we saw that there exist a generalized energy functional $E(n, v) = T(n, v) + F(n)$ which is stationary with respect to independent variations in the density n and the potential v. The variational properties of $E(n, v)$ mean that first order variations in n and v only lead to second order errors in $E(n, v)$. This can be used to understand the variations in adsorption energies from one metal to the next [20, 8, 9]. Assuming that the local densities and the one electron potential of the adsorbate and the metal does not change (the frozen density approximation) then the change in the adsorption energies for small changes in the metal electron density becomes:

$$\delta E_{ads} = \delta W_{1el} + \delta E_{es} \tag{2.22}$$

Where the difference in adsorption energy (δE_{ads}) is given by the change in one electron energies (δW_{1el}) and the change in inter-atomic electrostatic energy (δE_{es}). This is an extremely important result since it means that we can use models based on one electron energies to analyze and understand the trends and correlations in adsorption energies.

One electron models are widespread in chemistry and physics and several of these models based on the tight-binding approximation (or similar linear combination of atomic orbitals LCAO) are very useful to have in mind when investigating the changes in one electron energies induced by the formation of chemical bonds. The most noticeable models are the two level problem and the Newns-Anderson model which is a generalization of the two level problem.

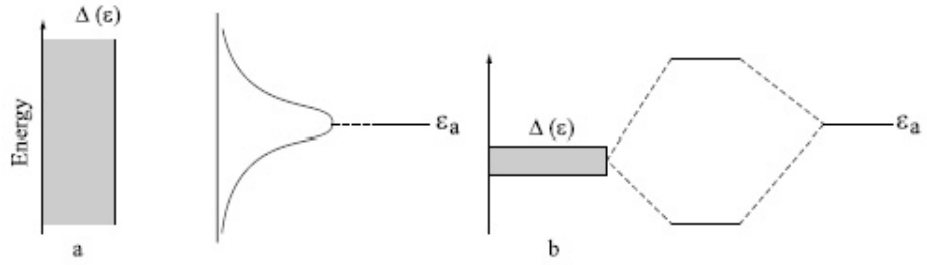

Figure 2.4: Newns Anderson Model [8].

Newns-Anderson Model

The main result of the Newns Anderson Model is Eq.

$$n_a(\varepsilon) = \frac{1}{\pi} \frac{\Delta(\varepsilon)}{(\varepsilon - \varepsilon_a - \Lambda(\varepsilon))^2 - \Delta(\varepsilon)^2} \tag{2.23}$$

Where $\Delta(\varepsilon)$ is the imaginary part of the self-energy and and $\Lambda(\varepsilon)$ is the real part of the self energy. $\Delta(\varepsilon) = \pi \sum_k |V_{ak}|^2 \delta(\varepsilon - \varepsilon_k)$ is the projected density of states. To understand trends in chemisorption two limiting cases of the Newns-Anderson model turn out to be of importance. One where $\Delta(\varepsilon)$ is a constant background which merely broadens the adsorbate level (Fig. 2.4 left) and another case where $\Delta(\varepsilon)$ is a single level which leads to splitting into bonding and anti-bonding states (Fig. 2.4 right). In between these two cases lie the interaction with sp electrons and d electrons. In these cases the overall picture is that the sp electrons shift down the adsorbate level and broadens it. The d electrons split the adsorbate level into two levels and broaden the levels.

d-band model

The main assumption in the d-band model is that the majority of the adsorption energy is given by the interactions with the sp-electrons. The interaction with the d-electrons is only a small perturbation on top of the sp-electrons. This means that the adsorption energy can be divided into a term due to the sp electrons and a term due to the d electrons. Fig 2.5 shows the d-band interpretation of adsorption, where the adsorption is initiated by a down shift and broadening of the adsorbate level followed by a splitting into bonding and anti bonding states by the d band.
The splitting and broadening of the renormalized adsorption level by the d-band electrons may be approximated as a two level problem, by simply treating the d-band as a single level with an energy equal to the center of the d-band. The two level approximation is motivated by the Newns-Anderson model where the d band is seen to split the adsorbate level and broaden the levels with the limit of a very narrow d band which simply splits the

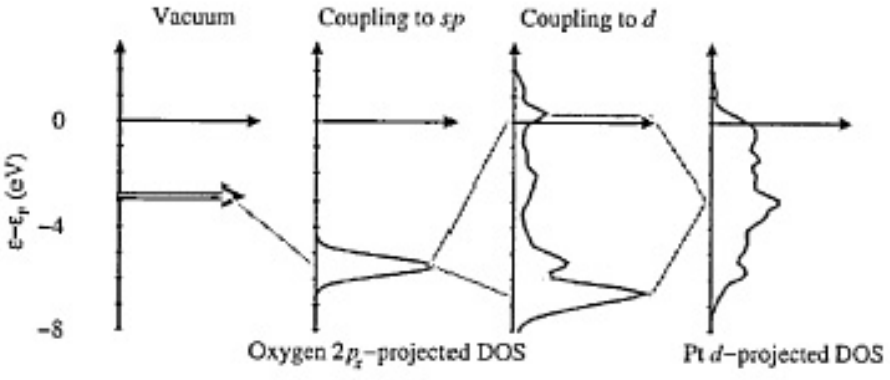

Figure 2.5: schematic of the d-band model [9].

adsorbate level into a bonding and antibonding state. This leads to the following equation for the hybridization energy due to the interaction with the d-band

$$E_{d-chem} = -(1-f)\left(\sqrt{4V_{ad}^2 + (\varepsilon_d - \varepsilon_a)^2} - (\varepsilon_d - \varepsilon_a)\right) - 2(1+f)V_{ad}S \tag{2.24}$$

Where f is filling of the d-band,V_{ad} is the coupling matrix element between the adsorbate state and the metal d states, ε_d is the center of the d band, ε_a is the energy of the adsorbate level, and S is the overlap matrix element. This apparently very simple model has successfully explained trends in adsorption energies across the periodic table, effects of strain, stress, and poisoning [53, 54, 55].

Chapter 3

Linear scaling

3.1 Introduction

Understanding trends in reactivity for heterogeneous catalysts has both an applied and a fundamental aspect. From an applied point of view trends may speed up the process of identifying new and better catalyst. From a more fundamental scientific point of view trends and correlations are interesting because they indicate that some underlying physics are determining the chemical reactivity thus trends may help researchers understand the physics of chemical reactions on surfaces.
In this chapter a series of computer "experiments" will investigate trends in adsorption energies. A series of empirical scaling laws will be derived from the computer "experiments" and a model describing the underlying physics that dictates the scaling laws will be proposed.

3.2 Calculational details

3.2.1 Transitions metals

The computer "experiments" are conducted on the close-packed fcc(111), hcp(0001), and bcc(110) surfaces, and the stepped fcc(211) and bcc(210) surfaces. Each of the surfaces is modeled by a (2x2) or a (1x2) surface unit cell for the close-packed and stepped surfaces, respectively. Each slab has a thickness of three layers in the direction perpendicular to the close-packed surface. The adsorbates and the topmost layer are allowed to relax fully in all configurations, and in the case of Fe, Ni, and Co, spin polarization is taken into account. The binding energies of the different species have been taken for the most stable adsorption sites on all surfaces. The GGA-RPBE functional is used to describe exchange and correlation effects [19]. A (4x4x1) k-point Monkhorst-Pack sampling is used [34]. A distance between layers of 10Å together with dipole correction in the z direction is used in order to decouple adjacent slabs. Ultra soft pseudopotentials are used except

for sulfur where a soft pseudopotential is used [33, 56]. A planewave cutoff of 340eV and a density cutoff of 540eV is used.

3.2.2 Transition metal nitrides, oxides, and sulfides

The calculational details are similar to the ones for transition metals with the following differences The valence wave functions are expanded in a basis set of plane waves with a kinetic energy cut-off of 350-400 eV. Spin magnetic moments for the oxides, Co-Mo-S, Ni-Mo-S, and Co-W-S are taken into account. We use the periodic slab approximation and the unit cells considered are modeled by a (2x2) unit cell for the nitrides and perovskite-type oxides, a (2x1) unit cell for PtO_2, a (2x1) unit cell for Co-W-S and MS_2 surfaces with M = Mo, Nb, Ta, and W, and a (4x1) unit cell for M-Mo- S surface with M = Ni and Co. A four layer slab for the nitrides and perovskite-type oxides, a four trilayer slab for PtO_2-type oxides, and a 8 or 12 layer slab for sulfides are employed in the calculations. Neighboring slabs are separated by more than 10Å of vacuum. The results for the MO_2 surfaces with M = Ir, Mn, Ru, and Ti are taken from Refs. [57] The adsorbate together with the two topmost layers for the nitrides and perovskite-type oxides, the two topmost trilayers for MO_2 oxides and all layers for the sulfides, are allowed to fully relax. The Brillouin zone of the systems is sampled with a 4x4x1 Monkhorst- Pack grid for nitride and oxide surfaces and with a 6x1x1 (4x1x1) for the 2x1 (4x1) supercell for the sulfide surfaces.

3.3 Transition metals

First, we will present calculated adsorption energies of CH_x, $x = 0, 1, 2, 3$, NH_x, $x = 0, 1, 2$, SH_x, $x = 0, 1$, OH_x,$x = 0, 1$. Then we will develop a model which explains the physical origin of the observed trends and finally we briefly outline one possible use of the presented correlations.

3.3.1 Adsorption energies

Figure 3.1 summarizes the adsorption energies of the DFT calculations. We find for all the AH_x molecules investigated that the adsorption energy as a function of the adsorption energy of the central atom follows equation 3.1.

$$\Delta E^{AH_x} = \gamma \Delta E^A + \xi \tag{3.1}$$

There is some scatter around the linear relation but we note that while the adsorption energy ΔE varies over several eV the mean absolute error (MAE) is only 0.13eV. Some of the scatter originates from the fact that the most stable adsorption site changes as the molecules are dehydrogenated. Figure 3.2 shows the adsorption energy of CH_3 at the ontop site as a function of C at the most stable site or C at the ontop site. Even though the scatter is not

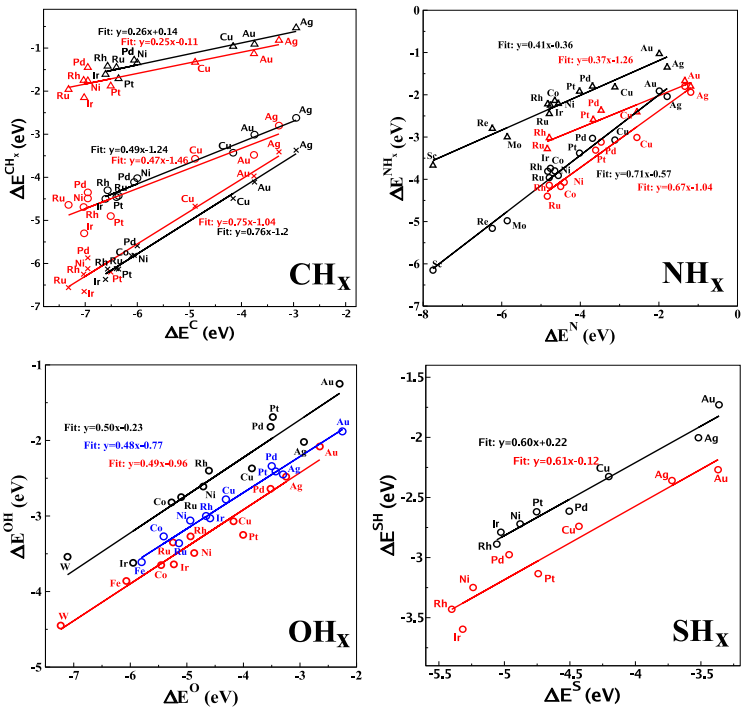

Figure 3.1: Adsorption energies of CH_x species. (crosses: x=1; circles: x=2; triangles: x=3), NH_x intermediates (circles: x=1; triangles: x=2), OH, and SH intermediates plotted against adsorption energies of C, N, O, and S, respectively. The adsorption energy of molecule A is defined as the total energy of A adsorbed in the lowest energy position outside the surface minus the sum of the total energies of A in vacuum and the clean surface. The data points represent results for close-packed (black) and stepped (red) surfaces on various transition-metal surfaces. In addition, data points for metals in the fcc(100) structure (blue) have been included for OH_x.

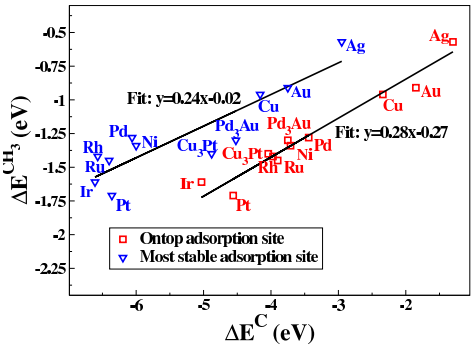

Figure 3.2: Adsorption energies of CH_3 against the binding energies of C for adsorption in the most stable sites (triangles) and in the case where both CH_3 and C have been fixed in the on-top site (squares)

large for CH_3 plotted against C at the most stable site the scatter decreases further when CH_3 and C are at the ontop site (MAE = 0.06eV).
The main observation is that the adsorption energies correlate in a linear fashion. The proportionality constant γ is a seen to be a function of the number of H atoms in AH_x and is to a good approximation given by equation

$$\gamma(x) = \frac{x_{max} - x}{x_{max}} \tag{3.2}$$

where x is the number of H atoms in AH_x and x_{max} is the maximum number of H atoms in AH_x, which for A equals C is 4 , A equals N is 3 and for A equals O or S it is 2. The valency of a molecule is given as $(x_{max} - x)$ and for the 4 systems considered in the present study the slope only depends on the valency. In the following section we will consider a model that allows us to understand the physics behind this effect.

3.3.2 Model of scaling laws for adsorption energies,

Simple bond counting [58] can explain the observed correlations between CH_3, CH_2, and CH which on the closed packed (111) surface prefer to adsorb in onefold, twofold, and threefold adsorption sites, respectively. The intuitive conclusion drawn from these observation is that the unsaturated molecular bonds form bonds to the surface. However, simple bond counting breaks down for atomic C, which is still adsorbed in a three fold site even though it is missing 4 bonds. Therefore it is not obvious from bond counting that all the CH_x species should correlate with the binding energy of atomic C. Furthermore, it is difficult to understand the apparent independence of the scaling relation on the adsorption site (Fig. 3.2) using bond counting

arguments . The scaling seen in Fig. 3.1 and 3.2 must therefore have a more general explanation which include the bond counting arguments as a special case.
The d-band model introduced in Sec. 2.3.2 has been quite successful in predicting trends in catalytic activity from one metal to the next [9, 59, 53, 60, 61, 62] and in the following we will use the d-band model to understand the correlations seen in Fig. 3.1 and 3.2. The main assumption in the d band model is that the adsorption energy can be divided into a part due to coupling to sp-electrons of the metal and a part due to the d electrons.

$$\Delta E = \Delta E_{sp} + \Delta E_d \tag{3.3}$$

The coupling to the sp states is usually the largest part of the binding and involves considerable hybridization and charge transfer. In the d band model it is assumed that the coupling to the sp states is constant from one transition metal to the next. This assumption is justified by the fact the the sp band is broad and half occupied for all transition metals. The variation from one metal to the next is then given by the d states. The d states form narrow bands of states close to the Fermi level, and the width and energy of the d bands vary substantially from one transition metal to the next. According to the d-band model all the variation seen in Fig.3.1 should be given by the variations in the d bands. This means that the x dependence of $\Delta E^{AH_x}(x)$ must be given by the d coupling alone. If one for a moment assumes that the d coupling for AH_x is proportional to the valency parameter defined above:

$$\Delta E_d^{AH_x} = \gamma(x)\Delta E_d^A \tag{3.4}$$

Following the same presciption as in the d band model the adsorption energy of AH_x (Eq. 3.1) can be written as:

$$\begin{aligned}\Delta E^{AH_x} = \Delta E_d^{AH_x} + \Delta E_{sp}^{AH_x} &= \gamma(x)\Delta E_d^A + \Delta E_{sp}^{AH_x} \\ &= \gamma(x)(\Delta E^A - \Delta E_{sp}^A) + \Delta E_{sp}^{AH_x} \\ &= \gamma(x)\Delta E^A + \xi\end{aligned} \tag{3.5}$$

where $\xi = \Delta E_{sp}^{AH_x} - \gamma(x)\Delta E_{sp}^A$ only includes sp terms and from the assumption about it follows that it is independent of the metal in question. The parameter $\gamma(x)$ can be read off Fig 3.1 for each AH_x/A combination, see Eq. 3.1 and the parameter ξ can be obtained from calculations on any transition metal. In the following all model data presented is obtained using Pt(111) as the reference system.

However, we still need to show that the assumption behind Eq 3.4 is valid. Hence, show that the coupling to d states scale with the valency of the adsorbate as in Eq. 3.1 which in mathematical terms equals to showing that:

$$\Delta E_d \propto V_{ad}^2 \propto \gamma(x) = (x_{max} - x)/x_{max} \tag{3.6}$$

Equation 3.6 will be correct if the number of bonds scale with x (CH, CH_2, CH_3) unless the bond lengths change. In the case where the bond lengths are unchanged the coupling matrix elements stay the same, and the hybridization energy of each extra bond will then be proportional to the coupling matrix elements. In the case where the site is unchange there must be a change in bond length. The change in bondlength will be given primarily by the change in sp coupling since $\Delta E_d << \Delta E_{sp}$. The change in sp coupling can be understood in terms of effective medium theory [20]. In effective medium theory the adsorption energy at a given density is approximated by the adsorption energy in an effective medium with the same density. Figure 3.3 shows the cohesive energy as function of the density, there exist an optimum electron density (n_0) where the cohesive energy has an minimum. In the case of adsorption on an surface the adsorption distance of a given species is given by $n(r) = n_0$ where n_0 is the optimum density. $n(r)$ can be viewed as a generalized bond order and the fact that the adsorption occurs at $n(r) = n_0$ expresses bond order conservation. Returning again to CH_4, C will adsorb where $n_{surf} = n_0$ and CH_4 which only adsorbs through weak van der Waal forces adsorbs where $n_{surf} = 0$ which means that the optimum density for the main atom C must be provided by the H atoms so that $4n_H = n_0$ following along these lines lead to $n_{surf} = (4 - x)/4n_0$ which in the general case is

$$n_{surf} = (x_{max} - x)/x_{max} n_0 = \gamma(x) n_0 \tag{3.7}$$

Since $n_{surf}(x) \propto V_{ad}^2(x)$, because the density at the surface i proportional to the overlap matrix element, which again is proportional to the coupling matrix element. Using this leaves us with

$$\Delta E_d(x) \propto V_{ad}^2(x) \propto n_{surf}(x) \propto \frac{x_{max} - x}{x_{max}} = \gamma(x) \tag{3.8}$$

which shows that there is good reason to believe that the d coupling will be proportional γ

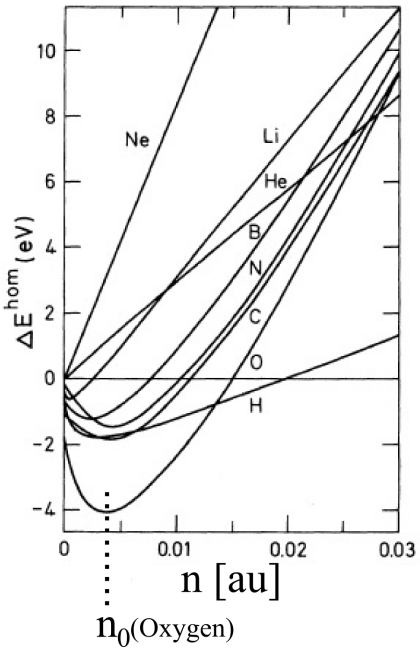

Figure 3.3: Cohesive energies of different atoms embedded in a homogeneous electron gas with density n. n_0(oxygen) marks the optimum density of oxygen. Adapted from [63, 64].

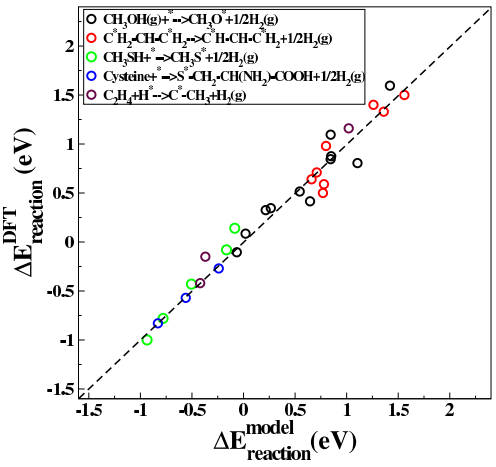

Figure 3.4: Calculated reaction energies for a series of dehydrogenation reactions plotted against the model predictions. The model data have been generated using calculated Pt(111) data as reference.

The scaling laws can for instance be used to calculate reaction energies for (de)hydrogenation reactions. The reaction energy will be given by equation 3.9

$$\Delta E = \sum_{i=1}^{N} \left(\Delta\gamma_i \Delta E^{A_i} + \Delta\xi_i\right) = \sum_{i=1}^{N} \left(\Delta\gamma_i \Delta E^{A_i}\right) + \Delta\xi \tag{3.9}$$

Where the sum runs over the i atoms bonding to the surface, $\Delta\gamma_i$ is the change in valency of atom i, and $\Delta\xi_i$ is the change in the y axis intercept for atom i. $\Delta\xi_i$ is metal independent, since it only depends on the sp electrons and therefore can be calculated once and for all for a given reaction on one metal. In Fig. 3.4 calculated reaction energies for different dehydrogenation reaction have been plotted against the reaction energy given by Eq. 3.9. The correlation is striking and it is clear that it is viable to use the scaling relation to estimate reaction energies. This opens op for the construction of entire energy diagrams for reactions at metal surfaces and combined with brønsted-Evans-Polanyi relationships activation barriers could also be included leading to the complete potential energy landscape based on the adsorption energies of the central atoms. In summary we observe in Fig. 3.1 that the adsorption energy of hydrogenated species correlate with the adsorption energy of the central atom. We have presented a model which indicate that the slope of the correlation is given by the interaction with the d electrons while the intercept is dependent on the sp coupling and therefore approximately transition metal independent. This is a result of a generalized bond order conservation, which requires that the local density of the central atom is unchange.

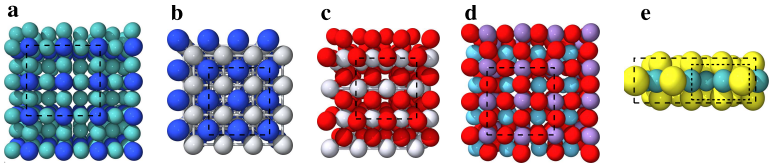

Figure 3.5: The investigated surfaces. a) fcc-like structure for the M_2N (100) surface, M = Mo and W. Dark blue and light blue spheres represent metal and nitrogen atoms, respectively. b) fcc-like rock salt structure for the TiN (100) surface. Dark blue and gray spheres represent Ti and N atoms, respectively, c) rutile-like (110) surface for the PtO2. Red and white spheres represent oxygen and metal atoms, respectively. d) perovskite structure for the $LaMO_3$ (100) surface , with M = Ti, Ni, Mn, Fe, and Co. Red, light blue, and violet spheres represent oxygen, lanthanum and metal atoms, respectively. e) hcp like $(\bar{1}010)$ surfaces for NbS_2, TaS_2, MoS_2, WS_2, Co-Mo-S, Ni-Mo-S and Co-W-S. Yellow and green spheres represent sulfur and metal atoms, respectively. The dotted lines mark the supercell.

3.4 Transition metal nitrides, oxides, and sulfides

Surface processes on nitrides, oxides and sulfides are of interest for a series of applications e.g. hardening of steel [65], fuel cells [57], hydrotreating catalysis [66, 67, 50, 68, 69].

Therefore, a series of studies of adsorption on these surfaces are undertaken in order to investigate whether scaling relations also exist for these more complex surfaces. Using the same approach as for the pure transition metals we have investigated the surfaces of some sample nitrides, oxides, and sulfides, these can be seen in Fig. 3.5 along with the investigated super cells. For the nitrides, the clean surface and the surface with a nitrogen vacancy are studied. For MX_2-type oxides (sulfides) an oxygen (sulfur) covered surface with an oxygen (sulfur) vacancy is studied.

We have investigated the adsorption of NH_x, $x = 0, 1, 2$, OH_x,$x = 0, 1$, SH_x, $x = 0, 1$ on the nitrides, oxides and sulfides, respectively. The calculated adsorption energies as a function of the adsorption energy of the central atom can be seen in Fig. 3.6. It is evident that scaling relations do also exist for these systems. The scaling is approximately given by the same linear expression found the for pure transition metals (Eq. 3.1). We find that the mean absolute error (MAE) is lower than 0.19eV for all the species considered here. The correlation is poorest for the nitrides, which is mainly due to TiN which is a clear outlier.

Fig. 3.7 compares adsorption energies on transition metals with adsorption energies on nitrides, oxides, and sulfides. It is interesting to note that for the nitrides the scaling is essentially the same for the two systems. For the oxides and partially for the sulfides the results for the compounds are shifted from those of the metals. This is due to a difference in the local geometry

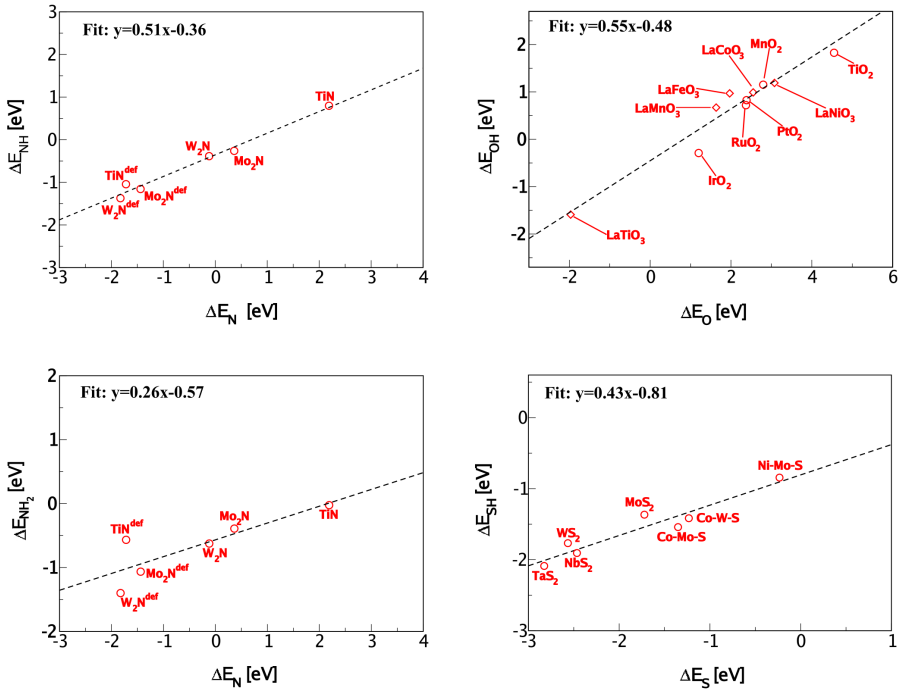

Figure 3.6: Adsorption energies. The adsorption energy of AH_x is defined as: $\Delta E(AH_x) = E(AH_x*) + (x_{max} - x)/2 * E(H_2) - E(*) - E(AH_{x_{max}})$ where $E(AH_x*)$ is the total energy of an AH_x molecule adsorbed on the most stable adsorption site, $E(*)$ is the total energy of the surface without the A atom adsorbed, and $E(H_2)$ and $E(AH_{x_{max}})$ are the total energy of the hydrogen molecule and the $AH_{x_{max}}$ molecule in vacuum, respectively.

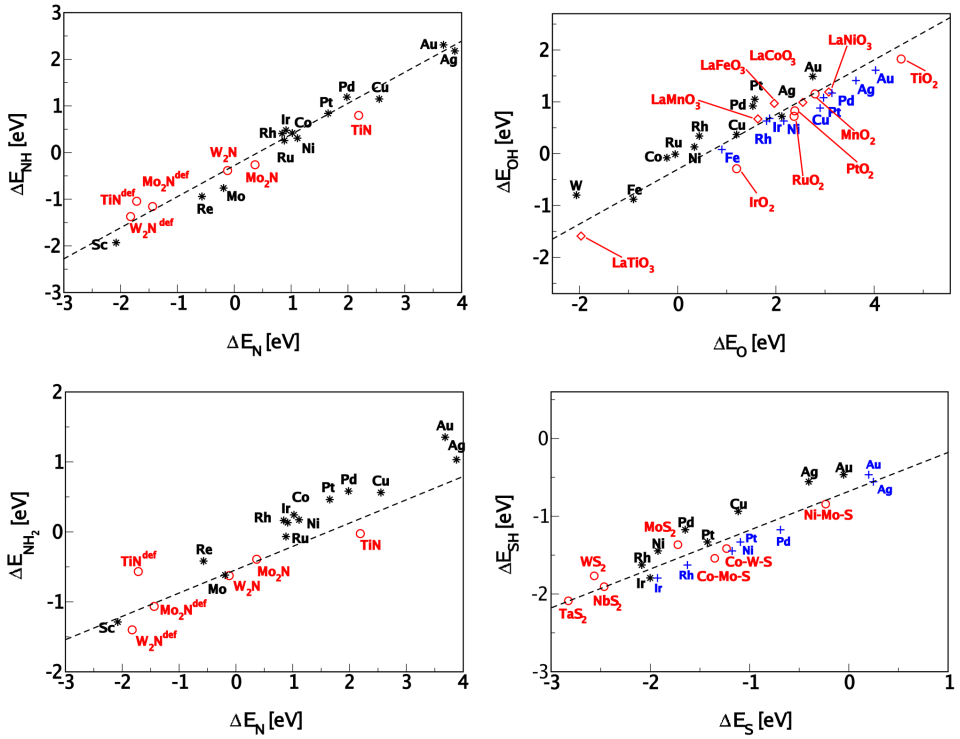

Figure 3.7: Adsorption energies. Close-packed surfaces for NH_x and OH_x intermediates and the stepped surface for SH_x intermediates are considered. The adsorption energies for the OH intermediate on top site and S intermediates on bridge site over transition metals are included (blue points). The dashed line is the exact slope, $\gamma(x)$, obtained by eq. 3.1.

for the S atoms, which on the sulfides is adsorbed in bridge positions while the most stable site on the transition metals (211) surface is the b5 site. If similar adsorption site i.e. bridge site on the (211) step is chosen then the agreement between the sulfides and the transition metals is better. For the oxides the O atom also adsorbs on a different site and if a similar adsorption site on the metal is considered then the data agrees with the oxide results, as we observed for the sulfides.

The results of Figs. 3.6 and 3.7 indicate that the nature of the adsorption is similar for transition metals and nitrides, oxides, and sulfides. In the case of transition metals we could explain the difference in terms of the d-band model, see Sec. 3.3.2. The scaling behavior of Figs. 3.6 and 3.7 suggest that the underlying physics of adsorption on the more complex surfaces is similar to the underlying physics on metals. The key to understand this can be found in recent work by Lundqvist *et al* [70, 71] where they show that a suitable modified d-band model can be used to understand trend in adsorption energies on transition metal carbides and nitrides.

3.5 Summary

We have presented linear scaling relations for adsorption on transition metals. We have presented an explanation within the d-band model framework, where the metal independent intercept is given by the sp-coupling and the slope is determined by the coupling to the d-band. We have demonstrated that the same kind of linear relationships also exist on nitrides, oxides, and sulfides. The existence of linear relationships opens up for fast predictions of reaction energies and the construction of entire energy diagrams for catalytic reactions. It is therefore proposed to be a very useful tool in a fast screening for new catalysts or materials with specific properties.

Chapter 4

Hydrodesulfurization

4.1 Introduction

The present chapter presents a short introduction to hydrodesulfurizaton (HDS) and the general computational details used to study the HDS process. Hydrotreating is a family of catalytic processes which remove contaminants such as, nitrogen, oxygen, sulfur, and metals from crude oil. This chapter focuses on the removal of sulfur which is called hydrodesulfurization. Refiners need to remove sulfur to meet present day regulations on sulfur content in diesel fuel and to ensure that sulfur does not contaminate catalyst of other refining processes. The legislations on sulfur contents are becoming increasingly stricter in order to decrease air pollution in densely populated areas and more recently to pave the way for exhaust catalyst on diesel fueled cars.

4.1.1 The HDS process

The research in HDS has been ongoing for several decades and is still an active field [72]. There exist a series of reviews on HDS e.g [73, 74, 75, 76, 77, 78, 79] covering all the corners of HDS catalysis.
The general reaction taking place in HDS is seen in reaction 4.1. The reaction conditions of HDS may vary over a large range of pressures and temperatures, where a few examples are given in Tab. 4.1. The choice of reaction conditions depends on parameters such as, the required conversion of sulfur containing compounds, the choice of catalyst, the quality of the crude oil including the amounts of pollutants such as nitrogen, sulfur, and oxygen, etc.

$$\begin{pmatrix} \text{Organic sulfur} \\ \text{compound} \end{pmatrix} + \mathrm{H_2(g)} \rightarrow \begin{pmatrix} \text{Desulfurized organic} \\ \text{compound} \end{pmatrix} + \mathrm{H_2S(g)} \quad (4.1)$$

Table 4.1: Reaction conditions for the hydrodesulfurization process,[73]

Fuel type	Total Pressure [MPa]	LHSV [h^{-1}]	Temperature[C°]
Naphtha(gasoline)	1.38-5.17	2-6	290-370
Kerosene/gas oil (jet/diesel fuels)	3.45-10.30	0.5-3.0	315-400
FCC feed pretreat	6.90-20.70	0.5-2.0	370-425

The need to reach present day strict legislations on sulfur content and upgrade increasingly heavier feedstock calls for improved catalysts. In order to aid the development of new and better catalyst atomic scale insight is needed. Commonly used catalysts for HDS consist of MoS_2 particles promoted with Co (CoMoS) or Ni (NiMoS) supported on γ-Al_2O_3 support or graphite. The atomic scale structure of CoMoS and NiMoS is the subject of chapter 5. Several experimental studies have investigated the kinetics of HDS catalysis [69] it is however not understood what the nature of the active site is, for instance it is not clear whether there is a difference in the chemistry of the different stable edges. In chapter 6 the reactivity of MoS_2 and Co promoted MoS_2 is investigated. The need to reach ultra low diesel levels has increased the focus on inhibition mechanisms of HDS, where among others nitrogen containing organic compounds acts as inhibitors. Chapter 7 presents an investigation of the inhibition mechanism and it is shown how the formation of a pyridinium ion plays a key role in inhibition by pyridine. DFT has a proven track record of calculating accurate adsorption energies of small molecules on metals. However, a large fraction of reactants and inhibitors in HDS catalysis are cyclic molecules with delocalized π electrons and for such molecules van der Waals forces are believed to play a role in adsorption. This is usually neglected, in lack of a tractable method of including van der Waals forces, when investigating adsorption of cyclic molecules. Recent developments in DFT theory have however shown that van der Waals forces may be included [25] and in chapter 8 we present calculations including van der Waals interaction of thiophene and butadiene on the basal plane of MoS_2 and find that the van der Waals part of the adsorption energy is quite significant.

4.2 General computational details for HDS

The computational details of the following chapters are very similar and below the archetypical computational details will be outlined. The specific chapters will have a short section describing differences from the details below. An infinite stripe model, which has previously been proven successful to investigate MoS_2 based systems [80,50,81], is used to investigate the edges of MoS_2 and is depicted in Fig. 4.1. The infinite stripe exposes both the Mo

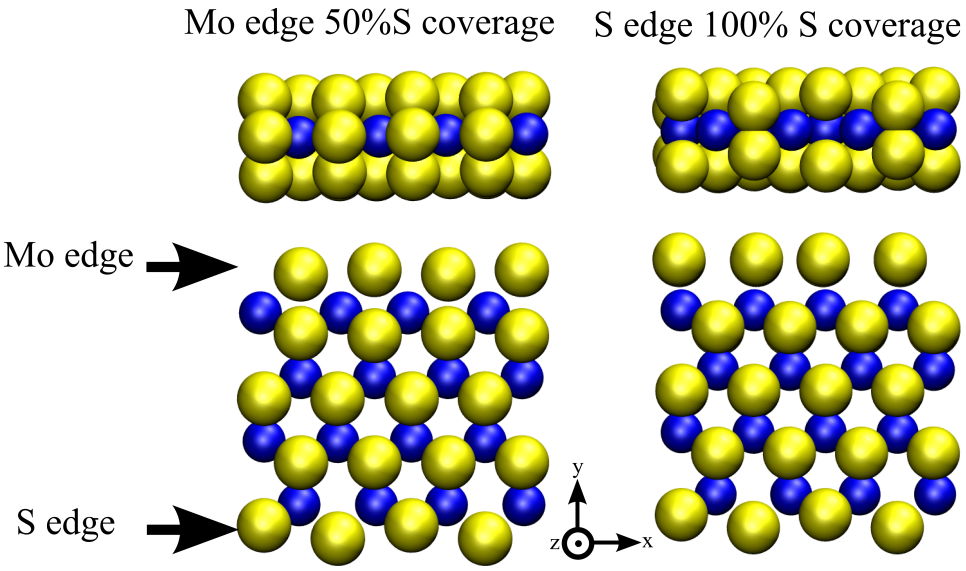

Figure 4.1: The 4x4 supercell. Molybdenum (blue), sulfur (yellow)

edge and the S edge. The supercell size is denoted as N_xxN_y corresponding to N_x Mo atoms in the x-direction and N_y Mo atoms in the y-direction. N_x must be an even integer in order to allow for important reconstructions with a period of 2 in the x-direction and N_y must insure decoupling of the Mo edge and the S edge in the y-direction. The stripes are separated by 14.8Å in the z-direction and 9Å in the y-direction. This model represents MoS_2 structures with no support interactions such structures are similar to the Type II structures found in present day high activity commercial catalysts [82, 83, 84]. The plane wave density functional theory code DACAPO [19,29] is used to perform the DFT calculations. The Brillouin zone is sampled using a Monkhorst-Pack k-point set [34] containing 12 k-points in the x-direction and 1 k-point in the y- and z-direction in the case of a single MoS_2 unit in the x-direction (N_x=1). The calculated equilibrium lattice constant of a=3.215Å compares well to the experimental lattice constant of 3.16Å [85]. A plane-wave cutoff of 30 Rydberg and a density wave cutoff of 45 Rydberg are employed using the double-grid technique [86]. Ultrasoft pseudopotentials are used except for sulfur, where a soft pseudopotential is employed [56,33]. A Fermi temperature of k_BT=0.1eV is used for all stripe calculations and energies are extrapolated to zero electronic temperature. The exchange correlation functional PW91 is used [18]. In the case of possible spin polarized metals (e.g Cobalt) or molecules the calculations are done spinpolarized. The convergence criterion for the atomic relaxation is that the norm of the total force should be smaller than 0.15eV/Å, which corresponds approximately to a max force on one atom below 0.05eV/Å. The nudged elastic band (NEB) method is used to find energy barriers [38] to-

gether with the adaptive nudged elastic band approach [87] and cubic spline fits to the energy and the forces. Furthermore a fixed bond length filter and a transition state search algorithm have been used to check NEB transition states. The algorithm utilizes a quasi Newton algorithm and an approach similar to the one presented in [88] to follow the eigenvector corresponding to the lowest eigenvalue to the saddle point. Figures of atomic structures have been made using VMD [89].
All adsorption energies have, unless otherwise noted, been calculated using the equation:

$$E_{ad} = E_{molecule+MoS_2} - E_{MoS_2} - E_{molecule(g)}$$

where $E_{molecule+MoS_2}$ is the energy of the system with the molecule bound to the surface, E_{MoS_2} the energy of the stripe and $E_{molecule(g)}$ is the energy of the molecule in vacuum. Molecules in vacuum have been calculated with the same setup as stripe calculations, except using a supercell which ensures at least 11Å vacuum between neighboring molecules, using a Fermi temperature of k_BT=0.01eV, using only the gamma point in the Brillouin zone sampling, and the norm of the total force should be smaller than 0.05eV/Å.

Chapter 5

Structure of HDS catalysts

5.1 Introduction

A key prerequisite for understanding the catalytic behavior is detailed understanding of the structure of the active catalyst. The structure and shape of the catalyst may depend on the support, the reaction conditions, and the incorporation of promoters. The present chapter presents a short introduction to the structure of HDS catalysts based on experiments (Sec. 5.1.1) and theory (Sec. 5.1.2). Finally new insight into Ni and Co promoted MoS_2 catalyst based on combined STM and DFT is presented (Sec. 5.2).

5.1.1 Experimental studies

Bulk MoS_2 is a layered structure consisting of MoS_2 hexagonal closed packed (hcp) layers held together by van der Waals forces. Each individual hcp layer is a sandwich structure with a Mo layer sandwiched between two sulfur layers. The structure of MoS_2 is similar to that of graphite and it can also form nanotubes [90, 91].
The common catalyst in industrial reactors is particulate Mo sulfide promoted by Co or Ni. The active phase has been identified by extended X-ray Adsorption Fine Structure (EXAFS) studies to be present as MoS_2 like structures, 10-20Å wide (Fig. 5.1) [92, 93, 94].
Transmission Electron Microscopy (TEM) experiments find that the active phase may be layered structures [95, 96, 97]. However, present day catalysts are mainly Type II catalysts, which are fully sulfided single layer structures with weak support interactions [82, 83, 84], a ball model of a MoS_2 particle can be seen in Fig. 5.1.
Insight into the structure of the smallest catalyst particles is hampered by the detection limit of TEM [98, 97, 99] which renders detection of the smallest particles impossible. Furthermore, TEM is also limited to only observing particles along the (0001) basal plane i.e. the layers are seen as lines. Recently is has, however, been possible using high angle annular dark field scan-

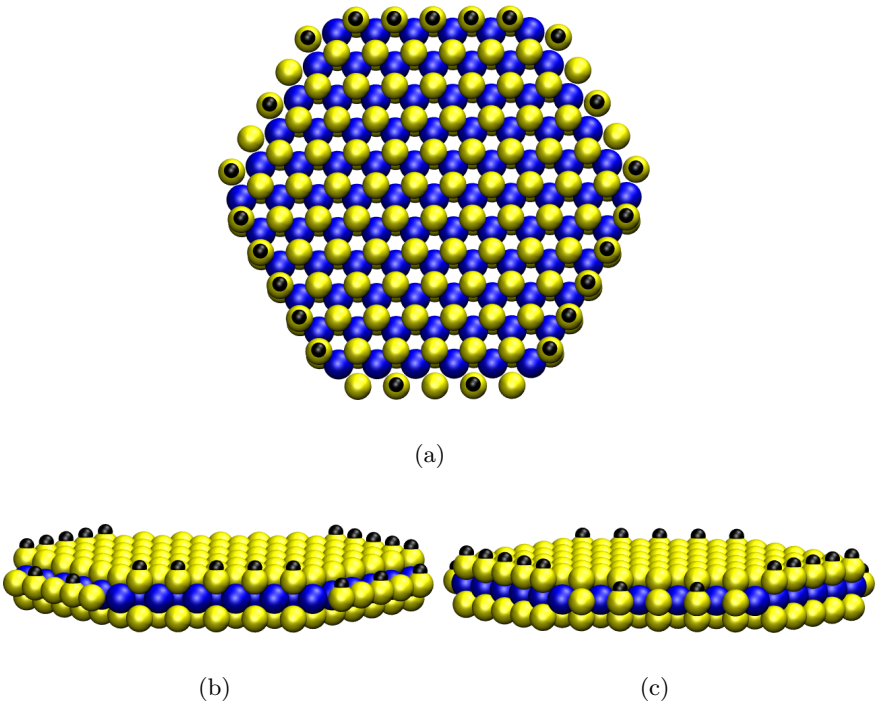

(a)

(b) (c)

Figure 5.1: MoS_2 Ballmodels:(a) topview of a MoS_2 particle, (b) S edge with 100% S and 100%H, (c) MoS_2 Mo edge with 50% S and 50% H.

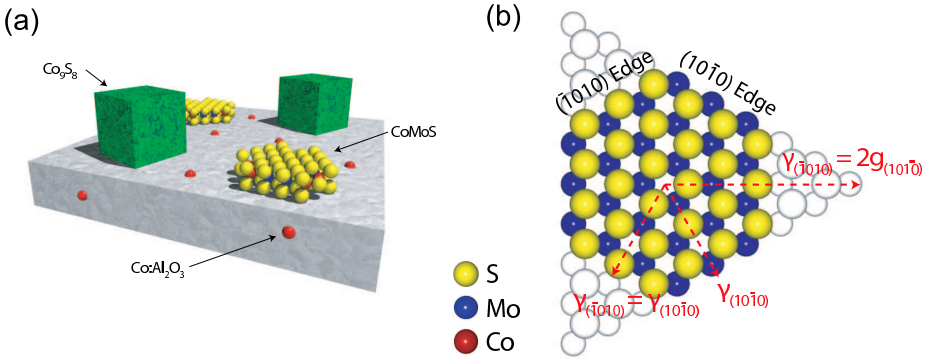

Figure 5.2: a) The three different phases of Co, b) ball model of MoS_2.

ning transmission electron microscopy (HAADF-STEM) [100, 101, 102, 103] to observe the shape of relative large MoS_2 and WS_2 particles supported on graphite.

Important information regarding the atomic scale structure and reactivity of MoS_2 based HDS catalysts has been obtained using STM. Such studies have provided atom resolved images of the MoS_2 nanostructures; and when combined with DFT calculations quite detailed information may be obtained from the images [104, 105, 106, 107, 108, 109, 50, 110, 111]. These combined studies clearly show that naked Mo $(10\bar{1}0)$ edges are not present at ultrahigh vacuum conditions. In contrast, the results show that the Mo atoms will tend to maintain the full sulfur coordination of six. This is achieved by extensive edge reconstructions. Quite surprisingly, it was found that these fully sulfur-saturated Mo $(10\bar{1}0)$ edges of MoS_2 have some sites with metallic character [104, 109, 50].

Promotion: The CoMoS phase

As all ready mentioned the industrial catalyst is promoted by Co or Ni. The effect of promotion of MoS_2 by Co and Ni has been the subject of a long discussion in the HDS literature but presently consensus has been reached on the CoMoS/NiMoS phase as the active phase [112]. The CoMoS phase was discovered using Mössbauer spectroscopy [113, 114]. Fig, 5.2 presents the three different positions for the Co atom: in the Al_2O_3 bulk, as Co_9S_8 and on the edges of MoS_2. The cobalt decorated MoS_2 phase was termed the CoMoS phase and was found to be the phase responsible for the catalytic activity [112].

5.1.2 Density functional theory studies

A series of DFT studies have investigated the structure of promoted and non-promoted HDS catalysts, including the position of promoters [68,67,115,116, 117], the influence of reaction conditions [50,67,118,119,120], support effects [81,121,122], and explorative catalysts like phosphides, carbides and zeolites [123, 124, 125, 126, 127, 128, 129, 130, 131]

In the first DFT study of MoS_2 and CoMoS structures, Byskov et al [68] found that it is energetically very unfavorably to create the "naked" Mo edges, where Mo is exposed at the edge and only 4 fold coordinated, and they concluded that such structures probably are not present under realistic HDS conditions [68]. Subsequent DFT studies have supported this conclusion [132, 50, 133]. Even though multiple vacancy sites may be very reactive [134, 135, 136], they are expected to readily react with H_2S; and reactions involving such sites should be extremely strongly inhibited by H_2S. The first study of mechanistic aspects of HDS using DFT studied the HDS of thiophene over Ni_xS_y clusters [66]. Although the study does not directly relate to MoS_2 catalysts, coordinatively unsaturated Ni sites were found to be very reactive.

DFT combined with thermodynamics in order to include temperature effects has proven to be a very useful tool to predict the edge configuration as a function of reaction conditions (see also Sec. 2.2). Several groups have investigated the stability of different edge configurations as a function of reaction conditions [50, 132, 67, 118, 119, 117, 116] and the accuracy of the approach has been validated by the ability to predict structures observed in STM experiments [50,107]. DFT based thermodynamics are the basis of theoretical investigation of the reaction mechanism involved in HDS since it provides a way to predict which surface configurations are most likely to exist during HDS. For instance, MoS_2 at HDS conditions ($P_{H_2} = 10bar$,$P_{H_2}/P_{H_2S} = 100$ and T=650K) will be fully covered with sulfur at the S $(\bar{1}010)$ edge (Fig. 5.3 *a*)) with hydrogen on top of every sulfur dimers and the Mo $(10\bar{1}0$ edge (Fig. 5.3 *b*)) will be covered with 50% S with hydrogen on top of every second S atom.

5.2 Atomic scale insight into the structure of CoMoS and NiMoS

In the following section we present a combined DFT and STM study of the Co or Ni promoted MoS_2, termed CoMoS or NiMoS respectively. CoMoS and NiMoS are the most widely used HDS catalyst and understanding the differences in atomic scale morphology and electronic structure is proposed to be very useful for future development of HDS catalysts.

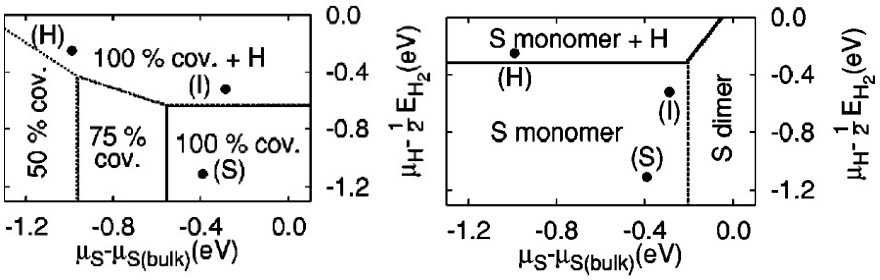

(a) (b)

Figure 5.3: (a) MoS_2 S edge phasediagram, (b) MoS_2 Mo edge phasediagram. Adapted from [50]

5.2.1 Experimental details

The experiments are conducted in a ultra high vacuum (UHV) champer equipped with standard surface analysis equipment and equipment for depositing metals by e-beam evaporation and introducing gasses into the champer. The homebuild Aarhus scanning tunneling microscope [137] is used for the experiments. Au(111) is used as support because it has previously proven to be very successful [105, 104, 108] due to the nucleation centers of the so-called Herringbone reconstruction [138]. The promoted MoS_2 structures are prepared by initial depositing of pure Mo in a sulfiding atmosphere, thereby forming sulfided Mo nucleation centers followed by co-deposition of additional Mo together with Ni or Co to form CoMoS or NiMoS. For a detail description of the experimental details see Paper V [110].

5.2.2 Computational details

We use the computational setup describe in Sec. 4.2 except the following details. The stripes used for the calculations in this work were composed of repeat units containing one or two MoS_2 units in the x direction and 6 repeat units in the y direction. Promoted structures are obtained by replacing Mo with Co or Ni at the relevant edge positions. In the case of Co, all Mo atoms at the $(\bar{1}010)$ are replaced by Co, which is known to be most energetically favorable location of Co [139, 67, 68]. In the case of Ni, locations at both edges are considered as well as partial substitution. Hydrogen adsorption are also investigated but based on the adsorption energies found, the concentrations of adsorbed hydrogen is estimated to be negligible under experimental conditions. The STM simulations are performed as reported in [50] by matching the corrugation on the MoS_2 basal plane to the experimentally measured value of 0.2Å and then plotting calculated contours

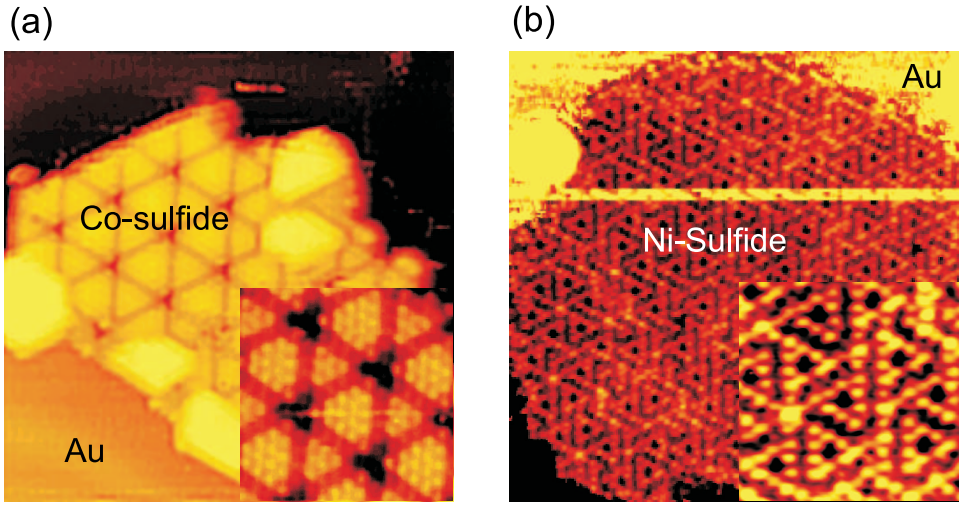

Figure 5.4: a) Cobalt sulfide formed on Au(111). The insert shows the proposed Co_3S_4(111) faces. Adapted from [105], b) Ni sulfide

of constant local density of the electron states. The edge free energies are calculated as described in Sec. 2.2 with Co_9S_8 and Ni_3S_2 as bulk sulfide references. Table 5.1 shows the chemical potential of sulfur and hydrogen at two different STM experimental conditions, Sulfiding (S) and Imaging (I).

Table 5.1: Chemical potential of sulfur at different working conditions

Working condition	T[K]	p_{H_2}[bar]	p_{H_2S}[bar]	$\mu_S - \mu_{S(bulk)}$[eV]	μ_H-$\frac{1}{2}E_{H_2}$[eV]
(I) STM Imaging	300	$2.0{\cdot}10^{-16}$	$1.0{\cdot}10^{-13}$	-0.242	-0.49
(S) STM Sulfiding	673	$2.0{\cdot}10^{-12}$	$1.0{\cdot}10^{-9}$	-0.344	-1.08

5.2.3 Morphology

The synthesis procedure for the promoted structures produces two significantly different sulfide structures. One which consists of Ni- or Co-sulfide islands at the step edges of Au (111) and another which is well dispersed nanoparticles of CoMoS or NiMoS.

The growth of Ni- or Co sulfides at the step edges (Fig. 5.4) is due to an excess of Co or Ni. The facets match the (111) facets of Co_3S_4 and Ni_3S_2 respectively and will not be considered further since such sulfides are not active in HDS [69].

Promotion by Co and Ni changes the morphology, from triangular shapes for MoS_2 (Fig 5.5 *a*)) to truncated shapes for CoMoS (Fig 5.5 *b*)) and NiMoS (Fig 5.5 *c*)). The triangular shape of MoS_2 has been investigated in details using STM [104, 107] and DFT [50, 109]. The MoS_2 triangles are found to expose only the $(10\bar{1}0)$ Mo edge, which is covered with sulfur dimers. The

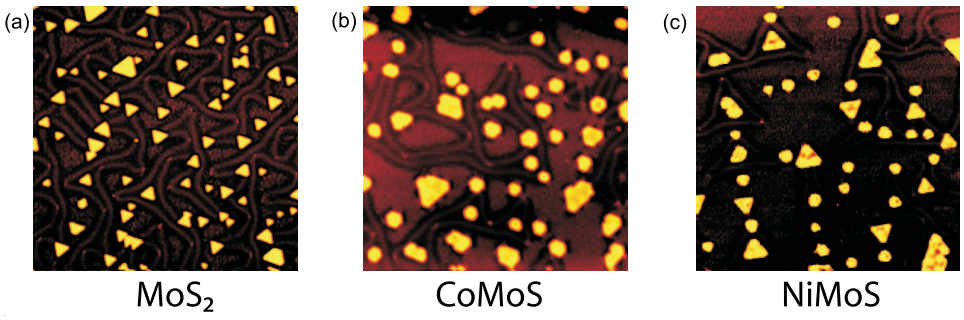

Figure 5.5: a) MoS_2, CoMoS, NiMoS

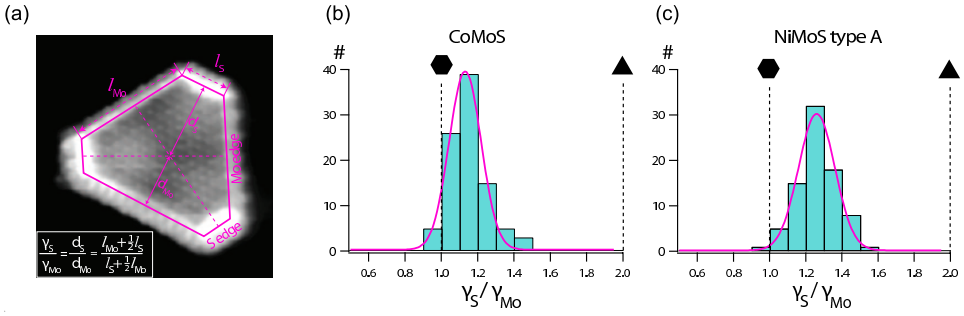

Figure 5.6: (a) Graphical presentation of the Wullf construction theory, where the ratio of the edge free energies determine the cluster shape, (b) Histogram as a function of relative edge free energies for CoMoS, and (c) for NiMoS. The dotted line marks $\gamma_{(\bar{1}010)}/\gamma_{(10\bar{1}0)} = 1$

truncated structures of the promoted clusters can be explained by a change in relative edge free energy induced by the substitution of Mo atoms with promotor atoms.

5.2.4 CoMoS

Promotion by Co changes the morphology to near hexagonal shaped clusters (Fig 5.7*a*) and Fig.5.8*b*)). The clusters expose both the $(\bar{1}010)$ and the $(10\bar{1}0)$ edges and both edges have bright brims (Fig 5.7*a*)). One of the edges can be identified as the MoS_2 $(10\bar{1}0)$ edge of triangular MoS_2 clusters, thus, Co substitution takes place at the $(\bar{1}010)$ edge. Thereby lowering the edge free energy of the $(\bar{1}010)$ edge which leads to the hexagonal shape. The mean edge free energy ratio γ_S/γ_{Mo} can be calculated from the STM images (5.8) and lies a little above the equilateral hexagon shape and much below the triangular shape of pure MoS_2

We have performed a series of DFT calculation in order to identify the nature of the $(\bar{1}010)$ CoMoS edge. The edge configurations of 100, 75 and 50% S can be seen in Fig.5.8*a*). The calculated edge free energies at sulfiding

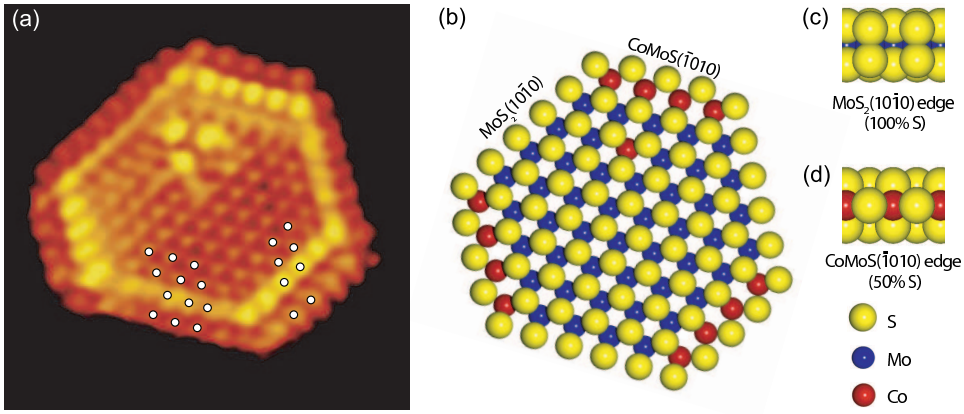

Figure 5.7: a) STM image of CoMoS, b) ball model, c) structure of Mo edge $(10\bar{1}0)$, d) structure of S edge $(\bar{1}010)$

and imaging conditions (Fig.5.8*a*)) rules out 100% S because the edge free energy at both sulfiding and imaging conditions is higher than the ones for 75 and 50%. The 75 and 50% edge free energies are, however, quite similar and from a free energy perspective both edges should be present. The STM simulations of 75% and 50% S show that the 75% S has a distinct periodicity of two which is not seen in the experimental STM image and this rules out the 75% S configuration. The 50% S configuration shows a a bright brim located on the S atoms behind the front row Co and a less pronounced corrugation located on the front row S atom. The shape of the 50% simulated brim fits the experimental brim and the conclusion is that the hexagonal CoMoS particles expose the $(10\bar{1}0)$ edge covered with S dimers similar to the non promoted MoS_2 and at the $(\bar{1}010)$ edge Mo atoms are fully substituted by Co atoms covered by 50%S positioned at the in registry bridge position. A ball model representing the STM image of CoMoS can be seen in Fig. 5.7*b*). The physical origin of the brim is the electronic structure of the CoMoS particle, where the band diagram shows that three bands are crossing the Fermi level (Fig. 5.8*c*)). State I and II are located on the Mo edge and have previously been described in details [109,50], while state III_{Co} is located at the S edge and is a feature of the Co promotion.

5.2.5 NiMoS

Promotion by Ni results in truncated clusters. The truncated clusters fall in two different categories, Type A which is a hexagon (Fig 5.10) and type B which is a truncated hexagon (Fig 5.12). Type A is typical for large clusters while type B is typical for small clusters (Fig. 5.9). The distribution in Type A or B is dependent on temperature, since increasing temperature results in relative more Type A structures (5.9). The distribution at higher

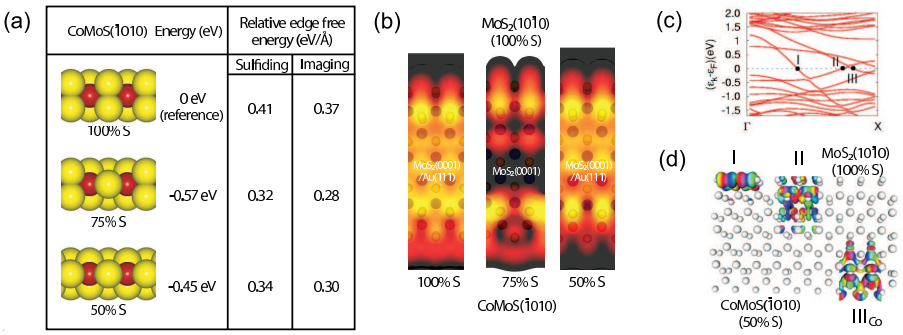

Figure 5.8: a) DFT results for CoMoS ($\bar{1}010$) edge (S: yellow, Co: red), (2x6 unit cell), b) STM simulation (1x6 unit cell) of the CoMoS ($\bar{1}010$) edge with 100, 75, and 50% sulfur, c)Band stucture of CoMoS with 50%S and Co at the ($\bar{1}010$) edge and 100% S at the ($10\bar{1}0$) edge, d) Plot of the wave function contours associated with the three metallic edge states in CoMoS.

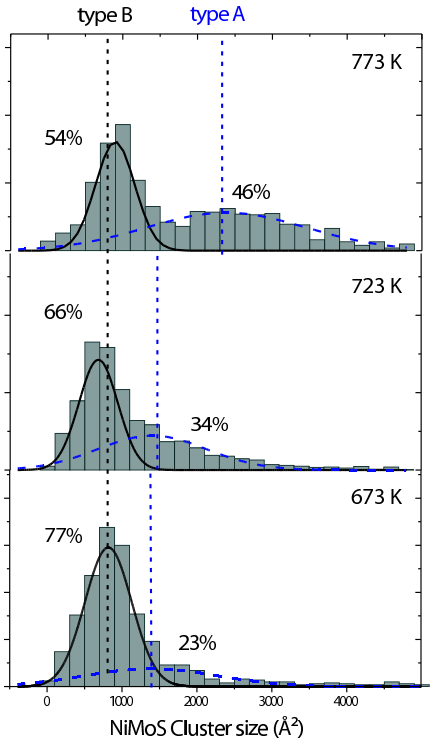

Figure 5.9: NiMoS particle size distribution corresponding to three different temperatures. The histogram has been fitted with gaussians assuming a bimodel distribution. The vertical dotted lines refer to type A or type B

temperatures (e.g Fig. 5.9) is observed to be stable over extended periods of sulfidation indicating that the observed structures are not due to kinetic limitations.

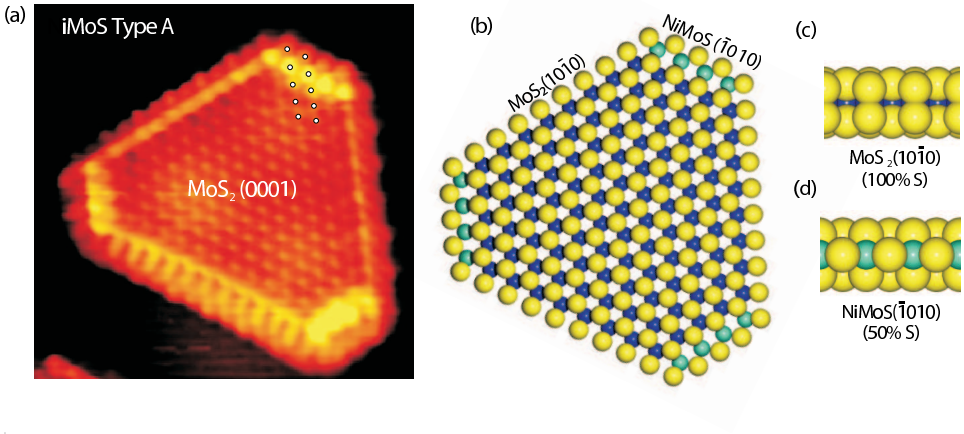

Figure 5.10: a) Atom-resolved STM image of type A NiMoS, b) Ball model of type A NiMoS, c) side view of the MoS_2 $(10\bar{1}0)$ edge, d) side view of the NiMoX $(\bar{1}010)$ edge, S:yellow, Mo:blue, Ni:cyan.

5.2.6 Type A NiMoS

The type A NiMoS clusters are hexagons, with bright brims on all edges. One of the edges has the characteristics of the MoS_2 $(10\bar{1}0)$ edge, which is a bright brim located on (or slightly in front of) the second row S atoms and protrusion out of registry with the basal plane S atoms at the front row. The existence of the $(10\bar{1}0)$ edge, identifies the Ni promoted edge as the $(\bar{1}010)$ edge. The $(\bar{1}010)$ NiMoS edge has a brim with protrusions on the second row S atoms and protrusion on the front row S atoms. The $(\bar{1}010)$ NiMoS edge brim is brighter than the MoS_2 $(10\bar{1}0)$ edge. The front row protrusions are regular indicating that Ni atoms are substituting all of the edge Mo atoms.
We have investigated numerous edge configurations and the three most stable edges are the 100, 75, and 50% S (Fig. 5.11*a*)). The edge free energies of these edge configurations are almost equal with the 100% S configuration being the most stable. However, comparing the STM simulated images (Fig. 5.11*b*)) with the experimental STM image (5.10) one finds that the 100% S configuration does not match the experimental image. The 50% S configuration is identified as the best match, since it has a brim located on the S atoms behind the front row Ni atoms and protrusion on the front row S atoms. Furthermore, the simulated 50% S $(\bar{1}010)$ NiMoS edge is brighter than the MoS_2 $(10\bar{1}0)$ edge. The STM images show no indications of the presence of different edge configurations on the NiMos type A $(\bar{1}010)$ edge as could be indicated by the lower edge free energy of the 100% S configuration found in the present study and also in reference [67]. The higher stability of the 50% S configuration could be due to corner or support effects.

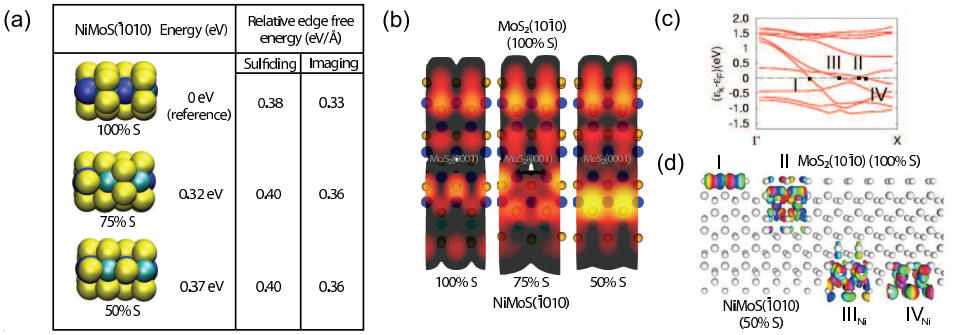

Figure 5.11: NiMos Type A: a)DFT results for the (100% Ni) NiMoS ($\bar{1}010$) edge (2x6 unit cell), b) STM simulation (1x6 unit cell) of the fully Ni-substituted NiMoS ($\bar{1}010$) edge with a 50,75, or 100% S coverage, c) Band structure, and d) plot of the wavefunction contours associated with the two metallic edge states in 50% S NiMoS ($\bar{1}010$)

5.2.7 Type B NiMoS

The smaller type B NiMoS clusters (Fig. 5.12) have a truncated hexagonal shape. The ($\bar{1}010$) NiMoS edge observed on Type A NiMoS is also present on type B NiMoS. However, on type B NiMoS the ($10\bar{1}0$) edge has bright protrusions and some of the corners are truncated. In the STM picture in Fig. 5.12 five of the six corners are truncated revealing an edge similar to ($11\bar{2}0$). In the specific STM picture in Fig. 5.12 one Ni atom appears to be missing on the ($\bar{1}010$) edge, this is a rare event and should be regarded as a defect and not a stable structure.
In order to identify the edge configuration on the ($10\bar{1}0$) edge we produce STM simulations of both the fully Ni substituted and 50% Ni substituted edge with different S coverage. The edge free energies are very similar for most stable 100% Ni and the 50% Ni substituted edge, with the fully substituted edge being the most stable. Non of the edges can be excluded on grounds of the edge free energies. The STM simulation of the 100% Ni and 0% S agrees with the ($10\bar{1}0$) edge next to the corner while the simulation of the 50% Ni and 50% S agrees with the center of the ($10\bar{1}0$) NiMoS type B edge. Besides a different ($10\bar{1}0$) edge configuration the type B clusters are also characterized by the presence of short ($11\bar{2}0$) edges. The existence of such edges, which has also been observed in very recent HAADF-STEM experiments [101], is quite interesting and indicates that under certain reaction conditions less closely packed edges may appear. Such edges can be speculated to have different activity than the closed packed edges.

Comparison of CoMoS and NiMoS

We have investigated both CoMoS and NiMoS and it is evident that type A NiMoS and CoMoS are quite similar in geometry. However, the electronic

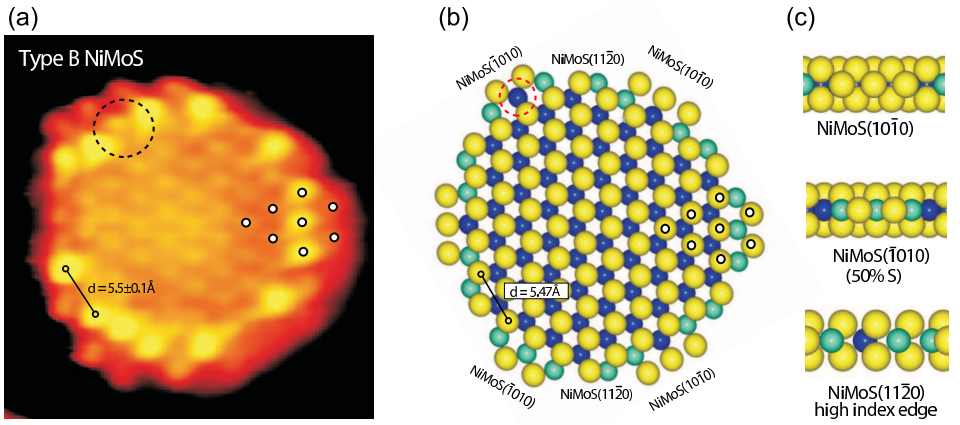

Figure 5.12: 1) Atom-resolved STM image of type B NiMoS, b) Ball model of type B NiMoS, c) Side views of NiMoS(1̄010), NiMoS(10$\bar{1}$0) and NiMoS(11$\bar{2}$0), S:yellow, Mo:blue, Ni:cyan

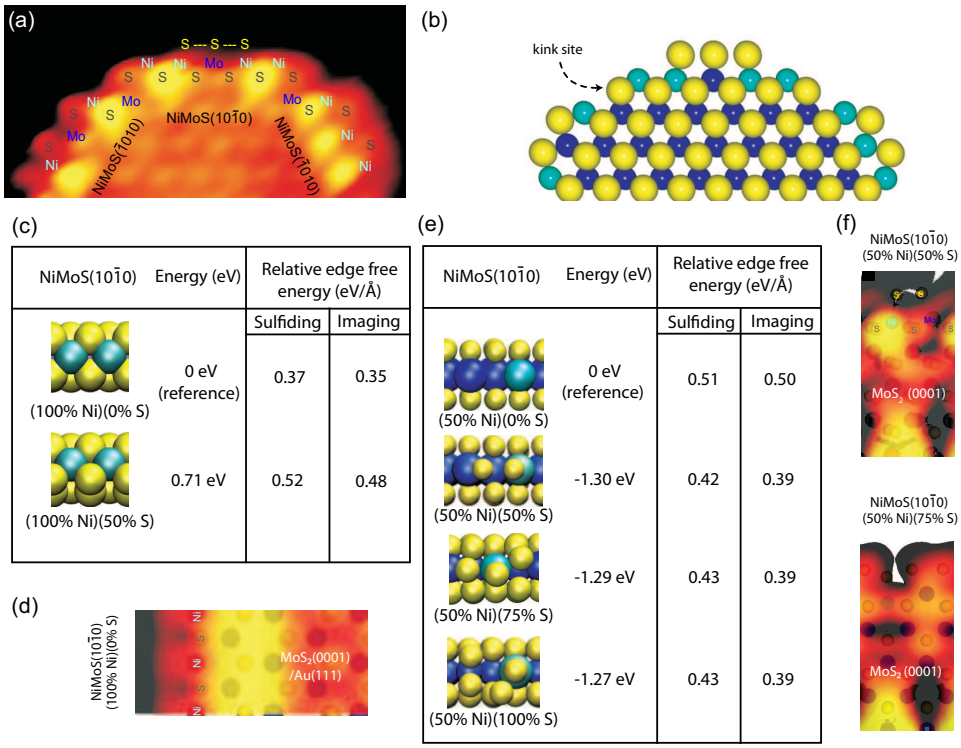

Figure 5.13: NiMos Type B: a) Zoom-in on a type B NiMoS cluster, b) A topview ball model, c) DFT results (2x6 unit cell) for a fully substituted (100% Ni) NiMoS (1̄010) edge, d) STM simulation of 100% and 0% S NiMoS (10$\bar{1}$0) edge, f) STM simulation of (50% Ni) NiMoS edge with 50% S or 75% S

structure is somewhat different. A closer look at the band diagrams of the $(\bar{1}010)$ edge of CoMoS (Fig. 5.14) and NiMoS (Fig. 5.15) reveals that the band diagrams are quite similar apart from the position of the Fermi level. Thus, the effect of Ni promotion is to raise the Fermi level such that a fourth band crosses the Fermi level. The fourth band introduces a metallic edge state which does not exist on CoMoS. One could speculate that this state could be partly responsible for the different chemical properties of NiMoS and CoMoS.

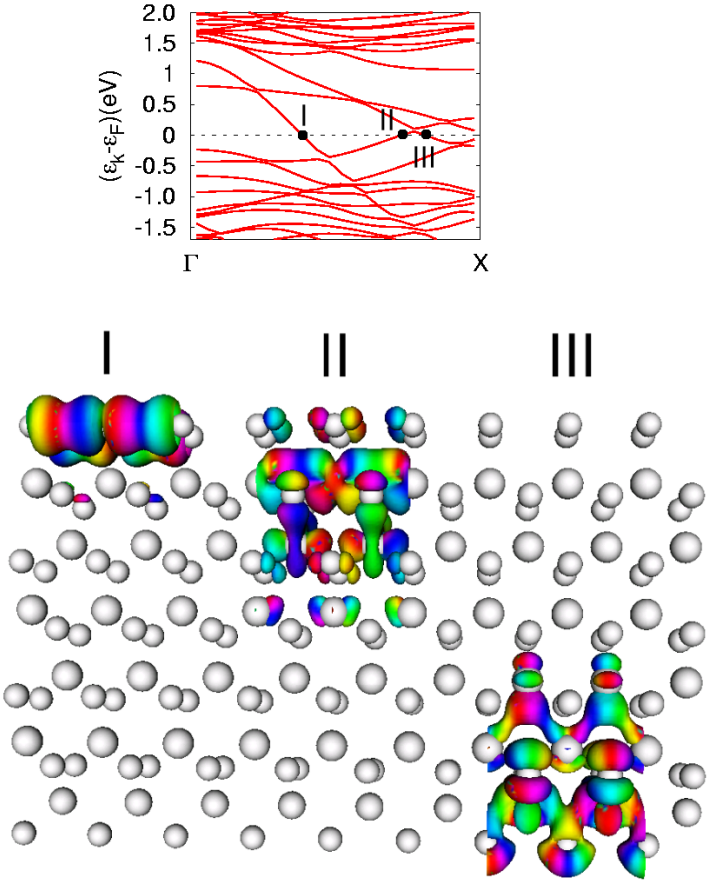

Figure 5.14: Upper: One-dimensional energy bands for a (1x6) CoMoS stripe with 50% S coverage at the S edge and a fully sulfided Mo edge. The band crossings at the Fermi level are labeled with Roman numbers, I-III. Lower: Contours of the Kohn-Sham wave functions corresponding to the metallic edge states at both the S and Mo edge. The contours are colored according to the phase of the wave functions. Edge state I corresponds to a wave vector of k_f =0.39 Å^{-1}, Edge state II corresponds to k_f = 0.71Å^{-1}, edge state III corresponds to k_f = 0.79Å^{-1}. Adapted from reference [30].

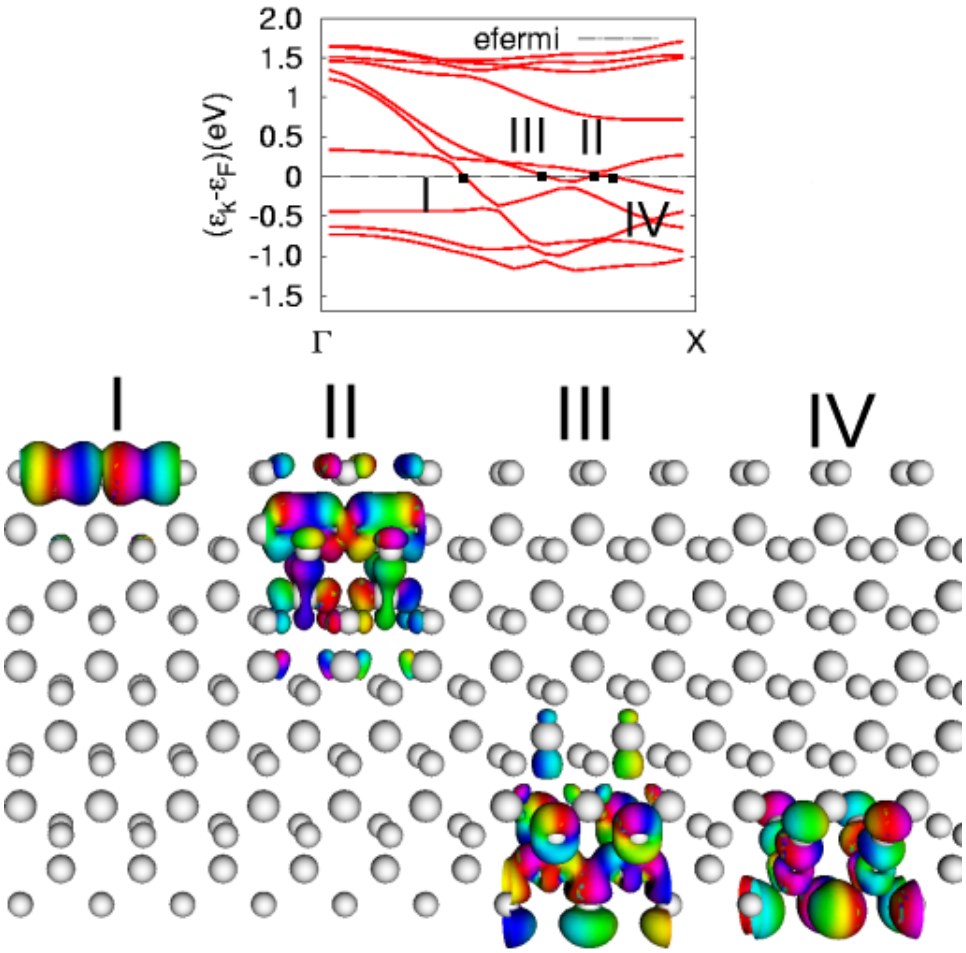

Figure 5.15: Upper: One-dimensional energy bands for a (1x6) NiMoS stripe with 50% S coverage at the S edge and a fully sulfided Mo edge. The band crossings at the Fermi level are labeled with Roman numbers, I-IV. Lower: Contours of the Kohn-Sham wave functions corresponding to the metallic edge states at both the S and Mo edge. The contours are colored according to the phase of the wave functions. Edge state I corresponds to a wave vector of k_f =0.39 Å^{-1}, Edge state II corresponds to $k_f = 0.71$Å^{-1}, edge state III corresponds to $k_f = 0.59$Å^{-1} and edge state IV corresponds to $k_f = 0.75$Å^{-1}.

5.2.8 Conclusion

We have used STM and DFT to investigate the atomic scale structure of CoMoS and NiMoS. Promotion does in general change the morphology of the nano particles from triangular shapes to more truncated shapes. The promotor substitution primarily takes place at $(\bar{1}010)$ edge even though there are some very significant differences between CoMoS and NiMoS. Co in CoMoS exclusively incorporates at the $(\bar{1}010)$ edge, which also stabilizes this edge and leads to hexagonal shaped particles. Using STM we have identified the CoMoS $(\bar{1}010)$ edge as a 50% S covered edge with 100% Co substitutions. The bright brim of CoMoS $(\bar{1}010)$ edge is due to a metallic state present near the edge.
Ni promotion results in two different types of clusters: Type A which is hexagonal in shape and Type B which is a truncated hexagon. Type A NiMoS hexagons have 100% Ni substitutions at the $(\bar{1}010)$ edge with 50% S coverage and is as such similar to the CoMoS cluster. However, the electronic structure is different and a second metallic edge state is present at the $(\bar{1}010)$ edge. Type B NiMoS is smaller and exposes the same type of $(\bar{1}010)$ edge as the Type A clusters. The $(10\bar{1}0)$ edge is different due to partly substitution of Mo by Ni. Furthermore Type B clusters are truncated hexagons and therefore also expose short edges belonging to the $(11\bar{2}0)$ family. It could be speculated that the chemical activity of Type B is different from the activity of Type A due to the presence of more open edges and a Ni promotion of the $(10\bar{1}0)$ edge.
The present study has shown that both CoMoS and NiMoS may be synthesized such that the promoters are present on the $(\bar{1}010)$ edge. In the case of NiMoS small Type B clusters with Ni on the $(10\bar{1}0)$ edge may also be synthesized. The present study uses a relatively inert Au substrate and it can be speculated that supports with stronger catalyst support interactions such as Al_2O_3 could be modified such that certain edges may be stabilized.

Chapter 6

Reactivity

6.1 Introduction

The structure of HDS catalyst has been investigated for many decades and quite detailed understanding has been obtained regarding the active catalysts (see chapter 5). However, much less is known about the reaction mechanisms and the nature of the active sites and many different views have been presented [79, 78, 140, 141, 142, 143, 69].

The challenge in HDS catalysis is to remove sulfur from the ring shaped sulfur containing molecules, since these are the most refractory species present in crude oil [144]. One approach which has been taken in a series of studies is to investigate HDS of model feeds with less complexity than real feeds [69, 141]. For such studies thiophene is a suitable test molecule, as it contains an S-atom in a benzene-like ring and at the same time it is the basic building block in larger ring formed sulfur containing molecules such as dibenzoethiophene. Therefore, thiophene HDS has been the most studied reaction; but also in this case there has been considerable debate regarding the mechanism [141, 145, 146, 147, 148, 149, 69, 150]. It also appears that the observed reaction products depend on the reaction conditions [69, 150]. Tetrahydrothiophene is typically not observed as an intermediate at atmospheric pressure [150], but it may be a major intermediate at high pressure [148] and low temperature [141], since the formation of tetrahydrothiophene is equilibrium limited at high temperature [141].

For the larger S-containing molecules like dibenzothiophene, it has been established that two parallel routes exist, a direct desulfurization route (DDS) through biphenyl and a hydrogenation route (HYD), where one of the benzene rings is hydrogenated first [149]. In order to produce the clean transport fuels demanded today, even the very refractory sulfur compounds like 4,6-dimethyldibenzoethiophene must be removed [69, 144, 73, 151, 152, 149, 153, 154]. For such molecules the HYD route may become more important than the DDS route, which dominates for unsubstituted dibenzothiophene

[144, 155].
Insight into the mechanism of HDS has also been obtained from a large number of studies on activity correlations [69, 156, 157], which have been taken as evidence for MoS_2 edge vacancies being the active sites in HDS, since vacancy formation has generally been assumed to take place at the MoS_2 edges. In support of this, basal plane surfaces have been observed to be inactive[158]. For hydrogenation reactions, the activity has also been observed to correlate with the number of MoS_2 or WS_2 edges sites [159,160, 111]. However, it is in general difficult to draw firm conclusions from such activity correlations [69], since a variety of other species, like -SH groups [161], may also be located at the edges. Further, support for the importance of vacancies has been provided from experimental studies of the effect of prereduction temperature [162,163]. Also, the observed activity correlation with the metal-sulfur bond strength, which leads to the formulation of the Bond Energy model (BEM), suggest that vacancy formation is a key aspect of HDS [164].
Since both HDS and hydrogenation activities have been observed to correlate with the number of MoS_2 (WS2) edge sites, some authors have suggested [165,166] that the sites for the DDS route and the HYD route are similar. However, a number of effects strongly suggest that DDS and hydrogenation sites are not the same. For example, the presence of methyl groups in dibenzothiophene may severely reduce the activity for S removal via DDS without significantly affecting the hydrogenation activity [144]. Also, H_2S is a strong inhibitor for S removal via DDS, but it has only a minor effect on hydrogenation [155]. Evidence for different sites for HYD and DDS also comes from studies of the effect of nitrogen compounds [69, 167, 154, 168, 169,170,171,172,173,174,175,176,177]. In contrast to the effect of H_2S, the presence of basic nitrogen compounds is observed to mainly inhibit the HYD route with only a moderate effect on DDS. The inhibiting effect was found to correlate with the proton affinity of the nitrogen compounds [170, 169] and this result also suggests that different sites are involved in HYD and DDS.

6.2 MoS_2 catalyst

An important problem with most reaction pathway studies has been that the assumed structures may be very different from those actually present at HDS conditions. Therefore, a key goal of the present study is to perform calculations on the type of structures, which will be present during HDS catalysis and in Sec. 6.2.2 we discuss the relevant structures and the investigated edge configurations to lay the groundwork for studying the reaction pathways. In Sec. 6.2.3, 6.2.4, and 6.2.5 we discuss the results on hydrogenation, S-C cleavage and site regeneration reactions at those edges. These detailed results are subsequently used to discuss some more general

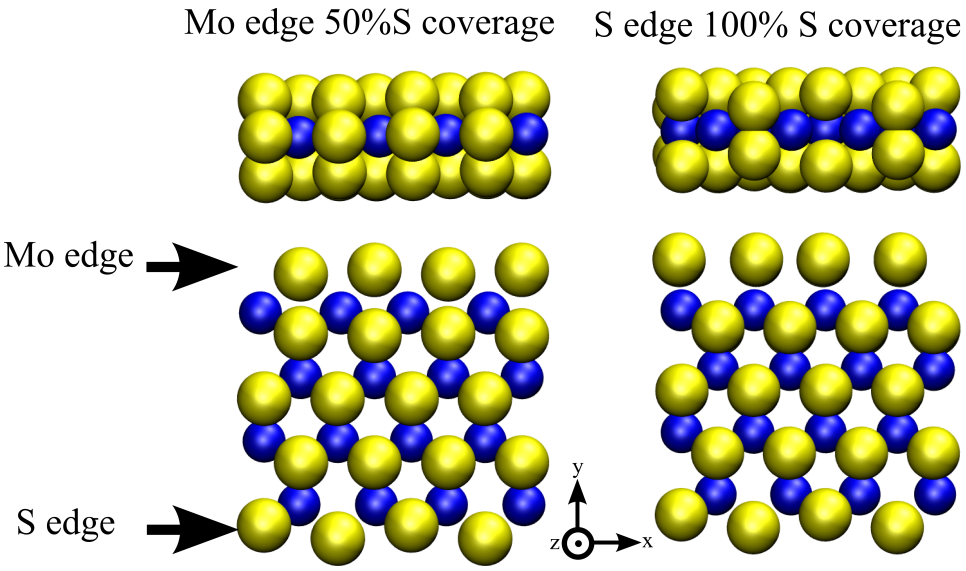

Figure 6.1: The 4x4 supercell. Molybdenum (blue), sulfur (yellow)

themes. The influence of reaction conditions is found to be quite significant, and these aspects are discussed in Sec. 6.2.6. Sec. 6.2.7 and 6.2.8 present an analysis of the hydrogenation and S-C bond scission reactions and interplay between the two different edge sites in those reactions based on the determined reaction paths and the availability of the active sites. In Sec. 6.2.9, we will discuss the relative role of different elementary reactions and pathways during HDS of thiophene. In order to avoid excessive repetition and to aid the presentation of the results, we have summarized many of the detailed results regarding the reaction pathways, the stabilities of the intermediates, and key activation energies in Fig. 6.3 to Fig. 6.7 and in Tab. 6.1. Detailed comments regarding each elementary step and the nature of the intermediates will be given in the following sections, and further details can be found in appendix C

6.2.1 Computational details

We use the computational setup described in Sec. 4.2 except the following details. We use a unit cell consisting of 4 Mo atoms in the x-direction and 4 Mo atoms in the y-direction (Fig. 6.1). The Brillouin zone is sampled using a Monkhorst-Pack k-point set [34] containing 4 k-points in the x-direction and 1 k-point in the y- and z-direction. The convergence criterion for the atomic relaxation is that the norm of the total force should be <0.15eV/Å, which correspond approximately to a max force on one atom <0.05eV/Å.

6.2.2 The choice of active surfaces and elementary reactions

Table 6.1: An overview of the reactions involved in HDS of thiophene over MoS_2 including the activation barriers (E_a) and energy changes (ΔE) of the reactions

	Reaction	S edge		Mo edge	
		E_a [eV]	ΔE [eV]	E_a [eV]	ΔE [eV]
I	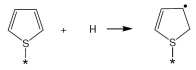	0.80	0.43	0.57	0.57
II	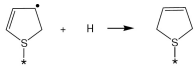	0.00	-1.02	0.00	-0.74
III	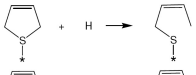	0.79[j]	-0.78	2.03	0.51
IV	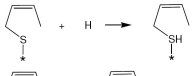	1.63	1.09	0.14	-0.26
V	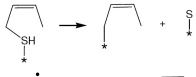	0.0	-0.66	0.12	-0.41
VI	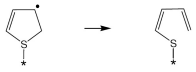	0.21	-1.11	1.10	1.09
VII	$2HS\text{-}* \longrightarrow H_2S\text{-}* + S\text{-}*$	1.70[a] 1.49[b]	1.57[a] 1.32[b]	1.00[c]	0.7[c]
VIII	$1/2H_{2(g)} + * \longrightarrow H\text{-}*$		-0.57 -0.11[b]		-0.33[d]
IX	$H_2S_{(g)} + * \longrightarrow H_2S\text{-}*$		-0.12[h]		-0.19[e]
X			0.21[g]		-0.07[f]
XI			-0.59[g]		-0.12[f]
XII	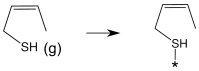		-0.52[g]		-0.12[d]
XIII	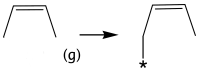		-0.05[i]		-0.28[d]

[a] Low H_2 pressures
[b] High H_2 pressures
[c] Calculated as $E_{VII} = \Delta E_1 + E_2$, where ΔE_1 is the reaction energy of reaction 1: 2H-S(25%H and 50%S)+ S(0%H and 62.5%S) + S-S (0% H and 62.5% S)→ 2(0%H and 50%S)+ H-S-S(50%H and 62.5%S) +H-S(50%H and 62.5%S) and E_2 = 0.54eV is the activation energy of reaction 2: H-S-S(50%H and 62.5%S) +H-S(50%H and 62.5%S)→ H_2S-S(50%S). ΔE is the energy change of reaction 1+reaction 2.
[d] Adsorption at the Mo edge with 50% S and 25% H.
[e] Adsorption at the Mo edge with 50% S and 0% H.
[f] Adsorption at the Mo edge with 50% S and 50% H.
[g] Adsorption at the S edge with 87.5% S and 75% H.
[h] Adsorption at the S edge with 87.5% S and 50% H.
[i] Adsorption at the S edge with 100% S and 25% H.
[j] Proceeds in two steps,1) S-C scission without involving H, 2) hydrogenation. The overall activation energy is given by step 1) since the hydrogenation reaction in step 2) has been found to have a barrier of 0.04eV

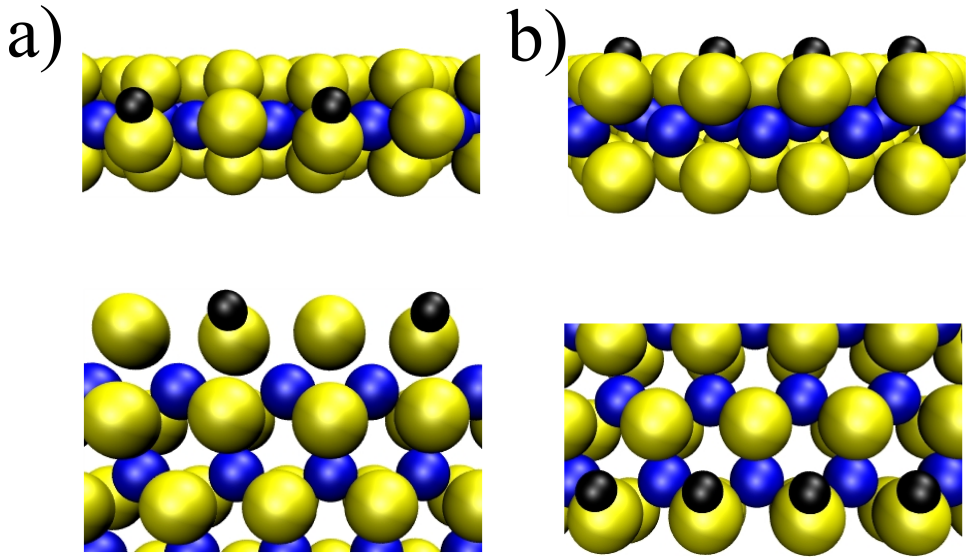

Figure 6.2: The equilibrium edge configurations at HDS conditions, P_{H_2} = $10bar$,P_{H_2}/P_{H_2S} =100 and T=650K. a) The Mo edge with 50% S coverage and 50% H coverage. b) The S edge with 100% S coverage and 100% H coverage.

The starting point of this investigation of HDS of thiophene is the recently improved understanding of the edge configurations at HDS conditions (see chapter 5). The phase diagrams developed in reference [50] (Fig. 5.3), which describe the edge structures as function of the chemical potential of S and H are used to determine the edge configurations. The equilibrium edge configuration at HDS conditions (for example $P_{H_2} = 10bar$,P_{H_2}/P_{H_2S} =100 and T=650K, these conditions will be used throughout the thesis as an example of HDS conditions) determined in reference [50] was recalculated with the calculational setup described in Sec. 6.2.1. We find essentially the same structures and adsorption energies as in reference [50], and these equilibrium edge structures are shown in Fig. 6.2. It should be noticed in Fig. 6.2 that the Mo coordination number is found to be 6 at both edges. The H coverage at the S and Mo edges given in Fig. 6.2 corresponds to $P_{H_2} = 10bar$. However, we show that it is possible to further increase the H coverage at the S edge by increasing the H_2 pressure, which results in a H coverage above 100% (see atomic configuration 2 in Fig. 6.4). Such an increase is not possible at the Mo edge due to strong interactions between H atoms as discussed further in Section 3.5 and also reported in reference [178].

The structure presented in Fig. 6.2 is the most stable structure over most of the pressure range, with the exception that at high hydrogen pressures there may be more H atoms present at the S edge. S and H adsorption at sites at

the edges of MoS_2 introduces structural changes, therefore, the definition of coverage of S and H needs to be refined and we define the S coverage as the percentage of S present at the edge with 100% being the S coverage of the fully sulfided edge i.e. completely covered by S dimers. Using this definition the S coverage at the Mo edge in Fig. 6.2 is 50%, and at the S edge it is 100%. Furthermore, we define the H coverage as the fraction of H atoms present per edge unit cell in the 4x4 structure, e.g. 4 H atoms correspond to 100% H coverage. Using this definition the H coverage in Fig. 6.2 is 50% at the Mo edge and 100% at the S edge. This definition allows for coverage above 100%, when more than four H atoms are present per unit cell.
Our calculations show that a basic requirement for the removal of S from thiophene and other S containing compounds is that there is a site available where the removed S can adsorb. In this connection, an interesting finding is that the equilibrium edge configuration at the Mo edge allows for the addition of a S atom, while the equilibrium configuration at the S edge is fully covered by S and H atoms and does not allow for such an addition. At the S edge, a vacancy must therefore be created prior to S removal.
Experimental studies of thiophene HDS have suggested that a number of different pathways may be involved and that the relative involvement of these pathways depends on the reaction conditions [141,69]. The elementary reactions in the different proposed reaction pathways include both hydrogenation and S-C bond scission reactions, and we have therefore chosen to investigate both elementary hydrogenation and S-C bond scission reaction steps. Many different steps have been considered, and in order to simplify the following discussion, we have summarized the elementary reactions investigated in the present study in Tab. 6.1 together with the calculated reaction and activation energies. The choice of elementary reactions and intermediates has been guided by recent STM and DFT studies, which have shown that thiophene hydrogenation and S-C scission can occur at the fully sulfided Mo edge [108]. Except for 2-hydrothiophene all the other intermediates given in Tab. 6.1 have been reported to be present during HDS of thiophene [179,180,69]. The reason that 2-hydrothiophene has not been observed experimentally is most likely related to the fact that it is not a stable molecule in the gas phase. Furthermore, the present study shows that the subsequent hydrogenation of 2-hydrothiophene to 2,5-dihydrothiophene is a non-activated process.
We investigate both the HYD and DDS pathway of thiophene HDS. We define the difference between the DDS and the HYD pathway so that it is the DDS pathway when the initial S-C cleavage (Reaction VI in Tab. 6.1) occurs in 2-hydrothiophene after the first hydrogenation step (Reaction I in Tab. 6.1) and the HYD pathway when S-C cleavage (Reaction III in Tab. 6.1) occurs in 2,5-dihydrothiophene, which is formed by two successive hydrogenation steps (Reaction I and II in Tab. 6.1). It is interesting to note that the thiophene DDS pathway and the HYD pathway involve a common prehydrogenation step, since a similar common prehydrogenation step has

been proposed in the HYD and DDS pathway for DBT and 4,6-DMDBT [166].

Under realistic HDS conditions, MoS_2 is likely to expose Mo edges as well as S edges and both edges have therefore been considered [107, 67]. In the following we summarize the reactions in the HYD pathway as we have investigated them both at the Mo edge and at the S edge. The HYD pathway involves reaction I-V and reactions VII to XIII in Tab. 6.1. The reactions occur in the following order: X-I-II-III-IV-V-VII-IX. The HYD pathway is initiated by thiophene adsorption (Reaction X). Reaction I in Table 1 hydrogenates thiophene and forms 2-hydrothiophene, which is then further hydrogenated (reaction II) to produce 2,5-dihydrothiophene. The removal of S from 2,5-dihydrothiophene proceeds via initial S-C bond scission of 2,5-dihydrothiophene (Reaction III) producing cis-2-butenethiolate. We have discovered that reaction III may proceed via two different reaction mechanism: 1) A concerted mechanism where H transfer occurs simultaneously with S-C scission or 2) initial S-C scission forming a stable intermediate thiolate which is then hydrogenated to cis-2-butenethiolate. Cis-2-butenethiolate then reacts with a H atom and forms cis-2-butenethiol by a H transfer reaction (Reaction IV) and then cis-2-butene is the product formed by the final S-C scission (Reaction V). In this context it should be noted that the present study also investigates the S extrusion from cis-2-butenethiol because it is an intermediate in the HYD pathway. It is quite likely that cis-2-butene will react further either by hydrogenation to butane or by intramolecular rotation to form trans-2-butene. These, we do not consider presently since they take place subsequently to S removal and are not important for sulfur removal. Further hydrogenation of 2,5-dihydrothiophene to tetrahydrothiophene has not been investigated, since we have assumed that tetrahydrothiophene is only a likely intermediate at high H_2 and low temperatures, because the presence of tetrahydrothiophene has been shown to be equilibrium-limited at temperatures typical for HDS conditions [141].

The DDS of thiophene is investigated using the following reaction path: reactions X-I- VI-(IV- V) in Tab. 6.1. The DDS pathway is initiated by thiophene adsorption (Reaction X), which is followed by hydrogenation of thiophene (Reaction I) forming 2-hydrothiophene. Then, the initial S-C bond is broken (Reaction VI) and cis-butadienethiolate is formed. The further removal of S from cis-butadienthiolate has not been investigated directly. It is, however, assumed that these reactions will be very similar to reaction IV and V since the involvement of the carbon chain is found to be insignificant in these reactions as we find them to be dominated by H diffusion and addition. The product of the DDS pathway will be cis-butadiene under the assumption that the final S-C bond scission reaction is similar to IV and V. Cis-butadiene may react further by hydrogenation or intramolecular rotation.

The reaction pathways shown in Fig. 6.3 to Fig. 6.6 have been constructed under the assumption that H_2 in the gas phase is in equilibrium with the H atoms adsorbed at the edge of MoS_2. This assumption is justified by the fact that experimentally H_2 dissociation is not found to be the rate determining step [141, 69]. Previous DFT studies have found the barrier to be 0.9-1eV at the Mo edge with 50% S coverage [181, 182]. However, these studies use a unit cell which results in a H coverage after dissociation which is 0.66% or 100% respectively. The H adsorption energy at the Mo edge is highly dependent on the H coverage [178] and it could be speculated that the barrier changes when the H coverage is lowered to 50%, corresponding to HDS conditions. There do not exist any studies of the H_2 dissociation at the S edge of MoS_2, the only similar result is for the S edge promoted with 50% Co and with a S coverage of 75%, where the barrier was found to be 0.6eV [183]. The DFT results indicate that at certain reaction conditions like low hydrogen pressures there could be an influence on the apparent activation energy due to H_2 dissociation. However, we have assumed in the present study that this is not the case at HDS conditions and the hydrogen addition steps are therefore not included in the reaction pathways. We have contracted the hydrogenation of thiophene reactions (Reaction I and Reaction II) to one barrier since we find that only Reaction I is activated. We have furthermore in the case where reaction III is proceeding in two steps contracted it to one reaction since we find that the hydrogenation step has a very low barrier.

6.2.3 The HYD pathway at the Mo edge

Using the elementary steps discussed in Sec. 6.2.2, the detailed potential energy diagram for the HYD reaction pathway at the Mo edge has been found and the results are depicted in Fig. 6.3. In order to arrive at the diagram shown in Fig. 6.3, we have investigated the intermediates in a variety of different configurations as part of determining the minimum energy and the optimal reaction pathway. The adsorption of the cyclic intermediates has been investigated both above edge S atoms and in bridge positions between edge S atoms. Furthermore, we have investigated both the $\eta 1$ (binding through the S atom) adsorption mode and the $\eta 5$ (binding through the π system) adsorption mode. For thiophene both adsorption modes have been considered in the literature based on IR or INS studies [184, 185, 186, 187] or proposed based on analogous structures observed in organometallic complexes [188]. We find that the preferred adsorption site for 2,5-dihydrothiophene is in between the front row S atoms, which is the location of the brim at the Mo edge at HDS conditions [50], thus there is no direct binding to the Mo atoms. Thiophene $\eta 1$ and $\eta 5$ adsorption at both the brim site and on top of a edge S atoms are very similar in energy (within 0.02eV) and it is therefore expected that all of these adsorption modes will

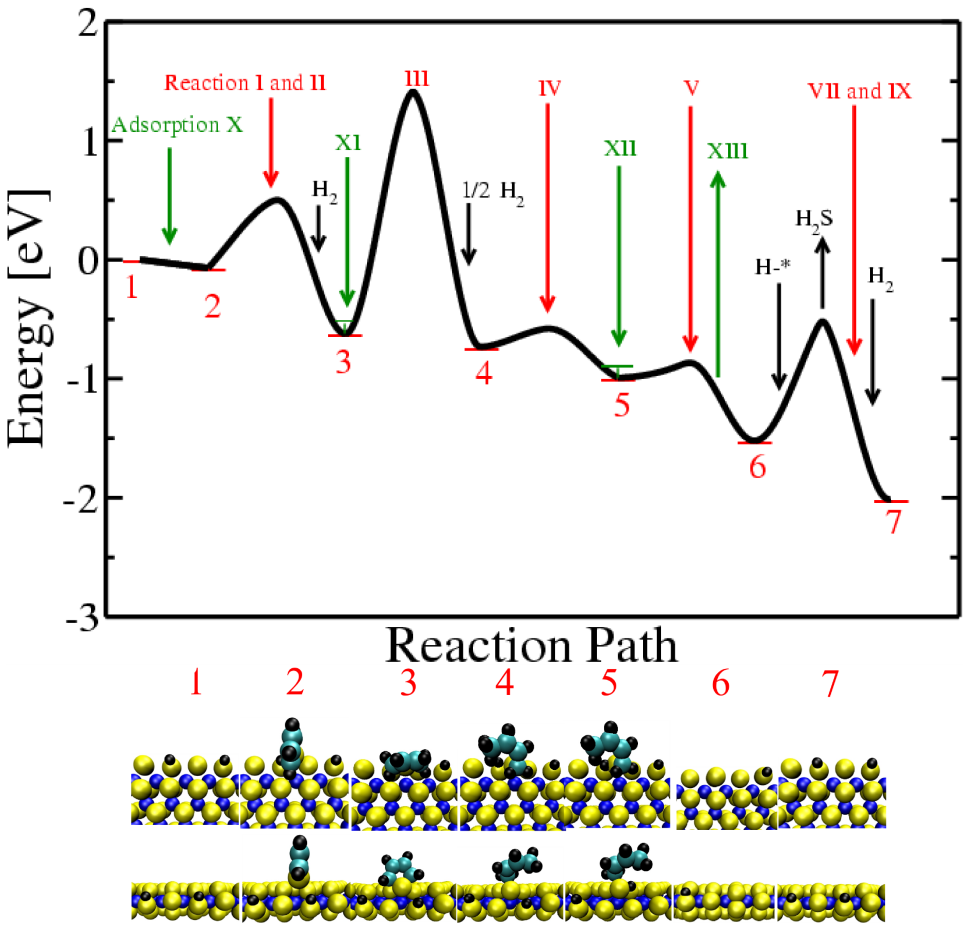

Figure 6.3: The Mo $(10\bar{1}0)$ edge HYD pathway. The reference energy is chosen as the equilibrium edge configuration at HDS conditions (Mo edge with 50%S and 50% H) and thiophene in the gas phase. The atoms are colored in the following color scheme: sulfur is yellow, molybdenum is blue, carbon is cyan, and hydrogen is black. Arabic numerals denote intermediates, Roman numerals denote reactions and refer back to Tab. 6.1.

be present at HDS conditions. The present results thus support the conclusion from the INS experiments where both the $\eta 1$ and $\eta 5$ adsorption modes were observed [186]. It can however, not be ruled out that van der Waals (vdW) forces will stabilize one of the adsorption configurations. Such forces are not included in present day exchange correlation functionals, and thus we cannot assess the importance of vdW forces at present. It should be emphasized that the present study investigates the adsorption at the equilibrium edge configurations under HDS conditions (50% H coverage, 50% S coverage). Clearly, the adsorption modes will change, when the experimental conditions are changed and new edge structures are created. For example, a recent theoretical investigation found the $\eta 1$ mode to be most stable at a reduced Mo edge with a vacancy [189] but such very reduced Mo edges will most likely only be present in insignificant numbers under HDS conditions.

The HYD pathway at the Mo edge (Fig. 6.3) is found to be initiated by thiophene adsorption at the brim site (Reaction X). Following this, we have two hydrogenation reactions (reaction I and II in Tab. 6.1) resulting in the formation of 2,5-dihydrothiophene. The overall barrier of the hydrogenation steps is given by the barrier of reaction I, since reaction II is non-activated. Thus, the reaction product (2-hydrothiophene) of reaction I is not expected to be abundant. This may explain, why 2-hydrothiophene has never been observed.

The initial hydrogenation steps are followed by reaction III, which breaks the first S-C bond in 2,5-dihydrothiophene and form cis-2-butenethiolate. Reaction III is found to proceed in a concerted mechanism where H transfer and S-C scission take place in a concerted motion. Cis-2-butene-thiol is formed by H transfer in reaction IV, and finally S is remove by breaking the last S-C bond in the thiol in reaction V. It is important to notice that the removal of S from cis-2-butenethiol (reaction V) has a very low barrier (0.1eV). The S removal from the thiol leaves a S atom behind. Subsequently, the active site must be regenerated in order to complete the catalytic cycle (Reaction VII). It is found that the activation energy of the first S-C bond scission (reaction III) is the highest barrier (2.0eV) followed by the regenerating the active site (Reaction VII). The relatively high barrier for S-C scission indicates that S-C scission will not take place at the Mo edge brim sites.

In the STM experiments one did not observe the removal of S from the thiolate [108] while the initial S-C scission was observed to take place. That S could not be removed from thiolate in ref. [108] is not in contradiction with the present findings, since the equilibrium edge structure under the STM experimental condition is different from the one under reaction conditions. Under STM condition the edges are covered completely with sulfur dimers (i.e. 100% sulfur coverage) and this surface does not allow the accommodation of an extra S atom, and thus the reaction stops after forming the

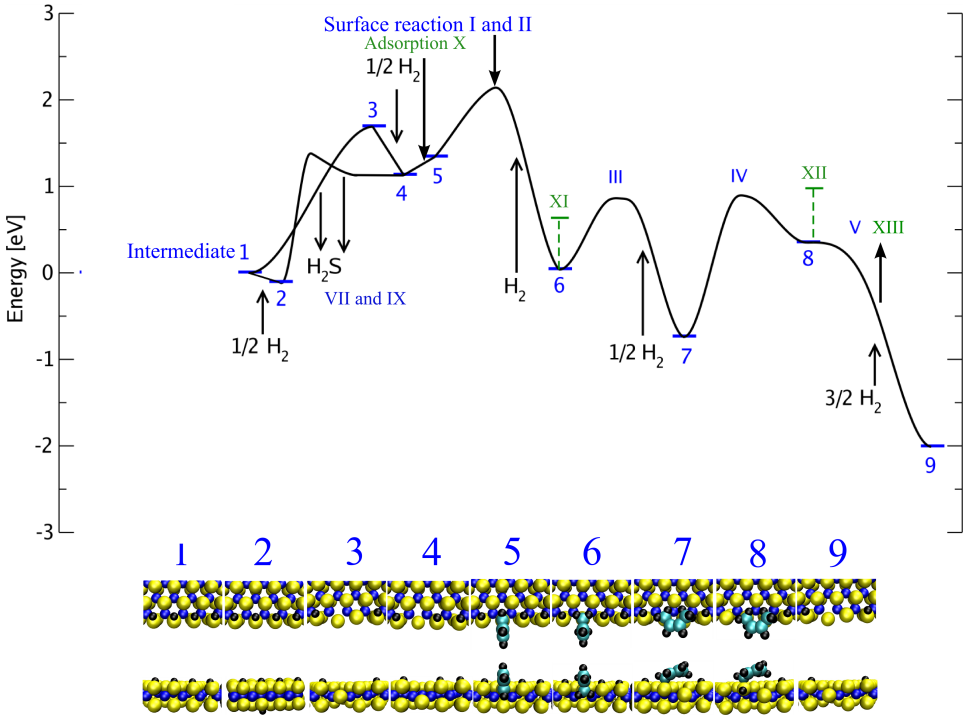

Figure 6.4: The S ($\bar{1}010$) edge HYD pathway of thiophene. The reference energy is chosen as the equilibrium edge configuration at HDS conditions (S edge with 100%S and 100% H) and thiophene in the gas phase. The atoms are colored in the following color scheme: sulfur is yellow, molybdenum is blue, carbon is cyan, and hydrogen is black. Arabic numerals denote intermediates, Roman numerals denote reactions and refer back to Tab. 6.1.

thiolate. The barrier for the initial S-C scission in the STM experiment was found to be 1.1eV [108] which is considerable lower than the barrier of 2.0eV found on the Mo edge present at HDS conditions. A possible explanation for the lower barrier in the STM experiment could be the presence of highly active H atoms.

The present results show that it is of key importance that H atoms are present at the Mo edge at HDS conditions and that these H atoms readily react with thiophene and the intermediates in hydrogenation reactions. The Mo edge configuration present at HDS conditions is therefore well suited for hydrogenation reactions.

The relative importance of the different hydrogenation reactions, the S-C bond scission reactions and regeneration of the active site will be discussed further in Sec. 6.2.6 to 6.2.9.

6.2.4 HYD pathway at the S edge

The HYD pathway at the S edge consist of the same reactions as on the Mo edge (reaction I-V, and reaction VII to XIII in Tab. 6.1) and the calculated potential energy diagram of the HYD reaction path at the S edge is shown in Fig. 6.4. The HYD reaction pathway is initiated by vacancy formation (reaction VII) since a vacancy is needed in order to bind the intermediates and for the final removal of S from the organic molecule. We have calculated the barrier for creating a vacancy at high and low hydrogen pressures corresponding to 125% H and 100% H coverage respectively, see Fig. 6.4. The binding energy of H decreases when there is more than one H atom per S dimer at the edge as seen in Tab. 6.1. The importance of such weakly bound and more reactive H atoms will be discussed further in Sec. 6.2.6, which also includes a discussion of the influence of the hydrogen pressure on the equilibrium H coverage.

Following the vacancy creation the HYD pathway continues with adsorption of thiophene (Reaction X) at the vacancy (corresponding to 75% S coverage and 75%H coverage) and this is endothermic (0.2eV at 75% H coverage and 0.0eV at 50%H coverage). The present adsorption mode is an end-on $\eta 1$ adsorption through the sulfur atom. Thiophene adsorption will therefore only take place if the van der Waals forces (which are not included in the present exchange correlation functional) are strong enough to give an exothermic adsorption energy otherwise hydrogenation and adsorption of thiophene may take place in a concerted manner. Thus we expect that thiophene will only be observed in high concentration at the S edge in $\eta 1$ adsorption mode at low temperatures or at edges far from HDS equilibrium edge configurations with vacancies and low H coverage. This is in agreement with a recent theoretical study where thiophene adsorption at the S edge of stacked MoS_2 has been investigated and found to be strongest at the S edge with multiple vacancies or 0% H coverage [189]. The thiophene coverage at the vacancy sites is expected to be very small at HDS conditions due to the endothermic adsorption energy (0.2eV). The first hydrogenation reaction (reaction I) resulting in the formation of 2-hydrothiophene is found to have a higher barrier than the same reaction at the Mo edge (0.8eV vs 0.6eV), whereas the second hydrogenation reaction is also non activated at the S edge vacancy. The higher reaction barrier of the first hydrogenation step is ascribed to the stronger binding energy of H at the S edge. In fact, the results show that the SH bond strength is a key parameter for all the hydrogenation reactions including the reaction involved in site regeneration. The hydrogenation reactions are followed by reaction III where we find that reaction III proceeds via initial S-C scission without involving a H atom and then subsequent hydrogenation leading to cis-2-butenethiolate. The concerted reaction mechanism identified at the Mo edge does not seem to have a counterpart at the S edge vacancy site. The barrier of the hydrogena-

tion reaction leading to cis-2-butenethiolate has been found to be 0.0eV. Thus, the overall S-C scission barrier will be given by the initial S-C scission reaction. The initial S-C scission (reaction III) is followed by reaction IV and V where the two S-C bond scission reactions (reaction III and V) have lower barriers than at the Mo edge, while the creation of cis-2-butenethiol has a higher barrier (reaction IV). The highest barrier involved in the HYD pathway is the initial vacancy and H_2S formation step.
On the Mo edge it was found that adsorption and hydrogenation reactions could proceed without the existence of a vacancy and we have investigated whether this could also be the case at the S edge. For this purpose the S edge is investigated with 100% S and 75% H, which is a slightly lower H coverage than the equilibrium edge configuration (100% H) in order to leave room for thiophene adsorption. Thiophene adsorption at the S edge with 100% S and 75% H is in fact slightly exothermic (-0.1eV). However, this adsorption energy is smaller than the H adsorption energy (-0.6eV) at the same site. Thus, H atoms will predominantly adsorb at these sites and create the equilibrium structure and the adsorption of thiophene is only favored at reaction conditions, where the hydrogen pressure is low and the thiophene pressure is high. Nevertheless, a full microkinetic model must be developed before the catalytic role of the "non-vacancy" sites can be evaluated in detail.
The relative catalytic importance of the hydrogenation reactions, S-C bond scission reactions and regeneration of the active site at the S and Mo edge will be further discussed in Sec. 6.2.6 to 6.2.9.

6.2.5 DDS pathway at the Mo edge and S edge

The DDS pathway is characterized by the initial S-C scission reaction occurring immediately after the formation of 2-hydrothiophene (Sec. 6.2.2). Thus, the first step after adsorption of thiophene (Reaction X) is hydrogenation to 2-hydrothiophene (reaction I) followed by S-C bond scission (reaction VI) to cisbutadienethiolate. The final S removal from cis-2-butadienethiolate is assumed to be similar to the final S removal from cis-2-butenethiolate. The calculated potential energy diagram of the DDS pathway at the Mo edge and the S edge can be found in Fig. 6.5 and Fig. 6.6 respectively. At the equilibrium Mo edge (50% S coverage and 50% H coverage), the DDS pathway is initiated by hydrogenation (reaction I) and then followed by S-C bond scission (reaction VI). The DDS pathway at the equilibrium S edge (100% S coverage and 100% H coverage) must, as discussed in Sec. 6.2.4, be initiated by vacancy formation (reaction VII). This is then followed by adsorption of thiophene (reaction X), the initial hydrogenation step (reaction I), and S-C bond scission (reaction VI). The barrier of reaction VI is 0.2eV at the S edge, which is 0.9eV lower than the barrier at the Mo edge. The present results indicate that the S edge vacancy site has a higher activ-

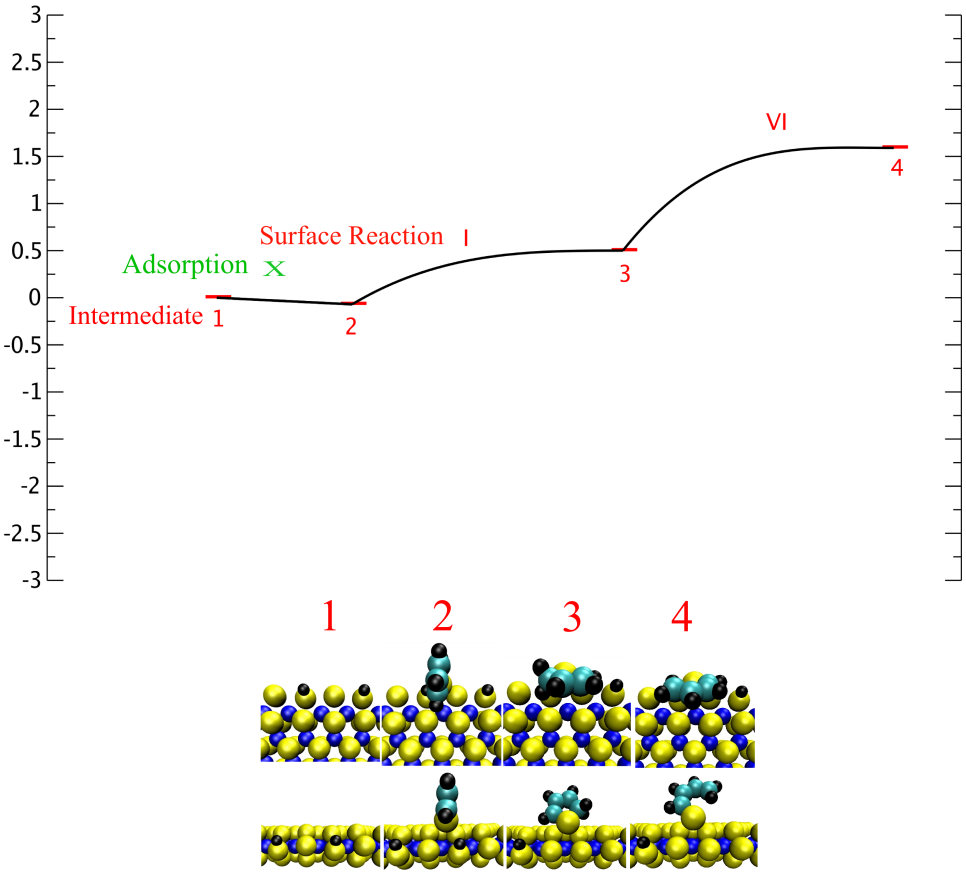

Figure 6.5: The Mo $(10\bar{1}0)$ edge DDS pathway of thiophene. The reference energy is chosen as the equilibrium edge configuration at HDS conditions (Mo edge with 50% S and 50% H) and thiophene in the gas phase. The atoms are colored in the following color scheme: sulfur is yellow, molybdenum is blue, carbon is cyan, and hydrogen is black. Arabic numerals denote intermediates, Roman numerals denote reactions and refer back to Tab. 6.1.

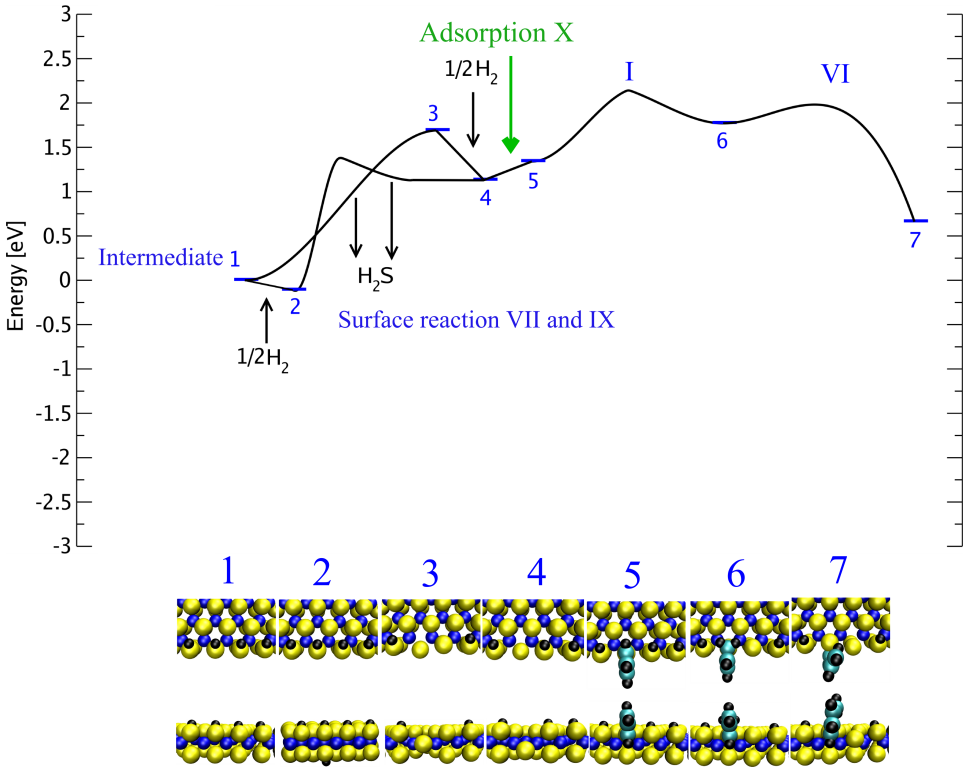

Figure 6.6: The S ($\bar{1}010$) edge DDS pathway of thiophene. The reference energy is chosen as the equilibrium edge configuration at HDS conditions (S edge with 100% S and 100% H) and thiophene in the gas phase. The atoms are colored in the following color scheme: sulfur is yellow, molybdenum is blue, carbon is cyan, and hydrogen is black. Arabic numerals denote intermediates, Roman numerals denote reactions and refer back to Tab. 6.1.

ity in elimination reactions of S-C bonds, which could indicate that the S edge vacancy site more readily eliminates the S-C bond in the DDS of DBT and similar molecules. The availability of the active site and the relative importance of the S and Mo edge in DDS will be discussed in Sec. 6.2.6 to 6.2.9.

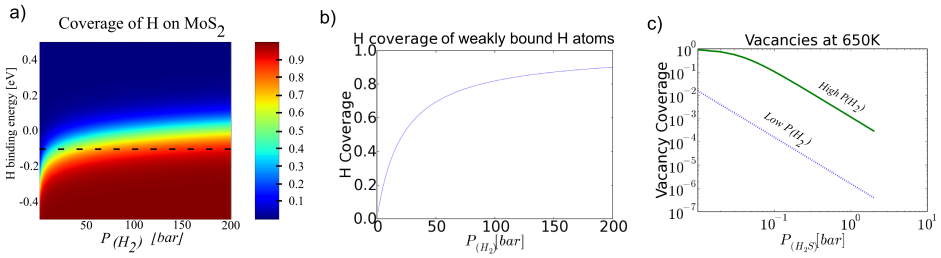

Figure 6.7: H and vacancy coverage. a) Contour plot of the H coverage as a function of the partial pressure of hydrogen and H binding energi. The dotted line marks the binding energy of weakly bound H atoms b) The H coverage of weakly bound H at the S edge dimers. c) The coverage of vacancies at high and low hydrogen pressure. All the coverages are at a temperature of 650K.

6.2.6 The influence of hydrogen and H_2S pressure on the availability of the active sites

The relative availabilities of the Mo edge brim site and the S edge vacancy site will influence their relative importance for the reactivity and the possibility of interplay between the two fundamentally different sites. The Mo edge brim site has a coverage of 1 since it is present at the equilibrium edge configuration. In contrast to the readily available brim site there is not a high concentration of vacancy sites at the S edge. From Tab. 6.1 and Fig. 6.4 one can see that the energy required to remove S from the S edge by creating H_2S depends on the H_2 pressure, in the sense that at high H_2 pressures the coverage of weakly bound H atoms becomes quite large, and this H gives a lower barrier for vacancy formation than the more strongly bound H. At low H_2 pressure and therefore at a low coverage of weakly bound H atoms, the overall barrier of H_2S formation is given by the lowest of $E_{overall} = E_a^{strong}$ and $E_{overall} = E_a^{weak} + \Delta E$ where E_a^{weak} is the activation energy of H_2S formation involving the weakly bound H atoms, E_a^{strong} is the activation energy of H_2S formation involving the strongly bound H atoms, and ΔE is the energy difference in binding energy between the weakly and strongly bound H atoms. At high H_2 pressure and therefore at high coverage of the weakly bound H atoms the overall energy barrier will be given by $E_{overall} = E_a^{weak}$. In the current work, high coverage is defined as 0.8, which corresponds to approximately 80bar hydrogen pressure, a quantification of high coverage could be possible using a micro kinetic model. The H binding energy is -0.6eV when there is only a single H bound to each S dimer, while an additional H added to a S dimer has a binding energy of -0.1eV. Fig. 6.7 (a) shows the calculated coverage of H as a function of the hydrogen pressure and H binding energy and it is seen that the strongly bound H will have a coverage of 100%, i.e. all available sites will be filled, while the coverage of

the weaker bound H will depend on the H_2 pressure. Fig. 6.7 (b) shows the coverage of the weakly bound and therefore more reactive H atoms. Many of the steps in the different HDS pathways involve H, and it is likely that the barriers of these reactions are also lowered, if the coverage of the weakly bound H is appreciable. A similar effect cannot take place at the Mo edge, since the differential H binding energy from 50% to 75% H coverage is 0.4eV which according to Fig. 6.7(a) corresponds to 0% coverage.
As discussed above, the creation of vacancies at the S edge involves reactions with H atoms, and the amount of vacancies will therefore depend on the partial pressure of hydrogen and the H coverage. Fig. 6.7 (c) shows an estimate of the coverage of vacancy sites at the S edge at different reaction conditions. High H_2 pressure referrers to the regime where only the weakly bound H is involved in vacancy formation, while low H_2 pressure referrers to the regime where only strongly bound H is involved in vacancy formation. The calculations are based on the dissociative H_2S adsorption energy [1] and they assume that equilibrium is reached and that the H_2S entropy of the adsorbed state is 0eV/K. For a particular choice of conditions like ($P_{H_2} = 10bar$, P_{H_2}/P_{H_2S} =100 and T=650K), which corresponds to the low pressure region, there is a vacancy coverage of 0.0001 but as can be seen in Fig. 6.7 (c) this changes with reaction conditions and the coverage of vacancy sites at the S edge will typically be in the range of 10^{-6} to 0.1. This is much lower than the coverage of Mo edge brim site which is close to 100%. The difference in availability of active sites has important catalytic consequences, and the active sites at the S edge must be far more active than the Mo edge brim site in order to play any role in HDS reactions.

6.2.7 Hydrogenation reactions

The HYD pathway is especially important for hydrodesulfurization of larger molecules like DBT and it is the dominating reaction pathway for the desulfurized of 4,6-DMDBT [69,149,144,155]. Although the present investigation deals with the desulfurization of the much simpler and more reactive thiophene molecule, it is likely that many of the hydrogenation steps observed presently will also be important for the key features of the hydrogenation steps of the aromatic rings in the more complex molecules. Below, we will present an analysis of the relative importance of the S edge vacancy site and the Mo edge brim site in hydrogenation reactions, and subsequently examine to what extend the elementary reactions and hydrogenation reaction pathways presented in the previous sections may describe the kinetic observations reported in the literature.
Thiophene is found to bind quite weakly (-0.1eV) to the Mo edge brim site but the bond is still 0.3eV stronger than at the S edge vacancy site. These adsorption energies will become more exothermic if van de Waals forces could

[1] Reaction: H_2S + S-S +*-S→2HS-S

be included. Moreover, the barrier for the initial hydrogenation elementary step at the Mo edge brim site is 0.2eV lower than at the S edge vacancy site. Based on this and the higher number of active sites at the Mo edge, it is concluded that hydrogenation reactions most likely occur at the Mo edge brim site. The difference between the Mo edge brim site and the S edge vacancy site in hydrogenation activation energy is probably related to the different H binding energy at the two edges. H is bound more weakly at the Mo edge than at the S edge. The differential desorption energy of $1/2H_2$ from the equilibrium structures is $0.3eV/(1/2H_2)$ at the Mo edge compared to $0.6eV/(H_2)$ at the S edge. Thus hydrogen may be bound too strongly at the S edge, and this could explain why the H transfer processes involved in hydrogenation of thiophene on the Mo edge in Fig. 6.3 only have barriers equal to or very close to the thermochemical differences, while Fig. 6.4 shows that there are significant barriers at the S edge.

In the literature, it has been reported that hydrogenation reactions are not significantly poisoned by H_2S [155]. This has been difficult to reconcile with vacancies being the active sites, but the present finding that the hydrogenation reactions occur at the Mo brim sites, without involving a vacancy, explains the low inhibiting effect of H_2S on hydrogenation.

In the literature the HYD pathway has been reported to be most important for sterically hindered molecules, like 4,6-DMDBT [155, 69, 144]. Therefore, the hydrogenation site must be able to adsorb the sterically hindered molecules. The Mo edge brim site is a very open site and we find that it can adsorb thiophene in both the $\eta 1$ and $\eta 5$ mode. These adsorption modes are of such a character that analogues adsorption of DBT or 4,6-DMDBT would not be sterically hindered. However, the vacancy site at the S edge is subject to steric constraints. This further supports the above conclusion that these sites are not expected to be play a significant role in the hydrogenation of both smaller and larger sulfur containing molecules.

6.2.8 S-C bond scission reactions

We have presently investigated the S-C scission reaction for three different S-C scission reactions: The S-C scission in 2-hydrothiophene (leading to DDS), the S-C scission in 2,5-dihydrothiophene, and the S-C scission in cis-2-butene-thiolate. The latter two steps are the first and second S-C scission steps involved in the HYD pathway. In Sec. 6.2.3 to 6.2.5, we have discussed, how the HYD or DDS pathways can occur at either the Mo or the S edge. However, the reactants and intermediates are not forced to go through all the elementary reactions at one edge exclusively, because the intermediates may move from one site to another, either by surface diffusion, or by desorption and gas phase diffusion. The probability of moving from a site at one type of edge to a site at the other via desorption and gas phase diffusion depends on the relative adsorption energy of the intermediates. The green lines in

Fig. 6.3 and Fig. 6.4 indicate the adsorption energies of reactants and intermediates (Reaction X to XIII) and the adsorption energies are also tabulated in Tab. 6.1. We observe the quite general trend that all the intermediates adsorb at the S edge vacancy site rather than at the Mo edge. In contrast to this, the reactant thiophene adsorbs most strongly at the Mo edge brim site. Therefore, it is possible that some of the elementary reactions may start at the Mo edge brim followed by desorption of intermediates and readsorption at the S edge, where the reaction may be completed.
Below we will discuss where the three different S-C reactions will take place, how reaction conditions influence the relative importance of the Mo edge brim site and the S edge vacancy site, and the interplay between these sites. The S-C scission in 2-hydrothiophene (reaction VI) is an intramolecular elimination reaction involved in DDS which does not involve a hydrogen from a neighboring -SH group. The activation energy at the S edge vacancy site is 0.2eV, while at the Mo edge brim site the activation energy is 1.1eV (see Tab. 6.1). The low barrier at the S edge vacancy site indicates that the S edge vacancy site is able to break S-C bonds by elimination, while the high barriers at the Mo edge brim show that this site is not well suited for the elimination reaction. It should be emphasized that reaction VI takes place after the initial hydrogenation reaction (reaction I) and as mentioned above (Sec. 6.2.7) this reaction will primarily take place at the Mo edge brim. The DDS path can, however, not easily continue at this edge, since reaction VI has a high barrier at the Mo edge brim site and this reaction is competing with the further hydrogenation reaction (reaction II) involved in the HYD pathway. However, it is possible that DDS of thiophene can take place if 2-hydrothiophene can move from the Mo edge to the S edge by surface diffusion. A region with high reactivity could therefore be close to the corner region between a Mo and S edge. Another possibility is that 2,5-dihydrothiophene formed at the Mo edge brim site desorbs and readsorbs at a S edge vacancy, where it is dehydrogenated to form 2-hydrothiophene before S-C scission occurs (Reaction VI). In all situations the results suggest that the S-C scission in the DDS pathway takes place at the S edge vacancy, and this is consistent with the fact that the DDS pathway is strongly inhibited by H_2S [69].
Apart from the S-C scission reactions involved in DDS, we have also studied the S-C scission reactions involved in the HYD pathway, which take place when S-C bonds are broken in 2,5-dihydrothiopene and in cis-2-butenethiolate. The S extrusion from cis-2-butenethiolate is found to consist of two elementary steps: the transfer of H from an SH group to the sulfur in cis-2-butenethiolate (Reaction IV) and the subsequent S-C scission reaction (Reaction V). The H transfer step (Reaction IV) turns out to be of key importance. It has a much lower barrier at the Mo edge brim site than at the S edge which we propose to be related to the weaker binding of H atoms at the Mo edge, see Sec. 6.2.7. In contrast to the H transfer step, the S-C scission

reaction has the highest barrier at the Mo edge brim site. This appears to be analogous to the situation for step VI . The final S-C scission (reaction V) will probably also take place at the Mo edge brim site as seen in Fig. 6.3 even though it has a 0.1eV higher barrier than at a S edge vacancy site.
The rate of S extrusion from cis-2-butenethiolate at the S edge vacancy site will be determined by the H transfer step. However, The H transfer step in S extrusion from cis-2-butenethiolate may be circumvented by surface diffusion of cis-2-butene-thiolate to the Mo edge. The corresponding diffusion barriers have not been calculated presently, but they may be estimated by the energy required to move cis-2-butenethiolate from a vacancy site to a site next to the vacancy. This energy is found to be 1.1eV. From the above discussion we draw the conclusion that the Mo edge brim site will be the primary site of cis-2-butenethiol formation. In view of the results shown in Fig. 6.7 and the discussion in Sec. 6.2.6, it could be speculated that the H transfer step and H transfer steps in general can more easily take place at the S edge vacancy site at high hydrogen partial pressures, where weakly bound H atoms are present.
Interplay between the Mo edge brim site and the S edge vacancy site is found to be important for desulfurization of cis-2-butenethiolate. For example, the final S-C scission step may take place at the S edge vacancy even though the cis-2-butenethiol intermediate is formed at the Mo edge site. For such an interplay between the S edge and Mo edge to take place, it requires that cis-2-butenethiol moves via surface diffusion or desorbs from the Mo brim site. The present study finds that cis-2-butenethiol will easily desorb due to the weak binding (-0.1eV) at the Mo edge brim site. In this connection it is interesting to note that thiols have been found as intermediates in HDS of thiophene [179]. Due to their high reactivity, they are expected to be present in very small concentrations, which was also observed experimentally [179].
The rate of S removal from cis-2-butenethiol will depend on the coverage of cis-2-butenethiol at the Mo edge brim site and at the S edge vacancy site. The coverage of cis-2-butene-thiol can presently not be calculated with high accuracy due to the lack of thermodynamic data on gas phase butane-thiols, but it is possible to obtain an estimate of the relative coverage. The coverage is a function of the Gibbs free energy of adsorption, and if one assumes that the entropy of cis-2-butene-thiol [190] in the gas phase is similar to the entropy of cis-2-pentene and furthermore uses the upper limit of the entropy loss, which is found by assuming that all the entropy is lost upon adsorption, then $-TS_{adsorb}$ equals 2.3eV at 650K and 1atm. The entropy loss therefore dominates the Gibbs free energy of adsorption and the coverage of cis-2-butene-thiol will be low. The large positive Gibbs free energy leads to the following simplification.

$$\theta = K \cdot P/(1 + K \cdot P) \approx K \cdot P$$

, where K is the equilibrium constant ($K = exp(-\Delta G/(k_B T))$), P is the

partial pressure of the reactant or intermediates, and θ is the coverage of the reactant or intermediates. If one assumes that the entropy loss is similar at the two edges, the relative coverage is given by:

$$\theta_{\text{S edge}}/\theta_{\text{Mo edge}} = exp(-(\Delta E_{\text{S edge}} - \Delta E_{\text{Mo edge}})/(k_B T))$$

, where $\Delta E_{\text{S edge}}$ is the adsorption energy at the S edge, $\Delta E_{\text{Mo edge}}$ is the adsorption energy at the Mo edge, and k_B is the Boltzmann constant.
The adsorption energy of cis-2-butenethiol is most exothermic at the S edge vacancy site where it is between -0.5 and -0.6eV (depending on H coverage), while it is -0.1eV at the Mo edge brim site. As a result, the coverage is 3 orders of magnitude larger at the S edge vacancy site. The S edge vacancy site has an activity for the final S-C scission, which is approximately 10 times higher than the Mo brim site (difference in barrier of 0.12eV). Combining this with the higher coverage of cis-2-butene-thiol at a S edge vacancy site means that the S edge vacancy site is approximately 10^4 times more active for the HDS of cis-2-butene-thiol than the Mo edge brim site.
The same analysis for 2,5-dihydrothiophene leads to the conclusion that the S edge vacancy site is approximately 10^{13} times more active in the initial S-C bond scission of 2,5-dihydrothiophene (Reaction III) than the Mo edge brim site. The S edge vacancy sites will therefore contribute more to the overall initial S-C scission than the Mo edge brim sites for the entire range of H_2S pressure. The final S extrusion will be dominated by the S edges if the S edge vacancy coverage is larger than about 10^{-4}, which by inspection of Fig. 6.7 (c) is the case at high H_2 pressures or at H_2S pressures below 0.1bar.
The present results, which show that the elimination step VI has a low barrier, indicate that the S edge vacancy site could also be the active site for other types of S-C elimination reactions like the S-C bond scission in the DDS mechanism of DBT or 4,6-DMDBT. It could also be speculated that the S edge vacancy site could be able to eliminate both S-C bonds in 2,5-dihydrothiophene and form butadiene in a reaction mechanism similar to the one found for very small clusters [191]. Furthermore the present findings substantiate the proposal that a S edge vacancy site is needed in order to remove S from DBT and 4,6-DMDBT [192, 50].
The picture is expected to be somewhat different for species like DBT and 4,6-DMDBT where geometrical hindrances of adsorption play a larger role. For these species, the difference in adsorption energy between the different sites may also be larger and this is also expected to play a role. It could be added that the relative contribution of the two MoS_2 edges will also depend on the sulfiding conditions since this has been observed to influence the relative abundance of the Mo and S edge [107].
The present study has investigated the reactions at a single MoS_2 slab, and represents the structures observed in many commercial catalysts quite well.

The present results indicate that the relative contribution of different pathways and interaction between the S edge and the Mo edge will be different in stacked multi slab MoS_2 structures. For example, in such cases only the top layer will expose readily accessible brim sites. This is proposed to be one of the reasons why it may be desirable to have mainly single slab catalyst in commercial catalysts and also proposed to be one of the reasons why differences in activity depending on the stacking degree has been reported experimentally to be an important factor [193].

6.2.9 Possible rate determining steps

The present results suggest that two different reactions play a major role in the HYD pathway of thiophene namely the initial SC scission (Reaction III) and the creation of the active site. At the S edge the vacancy site has a high barrier for creating the vacancy site (1.7eV), while on the other hand the S-C scission barrier is relatively low (0.8eV). It is the opposite case at the Mo edge where the S-C scission barrier is large (2eV) compared to the regeneration of the active site (1eV). However the barrier of regenerating the active site on the S edge is lower than the S-C scission barrier at the Mo which could indicate that the rate determining step is the generation of vacancies at the S edge. It is well know from the literature that H_2S acts as an inhibitor of S removal [69], and the present results are in agreement with this observation. The hydrogenation activity of the Mo edge brim site is higher than that of the S edge vacancy site and, therefore, the Mo edge brim sites are still of importance. Because even though the initial S-C scission most probably takes place at the S edge vacancy site thiophene must still be hydrogenated prior to the initial SC scission and hydrogenation is facile at the Mo edge brim site. The final SC scission may also require interplay between the S edge and the Mo edge since thiol formation has a high barrier at the S edge vacancy site. In future studies, a micro kinetic model would quite possibly be a useful tool in order to determine the importance of the interplay between the Mo and S edge.

6.2.10 Conclusions

It is important to emphasize that as a starting point, we have considered the edge configurations, which are thermodynamically most stable under realistic HDS conditions. These correspond to a Mo edge with 50% S coverage and 50% H coverage and a S edge with 100% S coverage and 100% H coverage and these structures are illustrated in Fig. 6.8. On these edges we have identified several HYD and DDS reaction pathways for thiophene HDS and they are summarized in Fig. 6.8. The active site for thiophene HDS at the Mo edge is the so-called brim site [50, 108]. It is important to point out that these brim sites are present at the equilibrium edge configuration and should therefore not be considered as vacancies. In fact the neighboring Mo

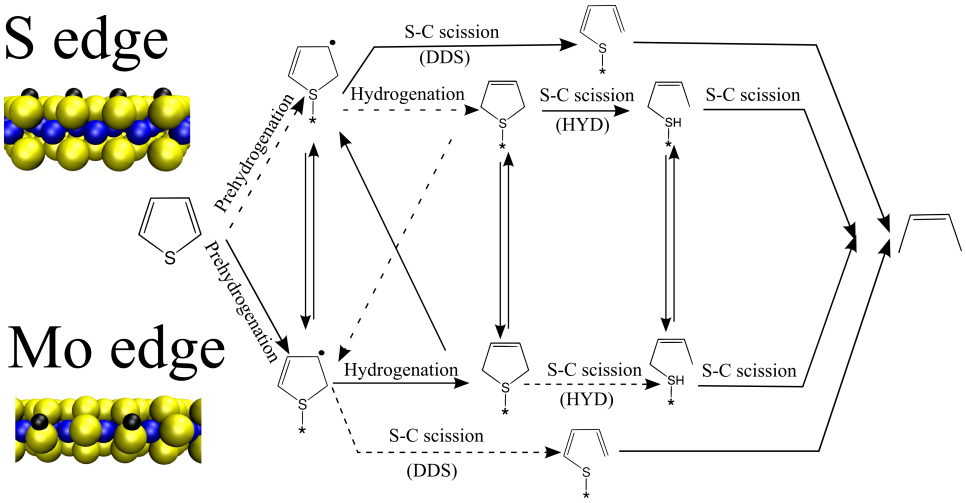

Figure 6.8: A schematic overview of the reactions involved in HDS of thiophene including the possible interaction between the S $(\bar{1}010)$ edge and the Mo $(10\bar{1}0)$ edge. Dotted arrows mark reactions found to be slow.

atoms are fully coordinated by sulfur (Fig. 6.8). Thus, this active site does not have to be created before the reaction can take place, but of course if sulfur is removed from an organic compound and thereby deposited at the Mo edge brim site it has to be regenerated between catalytic cycles. The active site for thiophene HDS at the S edge is a vacancy site, which is not present at the equilibrium edge structure (Fig. 6.8), but has to be created first and subsequently regenerated between cycles. The relative concentration of S edge vacancies is significantly smaller than the concentrations of the Mo edge brim sites, since the energy barrier involved in the creation of the vacancies is found to be quite large, especially at low H_2 partial pressures. Considering the elementary steps of thiophene hydrogenation and subsequent S-C bond scission, we find significant differences between the Mo edge and the S edge. Some of these can be summarized as follows:

1. H transfer and hydrogenation reactions have lower barriers at the Mo edge brim site (more than 0.2eV lower barriers than at the S edge vacancy site).

2. Thiophene prefers to adsorb at the Mo edge brim site (0.3eV stronger binding than at the the S edge vacancy site).

3. 2,5-dihydrothiophene and cis-2-butenethiol prefer to adsorb at the S edge vacancy site (more than 0.4eV stronger binding than at the Mo edge brim site).

4. S-C scission reactions have lower barriers at the S edge vacancy site (more than 0.1eV lower barriers than at the Mo edge brim site).

5. The regeneration of the active site has a higher barrier at the S edge (more than 0.5eV higher than at the Mo edge).

Our results suggest that the HYD pathway is initiated by hydrogenation at the Mo edge, as thiophene preferentially adsorbs at the Mo edge and hydrogenation is energetically unfavorable at the S edge. When 2,5-dihydrothiophene has been formed on the Mo edge it moves to the S edge vacancy site where the initial S-C-scission takes place. The subsequent S extrusion from the cis-2-butenethiolate may take place either at the S edge vacancy site or at the Mo edge brim site depending on the reaction conditions. The S edge vacancy site will be the primary site at high H_2 (above 80bars) pressures or at low H_2S pressures.
As the intermediates (e.g. 2,5-dihydrothiophene and cis-2-butenethiol) prefer to bind at the S edge compared to the Mo edge, it is possible that they diffuse to the S edge after initial hydrogenation at the Mo edge, since desorption and diffusion is facile. Thus, we suggest that the edges can catalyze the reaction in interplay between sites, i.e., thiophene adsorbs and gets hydrogenated at the Mo edge and subsequently diffuses to the S edge, where the final S-C bond scission is accomplished.
Cis-2-butenethiol is found to be an intermediate in the HYD pathway and the low barriers of S removal from thiol at both the Mo edge brim site and the S edge vacancy site explain the high reactivity of thiols observed in kinetic and reactivity studies [69].
For the DDS pathway, we find that it is initiated by a hydrogenation step which occurs preferably at the Mo edge and that the subsequent S-C scission takes place at the S edge. The calculated energies and barriers indicate that the DDS pathway is relatively less important than the HYD pathway for MoS_2. The main reason being that the initial hydrogenation to hydrothiophene has to take place at the Mo edge brim site and the S-C scission at the S edge vacancy site.
We find that our proposed model for thiophene HDS involving the HYD and DDS pathway clarifies several experimental observations in the literature. We identify the Mo edge brim sites as the hydrogenation sites for the aromatic like thiophene molecule, and it is seen that they do not require creation of a vacancy to be active. This explains the experimental observation that H_2S does not significantly inhibit hydrogenation of aromatics [69] [155].
Furthermore, the Mo edge brim site is a very "open" site and allows for adsorption of larger molecules without introducing significant steric hindrances. Thus, it is likely that hydrogenation of e.g. 4,6-DMDBT takes place at the Mo edge brim site prior to desulfurization. It is therefore proposed that the S edge vacancy site may also play a large role for final S removal from hydrogenated DBT and hydrogenated 4,6-DMDBT in a similar mechanism, where the stronger adsorption of hydrogenated intermediates

at the S edge vacancy site helps the S removal. This is indeed consistent with the observed inhibition by H_2S of these final steps [155].

The present results show that HDS of thiophene is a complicated interplay, between edge structures, adsorption energies of reactants and intermediates, activation barriers and reaction conditions. This may explain why it has been so difficult in the literature to arrive at agreement on the kinetics of thiophene HDS.

6.3 CoMoS catalyst

6.3.1 Introduction

Industrial HDS catalysts often consist of Co or Ni promoted MoS_2, since Ni or Co promotion increases the activity of the catalyst [69]. The promotion of MoS_2 by Co is due to the formation of the CoMoS phase [157] (see Sec. 5.1.1). Apart from a general agreement on that promotion by Co or Ni increases the activity of the catalyst, there is still much debate on the effect of promotion with regards to the relative increase in hydrogenation and SC-scission activity [155,166,194,195,196,152] and resistivity towards inhibitors such as H_2S [155,197,194]. In the following sections the effect of promotion by Co on HDS of thiophene is investigated. Sec. 6.3.3 presents the HDS equilibrium edge configuration and the investigated elementary reactions. The results show that creating a vacancy at the equilibrium edge requires more energy than creating a vacancy at the non promoted S edge, therefore we investigate a site similar in nature to the MoS_2 Mo edge brim site. The investigated site is characterized by it being present at the equilibrium edge configuration where a bright brim has been identified (Sec. 5.2.4) and due to the similarity to the MoS_2 brim site we call the site the CoMoS brim site. We investigate the HYD and DDS pathway in Sec. 6.3.4 and 6.3.5 with the definition given in Sec. 6.2.2. The DDS pathway is defined as the pathway which is initiated by an initial hydrogenation reaction forming 2-hydrothiophene which is reacting further by direct SC scission. The HDS pathway is defined as the HYD pathway when thiophene is hydrogenated twice and 2,5-dihydrothiophene is formed prior to the initial SC scission. We find that Co promotion significantly increases the hydrogenation activity of the S edge (Sec. 6.3.6). Furthermore, the SC scission barriers (Sec. 6.3.7) are increased to a level below the Mo edge brim site but well above the non promoted S edge vacancy site. In Sec. 6.3.8 we discuss the overall effect of promotion and come to the conclusion that promotion has two major effects, first of all it will increase the hydrogenation activity and secondly it will increase the relative importance of the DDS pathway compared to the HYD pathway.

6.3.2 Computational details

We use the computational setup describe in Sec. 4.2 except the following details. We use a unit cell consisting of 4 Mo atoms in the x-direction and 4 Mo atoms in the y-direction. The Brillouin zone is sampled using a Monkhorst-Pack k-point set [34] containing 4 k-points in the x-direction and 1 k-point in the y- and z-direction. All calculations have been performed spin polarized, due to the presence of cobalt.

6.3.3 The choice of active surfaces and elementary reactions

We investigate the Co promoted S edge since both experiment and theory have found that Co atoms substitute Mo atoms at the S ($\bar{1}010$) edge (see chapter 5). It is likely that Co only partially substitutes Mo atoms as suggested in reference [68, 198, 199]. We focus on the fully promoted S edge since this is a well defined limit. The equilibrium surface at HDS conditions is covered with 50% S and 25% H (Fig. 6.9). Therefore, Co is 4 fold coordinated to S and the H coverage is lower than for the unpromoted S edge. It is interesting to note that the HDS equilibrium edge is similar to the edge observed in STM experiments (Sec. 5.2), except for the H coverage. We do therefore have direct atomic insight into the edge present at HDS conditions. Creating a vacancy at the CoMoS ($\bar{1}010$) edge requires 1.8eV[2] and therefore it is more difficult to create a vacancy at the promoted S edge than at the non promoted S edge (ΔE_{vac}= 1.69eV). Thus, there is reason to believe that the barrier for creating a vacancy will be larger at the Co promoted S edge than at the non promoted S edge indicating that the active site at the CoMoS ($\bar{1}010$) edge is not a vacancy. However, Co promotion does also introduce non vacancy sites. The equilibrium edge has 50% S coverage and 25% H coverage and STM experiments have observed a bright brim present behind the edge with protrusion at the front row S atoms (Sec. 5.2). The site present on this edge will be termed the CoMoS brim site since it is analogous to the Mo edge brim site in the way that it has a bright brim and is not a vacancy in the equilibrium structure. The investigated CoMoS brim site has a coverage of one since it is present at the equilibrium edge configuration.
We have investigated both the HYD and the DDS pathway at the CoMoS brim site using the same definition of the two different pathways as for MoS_2. We assume that the second hydrogenation reaction (reaction II in Tab. 6.1), which hydrogenates 2-hydrothiophene into 2,5-dihydrothiophene and the final S removal from cis-2-butenethiol (reaction V in Tab. 6.1) have zero barrier as observed on both the S and Mo edge of MoS_2. In order to find the reaction path we have investigated several adsorption configurations for all the intermediates, an overview of the intermediates can be seen in

[2]Calculated as $\Delta E_{vac} = E_* + E_{H_2S(g)} - E_{H_2(g)} - E_{S-*}$

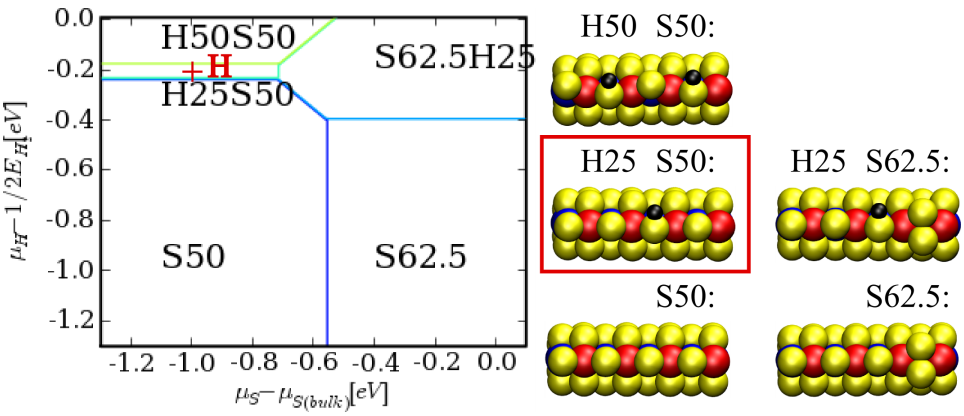

Figure 6.9: Phasediagram of the S ($\bar{1}010$) CoMoS edge. (+ H) mark the chemical potential at HDS condition (P_{H_2} = 10bar,P_{H_2}/P_{H_2S} =100 and T=650K). The stable edge configuration at HDS conditions is emphasized by a red square.

appendix D. We have summarized the HDS reactions at the CoMoS brim site in Tab. 6.2 where the numbering of the reactions are identical to the MoS_2 numbering. The contracted reaction seen in Fig. 6.10 have been constructed under the assumption that gas phase hydrogen is in equilibrium with the surface hydrogen.

Table 6.2: An overview of the reactions involved in HDS of thiophene over CoMoS including the activation barriers (E_a) and energy changes (ΔE) of the reactions

Reaction		E_a [eV]	ΔE [eV]
I	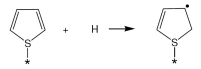	0.44	0.44
III	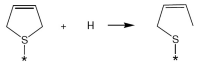	1.70[e]	-0.13
IV	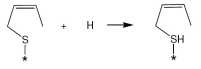	0.96	0.21
VI	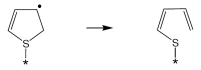	0.63	0.03
VII	$2HS\text{-}* \longrightarrow H_2S\text{-}* + S\text{-}*$	1.00[a]	-0.01
VIII	$1/2H_{2(g)} + * \longrightarrow H\text{-}*$		-0.24[b]
IX	$H_2S_{(g)} + * \longrightarrow H_2S\text{-}*$		-0.02[b]
X			-0.07[c]
XI			-0.57 [c]
XII			-0.55[c]
XIIII	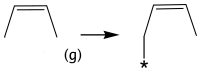		-0.03[d]

[a] Calculated as $E_{\mathrm{VII}} = \Delta E_1 + E_2$, where ΔE_1 is the reaction energy of reaction 1: 2H-S(25%H and 50%S)+ S(0%H and 62.5%S) + S-S (0% H and 62.5% S)→ 2(0%H and 50%S)+ H-S-S(50%H and 62.5%S) +H-S(50%H and 62.5%S) and E_2 = 0.54eV is the activation energy of reaction 2: H-S-S(50%H and 62.5%S) +H-S(50%H and 62.5%S)→ H_2S-S(50%S).

[b] 50%S and 0% H

[c] 50%S and 25% H

[d] 62.5%S and 0% H

[e] Proceeds in two steps, 1) S-C scission without involving H, 2) hydrogenation. The overall activation energy is given by step 1) since the hydrogenation reaction in step 2) has been assumed to be non activated. The barrier is calculated without spin polarization.

6.3.4 HYD pathway

The hydrogenation pathway can be seen in Fig. 6.10. The HYD pathway is initiated by thiophene adsorption (reaction X in Tab. 6.2). The weakly bound thiophene (-0.1eV) is then subsequently hydrogenated to 2-hydrothiophene (reaction I in Tab. 6.2) with a barrier of 0.4eV which is equal

to the energy change of the reaction. The second hydrogenation reaction whereby 2,5-dihydrothiophene is formed is assumed to be non activated. When 2,5-dihydrothiophene is formed the HYD pathway proceeds by the initial S-C scission reaction (reaction III in Tab. 6.2) where we find that the S-C bond can be broken without involving a H atom. We have investigated two different initial states of reaction III in an attempt to find the concerted reaction mechanism found for reaction III at the MoS_2 Mo edge brim site, however in both cases the pathway is found to proceed in two steps. Thus, the reaction mechanism is similar to the reaction mechanism found at the non promoted MoS_2 S edge. The subsequent hydrogenation reaction which leads to the formation of cis-2-butenethiolate is assumed to be non activated justified by the fact that the similar reaction at the S edge vacancy site is non activated and the low hydrogenation barrier of thiophene found at the CoMoS brim site. Therefore, the overall barrier is given by the SC scission barrier which is 1.70eV. Reaction III is followed by a H transfer reaction (reaction IV in Tab. 6.2) which forms cis-2-butenethiol with an activation energy of 1.0eV. The final S-C scission is assumed to be low as observed on non promoted MoS_2

6.3.5 DDS pathway

The potential energy diagram for the DDS pathway is shown in Fig. 6.10. The DDS pathway is initiated by thiophene adsorption (reaction X in Tab. 6.2). The weakly bound thiophene (-0.1eV) is then hydrogenated to 2-hydrothiophene (reaction I in Tab. 6.2) with a barrier of 0.4eV which is equal to the energy change of the reaction. The S-C bond between S and the hydrogenated C in 2-hydrothiophene is then broken without further hydrogenation forming cis-butadienethiolate with a barrier of 0.6eV (reaction VI in Tab. 6.2). The final S-C scission in the DDS pathway is assumed to take place in the same way as the final S-C scission in the HYD pathway. The low hydrogenation barrier combined with the relatively low S-C scission barrier indicate that the DDS pathway plays a major role at the CoMoS brim site.

6.3.6 Hydrogenation

The conclusion in the previous section on MoS_2 (Sec. 6.2) was that hydrogenation primarily takes place at the Mo edge, due to the stronger binding of thiophene and the lower barrier at the Mo edge compared to the S edge. Totally substitution of the Mo atoms at the S edge by Co atoms lowers the thiophene binding energy to -0.1eV, similar to the binding energy at the Mo edge brim site. Furthermore the barrier of 0.4eV is lower than the Mo edge brim site barrier of 0.6eV. The lower barrier could be due to the less tightly bound H atoms on CoMoS bound with 0.2eV compared to 0.3eV on the Mo edge of MoS_2. Promoting MoS_2 with Co is therefore predicted to

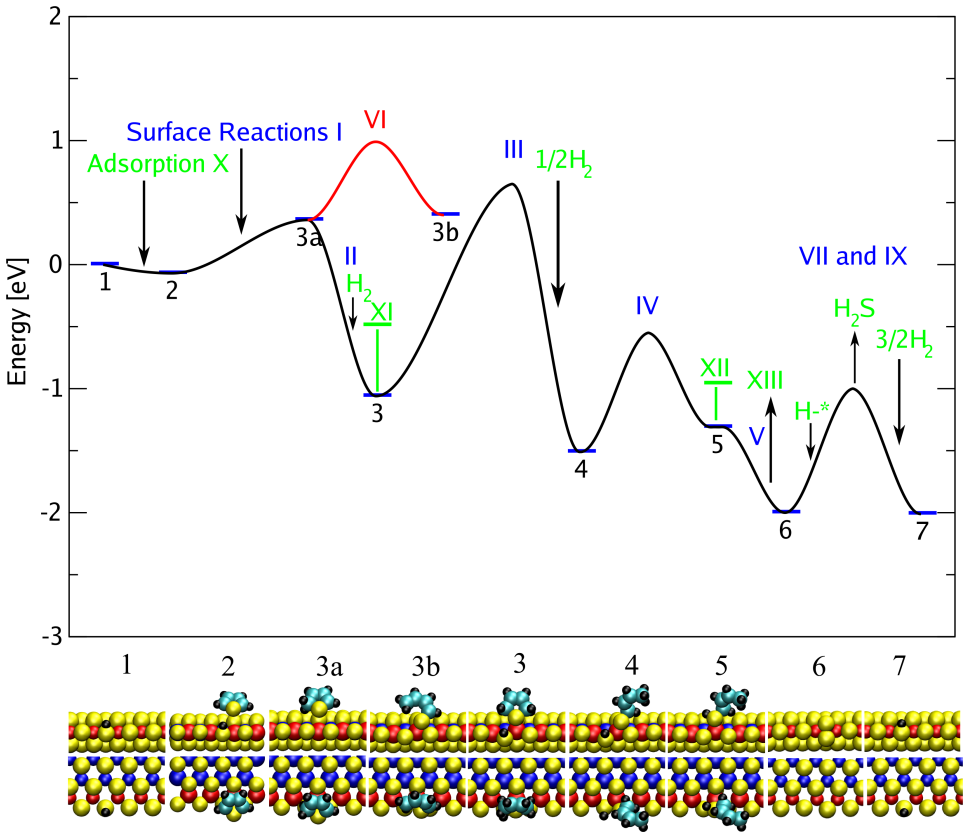

Figure 6.10: The S ($\bar{1}010$) CoMoS edge HYD and DDS pathway. The reference energy is chosen as the equilibrium edge configuration at HDS conditions (S edge with 50%S and 25% H) and thiophene in the gas phase. The atoms are colored in the following color scheme: sulfur is yellow, molybdenum is blue,cobalt is red, carbon is cyan, and hydrogen is black. Arabic numerals denote intermediates, Roman numerals refer to reactions numbers in Tab. 6.2.

increase the hydrogenation properties, an effect which also have been observed experimentally [155, 166]. The CoMoS ($\bar{1}010$) edge is similar to the MoS_2 Mo edge in the sense that it is an open structure where adsorption of large molecules like 4,6-DMDBT would not be sterically hindered. It could be speculated that the CoMoS ($\bar{1}010$) edge will be well suited for HDS of sterically hindered molecules where the HYD pathway is important.

6.3.7 SC scission

In Sec. 6.3.4 and 6.3.5 we described how the HYD pathway and the DDS pathway occur. The SC-scission of 2-hydrothiophene is the initial SC-scission reaction in the DDS pathway and the barrier of this reaction is 1.1eV lower than the SC-scission of 2,5-dihydrothiophen which is the initial S-C scission reaction of the HYD pathway. Compared to the non promoted MoS_2 both S-C scission reaction at the CoMoS brim site have lower barriers than at the Mo edge brim site but higher barriers than at the S edge vacancy site.
An important mechanism on the non promoted MoS_2 was proposed to be the interaction between the Mo edge and the S edge. This is likely also the case for Co promoted MoS_2 since the adsorption energies of the intermediates are more exothermic at the CoMoS ($\bar{1}010$) edge than on coexisting MoS_2 Mo ($10\bar{1}0$) edge, thus there is a thermodynamic driving force for the intermediate to move to the Co promoted S edge.

6.3.8 Effect of promotion

Total substitution of the S edge Mo atoms with Co atoms changes the catalytic properties of the S edge quite substantially. Relative to the non promoted S edge the S-C scission barriers increase and the hydrogenation barriers decrease. At the same time thiophene adsorption becomes exothermic and the adsorption energies of the intermediates like 2,5-dihydrothiophene and cis-2-butadienethiol remain almost constant. The Co promoted particles will most likely expose both CoMoS brim sites and MoS_2 Mo edge brim sites. Therefore, it is relevant to compare the CoMoS brim site and the Mo ($10\bar{1}0$) edge brim site and in this case the S-C scission and hydrogenation barriers are lower at the CoMoS brim site than at the Mo edge brim site. Furthermore, reactants and intermediates adsorb as strong or stronger at the CoMoS brim site than at the Mo edge brim sites.
The hydrogenation activity will go up as a consequence of promotion for the following reasons. First of all the hydrogenation barrier at the S edge CoMoS brim sites is lower that at the non promoted Mo edge brim site and S edge vacancy site. Secondly the adsorption energy of thiophene is the same at Mo edge brim sites and at the CoMoS brim sites. The per site activity will therefore be higher for CoMoS brim sites than for Mo edge brim sites. This implies that structural changes as a result of Co promotion (see

Sec. 5.2) which lower the number of Mo edge brim sites will not reduce the hydrogenation activity since at the same time the number of CoMoS brim sites will increase and therefore the hydrogenation activity will improve.

The DDS pathway will most likely be the dominant reaction path, because Co promotion makes it possible to form hydrothiophene at the S edge where the DDS S-C barrier is still low (0.6eV). This is a clear effect of promotion since the DDS pathway of non promoted MoS_2 was proposed to be low due to the inability of the S edge vacancy site to hydrogenate thiophene.

The initial S-C scission in the HYD pathway has a barrier of 1.7eV and therefore much higher than the DDS S-C scission (0.6eV), however the coverage of 2,5-dihydrothiophene is also larger due to the stronger binding of 2,5-dihydrothiophen so the HYD path could still play a role, especially in connection with 2,5-dihydrothiophene formed at the Mo edge. A micro kinetic model would be very useful in order to quantify the relative importance of the DDS and HYD pathway for the Co promoted MoS_2 catalyst. However, the effect of Co promotion is quite evident, since the DDS pathway will clearly play a larger role and hydrogenation activity will increase. Even though one should be cautious about drawing direct conclusions from the present study of thiophene to studies of larger molecules like DBT and 4,6-DM-DBT recent experimental studies of these larger molecules seem to agree with the present finding since they observed an increased hydrogenation and DDS activity upon Co promotion [166, 155].

6.3.9 Conclusion

In the case of no support interactions Co promotion will change the shape of the catalyst into hexagonal shape particles. The S edge Mo atoms will be substituted by Co and we have investigated the limiting case where all S edge Mo atoms are substituted by Co. On this edge we have identified an active site present at the equilibrium edge configuration, which has a bright brim. Since this site is analogues to the Mo edge brim site we have named it the CoMoS brim site. The hydrogenation properties of the catalyst will increase since the CoMoS brim site has slightly better hydrogenation properties than the MoS_2 Mo edge brim site.

The SC-scission barriers increase relative to the non promoted S edge. However, due to the increased hydrogenation activity and increased adsorption energy of thiophene the CoMoS brim site will have a higher activity in the DDS pathway. It could be speculated that less then 100% Co substituted $(\bar{1}010)$ edges like the edges investigated in [68, 183, 198, 199] could have sites which are a mixture of the fully promote and the non promoted S edge and that these sites would have lower SC-scission barriers than the fully promoted S edge and at the same time lower barriers for site generation.

6.4 Conclusion and outlook

We have established the HYD and DDS pathways on the Co promoted and non promoted S ($\bar{1}010$) edge and on the non promoted Mo ($10\bar{1}0$) edge. On the non promoted MoS_2 particles we find that interplay between the S and Mo edges plays a key role, since hydrogenation of thiophene takes place at the Mo edge brims site and SC-scission primarily takes place at the S edge vacancy site. Both the HYD and the DDS pathway may on the other hand take place exclusively at the Co promoted ($\bar{1}010$) edge, however, this does not rule out edge interplay for the promoted particles since the non promoted Mo edge will still be active as hydrogenation catalyst.
It is interesting to note that the present results can form the basis for the development of a micro kinetic model of HDS of thiophene which could be a very useful tool for quantifying the contributions of the different edges to thiophene HDS. Knowing the contribute to activity of the different sites involved in HDS could possibly guide future design of catalysts with specific HYD/DDS properties. One could speculate that certain additives or supports could stabilize either the S or the Mo edge and identifying such supports or additives could enable more intelligent catalyst design.

Chapter 7

Inhibition in HDS

7.1 Introduction

The need to upgrade crude oil to ultra clean diesel does not only require insight into the desulfurization process itself but also knowledge about other hydrotreating reactions like hydrodenitrogenation and insight into the role of inhibitors are needed. In the case of HDS several of the constituents of crude oil act as inhibitors, and in order to optimize catalysts for feeds with different levels of inhibitors, knowledge about the mechanism of inhibition is needed.

In the following, we will briefly recapitulate the HYD and DDS pathway and some of the important experimental findings with regard to inhibition of the two different pathways. Studies using model compounds have shown that the HDS reaction for the unsubstituted DBT molecule proceeds mainly via the direct (DDS) route [149, 144, 69]. However, in the case of sterically hindered alkyl substituted molecules like 4,6–DMDBT, the HYD route become important [153,144,77,151,69,200,201,155,202,203]. In the industrial reactor, the desulfurization pathway will depend on parameters such as the composition of the crude oil, the partial pressures of H_2 and H_2S, and the desired sulfur content in the product stream [151,202]. Many of these effects appear to be related to the fact that different molecules in the feed may have quite different inhibiting effects on the two reaction routes. The presence of nitrogen compounds is, for example, a key parameter, which may influence the HDS activity [73,69,202,203,168,169,170,171,172,174,177,175,176,173].

Detailed studies of inhibition effects under real feed conditions [171] showed that especially basic heterocyclic nitrogen compounds inhibit the HDS reaction and that the inhibition is most pronounced for the HYD route. Thus, the inhibition effects are particular important for deep HDS of refractory compounds like 4,6–DMDBT which must be hydrogenated before desulfurization can take place. Kinetic studies using model compounds also support this conclusion [174, 161]. For non–sterically hindered heterocyclic

compounds with nitrogen in a six–membered ring, there appears to be a good correlation between the inhibitor strength and the gas phase proton affinities, where stronger inhibitors have higher gas phase proton affinity [169, 170]. This could indicate that the poisoning of the HYD route by nitrogen compounds involves the interaction with a proton from a Brønsted acid site on the catalytically active nanostructures.
Infrared measurements have shown that SH groups exist at the edges of MoS_2 nanoparticles [161] and IR studies also revealed their interaction with pyridine to form pyridinium ions [204]. The inhibiting effect of other molecules on the HYD route has also been investigated. Aromatic hydrocarbons have been observed to poison the HYD route more than the DDS route [69, 203, 195] but for real–life operating conditions, the poisoning effect on HYD may be quite small [202, 174]. In contrast, the H_2S inhibiting effect is much less for HYD than for DDS [69, 202, 205].
While there is a relatively good general agreement in the literature on the different reactivity, kinetic and poisoning effects, very limited direct mechanistic insight has been obtained. Nevertheless, many of the above-mentioned observations have been taken as evidence for the HYD and DDS pathways occurring on different sites [69, 155]. Sulfur vacancies are in general believed to play a key role in the DDS pathway. The nature of the hydrogenation sites is less well understood but many authors have also proposed vacancies to be involved in HYD reactions (see e.g. [69]). In view of the observation that quite large molecules may be desulfurized via the HYD pathway, it has been proposed that multiple vacancy sites or ensembles of vacancies are involved in HYD. It has, for example, been suggested [74] that the HYD reaction occurs at the so–called naked MoS_2 edge (i.e. the $(10\bar{1}0)$ Mo edge without terminal sulfur atoms). However such naked $(10\bar{1}0)$ Mo edges are energetically extremely unfavorable (see Sec. 5.1.2) since the edges bind sulfur very strongly and are not likely to be present at HDS conditions. The observation that the HYD reaction is not very strongly inhibited by H_2S excludes that naked Mo edges play an important role in hydrogenation. In chapter 6 we found that hydrogenation of thiophene can take place without involving a vacancy site instead the catalytic reaction takes place on a so–called brim site. That is present on the equilibrium edge structures and does not introduce significant sterical hindrance for adsorption of large molecules like 4,6–DMDBT due to its open geometry. On such open sites the adsorption energy of thiophene is weak (on the order of -0.1eV) which indicates that thiophene adsorption could be inhibited by molecules binding more strongly to the active sites.
In the present chapter, we investigate poisoning effects using three different known inhibitors, i.e. benzene, pyridine and H_2S. DFT calculations have been performed on the interaction of these molecules with the Mo edge and the S edge of MoS_2 at S and H coverages, that are likely to be present under industrial HDS conditions. The effect of protonation of the basic

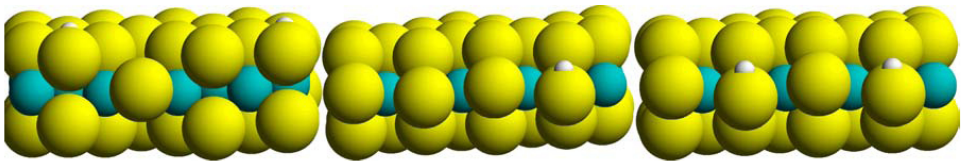

Figure 7.1: The edge geometries: **Left:** The S ($\bar{1}010$) edge with a vacancy and 50% H coverage, **Middle:** Mo ($10\bar{1}0$) edge with 50% S and 25% H coverage, **Right:** Mo ($10\bar{1}0$) edge with 50% S and 50% H coverage.

pyridine molecule has also been investigated in order to elucidate the effect of Brønsted sites. The results provide insight into the nature of the HYD sites; the strong inhibition by pyridine and the weak inhibition of the HYD route by H_2S.

7.2 Computational details

7.2.1 Computational details

We use the computational setup described in Sec. 4.2 apart from the following details. We use a unit cell consisting of 4 Mo atoms in the x-direction and 4 Mo atoms in the y–direction (Fig. 6.1). The edge configurations investigated can be seen in Fig. 7.1 The Brillouin zone is sampled using a Monkhorst–Pack k–point set [34] containing 3 k–points in the x–direction and 1 k–point in the y–direction for edge calculations and 3 k–point in the y–direction for basal plane calculations and 1–kpoint in the z–direction.

7.3 Benzene

The adsorption of benzene has been investigated both at different regions along the Mo and the S edge and on the basal plane as a reference.

Table 7.1: Benzene adsorption sites

	Configuration[a]					
	a	b	c	d	e	f
	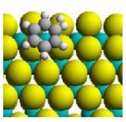	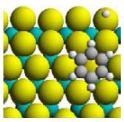	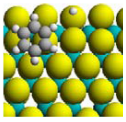	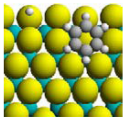	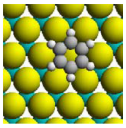	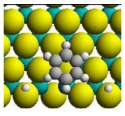
H coverage [%]	25	25	25	25		50
ΔE_{ad} [eV]	-0.14	-0.17	-0.16	-0.16	-0.02	0.00

[a] Configurations a–d is at the Mo ($10\bar{1}0$) edge, configuration e is on the basalplane (0001), and configuration f is at the S ($\bar{1}010$) edge.

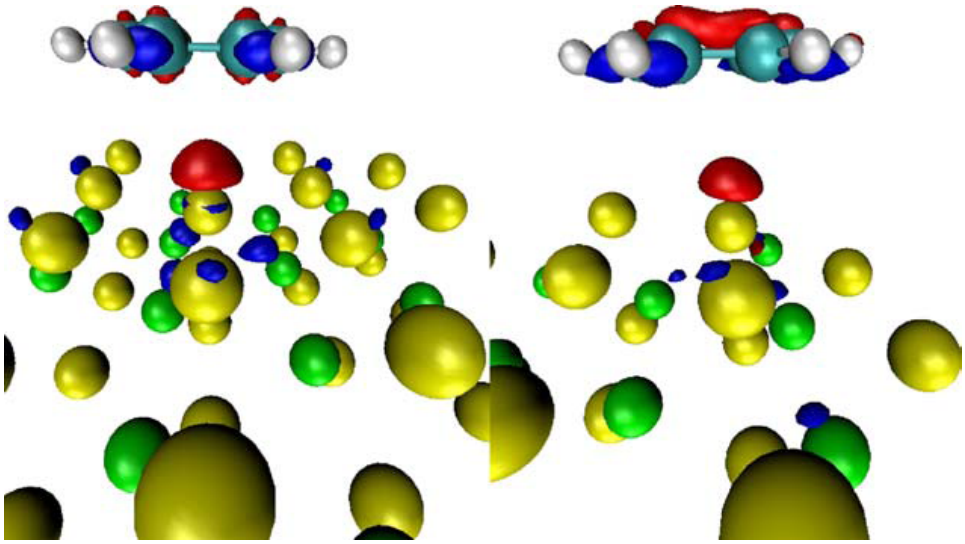

Figure 7.2: Benzene electron–density difference plot. **Left:** Benzene on the basal plane. **Right:** Benzene at the Mo $(10\bar{1}0)$ edge. Color code: Depletion of electron density (red) , increase in the electron density (blue) plotted at a contour value of -0.003$e^3/\mathring{A}$ and +0.003$e^3/\mathring{A}$, respectively.

7.3.1 Mo edge

Benzene adsorption at the Mo edge has been investigated with a S coverage corresponding to HDS conditions and a H coverage of 25%. The H coverage chosen is below the 50% H coverage at equilibrium in order to investigate the influence of the distance between the adsorbed molecule and the H atom. The brim sites, which have been shown to be able to participate in hydrogenation [108, 50] (see chapter 6) are positioned close to the front row S atoms and adsorption on these sites is also investigated. The adsorption configurations at the Mo edge can be seen in Tab. 7.1. The adsorption energy at the Mo edge is slightly exothermic being similar for all configurations, while adsorption on the basal plane is thermoneutral as shown in configuration e in Tab. 7.1. The exchange correlation functional used does not take van der Waals interactions into account and the difference in adsorption energies is therefore only related to chemisorption.

The changes in electron density upon benzene adsorption are somewhat larger at the Mo edge than on the basal plane (Fig. 7.2) indicating that the adsorption energy on the Mo edge is due to chemisorption. Adsorption at the edge or on the basal plane results in a lowering of the density directly below the center of the benzene ring. This could be an orthogonalization hole similar to what has been observed for e.g H_2 [206]. The larger change in electron density combined with the stronger binding energy on the edge means that there is a preference for the benzene molecule to adsorb at

the Mo edge rather than on the basal plane. Furthermore, we have tested whether hydrogenation of benzene can stabilize the adsorption, and we find that hydrogenation makes the adsorption energy endothermic.

7.3.2 S edge

Benzene adsorption at the S edge has been investigated with H and S coverages corresponding to HDS conditions and the S edge has been activated by the creation of a single vacancy. Benzene adsorption at the S edge has been investigated at a site next to the vacancy, as shown in configuration f Tab. 7.1. Only one adsorption site has been investigated since the benzene adsorption energy is thermoneutral at the vacancy site, which is the chemical most reactive site, because it is not covered by H and has an undercoordinated Mo atom. It is therefore presently assumed that the adsorption will not become more exothermic by moving the benzene molecule away from the vacancy. The adsorption energy at the S edge (configuration f) is similar to the adsorption energy on the basal plane (configuration e), indicating that there is no preference for the benzene to move from the Mo edge to the S edge. Thus, we can conclude that benzene does not adsorb at the S edge. This indicates that the S edge is not important for hydrogenation as benzene inhibits this reaction.

7.4 Pyridine and Pyridinium ion

Adsorption of pyridine and the formation of a pyridinium ion have been investigated at both the Mo edge and the S edge and as reference also on the basal plane.

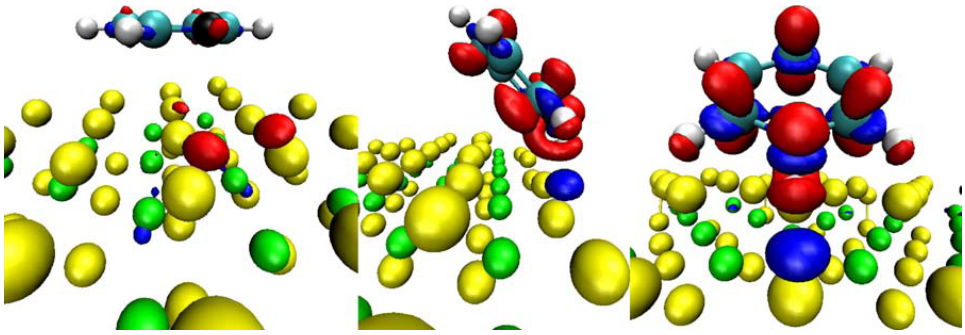

Figure 7.3: Pyridine and pyridinium ion electron–density difference plot. **Left:** Pyridine on basal plane. **Middle:** Sideview of pyridinium ion at the Mo edge. **Right:** Frontview of pyridinium ion at the Mo edge. Color code: Depletion of electron density (red), increase in the electron density (blue) plotted at a contour value of -0.03$e^3/\AA$ and +0.03$e^3/\AA$, respectively.

Table 7.2: Mo (10$\bar{1}$0) edge and basalplane pyridine and pyridinium ion adsorption sites

	Configuration[a]					
	a	b	c	d	e	f
	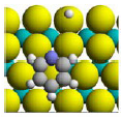	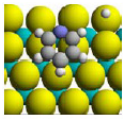	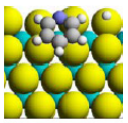	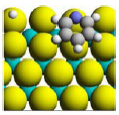	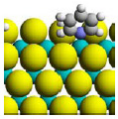	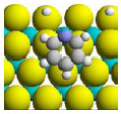
H coverage [%]	25	25	25	25	50	50
ΔE_{ad} [eV]	-0.12	-0.08	-0.09	-0.08	-0.09	-0.03
	Configuration[a]					
	g	h	i	j	k	l
	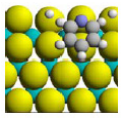	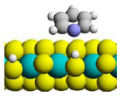	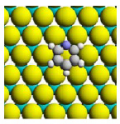	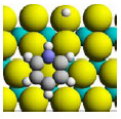	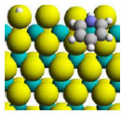	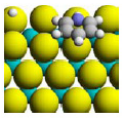
H coverage [%]	50	50		25		50
ΔE_{ad} [eV]	-0.01	-0.11	-0.03	-0.40[b]	-0.45 [b]	-0.59[b]

[a] Configurations a–h is pyridine at the Mo (10$\bar{1}$0) edge, configuration i is pyridine on the basalplane (0001), and configuration j–k is the pyridinium ion at the Mo (10$\bar{1}$0) edge.

[b] ΔE_{ad} is calculated as $\Delta E_{ad} = E_{\text{S-*-pyridinium ion}} - E_{\text{HS-*}} - E_{\text{Pyridine(g)}}$

7.4.1 Mo edge

Pyridine adsorption at the Mo edge has been investigated with S coverage corresponding to HDS conditions, i.e. 50% S coverage with 25 or 50% H coverages. The formation of pyridinium ions has been investigated with 25% H coverage, which corresponds to a transfer of a proton to the pyridine

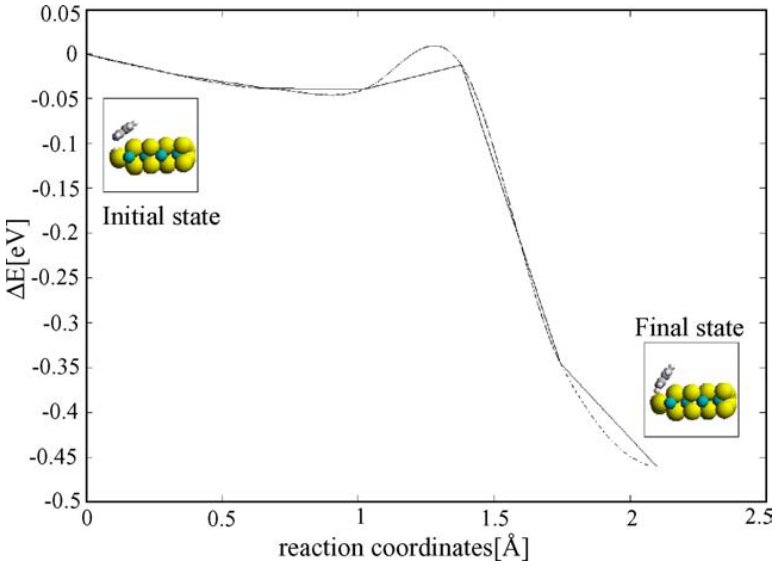

Figure 7.4: The energy barrier for creating a pyridinium ion. The straight line connects the individual NEB Images and the curved line is splines fitted to the forces on the individual images.

molecule from the edge. The adsorption configurations of pyridine at the Mo edge (configurations a–h) and basal plane (configuration i) can be seen in Tab. 7.2. It is seen that the adsorption energies are slightly exothermic on the edge and more exothermic than on the basal plane where it is almost thermoneutral. Under HDS conditions, there is adsorbed hydrogen in form of SH groups in the vicinity of the pyridine. That allows a proton to be transferred from the neighboring SH group to the pyridine molecule, resulting in the formation of a pyridinium ion. The significant exothermic energies for pyridinium ions (configurations j-l in Tab. 7.2) show that pyridinium ions are very stable at the Mo edge. The adsorption energies become approximately 0.4eV more exothermic than for pyridine itself. The barrier for the proton transfer has also been calculated and the result is shown in Fig. 7.4. The H transfer reaction is apparently non–activated, suggesting that pyridine will form pyridinium ions readily upon adsorption at the Mo edge. The electron density difference plots of pyridine and the pyridinium ion adsorbed at the Mo edge and basal plane (Fig. 7.3) show a more pronounced change in the electron density when the adsorption occurs at the edge. The change in electron density is also significantly larger than found for benzene (note that the contour value is a factor of 10 larger than the one used in the benzene density). Most importantly it is also seen that as H^+ is transferred from the catalyst to pyridine, some electron density is shifted to the catalyst, which, indicates the formation of a pyridinium ion–like species.

7.4.2 S edge

Table 7.3: S ($\bar{1}010$) edge pyridine and pyridinium ion adsorption sites

	Configuration[a]			
	a	b	c	d
	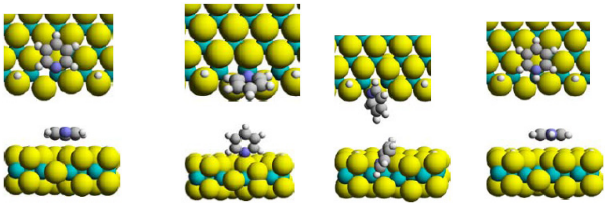			
H coverage [%]	25	25	25	25
ΔE_{ad} [eV]	-0.02	-0.05	-0.28	0.17[b]

[a] Configurations a–c is at the S ($\bar{1}010$) edge with a vacancy and configuration d is the pyridinium ion at the S ($\bar{1}010$) edge with a vacancy.
[b] ΔE_{ad} is calculated as $\Delta E_{ad} = E_{\text{S-*-pyridinium ion}} - E_{\text{HS-*}} - E_{\text{Pyridine(g)}}$

Pyridine adsorption at the S edge has been investigated with H and S coverage corresponding to HDS conditions and as for the benzene study, the S edge has been activated by the creation of a single vacancy. Such a vacancy is likely to be involved in the DDS pathway and the present calculations, therefore, also allow us to get insight into poisoning effects of this route. The adsorption configurations are shown in configurations a-c in Tab. 7.3. Pyridine binds strongest when the N atom is positioned in the vacancy, as seen in configuration c and less strongly when the adsorption configurations are similar to those at the Mo edge, as in configurations a and b. The observation that pyridine binds strongly to the vacancy is in agreement with the observation that the DDS route is poisoned by basic N compounds [69]. In configuration d, a H atom is added to the pyridine making the adsorption energy endothermic. The adsorption at the S edge is less exothermic than at the Mo edge except for configuration c where pyridine is adsorbed in the vacancy. Pyridine in the vacancy is, on the other hand, less exothermic than the adsorption energies of pyridinium ions on the Mo edge (configuration j–l in Tab. 7.2). The edge preference follows the same trend as for benzene adsorption, with the difference of being more pronounced for pyridine. The reason why H does not stabilize pyridine as pyridinium at the S edge could be related to the S edge SH groups being less acidic than SH groups at the Mo edge. This is reflected by a stronger binding energy at the S edge, -0.6eV at the S edge compared to -0.4eV at the Mo edge.

7.5 H_2S

H_2S is generally not considered to be a significant inhibitor for hydrogenation and should thus adsorb much weaker than benzene and pyridine on the hydrogenation site. Studies of the H_2S adsorption therefore offer a way to supplement the above investigations. H_2S adsorption has therefore also been investigated at both the S and Mo edges.

Table 7.4: H_2S adsorption sites at the Mo edge and the S edge

	Configuration[a]				
	a	b	c	d	e
	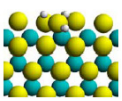	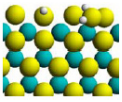	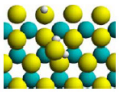	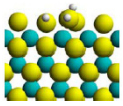	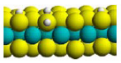
H coverage [%]	25	25	25	25	50
ΔE_{ad} [eV]	0.00	0.00	-0.06	-0.16	-0.12

[a] Configurations a–d are at the Mo $(10\bar{1}0)$ edge, Configuration e is a vacancy site at the S edge.

7.5.1 Mo edge

H_2S adsorption at the Mo edge has been investigated with a S coverage corresponding to HDS conditions and with a 25% H coverage. The lower than equilibrium H coverage is again chosen in order to investigate the influence of the distance between the adsorbed molecule and H. The adsorption configurations of H_2S at the Mo edge are shown in Tab. 7.4(a-d). Adsorption configuration d where H_2S is located next to the SH group is found to be slightly exothermic (-0.16eV), with approximately the same adsorption energy as benzene at the Mo edge (see Tab. 7.1). It should, however, be stressed that the van der Waals part of the adsorption energy for molecules with π systems is generally larger than for small molecules like H_2S. The adsorption of benzene and pyridine at the Mo edge is therefore expected to be stronger than H_2S.

7.5.2 S edge

H_2S adsorption at the S edge has been investigated at the S edge with H and S coverages corresponding to HDS conditions, where the S edge is again activated by the creation of one vacancy. The adsorption has been investigated at the vacancy as shown in configuration e in Tab. 7.4. The adsorption energy is exothermic (-0.12eV), which is similar to that on the Mo edge. The adsorption of H_2S is, therefore, equally likely at both edges. The dissociative chemisorption of H_2S at the vacancy site was found to be highly exothermic (-1.69eV see Sec. 6.2), and it is suggested that this is the

reason why H_2S inhibits the DDS pathway.

7.6 Discussion

Recent STM and DFT results have indicated that sites that are quite different from vacancies might be involved in HYD, namely, the metallic like brim sites located adjacent to the edges [50, 108, 107, 105]. The involvement of such sites has also been proposed to be consistent with the different observed inhibition effects [207]. In chapter 6 we presented the DDS and HYD pathways for HDS of thiophene and we found that the brim sites are well suited for hydrogenation. The present results have confirmed these finding and have provided additional insight into the nature of the inhibiting effects. It is presently observed that the availability of hydrogen at the catalyst surface plays an essential role in the poisoning by basic nitrogen compounds like pyridine. Pyridine reacts with hydrogen and forms the pyridinium ion and this stabilizes its adsorption. This process is favored at the Mo edge. Pyridinium ions were previously observed in IR experiments [204] and our findings substantiate the proposal that SH groups are involved in the pyridinium ion formation. It is interesting to note that the present results show that the formation of pyridinium ions is expected to occur predominantly at the Mo edge. Without the formation of pyridinium ions benzene would have been a stronger inhibitor than pyridine since its adsorption is stronger. However, due to the influence of hydrogen, pyridine becomes a much stronger poison. In this context, it is important that hydrogen binds less strongly at the Mo edge as compared to the S edge and, therefore, can be easily transferred to the pyridine molecule. This result confirms the results in Sec. 6.2 showing that the hydrogenation occurs at the Mo edge brim sites. In addition, both benzene and pyridine/pyridinium ions preferably adsorb at the Mo edge, underpinning that the active site for hydrogenation is located at the Mo edge. This is substantiated by the adsorption study of H_2S since H_2S adsorbs weakly in agreement with the very weak poisoning of the HYD pathway. Benzene is found to be less strongly bound than the pyridinium ion, which explains the less poisonous effect of benzene compared to pyridine.

Inhibition of hydrogenation reactions by pyridine is not only due to blocking. When it is protonated it also uses H from the Brønsted acid sites, thereby reducing the number of H atoms available for hydrogenation. The observation that heavier molecules, like quinolines and acridines are stronger poisons than pyridine [169, 170], can be explained by two effects. Firstly, the van der Waals interaction increases for molecules with more π systems [208]. The second and probably more important effect is that the inhibition by basic nitrogen compounds increases with higher proton affinity as found in experimental studies [169, 170]. The present study has shown that there is no significant barrier for proton transfer from the SH groups to pyridine

at the Mo edge. Assuming that this is also the case for larger molecules than pyridine, means that the proton transfer will only be equilibrium limited. It is therefore reasonable to expect that the gas phase proton affinity correlates quite well with the inhibitor strength because a similar proton transfer process is taking place on the catalyst.
While the present investigation has mainly focused on the poisoning of the HYD pathway several of the results also provide insight into the poisoning of the DDS pathway. For example, it is seen that pyridine adsorbs quite strongly in a vacancy site at the S edge. This may be the origin of the poisoning effects by N compounds of the DDS pathway [69, 168].

7.7 Conclusion

Detailed understanding of the inhibition mechanism of the HYD pathway has been quite difficult to obtain due to the lack of data on the nature of the active sites. We have used DFT to investigate the adsorption of some key model inhibitors at sites which have been found to be the active sites in HDS of thiophene (see Chapter 6). It is seen that the poisoning of the HYD route occurs quite differently from the most commonly accepted proposals in the literature. For example, it is seen that the inhibiting effect by aromatics is not due to the interactions with highly uncoordinated vacancies (like the naked Mo edges) but rather with the Mo edge brim sites which are present at the Mo edge with fully coordinated molybdenum atoms. The π–bonding to such sites explains the poisoning by aromatics. This bonding is not much affected by substituents in DBT and this explains why the HYD route is more favored for refractory molecules than the DDS route. The present results show that the fully coordinated brim sites bind H_2S very weakly. Thus, the lack of significant inhibition by H_2S, which has intrigued researchers for decades, can readily be explained. The strong poisoning by pyridine is observed to be due to an increase in adsorption energy upon protonation of the pyridine molecule. The proton donor is a neighboring SH Brønsted acid site located at the Mo edge. The pyridine to pyridinium ion reaction is found to be non–activated. Both benzene and pyridine prefer to adsorb at the Mo edge and both act as poisons for the hydrogenation pathway, supporting the conclusion that the hydrogenation site is located at the Mo edge. This is also supported by the low energy barrier of hydrogenation found in Sec. 6.2. The present results also show that pyridine will poison vacancy sites involved in the direct desulfurization path. In this case, the poisoning occurs via direct coordination and without pyridinium ion formation.
In the future, the present studies should be extended to include promoted systems. It would for instance be very interesting to extend the study to CoMoS, since the CoMoS ($\bar{1}010$) edge has been found to be able to hydrogenate thiophene (Sec. 6.3). DFT studies of the HDN reaction like those in reference [209,210] may also provide insight relevant for an understanding of

the inhibition by nitrogen compounds since the additional H_2 consumption by HDN may also be of importance.

Chapter 8

Influence of vdW forces on adsorption energies

Compounds like benzene, thiophene, and dibenzothiophene have in a series of studies been found to bind quite weakly to the edge structures of MoS_2 and WS_2 [192, 189, 211, 212] unless multiple vacancies have been formed [192,136]. This is also the case at the equilibrium edge configurations as we have seen in chapter 6 and chapter 7 where we attributed the weak binding to the lack of van der Waals interaction in the GGA exchange-correlation approximation. Thus, it is problematic to predict the coverage of the main reactants in HDS catalysis, making it difficult to construct micro-kinetic models for HDS. Even simple analysis of inhibition based on the adsorption energies of different inhibitors and reactants may be qualitatively wrong due to the neglect of vdW interactions.

However, recent developments in exchange-correlation functionals [25] have shown promising results for adsorption and binding of systems dominated by vdW interactions [25, 208, 213, 214]. The scheme presented by [25] have been implemented in the real space code GPAW as described in chapter 2.

In the present chapter we investigate the adsorption of thiophene and butadiene on the basal plane of MoS_2 using the novel exchange correlation functional, vdW-DF [25]. The adsorption energies of thiophene and butadiene on the basal plane of MoS_2 are found to be dominated by vdW interactions and the theoretical predictions agree with well defined ultra high vacuum surface science experimental results [158]. The present results indicate that the vdW interaction for adsorption on MoS_2-based systems is well described by the vdW-DF functional. The vdW forces are found to be of such size that they can not without caution be neglected when calculating adsorption energies for systems with delocalized electrons.

8.1 Calculational details

The general computational details (Sec. 4.2) are used except for the following changes. A slab model is used to investigate the basal plane (0001) of MoS_2. The supercell has 4 MoS_2 units in the x- and y-direction. The slabs are separated by 21.82 in the z-direction. This model represents the basal plane of MoS_2 single crystal where the effect of the second layer of MoS_2 is assumed to be small, which has been shown to be a reasonable approximation for graphite [208]. DACAPO is used to perform the DFT calculations [29,19]. The Brillouin zone is sampled using a Monkhorst-Pack k-point set [34] containing 4 k-points in the x- and y-direction and 1 k-point in z-direction. A plane-wave cutoff of 30 Rydberg and a density wave cutoff of 60 Rydberg are employed using the double-grid technique [86]. The convergence criterion for the atomic relaxation is that the maximum force on one atom should be smaller than 0.01eV/Å.

The exchange correlation functional RPBE is used [19] for structure optimization. The binding curves have been constructed using the vdW-DF functional [25] implemented as described in chapter 2. The E_{vdW-DF} is calculated as described in chapter 2 on the density grid with 0.11Å between points and for densities above $0.0001/a_0^3$. The binding site and orientation of the molecule have been identified by constrained minimization fixing the slab and the z coordinate of the molecule or free minimization of the molecule fixing the slab. The binding curves have been calculated by moving the molecule in the z direction while at the same time fixing the geometry of the molecule and the slab.

8.2 Results and discussion

We have investigated the adsorption of thiophene and butadiene. The adsorption of these molecules have previously been investigated in a well defined surface science experiment which found that the binding on the basal plane is weak, with thiophene adsorption energy of -0.42eV and butadiene adsorption energy of -0.37eV.

8.2.1 Thiophene

Table 8.1: Thiophene adsorption

	a)	b)
Front	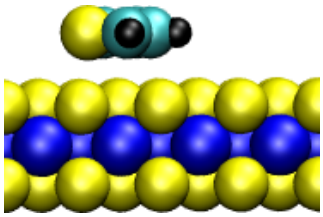	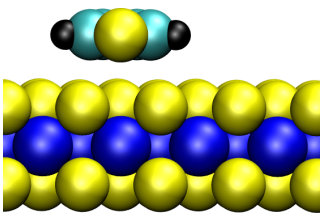
Top	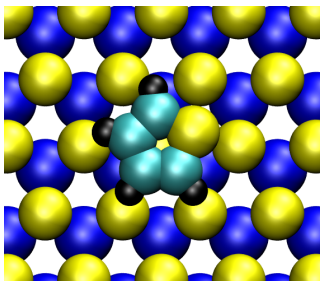	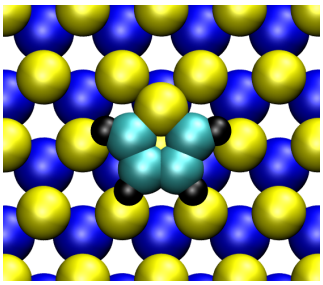
Binding	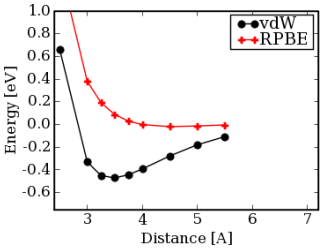	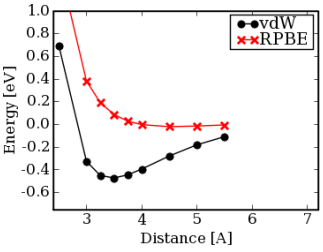
Exp [eV]	-0.42 [a]	
RPBE [eV]	-0.02	-0.02
vdW [eV]	-0.47	-0.47

[a] Reference [158]

The adsorption configurations (a,b in Tab. 8.1) of thiophene have very similar binding energies and the binding curves are also similar. There is little or no chemical bonding and the entire bond is given by vdW interaction. The adsorption energy is -0.47eV which compares well with the experimental adsorption energy of -0.42eV.

8.2.2 Butadiene

Table 8.2: Butadiene adsorption, The abscissa in the binding curves is the distance from the center of mass of butadiene to the z position of the top sulfur layer.

	a)	b)	c)
Front / Top	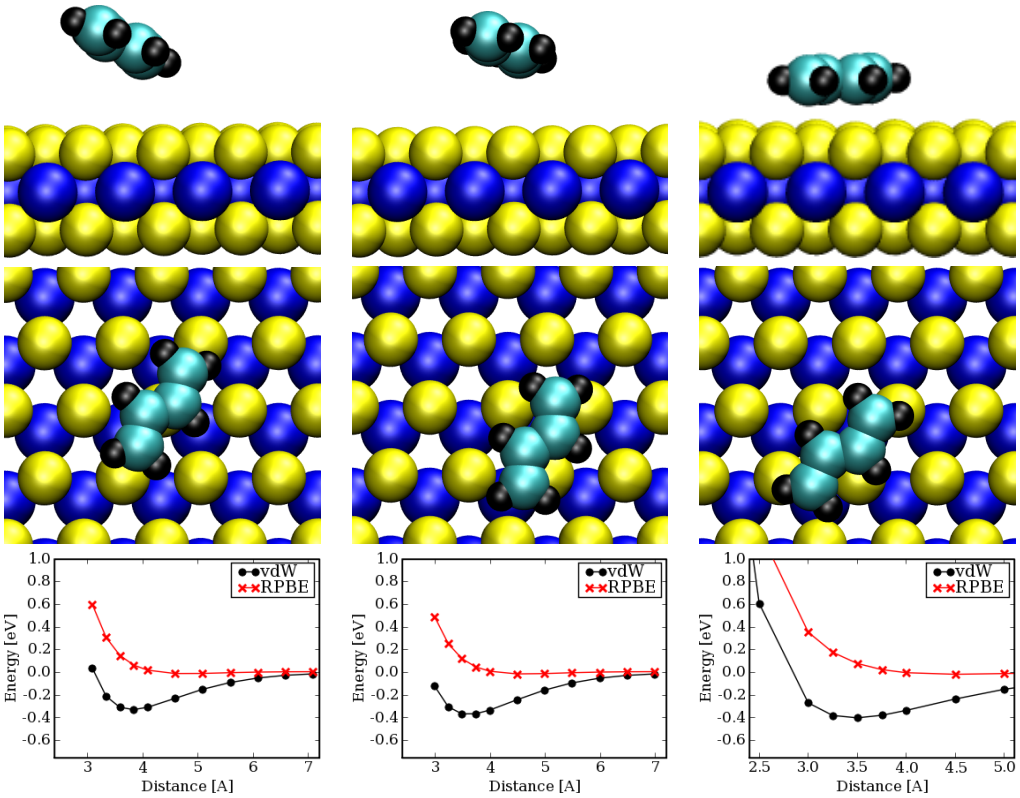		
Binding Exp [eV]		-0.37[a]	
RPBE [eV]	-0.01	-0.01	-0.01
vdW [eV]	-0.33	-0.36	-0.40

[a] Reference [158]

Three different butadiene adsorption configurations (seen in Tab. 8.2) have been investigated and the binding curves can be seen in Tab. 8.2. The binding energies for the different adsorption configurations are very similar and the maximum binding energy is -0.40eV, The binding energies are as for thiophene dominated by vdW interactions. The agreement between the experimental binding energy of -0.37eV and the calculated binding energy is high.

8.3 Discussion

The overall picture is that the adsorption energy is highest for thiophene followed by butadiene and the agreement between experiment and theory

is good. For thiophene and butadiene the calculated binding energies are approximately 0.05eV stronger than the experimental values. Furthermore, the difference between thiophene and butadiene adsorption energy is 0.07eV which is in very good agreement with the experimental difference of 0.05eV. The binding energy is to a high degree determined by the distance to the surface while different adsorption geometries introduce very small changes in the binding energy. The adsorption energies of both molecules are found to be due to vdW interactions while the chemisorption energies which are well described by RPBE show very little or no binding.
The relatively strong vdW binding energy of thiophene and butadiene could be due to the fact that these molecules have delocalized electrons because of the aromatic structure of thiophene and the conjugated double bonds in butadiene. The present results indicate that including vdW forces will significantly affect the adsorption energy and thereby the coverage of aromatic compounds on MoS_2 based catalysts. Increasing the adsorption energies by 0.5eV and possibly more for larger molecules will be of significant importance since molecules like thiophene and DBT have been found to make weak chemical bonds with the equilibrium edge structures and single vacancies on the equilibrium edges [215, 192, 211, 212].

8.4 Conclusion and outlook

We have calculated the adsorption energy of thiophene and butadiene on the basal plane of MoS_2 using the recently developed exchange correlation functional vdW-DF [25] and we find a high degree of agreement between experiment and theory. The binding energies of both molecules are found to be due to vdW interactions. The present results show that the vdW binding energy of thiophene and butadiene is -0.47eV and -0.40eV, respectively. This will influence the coverage of these species considerably and it is proposed that the van der Waals forces can not without caution be neglected when calculating adsorption energies of aromatic compounds on MoS_2. The high degree of agreement between theory and experiment shows that the vdW-DF functional is promising for accurately calculating adsorption energies.

Chapter 9

Designing new hydrogen evolution catalyst based on DFT

Design of new materials with certain properties using DFT requires that the material properties can be reliably predicted directly from DFT results. In the case of heterogeneous catalysis this does in practice mean that the activity of a given catalyst has to be linked to a key activity descriptor such as the adsorption energy. This is required since directly calculating barriers for a series of elementarily steps on a large number of test materials is not with the present computer power feasible.
Determining the key activity descriptors are often not an easy task as we have seen in chapter 6. The present chapter therefore focuses on a much simpler reaction than the HDS reaction of thiophene, namely the hydrogen evolution reaction. In the following chapter we will present a key descriptor for hydrogen evolution. This descriptor has successfully been used in a large scale computational screening study to investigate hydrogen evolution on transition metal alloys [3]. Using this approach a PtBi system was identified as a promising catalyst. However, PtBi is still relatively expensive thus in the following we calculate the descriptor on a series of non nobel transition metal sulfides which are considerably cheaper.

9.1 Transition metal sulfides in hydrogen evolution reactions

Hydrogen has been proposed as a future energy carrier [216]. One of the reasons for this is that the only product of hydrogen oxidation is water. Hydrogen is therefore, in principal CO_2 and emission neutral if produced in a sustainable fashion. Pt is today used as a catalyst for hydrogen evolution and hydrogen oxidation. Since Pt is rare and expensive alternative materials

are desired to catalyze these reactions. Nature is able to produce hydrogen at room temperature and atmospheric pressure using enzyme catalysis. Two enzymes which are able to produce hydrogen are nitrogenase and hydrogenase [217, 30]. The enzymes do not contain Pt but less expensive transition metal sulfides. Thus there is hope that hydrogen evolution catalysts based on non-precious metals exists.
The basic reactions, which occur under hydrogen evolution are listed below. The overall hydrogen evolution reaction can be seen in reaction 9.1, Where H^+ ions and electrons combine to from H_2.

$$2H^+ + 2e^- \rightarrow H_2 \tag{9.1}$$

The H^+ ion must be adsorbed to the catalyst which happens as in reaction 9.2

$$H^+ + e^- + {}^* \rightarrow H^* \tag{9.2}$$

The adsorbed H atom must finally be released as hydrogen through one of the two hydrogen evolution reactions seen in reaction 9.3 and reaction 9.4.

$$2H^* \rightarrow H_2 + 2^* \tag{9.3}$$

or

$$H^+ + e^- + H^* \rightarrow H_2 + * \tag{9.4}$$

9.1.1 The hydrogen evolution activity descriptor: $\Delta G_H \approxeq 0eV$

It was suggested by Parsons in 1958 [219] that the Gibbs free energy of hydrogen adsorption ΔG_H would be a descriptor for the hydrogen evolution activity, and that it should be approximately 0eV for a good catalyst. However, it has turned out to be very difficult to accurately measure ΔG_H, thus DFT is a very useful tool because calculating ΔG_H is a relatively simple task. In general the change in Gibbs free energy of a reaction is the lower bound on the energy barrier associated with the reaction. A necessary condition for reactions to take place at or close to room temperature is, therefore, that no reaction step can involve large changes in Gibbs free energy. This means that the hydrogen adsorption energy can not be too high, as on Ni and Mo (see figure 9.1), because that will make the hydrogen release reaction (reaction 9.3 or 9.4) slow. A very low hydrogen adsorption energy, as on gold (see figure 9.1), will on the other hand slow down the proton electron transfer step (reaction 9.2) because it will be thermodynamically uphill. Kinetics are, of course, also important since it can not be excluded that some of the involved reactions have additional energy barriers. The thermodynamical criterion that $\Delta G_H \approxeq 0$eV is therefore a necessary, but not a sufficient criteria for a catalyst to be a good catalyst.

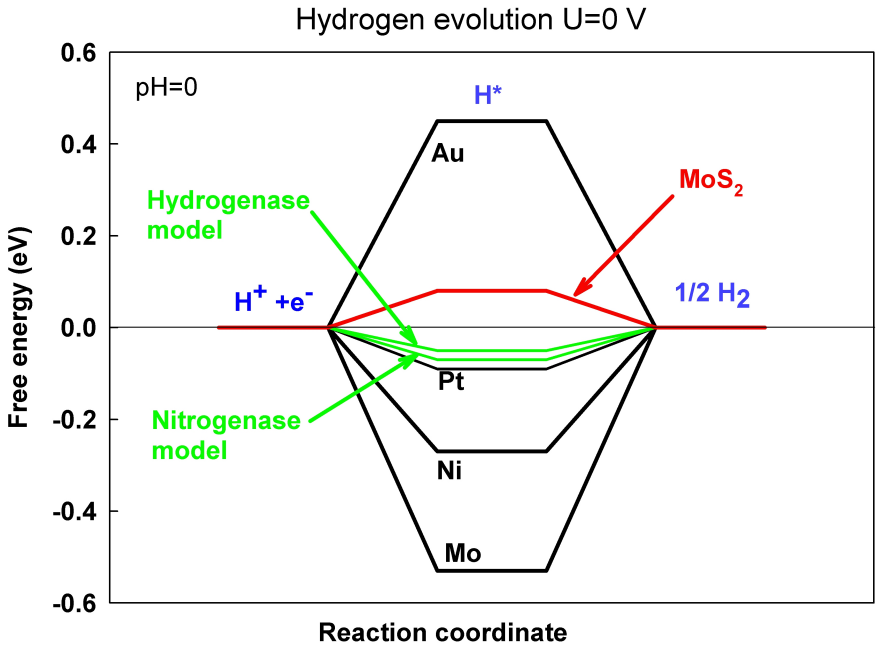

Figure 9.1: Calculated free energy diagram for hydrogen evolution at a potential U=0 relative to the standard hydrogen electrode. We have used the fact that the free energy of $H^+ + e^-$ is by definition the same as that of $^1/_2H_2$ at these standard conditions. The free energy of H atoms bound to different catalysts is then found by calculating the free energy with respect to molecular hydrogen including zero point energies and entropy terms. The comparison of different elemental metals is taken from [218]. The results for hydrogenase are from [217]. The results for nitrogenase are from [30] The included result for MoS_2 is the free energy required to increase the hydrogen coverage from 25% to 50% on the MoS_2 $(10\bar{1}0)$ edge. Adapted from [178].

9.1.2 Validation of the criterion

The validity of the criterion has been tested and documented in article [178]. This criterion has been shown to agree well with the high hydrogen evolution activity of Pt, nitrogenase and hydrogenase, (see figure 9.1). The criterion is thus a good descriptor of the hydrogen evolution activity and thus, it may be used to search for new hydrogen evolution catalyst.

9.2 Possible candidate catalysts for hydrogen evolution

9.2.1 Calculational details

We use the general calculational details described in Sec. 4.2 with the following changes. We use a 4x4 MeS_2 unit cell, with Me being either Mo or W. In the case of MoS_2 $(10\bar{1}0)$ edge we use a 4x6 unit cell. Furthermore, we use the RPBE exchange correlation functional in order to increase the accuracy of the binding energies of H [19]. ΔG_H is calculated in the following way.

$$\Delta G_H = \Delta E_{ad} + \Delta E_{ZPE} - T\Delta S_{vib} \tag{9.5}$$

Where ΔE_{ad} is the energy of adsorption, ΔE_{ZPE} is the change in zero point energies, and ΔS_{vib} is the change in entropy. We neglect the PV term in the enthalpy which is on the order of 0.025eV for the gas phase and assume that the configurational and the surface vibrational entropy are small. This is reasonable at room temperature, for details see reference [178].

9.2.2 Promoted and non-promoted Mo and W sulfides

We calculate ΔG_H for Co promoted and non-promoted WS_2 and MoS_2, which are all known HDS catalyst. The choice of transition metal sulfides has been guided by the following considerations. First, all sulfides look promising since the active centers of nitrogenase and hydrogenase are sulfides. Secondly the stable edges of HDS catalysts have been established in connection with HDS catalysis. Finally synthesis routes for HDS catalysts exist in the HDS literature.
We have calculated the free energy of H adsorption over a wide range of S and H coverages at the S $(\bar{1}010)$ edge of WS_2, Co promoted WS_2, MoS_2, and CoMoS and on the Mo/W $(10\bar{1}0)$ edge of WS_2 and MoS_2. The choice of the relevant edge configurations are based on the chemical potential of hydrogen and sulfur at the experimental sulfiding conditions using the thermodynamic model presented in Sec. 2.2. The structure and the corresponding differential free energies of H adsorption can be seen in Fig. 9.2.
The results indicate that non-promoted WS_2 and MoS_2 nanoparticles should be reasonably good hydrogen evolution catalysts since both systems have

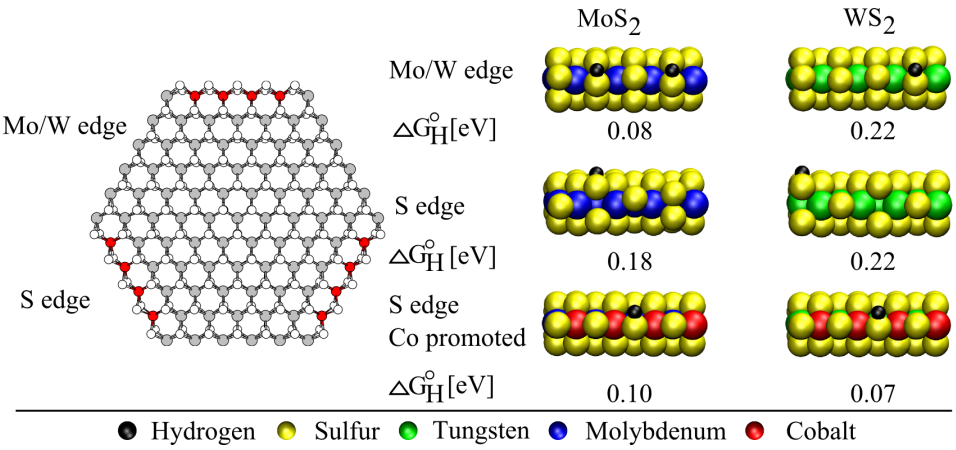

Figure 9.2: **Left**: Ball model of a MoS_2 particle exposing both S edge and Mo/W edge. **Right**: Differential free energies of hydrogen adsorption. The atoms has the following color scheme: yellow is sulfur; blue is molybdenum; green is tungsten; red is cobalt; black is hydrogen.

free energies of adsorption close to zero. The active site for hydrogen evolution on MoS_2 is expected to be present at the Mo edge ($\Delta G_H = 0.08eV$) rather than at the S edge ($\Delta G_H = 0.18eV$). The picture is different for WS_2 since both the W and the S edge have similar adsorption energies ($\Delta G_H = 0.22eV$). Thus there will be no difference in hydrogen evolution activity on the W or the S edge. However, WS_2 with $\Delta G_H = 0.22eV$ is expected to be less active compared to MoS_2 with $\Delta G_H = 0.08eV$.
Co promotion increases the activity of both WS_2 and MoS_2 because it reduces the free energy of hydrogen adsorption. In the case of MoS_2 the promoted S edge adsorbs H with $\Delta G_H = 0.10eV$ which is very similar to the free energy of hydrogen adsorption at the Mo edge of MoS_2 ($\Delta G_H = 0.08eV$). Therefore, promotion of MoS_2 increases the number of sites with the same activity. Promoting WS_2 with Co reduces ΔG_H to 0.07eV. Thus, promoting WS_2 leads to the creation of new sites with a higher activity than without promotion. Under the assumption that the size and shape of Co promoted MoS_2 and Co promoted WS_2 are identical Co promoted MoS_2 (CoMoS) should be the best catalyst since it would have active sites on both edges and therefore a higher total number of active sites.

9.2.3 Experimental testing

The WS_2 and MoS_2-based catalysts were synthesized directly onto a Toray carbon paper support. The area of the catalyst was measured by electrochemical oxidation and the hydrogen evolution activity was normalized with respect to the area based on charge (See paper IX). Ideally the activity should be normalized with respect to the number and types of active sites

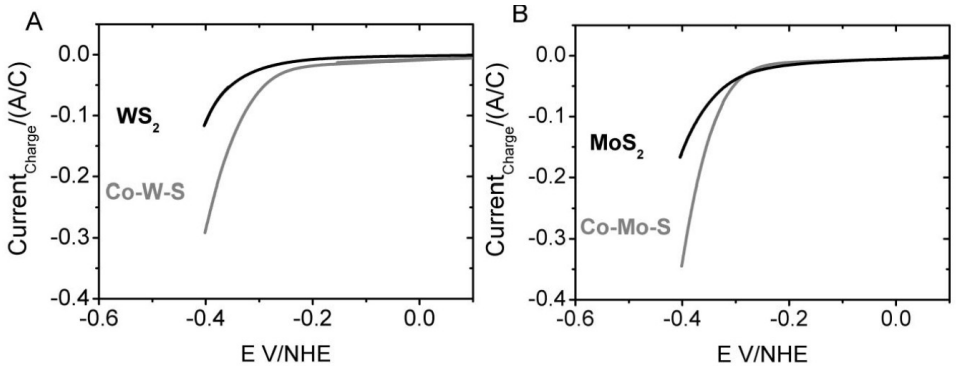

Figure 9.3: Polarization curves (i.e. current as a function of potential) where the currents have been normalized with the total area.**A**:WS_2 based catalysts **B**: MoS_2 based catalysts

but such measurements are not easily carried out. The hydrogen evolution activity is in general good for all sulfides as predicted by DFT. MoS_2 have previously been reported by Sobczynski to be as good a hydrogen evolution catalysts as Pt [220]. However, this was not based on a per area activity or on measuring the overpotential, but merely on H_2 production and the high amount of H_2 production could have been due to differences in dispersion. The general trend observed in the present study is that Co promotion increases the activity of the catalyst (Fig. 9.3). According to DFT this is due to a larger number of active sites on MoS_2 while for WS_2 the increased activity is explained by the appearance of new and more active sites.

9.3 Discussion and conclusion

Efficient search for new catalysts requires that a key descriptor is determined. In the case of hydrogen evolution catalysis, $\Delta G_H \approx 0.0eV$ has been presented by Parsons [219] and we have validated that for a series of well known hydrogen evolution catalysts it is indeed a good descriptor. A recent study has shown that it is possible to find new promising hydrogen evolution catalysts by computational screening of transition metal alloys. In the present chapter we have chosen to investigate sulfides as hydrogen evolution catalyst. Studying sulfides is more complicated than transition metal surface alloys, due to the complex structures of sulfides. We have, therefore, inspired by the nitrogenase FeMo-cofactor and HDS catalysis chosen to look at promoted MoS_2 and WS_2. These sulfides turn out to have very promising descriptors with regard to hydrogen evolution catalysis. Experimental testing confirms this along with the enhancing effect of promotion.
In the present chapter we have only tested a handful of transition metal sulfides for hydrogen evolution activity. It is evident from the present limited screening study that it is possible to identify new hydrogen evolution

catalysts, thus one would expect that an extended study could be worthwhile. To perform DFT based screening on the same scale as for transition metal alloys where over 700 bimetallic alloys were investigated would require considerable amount of computer power. Sulfides are demanding in terms of computer power since the required super cells are usually larger than the ones used for metals. Also one must calculate on the order of 10 different edge configurations for each sulfide to determine which structure is likely to be present. In order to save computer time future screening studies could possibly benefit from scaling relations like the ones presented in Sec. 3.4 which could be used to determine hydrogen adsorption energies directly from S adsorption energies.

Chapter 10

Summary and outlook

In this thesis several topics related to hydrodesulfurization catalysis have been addressed using DFT. The long term goal of designing new HDS catalysts based on first principles is approached from two different angles. The first one investigates correlations in adsorption energies on both transition metal and more complicated structures like oxides, nitrides and sulfides. This approach reveals that linear relations exist which could prove useful in future design studies.

The other approach towards design of new HDS catalysts investigates important aspects of HDS catalysis such as structure, reactivity, and inhibition. Ni and Co promotion of MoS_2 are found to change both the morphology and the electronic structure of the catalytic nanoparticles. HDS of thiophene has been investigated on Co promoted and non-promoted MoS_2 and care is taken to investigate active sites at the stable edge configurations at HDS conditions. On the non-promoted MoS_2 particle two different active sites have been identified. Interplay between the two stable edges on non-promoted MoS_2 is found to be important due to the high hydrogenation activity of the Mo edge and the high SC-scission activity of the S edge vacancy site. Co promotion increases the hydrogenation activity of the S edge. Inhibition by pyridine of the hydrogenation pathway is seen to be due to the formation of strongly bound pyridinium ions and the consumption of hydrogen. In order to improve the accuracy of calculated adsorption energies the vdW-DF functional has been implemented and it is found that vdW forces give an important contribution to the adsorption energy of key molecules on the basal plane of MoS_2. Thus proposing that vdW forces should be included in order to obtain accurate adsorption energies at the active sites on the edges.

Finally a limited screening study for new hydrogen evolution catalyst has been carried out identifying Co promoted WS_2 and MoS_2 as promising hydrogen evolution catalysts. The theoretical predictions have been confirmed by experiments.

Outlook

The present study shows that HDS catalysis is a complicated interplay between edges, pathways, inhibitors and reaction conditions. A micro-kinetic model could be a very useful tool to identify the important parameters determining the overall reactivity. This would require accurate adsorption energies of reactants, intermediates and products at the active sites. Thus, it would be interesting to apply the vdW-DF functional in order to include vdW forces in the adsorption energies. A self-consistent implementation of the vdW-DF functional would simplify such a study since it would allow evaluation of the forces.
Further investigations of correlations in adsorption energies on different transition metal sulfides could prove useful for future investigation of HDS catalysis. The possibility of extending the correlations to activation energies would also be an interesting topic to investigate.
One thing is to find a new and better HDS catalyst using DFT another and not less complicated task is to synthesize it. Rational routes to synthesis could be found using DFT where studies of support interactions could prove fruitful. Such investigation have been undertaken in a few studies [121, 122, 81] however much more is to be learned with regards to the influence of support interactions on morphology and reactivity.
The search for better hydrogen evolution catalyst is not finished with the present work since non of the identified catalysts can match Pt. However, the number of positive candidates among the small test set of sulfides is encouraging and does call for a broader screening study.

Bibliography

[1] http://www.imo.org/.

[2] W. Kohn. Nobel lecture: Electronic structure of matter-wave functions and density functionals. *Reviews Of Modern Physics*, 71(5):1253–1266, October 1999.

[3] J. Greeley, T. F. Jaramillo, J. Bonde, I. Chorkendorff, and J. K. Nørskov. Computational high-throughput screening of electrocatalytic materials for hydrogen evolution. *Nature Materials*, 5(11):909–913, November 2006.

[4] M. P. Andersson, T. Bligaard, A. Kustov, K. E. Larsen, J. Greeley, T. Johannessen, C. H. Christensen, and J. K. Nørskov. Toward computational screening in heterogeneous catalysis: Pareto-optimal methanation catalysts. *Journal Of Catalysis*, 239(2):501–506, April 2006.

[5] J. Sehested, K. E. Larsen, A. L. Kustov, A. M. Frey, T. Johannessen, T. Bligaard, M. P. Andersson, J. K. Nørskov, and C. H. Christensen. Discovery of technical methanation catalysts based on computational screening. *Topics In Catalysis*, 45(1-4):9–13, August 2007.

[6] Ture Rønved Munter. *Towards Catalysis Informatics - Materials design using Density Functional Theory*. PhD thesis, Center for Atomic-scale Materials Dhysics Department of Physics Technical University of Denmark, 2008.

[7] R. A. Van santen and M. Neurock. Concepts in theoretical heterogeneous catalytic reactivity. *Catalysis Reviews-Science And Engineering*, 37(4):557–698, 1995.

[8] J. K. Nørskov. Chemisorption on metal-surfaces. *Reports On Progress In Physics*, 53(10):1253–1295, October 1990.

[9] B. Hammer and J. K. Nørskov. Theoretical surface science and catalysis–calculations and concepts. In Bruce C. Gates and Helmut

Knozinger, editors, *Impact of Surface Science on Catalysis*, volume Volume 45, pages 71–129. Academic Press, 2000.

[10] R. A. Van santen and M. Neurock. *Molecular Heterogeneous Catalysis: A conceptual and computational approach*. Wiley-VCH, 2006.

[11] D.P. Woodruff, A. Nilsson, L.G. Moody Petersson, A.C. Luntz, J.K. Nørskov T. Bligaard, S.F. Bent, P. Strasser, H. Ogasawara, and G.E. Brown. *Chemical bonding at surfaces and interfaces*. Elsevier, 2008.

[12] I. Chorkendorff and J. W. Niemantsverdriet. *Concepts of Modern Catalysis and Kinetics*. Wiley Publisher, 2003.

[13] J. A. Pople. Nobel Lecture: Quantum chemical models. *Reviews of Modern Physics*, 71:1267–1274, 1999.

[14] Robert G. Parr and Weitao Yang. *Density-Functional Theory of Atoms and Molecules*. Oxford University Press, Oxford, 1989.

[15] Richard M. Martin. *Electronic Structure Basic Theory and Practical Methods*. Cambridge University Press, 2004.

[16] P. Hohenberg and W. Kohn. Inhomogeneous Electron Gas. *Physical Review*, 136(3B):B864, November 1964.

[17] W. Kohn and L. J. Sham. Self-consistent equations including exchange and correlation effects. *Physical Review*, 140(4A):1133–&, 1965.

[18] J. P. Perdew, J. A. Chevary, S. H. Vosko, K. A. Jackson, M. R. Pederson, D. J. Singh, and C. Fiolhais. Atoms, molecules, solids, and surfaces: Applications of the generalized gradient approximation for exchange and correlation. *Physical Review B*, 46(11):6671, 1992.

[19] B. Hammer, L. B. Hansen, and J. K. Nørskov. Improved adsorption energetics within density-functional theory using revised Perdew-Burke-Ernzerhof functionals. *Physical Review B*, 59(11):7413, 1999.

[20] K. W. Jacobsen, J. K. Nørskov, and M. J. Puska. Interatomic interactions in the effective-medium theory. *Physical Review B*, 35(14):7423–7442, May 1987.

[21] D. M. Ceperley and B. J. Alder. Ground state of the electron gas by a stochastic method. *Physical Review Letters*, 45(7):566–569, 1980.

[22] S. H. Vosko, L. Wilk, and M. Nusair. Accurate spin-dependent electron liquid correlation energies for local spin-density calculations - a critical analysis. *Canadian Journal Of Physics*, 58(8):1200–1211, 1980.

[23] J. H. Perdew, K. Burke, and M. Ernzerhof. Generalized Gradient Approximation Made Simple. *Physical Review Letters*, 77(18):3865, 1996.

[24] Y. K. Zhang and W. T. Yang. Comment on "generalized gradient approximation made simple". *Physical Review Letters*, 80(4):890–890, January 1998.

[25] M. Dion, H. Rydberg, E. Schroder, D. C. Langreth, and B. I. Lundqvist. Van der waals density functional for general geometries. *Physical Review Letters*, 92(24):246401, June 2004.

[26] J. J. Mortensen, L. B. Hansen, and K. W. Jacobsen. Real-space grid implementation of the projector augmented wave method. *Physical Review B*, 71(3):035109, January 2005.

[27] M. M. Pant and A. K. Rajagopal. Theory of inhomogeneous magnetic electron gas. *Solid State Communications*, 10:1157–1160, 1972.

[28] U. von Barth and L. Hedin. A local exchange-correlation potential for the spin polarized case: I. *Journal of Physics C: Solid State Physics*, 5:1629–1642, 1972.

[29] S. R. Bahn and K. W. Jacobsen. An object-oriented scripting interface to a legacy electronic structure code. *Computing In Science & Engineering*, 4(3):56–66, May 2002.

[30] Berit Hinnemann. *Transition Metal Sulfides as Biological and Inorganic Catalysts*. PhD thesis, Center for Atomic-scale Materials Physics Department of Physics Technical University of Denmark, 2003.

[31] D. R. Hamann, M. Schlüter, and C. Chiang. Norm-conserving pseudopotentials. *Physical Review Letters*, 43(20):1494–1497, 1979.

[32] G. B. Bachelet, D. R. Hamann, and M. Schlüter. Pseudopotentials that work: From H to Pu. *Physical Review B*, 26(8):4199–4228, 1982.

[33] D. Vanderbilt. Soft self-consistent pseudopotentials in a generalized eigenvalue formalism. *Physical Review B*, 41(11):7892–7895, 1990.

[34] H. J. Monkhorst and J. D. Pack. Special points for Brillouin-zone integrations. *Physical Review B*, 13(12):5188–5192, 1976.

[35] D. J. Chadi and M. L. Cohen. Special points in the Brillouin zone. *Physical Review B*, 8(12):5747–5753, 1973.

[36] N. D. Mermin. Thermal properties of the inhomogeneous electron gas. *Physical Review*, 137(5A):A1441–A1443, 1965.

[37] R. P. Feynman. Forces in Molecules. *Physical Review*, 56:340–343, 1939.

[38] H. Jónsson, G. Mills, and K. W. Jacobsen. Nudged Elastic Band Method for Finding Minimum Energy Paths of Transitions. In *Proceedings*. Enrico Fermi Summer School 97, 1997.

[39] G. Henkelman, B. P. Uberuaga, and H. Jónsson. A climbing image nudged elastic band method for finding saddle points and minimum energy paths. *Journal of Chemical Physics*, 113(22):9901, 2000.

[40] J. V. Lauritsen. *Atomic-scale study of a hydrodesulfurization model catalyst*. PhD thesis, Department of physics and astronomy, University of Aarhus, 2002.

[41] J. Bardeen. Tunneling from a many-particle point of view. *Physical Review Letters*, 6(2):57–59, 1961.

[42] J. Tersoff and D. R. Hamann. Theory and Application for the Scanning Tunnelling Microscope. *Physical Review Letters*, 50(25):1998, 1983.

[43] J. Tersoff and D. R. Hamann. Theory of the scanning tunnelling microscope. *Physical Review B*, 31(2):801, 1985.

[44] C. J. Chen. Tunneling matrix elements in three-dimensional space: The derivative and the sum rule. *Physical Review B*, 42(14):8857–8841, 1990.

[45] S. Heinze, S. Blügel, R. Pascal, M. Bode, and R. Wiesendanger. Prediction of bias-voltage-dependent corrugation reversal for STM images of bcc (110) surfaces: W(110),Ta(110), and Fe(110). *Physical Review B*, 58(24):16432–16445, 1998.

[46] C. J. H. Jacobsen, N. Y. Topsøe, H. Topsøe, L. Kellberg, and H. J. Jakobsen. Quantitative ^{1}H MAS NMR Studies of Structurally Different OH Surface Groups on η-Al_2O_3 and Mo/η-Al_2O_3 Catalysts. *Journal of Catalysis*, 154:65–68, 1995.

[47] W. A. Hofer and J. Redinger. Scanning tunneling microscopy of binary alloys: first principles calculation of the current for PtX(100) surfaces. *Surface Science*, 447:51–61, 2000.

[48] M. L. Bocquet, J. Cerdà, and P. Sautet. Transformation of molecular oxygen on a platinum surface: A theoretical calculation of STM images. *Physical Review B*, 59(23):15437–15445, 1999.

[49] M. V. Bollinger. *Structure and electronic properties of MoS_2 and metallic nano-scale systems*. PhD thesis, Technical University of Denmark, September 2002.

[50] M. V. Bollinger, K. W. Jacobsen, and J. K. Nørskov. Atomic and electronic structure of MoS_2 nanoparticles. *Physical Review B*, 67:085410, 2003.

[51] K. Reuter and M. Scheffler. First-principles atomistic thermodynamics for oxidation catalysis: Surface phase diagrams and catalytically interesting regions. *Physical Review Letters*, 90(4):046103, January 2003.

[52] Y. Xu, W. A. Shelton, and W. F. Schneider. Thermodynamic equilibrium compositions, structures, and reaction energies of Pt_xO_y (x=1-3) clusters predicted from first principles. *Journal Of Physical Chemistry B*, 110(33):16591–16599, August 2006.

[53] B. Hammer and J. K. Nørskov. Why gold is the noblest of all the metals. *Nature*, 376(6537):238–240, July 1995.

[54] F. Abild-Pedersen, J. Greeley, and J. K. Nørskov. Understanding the effect of steps, strain, poisons, and alloying: Methane activation on Ni surfaces. *Catalysis Letters*, 105(1-2):9–13, November 2005.

[55] A. Ruban, B. Hammer, P. Stoltze, H. L. Skriver, and J. K. Nørskov. Surface electronic structure and reactivity of transition and noble metals. *Journal Of Molecular Catalysis A-Chemical*, 115(3):421–429, February 1997.

[56] N. Troullier and J. L. Martins. Efficient pseudopotentials for plane-wave calculations. *Physical Review B*, 43(3):1993–2006, January 1991.

[57] J. Rossmeisl, Z. W. Qu, H. Zhu, G. J. Kroes, and J. K. Nørskov. Electrolysis of water on oxide surfaces. *Journal Of Electroanalytical Chemistry*, 607(1-2):83–89, September 2007.

[58] G. Papoian, J. K. Nørskov, and R. Hoffmann. A comparative theoretical study of the hydrogen, methyl, and ethyl chemisorption on the pt(111) surface. *Journal Of The American Chemical Society*, 122(17):4129–4144, May 2000.

[59] B. Hammer and J. K. Nørskov. Electronic factors determining the reactivity of metal surfaces. *Surface Science*, 343(3):211–220, December 1995.

[60] A. Eichler, F. Mittendorfer, and J. Hafner. Precursor-mediated adsorption of oxygen on the (111) surfaces of platinum-group metals. *Physical Review B*, 62(7):4744–4755, August 2000.

[61] J. Greeley and M. Mavrikakis. Alloy catalysts designed from first principles. *Nature Materials*, 3(11):810–815, November 2004.

[62] A. Roudgar and A. Gross. Local reactivity of metal overlayers: Density functional theory calculations of Pd on Au. *Physical Review B*, 67(3):033409, January 2003.

[63] J. K. Nørskov. Covalent effects in the effective-medium theory of chemical-binding - hydrogen heats of solution in the 3d-metals. *Physical Review B*, 26(6):2875–2885, 1982.

[64] M. J. Puska, R. M. Nieminen, and M. Manninen. Atoms embedded in an electron-gas - immersion energies. *Physical Review B*, 24(6):3037–3047, 1981.

[65] A. Vojvodic, C. Ruberto, and B. I. Lundqvist. Trends in atomic adsorption on titanium carbide and nitride. *Surface Science*, 600(18):3619–3623, September 2006.

[66] M. Neurock and R. A. van Santen. Theory of Carbon-Sulfur Bond Activation by Small Metal Sulfide Particles. *Journal of American Chemical Society*, 116:4427–4439, 1994.

[67] H. Schweiger, P. Raybaud, and H. Toulhoat. Promoter Sensitive Shapes of Co(Ni)MoS Nanocatalysts in Sulfo-Reductive Conditions. *Journal of Catalysis*, 212:33–38, 2002.

[68] L. S. Byskov and B. Hammer and J. K. Nørskov and B. S. Clausen and H. Topsøe. Sulfor bonding in MoS_2 and Co-Mo-S structures. *Catalysis Letters*, 47:177–182, 1997.

[69] H. Topsøe, B. S. Clausen, and F. E. Massoth. *Hydrotreating Catalysis*. Science and Technology. Springer-Verlag, Berlin, 1996.

[70] C. Ruberto, A. Vojvodic, and B. I. Lundqvist. Nature of chemisorption on titanium carbide and nitride. *Surface Science*, 600(8):1612–1618, April 2006.

[71] C. Ruberto, A. Vojvodic, and B. I. Lundqvist. Nature of versatile chemisorption on TiC(111) and TiN(111) surfaces. *Solid State Communications*, 141(1):48–52, January 2007.

[72] Sonja Eijsbouts, J.A. Rob van Veen, Emiel J.M. Hensen, and Guido Mul. Preface. *Catalysis Today*, 130(1):1–2, January 2008.

[73] C. Song. An overview of new approaches to deep desulfurization for ultra-clean gasoline, diesel fuel and jet fuel. *Catalysis Today*, 86:211–263, 2003.

[74] C. Song and X. L. Ma. New design approaches to ultra-clean diesel fuels by deep desulfurization and deep dearomatization. *Applied Catalysis B-Environmental*, 41(1-2):207–238, March 2003.

[75] C. S. Song and X. L. Ma. Ultra-deep desulfurization of liquid hydrocarbon fuels: Chemistry and process. *International Journal Of Green Energy*, 1(2):167–191, May 2004.

[76] M. V. Landau. Deep hydrotreating of middle distillates from crude and shale oils. *Catalysis Today*, 36:393–429, 1997.

[77] D. D. Whitehurst, T. Isoda, and I. Mochida. Present state of the art and future challenges in the hydrodesulfurization of polyaromatic sulfur compounds. *Advances In Catalysis, Vol 42*, 42:345–471, 1998.

[78] I. V. Babich and J. A. Moulijn. Science and technology of novel processes for deep desulfurization of oil refinery streams: A review. *Fuel*, 82(6):607–631, April 2003.

[79] R. Prins, V. H. J. Debeer, and G. A. Somorjai. Structure And Function Of The Catalyst And The Promoter In Co-Mo Hydrodesulfurization Catalysts. *Catalysis Reviews-Science And Engineering*, 31(1-2):1–41, 1989.

[80] L. S. Byskov, J. K. Nørskov, B. S. Clausen, and H. Topsøe. DFT calculations of unpromoted and promoted MoS_2-based hydrodesulfurization catalysts . *Journal of Catalysis*, 187:109–122, 1999.

[81] B. Hinnemann, J. K. Nørskov, and H. Topsøe. A density functional study of the chemical differences between type I and type II MOS_2-based structures in hydrotreating catalysts. *Journal Of Physical Chemistry B*, 109(6):2245–2253, February 2005.

[82] E. J. M. Hensen, V. H. J. de Beer, J. A. R. van Veen, and R. A. van Santen. A refinement on the notion of type I and II (Co)MoS phase in hydrotreating catalysts. *Catalysis Letters*, 84(1–2):59–67, 2002.

[83] R. Candia, O. Sørensen, J. Villadsen, N. Y. Topsøe, B. S. Clausen, and H. Topsøe. Effect Of Sulfiding Temperature On Activity And Structures Of Co-Mo-Al_2O_3 Catalysts .2. *Bulletin Des Societes Chimiques Belges*, 93(8-9):763–773, 1984.

[84] N. Y. Topsøe. Infrared Study of Sulfided Co-Mo/Al_2O_3 Catalysts: The Nature of Surface Hydroxyl Groups. *Journal of Catalysis*, 64:235–237, 1980.

[85] Th. Böker, R. Severin, A. Müller, C. Janowitz, R. Manzke, D. Voss, P. Krüger, A. Mazur, and J. Pollmann. Band structure of MoS_2, $MoSe_2$ and α-$MoTe_2$: Angle resolved photoelectron spectroscopy and *ab initio* calculations. *Physical Review B*, 64:235305–1–235305–11, 2001.

[86] K. Laasonen, A. Pasquarello, R. Car, C. Lee, and D. Vanderbilt. Car-parrinello molecular-dynamics with vanderbilt ultrasoft pseudopotentials. *Physical Review B*, 47(16):10142–10153, April 1993.

[87] P. Maragakis, S. A. Andreev, Y. Brumer, D. R. Reichman, and E. Kaxiras. Adaptive nudged elastic band approach for transition state calculation. *Journal Of Chemical Physics*, 117(10):4651–4658, September 2002.

[88] P. Culot, G. Dive, V. H. Nguyen, and J. M. Ghuysen. A quasi-newton algorithm for 1st-order saddle-point location. *Theoretica Chimica Acta*, 82(3-4):189–205, April 1992.

[89] W. Humphrey, A. Dalke, and K. Schulten. VMD: Visual molecular dynamics. *Journal Of Molecular Graphics*, 14(1):33–&, February 1996.

[90] G. Seifert, H. Terrones, M. Terrones, G. Jungnickel, and T. Frauenheim. Stucture and electronic properties of MoS_2 nanotubes. *Physical Review Letters*, 85(1):146–149, 2000.

[91] Y. Feldman, E. Wasserman, D. J. Srolovitz, and R. Tenne. High-rate, gas-phase growth of MoS_2 nested inorganic fullerenes and nanotubes. *Science*, 267(5195):222–225, 1995.

[92] B. S. Clausen, H. Topsøe, R. Candia, J. Villadsen, B. Lengeler, J. A. Nielsen, and F. Christensen. Extended X-ray Absorption Fine Structure Study of Co-Mo Hydrodesulfurization Catalysts. *Journal of Physical Chemistry*, 85:3868–3872, 1981.

[93] Thomas G. Parham and Robert P. Merrill. An EXAFS study of the structure of supported cobalt molybdate catalysts as a function of sulfiding temperature. *Journal of Catalysis*, 85(2):295–310, February 1984.

[94] S. M. A. M. Bouwens, R. Prins, V. H. J. Debeer, and D. C. Koningsberger. Structure of the molybdenum sulfide phase in carbon-supported Mo and Co-Mo sulfide catalysts as studied by extended x-ray absorption fine-structure spectroscopy. *Journal Of Physical Chemistry*, 94(9):3711–3718, May 1990.

[95] P. J. Kooyman, J. G. Buglass, H. R. Reinhoudt, A. D. van Langeveld, E. J. M. Hensen, H. W. Zandbergen, and J. A. R. van Veen. Quasi in Situ Sequential Sulfidation of $CoMo/Al_2O_3$ Studied Using High-Resolution Electron Microscopy . *Journal of Physical Chemistry B*, 106:11795–11799, 2002.

[96] S. Eijsbouts. On the flexibility of the active phase in hydrotreating catalysts. *Applied Catalysis A: General*, 158:53–92, 1997.

[97] S. Eijsbouts, J. J. L. Heinerman, and H. J. W. Elzerman. MoS_2 Structures In High-Activity Hydrotreating Catalysts .1. Semiquantitative Method For Evaluation Of Transmission Electron-Microscopy Results - Correlations Between Hydrodesulfurization And Hydrodenitrogenation Activities And MoS_2 Dispersion. *Applied Catalysis A-General*, 105(1):53–68, November 1993.

[98] R. Candia, H. Topsøe, and B. S. Clausen. Effect of sulfiding temperature on activity and structure of Co-Mo/Al_2O_3. In *9th Iberoamerican symposium on catalysis*, pages 1–11, Lisbon Portugal, 1984.

[99] R. M. Stockmann, H. W. Zandbergen, A. D. Vanlangeveld, and J. A. Moulijn. Investigation Of MoS_2 On Gamma-Al_2O_3 By HREM With Atomic-Resolution. *Journal Of Molecular Catalysis A-Chemical*, 102(3):147–161, October 1995.

[100] F. Besenbacher, M. Brorson, B. S. Clausen, S. Helveg, B. Hinnemann, J. Kibsgaard, J. Lauritsen, P. G. Moses, J. K. Nørskov, and H. Topsøe. Recent STM, DFT and HAADF-STEM studies of sulfide-based hydrotreating catalysts: Insight into mechanistic, structural and particle size effects. *Catalysis Today*, 130(1):86–96, January 2008.

[101] M. Brorson, A. Carlsson, and H. Topsøe. The morphology of MoS_2, WS_2, Co-Mo-S, Ni-Mo-S and Ni-W-S nanoclusters in hydrodesulfurization catalysts revealed by HAADF-STEM. *Catalysis Today*, 123(1-4):31–36, May 2007.

[102] Anna Carlsson, Michael Brorson, and Henrik Topsøe. Morphology of WS_2 nanoclusters in WS_2/C hydrodesulfurization catalysts revealed by high-angle annular dark-field scanning transmission electron microscopy (HAADF-STEM) imaging. *Journal of Catalysis*, 227(2):530–536, October 2004.

[103] A. Carlsson, M. Brorson, and H. Topsøe. Supported metal sulphide nanoclusters studied by HAADF-STEM. *Journal Of Microscopy-Oxford*, 223:179–181, September 2006.

[104] S. Helveg, J. V. Lauritsen, E. Lægsgaard, I. Stensgaard, J. K. Nørskov, B. S. Clausen, H. Topsøe, and F. Besenbacher. Atomic-Scale Structure of Single-Layer MoS_2 Nanoclusters. *Physical Review Letters*, 84(5):951–954, 2000.

[105] J. V. Lauritsen, S. Helveg, E. Lægsgaard, I. Stensgaard, B. S. Clausen, H. Topsøe, and F. Besenbacher. Atomic-Scale Structure of Co-Mo-S Nanoclusters in Hydrotreating Catalysts. *Journal of Catalysis*, 197:1–5, 2001.

[106] J. V. Lauritsen, M. Nyberg, R. T. Vang, M. V. Bollinger, B. S. Clausen, H. Topsøe, K. W. Jacobsen, E. Lægsgaard, J. K. Nørskov, and F. Besenbacher. Chemistry of one-dimensional metallic edge states in MoS_2 nanoclusters. *Nanotechnology*, 14:385–389, 2003.

[107] J. V. Lauritsen, M. V. Bollinger, E. Lægsgaard, K. W. Jacobsen, J. K. Nørskov, B. S. Clausen, H. Topsøe, and F. Besenbacher. Atomic-scale insight into structure and morphology changes of MoS_2 nanoclusters in hydrotreating catalysts. *Journal of Catalysis*, 221:510–522, 2004.

[108] J. V. Lauritsen, M. Nyberg, J. K. Nørskov, B. S. Clausen, H. Topsøe, E. Lægsgaard, and F. Besenbacher. Hydrodesulfurization reaction pathways on MoS_2 nanoclusters revealed by scanning tunneling microscopy. *Journal of Catalysis*, 224:94–106, 2004.

[109] M. V. Bollinger, J. V. Lauritsen, K. W. Jacobsen, J. K. Nørskov, S. Helveg, and F. Besenbacher. One-Dimensional Metallic Edge States in MoS_2. *Physical Review Letters*, 87:196803–1, 2001.

[110] Jeppe V. Lauritsen, Jakob Kibsgaard, Georg H. Olesen, Poul G. Moses, Berit Hinnemann, Stig Helveg, Jens K. Nørskov, Bjerne S. Clausen, Henrik Topsøe, Erik Lægsgaard, and Flemming Besenbacher. Location and coordination of promotor atoms in Co- and Ni-promoted MoS_2 based hydrotreating catalysts. *Journal of Catalysis*, 249:220–233, 2007.

[111] T. F. Jaramillo, K. P. Jørgensen, J. Bonde, J. H. Nielsen, S. Horch, and I. Chorkendorff. Identification of active edge sites for electrochemical H-2 evolution from MoS2 nanocatalysts. *Science*, 317(5834):100–102, July 2007.

[112] R. Candia, B. S. Clausen, J. Bartholdy, N. Y. Topsøe, B. Lengeler, and H. Topsøe. Nature of active sites in sulfided HDS catalysts. In *Proc. 8th Int. Congr. Catal.*, volume II, pages 375–386, Weinheim, 1984. Verlag Chemie.

[113] H. Topsøe, B. S. Clausen, R. Candia, C. Wivel, and S. Mørup. In Situ Mössbauer Emission Spectroscopy Studies of Unsupported and Supported Sulfided Co-Mo Hydrodesulfurization Catalysts: Evidence for and Nature of a Co-Mo-S Phase. *Journal of Catalysis*, 68:433–452, 1981.

[114] C. Wivel, R. Candia, B. S. Clausen, S. Mørup, and H. Topsøe. On the Catalytic Significance of a Co-Mo-S Phase in Co-Mo-/Al_2O_3 Hydrodesulfurization Catalysts: Combined *in Situ* Mössbauer Emission Spectroscopy and Activity Studies. *Journal of Catalysis*, 68:453–463, 1981.

[115] H. Schweiger, P. Raybaud, G. Kresse, and H. Toulhoat. Shape and Edge Sites Modifications of MoS_2 Catalytic Nanoparticles Induced by Working Conditions: A Theoretical Study. *Journal of Catalysis*, 207:76–87, 2002.

[116] M. Sun, A. E. Nelson, and J. Adjaye. On the incorporation of nickel and cobalt into MoS_2-edge structures. *Journal of Catalysis*, 226:32–40, 2004.

[117] Mingyong Sun, Alen E. Nelson, and J. Adjaye. A DFT study of WS_2, NiWS, and CoWS hydrotreating catalysts: energetics and surface structures. *Journal of Catalysis*, 226:41–53, 2004.

[118] S. Cristol, J. F. Paul, E. Payen, D. Bougeard, S. Clémendot, and F. Hutschka. Theoretical Study of the $MoS_2(100)$ Surface: A Chemical Potential Analysis of Sulfur and Hydrogen Coverage. *Journal of Physical Chemistry B*, 104:11220–11229, 2000.

[119] S. Cristol, J. F. Paul., E. Payen, D. Bougeard, S. Clémendot, and F. Hutschka. Theoretical Study of the $MoS_2(100)$ Surface: A Chemical Potential Analysis of Sulfur and Hydrogen Coverage. 2. Effect of the Total Pressure on Surface Stability. *Journal of Physical Chemistry B*, 106:5659–5667, 2002.

[120] M. Sun, J. Adjaye, and A. E. Nelson. Theroretical investigations of the structure and properties of molybdenum-based sulfide catalysts. *Applied Catalysis A: General*, 263:131–143, 2004.

[121] D. Costa, C. Arrouvel, M. Breysse, H. Toulhoat, and P. Raybaud. Edge wetting effects of gamma-Al_2O_3 and anatase-TiO_2 supports by MoS_2 and CoMoS active phases: A DFT study. *Journal Of Catalysis*, 246(2):325–343, 2007.

[122] C. Arrouvel, M. Breysse, H. Toulhoat, and P. Raybaud. A density functional theory comparison of anatase (TiO_2)- and gamma-Al_2O_3-supported MoS_2 catalysts. *Journal Of Catalysis*, 232(1):161–178, 2005.

[123] X. Rozanska, R. A. van Santen, and F. Hutschka. A DFT study of the cracking reaction of thiophene activated by small zeolitic clusters. *Journal of Catalysis*, 200:79–90, 2001.

[124] X. Rozanska, R. A. van Santen, F. Hutschka, and J. Hafner. A periodic DFT study of the isomerization of thiophenic derivatives catalyzed by acidic mordenite. *Journal of Catalysis*, 205:388–397, 2002.

[125] X. Rozanska, X. Saintigny, R. A. van Santen, S. Clémendot, and F. Hutschka. A theoretical study of hydrodesulfurization and hy-

drogenation of dibenzothiophene catalyzed by small zeolitic cluster . *Journal of Catalysis*, 208:89–99, 2002.

[126] X. Rozanska, R. A. van Santen, F. Hutschka, and J. Hafner. A periodic density functional theory study of thiophenic derivative cracking catalyzed by mordenite. *Journal of Catalysis*, 215:20–29, 2003.

[127] P. Liu, J. A. Rodriguez, and J. T. Muckerman. The Ti_8C_{12} metcar: A new model catalyst for hydrodesulfurization. *Journal Of Physical Chemistry B*, 108(49):18796–18798, 2004.

[128] P. Liu and J. A. Rodriguez. Effects of Carbon on the stability and chemical performance of transition metal carbides: A density functional study. *Journal of Chemical Physics*, 120(11):5414–5423, 2004.

[129] P. Liu, J. A. Rodriguez, T. Asakura, J. Gomes, and K. Nakamura. Desulfurization reactions on ni2p(001) and alpha-mo2c(001) surfaces: Complex role of p and c sites. *Journal Of Physical Chemistry B*, 109(10):4575–4583, March 2005.

[130] P. Liu, J. A. Rodriguez, and J. T. Muckerman. Sulfur adsorption and sulfidation of transition metal carbides as hydrotreating catalysts. *Journal Of Molecular Catalysis A-Chemical*, 239(1-2):116–124, 2005.

[131] P. Liu, J. M. Lightstone, M. J. Patterson, J. A. Rodriguez, J. T. Muckerman, and M. G. White. Gas-phase interaction of thiophene with the ti8c12+ and ti8c12 met-car clusters. *Journal Of Physical Chemistry B*, 110(14):7449–7455, 2006.

[132] P. Raybaud, J. Hafner, G. Kresse, S. Kasztelan, and H. Toulhoat. Ab Initio Study of the H_2-H_2S/MoS_2 Gas-Solid Interface: The Nature of the Catalytically Active Sites. *Journal of Catalysis*, 189:129–146, 2000.

[133] J. F. Paul and E. Payen. Vacancy Formation on MoS_2 Hydrodesulfurization Catalyst: DFT Study of the Mechanism. *Journal of Physical Chemistry B*, 107:4057–4064, 2003.

[134] T. Todorova, R. Prins, and Th. Weber. A density functional theory of the hydrogenolysis reaction of CH_3SH to CH_4 on the catalytically active (100) edge of 2H-MoS_2. *Journal of Catalysis*, 236:190, 2005.

[135] P. Raybaud, J. Hafner, G. Kresse, and H. Toulhoat. Adsorption of thiophene on the catalytically active surface of MoS_2: An *ab initio* local-density-functional study. *Physical Review Letters*, 80(7):1481–1484, 1998.

[136] P. Raybaud, J. Hafner, G. Kresse, and H. Toulhoat. Ab-initio energy profiles for thiophene HDS on the MoS_2 $(10\bar{1}0)$ edge-surface. *Hydrotreatment And Hydrocracking Of Oil Fractions*, 127:309–317, 1999.

[137] F. Besenbacher. Scanning tunnelling microscopy studies of metal surfaces. *Reports On Progress In Physics*, 59(12):1737–1802, December 1996.

[138] J. V. Barth, H. Brune, G. Ertl, and R. J. Behm. Scanning tunneling microscopy observations on the reconstructed au(111) surface - atomic-structure, long-range superstructure, rotational domains, and surface-defects. *Physical Review B*, 42(15):9307–9318, November 1990.

[139] P. Raybaud, J. Hafner, G. Kresse, S. Kasztelan, and H. Toulhoat. Structure, Energetics , and Electronic Properties of the Surface of a Promoted MoS_2 Catalyst: An ab Initio Local Density Functional Study. *Journal of Catalysis*, 190:128–143, 2000.

[140] T. Kabe, A. Ishihara, and W. Qian. Elucidation of Hydrodesulfurization Mechanism on Molybdenum-based Catalysts using ^{35}S Radioisotope Pulse Tracer Methods. *Catalysis Surveys from Japan*, 3:17–25, 1999.

[141] M. L. Vrinat. The kinetics of the hydrodesulfurization process- a review. *Applied Catalysis*, 6:137–158, 1983.

[142] M. J. Girgis and B. C. Gates. Reactivities, reaction networks, and kinetics in high-pressure catalytic hydroprocessing. *Ind. Eng. Chem. Res.*, 30:2021–2058, 1991.

[143] T. C. Ho. Hydrodenitrogenation catalysis. *Catalysis Reviews-Science And Engineering*, 30(1):117–160, 1988.

[144] B. C. Gates and H. Topsøe. Reactivities in deep catalytic hydrodesulfurization: challenges, opportunities, and the importance of 4-methyldibenzothiophene amd 4,6-dimethyldibenzothiophene. *Polyhedron*, 16(18):3213–3217, 1997.

[145] P. J. Owens and C. H. Amberg. Thiophene desulfurization by a microreactor technique. *Advances in Chemistry series*, (33):182, 1961.

[146] A. E. Hargreaves and J. R. H. Ross. An investigation of the mechanism of the hydrodesulfurization of thiophene over sulfided Co-Mo/Al_2O_3 catalysts II. The effect of promotion by cobalt on the C-S bond cleavage and double-bond hydrogenation/dehydrogenation activities of tetrahydrothiophene and related compounds. *Journal of Catalysis*, 56:363–376, 1979.

[147] K. F. Mccarty and G. L. Schrader. Deuterodesulfurization of thiophene - an investigation of the reaction-mechanism. *Journal Of Catalysis*, 103(2):261–269, February 1987.

[148] H. Schulz and D. V. Do. Fast and slow steps of hydrodesulfurization. *Bulletin Des Societes Chimiques Belges*, 93(8-9):645–651, 1984.

[149] M. Houala, N. K. Nag, A. V. Sapre, D. H. Broderick, and B. C. Gates. Hydrodesulfurization of dibenzothiophene catalyzed by sulfided CoO-MoO_3-Al_2O_3: The reaction network. *AIChE Journal*, 24(6):1015–1021, 1978.

[150] A. Borgna, E. J. M. Hensen, L. Coulier, M. H. J. M. de Croon, J. C. Schouten, J. A. R. van Veen, and J. W. Niemantsverdriet. Intrinsic thiophene hydrodesulfurization kinetics of a sulfided NiMo/SiO_2 model catalyst: volcano-type behavior. *Catalysis Letters*, 90(3–4):117–122, 2003.

[151] K. G. Knudsen, B. H. Cooper, and H. Topsøe. Catalyst and process technologies for ultra low sulfur diesel. *Applied Catalysis A: General*, 189:205–215, 1999.

[152] D. D. Whitehurst, H. Farag, T. Nagamatsu, K. Sakanishi, and I. Mochida. Assessment of limitations and potentials for improvement in deep desulfurization through detailed kinetic analysis of mechanistic pathways. *Catalysis Today*, 45:299–305, 1998.

[153] X. L. Ma, K. Sakanishi, and I. Mochida. Hydrodesulfurization reactivities of various sulfur compounds in vacuum gas oil. *Industrial & Engineering Chemistry Research*, 35(8):2487–2494, August 1996.

[154] M. Breysse, P. Afanasiev, C. Geantet, and M. Vrinat. Overview of support effects in hydrotreating catalysts. *Catalysis Today*, 86:5–16, 2003.

[155] M. Egorova and R. Prins. Hydrodesulfurization of dibenzothiophene and 4,6-dimethyldibenzothiophene over sulfided NiMo/γ-Al_2O_3, CoMo/γ-Al_2O_3, and Mo/γ-Al_2O_3 catalysts. *Journal of Catalysis*, 225:417–427, 2004.

[156] S. J. Tauster, T. A. Pecoraro, and R. R. Chianelli. Structure and properties of molybdenum sulfide - correlation of o-2 chemisorption with hydrodesulfurization activity. *Journal Of Catalysis*, 63(2):515–519, 1980.

[157] H. Topsøe, R. Candia, N. Y. Topsøe, and B. S. Clausen. On the state of the Co-Mo-S Model. *Bull. Soc. Chim. Belg.*, 93(8–9):783–806, 1984.

[158] M. Salmeron, G. A. Somorjai, A. Wold, R. Chianelli, and K. S. Liang. The Adsorption And Binding Of Thiophene, Butene And H_2S On The Basal-Plane Of MoS_2 Single-Crystals. *Chemical Physics Letters*, 90(2):105–107, 1982.

[159] Voorhoev.Rj. Electron spin resonance study of active centers in nickel-tungsten sulfide hydrogenation catalysts. *Journal Of Catalysis*, 23(2):236–&, 1971.

[160] Voorhoev.Rj and J. C. M. Stuiver. Mechanism of hydrogenation of cyclohexene and benzene on nickel-tungsten sulfide catalysts. *Journal Of Catalysis*, 23(2):243–&, 1971.

[161] N. Y. Topsøe and H. Topsøe. FTIR Studies of Mo/Al_2O_3-Based Catalysts II. Evidence for the Presence of SH Groups and Their Role in Acidity and Activity. *Journal of Catalysis*, 139:641–651, 1993.

[162] B. Scheffer, N. J. J. Dekker, P. J. Mangnus, and J. A. Moulijn. A temperature-programmed reduction study of sulfided co-mo/al2o3 hydrodesulfurization catalysts. *Journal Of Catalysis*, 121(1):31–46, January 1990.

[163] D. G. Kalthod and S. W. Weller. Studies of molybdenum sulfide catalysts - effects of pretreatment on olefin hydrogenation activity. *Journal Of Catalysis*, 98(2):572–576, April 1986.

[164] J. K. Nørskov, B. S. Clausen, and H. Topsøe. Understanding the trends in the hydrodesulfurization activity of the transition metal sulfides. *Catalysis Letters*, 13:1–8, 1992.

[165] P. Zeuthen, P. Stolze, and U. B. Pedersen. Kinetics For Simultaneous HDS, HDN And Hydrogenation Model Reactions On A $Co\text{-}Mo/Al_2O_3$ Catalyst. *Bulletin Des Societes Chimiques Belges*, 96(11-12):985–995, November 1987.

[166] F. Bataille, J. L. Lemberton, P. Michaud, G. Pérot, M. Vrinat, M. Lemaire, E. Schulz, M. Breysse, and S. Kaztelan. Alkyldibenzothiophenes hydrodesulfurization-promoter effect, reactivity, and reaction mechanism. *Journal of Catalysis*, 191:409–422, 2000.

[167] F. van Looij, P. van der Laan, W. H. J. Stork, D. J. DiCamillo, and J. Swain. Key parameters in deep hydrodesulfurization of diesel fuel. *Applied Catalysis A-General*, 170(1):1–12, May 1998.

[168] M. Nagai and T. Kabe. Selectivity of molybdenum catalyst in hydrodesulfurization, hydrodenitrogenation, and hydrodeoxygenation - effect of additives on dibenzothiophene hydrodesulfurization. *Journal Of Catalysis*, 81(2):440–449, 1983.

[169] M. Nagai, T. Sato, and A. Aiba. Poisoning effect of nitrogen compounds on dibenzothiophene hydrodesulfurization on sulfided $NiMo/Al_2O_3$ catalysts and relation to gas-phase basicity. *Journal of Catalysis*, 97:52–58, 1986.

[170] V. LaVopa and C. N. Satterfield. Poisoning of thiophene hydrodesulfurization by nitrogen compounds. *Journal of Catalysis*, 110:375–387, 1988.

[171] P. Zeuthen, K. G. Knudsen, and D. D. Whitehurst. Organic nitrogen compounds in gas oil blends, their hydrotreated products and the importance to hydrotreatment. *Catalysis Today*, 65(2-4):307–314, February 2001.

[172] P. Wiwel, K. Knudsen, P. Zeuthen, and D. Whitehurst. Assessing compositional changes of nitrogen compounds during hydrotreating of typical diesel range gas oils using a novel preconcentration technique coupled with gas chromatography and atomic emission detection. *Industrial & Engineering Chemistry Research*, 39(2):533–540, February 2000.

[173] M. Egorova and R. Prins. Mutual influence of the HDS of dibenzothiophene and HDN of 2-methylpyridine. *Journal of Catalysis*, 221:11–19, 2004.

[174] M. Egorova and R. Prins. Competitive hydrodesulfurization of 4,6-dimethyldibenzothiophene, hydrodenitrogenation of 2-methylpyridine, and hydrogenation of naphthalene over sulfided $NiMo/\gamma\text{-}Al_2O_3$. *Journal of Catalysis*, 224:278–287, 2004.

[175] T. C. Ho. Inhibiting effects in hydrodesulfurization of 4,6-diethyldibenzothiophene. *Journal of Catalysis*, 219:442–451, 2003.

[176] U. T. Turaga, X. L. Ma, and C. S. Song. Influence of nitrogen compounds on deep hydrodesulfurization of 4,6-dimethyldibenzothiophene over Al_2O_3- and MCM-41-supported Co-Mo sulfide catalysts. *Catalysis Today*, 86(1-4):265–275, November 2003.

[177] E. Furimsky and F. E. Massoth. Deactivation of hydroprocessing catalysts. *Catalysis Today*, 52:381–495, 1999.

[178] B. Hinnemann, P. G. Moses, J. Bonde, K. P. Jørgensen, J. H. Nielsen, S. Horch, I. Chorkendorff, and J. K. Nørskov. Biomimetic hydrogen evolution: MoS_2 nanoparticies as catalyst for hydrogen evolution. *Journal Of The American Chemical Society*, 127(15):5308–5309, April 2005.

[179] D. L. Sullivan and J. G. Ekerdt. Mechanisms of thiophene hydrodesulfurization on model molybdenum catalysts. *Journal of Catalysis*, 178:226–233, 1998.

[180] A. Borgna, E. J. M Hensen, J. A. R. van Veen, and J. W. Niemantsverdriet. Intrinsic kinetics of thiophene hydrodesulfurization on a sulfided $NiMo/SiO_2$ planar model catalyst. *Journal of Catalysis*, 221:541–548, 2004.

[181] A. Travert, H. Nakamura, R. A. van Santen, S. Cristol, J. F. Paul, and E. Payen. Hydrogen Activation on Mo-Based Sulfide Catalysts, a Periodic DFT Study. *Journal of American Chemical Society*, 124:7084–7095, 2002.

[182] Mingyong Sun, Alen E. Nelson, and J. Adjaye. Ab initio DFT study of hydrogen dissociation on MoS_2, NiMoS, and CoMoS: mechanism, kinetics, and vibrational frequencies. *Journal of Catalysis*, 233:411–421, 2005.

[183] L. S. Byskov, M. Bollinger, J. K. Nørskov, B. S. Clausen, and H. Topsøe. Molecular aspects of the H_2 activation on MoS_2 based catalysts- the role of dynamic surface arrangements. *Journal of Molecular Catalysis A*, Chemical 163(163):117–122, 2000.

[184] T. L. Tarbuck, K. R. McCrea, J. W. Logan, J. L. Heiser, and M. E. Bussell. Identification of the adsorption mode of thiophene on sulfided Mo catalysts. *Journal of Physical Chemistry B*, 102:7845–7857, 1998.

[185] P. Mills, D. C. Phillips, B. P. Woodruff, R. Main, and M. E. Bussell. Investigation of the adsorption and reactions of thiophene on sulfided Cu, Mo, and Rh catalysts. *Journal of Physical Chemistry B*, 104:3237–3249, 2000.

[186] P. C. H. Mitchell, D. A. Green, E. Payen, J. Tomkinson, and S. F. Parker. Interaction of thiophene with a molybdenum disulfide catalyst -an inelastic neutron scattering study. *Physical Chemistry Chemical Physics*, 1:3357–3363, 1999.

[187] P. Mills, S. Korlann, M. E. Bussell, M. A. Reynolds, M. V. Ovchinnikov, R. J. Angelici, C. Stinner, T. Weber, and R. Prins. Vibrational study of organometallic complexes with thiophene ligands: Models for adsorbed thiophene on hydrodesulfurization catalysts. *Journal of Physical Chemistry A*, 105:4418–4429, 2001.

[188] R. J. Angelici. An overview of modeling studies in HDS, HDN and HDO catalysis. *Polyhedron*, 16(18):3073–3088, 1997.

[189] S. Cristol, J. F. Paul, C. Schovsbo, E. Veilly, and E. Payen. DFT study of thiophene adsorption on molybdenum sulfide. *Journal Of Catalysis*, 239(1):145–153, April 2006.

[190] D.R.Lide, editor. *CRC Handbook of Chemistry and Physics 83th edition.* CRC Press, Boca Raton, 2002.

[191] Xiao-Qian Yao, Yong-Wang Li, and Haijun Jiao. Mechanism of thiophene hydrodesulfurization on a Mo_3S_9 model catalyst. A computational study. *Journal of Molecular Structure: THEOCHEM*, 726:81, 2005.

[192] S. Cristol, J. F. Paul, E. Payen, D. Bougeard, F. Hutschka, and S. Clémendot. DBT derivatives adsorption over molybdenum sulfide catalysts: a theoretical study. *Journal of Catalysis*, 224:138–147, 2004.

[193] M. Daage and R. R. Chianelli. Structure-Function Relations in Molybdenum Sulfide Catalysts: The "Rim-Edge" Model. *Journal of Catalysis*, 149:414–427, 1994.

[194] D. Kasahara, T. Shimizu, and M. Yamada. Inhibiting effects of H_2S on HDS activity of CoMo-, NiMo, and Mo/Al_2O_3. *Catalysis Today*, 35:59–64, 1997.

[195] X. L. Ma, K. Sakanishi, T. Isoda, and I. Mochida. Hydrodesulfurization reactivities of narrow-cut fractions in a gas oil. *Industrial & Engineering Chemistry Research*, 34(3):748–754, March 1995.

[196] M. V. Landau, D. Berger, and M. Herskowitz. Hydrodesulfurization of methyl-substituted dibenzothiophenes: Fundamental study of routes to deep desulfurization. *Journal Of Catalysis*, 159(1):236–245, March 1996.

[197] E. Lecrenay, K. Sakanishi, I. Mochida, and T. Suzuka. Hydrodesulfurization activity of CoMo and NiMo catalysts supported on some acidic binary oxides. *Applied Catalysis A: General*, 175:237–243, 1998.

[198] E. Krebs, B. Silvi, and P. Raybaud. Mixed sites and promoter segregation: A DFT study of the manifestation of Le Chatelier's principle for the Co(Ni)MoS active phase in reaction conditions. *Catalysis Today*, 130(1):160–169, January 2008.

[199] A. D. Gandubert, E. Krebs, C. Legens, D. Costa, D. Guillaume, and P. Raybaud. Optimal promoter edge decoration of CoMoS catalysts: A combined theoretical and experimental study. *Catalysis Today*, 130(1):149–159, January 2008.

[200] Toshiaki Kabe, Atsushi Ishihara, and Haruhiko Tajima. Hydrodesulfurization of sulfur-containing polyaromatic compounds in light oil. 31:1577–1590, 1992.

[201] V. Meille, E. Schulz, M. Lemaire, and M. Vrinat. Hydrodesulfurization of alkyldibenzothiophenes over a $NiMo/Al_2O_3$ catalyst: Kinetics and mechanism. *Journal Of Catalysis*, 170(1):29–36, August 1997.

[202] F. van Looij, P. van der Laan, W. H. J. Stork, D. J. DiCamillo, and J. Swain. Key Parameters in deep hydrodesulfurization of diesel fuel. *Applied Catalysis A: General*, 170:1–12, 1998.

[203] M. Breysse, G. Djega-Mariadassou, S. Pessayre, C. Geantet, M. Vrinat, G. Perot, and M. Lemaire. Deep desulfurization: reactions, catalysts and technological challenges. *Catalysis Today*, 84(3-4):129–138, September 2003.

[204] N. Y. Topsøe, H. Topsøe, and F. E. Massoth. Evidence of Brønsted acidity on sulfided promoted and unpromoted Mo/Al_2O_3 catalysts. *Journal of Catalysis*, 119:252–255, 1989.

[205] T. Kabe, W. H. Qian, and A. Ishihara. Elucidation of hydrodesulfurization mechanism using S-35 radioisotope pulse tracer methods. *Catalysis Today*, 39(1-2):3–12, December 1997.

[206] B. Hammer, K. W. Jacobsen, and J. K. NøRskov. Role of nonlocal exchange-correlation in activated adsorption. *Physical Review Letters*, 70(25):3971–3974, June 1993.

[207] H. Topsøe, B. Hinnemann, J. K. Nørskov, J. V. Lauritsen, F. Besenbacher, P. L. Hansen, G. Hytoft, R. G. Egeberg, and K. G. Knudsen. The role of reaction pathways and support interactions in the development of high activity hydrotreating catalysts. *Catalysis Today*, 107-08:12–22, October 2005.

[208] S. D. Chakarova-Kack, E. Schroder, B. I. Lundqvist, and D. C. Langreth. Application of van der waals density functional to an extended system: Adsorption of benzene and naphthalene on graphite. *Physical Review Letters*, 96(14):146107, April 2006.

[209] M. Sun, A. E. Nelson, and J. Adjaye. Correlating the electronic properties and hdn reactivities of organonitrogen compounds: an ab initio dft study. *Journal Of Molecular Catalysis A-Chemical*, 222(1-2):243–251, November 2004.

[210] Mingyong Sun, Alen E. Nelson, and J. Adjaye. Adsorption and hydrogenation of pyridine and pyrrole on nimos: an ab initio density-functional theory study. *Journal of Catalysis*, 231:223–231, 2005.

[211] R. Koide, E. J. M. Hensen, J. F. Paul, S. Cristol, E. Payen, H. Nakamura, and R. A. van Santen. A DFT study on benzene adsorption over tungsten sulfides: surface model and adsorption geometries. *Topics In Catalysis*, 45(1-4):175–179, August 2007.

[212] R. Koide, E. J. M. Hensen, J. F. Paul, S. Cristol, E. Payen, H. Nakamura, and R. A. van Santen. A DFT study on benzene adsorption over a corner site of tungsten sulfides. *Catalysis Today*, 130(1):178–182, January 2008.

[213] S. D. Chakarova-Kack, O. Borck, E. Schroder, and B. I. Lundqvist. Adsorption of phenol on graphite(0001) and alpha-Al_2O_3(0001): Nature of van der Waals bonds from first-principles calculations. *Physical Review B*, 74(15):155402, October 2006.

[214] J. Kleis, B. I. Lundqvist, D. C. Langreth, and E. Schoder. Towards a working density-functional theory for polymers: First-principles determination of the polyethylene crystal structure. *Physical Review B*, 76(10):100201, September 2007.

[215] J. F. Paul, S. Cristol, and E. Payen. Computational studies of (mixed) sulfide hydrotreating catalysts. *Catalysis Today*, 130(1):139–148, January 2008.

[216] M. S. Dresselhaus and I. L. Thomas. Alternative energy technologies. *Nature*, 414(6861):332–337, November 2001.

[217] P. E. M. Siegbahn. Proton and electron transfers in [nife] hydrogenase. *Advances In Inorganic Chemistry - Including Bioinorganic Studies, Vol 56*, 56:101–125, 2004.

[218] J. K. Norskov, T. Bligaard, A. Logadottir, J. R. Kitchin, J. G. Chen, S. Pandelov, and J. K. Norskov. Trends in the exchange current for hydrogen evolution. *Journal Of The Electrochemical Society*, 152(3):J23–J26, 2005.

[219] R. Parsons. The rate of electrolytic hydrogen evolution and the heat of adsorption of hydrogen. *Transactions Of The Faraday Society*, 54(7):1053–1063, 1958.

[220] A. Sobczynski. Molybdenum-disulfide as a hydrogen evolution catalyst for water photodecomposition on semiconductors. *Journal Of Catalysis*, 131(1):156–166, September 1991.

[221] D. C. Langreth, M. Dion, H. Rydberg, E. Schroder, P. Hyldgaard, and B. I. Lundqvist. Van der waals density functional theory with applications. *International Journal Of Quantum Chemistry*, 101(5):599–610, February 2005.

[222] H. Rydberg, B. I. Lundqvist, D. C. Langreth, and M. Dion. Tractable nonlocal correlation density functionals for flat surfaces and slabs. *Physical Review B*, 62(11):6997–7006, September 2000.

[223] W. Kohn, Y. Meir, and D. E. Makarov. vanderwaals energies in density functional theory. *Physical Review Letters*, 80(19):4153–4156, May 1998.

[224] B Lundqvist. Characteristic structure in core electron spectra of metals due to electron-plasmon coupling. *Physik Der Kondensiterten Materie*, 9(3):236–, 1969.

[225] O. Gunnarsson and B. I. Lundqvist. Exchange and correlation in atoms, molecules, and solids by spin-density functional formalism. *Physical Review B*, 13(10):4274–4298, 1976.

[226] D. C. Langreth and J. P. Perdew. Exchange-correlation energy of a metallic surface. *Solid State Communications*, 17(11):1425–1429, 1975.

[227] D. C. Langreth and J. P. Perdew. Exchange-correlation energy of a metallic surface - wave-vector analysis. *Physical Review B*, 15(6):2884–2901, 1977.

[228] T. Thonhauser, V. R. Cooper, S. Li, A. Puzder, P. Hyldgaard, and D. C. Langreth. Van der waals density functional: Self-consistent potential and the nature of the van der waals bond. *Physical Review B*, 76(12):125112, September 2007.

[229] M.A.L. Marques, C.A. Ullrich, F. Nogueira, A. Rubio, K. Burke, and E.K.U. Gross, editors. *Lecture Notes in Physics: Time-Dependent Density Functional Theory*. Springer, 2006.

[230] Henrik Bruus and Karsten Flensberg. *Many-Body Quantum Theory in Condensed Matter Physics*. Oxford University Press, 2004.

[231] E. K. U. Gross and W. Kohn. Local density-functional theory of frequency-dependent linear response. *Physical Review Letters*, 55(26):2850–2852, 1985.

[232] Maxine Dion. *van der Waals Forces in Density Functional Theory*. PhD thesis, Rutgers University, 2004.

[233] S. D. Chakarova and E. Schroder. van der waals interactions of the benzene dimer: Towards treatment of polycyclic aromatic hydrocarbon dimers. *Materials Science & Engineering C-Biomimetic And Supramolecular Systems*, 25(5-8):787–792, December 2005.

Appendix A

Background on the vdW-DF XC functional

A long line of research has led to the van der Waals XC-functional for general geometries (vdW-DF) [25] and the developments have been publish in a series of articles which reach back to some of the basic developments in the theory of the homogeneous electron gas [221,222,223,224,225,226,227,228]. The present appendix gives an overview of the derivation of the vdW-DF functional which leads to the result in reference [25]. For a more general introduction to van der Waals forces in DFT see reference [229].

A.1 The adiabatic connection formula

The adiabatic connection formula was originally introduced in [225,226,227]. The electron electron interaction is scaled by a factor λ, called the coupling strength, while keeping the density fixed at the ground state density by changing the external potential. $\lambda = 0$ corresponds to the non interacting system and $\lambda = 1$ corresponds to the fully interacting system. The Hamiltonian is then given by equation A.1.

$$\hat{H} = \hat{T} + \hat{V}_{ext}(\lambda) + \lambda \hat{V}_{ee} \tag{A.1}$$

$\hat{V}_{ext}(\lambda)$ is given by Eq. A.2:

$$\hat{V}_{ext}(\lambda) = \int d^3 \hat{n}(r) v_\lambda(r) \tag{A.2}$$

From Eq. A.1 it follows that $\hat{H}_{KS} = \hat{H}(\lambda = 0)$ and $\hat{H} = \hat{H}(\lambda = 1)$
The total energy is given by equation A.3

$$E = V_{ext} + T_{KS} + E_H + E_{XC} \tag{A.3}$$

Rewriting the total energy (eq. A.3) yields:

$$\begin{aligned} E_{XC} &= E - V_{ext} - T_{KS} - E_H \\ &= E - V_{ext} - (E_{KS} - V_{KS}) - E_H \\ &= \int d\lambda \frac{d}{d\lambda} \left[E(\lambda) - V_{ext}(\lambda) \right] - E_H \end{aligned} \tag{A.4}$$

We introduce the ground state wave function using that the derivative of the energy can be written as:

$$\frac{dE(\lambda)}{d\lambda} = \frac{d}{d\lambda} < \Psi | \hat{H}(\lambda) | \Psi >_\lambda = < \Psi | \frac{d\hat{H}(\lambda)}{d\lambda} | \Psi >_\lambda \tag{A.5}$$

Where $|\Psi >_\lambda$ is the ground state wavefunction at a given λ. The derivative of the external potential is given as

$$\frac{dV_{ext}(\lambda)}{d\lambda} = \int d^3 r n(r) \frac{dv_\lambda(r)}{d\lambda} = < \Psi | \frac{d\hat{V}_{ext}(\lambda)}{d\lambda} | \Psi >_\lambda \tag{A.6}$$

The derivative of the Hamiltonian in eq. A.5 is given by eq. A.7

$$\frac{d\hat{H}(\lambda)}{d\lambda} = \frac{d\hat{V}_{ext}(\lambda)}{d\lambda} + \hat{V}_{ee} \tag{A.7}$$

inserting eq. A.7 into eq. A.5 gives

$$\frac{dE(\lambda)}{d\lambda} = < \Psi | \frac{d\hat{V}_{ext}(\lambda)}{d\lambda} + \hat{V}_{ee} | \Psi >_\lambda \tag{A.8}$$

Then finally inserting equation A.8 and eq. A.6 into eq. A.4 leads to equation A.9 which is the adiabatic connection formula.

$$\begin{aligned} E_{XC} &= \int_0^1 d\lambda < \Psi | \frac{d\hat{V}_{ext}(\lambda)}{d\lambda} + \hat{V}_{ee} | \Psi >_\lambda - < \Psi | \frac{d\hat{V}_{ext}(\lambda)}{d\lambda} | \Psi >_\lambda - E_H \\ &= \int_0^1 d\lambda < \Psi | \hat{V}_{ee} | \Psi >_\lambda - E_H \end{aligned} \tag{A.9}$$

A.2 The response function and the adiabatic connection formula

A few steps are necessary in order to introduce the density density response function. First of all the density operator must be introduced which is done be rewriting the electron electron interaction. The electron electron interaction is in second quantization given by equation A.10:

$$\hat{V}_{ee} = \frac{1}{2}\int d^3r \int d^3r' \frac{1}{|r'-r|}\hat{\Psi}^+(r)\hat{\Psi}^+(r')\hat{\Psi}(r')\hat{\Psi}(r) \tag{A.10}$$

The expectation value of the electron electron interaction for a given λ is the following

$$\begin{aligned}
&< \Psi|\hat{V}_{ee}|\Psi >= \\
&= \frac{1}{2}\int d^3r \int d^3r' \frac{1}{|r'-r|} < \hat{\Psi}^+(r)\hat{\Psi}^+(r')\hat{\Psi}(r')\hat{\Psi}(r) >_\lambda \\
&= \frac{1}{2}\int d^3r \int d^3r' \frac{1}{|r'-r|} - < \hat{\Psi}^+(r)\hat{\Psi}^+(r')\hat{\Psi}(r)\hat{\Psi}(r') >_\lambda \\
&\text{using the commutator relationship} \{\hat{\Psi}(r), \hat{\Psi}^+(r')\} = \delta(r-r') \\
&= \frac{1}{2}\int d^3r \int d^3r' \frac{1}{|r'-r|} - < \hat{\Psi}^+(r)\left(\delta(r-r') - \hat{\Psi}(r)\hat{\Psi}^+(r')\right)\hat{\Psi}(r') >_\lambda \\
&= \frac{1}{2}\int d^3r \int d^3r' \frac{1}{|r'-r|}\left(- < \hat{\Psi}^+(r)\delta(r-r')\hat{\Psi}(r') >_\lambda + < \hat{\Psi}^+(r)\hat{\Psi}(r)\hat{\Psi}^+(r')\hat{\Psi}(r') >_\lambda\right) \\
&= \frac{1}{2}\int d^3r \int d^3r' \frac{1}{|r'-r|}\left(-\delta(r-r')n(r) + < \hat{n}(r)\hat{n}(r') >_\lambda\right)
\end{aligned} \tag{A.11}$$

where in the last line is has been used that for a given λ, the external potential is set (by definition) so that the ground state density is reproduced. The key to introduce the response function is $< \hat{n}(r)\hat{n}(r') >_\lambda$. We introduce the time dependence via the density deviation operator $\hat{\tilde{n}}(r,t) = \hat{n}(r,t) - n(r)$.

$$\begin{aligned}
< \hat{n}(r)\hat{n}(r') >_\lambda = &< \left(\hat{\tilde{n}}(r,t) + n(r)\right)\left(\hat{\tilde{n}}(r',t') + n(r')\right) >_\lambda |_{t=t'} \\
&= < \hat{\tilde{n}}(r,t)\hat{\tilde{n}}(r',t') >_\lambda \\
&+ \underbrace{< \hat{\tilde{n}}(r,t) >_\lambda n(r')}_{=0} + \underbrace{n(r) < \hat{\tilde{n}}(r',t') >_\lambda}_{=0} \\
&+ n(r)n(r')\underbrace{<>_\lambda}_{=1} \\
&= < \hat{\tilde{n}}(r,t)\hat{\tilde{n}}(r',t') >_\lambda + n(r)n(r')
\end{aligned} \tag{A.12}$$

The next step is to introduce the fluctuation-dissipation theorem.

A.2.1 The fluctuation dissipation theorem at 0 Kelvin

$$< \hat{A}(tr)\hat{B}(r') >_\lambda = < e^{i\hat{H}t}\hat{A}e^{-i\hat{H}t}\hat{B}(r') >_\lambda \tag{A.13}$$

using that for a complete set of states $\sum_m |m><m| = 1$

$$\begin{aligned} < \hat{A}(tr)\hat{B}(r') >_\lambda &= \sum_m < e^{i\hat{H}t}\hat{A}(r)e^{-i\hat{H}t}|m >< m|\hat{B}(r') >_\lambda \\ &= \sum_m < e^{i\hat{E}_0 t}\hat{A}(r)e^{-iE_m t}|m >< m|\hat{B}(r') >_\lambda \\ &= \sum_m < \hat{A}(r)|m >< m|\hat{B}(r') >_\lambda \, e^{i(E_0-E_n)t} \end{aligned} \quad (A.14)$$

Fourier transforming $< \hat{A}(tr)\hat{B}(r') >_\lambda$ leads to

$$\begin{aligned} J_1(\omega) &= \int_{-\infty}^{\infty} dt < \hat{A}(tr)\hat{B}(r') >_\lambda \, e^{i\omega t} \\ &= \int_{-\infty}^{\infty} dt \sum_m < \hat{A}(r)|m >< m|\hat{B}(r') >_\lambda \, e^{i(E_0-E_m)t}e^{i\omega t} \\ &= 2\pi \sum_m < \hat{A}(r)|m >< m|\hat{B}(r') >_\lambda \, \delta(E_0 - E_m + \omega) \end{aligned} \quad (A.15)$$

Due to the variational principle $E_0 - E_m < 0$ and therefore $J_1 = 0$ for $\omega < 0$.

$$\begin{aligned} J_2(\omega) &= \int_{-\infty}^{\infty} dt < \hat{B}(r')\hat{A}(rt) >_\lambda \, e^{i\omega t} \\ &= 2\pi \sum_m < \hat{B}(r')|m >< m|\hat{A}(r) >_\lambda \, \delta(E_m - E_0 + \omega) \end{aligned} \quad (A.16)$$

Due to the variational principle $E_m - E_0 < 0$ and therefore $J_2 = 0$ for $\omega > 0$. Rewriting the correlation function in terms of J_1 and J_2. The correlation function becomes:

$$\begin{aligned} C^R(r', rt) &= -i\theta(t) < [\hat{A}(tr)B(r')] >_\lambda \\ &= -i\theta(t) < \hat{A}(tr)\hat{B}(r') - \hat{B}(r')\hat{A}(tr) >_\lambda \\ &= -i\theta(t) < \int_{-\infty}^{\infty} \frac{d\omega}{2\pi} \left[J_1(\omega', r, r') - J_2(\omega', r, r')\right] e^{-i\omega' t} \end{aligned} \quad (A.17)$$

Fourier transforming $C^R(r', rt)$ leads to

$$\begin{aligned} C^R(r', r, \omega) &= -i \int_0^{\infty} dt \int_{-\infty}^{\infty} \frac{d\omega}{2\pi} \left[J_1(\omega', r, r') - J_2(\omega', r, r')\right] e^{i(\omega-\omega'+i\eta)t} \\ &= \int_{-\infty}^{\infty} \frac{d\omega'}{2\pi} \frac{[J_1(\omega', r, r') - J_2(\omega', r, r')]}{\omega - \omega' + i\eta} \end{aligned} \quad (A.18)$$

Taking the imaginary part of the correlation function and using that $\Im\frac{1}{\omega+i\eta} = -\pi\delta(\omega)$ for $\eta \to 0$

$$\Im C^R(r', r, \omega) = -\pi \int_{-\infty}^{\infty} \frac{d\omega'}{2\pi} \left[J_1(\omega', r, r') - J_2(\omega', r, r')\right] \delta(\omega - \omega') \quad \text{(A.19)}$$

This leads to the fluctuation-dissipation theorem

$$\Im C^R(r', r, \omega) = -\frac{1}{2} \left[J_1(\omega, r, r') - J_2(\omega, r, r')\right] \quad \text{(A.20)}$$

Which due to the symmetry of J_1 and J_2 for $\omega > 0$ becomes:

$$-2\Im C^R(r', r, \omega) = J_1(r, r', \omega) \quad \text{(A.21)}$$

A.2.2 The density density response function

We will use the fluctuation-dissipation theorem to introduce the response function into the adiabatic-connection formula. The relevant response is the response of the density due to a change in external potential. The Kubo formular gives the linear response in an observable due to a perturbation of the hamiltonian [230].

$$\begin{aligned} \delta < A(t) > &\equiv < A(t) > - < A >_\lambda \\ &= \int_{t_0} dt' - i\theta(t - t') < [\hat{A}(t), \hat{H}'(t')] >_\lambda e^{-\eta(t-t')} \end{aligned} \quad \text{(A.22)}$$

the linear responds due to an external potential,

$$\hat{H}' = \int dr \hat{n}(r)\phi_{ext}(r, t) \quad \text{(A.23)}$$

The induced density $n_{induced}$ is then given by insertion of the Hamiltonian in Eq. A.23 into the Kubo formula (Eq. A.22):

$$\begin{aligned} n_{induced} &= \int_{t_0}^{\infty} dt' - i\theta(t - t') < [\hat{n}(rt), \hat{H}'(r't')] >_\lambda \\ &= \int dr' \int_{t_0}^{\infty} dt' \underbrace{i\theta(t - t') < [\hat{n}(rt), \hat{n}(r't')] >_\lambda}_{C^R_{nn}(rt,r't') \equiv \chi^R(rt,r't')} e^{-\eta(t-t')} \phi_{ext}(r', t') \end{aligned} \quad \text{(A.24)}$$

Where we have changed to the notation used by Langreth *et al* and Lundqvist *et al* who use $\chi^R(rt, r't')$ as the density density response function.
Now returning to the adiabatic-connection formula. By inserting into the first term on the right side of Eq. A.12:

$$< \hat{\tilde{n}}(rt), \hat{\tilde{n}}(r't') >_\lambda = \int_0^{\infty} \frac{d\omega}{2\pi} J_1(r, r', \omega) e^{-i\omega(t-t')} \quad \text{(A.25)}$$

The integral lower bound is 0 because $J_1(r,r',\omega) = 0$ for $\omega < 0$ Using the fluctuation dissipation theorem (see Sec. A.21):

$$-2\Im\{\chi_\lambda^R\} = J_1(r,r',\omega), \omega > 0 \tag{A.26}$$

Inserting Eq. A.25 and Eq. A.26 into Eq. A.12 we obtain Eq. A.27:

$$< \hat{n}(r)\hat{n}(r') >_\lambda = n(r)n(r') - \frac{1}{\pi}\int_0^\infty d\omega \Im\chi_\lambda^R(r,r',\omega) \tag{A.27}$$

changing to imaginary frequency $u = -i\omega$

$$< \hat{n}(r)\hat{n}(r') >_\lambda = n(r)n(r') - \frac{1}{\pi}\int_0^\infty idu \Im\chi_\lambda^R(r,r',iu) \tag{A.28}$$

Insertion into the adiabatic-connection formula and using that $\Im\chi_\lambda^R(r,r',iu)$ is real valued [229].

$$E_{XC} = -\frac{1}{2}\int_0^1 d\lambda \int d^3r \int d^3r' \frac{1}{|r-r'|}\left(n(r)\delta(r-r') + \frac{1}{\pi}\int_0^\infty du \chi_\lambda^R(r,r',iu)\right) \tag{A.29}$$

Eq. A.29 is now the adiabatic connection formula in terms of the response function. Eq. A.29 is a good starting point for introduction vdW forces, because even though the exact form of $\chi_\lambda^R(r,r',iu)$ is not know, some important limiting cases are known [229]. Eq A.29 may be written in short hand notation as seen in eq. A.30:

$$E_{XC} = -\int_0^1 \frac{d\lambda}{\lambda}\int_0^\infty \frac{du}{2\pi} Tr[\chi_\lambda V_\lambda] - E_{self} \tag{A.30}$$

where

$$\mathrm{Tr}[\chi_\lambda V_\lambda] = \int d^3r \int d^3r' \frac{1}{|r-r'|}\chi_\lambda^R(r,r',iu)$$

and

$$E_{self} = \int d^3r \int d^3r' \frac{1}{|r-r'|} n(r)\delta(r-r')$$

A.3 The Full Potential approximation

Eq. A.29 is in itself not viable for any practical applications in heterogeneous catalysis, and in order for it to become tractable Lundqvist *et al* and Langreth *et al* make a series of approximation. In order to simplify the

response function, a Dyson like equation linking the response of the homogeneous electron gas with the real interacting response function, is introduced [231]:

$$\chi = \chi_{KS} + \chi_{KS}(V_\lambda + f_{XC,\lambda})\chi_\lambda \tag{A.31}$$

Where χ_{KS} is the response function of the homogeneous electron gas and $f_{XC,\lambda}$ is the exchange correlation kernel. Then the following trick is introduced in reference [232]:

$$\chi_\lambda = \tilde{\chi}_\lambda + \tilde{\chi}_\lambda V_\lambda \chi_\lambda \tag{A.32}$$

$$\tilde{\chi}_\lambda = \chi_0 + \chi_0 f_{XC}^\lambda \tilde{\chi}_\lambda \tag{A.33}$$

Where $\tilde{\chi}_\lambda$ is the response to the screened potential. The usual approximation in eq. A.33 is to set $f_{XC} = 0$ or equivalent $\tilde{\chi}_\lambda = \chi_0$ which is called the random phase approximation. However, it has turned out to be more fruitful to do a different type of approximation called the full potential approximation (FPA) where $\tilde{\chi}_\lambda = \tilde{\chi}_{\lambda=1}$. Inserting eq. A.32 into eq. A.30 and using the FPA approximation lead to:

$$E_{XC}^{FPA} = \int_0^\infty \frac{du}{2\pi} \mathrm{Tr}[ln(1 - \tilde{\chi}_{\lambda=1} V)] - E_{self} \tag{A.34}$$

The last step is to subtract the local exchange-correlation term this is done by introduction the dielectric function ϵ [232]:

$$\tilde{\chi} = \vec{\nabla} \cdot \frac{\epsilon - 1}{4\pi} \vec{\nabla} \tag{A.35}$$

For the homogeneous electron gas the exchange correlation energy is [232]:

$$E_{XC}^{FPA}(H.E.G) = \int_0^\infty \frac{du}{2\pi} \mathrm{Tr}[ln(\epsilon)] - E_{self} \tag{A.36}$$

Subtracting eq. A.36 from eq. A.34:

$$E_c^{nl} = \int_0^\infty \frac{du}{2\pi} \mathrm{Tr}[ln(1 - V\tilde{\chi}) - ln\epsilon] \tag{A.37}$$

expanding this equation to second order in $S \equiv 1 - \epsilon^{-1}$ leads to [25]:

$$E_c^{nl} \approx \int_0^\infty \frac{du}{4\pi} \mathrm{Tr}[S^2 - \left(\frac{\nabla S \cdot \nabla V}{4\pi e^2}\right)^2] \tag{A.38}$$

S is then approximated by a plasmon pole approximation and this leads to the vdW-DF functional for the non-local part [25].

$$E_c^{nl} = \iint dr dr' n(r) \phi(r, r') n(r') \tag{A.39}$$

Where $\phi(r, r')$ can be calculated in advance and tabulated, see reference [25].

Appendix B

vdW-DF implementation issues

B.1 Overview

We have implemented the recently developed XC-functional vdW-DF [25] in the grid based projected augmented wave density functional theory code GPAW [26]. The required input is the density and the super cell. The input density may be taken from any DFT program with the one restriction implied by GPAW that the super cell must have orthogonal unit cell vectors. Periodic boundary conditions are included using the minimum image convention. A density cutoff (not to be confused with the density cutoff used in the double grid technique in plane wave DFT codes) is introduced which leaves densities below a certain threshold out of the 6d-realspace integral (Eq. A.39) in order to speed up the calculations.

B.1.1 Convergence tests

To insure convergence of E_c^{nl} one should test the following parameters for convergence

1. The grid spacing
2. The density cutoff

B.2 Tests of the current implementation

We have performed a series of test of our implementation of vdW-DF.

- Visual inspection of the interaction kernel ϕ
- Convergence of the interaction kernel with the asymptotic limit at large separations

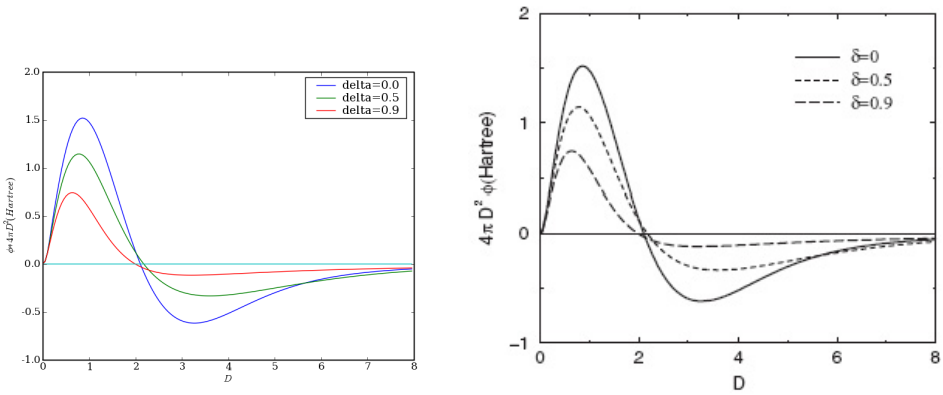

Figure B.1: Left: The interaction kernel ϕ. Right: The interaction kernel ϕ from reference [25].

- C6 coefficients
- Rare gas dimer binding curve
- Benzene dimer binding curve

When possible we compare our results with the results of reference [25].

B.2.1 The interaction kernel ϕ

The interaction kernel has been calculated as describe in reference [25]. We have tabulated it on a uniform grid with a grid spacing of 0.05 in both δ and D. The upper limit of D is set to 60 which is well beyond the asymptotic limit. D and δ depend on q_0 which is a function of the density and the gradient of the density [25].

B.2.2 C6 coefficients

Reference [25] calculates the C6 coefficients based on Hartree-Fock densities. No information is given as to the size of the basis used in the HF calculations and we have therefore chosen to calculated the C6 coefficients using GGA DFT with either a plane wave basis or a grid basis. The C6 coefficients are calculated using the asymptotic limit of the interaction kernel. Therefore, they only depend on q_0 [25].

Plane wave basis

We have found it very difficult to calculate C6 coefficients using plane wave DFT. The oscillations at low densities due to the planewave basis introduce large unphysical oscillations in q_0. A very high planewave cutoff and a dense density grid are required in order to minimize these effects. The calculated

C6 coefficients are very dependent on the vdw density cutoff and we have therefore chosen only to test C6 coefficients using a grid based code which does not have the inherent problems of plane waves.

Grid basis

The smooth density and reduced gradient of the grid based code remove the large unphysical oscillations of q_0 at low densities. The projected augmented wave representation of the core electrons does allow us to introduce the real valence density. We have calculated C6 coefficients for He, Ne, Ar, and Mg in non periodic cubic unit cell with edge lengths of 12Å and a grid spacing of 0.15Å. The obtained results can be seen in Fig. B.2.
Comparing the converged C6 coefficients with the results from [25] we find a generally good agreement even though one should be careful with direct comparison since the exact convergence criteria of the results in [25] are not reported.

B.2.3 Kr dimer

We have calculated the interaction energy of a Kr dimer. The density is calculated using Dacapo, with an energy cutoff of 30Rydberg and a density cutoff of 45Rydberg. The vdW energy is calculated using the Dacapo density with a density grid distance of 0.12Åand including densities above $0.0005 a_0^{-3}$ in the 6d integral. We get the same binding curve as in reference [25] with one exception which is a small offset of the energy which could be an effect of the unit cell size.

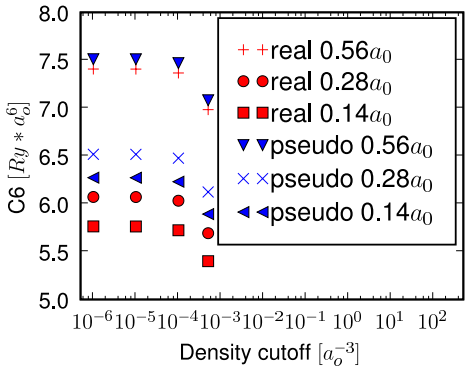

(a) He (4.8)

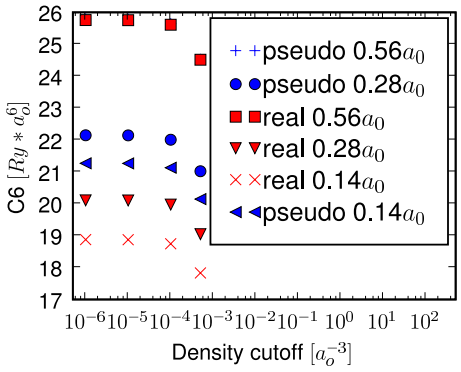

(b) Ne (14.6)

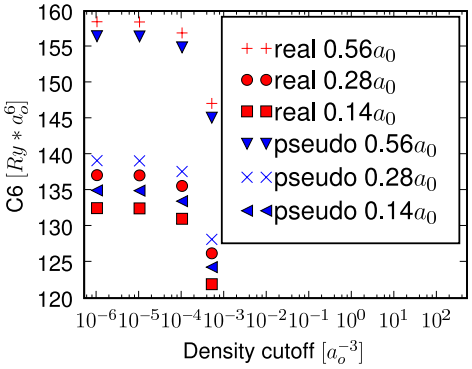

(c) Ar (124)

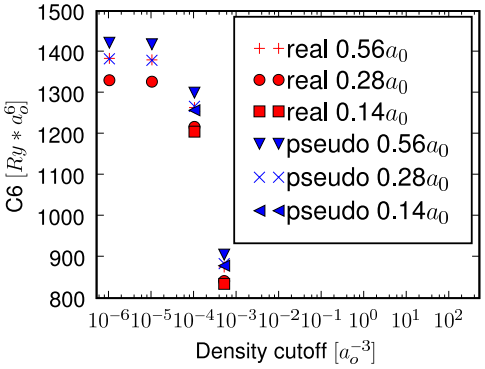

(d) Mg (1598)

Figure B.2: C6 coefficients as a function of density cutoff and real or pseudo density from GPAW for a) He, b) Ne, c) Ar, and d) Mg. a_0 is the bohr radii. numbers in parenthesis are the C6 values from reference [25].

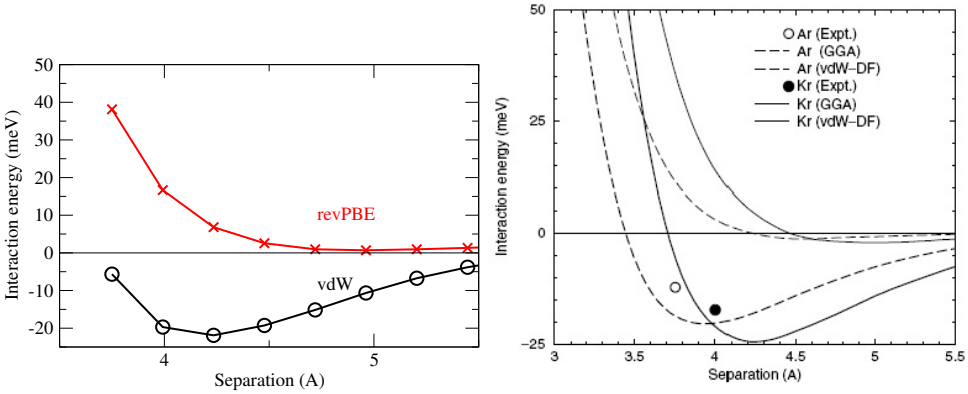

Figure B.3: Left: Kr dimer. Right: Kr and Ar dimer from reference [25].

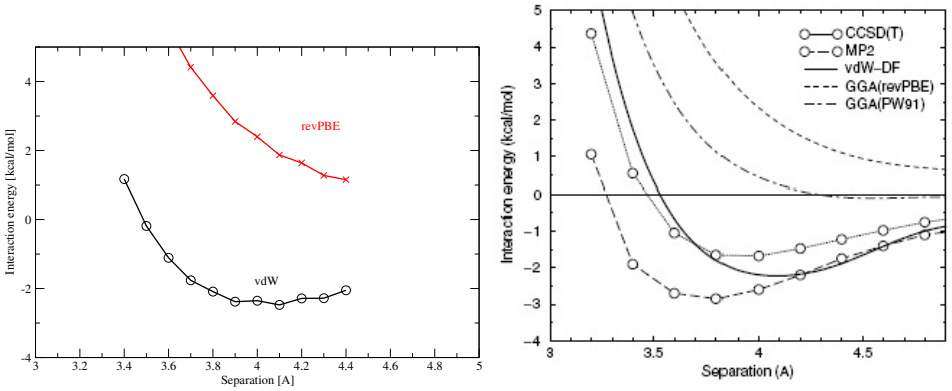

Figure B.4: Left: Benzene dimer Right: Benzene dimer from reference [25].

B.2.4 Benzene dimer

We have calculated the interaction energy of parallel benzene dimers (Fig. B.4). The density is calculated using Dacapo, with an energy cutoff of 30Rydberg and a density cutoff of 60Rydberg. The vdW energy is calculated using the Dacapo density with a density grid distance of 0.11Å and including densities above $0.0005\mathrm{a}_0^{-3}$ in the 6d integral. We get a similar binding curve to reference [25]. We have small oscillations in the revPBE energy, which have also been observed in other vdW studies [233]. This effect does not disappear with a larger density grid and we refer to [233] for a more thorough discussion of this very small anomaly, which for most practical problems will be insignificant.

B.2.5 Choice of density cutoff and grid spacing in 6d integral

We will use thiophene adsorption on the MoS_2 basal plane as an example of the importance of the density cutoff (ncut) in the 6d real space integration. Fig. B.5 shows the binding curve of thiophene as it is moved towards the surface of MoS_2. ncut is varied from 0.0005 to $0.000001a_0^{-3}$ and the grid spacing of the 6d integral is varied between from 0.106Å and 0.212Å. The influence of the density cutoff (ncut) is small relative to the total binding energy. A closer look at a distance of 3.5Å reveals that lowering ncut from $0.0005a_0^{-3}$ to $0.000001a_0^{-3}$ while keeping the grid spacing fixed at 0.212Å changes the binding energy with less than 10meV. Changing the grid spacing from 0.212Å to 0.106Å changes the binding energy with 30meV. Thus, for this particular system it is reasonable to use a grid spacing of 0.106Å and a density cutoff of $0.0001a_0^{-3}$.

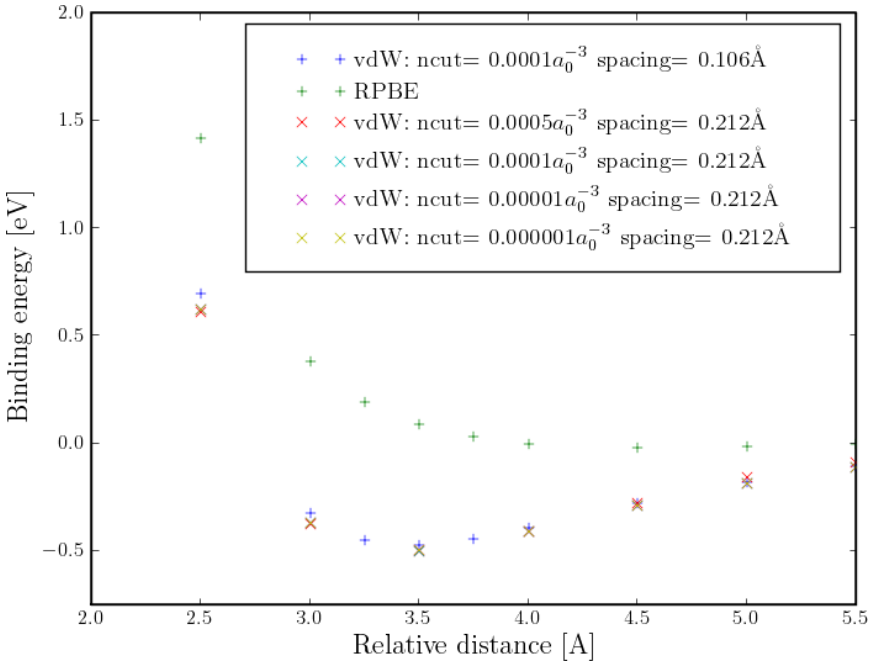

Figure B.5: Thiophene on the basal plane of MoS_2.

B.3 Summary and future improvements

The minimum image convention should be extended so that points further away can be included. The current implementation is performed as a perturbation to the GGA density. Implementation of a self consistent scheme [228] will provide the real forces and allows the user to directly minimize the atomic positions of a given problem, which will be of importance for problems with several degrees of freedom.

Appendix C

Adsorption energies on MoS_2

The adsorption energies E_{ad} have been calculated as

$$E_{ad} = E_{molecule+MoS_2} - E_{MoS_2} - E_{molecule(g)}$$

except for thiolates where the adsorption energy is calculated as

$$E_{ad} = E_{Thiolate+MoS_2} + E_{1/2H_2(g)} - E_{MoS_2} - E_{Thiol(g)}$$

Table 1 Mo edge intermediates. Color scheme for online version: Sulfur is yellow, Molybdenum is blue, Carbon is cyan, and Hydrogen is black.

	Thiophene	Thiophene (90deg)	Thiophene	Thiophene
S[%]	50	50	50	50
H [%]	50	50	50	50
Adsorption energy [eV]	-0.02	-0.07	-0.05	-0.05
Front View	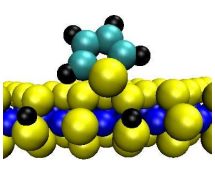	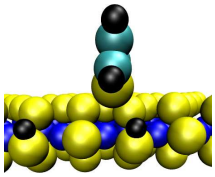	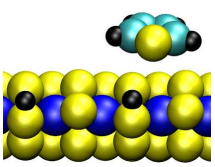	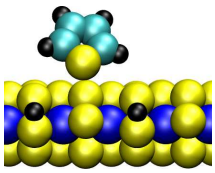
Top view	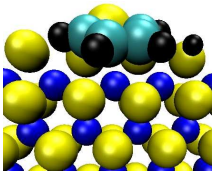	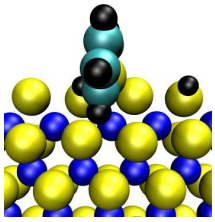	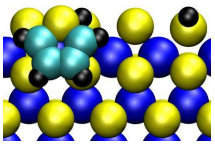	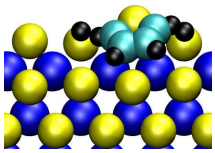
	Thiophene	2-Hydrothiophene	2-Hydrothiophene	
S[%]	50	50	50	
H[%]	50	25	50	
Adsorption energy [eV]	-0.08	-0.74	-0.42	
Front View	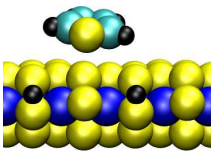	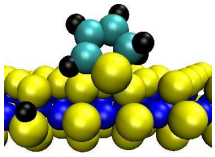	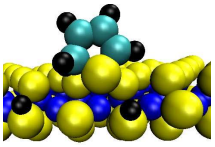	
Top view	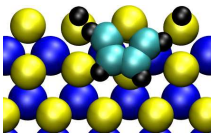	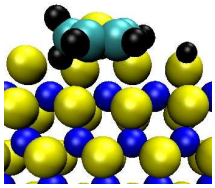	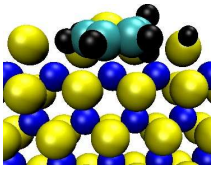	

[a] The adsorption energy is calculated according to the reaction: $C_4H_xSH(g) + * \rightarrow 1/2\ H_2(g) + C_4H_xS\text{-}*$

Table 2 Mo edge intermediates. Color scheme for online version: Sulfur is yellow, Molybdenum is blue, Carbon is cyan, and Hydrogen is black.

	2,5-Dihydrothiophene	2,5-Dihydrothiophene	2,5-Dihydrothiophene(90)
S[%]	50	50	50
H[%]	25	50	50
Adsorption energy [eV]	-0.09	-0.12	0.04
Front View	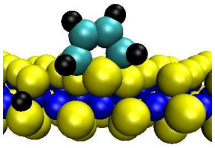	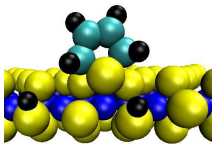	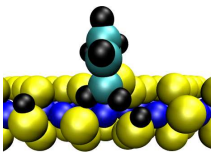
Top view	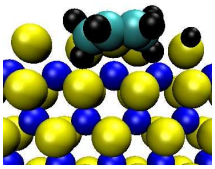	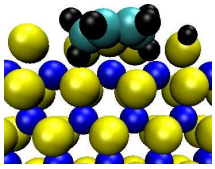	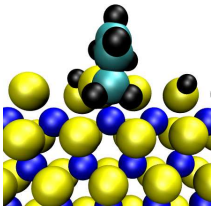
	2,5-Dihydrothiophene	Cis-butadien-thiolate	Cis-butadien-thiolate
S[%]	50	50	50
H[%]	50	25	25
Adsorption energy [eV]	-0.07	1.10[a]	1.15[a]
Front View	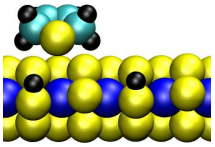	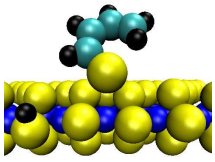	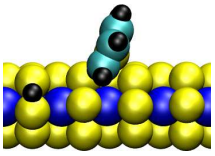
Top view	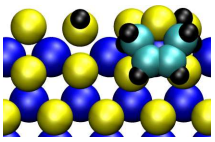	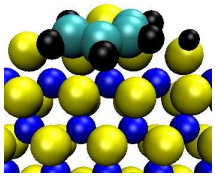	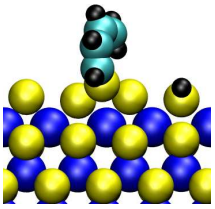

[a] The adsorption energy is calculated according to the reaction: $C_4H_xSH(g) + * \rightarrow 1/2\ H_2(g) + C_4H_xS\text{-}*$

Table 3 Mo edge intermediates. Color scheme for online version: Sulfur is yellow, Molybdenum is blue, Carbon is cyan, and Hydrogen is black.

	Cis-butadien-thiolate	Cis-2-butene-thiolate	Cis-2-butene-thiolate	Cis-2-butene-thiolate
S[%]	50	50	50	50
H[%]	25	25	25	25
Adsorption energy [eV]	1.11[a]	0.92[a]	0.74[a]	1.12[a]
Front View	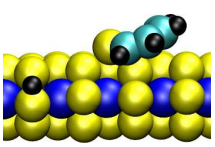	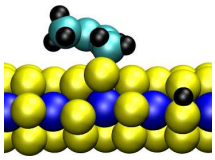	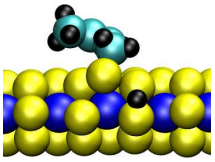	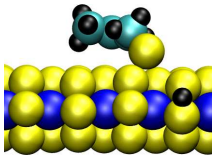
Top view	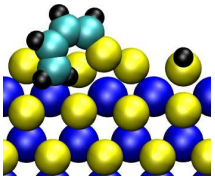	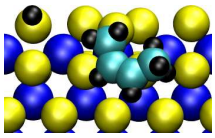	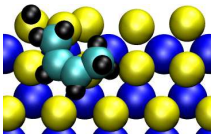	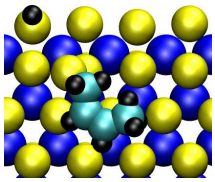
	Cis-2-butene-thiolate	Cis-2-butene-thiolate	Cis-2-butene-thiolate	Cis-2-butene-thiol
S[%]	50	50	50	50
H[%]	25	50	50	25
Adsorption energy [eV]	0.77[a]	0.61[a]	0.47[a]	-0.12
Front View	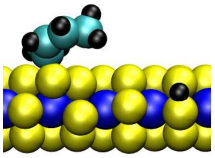	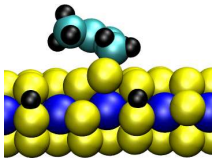	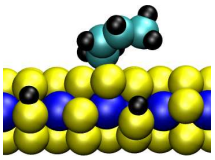	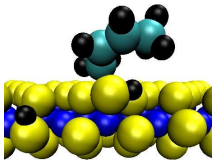
Top view	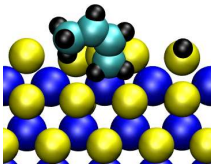	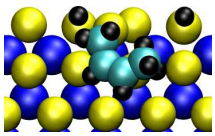	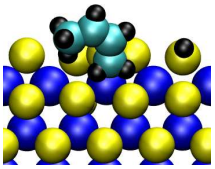	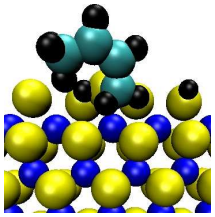

[a] The adsorption energy is calculated according to the reaction: $C_4H_xSH(g) + * \rightarrow 1/2\ H_2(g) + C_4H_xS\text{-}*$

Table 4 Mo edge intermediates. Color scheme for online version: Sulfur is yellow, Molybdenum is blue, Carbon is cyan, and Hydrogen is black.

	Cis-2-butene	H_2S	H_2S	H_2S
S[%]	50	50	50	50
H[%]	25	0	0	0
Adsorption energy [eV]	0.28	-0.16	-0.19	-0.14
Front View	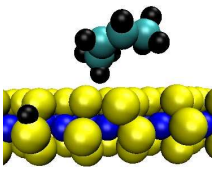	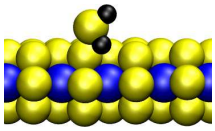	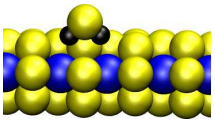	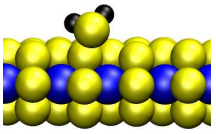
Top view	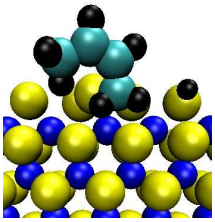	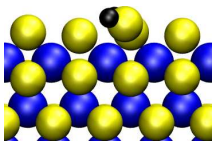	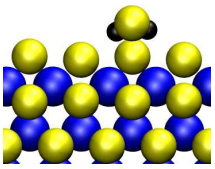	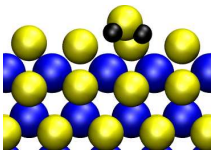

Table 1 S edge intermediates. Color scheme for online version: Sulfur is yellow, Molybdenum is blue, Carbon is cyan, and Hydrogen is black.

	Thiophene	Thiophene	Thiophene	Thiophene
S[%]	100	100	100	100
H [%]	75	75	75	75
Adsorption energy [eV]	0.02	-0.08	-0.05	-0.04
Front View	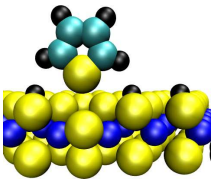	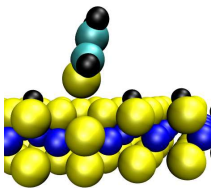	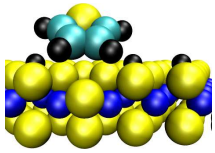	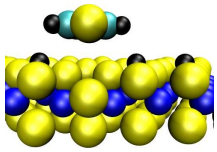
Top view	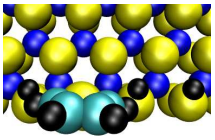	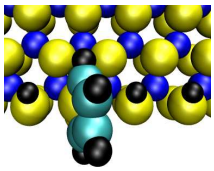	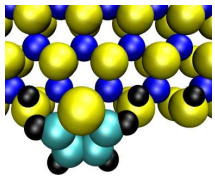	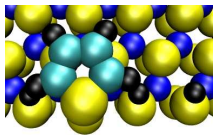
	Thiophene	Thiophene	2,Hydrothiophene	2,Hydrothiophene
S[%]	87.5	87.5	87.5	87.5
H [%]	50	75	50	75
Adsorption energy [eV]	0.04	0.21	-0.82	-0.67
Front View	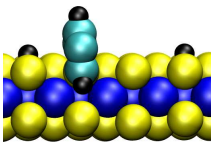	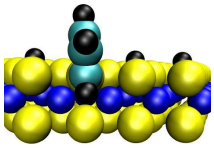	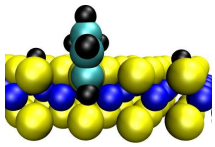	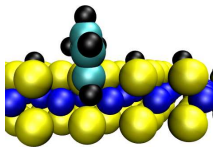
Top view	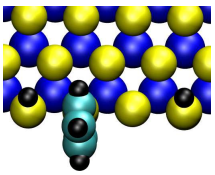	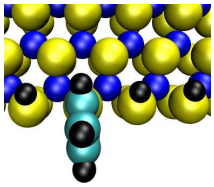	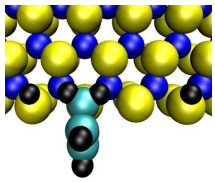	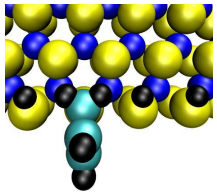

[a] The adsorption energy is calculated according to the reaction: $C_4H_xSH(g) + * \rightarrow 1/2\ H_2(g) + C_4H_xS\text{-}*$

Table 2 S edge intermediates. Color scheme for online version: Sulfur is yellow, Molybdenum is blue, Carbon is cyan, and Hydrogen is black.

	2,5-Dihydrothiophene	2,5-Dihydrothiophene	Cis-butadien-thiolate	Cis-2-butene-thiolate
S[%]	87.5	87.5	87.5	87.5
H[%]	50	75	50	50
Adsorption energy [eV]	-0.85	-0.59	-0.95[a]	-1.23[a]
Front View	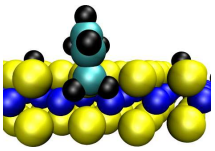	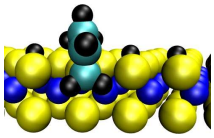	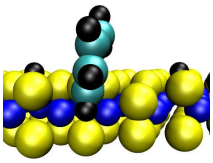	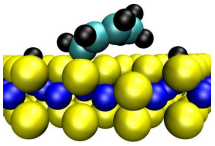
Top view	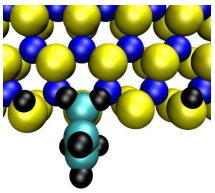	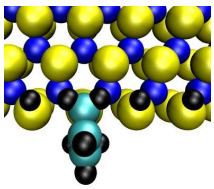	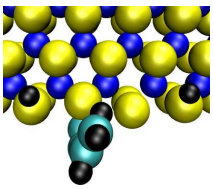	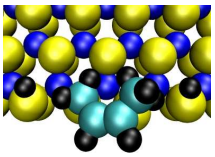

	Cis-2-butene-thiolate	Cis-2-butene-thiol	Cis-2-butene-thiol	Cis-2-butene
S[%]	87.5	87.5	87.5	100
H[%]	50	25	50	25
Adsorption energy [eV]	-0.14[a]	-0.62	-0.52	-0.05
Front View	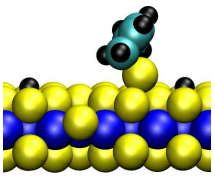	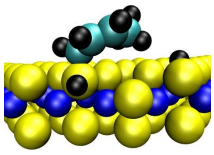	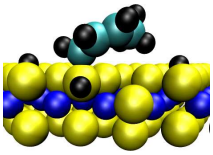	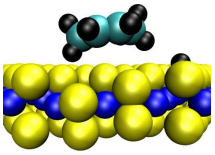
Top view	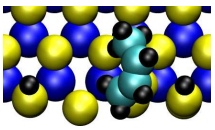	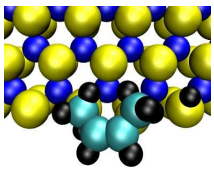	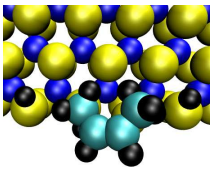	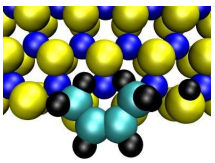

[a] The adsorption energy is calculated according to the reaction: $C_4H_xSH(g) + * \rightarrow 1/2\ H_2(g) + C_4H_xS\text{-}*$

Table 3 S edge intermediates. Color scheme for online version: Sulfur is yellow, Molybdenum is blue, Carbon is cyan, and Hydrogen is black.

	H_2S	H_2S	H_2S	H_2S
S[%]	87.5	87.5	87.5	87.5
H[%]	50	50	50	75
Adsorption energy [eV]	-0.12	-0.2	0.1	0.09
Front View	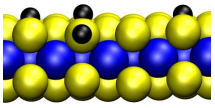	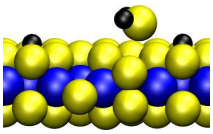	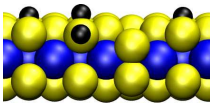	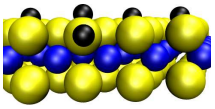
Top view	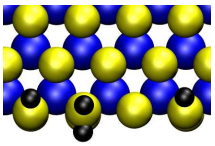	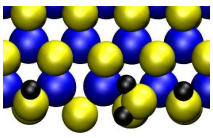	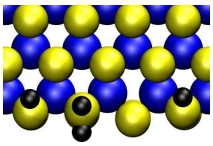	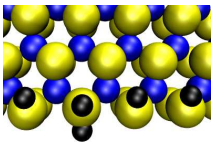

Appendix D

Adsorption energies on CoMoS

The adsorption energies E_{ad} have been calculated as

$$E_{ad} = E_{molecule+MoS_2} - E_{MoS_2} - E_{molecule(g)}$$

except for thiolates where the adsorption energy is calculated as

$$E_{ad} = E_{Thiolate+MoS_2} + E_{1/2H_2(g)} - E_{MoS_2} - E_{Thiol(g)}$$

Table 1 Adsorption on CoMoS S edge

	25DHThiophene	25DHThiophene	25DHThiophene	25DHThiophene
S[%]	50	50	50	50
H[%]	25	25	25	25
Adsorption Energy [eV]	-0.57	-0.06	-0.53	-0.54
Mag mom [μ_B]	0.0	NA	0.0	0.0
Top View	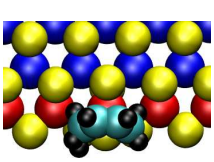	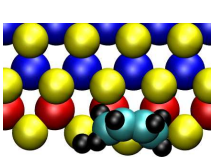	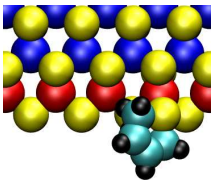	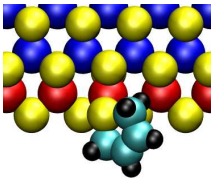
Front View	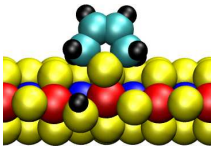	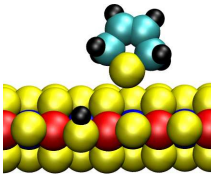	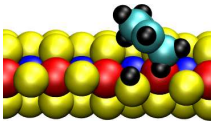	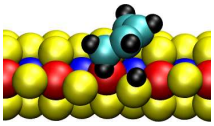
	25DHThiophene	25DHthiophene	25DHthiophene	25DHthiophene
S[%]	50	50	50	50
H[%]	25	0	0	0
Adsorption Energy [eV]	-0.33	-0.35	-0.40	-0.4
Mag mom [μ_B]	0.0	NA	0.0	0.0
Top View	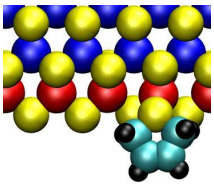	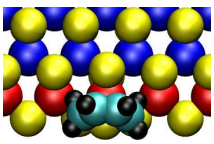	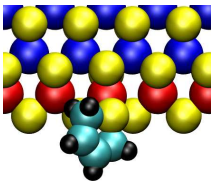	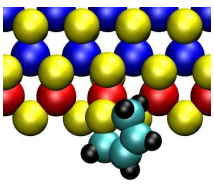
Front View	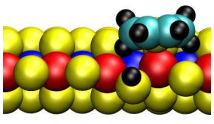	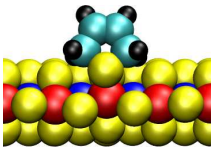	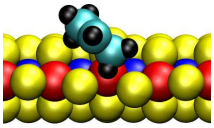	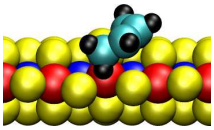

Table 2 Adsorption on CoMoS S edge

	Hthiophene	Hthiophene	Hthiophene	Hthiophene
S[%]	50	50	50	50
H[%]	0	0	0	0
Adsorption Energy [eV]	-0.78	-0.78	-0.81	-0.60
Mag mom [μ_B]	0.46	0.48	0.48	NA
Top View	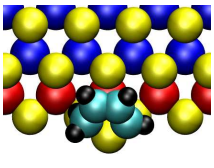	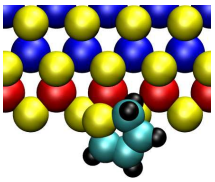	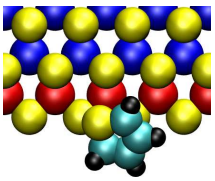	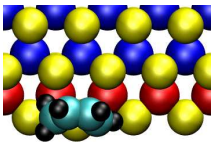
Front View	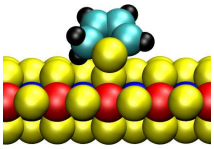	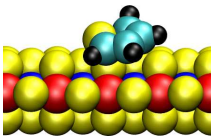	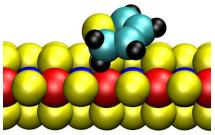	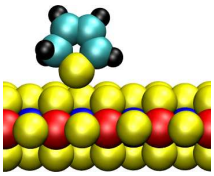
	Cis-2-butenethiolate	Cis-2-butenethiolate	Cis-butadien-thiolate	Cis-butadien-thiolate
S[%]	50	50	50	50
H[%]	0	0	0	0
Adsorption Energy [eV]	-0.2	-0.15	0.01	0.0
Mag mom [μ_B]	0.0	0.0	0.0	0.0
Top View	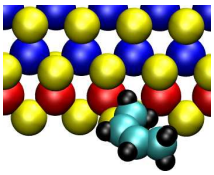	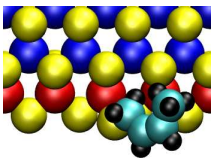	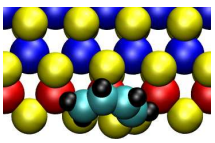	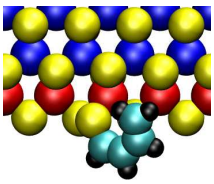
Front View	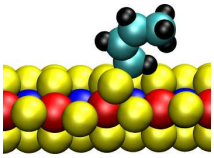	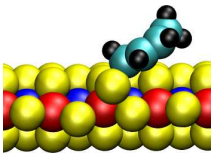	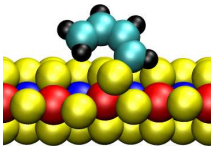	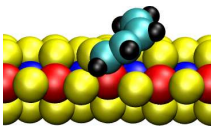

Table 3 Adsorption on CoMoS S edge

	Cis-butadien-thiolate	Cis-2-butenethiol	Cis-2-butenethiol	H_2S
S[%]	50	50	50	50
H[%]	0	0	0	0
Adsorption Energy [eV]	1.17	-0.23	-0.34	-0.02
Mag mom [μ_B]	NA	NA	0.0	0.0
Top View	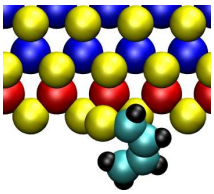	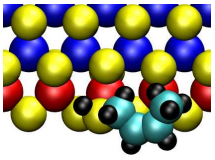	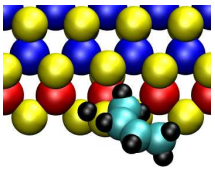	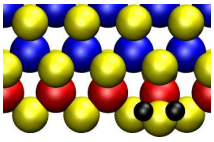
Front View	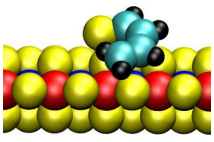	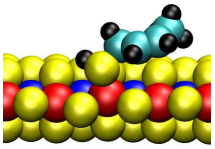	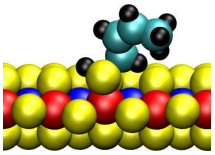	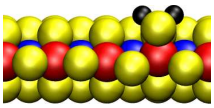
	H_2S	Thiophene	Thiophene	Thiophene
S[%]	50	50	50	50
H[%]	0	25	25	25
Adsorption Energy [eV]	-0.02	0.0	-0.03	0.03
Mag mom [μ_B]	0.0	0.0	0.0	0.0
Top View	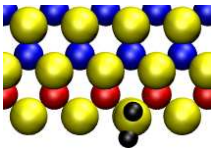	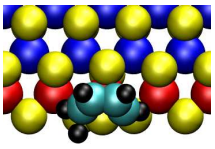	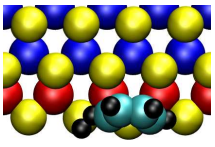	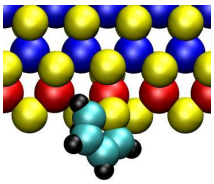
Front View	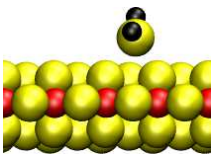	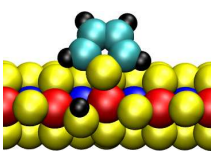	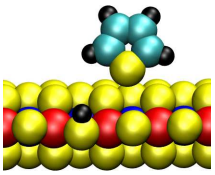	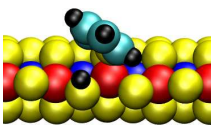

Table 4 Adsorption on CoMoS S edge

	Thiophene	Cis-2-butene-thiolate	Cis-2-butene-thiolate	Cis-2-butene-thiolate
S[%]	50	50	50	50
H[%]	25	25	25	25
Adsorption Energy [eV]	-0.07	-0.32	-0.28	-0.02
Mag mom [μ_B]	0.0	0.0	0.0	NA
Top View	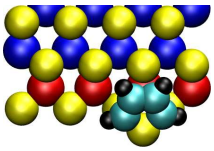	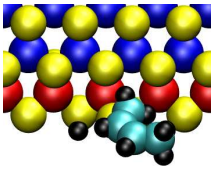	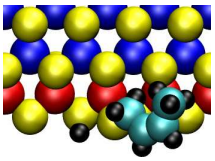	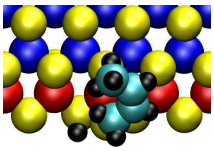
Front View	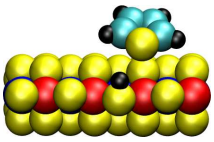	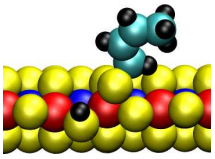	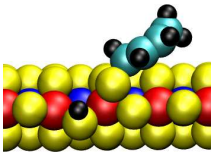	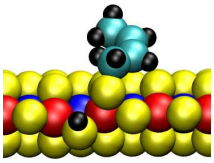
	Cis-2-butene-thiol	Cis-2-butene-thiol	Cis-2-butadien	
S[%]	50	50	62.5	
H[%]	25	25	25	
Adsorption Energy [eV]	-0.55	-0.46	-0.04	
Mag mom [μ_B]	0.0	0.0	0.0	
Top View	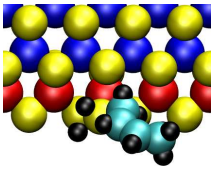	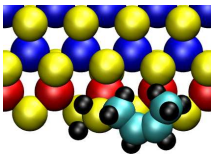	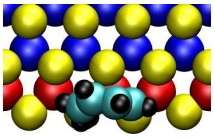	
Front View	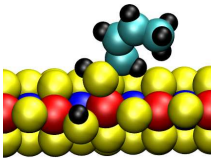	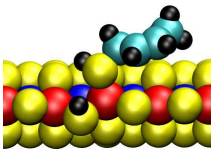	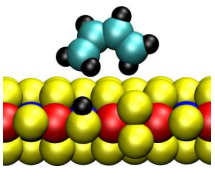	

Appendix E

Included Publications

Paper 1

J|A|C|S
COMMUNICATIONS

Published on Web 03/25/2005

Biomimetic Hydrogen Evolution: MoS_2 Nanoparticles as Catalyst for Hydrogen Evolution

Berit Hinnemann, Poul Georg Moses, Jacob Bonde, Kristina P. Jørgensen, Jane H. Nielsen, Sebastian Horch, Ib Chorkendorff, and Jens K. Nørskov*

Center for Atomic-scale Materials Physics, Department of Physics, NanoDTU, Technical University of Denmark, DK-2800 Lyngby, Denmark

Received January 24, 2005; E-mail: norskov@fysik.dtu.dk

The electrochemical hydrogen evolution process whereby protons and electrons are combined into molecular hydrogen is catalyzed most effectively by the Pt group metals.[1] The interest in hydrogen evolution catalysts is currently increasing, as molecular hydrogen, H_2, is being considered as an energy carrier.[2] Unlike the hydrocarbon fuels used today, hydrogen produces only water during oxidation, for instance in a fuel cell. For hydrogen to be a real alternative to hydrocarbons, it must be produced in a sustainable fashion. One possibility is to use sunlight directly or indirectly (through wind power, for instance) to split water.[2] This requires an efficient catalyst for hydrogen evolution, preferably based on materials that are cheap and abundant. It is therefore important to find alternatives to the Pt group metals.

Hydrogenases and nitrogenases are also effective catalysts for the hydrogen evolution process[3,4] even though the catalytically active site of these enzymes contains the much less noble metals Fe, Ni, and Mo. Recently it has become possible to anchor hydrogenase to an electrode surface,[5] and considerable progress has been made in the synthesis of compounds in solution resembling the hydrogenase active site and showing activity for hydrogen evolution.[6]

In the present communication, we use density functional calculations to guide us to a new inorganic analogue of the other hydrogen-producing enzyme, nitrogenase. We analyze the difference between the metallic and the biological catalysts and show that in terms of being able to stabilize intermediates involving atomic hydrogen they have very similar properties. This allows us to identify a parameter determining whether a certain compound will be suitable as a catalyst in electrochemical hydrogen evolution, and it provides an efficient way to search for new systems.

Most water-splitting processes rely on electrochemical hydrogen evolution $2H^+ + 2e^- \rightarrow H_2$ in the final step. The hydrogen evolution reaction must in the first step involve bonding of hydrogen to the catalyst $H^+ + e^- + * \rightarrow H^*$, where * denotes a site on the surface able to bind to hydrogen. The second step is the release of molecular hydrogen through one of the two processes:[1] $2H^* \rightarrow H_2 + 2^*$ or $H^+ + e^- + H^* \rightarrow H_2 + *$.

Using density functional theory (DFT) calculations, we can elucidate the thermochemistry (which is independent on the precise mechanism of the second step) of the reaction; see Figure 1.[7] By calculating the free energy of atomic hydrogen bonding to the catalyst, one can compare different metal surfaces as catalysts. For a chemical process to proceed at or around room temperature, no reaction step can be associated with large changes in the free energy. This immediately excludes the metals that form strong bonds to atomic hydrogen (Ni and Mo in Figure 1) as good catalysts because the hydrogen release step will be slow. Metals that do not bind to atomic hydrogen (Au in Figure 1) are also excluded because here the proton/electron-transfer step will be thermodynamically uphill and therefore slow. There could be extra energy barriers associated with the proton-transfer steps or H_2 recombination, but independent of this it is a necessary, but not sufficient, criterion for a material to be a good catalyst that the free energy of adsorbed H is close to that of the reactant or product (i.e., $\Delta G_H^\circ \cong 0$). This principle can explain available experimental observations regarding metals as catalysts and electrode materials for hydrogen evolution.[7]

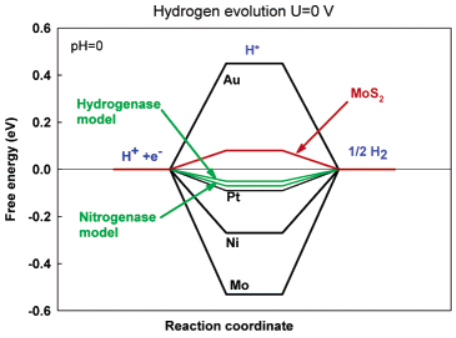

Figure 1. Calculated free energy diagram for hydrogen evolution at a potential $U = 0$ relative to the standard hydrogen electrode at pH = 0. The free energy of $H^+ + e^-$ is by definition the same as that of $^1/_2\ H_2$ at standard conditions. The free energy of H atoms bound to different catalysts is then found by calculating the free energy with respect to molecular hydrogen including zero-point energies and entropy terms. The comparison of different elemental metals is taken from ref 7. The results for hydrogenase are from ref 11. The included result for MoS_2 is the free energy required to increase the hydrogen coverage from 25 to 50%; see Figure 2.

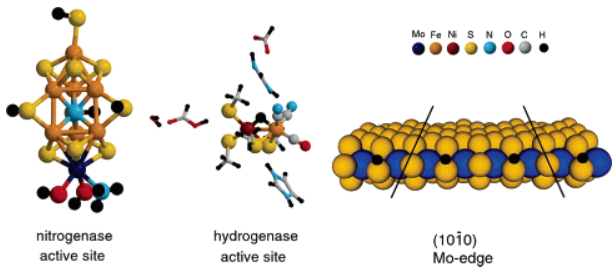

Figure 2. (Left) Nitrogenase FeMo cofactor (FeMoco) with three hydrogen atoms bound at the equatorial μ_2S sulfur atoms. (Middle) Hydrogenase active site with one hydrogen atom bound. The structure is taken from ref 11. (Right) MoS_2 slab with sulfur monomers present at the Mo edge. The coverage is 50%, i.e., hydrogen is bound at every second sulfur atom. The lines mark the dimension of the unit cell in the *x*-direction.

It is interesting to apply the same analysis to the active sites in nitrogenases and hydrogenases. For nitrogenase we have considered the model of the active site, the FeMo cofactor (FeMoco) shown in Figure 2.[8] We find that hydrogen atoms can only bind exothermically to the three equatorial sulfur ligands (μ_2S ligands) on the FeMoco. When the free energy of hydrogen atoms bound to the equatorial sulfur of the FeMoco is included in Figure 1, it

10.1021/ja0504690 CCC: $30.25

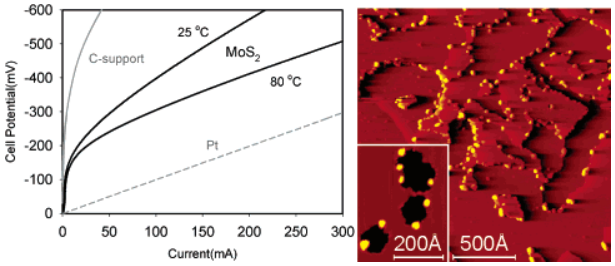

Figure 3. (Left) Polarization curve for hydrogen evolution on Pt, daihope C-support, and MoS_2 cathodes. The polarization curves for Pt and C support are made at 25 °C. The potentials are measured with respect to a carbon-supported Pt anode in a proton exchange membrane electrode assembly. (Right) STM images of MoS_2 nanoparticles on modified graphite.

results in a binding energy close to that of Pt. The FeMoco thus complies with the $\Delta G_H^\circ \cong 0$ requirement.[9] A number of researchers have performed computational studies of hydrogenase,[10,11] and the results obtained by Siegbahn[11] allow us to calculate the atomic hydrogen adsorption free energy for a [NiFe]-hydrogenase system. The Siegbahn model for the hydrogenase active site is shown in Figure 2. When the free energy is included in Figure 1, one can see that hydrogenase also fulfils the $\Delta G_H^\circ \cong 0$ requirement and fulfils it best for all considered systems.[9]

We therefore conclude that ΔG_H° is a good descriptor of materials that can catalyze hydrogen evolution and applies to a broad range of systems, both metals and enzymes. This means that we can use the same calculations to search for other systems, which could be candidates as catalysts for hydrogen evolution. One compound we have found computationally to obey the criterion is MoS_2; see Figure 1. Comparing the nitrogenase active site and the MoS_2 edge structure, we see that they bear a close resemblance, as shown in Figure 2. In both structures, the sulfur atom, which binds the hydrogen, is 2-fold coordinated to metal atoms, either to molybdenum or to iron. Only the edges of MoS_2 are interesting in this context, as the basal plane of MoS_2 is catalytically inactive.[12] The first H that bonds to the edge is strongly bound, but at an H coverage above 0.25, the differential free energy of adsorption is 0.1 eV. According to the calculations, additional H atoms should then be able to adsorb with a low barrier or, equivalently, a low overpotential of the order 0.1 V. A good material would be nanometer-large MoS_2 crystallites supported on, for example, graphite, which is conducting but otherwise inert. Such materials are used as catalysts for hydrotreating (hydrogenation of sulfur compounds in crude oil[13]), and methods for their preparation can be found in the literature.[14] It is indeed possible to prepare nanosized MoS_2 clusters on a graphite support, as can be seen in the scanning tunnel microscope (STM) image shown in Figure 3. The MoS_2 nanoparticles are approximately 4 nm in diameter and 1 nm in apparent height, and nucleate along the graphitic steps.

We have tested experimentally whether MoS_2 nanoparticles supported on carbon can be used as catalyst for electrochemical hydrogen evolution. This was done by preparing a membrane electrode assembly (MEA), based on a Nafion proton exchange membrane, with a standard platinum electrode on one side and a MoS_2/graphite electrode on the other side. By having the same hydrogen pressure on both sides, we could make the electrochemical measurements using a Parstat 2273 potentiostat resulting in the $I-V$ curve shown in Figure 3. The experimental approach has been used successfully in other studies.[15] The conditions of the experiment correspond to pH = 0 as in the calculations. As shown in Figure 3, MoS_2/graphite is a quite reasonable material for hydrogen evolution with an overpotential in the range 0.1−0.2 V.

We note that MoS_2 has been found to be a promoter for the hydrogen evolution activity of NiS_x electrodes,[16] which can be understood from our findings. Furthermore, MoS_2 has been tested for photocatalytic hydrogen evolution and shows activity but with significantly lower currents.[17]

Our findings suggest that we can begin searching for new catalytic materials using quantum chemical methods. The MoS_2 nanoparticles supported on graphite may be an example of a new class of electrode materials.

Acknowledgment. M. Brorson is gratefully thanked for providing us the samples. We thank P. E. M. Siegbahn for providing us results and structures prior to publication. We acknowledge support from the Danish Center of Scientific Computing through Grant No. HDW-1101-05.

Supporting Information Available: Details of the DFT calculations, experimental setup, and obtained data. This material is available free of charge via the Internet at http://pubs.acs.org.

References

(1) (a) Trasatti, R. S. *J. Electroanal. Chem.* **1972**, *39*, 163. (b) Bockris, J. O'M.; Reddy, A. K. N.; Gamboa-Aldeco, M. *Modern Electrochemistry 2A* 2nd ed.; Kluwer Academic/Plenum Publishers: New York, 1998.
(2) Dresselhaus, M. S.; Thomas, I. L. *Nature* **2001**, *414*, 332.
(3) (a) Evans, D. J.; Pickett C. J. *Chem. Soc. Rev.* **2003**, *32*, 268. (b) Vollbeda, A.; Fontecilla-Camps, J. C. *J. Chem. Soc., Dalton Trans.* **2003**, *21*, 4030.
(4) (a) Rees, D. C.; Howard, J. B. *Science* **2003**, *300*, 929. (b) Lee, S. C.; Holm, R. H. *Proc. Natl. Acad. Sci. U.S.A.* **2003**, *100*, 3595.
(5) Lamle, S. E.; Vincent, K. A.; Halliwell, L. M.; Albracht, S. P. J.; Armstrong, F. A. *J. Chem. Soc., Dalton Trans.* **2003**, *21*, 4152.
(6) (a) Rauchfuss, T. B. *Inorg. Chem.* **2004**, *43*, 14. (b) Meija-Rodriguez, Chong, D.; Reibenspies, J. H.; Soriaga, M. P.; Darensbourg, M. Y. *J. Am. Chem. Soc.* **2004**, *126*, 12004. (c) Razavet, M.; Davies, S. C.; Hughes, D. L.; Barclay, J. E.; Evans, D. J.; Fairhurst, S. A.; Liu, X.; Pickett, C. *J. Chem. Soc., Dalton Trans.* **2003**, *4*, 586.
(7) Nørskov, J. K.; Bligaard, T.; Logadóttir, Á.; Kitchin, J. R.; Chen, J. G.; Pandelov, S.; Stimming, U. *J. Electrochem. Soc.* **2005**, *152*. J23.
(8) Hinnemann, B.; Nørskov, J. K. *J. Am. Chem. Soc.* **2004**, *126*, 3920.
(9) The difference in pH and chemical potential for electron transfer is of the same order and cancel each other; see Supporting Information.
(10) (a) Cao, Z.; Hall, M. B. *J. Am. Chem. Soc.* **2001**, *123*, 3734. (b) Liu, Z.-P.; Hu, P. *J. Chem. Phys.* **2002**, *117*, 8177. (c) Bruschi, M.; Fantucci, P.; De Goia, L. *Inorg. Chem.* **2004**, *43*, 3733.
(11) Siegbahn, P. E. M. *Adv. Inorg. Chem.* **2004**, *56*, 101.
(12) Raybaud, P.; Hafner, J.; Kresse, G.; Kasztelan, S.; Toulhoat, H. *J. Catal.* **2000**, *189*, 129.
(13) Topsøe, H.; Clausen, B. S.; Massoth, F. E. *Hydrotreating Catalysis—Science and Technology*, Springer-Verlag: Berlin, 1996.
(14) Chorkendorff, I.; Niemantsverdriet, J. W. *Concepts of Modern Catalysis and Kinetics*; Wiley-VCH: New York, 2003.
(15) Davies, J. C.; Nielsen, R. M.; Thomsen, L. B.; Chorkendorff, I.; Logadóttir, Á.; Łodziana, Z.; Nørskov, J. K.; Li, W. X.; Hammer, B.; Longwitz, S. R.; Schnadt, J.; Vestergaard, E. K.; Vang, R. T.; Besenbacher, F. *Fuel Cells* **2004**, *4*, 309.
(16) Nidola, A.; Schira, R. *Int. J. Hydrogen Energy* **1986**, *11*, 449.
(17) Sobczynski, A. *J. Catal.* **1991**, *131*, 156.

JA0504690

Paper 2

Available online at www.sciencedirect.com
SCIENCE DIRECT
Catalysis Today 111 (2006) 44–51
CATALYSIS TODAY
www.elsevier.com/locate/cattod

A density functional study of inhibition of the HDS hydrogenation pathway by pyridine, benzene, and H_2S on MoS_2-based catalysts

Áshildur Logadóttir [a], Poul Georg Moses [b], Berit Hinnemann [b], Nan-Yu Topsøe [a], Kim G. Knudsen [a], Henrik Topsøe [a,**], Jens K. Nørskov [b,*]

[a] *Haldor Topsøe A/S, Nymøllevej 55, DK-2800 Lyngby, Denmark*
[b] *Center for Atomic-scale Materials Physics (CAMP), Nano DTU, Department of Physics, Building 307, Technical University of Denmark, DK-2800 Lyngby, Denmark*

Available online 28 November 2005

Abstract

The inhibition of catalytic hydrodesulfurization (HDS) by basic nitrogen compounds is an important problem in the production of ultra low sulfur transportation fuels and the origin of the inhibition effects is presently elucidated by performing density functional theory (DFT) calculations on the interaction of pyridine with the two types of edges of MoS_2 catalyst nanoparticles. Particular attention is given to studies of the hydrogenation (HYD) pathway in HDS since this is the favored pathway for refractory sulfur compounds and it is the pathway, which is most severely poisoned by basic nitrogen compounds. In order to understand the observed inhibitor trends, DFT studies on the adsorption of benzene, which is a weaker poison than pyridine, and H_2S, which has no or only a very minor influence on the HYD pathway, have also been made. We find that the adsorption of pyridine is quite strong and especially strong at positions along the so-called Mo edge. Thus, the HYD reaction most likely involves sites at this edge. This suggestion is substantiated by the observation that the adsorption blocks the metallic like so-called brim sites, which were recently shown to be involved in the HYD pathway. Furthermore, H_2S is observed not to interact strongly with these sites. The present results have also provided insight into the nitrogen compound inhibition of the direct desulfurization DDS pathway. The difference in the poisoning by benzene and pyridine is observed to be related to the ease with which hydrogen from neighboring SH group can be transferred to the pyridine molecule resulting in the creation of more strongly held pyridinium ions. At the so-called S edge, hydrogen is tightly bound and this transfer is not favored. The present results, therefore, also stress the importance of the hydrogen binding properties of HDS catalysts.

Keywords: Hydrodesulfurization; Hydrogenation; Inhibition; DFT; Brim sites; Brønsted acid sites; MoS_2; Pyridine; Benzene; H_2S

1. Introduction

It has been known for many years that dibenzothiophene (DBT) may be desulfurized by two different reaction pathways, i.e., the direct desulfurization (DDS) pathway and the hydrogenation (HYD) pathway [1]. Early studies [2] also showed that the presence of alkyl groups on the DBT skeleton might reduce the reactivity, especially if the substituents are located close to the sulfur like in the case of 4,6-dimethyldibenzothiophene (4,6-DMDBT). Recently, there has been a worldwide demand for producing transportation fuels with ultra low sulfur contents [3–12] and real feed studies have shown that this requires the removal of refractory compounds like 4,6-DMDBT. Model compound studies have shown that the HDS reaction for the unsubstituted DBT molecule proceeds mainly via the direct (DDS) route [1,7,13]. However, in the case of sterically hindered alkyl substituted molecules like 4,6-DMDBT, the rate for the DDS route is diminished whereas the rate for sulfur removal via the prehydrogenation HYD route may remain relatively unaffected [7]. Thus, for HDS of sterically hindered molecules the HYD route may become very important [5,7–9,13–18].

In real feed operation, the extent to which a given catalyst desulfurizes via one route or the other will depend on the hydrogen and H_2S partial pressures, on the conversion, and on the properties of the feed [9,17]. Many of these effects appear to

* Corresponding author. Tel.: +45 4525 3175; fax: +45 4593 2399.
** Corresponding author. Tel.: +45 4527 2000; fax: +45 4527 2999.
E-mail addresses: het@topsoe.dk (H. Topsøe), norskov@fysik.dtu.dk (J.K. Nørskov).

0920-5861/$ – see front matter
doi:10.1016/j.cattod.2005.10.018

be related to the fact that different molecules in the feed may have quite different inhibiting effects on the two reaction routes. The presence of nitrogen compounds is, for example, a key parameter, which may influence the HDS activity [11,13,17–28]. Recent detailed studies of inhibition effects under real feed conditions [22] showed that it is especially basic heterocyclic nitrogen compounds that inhibit the HDS reaction and the inhibition is most pronounced for the HYD route. Thus, the inhibition effects are particular important for deep HDS of refractory compounds. Kinetic studies using model compounds also support this conclusion [24,29]. For non-sterically hindered heterocyclic compounds with nitrogen in a six-membered ring, there appears to be a good correlation between the inhibitor strength and the gas phase proton affinities, where stronger inhibitors have higher gas phase proton affinity [20,21]. This could indicate that the poisoning of the HYD route by nitrogen compounds involves the interaction with a proton from a Brønsted acid site on the catalytically active nanostructures. Infrared measurements have shown that SH groups exist at the edges of MoS_2 nanoparticles [29] and IR studies have also revealed their interaction with pyridine to form pyridinium ions [30]. The inhibiting effect of other molecules on the HYD route has also been investigated. Aromatic hydrocarbons have been observed to poison the HYD route more than the DDS route [13,18,31,32] but for real-life operating conditions, the poisoning effect on HYD may be quite small [17,24]. In contrast, the H_2S inhibiting effect is much less for HYD than for DDS [13,17,33]. Recently, it was found that the H_2S inhibition of the HYD route could be related to the poisoning of the final hydrogenolysis step of this route (which is similar to DDS) and not to poisoning of the preceding hydrogenation steps [16].

While there is a quite good general agreement in the literature on the different reactivity, kinetic and poisoning effects, very limited direct mechanistic insight has resulted. Nevertheless, many of the above-mentioned observations have been taken as evidence for the HYD and DDS pathways occurring on different sites [13,16,34]. Sulfur vacancies are in general believed to play a key role in the DDS pathway. The nature of the hydrogenation sites is less well understood but many authors have also proposed vacancies to be involved in HYD reactions (see e.g. [13]). In view of the observation that quite large molecules may be desulfurized via the HYD pathway it has been proposed that multiple vacancy sites or ensembles of vacancies are involved in HYD. It has, for example, been suggested [35] that the HYD reaction occurs at the so-called naked MoS_2 edge (i.e. the $10\bar{1}0$ Mo edge without terminal sulfur atoms). Many DFT studies [36–40] have used the naked Mo edge as a starting point for addressing mechanistic issues. However, recent results have shown that it is energetically extremely unfavorable to create such naked Mo edges [41,42]. The edges bind sulfur very strongly and naked edges will not be present under realistic reaction conditions. The observation that the HYD reaction is not strongly inhibited by H_2S also allows one to exclude that naked Mo edges can play an important role in hydrotreating.

Recently, it has been possible to obtain important clues about the HYD pathway since atomically resolved scanning tunneling microscopy (STM) images could be obtained of key intermediates of this path [43]. DFT calculations provided detailed insight into the origin of the observations and the reaction was shown to involve metallic edge states (the so-called brim sites) located slightly inside the MoS_2 nanoparticles adjacent to the Mo edge itself.

Several DFT studies have investigated the equilibrium edge configuration of MoS_2 [41,42,44]. These studies have led to the construction of phase diagrams of edge configurations at different reaction conditions. The theoretical studies by Bollinger et al. [42] have shown that it is important to take the adsorption of H into account when constructing such phase diagrams. The validity of these phase diagrams has been supported experimentally by STM images [45]. The phase diagrams, which includes the effect of hydrogen show that under typical HDS conditions the S edge ($\bar{1}010$) exposes S dimers, which are fully covered by adsorbed hydrogen (SH groups), whereas the Mo edge exposes S monomers, which are partly covered by adsorbed hydrogen [42,46].

In the present paper, we investigate poisoning effects using three different known inhibitors, i.e. benzene, pyridine and H_2S. DFT calculations have been performed on the interaction of these molecules with the Mo edge and the S edge of MoS_2 at S and H coverages, which are likely to be present under industrial HDS conditions. The effect of protonation of the basic pyridine molecule has also been investigated in order to elucidate the effect of Brønsted sites. The results provide insight into the nature of the HYD sites, the strong inhibition by pyridine and the weak inhibition of the HYD route by H_2S.

2. Calculation details

An infinite stripe model, which has previously proved suitable for providing insight into MoS_2, is used to investigate the edges of MoS_2, see Fig. 1 [41,42,47]. The edge configurations investigated in the present study can be seen in Fig. 2. The infinite stripe exposes both the Mo edge and the S edge. The supercell has four Mo atoms in the *x*-direction and four Mo atoms in the *y*-direction. The periodicity of four in the *x*-direction is necessary to allow for important reconstructions with a period of two. The dimension of the slab in the *y*-direction has been tested to be sufficient to decouple the Mo edge and the S edge in the *y*-direction. The stripes are separated by 14.8 Å in the *z*-direction and 9 Å in the *y*-direction in order to decouple the individual stripes. The basal plane of MoS_2 is investigated using a supercell with four Mo atoms in the *x*- and *y*-direction and a separation of 14.8 Å in the *z*-direction between individual MoS_2 slabs, see Fig. 1.

The plane wave density functional theory code *DACAPO* is used [48]. The Brillouin zone is sampled by three *k*-points in the *x*-direction and one *k*-point in the *y*- and *z*-direction for the stripe, and the three *k*-points in the *x*- and *y*-direction for the basal plane slab [49]. A plane-wave cutoff of 30 Rydberg is used and a density wave cutoff of 45 Rydberg is used, in order to improve the precision of the forces [50]. Ultrasoft pseudopotentials are used except for sulfur, where a soft pseudopotential has been used [51]. A Fermi temperature of

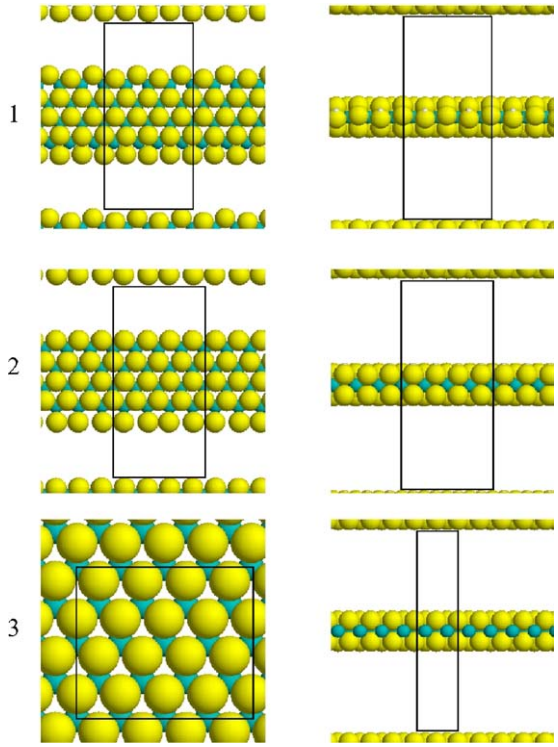

Fig. 1. Super cells used for studies on: (1) Mo edge; (2) S edge; (3) Basal Plane. Left side shows the top view and right side the side view. Color code: sulfur (yellow), molybdenum (green), hydrogen (white). For interpretation of the references to colour in this figure legend, the reader is referred to the web version of the article.

$k_BT = 0.1$ eV is used and all energies are extrapolated to zero electronic temperature. The exchange correlation functional PW91 has been used throughout the study [52]. The convergence criterion for the atomic relaxation is 0.15 eV/Å. The Nudge Elastic Bands (NEB) method is used to find energy barriers [53]. The adsorption energies are calculated using Eq. (1).

$$\Delta E_{ad} = (E_{molecule/MoS_2} - E_{MoS_2} - E_{molecule(g)}) \quad (1)$$

where $E_{molecule/MoS_2}$ is the energy of the system with the molecule bound to the surface, E_{MoS_2} the energy of the stripe/slab and $E_{molecule(g)}$ the energy of the free molecule. All energies are given at 0 K and do not include vibrational ground state energies. The lattice constant of MoS_2 is calculated to be $a = 3.215$ Å, which compares well with the experimental value of 3.16 Å. Figures have been made using Rasmol and VMD [54].

3. Results

3.1. Benzene

The adsorption of benzene has been investigated both at different regions along the Mo and the S edge and on the basal plane as a reference.

3.1.1. Mo edge

Benzene adsorption at the Mo edge has been investigated with a S coverage corresponding to HDS conditions and a H coverage of 25%. The H coverage chosen is below the 50% H coverage at equilibrium in order to investigate the influence of the distance between the adsorbed molecule and the H atom. The brim sites, which have been shown to be able to participate in hydrogenation [43] are positioned close to the front row S atoms and adsorption on these sites is also investigated. The investigated adsorption configurations at the Mo edge can be seen in Table 1. It is seen that the adsorption energy at the Mo edge is slightly exothermic and is similar for all configurations, while adsorption on the basal plane is thermoneutral as shown in configuration e in Table 1. The exchange correlation functional (XC-functional) used does not take van der Waals interactions into account and the difference in adsorption energies is therefore due to chemisorption. The change in

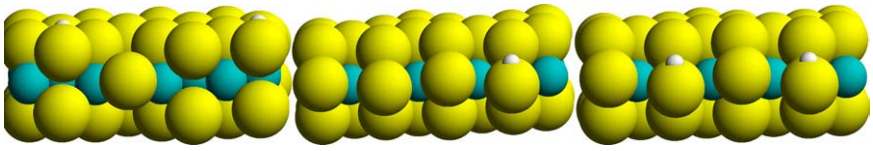

Fig. 2. Edge configurations investigated. Left is the S edge with a vacancy and 50% H coverage. Middle is the Mo edge with 50% S coverage and 25% H. Right is the Mo edge with 50% S coverage and 50% H.

Table 1
Benzene adsorption sites

	Configuration					
	a	b	c	d	e	f
	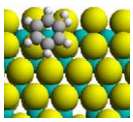	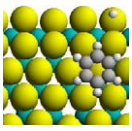	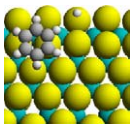	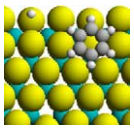	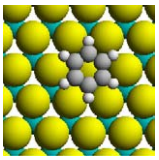	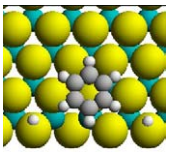
H coverage [%]	25	25	25	25		50
ΔE_{ad} [eV]	−0.14	−0.17	−0.16	−0.16	−0.02	0.02

Configurations a–d is at the Mo edge, configuration e is on the basal plane, and configuration f is at the S edge.

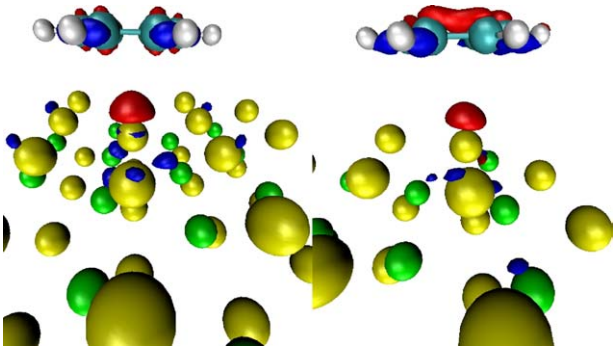

Fig. 3. Benzene electron-density difference plot. Left: Benzene on basal plane. Right: Benzene at Mo edge. Color code: Depletion of electron density (red) plotted at a contour value of −0.003 e^3/Å increase in electron density (blue) plotted at a contour value of 0.003 e^3/Å. For interpretation of the references to colour in this figure legend, the reader is referred to the web version of the article.

electron density can be seen in Fig. 3. The figure clearly shows that the changes in electron density upon adsorption are somewhat larger at the Mo edge than on the basal plane. Thus, there is a preference for the benzene molecule to adsorb at the Mo edge rather than on the basal plane. Furthermore, we have tested whether hydrogenation of benzene can stabilize the adsorption. We find that hydrogenation makes the adsorption energy endothermic.

3.1.2. S edge

Benzene adsorption at the S edge has been investigated with H and S coverages corresponding to HDS conditions and the S edge has been activated by the creation of a single vacancy. Benzene adsorption at the S edge has been investigated at a site next to the vacancy, as shown in configuration f Table 1. Only one adsorption site has been investigated since the benzene adsorption energy is thermoneutral at the vacancy site and the Mo edge results indicated that small variation in the local structure at the adsorption site only lead to small changes in the adsorption energy. It is, therefore, presently assumed that the adsorption will not become more exothermic by moving the benzene molecule away from the vacancy. The adsorption energy at the S edge (configuration f) is similar to the adsorption energy on the basal plane (configuration e), indicating that there is no preference for the benzene to move from the Mo edge to the S edge. Thus, we can conclude that benzene does not adsorb at the S edge. This indicates that the S edge is not important for hydrogenation as benzene inhibits this reaction.

3.2. Pyridine and pyridinium

Adsorption of pyridine and the formation of pyridinium ion have been investigated at both the Mo edge and the S edge and as reference also on the basal plane.

3.2.1. Mo edge

Pyridine adsorption at the Mo edge has been investigated with S coverage corresponding to HDS conditions, i.e. 50% S coverage and with 25 or 50% H coverages. Formation of pyridinium has been investigated with 25% H coverage, which corresponds to moving a proton to the pyridine molecule and thereby lowering the edge coverage of H. The adsorption configurations of pyridine at the Mo edge (configurations a–h) and basal plane (configuration i) can be seen in Table 2. It is seen that the adsorption energies are slightly exothermic, and more exothermic than on the basal plane. Under HDS conditions, there is adsorbed hydrogen in form of SH groups in the vicinity of the pyridine. Therefore, one could imagine

Table 2
Pyridine and pyridinium ion adsorption sites

	Configuration					
	a	b	c	d	e	f
	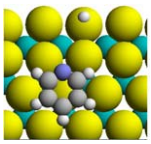	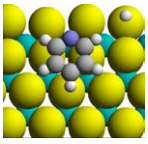	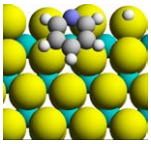	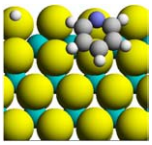	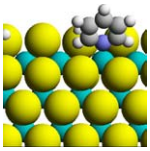	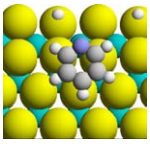
H coverage [%]	25	25	25	25	50	50
ΔE_{ad} [eV]	−0.12	−0.08	−0.09	−0.08	−0.09	−0.03
	Configuration					
	g	h	i	j	k	l
	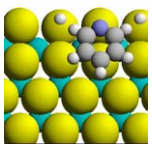	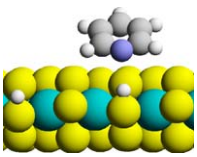	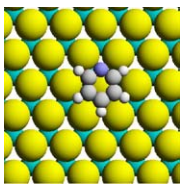	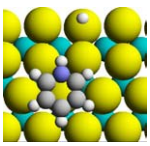	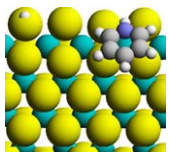	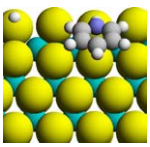
H coverage [%]	50	50		25	25	25
ΔE_{ad} [eV]	−0.01	−0.11	−0.03	−0.40	−0.45	−0.59

Configurations a–h is for pyridine at the Mo edge, configuration i is pyridine on the basal plane, and configurations j–k is the pyridinium ion at the Mo edge.

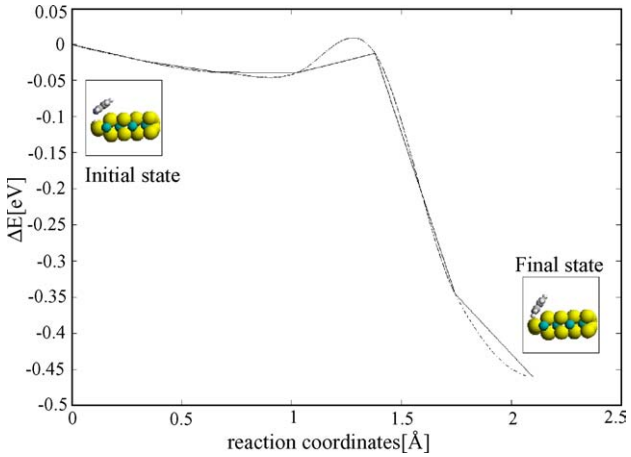

Fig. 4. The energy barrier for creating pyridium. The straight line connects the individual NEB Images and the curved line is splines fitted to the forces on the individual NEB images.

that a proton could be transferred from the neighboring SH group to the pyridine molecule, resulting in the formation of a pyridinium ion. Thus the formation of the pyridinium ion has also been investigated (configurations j–l in Table 2). The significant exothermic energies show that pyridinium ions are very stable at the Mo edge. The adsorption energies become approximately 0.4 eV more exothermic than for pyridine itself.

The barrier for the proton transfer has also been calculated and the results are shown in Fig. 4. The H transfer reaction is apparently non-activated, suggesting that pyridine will form pyridinium ions readily upon adsorption at the Mo edge. The electron density plots of pyridine and pyridinium ion adsorbed at the Mo edge and basal plane (Fig. 5) show a more pronounced change in the electron density when the adsorption occurs at the edge. The change in electron density is also significantly larger than for benzene (note that the contour value is a factor of 10 larger than the one used in the benzene density). It is also seen that as H^+ is transferred from the catalyst to pyridine, electron density is shifted to the catalyst, thus, indicating the formation of a pyridinium ion-like species.

3.2.2. S edge

Pyridine adsorption at the S edge has been investigated with H and S coverage corresponding to HDS conditions and as for the benzene study, the S edge has been activated by the creation of a single vacancy. Such a vacancy is likely to be involved in the DDS pathway and the present calculations, therefore, also allow us to get insight into poisoning effects on this route. The adsorption configurations are shown in configurations a–c in Table 3. Pyridine binds strongest when the N atom is positioned in the vacancy, as seen in configuration c and less strongly when the adsorption configurations are similar to those at the Mo

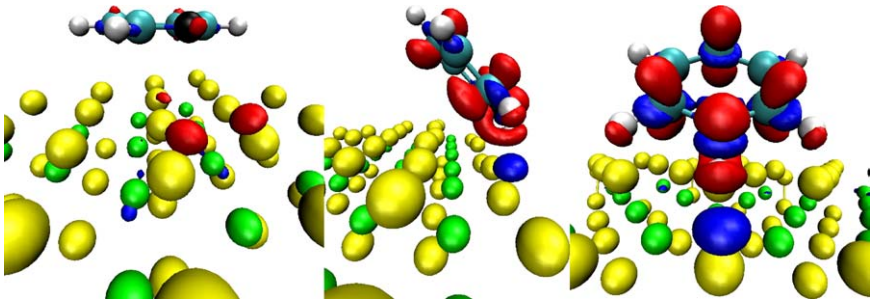

Fig. 5. Pyridine and pyridinium ion electron-density difference plot. Left: Pyridine on basal plane. Middle: Sideview of pyridinium ion at the Mo edge. Right: Frontview of pyridinium ion at the Mo edge. Color code: Depletion of electron density (red) plotted at a contour value of −0.03 e^3/Å increase in electron density (blue) plotted at a contour value of 0.03 e^3/Å. Nitrogen is black. For interpretation of the references to colour in this figure legend, the reader is referred to the web version of the article.

Table 3
S edge pyridine and pyridinium ion adsorption sites

	Configuration			
	a	b	c	d
Top view	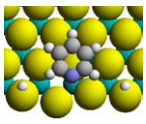	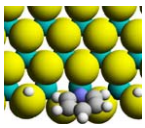	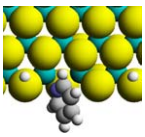	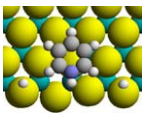
Front view	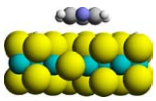	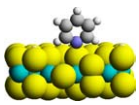	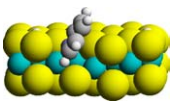	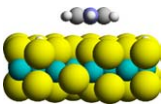
H coverage [%]	25	25	25	25
ΔE_{ad} [eV]	−0.02	−0.05	−0.28	0.17

Configurations a–c is pyridine at the S edge with a vacancy and configuration d is the pyridinium ion at the S edge with a vacancy.

Table 4
H_2S adsorption sites at the Mo edge and the S edge

	Configuration				
	a	b	c	d	e
	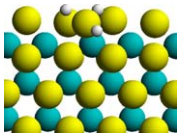	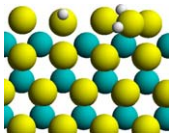	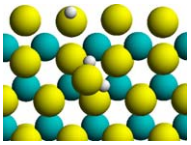	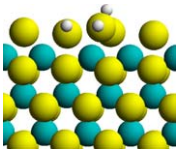	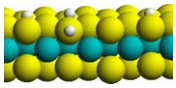
H coverage [%]	25	25	25	25	50
ΔE_{ad} [eV]	0.09	0.10	−0.06	−0.16	−0.12

Configurations a–d are at the Mo edge. Configuration e is a vacancy site at the S edge.

edge, as in configuration a and b. The observation that pyridine binds strongly to the vacancy is in agreement with the observation that the DDS route is poisoned by basic N compounds [13]. In configuration d, a H atom is added to the pyridine as shown in configuration a. This makes the adsorption endothermic. The adsorption at the S edge are less exothermic than at the Mo edge except for configuration c where pyridine is adsorbed in the vacancy. Pyridine in the vacancy is on the other hand less exothermic than the adsorption energies of pyridinium ions on the Mo edge (configuration j-l in Table 2). Therefore, the edge preference follows the same trend as for benzene adsorption, but the trend is more pronounced for pyridine. The reason why H does not stabilize pyridine as pyridinium at the S edge may be related to that the S edge S–H groups are less acidic than S–H groups at the Mo edge. This is reflected by a stronger binding energy at the S edge, 0.58 eV at the S edge compared to 0.37 eV at the Mo edge.

3.3. H_2S

H_2S is generally not considered to be a significant inhibitor for hydrogenation and, thus, it should adsorb much weaker than benzene and pyridine on the hydrogenation site. Studies of the H_2S adsorption, therefore, offer a way to supplement the above investigations. H_2S adsorption has, therefore, also been investigated at both the S and Mo edges.

3.3.1. Mo edge

H_2S adsorption at the Mo edge has been investigated with S coverage corresponding to HDS conditions and with a 25% H coverage. The lower than equilibrium H coverage is again chosen in order to investigate the influence of the distance between the adsorbed molecule and H. The adsorption configurations of H_2S at the Mo edge are shown in Table 4(a–d). Adsorption configuration d where H_2S is located next to the S–H group is found to be slightly exothermic (−0.16 eV), which is approximately the same adsorption energies as benzene at the Mo edge see Table 1. It should, however, be stressed that the van der Waals part of the adsorption energy for molecules with π systems is generally larger than for small molecules like H_2S. The adsorption of benzene and pyridine at the Mo edge is, therefore, expected to be stronger than H_2S.

3.3.2. S edge

H_2S adsorption at the S edge has been investigated at the S edge with H and S coverage corresponding to HDS conditions, where the S edge is again activated by the creation of one vacancy. The adsorption has been investigated at the vacancy as shown in configuration e in Table 4. The adsorption energy is seen to be exothermic (−0.12 eV), which is similar to that on the Mo edge. The adsorption of H_2S is, therefore, equally likely at both edges. Dissociation of H_2S is not considered in this study but has been found elsewhere to be highly exothermic (−1.6 eV). This result explains the strong inhibition of the DDS pathway by H_2S [55].

4. Discussion

One of the main reasons why it has been difficult to understand the reactivity and inhibition effects observed under deep HDS can be related to the fact that very little information has been available regarding the HYD pathway, which plays an important role under such conditions [5,7–9,11,13,14,16,18]. The fact that large sterically hindered alkyl substituted molecules like 4,6-DMDBT can react via the HYD route has led researchers to propose that multiple vacancies are involved in the reaction via an initial π bonding of the reactants [35,56]. This proposal can rationalize several observations but it has not allowed one to understand several observations including the large difference in the inhibition effects between molecules such as benzene and pyridine. Also, the absence of a strong inhibition effect by H_2S has been difficult to understand using the above proposal for the HYD sites, since one might expect that such sites would have a large affinity toward sulfur. Indeed, recent DFT results [41,42] have shown that such vacancy sites bind sulfur strongly again suggesting that other sites may be involved. For a long time, the nature of such sites remained unclear but recently STM and DFT results revealed that quite different sites might be involved in HYD, namely, the metallic like brim sites located adjacent to the edges [42,43,45,57]. It was proposed that the involvement of such sites might also be consistent with the different observed inhibition effects [58]. The present results have confirmed this and have provided detailed insight into the nature of the inhibiting effects.

It is, presently, observed that the availability of hydrogen at the catalyst surface plays an essential role in the poisoning by

basic nitrogen compounds like pyridine. Hydrogen reacts with pyridine and forms the pyridinium ion and this stabilizes its adsorption. This process is favored at the Mo edge. Pyridinium ions were previously observed in IR experiments [30] and our present findings substantiate the proposal that S–H groups are involved in the pyridinium ion formation. It is interesting that the present results show that the formation of pyridinium ions is expected to occur predominantly at the Mo edge. Without the formation of pyridinium ions benzene would have been a stronger inhibitor than pyridine because it is seen to bind stronger. However, due to the influence of hydrogen, pyridine is a much stronger poison. In this context, it is important that hydrogen binds less strongly at the Mo edge (but it still binds) as compared to the S edge. Actually, at the Mo edge, hydrogen is bound almost with zero free energy [46] and, therefore, can be easily transferred to the pyridine molecule. It is also likely that the weakly bound H atoms at the Mo edge could be important in hydrogenation reactions at the Mo edge.

Benzene is found to be less strongly bound than the pyridinium ion, and this explains why benzene is less poisonous than pyridine. Both benzene and pyridine/pyridinium ion preferably adsorb at the Mo edge indicating that the active site for hydrogenation is located at the Mo edge. The adsorption study of H_2S substantiates that the hydrogenation site is at the Mo edge, since H_2S adsorbs weakly here in agreement with the very weak poisoning of the HYD pathway. This result confirms STM and DFT results showing that the hydrogenation occurs at regions close to the Mo edge (the brim sites) [43]. Inhibition of hydrogenation reactions by pyridine is not only due to blocking, since when it is protonated it also uses H from the Brønsted acid sites, thereby, reducing the number of H atoms available for hydrogenation.

The observation that heavier molecules, like quinolines and acridines are stronger poisons than pyridine [20,21], can be explained by two effects. Firstly, the van der Waals interaction increases for molecules with more π systems. This increase in van der Waals interaction can probably be assumed to be quite independent of the nature of the adsorption site, meaning that the adsorption energy would also increase similarly for all sites. The second and probably more important effect is that the inhibition by basic nitrogen compounds increases with higher proton affinity as found in experimental studies [20,21]. The present study has shown that there is no significant barrier for proton transfer from the S–H groups to pyridine at the Mo edge and if one assumes that this is also the case for larger molecules than pyridine, then the proton transfer will only be equilibrium limited. It is, therefore, reasonable to expect that the gas phase proton affinity correlate quite well with the inhibitor strength because a similar proton transfer process is taking place on the catalyst.

While the present investigation has mainly focused on the poisoning of the HYD pathway several of the results also provide insight into the poisoning of the DDS pathway. For example, it is seen that pyridine adsorbs quite strongly in a vacancy site at the S edge. This may be the origin of the poisoning effects by N compounds of the DDS pathway, which dominates for the HDS reaction of rather reactive sulphur compounds like DBT [13].

Promoted catalysts have not been studied, presently, but the present results allow a basis for understanding certain inhibition effects in such catalysts. For Co promoted catalyst, the promoter prefers to be located at the S edge resulting in the formation of the CoMoS phase [13,41,44,57]. This results in the creation of new sites, which may interact with inhibitors. Mo edges will, however, also be present and they will resemble those in unpromoted catalysts. The present results may, thus, provide a starting point for understanding promoted catalysts.

5. Conclusion

In order to develop new catalysts, which can meet the increasing demands for the production of ultra low sulfur transportation fuels, it is necessary to understand in detail the reaction involved in the removal of sterically hindered sulfur containing molecules and how other molecules in the feed may inhibit these reactions. The present results have provided new insight in this regard. It is seen that the poisoning of the important HYD route occurs quite differently from the most commonly accepted proposals in the literature. For example, it is seen that the inhibiting effect by aromatics is not due to the interactions with highly uncoordinated vacancies (like the naked Mo edges) but rather with the fully coordinated molybdenum sites like the metallic-like brim sites located adjacent to the edge itself. The π-bonding to such sites explains the poisoning by aromatics. This bonding is not much affected by substituents in DBT and this explains why the HYD route is more favored for refractory molecules than the DDS route. The present results show that the fully coordinated brim sites bind H_2S very weakly. Thus, the lack of significant inhibition by H_2S, which has intrigued researchers for decades, can readily be explained. The strong poisoning by pyridine is observed to be due to an increase in adsorption energy upon protonation of the pyridine molecule. The proton donor is a neighboring S–H Brønsted acid site located at the Mo edge. The pyridine to pyridinium ion reaction is found to be non-activated. Both benzene and pyridine prefers to adsorb at the Mo edge and both acts as poison for the hydrogenation pathway, which support the conclusion that the hydrogenation site is located at the Mo edge. The present results also show that pyridine will poison vacancy sites involved in the direct desulfurization path. In this case, the poisoning occurs via direct coordination and without pyridinium ion formation.

In the future, the present studies should be extended to include promoted systems, support interactions, and other active phase modifications. DFT studies of the HDN reaction like those in [59,60] may also provide insight relevant for understanding the inhibition by nitrogen compounds. Recently, DFT calculations have shown that changes in support interactions influence the binding properties of MoS_2-based structures [47]. In fact, such changes may influence the hydrogenation sites, the binding of hydrogen and the apparent acidity of the hydrogen. Thus, support effects are also expected to influence the inhibition by different molecules and the

present type studies may provide a better basis for understanding and controlling the effect of inhibitors.

Acknowledgements

Fruitful discussions with Per Zeuthen and Duayne Whitehurst are gratefully acknowledged. We acknowledge support from the Danish center for scientific computing through grant number HDW-1101-05.

References

[1] M. Houalla, N.K. Nag, A.V. Sapre, D.H. Broderick, B.C. Gates, AIChE J. 24 (1978) 1015.
[2] M. Houalla, D.H. Broderick, A.V. Sapre, N.K. Nag, V.H.J. de Beer, B.C. Gates, H. Kwart, J. Catal. 61 (1980) 523.
[3] A. Amorelli, Y.D. Amos, C.P. Halsig, J.J. Kosman, R.R.J. Jonke, M. DeWind, J. Vrieling, Hydrocarb. Process. 71 (1992) 93.
[4] I. Mochida, K. Sakanishi, X. Ma, S. Nagao, T. Isoda, Catal. Today 29 (1996) 185.
[5] X. Ma, K. Sakanishi, I. Mochida, Ind. Eng. Chem. Res. 35 (1996) 2487.
[6] M.V. Landau, Catal. Today 36 (1997) 393.
[7] B.C. Gates, H. Topsøe, Polyhedron 16 (1997) 3213.
[8] D.D. Whitehurst, T. Isoda, I. Mochida, Adv. Catal. 42 (1998) 345.
[9] K.G. Knudsen, B.H. Cooper, H. Topsøe, Appl. Catal. A 189 (1999) 205.
[10] H. Schulz, W. Bohringer, P. Waller, F. Ousmanov, Catal. Today 49 (1999) 87.
[11] C. Song, Catal. Today 86 (2003) 211.
[12] T.C. Ho, Catal. Today 98 (2004) 3.
[13] H. Topsøe, B.S. Clausen, F.E. Massoth, Hydrotreating catalysis, in: J.R. Anderson, M. Boudart (Eds.), Science and Technology, vol. 11, Springer-Verlag, Berlin, New York, 1996.
[14] T. Kabe, A. Ishihara, H. Tajima, Ind. Eng. Chem. Res. 31 (1992) 1577.
[15] V. Meille, E. Schulz, M. Lemaire, M. Vrinat, J. Catal. 170 (1997) 29.
[16] M. Egorova, R. Prins, J. Catal. 225 (2004) 417.
[17] F. van Looij, P. van der Laan, W.H.J. Stork, D.J. Di Camillo, J. Swain, Appl. Catal. A 170 (1998) 1.
[18] M. Breysse, G. Djega-Maridassou, S. Pessayre, C. Geantet, M. Vrinat, G. Perot, M. Lemarie, Catal. Today 84 (2003) 129.
[19] M. Nagai, T. Kabe, J. Catal. 81 (1983) 440.
[20] M. Nagai, T. Sato, A. Aiba, J. Catal. 97 (1986) 52.
[21] V. LaVopa, C.N. Satterfield, J. Catal. 110 (1988) 375.
[22] P. Zeuthen, K.G. Knudsen, D.D. Whitehurst, Catal. Today 65 (2001) 307.
[23] P. Wiwel, K.G. Knudsen, P. Zeuthen, D.D. Whitehurst, Ind. Eng. Chem. Res. 39 (2002) 533.
[24] M. Egorova, R. Prins, J. Catal. 224 (2004) 278.
[25] E. Furimsky, F.E. Massoth, Catal. Today 52 (1999) 381.
[26] T.C. Ho, J. Catal. 219 (2003) 442.
[27] U.T. Turaga, X. Ma, C. Song, Catal. Today 86 (2003) 265.
[28] M. Egorova, R. Prins, J. Catal. 221 (2004) 11.
[29] N.-Y. Topsøe, H. Topsøe, J. Catal. 139 (1993) 641.
[30] N.-Y. Topsøe, H. Topsøe, F.E. Massoth, J. Catal. 119 (1989) 252.
[31] X.L. Ma, K. Sakanishi, I. Mochida, Ind. Eng. Chem. Res. 34 (1995) 748.
[32] E.A. Blekkan, A. Virnovskaia, H. Bergen, P. Steiner, ACS Fuel Chem. Div. Prepr. 48 (2003) 37.
[33] T. Kabe, W. Qian, A. Ishihara, Catal. Today 39 (1997) 2.
[34] J. Miciukiewicz, W. Zmierczak, F.E. Massoth, in: Proceedings of the Eighth International Conference of Catal. Verlag Chemie, Berlin, 1984), p. 671.
[35] X.L. Ma, H.H. Schobert, ACS. Div. Petrol. Chem. Prepr. 213 (1997) 15.
[36] S. Cristol, J.F. Paul, E. Payen, D. Bougeard, F. Hutschka, S. Clemendot, J. Catal. 224 (2004) 138.
[37] P. Raybaud, J. Hafner, G. Kresse, H. Touilhoat, in: B. Delmon, G.F. Froment, P. Grange (Eds.), Hydrotreatment and Hydrocracking of Oil Fractions, Elsevier, 1999, p. 309.
[38] P. Raybaud, J. Hafner, G. Kresse, H. Toulhaut, Phys. Rev. Lett. 80 (1998) 1481.
[39] H. Yang, C. Fairbridge, Z. Ring, Energy Fuels 17 (1993) 387.
[40] H. Orita, K. Uchida, N. Itoh, J. Mol. Catal. A 193 (2003) 197.
[41] L.S. Byskov, J.K. Nørskov, B.S. Clausen, H. Topsøe, J. Catal. 187 (1999) 109.
[42] M.V. Bollinger, K.W. Jacobsen, J.K. Nørskov, Phys. Rev. B 67 (2003) 085410.
[43] J.V. Lauritsen, M. Nyberg, J.K. Nørskov, B.S. Clausen, H. Topsøe, E. Lægsgaard, F. Besenbacher, J. Catal. 224 (2004) 94.
[44] H. Schweiger, P. Raybaud, H. Toulhaut, J. Catal. 212 (2002) 33.
[45] J.V. Lauritsen, M.V. Bollinger, E. Lægsgaard, K.W. Jacobsen, J.K. Nørskov, B.S. Clausen, H. Topsøe, F. Besenbacher, J. Catal. 221 (2004) 510.
[46] B. Hinnemann, P.G. Moses, J. Bonde, K.P. Jørgensen, J.H. Nielsen, S. Horch, I. Chorkendorff, J.K. Nørskov, J. Am. Chem. Soc. 127 (15) (2005) 5308.
[47] B. Hinnemann, J.K. Nørskov, H. Topsøe, J. Phys. Chem. B 109 (6) (2005) 2245.
[48] www.camp.dtu.dk/campos/.
[49] H.J. Monkhorst, J.D. Pack, Phys. Rev. B 13 (1976) 5188.
[50] K. Laasonen, A. Pasquarello, R. Car, C. Lee, D. Vanderbildt, Phys. Rev. B 47 (1993) 10142.
[51] D. Vanderbilt, Phys. Rev. B 41 (1990) 7892.
[52] J.P. Perdew, J.A. Chevary, S.H. Vosko, K.A. Jackson, M.R. Pederson, D.J. Singh, C. Fiolhais, Phys. Rev. B 46 (11) (1992) 6671.
[53] H. Jonsson, G. Mills, K.W. Jacobsen, in: B.J. Berne, G. Cicotti, D.F. Coker (Eds.), Classical and Quantum Dynamics in Condensed Phase Systems, World Scientific, 1998.
[54] W. Humphrey, A. Dalke, K. Schulten, J. Mol. Graphics 14 (1996) 33–38.
[55] P.G. Moses, Unpublished results.
[56] X. Ma, H.H. Schobert, J. Mol. Cat. A 160 (2000) 409.
[57] J.V. Lauritsen, S. Helveg, M. Nyberg, E. Lægsgaard, I. Stensgaard, B.S. Clausen, H. Topsøe, F. Besenbacher, J. Catal. 197 (2001) 1.
[58] H. Topsøe, B. Hinnemann, J.K. Nørskov, J.V. Lauritsen, F. Besenbacher, P.L. Hansen, G. Hyltoft, R.G. Egeberg, K.G. Knudsen, Catal. Today 107–108 (2005) 12.
[59] M. Sun, A.E. Nelson, J. Adjaye, J. Mol. Catal. A 222 (2004) 243.
[60] M. Sun, A.E. Nelson, J. Adjaye, J. Catal. 231 (2005) 223.

Paper 3

Available online at www.sciencedirect.com
ScienceDirect
Journal of Catalysis 248 (2007) 188–203
JOURNAL OF CATALYSIS
www.elsevier.com/locate/jcat

The hydrogenation and direct desulfurization reaction pathway in thiophene hydrodesulfurization over MoS_2 catalysts at realistic conditions: A density functional study

Poul Georg Moses [a], Berit Hinnemann [b], Henrik Topsøe [b], Jens K. Nørskov [a,*]

[a] *Center for Atomic-Scale Materials Design (CAMD), Department of Physics, Building 307, Nano DTU, Technical University of Denmark, DK-2800 Kgs. Lyngby, Denmark*

[b] *Haldor Topsøe A/S, Nymøllevej 55, DK-2800 Kgs. Lyngby, Denmark*

Received 5 December 2006; revised 20 February 2007; accepted 23 February 2007

Available online 20 April 2007

Abstract

We present density functional theory (DFT) calculations of reaction pathways for both the hydrogenation (HYD) and direct desulfurization (DDS) routes in the hydrodesulfurization (HDS) of thiophene over the different MoS_2 edge structures, which will dominate under typical HDS reaction conditions. Contrary to the generally accepted view, we find that the HYD reaction path, which involves hydrogenation to 2-hydrothiophene followed by hydrogenation to 2,5-dihydrothiophene and subsequent S–C scission, can occur at the equilibrium Mo($10\bar{1}0$) edge without the creation of coordinatively unsaturated Mo edge sites. This is related to the presence of the metallic-like brim sites also observed in previous STM studies. It is found that the HYD reaction pathway also can occur at the S($\bar{1}010$) edge. At this edge, the equilibrium edge structure itself is not active, and sulfur vacancies must be created for the reaction to proceed. It is found that the effective energy barrier for vacancy creation depends on the H_2 partial pressure. The sulfur vacancies at the S($\bar{1}010$) edge are also found to be active sites for the DDS pathway. This pathway does involve an initial hydrogenation step to 2-hydrothiophene, followed by S–C scission. Analyzing the relative stabilities of reactants and intermediates suggests that a catalytic cycle may involve elementary steps that start at one type of edge and are completed at the other; for example, many intermediates are more stable at the S edge. The regeneration of the active sites is found to be a crucial step for all of the reaction pathways, and the importance of reactions at Mo brim sites is related to the observation that regeneration is least activated here. It is proposed that an important activity descriptor is the minimum energy required to either add or remove S from the different equilibrium edge structures.

Keywords: Hydrodesulfurization; Hydrogenation; DFT; Brim Sites; MoS_2; Thiophene; Reaction Mechanism; DDS; HYD

1. Introduction

As the global energy consumption rapidly increases and environmental legislation becomes stricter, the need to upgrade low-quality oil to clean transport fuels increases. To meet current environmental regulations, refiners must remove even the most refractory sulfur-containing species [1–6]. This is generating increased interest in obtaining a detailed description of the catalytic hydrotreating reactions occurring during desulfurization. Hydrodesulfurization (HDS) has been investigated for many decades, leading to increased insight into the structure of the active catalyst particles, their interactions with the support, the effect of promoters, and the kinetics of the reactions [7]. However, much less is known about the reaction mechanisms and the nature of the active sites, and many different views have been presented [6–12].

Thiophene is a suitable test molecule for studying the HDS reaction because it contains an S atom in a benzene-like ring and also is small. Therefore, thiophene HDS has been the most studied reaction; but there has been considerable debate regarding the mechanism [7,10,13–23]. For instance, it has been difficult to establish to what extent prehydrogenation to dihydrothiophene or tetrahydrothiophene may be necessary before S–C bond cleavage. It also appears that the observed reaction

* Corresponding author.
E-mail address: norskov@fysik.dtu.dk (J.K. Nørskov).

0021-9517/$ – see front matter
doi:10.1016/j.jcat.2007.02.028

products depend on the reaction conditions [7,22,23]. Tetrahydrothiophene typically is not an intermediate at atmospheric pressure [23], but it may be a major intermediate at high pressure [17] and low temperature [10], because the formation of tetrahydrothiophene is equilibrium-limited at high temperature [10]. A detailed study of the HDS of 2-methylthiophene at high pressure [22] found that the splitting of the S–C bond in tetrahydro-2-methylthiophene (resulting in the formation of a thiol) is faster than the hydrogenation of the thiophene ring or of the pentene to yield pentane. Thus, the hydrogenation activity of the catalyst appears to be an important feature, which can influence the concentration of the reaction products. The proposed thiol intermediate was not observed, leading to the conclusion that the splitting of S–C bonds in thiols is very fast.

For the larger S-containing molecules like dibenzothiophene, it has been established that two parallel routes exist, a direct desulfurization route (DDS) through biphenyl and a hydrogenation route (HYD) in which one of the benzene rings is hydrogenated first [24]. In order to produce the clean transport fuels demanded today, even the very refractory sulfur compounds like 4,6-dimethyldibenzothiophene must be removed [1,2,4,5,7,19,25,26]. For such molecules, the HYD route may become more important than the DDS route, which dominates for unsubstituted dibenzothiophene [4,27]. Despite the established understanding of the pathways and the overall kinetics, little direct insight has been obtained regarding the reaction mechanisms and the surface sites involved in the DDS and HYD pathways. It has even been difficult to reach agreement on the mode of adsorption of the reactants. For instance, thiophene has been found to either exclusively adsorb in a so-called η_1 mode (e.g., standing up and binding only through S [28,29]) or adsorb primarily in a so-called η_5 mode (e.g., lying down, bonded through S and the four C atoms), with only a small fraction of the molecules being present in the η_1 mode [30].

Insight into the mechanism of HDS also has been obtained from numerous studies on activity correlations [7,31,32], which have been taken as evidence for MoS_2 edge vacancies being the active sites in HDS, because vacancy formation generally has been assumed to take place at the MoS_2 edges. In support of this, basal plane surfaces have been observed to be inactive [33]. For hydrogenation reactions, the activity also has been observed to correlate with the number of MoS_2 or WS_2 edges sites [34,35], and vacancies have been concluded to be the active sites for such reactions. However, in general it is difficult to draw firm conclusions from such activity correlations [7], because a variety of other species, like SH groups [36], also may be located at the edges. Further support for the importance of vacancies has been provided from experimental studies of the effect of prereduction temperature [37,38]. Moreover, the observed activity correlation with the metal–sulfur bond strength, leading to the formulation of the bond energy model (BEM), suggest that vacancy formation is a key aspect of HDS [39].

Because both HDS and hydrogenation activities have been observed to correlate with the number of MoS_2 (WS_2) edge sites, some authors have suggested [40,41] that the sites for the DDS route and the HYD route are similar. Indeed, kinetic models based on this proposal can provide a good fit of kinetic results. However, a number of effects strongly suggest that DDS and hydrogenation sites are not the same. For example, the presence of methyl groups in dibenzothiophene may severely reduce the activity for S removal via DDS without significantly affecting the hydrogenation activity [4]. In addition, H_2S is a strong inhibitor for S removal via DDS but has only a minor effect on hydrogenation [27]. Evidence for different sites for HYD and DDS also comes from studies of the effect of nitrogen compounds [7,26,42–52]. In contrast to the effect of H_2S, the presence of basic nitrogen compounds is observed to mainly inhibit the HYD route with only a moderate effect on DDS. The inhibiting effect was found to correlate with the proton affinity of the nitrogen compounds [44,45]; this result also suggests that different sites are involved in HYD and DDS. Based on the observation that quite large molecules may be desulfurized via the HYD route, Ma and Schobert [53] suggested that the hydrogenation sites are multiple vacancy sites on the Mo(10$\bar{1}$0) edges capable of π-bonding the large molecules. The presence of such sites has been discussed in the literature [7], because the single-bonded sulfur atoms created by simply cleaving the bulk structures at the Mo(10$\bar{1}$0) edges were proposed to be unstable.

Recently, it has become possible to use density functional theory (DFT) methods to address a number of issues relevant for HDS [54–72]. In the first DFT study of MoS_2 and Co-MoS structures, Byskov et al. [71] found that it is energetically very unfavorable to create the "naked" Mo edges, where Mo is exposed at the edge and only 4-fold coordinated, and they concluded that such structures probably are not present under realistic HDS conditions [71]. Subsequent DFT studies have supported this conclusion [56,67,70]. Even though multiple vacancy sites may be very reactive [59,62,64], they are expected to readily react with H_2S, and reactions involving such sites should be extremely strongly inhibited by H_2S. Because the hydrogenation reactions are not poisoned by H_2S, these results show that some other sites must be involved in HYD. The first study of mechanistic aspects of HDS using DFT was carried out by Neurock and Van Santen, who studied the HDS of thiophene over Ni_xS_y clusters [65]. Although the study does not directly relate to MoS_2 catalysts, coordinatively unsaturated Ni sites were found to be very reactive.

Recently, it has been possible to obtain important clues regarding the hydrogenation sites and the HYD pathway from scanning tunneling microscopy (STM) studies [61]. Such studies have provided atom resolved images of the MoS_2 nanostructures; when they are combined with DFT calculations, quite detailed information may be obtained from the images [56,57,61,73,74]. These combined studies clearly show that naked Mo(10$\bar{1}$0) edges are not present at ultrahigh vacuum conditions. In contrast, the results show in agreement with the DFT calculations [54,56,63,69,71] that the Mo atoms will tend to maintain the full sulfur coordination of 6. This is achieved by extensive edge reconstruction. Quite surprisingly, it was found that these fully sulfur-saturated Mo(10$\bar{1}$0) edges of MoS_2 have some sites with metallic character [56,73,75]. These so-called "brim" sites could bind thiophene and were observed to be involved in further hydrogenation reactions [61]. One S–C bond in thiophene appeared to be cleaved at the brim site, and the resulting ad-

sorbed butenethiolate could be observed [61]. This is interesting, because such thiolates or thiols have been proposed to be key intermediates in many of the HDS mechanisms proposed in the literature [7,22]. However, at realistic HDS conditions, this intermediate has not yet been detected, presumably due to its high reactivity. In the STM study [61], the completion of the HDS reaction could not be observed. Because the MoS_2 clusters only exposed the Mo($10\bar{1}0$) edge, this study [61] did not yield any information about the possible role of S($\bar{1}010$) edges. Also note that the structures observed in the STM experiments might not be those structures, which are stable under reaction conditions [61].

The structures and intermediates present under reaction conditions generally are not accessible for study by direct imaging methods, but they can be studied by DFT calculations. Indeed, it has been found experimentally [57] and theoretically [54,56, 63,69,70] that the MoS_2 edge structures may be very labile, and quite different structures may exist depending on the reaction conditions. In the real HDS catalyst, the MoS_2 and WS_2 structures also may expose the S($\bar{1}010$) edges [57,76]. A key objective of the present study is to examine reactions at the S($\bar{1}010$) edges, which are predicted to be present at reaction conditions.

The present study used DFT to investigate HDS of thiophene. The calculational details are described in Section 2. An important problem with most reaction pathway studies has been that the assumed structures may be very different from those actually present at HDS conditions. Therefore, a key goal of the present study is to perform calculations on the type of structures that will be present during HDS catalysis. Section 3.1 discusses the relevant structures and edge configurations to lay the groundwork for studying the reaction pathway. The energetically most stable structures for both the Mo($10\bar{1}0$) edge and the S($\bar{1}010$) edge under typical reaction conditions are described. Sections 3.2–3.4 discuss the results on hydrogenation, S–C cleavage and site regeneration reactions at those edges. These detailed results are subsequently used to discuss some more general themes. The influence of reaction conditions is found to be quite significant, and these aspects are discussed in Section 3.5. Sections 3.6 and 3.7 present an analysis of the hydrogenation and S–C bond scission reactions and interplay between the two different edge sites in those reactions based on the determined reaction paths and the availability of the active sites. Section 3.8 discusses the relative role of different elementary reactions and pathways during HDS of thiophene. To avoid excessive repetition and to aid the presentation of the results, we have summarized many of the detailed results regarding the reaction pathways, the stabilities of the intermediates, and key activation energies in Figs. 3–7 and Table 1. Detailed comments regarding each elementary step and the nature of the intermediates are given in the following sections, and further details are provided in supplementary information.

2. Calculational details

An infinite stripe model, which previously has been proven successful to investigate MoS_2-based systems [55,56,77,78],

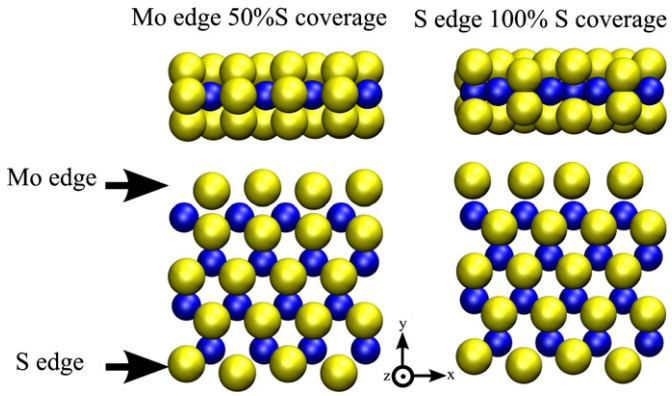

Fig. 1. The 4 × 4 supercells used for studies of the Mo edge with 50% S coverage and the S edge with 100% S coverage. Color code: sulfur (yellow), molybdenum (blue). (For interpretation of the references to color in this figure legend, the reader is referred to the web version of this article.)

is used to investigate the edges of MoS_2 and is depicted in Fig. 1. The infinite stripe exposes both the Mo edge and the S edge. The supercell has 4 Mo atoms in the x-direction and 4 Mo atoms in the y-direction, to allow for important reconstructions with a period of 2 in the x-direction and to allow decoupling of the Mo edge and the S edge in the y-direction. The stripes are separated by 14.8 Å in the z-direction and 9 Å in the y-direction. This model represents MoS_2 structures with no support interactions such structures are similar to the type II structures found in today's high-activity commercial catalysts [78].

The plane wave density functional theory code DACAPO [79,80] was used to perform the DFT calculations. The Brillouin zone was sampled using a Monkhorst–Pack k-point set [81] containing 4 k-points in the x-direction and 1 k-point in the y- and z-directions. The calculated equilibrium lattice constant of $a = 3.215$ Å and compares well to the experimental lattice constant of 3.16 Å [82]. A plane-wave cutoff of 30 Rydberg and a density wave cutoff of 45 Rydberg were used using the double-grid technique [83]. Ultrasoft pseudopotentials are used except for sulfur, where a soft pseudopotential was used [84,85]. A Fermi temperature of $k_B T = 0.1$ eV was used for all calculations, and energies were extrapolated to zero electronic temperature. The exchange correlation functional PW91 [86] was used. The convergence criterion for the atomic relaxation is that the norm of the total force should be <0.15 eV/Å, which corresponds approximately to a max force on one atom <0.05 eV/Å. The nudged elastic band (NEB) method was used to find energy barriers [87], together with the adaptive nudged elastic band approach [88] and cubic spline fits to the energy and the forces. Figures of atomic structures were created using VMD [89].

Unless notes otherwise, all adsorption energies were calculated using the equation

$$\Delta E_{\mathrm{ad}} = E_{\mathrm{molecule/MoS_2}} - E_{\mathrm{MoS_2}} - E_{\mathrm{molecule(g)}},$$

where $E_{\mathrm{molecule/MoS_2}}$ is the energy of the system with the molecule bound to the surface, $E_{\mathrm{MoS_2}}$ is the energy of the stripe, and $E_{\mathrm{molecule(g)}}$ is the energy of the molecule in vacuum. Molecules in vacuum were calculated using the same setup as for

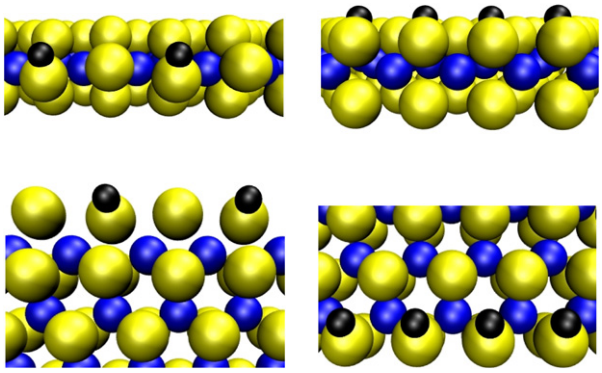

(a) (b)

Fig. 2. The equilibrium edge configurations at HDS conditions (P_{H_2} = 10 bar, P_{H_2}/P_{H_2S} = 100, and T = 650 K). (a) The Mo edge with 50% S coverage and 50% H coverage. (b) The S edge with 100% S coverage and 100% H coverage.

stripe calculations but using a supercell, which ensures at least 11 Å vacuum between neighboring molecules, using a Fermi temperature of k_BT = 0.01 eV, using only the gamma point in the Brillouin zone sampling. For all structural relaxations, the convergence criterion is that the norm of the total force should be <0.05 eV/Å.

3. Results and discussion

3.1. The choice of active surfaces and elementary reactions

The starting point of this investigation of HDS of thiophene is the recently improved understanding of the edge configurations at HDS conditions, which has been provided by several DFT studies [54,56,63,69,70]. As a starting point, we use the phase diagrams developed previously [56], which describe the edge structures as function of the chemical potential of S and H. The equilibrium edge configuration at HDS conditions (e.g., P_{H_2} = 10 bar, P_{H_2}/P_{H_2S} = 100 and T = 650 K, which are used throughout the article as an example of HDS conditions) determined in previous work [56] was recalculated with the calculational setup described in Section 2. We find essentially the same structures and adsorption energies as reported previously [56]; these equilibrium edge structures are shown in Fig. 2. HDS conditions vary depending on the crude oil being treated; the hydrogen pressure may vary from 10 to 200 bar, and P_{H_2}/P_{H_2S} also may vary depending on the reactor setup. The structure presented in Fig. 2 is the most stable structure over most of this range, with the exception that there may be more H atoms present at the S edge at high hydrogen pressures. S and H adsorption at sites at the edges of MoS_2 introduces structural changes; therefore, the definition of coverage of S and H needs to be refined; in this paper, we define the S coverage as the percentage of S present at the edge, with 100% being the S coverage of the fully sulfided edge (i.e., completely covered by S dimers). Using this definition, the S coverage is 50% at the Mo edge and 100% at the S edge (Fig. 2). Furthermore, we define the H coverage as the fraction of H atoms present per edge unit cell in the 4 × 4 structure; for example, 4 H atoms correspond to 100% H coverage. Using this definition, the H coverage in Fig. 2 is 50% at the Mo edge and 100% at the S edge. This definition allows for coverage above 100%, when more than four H atoms are present per unit cell. It should be emphasized that the structure for each "coverage" represents a new unique structure, and thus "coverage" should not be understood in the traditional sense, where it is the coverage of identical sites.

In the literature, "naked" Mo($10\bar{1}0$) edges with a coverage of 0% S have been considered as possible sites for hydrogenation reactions [53]. In this configuration, the Mo($10\bar{1}0$) edge contains Mo atoms coordinated to only four sulfur atoms, compared with a coordination number of 6 in the bulk. This situation is energetically very unfavourable under HDS conditions. In contrast, we find [56] an equilibrium S coverage of 50% at the Mo edge under HDS conditions. Note that in Fig. 2, the Mo coordination number is 6 at both edges. The H coverage at the S and Mo edges given in Fig. 2 corresponds to P_{H_2} = 10 bar. However, we show that it is possible to further increase the H coverage at the S edge by increasing the H_2 pressure, resulting in a H coverage above 100% (see atomic configuration 2 in Fig. 4). Such an increase is not possible at the Mo edge due to strong interaction between H atoms, as discussed further in Section 3.5 and also reported previously [78]. Our calculations show that a basic requirement for the removal of S from thiophene and other S-containing compounds is an available site for the adsorption of removed S. In this connection, an interesting finding is that the equilibrium edge configuration at the Mo edge allows for the addition of an S atom, whereas the equilibrium configuration at the S edge is fully covered by S and H atoms and does not allow for such an addition. Therefore, at the S edge, a vacancy must be created before S removal at the S edge.

Experimental studies of thiophene HDS have suggested that various pathways may be involved, and that the relative involvement of these pathways depends on the reaction conditions [7,10]. The elementary reactions in the different proposed reaction pathways include both hydrogenation and S–C bond scission reactions; thus, we have chosen to investigate both elementary hydrogenation and S–C bond scission reaction steps. Many different steps have been considered; to simplify the subsequent discussion, we summarize the elementary reactions investigated in the present study in Table 1, together with the calculated reaction and activation energies. The choice of elementary reactions and intermediates has been guided by recent STM and DFT studies, which have shown that thiophene hydrogenation and S–C scission can occur at the fully sulfided Mo edge [61]. Except for 2-hydrothiophene, all of the other intermediates given in Table 1 have been reported to be present during HDS of thiophene [7,90,91]. The reason that 2-hydrothiophene has not been observed experimentally is most likely related to the fact that it is not a stable molecule in the gas phase. Furthermore, the present study shows that the subsequent hydrogenation of 2-hydrothiophene to 2,5-dihydrothiophene is a nonactivated process.

We investigate both the HYD and DDS pathway of thiophene HDS. We define the difference between the DDS and the HYD pathway so that it is the DDS pathway when the initial S–C cleavage (reaction VI in Table 1) occurs in 2-hydrothiophene after the first hydrogenation step (reaction I in Ta-

Table 1
An overview of the reactions involved in HDS of thiophene including the activation barriers (E_a) and energy change (ΔE) of the reactions

Reaction	S edge		Mo edge	
	E_a (eV)	ΔE (eV)	E_a (eV)	ΔE (eV)
I 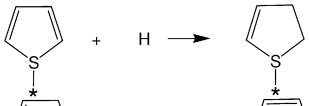	0.80	0.43	0.57	0.57
II 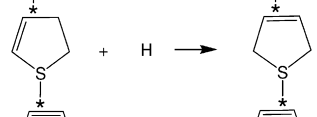	0.00	−1.02	0.00	−0.74
III 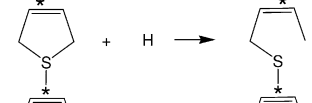	0.82	−0.78	1.13	0.51
IV 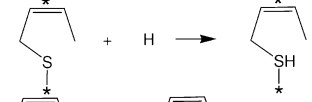	1.63	1.09	0.14	−0.26
V 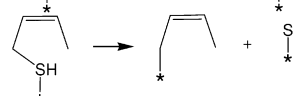	0.00	−0.66	0.12	−0.41
VI 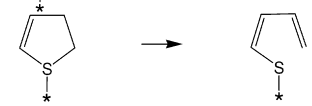	0.21	−1.11	1.10	1.09
VII $2HS–* \rightarrow H_2S–* + S–*$	1.70[a] 1.49[b]	1.57[a] 1.32[b]	1.00[c]	0.7[c]
VIII $(1/2)H_{2(g)} + * \rightarrow H–*$		−0.57[a] −0.11[b]		−0.33[d]
IX $H_2S_{(g)} + * \rightarrow H_2S–*$		−0.12[h]		−0.19[e]
X 		0.21[g]		−0.07[f]
XI 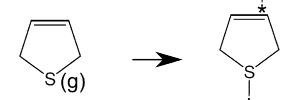		−0.59[g]		−0.12[f]
XII 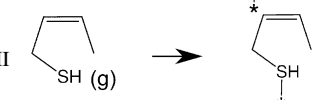		−0.52[g]		−0.12[d]
XIII 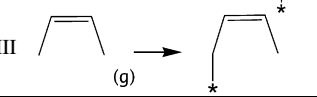		−0.05[i]		−0.28[d]

[a] Low H_2 pressures.
[b] High H_2 pressures.
[c] Calculated as $E_{VII} = \Delta E_1 + E_2$, where ΔE_1 is the energy change of reaction 1: 2H–S (50% H coverage 50% S) + S (0% H and 62.5% S) + S–S (0% H and 62.5% S) → S (25% H coverage 50% S) + HS (50% H and 62.5% S) + H–S–S (50% H and 62.5% S) and E_2 is the activation energy of reaction 2: HS (50% H and 62.5% S) + H–S–S (50% H and 62.5% S) → H_2S–S (Mo edge 50% S).
[d] Adsorption at the Mo edge with 50% S and 25% H.
[e] Adsorption at the Mo edge with 50% S and 0% H.
[f] Adsorption at the Mo edge with 50% S and 50% H.
[g] Adsorption at the S edge with 87% S and 75% H.
[h] Adsorption at the S edge with 87% S and 50% H.
[i] Adsorption at the S edge with 100% S and 25% H.

ble 1) and the HYD pathway when S–C cleavage (reaction III in Table 1) occurs in 2,5-dihydrothiophene, which is formed by two successive hydrogenation steps (reactions I and II in Table 1). It is interesting to note that the thiophene DDS and HYD pathways involve a common prehydrogenation step, because a similar common prehydrogenation step has been proposed in the HYD and DDS pathway for DBT and 4,6-DMDBT [41].

In what follows, we summarize the reactions in the HYD pathway as we have investigated them at both the Mo and S edges. The HYD pathway involves reactions I–V and reactions VII–XIII in Table 1. The reactions occur in the following order: X–I–II–III–IV–V–VII–IX. Reaction I in Table 1 hydrogenates thiophene and forms 2-hydrothiophene, which is then further hydrogenated (reaction II) to produce 2,5-dihydrothiophene.

The removal of S from 2,5-dihydrothiophene proceeds via initial S–C bond scission (reaction III) with *cis*-2-butenethiolate as a product, followed by *cis*-2-butenethiol formation by a H transfer reaction (reaction IV). Then *cis*-2-butene is the product formed by the final S–C scission (reaction V). In this context, it should be noted that the present study also investigates the S extrusion from *cis*-2-butenethiol, because it is an intermediate in the HYD pathway. It is quite likely that *cis*-2-butene will react further either by hydrogenation to butane or by intramolecular rotation to form *trans*-2-butene. We do not consider these here because they occur after S removal and are not important for sulfur removal. Further hydrogenation of 2,5-dihydrothiophene to tetrahydrothiophene has not been investigated, because we have assumed that tetrahydrothiophene is a likely intermediate only at high H_2 and low temperatures, because the presence of tetrahydrothiophene has been shown to be equilibrium-limited at temperatures typical for HDS conditions [10].

The DDS of thiophene was investigated using the following reaction path: reactions X–I–VI–(IV–V) in Table 1. The DDS pathway was initiated by thiophene adsorption (reaction X), followed by the hydrogenation of thiophene (reaction I), forming 2-hydrothiophene. Then the initial S–C bond was broken (reaction VI) and *cis*-butadienethiolate was formed. The further removal of S from *cis*-butadienethiolate was not investigated directly; however, these reactions are assumed to be very similar to reactions IV and V, because the involvement of the carbon chain is insignificant in these reactions, which are dominated by H diffusion and addition. The product of the DDS pathway is *cis*-butadiene under the assumption that the final S–C bond scission reaction is similar to reactions IV and V. *Cis*-butadiene may react further by hydrogenation or intramolecular rotation.

The reaction pathways shown in Figs. 3–6 have been constructed under the assumption that H_2 in the gas phase is in equilibrium with the H atoms adsorbed at the edge of MoS_2. This assumption is justified by the fact that experimentally H_2 dissociation is not found to be the rate-determining step [7,10]. Previous DFT studies have found the barrier to be 0.9–1 eV at the Mo edge with 50% S coverage [72,92]; however, these studies used a unit cell, which resulted in a H coverage after dissociation equal to 66 or 100%, respectively. The H adsorption energy at the Mo edge is highly dependent on the H coverage [78], and it can be speculated that the barrier changes when the H coverage is lowered to 50%, corresponding to HDS conditions. There have been no studies of the H_2 dissociation at the S edge of MoS_2; the only similar result is for the S edge promoted with 50% Co and with S coverage of 75%, where the barrier was found to be 0.6 eV [68]. The DFT results indicate that at certain reaction conditions (e.g., low hydrogen pressures), there could be an influence on the apparent activation energy due to H_2 dissociation; however, in the present study we have assumed that this is not the case at HDS conditions, and thus the hydrogen addition steps are not included in the reaction pathways. (A complete reaction path in which H addition steps are included is provided in supplementary information.) Furthermore, we contracted the hydrogenation of thiophene reactions (reactions I and II) to one barrier, because we found that only reaction I was activated.

3.2. The HYD pathway at the Mo edge

Using the elementary steps discussed in Section 3.1, we determined the detailed potential energy diagram for the HYD reaction pathway at the Mo edge; the results are depicted in Fig. 3. To arrive at the diagram shown in Fig. 3, we investigated the intermediates in various configurations as part of determining the minimum energy and the optimal reaction pathway. We evaluated the adsorption of the cyclic intermediates both above edge S atoms and in bridge positions between edge S atoms. Furthermore, we investigated both the η_1 (binding through the S atom) adsorption mode and the η_5 (binding through the π system) adsorption mode. For thiophene, we considered both adsorption modes proposed in the literature based on IR or INS studies [28–30,93] or proposed based on analogous structures observed in organometallic complexes [94]. We find that the preferred adsorption site for 2,5-dihydrothiophene is in between the front row S atoms, which is the location of the brim at the Mo edge at HDS conditions [56]; thus, there is no direct binding to the Mo atoms. Thiophene η_1 and η_5 adsorption at both the brim site and on top of edge S atoms are very similar in energy (within 0.02 eV); therefore, all of these adsorption modes will be expected to be present at HDS conditions. The present results thus support the conclusion from the INS experiments where both the η_1 and η_5 adsorption modes were observed [30]. However, the possibility that van der Waals (vdW) forces will stabilize one of the adsorption configurations cannot be ruled out. Such forces are not included in present-day exchange correlation functionals, and thus we cannot assess the importance of vdW forces. It should be emphasized that the present study investigates the adsorption at the equilibrium edge configurations under HDS conditions (50% H coverage, 50% S coverage). Clearly, the adsorption modes will change when the experimental conditions are changed and new edge structures are created. For example, a recent theoretical investigation found that the η_1 mode was most stable at a reduced Mo edge with a vacancy [95], but such very reduced Mo edges most likely will be present only in insignificant numbers under HDS conditions.

The HYD pathway at the Mo edge (Fig. 3) is initiated by thiophene adsorption at the brim site (reaction X). Following this, two hydrogenation reactions occur (reactions I and II in Table 1), resulting in the formation of 2,5-dihydrothiophene. Furthermore, the overall barrier of the hydrogenation steps is given by the barrier of reaction I, because reaction II is nonactivated. Thus, the reaction product (2-hydrothiophene) of reaction I is not expected to be abundant. This may explain why 2-hydrothiophene has never been observed. The hydrogenation reactions involve H from SH groups, which are present at the Mo edge. The binding energy of H at the 50% S-covered Mo edge depends on the H coverage, as also reported previously [78]; therefore, it will primarily be the H atoms corresponding to 50%, which will participate because H is too strongly bound (-0.7 eV) at lower coverage. H adsorption at coverage $>50\%$

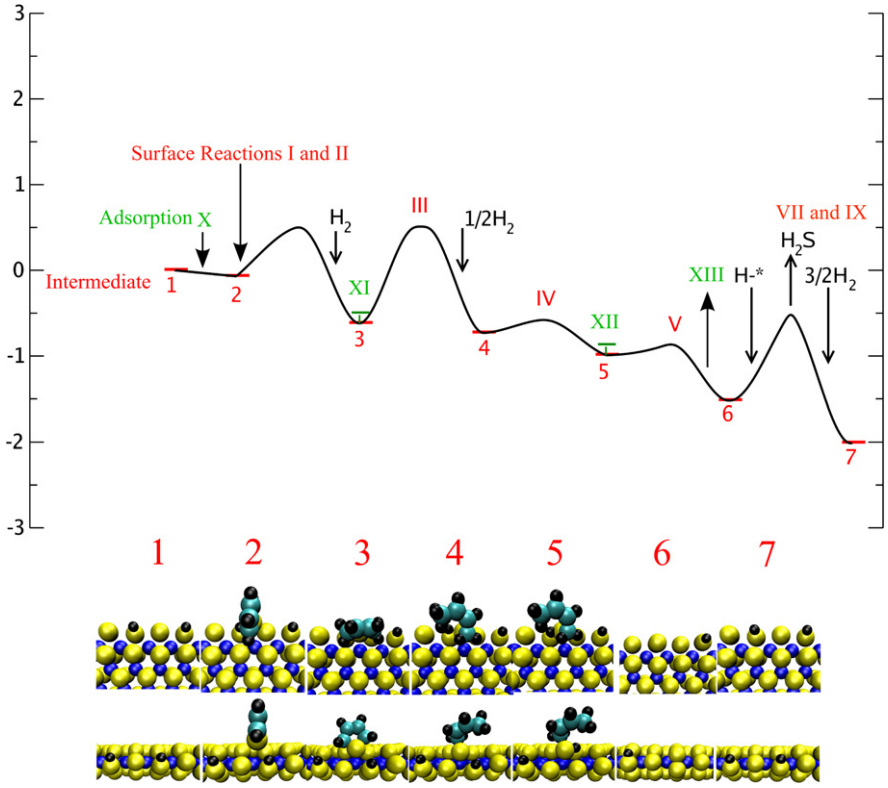

Fig. 3. The Mo-edge thiophene HYD pathway. The reference energy is the equilibrium edge configuration under HDS conditions (Mo edge with 50% S and 50% H) and thiophene in the gas phase. The atoms have the following color scheme: yellow, sulfur; blue, molybdenum; cyan, carbon; black, hydrogen. Arabic numerals denote intermediates, and Roman numerals denote reactions. (For interpretation of the references to color in this figure legend, the reader is referred to the web version of this article.)

has an endothermic binding energy (0.4 eV) [78] and are not occupied.

The initial hydrogenation steps are followed by reaction III, which breaks the first S–C bond in 2,5-dihydrothiophene and forms *cis*-2-butenethiolate. *Cis*-2-butenethiol is formed by H transfer in reaction IV, and finally S is removed by breaking the last S–C bond in the thiol in reaction V. Note that the removal of S from *cis*-2-butenethiol (reaction V) has a very low barrier (0.1 eV) and that the most difficult step is the initial S–C bond breaking. Removal of S from the thiol leaves behind an S atom. Subsequently, the active site must be regenerated to complete the catalytic cycle. The activation energy of regenerating the active site (reaction VII) is similar to the activation energy of the cleavage of the first S–C bond (reaction III).

STM experiments did not reveal the removal of S from thiolate [61]. This is not in contradiction with the present findings, because the equilibrium edge structure under the STM experimental conditions differs from that under reaction conditions. Under the STM conditions, the edges are completely covered with sulfur dimers (100% sulfur coverage). This surface does not allow the accommodation of an extra S atom, and thus the reaction stops once thiolate is formed. The present results show that it is of key importance that H atoms are present at the Mo edge at HDS conditions and that these H atoms react readily with thiophene and the intermediates. Thus, the Mo edge configuration present at HDS conditions is more suitable for HDS reactions than the highly sulfided Mo edge present at STM experimental conditions. The relative importance of the different hydrogenation reactions, the S–C bond scission reactions, and regeneration of the active site are explored further in Sections 3.5–3.8.

3.3. HYD pathway at the S edge

In the preceding section, we dealt with the HYD reaction pathway at the Mo edge. Under realistic HDS conditions, MoS_2 is likely to expose S edges as well, and possible reactions at this edge must also be considered [54,57]. The calculated potential energy diagram of the HYD reaction path at the S edge is shown in Fig. 4. It consists of reactions I–V and reactions VII–XIII in Table 1.

The HYD reaction pathway is initiated by vacancy formation (reaction VII), because a vacancy is needed to bind the intermediates and for the final removal of S from the organic molecule. We calculated the barriers for creating vacancies at high and low hydrogen pressures corresponding to 125% H and 100% H coverage, respectively; see Fig. 4. The binding energy of H decreases when there is more than one H atom per S dimer at the edge, as seen in Table 1. The importance of such weakly bound and more reactive H atoms is discussed further in Section 3.5, which also includes a discussion of the influence of the hydrogen pressure on the equilibrium H coverage.

After vacancy creation, the HYD pathway continues with adsorption of thiophene (reaction X) at the vacancy (corre-

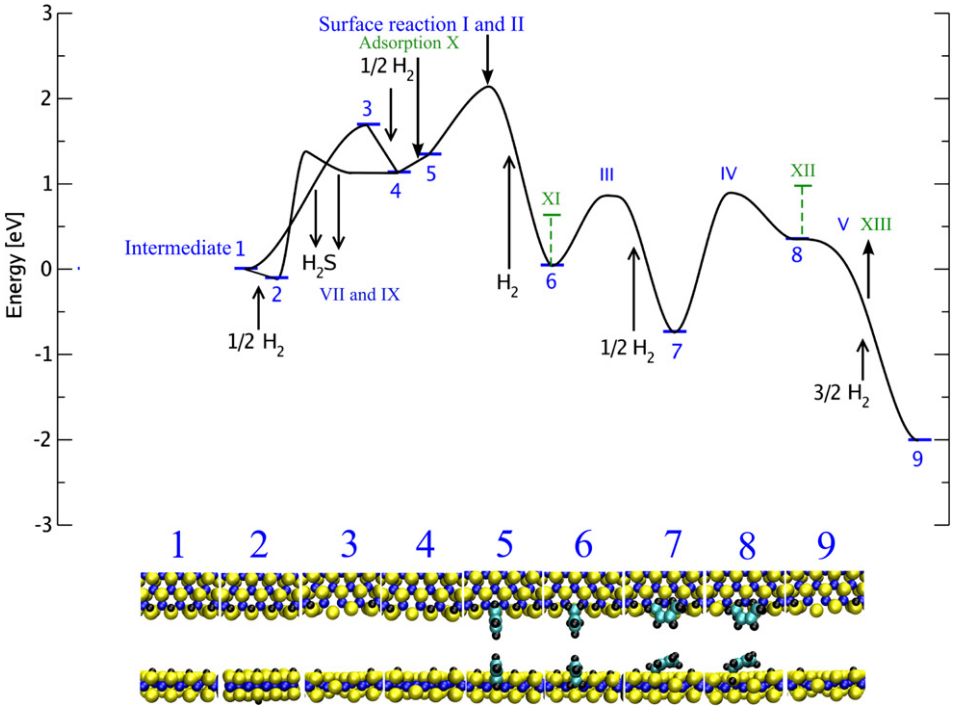

Fig. 4. The S-edge thiopene HYD pathway. The reference energy is the equilibrium edge configuration under HDS conditions (S edge with 100% S and 100% H) and thiophene in the gas phase. The color scheme for the atoms is the same as in Fig. 1. Arabic numerals denote intermediates, and Roman numerals denote reactions. (For interpretation of the references to color in this figure legend, the reader is referred to the web version of this article.)

sponding to 75% S coverage and 75% H coverage); this is endothermic (0.2 eV at 75% H coverage and 0.0 eV at 50% H coverage). The present adsorption mode is an end-on η_1 adsorption through the sulfur atom. Thus, thiophene adsorption will occur only if the van der Waals forces (which are not included in the present exchange correlation functional) are strong enough to give an exothermic adsorption energy; otherwise, thiophene hydrogenation and adsorption may occur in a concerted manner. Thus we expect that thiophene will be observed in high concentration only at the S edge in η_1 adsorption mode at low temperatures or at edges far from HDS equilibrium edge configurations with vacancies and low H coverage. This is in agreement with a recent theoretical study of thiophene adsorption at the S edge of stacked MoS_2 that found it to be strongest at the S edge with multiple vacancies or 0% H coverage [95]. The thiophene coverage at the vacancy sites is expected to be very small at HDS conditions, due to the endothermic adsorption energy (0.2 eV). The first hydrogenation reaction (reaction I), resulting in the formation of 2-hydrothiophene, had a higher barrier than the same reaction at the Mo edge (0.8 eV vs 0.6 eV), and the second hydrogenation reaction was also nonactivated at the S edge vacancy. The higher reaction barrier of the first hydrogenation step is ascribed to the stronger binding energy of H at the S edge. In fact, the results show that the SH bond strength is a key parameter for all the hydrogenation reactions including the reaction involved in site regeneration. The hydrogenation reactions are followed by reactions III, IV, and V, where the two S–C bond scission reactions (reactions III and V) have lower barriers than at the Mo edge, whereas the creation of *cis*-2-butenethiol has a higher barrier (reaction IV). The highest barrier involved in the HYD pathway is the initial vacancy and the H_2S formation step.

We investigated to what extent it could be possible that adsorption and hydrogenation could occur without the presence of an S vacancy at the S edge. For this purpose, we evaluated the S edge with 100% S and 75% H, which is a slightly lower H coverage than the equilibrium edge configuration (100% H), to leave room for thiophene adsorption. Thiophene adsorption at the S edge with 100% S and 75% H is in fact slightly exothermic (−0.1 eV). But this adsorption energy is smaller than the H adsorption energy (−0.6 eV) at the same site. Thus, H atoms will adsorb predominately at these sites and create the equilibrium structure, and the adsorption of thiophene is favored only at reaction conditions, where hydrogen pressure is low and thiophene pressure is high. Nevertheless, a full microkinetic model must be developed before the catalytic role of the "nonvacancy" sites can be evaluated in detail.

The relative catalytic importance of the hydrogenation reactions, S–C bond scission reactions, and regeneration of the active site at the S and Mo edge are further discussed in Sections 3.5–3.8.

3.4. DDS pathway at the Mo and S edges

As discussed in Section 3.1, the DDS pathway is characterized by the initial S–C scission reaction occurring immediately after the formation of 2-hydrothiophene. Thus, the first step after adsorption of thiophene (reaction X) is hydrogenation to 2-hydrothiophene (reaction I), followed by S–C bond scission (reaction VI) to *cis*-butadienethiolate. The final S removal from *cis*-2-butadienethiolate is assumed to be similar to the final S

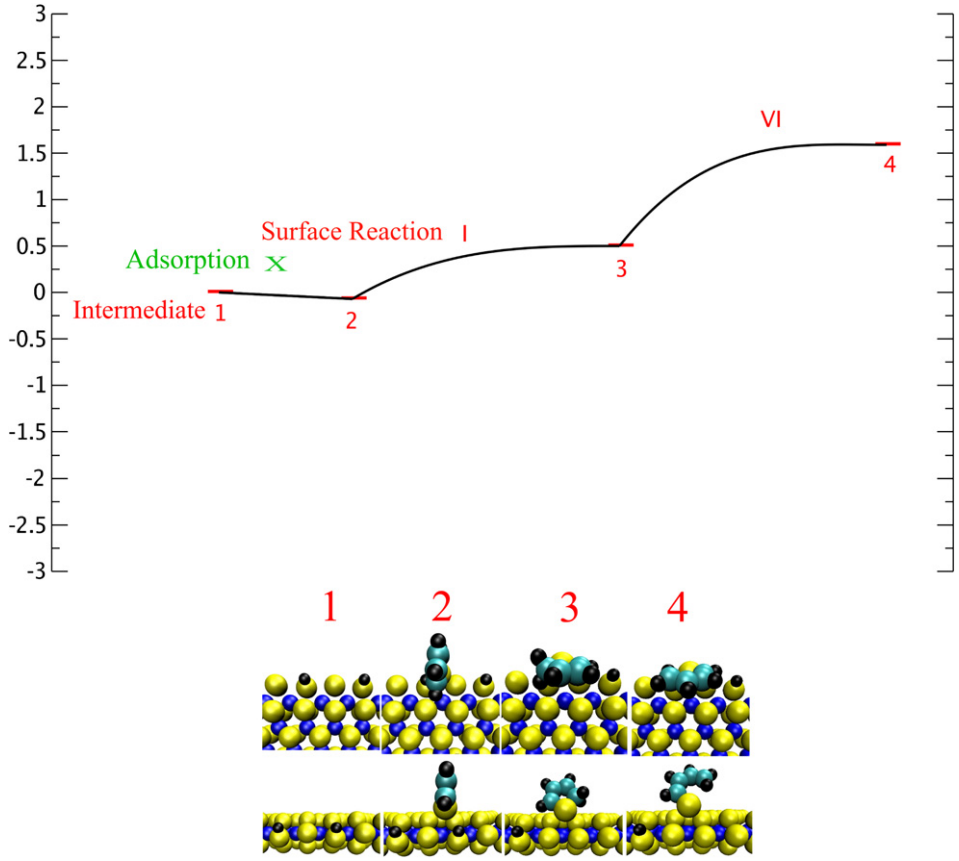

Fig. 5. The Mo-edge DDS pathway of thiophene. The reference energy is the equilibrium edge configuration at HDS conditions (Mo edge with 50% S and 50% H) and thiophene in the gas phase. The color scheme for the atoms is the same as in Fig. 1. Arabic numerals denote intermediates, and Roman numerals denote reactions. (For interpretation of the references to color in this figure legend, the reader is referred to the web version of this article.)

removal from *cis*-2-butenethiolate. The calculated potential energy diagrams of the DDS pathway at the Mo edge and the S edge are shown in Figs. 5 and 6, respectively. At the equilibrium Mo edge (50% S coverage and 50% H coverage), the DDS pathway is initiated by hydrogenation (reaction I), followed by S–C bond scission (reaction VI). The DDS pathway at the equilibrium S edge (100% S coverage and 100% H coverage) must (as discussed in Section 3.3) be initiated by vacancy formation (reaction VII). This is then followed by adsorption of thiophene (reaction X), the initial hydrogenation step (reaction I), and S–C bond scission (reaction VI). The barrier of reaction VI is 0.2 eV at the S edge, which is 0.9 eV lower than the barrier at the Mo edge. The present results indicate that the S edge vacancy site has a higher activity in elimination reactions of S–C bonds, which could indicate that the S edge vacancy site more readily eliminates the S–C bond in the DDS of DBT and similar molecules. The availability of the active site and the relative importance of the S and Mo edge in DDS are discussed in Sections 3.1 and 3.7.

3.5. The influence of hydrogen and H_2S pressure on the availability of the active sites

The brim site at the Mo edge and the vacancy site at the S edge are fundamentally different, and the interplay between the sites will depend on the relative availabilities of the sites. The Mo edge brim site is present at the equilibrium edge configuration, which has 50% S coverage and 50% H coverage, and the site is located in between the front-row S atoms with a neighboring H atom. In contrast to the readily available brim site, a large concentration of vacancy sites is not present at the S edge. Table 1 and Fig. 4 show that the energy required to remove S from the S edge by creating H_2S depends on the H_2 pressure, in the sense that at high H_2 pressures, the coverage of weakly bound H atoms becomes quite large, and this H gives a lower barrier for vacancy formation than the more strongly bound H. At low H_2 pressure, and thus at low coverage of weakly bound H atoms, the overall barrier of H_2S formation is given by the lowest of $E_{\text{overall}} = E_a^{\text{strong}}$ and $E_{\text{overall}} = E_a^{\text{weak}} + \Delta E$, where E_a^{weak} is the activation energy of H_2S formation involving the weakly bound H atoms, E_a^{strong} is the activation energy of H_2S formation involving the strongly bound H atoms, and ΔE is the energy difference in binding energy between the weakly and strongly bound H atoms. At high H_2 pressure, and thus at high coverage of the weakly bound H atoms, the overall energy barrier is given by $E_{\text{overall}} = E_a^{\text{weak}}$. In the current work, high coverage is defined as 0.8, which corresponds to approximately 80 bar hydrogen pressure. Quantification of high coverage could be possible using a microkinetic model. The H binding energy is −0.6 eV when only a single H is bound to each S dimer, whereas an additional H added to an S dimer has a binding en-

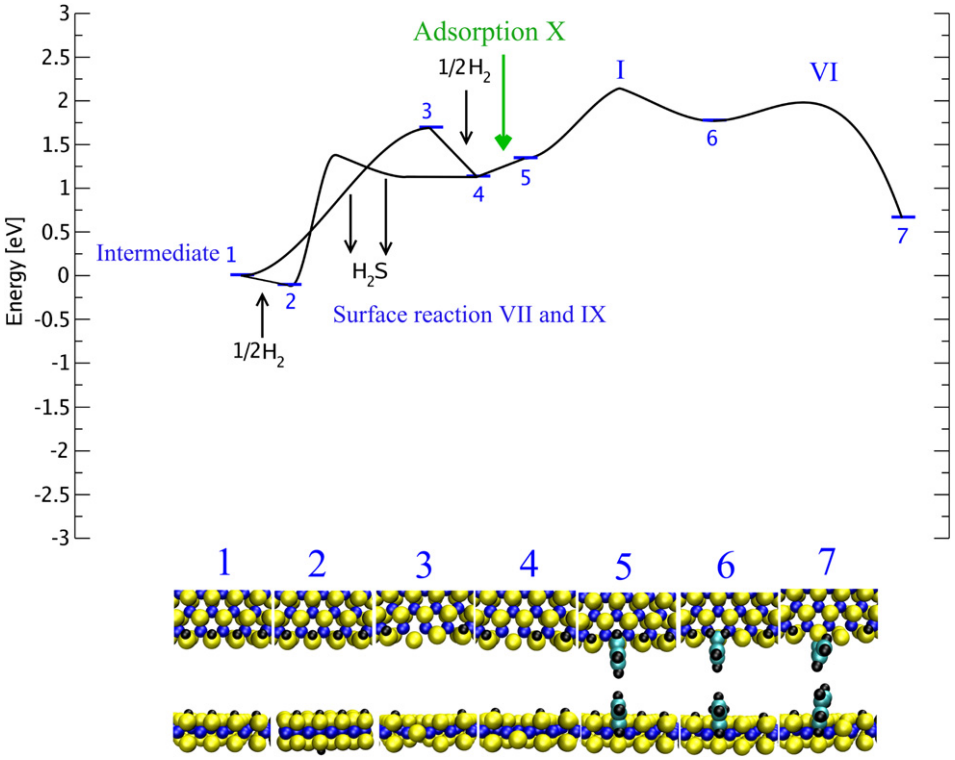

Fig. 6. The S-edge DDS pathway of thiophene. The reference energy is the equilibrium edge configuration at HDS conditions (S edge with 100% S and 100% H) and thiophene in the gas phase. The color scheme for the atoms is the same as in Fig. 1. Arabic numerals denote intermediates, and Roman numerals denote reactions. (For interpretation of the references to color in this figure legend, the reader is referred to the web version of this article.)

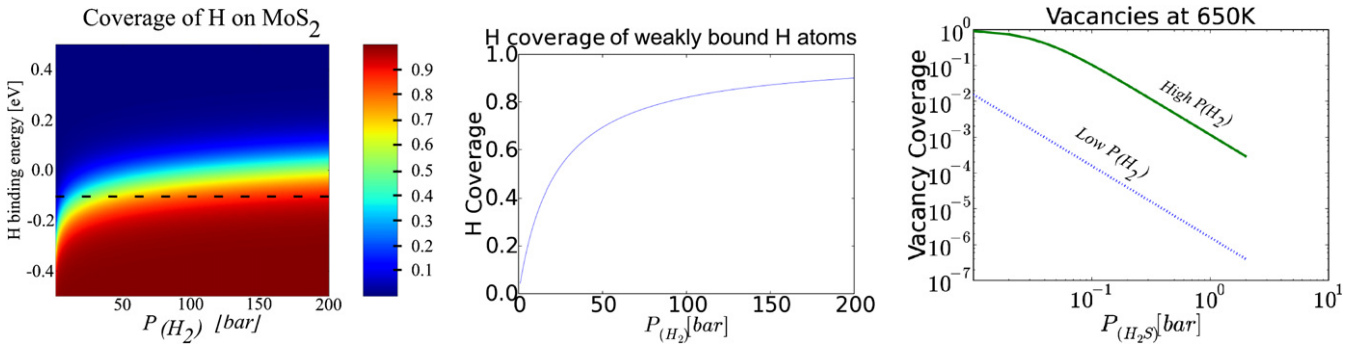

Fig. 7. H and vacancy coverages at 650 K. (a) Contour plot of the H coverage as a function of the partial pressure of hydrogen and H binding energies. The dotted line marks the binding energy of weakly bound H atoms. (b) H coverage of weakly bound H at the S edge dimers. (c) Coverage of vacancies at high and low hydrogen pressure.

ergy of −0.1 eV. Fig. 7a shows the calculated coverage of H as a function of the hydrogen pressure and H binding energy. It is seen that the strongly bound H will have 100% coverage; that is, all available sites will be filled, whereas the coverage of the weaker bound H will depend on the H_2 pressure. Fig. 7b shows the coverage of the weakly bound and thus more reactive H atoms. Many of the steps in the different HDS pathways involve H, and the barriers of these reactions likely are also lowered if the coverage of the weakly bound H is appreciable. A similar effect cannot occur at the Mo edge, because the differential H binding energy from 50 to 75% H coverage is 0.4 eV, which, according to Fig. 7a, corresponds to 0% coverage.

As discussed above, the creation of vacancies at the S edge involves reactions with H atoms, with the amount of vacancies depending on the partial pressure of hydrogen and the H coverage. Fig. 7c shows an estimate of the coverage of vacancy sites at the S edge under different reaction conditions. High H_2 pressure refers to the regime in which only the weakly bound H is involved in vacancy formation, and low H_2 pressure refers to the regime in which only strongly bound H is involved in vacancy formation. The calculations are based on the dissociative H_2S adsorption energy and assume that equilibrium is reached and that the H_2S entropy of the adsorbed state is 0 eV/K. For a particular choice of conditions like

(P_{H_2} = 10 bar, P_{H_2}/P_{H_2S} = 100, and T = 650 K), which correspond to the low-pressure region, there is a vacancy coverage of 0.0001; however, as can be seen in Fig. 7c, this changes with reaction conditions, and the coverage of vacancy sites at the S edge typically will be in the range of 10^{-6}–0.1. This is much lower than the coverage of Mo edge brim site, which is close to 100%. The difference in availability of active sites has important catalytic consequences, and the active sites at the S edge must be far more active than the Mo edge brim site to play any role in HDS reactions.

3.6. Hydrogenation reactions

The HYD pathway is especially important for the HDS of larger molecules like DBT and is the dominating reaction pathway for the desulfurization of 4,6-DMDBT [4,7,19,27]. Although the present investigation deals with desulfurization of the much simpler and more reactive thiophene molecule, many of the hydrogenation steps observed presently likely will also be important for the key features of the hydrogenation steps of the aromatic rings in the more complex molecules. Here we analyze the relative importance of the S edge vacancy site and the Mo edge brim site in hydrogenation reactions, then examine to what extent the elementary reactions and hydrogenation reaction pathways presented in the preceding sections may describe the kinetic observations reported in the literature.

Thiophene is found to bind quite weakly (−0.1 eV) to the Mo edge brim site, but the bond is still 0.3 eV stronger than that at the S edge vacancy site. These adsorption energies will become more exothermic if van der Waals forces can be included. Moreover, the barrier for the initial hydrogenation elementary step at the Mo edge brim site is 0.2 eV lower than at the S edge vacancy site. Based on this and the higher number of active sites at the Mo edge, it is concluded that hydrogenation reactions most likely occur at the Mo edge brim site. The difference in hydrogenation activation energy between the Mo edge brim site and the S edge vacancy site is probably related to the different H binding energy at the two edges. H is bound more weakly at the Mo edge than at the S edge. The differential desorption energy of 0.5 H_2 from the equilibrium structures is 0.3 eV/(0.5 H_2) at the Mo edge, compared with 0.6 eV/(0.5 H_2) at the S edge. Thus hydrogen may be bound too strongly at the S edge, which could explain why the H transfer processes involved in hydrogenation of thiophene on the Mo edge in Fig. 3 have barriers only equal to or very close to the thermochemical differences, whereas Fig. 4 shows that there are significant barriers at the S edge.

It has been reported that hydrogenation reactions are not significantly poisoned by H_2S [27]. This has been difficult to reconcile with vacancies as the active sites, but the present finding that the hydrogenation reactions occur at the Mo brim sites without involving a vacancy explains the low inhibiting effect of H_2S on hydrogenation.

The literature reports that the HYD pathway is most important for sterically hindered molecules like 4,6-DMDBT [4,7, 27]. Therefore, the hydrogenation site must be able to adsorb the sterically hindered molecules. The Mo edge brim site is a very open site that can adsorb thiophene in both the η_1 and η_5 modes. These adsorption modes are of such a character that analogue adsorption of DBT or 4,6-DMDBT is probably not sterically hindered. However, the vacancy site at the S edge is subject to steric constraints. This further supports the aforementioned conclusion that these sites are not expected to be involved in the hydrogenation of both smaller and larger sulfur-containing molecules.

During real feed HDS, the catalysts are also exposed to high concentrations of aromatics and different types of nitrogen-containing compounds [1,2]. The present findings elucidate the inhibition mechanism of the HYD pathway, in which such heterocyclic organic compounds are found to inhibit hydrogenation. Recently, we have investigated the inhibiting effect of basic nitrogen compounds using pyridine as an example. We found that pyridine is an inhibitor [58], because it not only can adsorb like benzene to the brim site, but also is able to react with H^+ from neighboring SH groups, resulting in the formation of a pyridinium ion, which adsorbs more strongly than pyridine. The thiophene adsorption energy is −0.1 eV, significantly lower than that of the pyridinium ion (−0.6 eV) [58]. These results allow us to explain the role of pyridine as an inhibitor and to understand the different observed kinetics of feeds including basic nitrogen-containing organic compounds.

3.7. S–C bond scission reactions

We investigated S–C scission reactions belonging to either the HYD or the DDS pathway. The distinction between the HYD and the DDS pathways is that in the DDS pathway, scission of the S–C bond (reaction VI) occurs after the first hydrogenation reaction (reaction I), whereas in the HYD pathway, S–C scission occurs after further hydrogenation (reaction II) of 2-hydrothiophene into 2,5-dihydrothiophene. We investigated the S–C scission reaction for three different S–C scission reactions: in 2-hydrothiophene (leading to DDS), in 2,5-dihydrothiophene, and in *cis*-2-butenethiolate. The latter two steps are the first and second S–C scission steps involved in the HYD pathway. In Sections 3.2–3.4 we discuss how the HYD or DDS pathways can occur at either the Mo or S edge. However, the reactants and intermediates are not forced to go through all of the elementary reactions at one edge exclusively, because the intermediates may move from one site to another, either by surface diffusion or by desorption and gas-phase diffusion. The likelihood of moving from a site at one type of edge to a site at another through desorption and gas-phase diffusion depends on the relative adsorption energy of the intermediates. The green lines in Figs. 3 and 4 indicate the adsorption energies of reactants and intermediates (reactions X–XIII); the adsorption energies are also tabulated in Tables 1 and 2. We see the quite general trend that all of the intermediates adsorb at the S edge vacancy site rather than at the Mo edge; in contrast, the reactant thiophene adsorbs most strongly at the Mo edge brim site. Therefore, it is possible that some of the elementary reactions may start at the Mo edge brim, followed by desorption of intermediates and readsorption at the S edge, where the reaction may be completed.

Table 2
Differential adsorption energies of the intermediates in thiophene HDS

	H coverage	0.5 H_2 (eV)	Thiophene (eV)	2,5-Dihydro-thiophene (eV)	*Cis*-2-butene-thiol (eV)
S edge	100% H, 100% S	−0.11			
	75% H, 87.5% S		0.21	−0.59	−0.52
	50% H, 87.5% S	−0.56	0.05	−0.85	−0.62
	25% H, 87.5% S	−0.48			
Mo edge	50% H, 50% S		−0.07[a] (−0.02)[b]	−0.12	
	25% H, 50% S	−0.33		−0.09	−0.12

[a] Perpendicular adsorption.
[b] Parallel adsorption.

Later we discuss where the three different S–C reactions will occur, how reaction conditions influence the relative importance of the Mo edge brim site and the S edge vacancy site, and the interplay between these sites. The S–C scission in 2-hydrothiophene (reaction VI) is an intramolecular elimination reaction involved in DDS that does not involve a hydrogen from a neighboring –SH group as for the other S–C scission reactions investigated. The activation energy is 0.2 eV at the S edge vacancy site and 1.1 eV at the Mo edge brim site (see Table 1). The low barrier at the S edge vacancy site indicates that this site is able to break S–C bonds by elimination, whereas the high barriers at the Mo edge brim show that this site is not well suited for the elimination reaction. It should be emphasized that reaction VI occurs after the initial hydrogenation reaction (reaction I), and, as mentioned in Section 3.6, this reaction occurs primarily at the Mo edge brim. But the DDS path cannot easily continue at this edge, because reaction VI has a high barrier at the Mo edge brim site, and this reaction is competing with the further hydrogenation reaction (reaction II) involved in the HYD pathway. However, the DDS of thiophene possibly can occur if 2-hydrothiophene can move from the Mo edge to the S edge by surface diffusion. Thus, a region with high reactivity could be close to the corner region between a Mo edge and an S edge. Another possibility is that 2,5-dihydrothiophene formed at the Mo edge brim site desorbs and readsorbs at a S edge vacancy, where it is dehydrogenated to form 2-hydrothiophene before S–C scission occurs (reaction VI). In all situations, the results suggest that the S–C scission in the DDS pathway occurs at the S edge vacancy, which is consistent with the fact that the DDS pathway is strongly inhibited by H_2S [7]. The relative rate of the DDS pathway compared with the HYD pathway seems to be quite low due to the low barriers for the competing hydrogenation reaction of 2-hydrothiophene (reaction II), but a more quantitative assessment of the relative rate of the DDS and the HYD pathway requires development of a complete microkinetic model. The present results, which show that the elimination step VI has a low barrier, indicate that the S edge vacancy site also could be the active site for other types of S–C elimination reactions, such as for thiols or S–C bond scission in the DDS mechanism of DBT or 4,6-DMDBT. It also can be speculated that the S edge vacancy site may be able to eliminate both S–C bonds in 2,5-dihydrothiophene and form butadiene in a reaction mechanism similar to that found for very small clusters [60]. Furthermore, the present findings support the proposal that an S edge vacancy site is needed to remove S from DBT and 4,6-DMDBT [56,66].

Along with the intramolecular elimination reactions involved in DDS, we also studied the hydrogenolysis reactions involved in the HYD pathway that occur when S–C bonds are broken in 2,5-dihydrothiopene and *cis*-2-butenethiolate. The S extrusion from *cis*-2-butenethiolate consists of two elementary steps: the transfer of H from an SH group to the sulfur in *cis*-2-butenethiolate (reaction IV) and the subsequent S–C scission reaction (reaction V). The H transfer step (reaction IV) turns out to be of key importance. It has a much lower barrier at the Mo edge brim site than at the S edge, which we propose to be related to the weaker binding of H atoms at the Mo edge (see Section 3.6). In contrast to the H transfer step, the S–C scission reaction has the highest barrier at the Mo edge brim site. This appears to be analogous to the situation for step VI. The final S–C scission (reaction V) likely also will occur at the Mo edge brim site, as shown in Fig. 3, even though it has a 0.1 eV higher barrier than at a S edge vacancy site. The rate of S extrusion from *cis*-2-butenethiolate at the S edge vacancy site will be determined by the H transfer step. S extrusion from *cis*-2-butenethiolate at the S edge vacancy site is competing with the backward reaction of step III, which leads to the formation of 2,5-dihydrothiophene. The barrier of 2,5-dihydrothiophene formation is similar to the barrier of H transfer (reaction IV); thus, 2,5-dihydrothiophene may be formed and subsequently desorbed and readsorbed at the Mo edge, where *cis*-2-butenethiol formation can occur. The other possibility is that *cis*-2-butenethiolate moves to the Mo edge by surface diffusion. We did not calculate the corresponding diffusion barriers, but they can be estimated by the energy required to move *cis*-2-butenethiolate from a vacancy site to a site next to the vacancy, which is 1.1 eV.

From the foregoing discussion, we can conclude that the Mo edge brim site is the primary site of *cis*-2-butenethiol formation. In view of the results shown in Fig. 7 and the discussion in Section 3.5, it can be speculated that the H transfer step and H transfer steps in general can occur more easily at the S edge vacancy site under high hydrogen partial pressure, where weakly bound H atoms are present.

Interplay between the Mo edge brim site and the S edge vacancy site is important for the desulfurization of *cis*-2-butenethiolate. For example, the final S–C scission step may

occur at the S edge vacancy even though the *cis*-2-butenethiol intermediate is formed at the Mo edge site. Such interplay between the S and Mo edges requires that *cis*-2-butenethiol move via surface diffusion or desorb from the Mo brim site. The present study found that *cis*-2-butenethiol will easily desorb due to the weak binding (−0.1 eV) at the Mo edge brim site. In this connection, it is interesting to note that thiols have been found as intermediates in the HDS of thiophene [90]. Because of their high reactivity, they are expected to be present in very small concentrations, as also has been observed experimentally [22,90].

The rate of S removal from *cis*-2-butenethiol will depend on the coverage of *cis*-2-butenethiol at the Mo edge brim site and the S edge vacancy site. At present, the coverage of *cis*-2-butenethiol cannot be calculated with high accuracy, due to the lack of thermodynamic data on gas-phase butane thiols; nonetheless, the relative coverage can be estimated. This coverage is a function of the Gibbs free energy of adsorption. Assuming that the entropy of *cis*-2-butenethiol [96] in the gas phase is similar to the entropy of *cis*-2-pentene, and using the upper limit of the entropy loss (found by assuming that all of the entropy is lost upon adsorption), $-T\Delta S_{\text{adsorb}}$ is 2.3 eV at 650 K and 1 atm. Thus, the entropy loss dominates the Gibbs free energy of adsorption, and the coverage of *cis*-2-butenethiol will be low. The large positive Gibbs free energy leads to the following simplification

$$\theta = K \cdot P/(1 + K \cdot P) \approx K \cdot P,$$

where K is the equilibrium constant ($K = \exp(-\Delta G/k_{\text{B}}T)$), P is the partial pressure of the reactant or intermediates, and θ is the coverage of the reactant or intermediates. Assuming that the entropy loss is similar at the two edges, the relative coverage is given by

$$\theta_{\text{S edge}}/\theta_{\text{Mo edge}} = \exp^{\square}-(\Delta E_{\text{S edge}} - \Delta E_{\text{Mo edge}})/(k_{\text{B}}T)^{\square},$$

where $\Delta E_{\text{S edge}}$ is the adsorption energy at the S edge, $\Delta E_{\text{Mo edge}}$ is the adsorption energy at the Mo edge, and k_{B} is the Boltzmann constant.

The adsorption energy of *cis*-2-butenethiol is most exothermic at the S edge vacancy site: between −0.5 and −0.6 eV, depending on H coverage. In contrast, it is −0.1 eV at the Mo edge brim site. Consequently, the coverage is 3 orders of magnitude larger at the S edge vacancy site. The activity for the final S–C scission is approximately 10 times higher at the S edge vacancy site than at the Mo brim site (a barrier difference of 0.12 eV). Combining this with the higher coverage of *cis*-2-butenethiol at an S edge vacancy site means that the S edge vacancy site is approximately 10^4 times more active for the HDS of *cis*-2-butenethiol than the Mo edge brim site. The same analysis for 2,5-dihydrothiophene leads to the conclusion that the S edge vacancy site is approximately 10^6 times more active in the initial S–C bond scission of 2,5-dihydrothiophene than the Mo edge brim site.

Consequently, the S edges will contribute more to the overall activity than the Mo edge if the S edge vacancy coverage is larger than approximately 10^{-4}, which (as shown in Fig. 7c) is the case at high H_2 pressure or H_2S pressure <0.1 bar. The picture is expected to differ somewhat for species like DBT and 4,6-DMDBT, in which geometrical hindrance of adsorption plays a larger role. For these species, the difference in adsorption energy between the different sites also may be larger and this also is expected to play a role. It can be added that the relative contributions of the different MoS_2 edges also depend on the sulfiding conditions, which influence the relative abundance of the Mo and S edges [57].

The present study, which investigated the reactions at a single MoS_2 slab, represents the structures observed in many commercial catalysts quite well. The results indicate that the relative contribution of different pathways and interaction between the S edge and the Mo edge are different in stacked multislab MoS_2 structures; for example, in such cases, only the top layer will expose readily accessible brim sites. This may be one reason why it is desirable to have mainly single slab catalysts in commercial catalysis, as well as why differences in activity depending on the degree of stacking degree has been found experimentally to be an important factor [97].

3.8. Possible rate-determining steps

The present results suggest that the regeneration of the active site is the crucial step in S removal. Regeneration of the active site at the Mo edge is comparable in energy barrier to the first S–C scission; at the S edge, the regeneration of the active site is the highest barrier involved in the HDS of thiophene. The barrier for regenerating the active site has the lowest value at the Mo edge; however, the barrier at the S edge can be lowered by high H_2 pressure, as discussed in Section 3.5. It is well known from the literature that H_2S acts as an inhibitor of S removal [7]; our results agree with this observation. The present results indicate that the S edge is inactive at low H_2 pressure and that catalytic reactions thus occur at the Mo edge. It is important to note that depending on the type of the active site, it can be either a site at which S is added to the equilibrium edge configuration or a site at which S is removed from the equilibrium edge configuration. Thus, a possible activity parameter could be the minimum energy required to either add or remove S from the equilibrium edge configuration. This insight can form the basis for refining the BEM model using S binding energy as the descriptor.

Various experimental studies have reported apparent activation energies in the ranges of 0.62–0.68 eV [98] and 0.83–1.01 eV [99]. Although a direct comparison to these apparent activation energies must await further study, the barriers found in the present study appear to compare well with the experimental values.

4. Conclusions

The present study has identified several HYD and DDS reaction pathways for thiophene HDS at both the Mo edge and the S edge, as summarized in Fig. 8. Note that as a starting point, we considered the edge configurations, which are thermodynamically most stable under realistic HDS conditions. These correspond to a Mo edge with 50% S coverage and 50% H

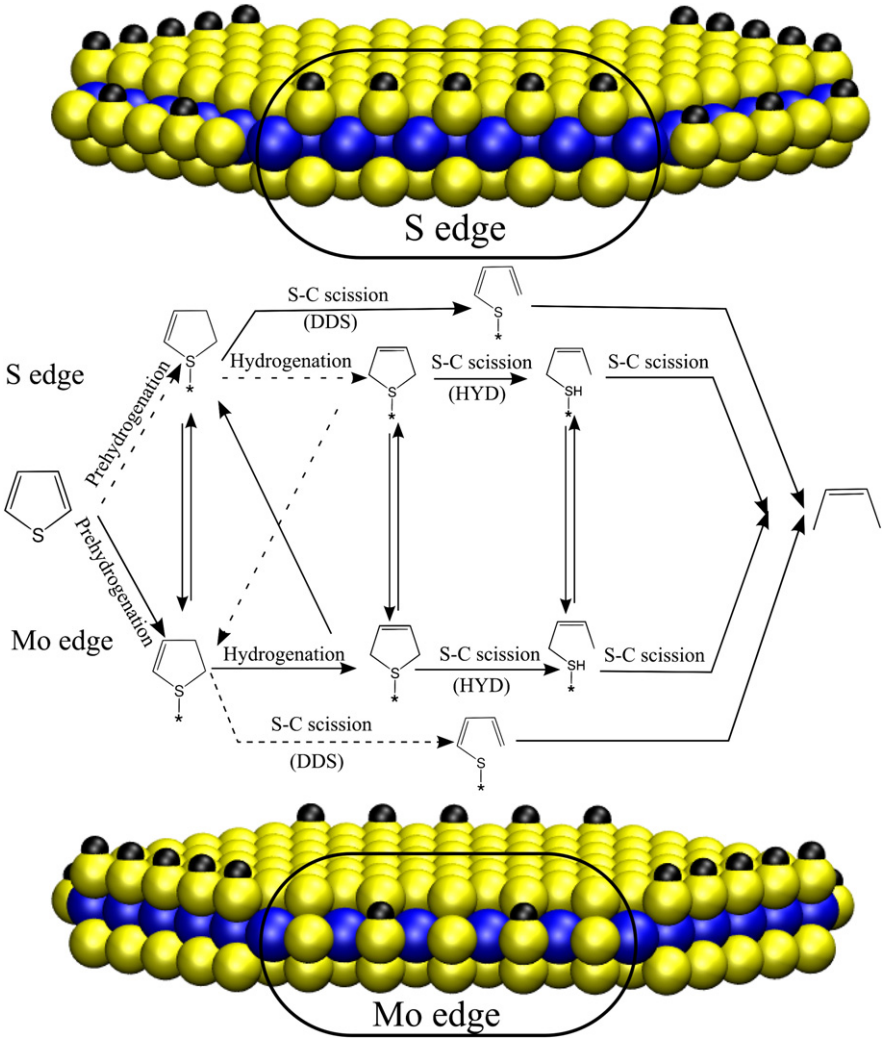

Fig. 8. Schematic overview over the reactions and MoS_2 structures involved in the HDS of thiophene. The upper part is a side view of MoS_2 perpendicular to the S($\bar{1}010$) edge, with the S and H coverage present at HDS conditions. The middle part is a schematic overview of the reactions involved in HDS of thiophene, including the possible interaction between the S($\bar{1}010$) edge and the Mo($10\bar{1}0$) edge. The dotted arrows denote reactions found to be slow. The lower part is a side view of MoS_2 perpendicular to the Mo($10\bar{1}0$) edge, with the S and H coverage present at HDS conditions.

coverage and an S edge with 100% S coverage and 100% H coverage; these structures are illustrated in Fig. 8.

Considering the elementary steps of thiophene hydrogenation and subsequent S–C bond scission, we have found some significant differences between the Mo and S edges, which can be summarized as follows:

1. H transfer and hydrogenation reactions have lower barriers at the Mo edge brim site (>0.2 eV lower than those at the S edge vacancy site).
2. Thiophene prefers to adsorb at the Mo edge brim site, where the binding is 0.3 eV stronger than at the S edge vacancy site.
3. 2,5-Dihydrothiophene and *cis*-2-butenethiol prefer to adsorb at the S edge vacancy site, where the binding is >0.4 eV stronger than at the Mo edge brim site.
4. S–C scission reactions have lower barriers at the S edge vacancy site (>0.1 eV lower than at the Mo edge brim site).
5. Regeneration of the active site has a higher barrier at the S edge (>0.5 eV higher than at the Mo edge).

Our results suggest that the HYD pathway is initiated by hydrogenation at the Mo edge, because thiophene preferentially adsorbs at the Mo edge and hydrogenation is energetically unfavorable at the S edge. In contrast, the S–C scission reaction can occur at both the Mo and S edges; which edge is preferred depends on the reaction conditions. Specifically, S–C scission preferably occurs at the Mo edge at high H_2S partial pressure and low H_2 pressures ($P_{H_2} < 80$ bar and $P_{H_2S} > 0.1$ bar), whereas the S edge is more reactive at low H_2S partial pressure or high H_2 partial pressures. This is due to the presence of different forms of adsorbed hydrogen and the resulting changes in the availability of S edge vacancy sites, which exhibit a low barrier for S–C scission.

Because the intermediates (e.g., 2,5-dihydrothiophene and *cis*-2-butenethiol) prefer to bind at the S edge rather than the Mo edge, it is possible that they diffuse to the S edge after initial

hydrogenation at the Mo edge, because desorption and diffusion are facile. Therefore, we suggest that the edges can catalyze the reaction in interplay between sites; that is, thiophene adsorbs and becomes hydrogenated at the Mo edge and subsequently diffuses to the S edge, where final S–C bond scission occurs. *Cis*-2-butenethiol is found to be an intermediate in the HYD pathway, and the low barriers of S removal from thiol at both the Mo edge brim site and the S edge vacancy site explain the high reactivity of thiols observed in kinetic and reactivity studies [7].

We find that the DDS pathway is initiated by a hydrogenation step occurring preferentially at the Mo edge, and the subsequent S–C scission occurs at the S edge. The calculated energies and barriers indicate that the DDS pathway is relatively less important than the HYD pathway for MoS_2.

The active site for thiophene HDS at the Mo edge is the so-called "brim" site, located 0.8 Å away from the edge. Note that these brim sites are present at the equilibrium edge configuration and thus should not be considered vacancies. In fact, the neighboring Mo atoms are fully coordinated by sulfur (see Fig. 8). Thus, this active site does not have to be created before the reaction can occur, but of course it must be regenerated between cycles. The active site for thiophene HDS at the S edge is a vacancy site that is not present at the equilibrium edge structure (see Fig. 8), but must be created first and subsequently regenerated between cycles. The relative concentration of S edge vacancies is significantly lower than that of the Mo edge brim sites, because the energy barrier involved in the creation of the vacancies is quite large, especially at low H_2 partial pressures. Therefore, they are present only at high H_2 partial pressures. In their absence (i.e., at low H_2 partial pressures), S–C scission must proceed by the energetically less favorable route involving the Mo edge.

Our results suggest that regeneration of the active site is a key step in the extrusion of S from thiophene at both edges. Thus, an important activity descriptor is the energy required to either add or remove S from the equilibrium edge configurations under reaction conditions.

We find that our proposed model for thiophene HDS involving the HYD and DDS pathways clarifies several experimental observations reported in the literature. We identify the Mo edge brim sites as the hydrogenation sites for the aromatic-like thiophene molecule and see that they do not require creation of a vacancy to be active. This explains the experimental observation that H_2S does not significantly inhibit hydrogenation of aromatics [7,27]. The present findings also elucidate the inhibiting effect of nitrogen-containing compounds on hydrogenation, because these species were found to preferably bind to the Mo edge brim sites [58]. At these edges, basic nitrogen containing molecules can gain extra stability through protonation by a SH group. Furthermore, the Mo edge brim site is a very "open" site that allows for adsorption of larger molecules without introducing significant steric hindrances. Thus, hydrogenation of, for example, 4,6-DMDBT likely occurs at the Mo edge brim site before desulfurization. Consequently, the S edge vacancy site also may play a large role in final removal of S from hydrogenated DBT and hydrogenated 4,6-DMDBT in a similar mechanism, where the stronger adsorption of hydrogenated intermediates at the S edge vacancy site aids S removal. This is consistent with the observed inhibition of these final steps by H_2S [27].

The present results show that HDS of thiophene involves a complicated interplay among edge structures, adsorption energies of reactants and intermediates, activation barriers, and reaction conditions. This may explain why researchers have found it so difficult to concur on the kinetics of thiophene HDS. It is interesting that the present results can form the basis for the development of a microkinetic model of HDS of thiophene that could be a very useful tool in quantifying the contributions of the different edges to thiophene HDS. Knowing the nature of the different sites involved in HDS can guide future design of catalysts with specific HYD/DDS properties. We can speculate that certain additives or supports may stabilize either the S or the Mo edge, and identifying such supports or additives can enable more intelligent catalyst design.

Acknowledgments

The authors thank Michael Brorson for fruitful discussions. This work was supported by the Danish Center for Scientific Computing (grant HDW-1103-06).

Supplementary information

The online version of this article contains additional supplementary information.

Please visit DOI: 10.1016/j.jcat.2007.02.028.

References

[1] K.G. Knudsen, B.H. Cooper, H. Topsøe, Appl. Catal. A Gen. 189 (1999) 205–215.
[2] C. Song, Catal. Today 86 (2003) 211–263.
[3] M.V. Landau, Catal. Today 36 (1997) 393–429.
[4] B.C. Gates, H. Topsøe, Polyhedron 16 (1997) 3213–3217.
[5] D.D. Whitehurst, T. Isoda, I. Mochida, Adv. Catal. 42 (1998) 345–471.
[6] I.V. Babich, J.A. Moulijn, Fuel 82 (2003) 607–631.
[7] H. Topsøe, B.S. Clausen, F.E. Massoth, Hydrotreating Catalysis, Springer-Verlag, Berlin, 1996.
[8] R. Prins, V.H.J. De beer, G.A. Somorjai, Catal. Rev. 31 (1989) 1–41.
[9] T. Kabe, A. Ishihara, W. Qian, Catal. Surv. Jpn. 3 (1999) 17–25.
[10] M.L. Vrinat, Appl. Catal. 6 (1983) 137–158.
[11] M.J. Girgis, B.C. Gates, Ind. Eng. Chem. Res. 30 (1991) 2021–2058.
[12] T.C. Ho, Catal. Rev. 30 (1988) 117–160.
[13] P.J. Owens, C.H. Amberg, Adv. Chem. Ser. 33 (1961) 182.
[14] A.E. Hargreaves, J.R.H. Ross, J. Catal. 56 (1979) 363–376.
[15] K.F. McCarty, G.L. Schrader, J. Catal. 103 (1987) 261–269.
[16] A.N. Startsev, in: 10th Int. Congr. Catal., 1992, p. 585.
[17] H. Schulz, D.-V. Do, Bull. Soc. Chim. Belg. 93 (1984) 645.
[18] J. Leglise, J. van Gestel, J.-C. Duchet, Adv. Hydrotreat. Catal. Prepr. Am. Chem. Soc. Div. Petrol. Chem. 39 (1994) 533–537.
[19] M. Houala, N.K. Nag, A.V. Sapre, D.H. Broderick, B.C. Gates, AIChE J. 24 (1978) 1015–1021.
[20] K.F. McCarty, G.L. Schrader, in: 8th Int. Congr. Catal. IV, 1984.
[21] P. Pokorny, M. Zdrazil, Collect. Czech. Chem. Commun. 46 (1981) 2185–2196.
[22] H. Schulz, M. Schon, H.M. Rahman, in: L. Cerveny (Ed.), Studies in Surface Science and Catalysis, Elsevier, Amsterdam, 2000, p. 204.
[23] A. Borgna, E.J.M. Hensen, L. Coulier, M.H.J.M. de Croon, J.C. Schouten, J.A.R. van Veen, J.W. Niemantsverdriet, Catal. Lett. 90 (2003) 117–122.

[24] M. Houalla, D.H. Broderick, V.H.J. De Beer, B.C. Gates, H. Kwart, Am. Chem. Soc. Div. Petrol. Chem. Prepr. 22 (1977) 941.
[25] X.L. Ma, K. Sakanishi, I. Mochida, Ind. Eng. Chem. Res. 35 (1996) 2487–2494.
[26] M. Breysse, P. Afanasiev, C. Geantet, M. Vrinat, Catal. Today 86 (2003) 5–16.
[27] M. Egorova, R. Prins, J. Catal. 225 (2004) 417–427.
[28] T.L. Tarbuck, K.R. McCrea, J.W. Logan, J.L. Heiser, M.E. Bussell, J. Phys. Chem. B 102 (1998) 7845–7857.
[29] P. Mills, D.C. Phillips, B.P. Woodruff, R. Main, M.E. Bussell, J. Phys. Chem. B 104 (2000) 3237–3249.
[30] P.C.H. Mitchell, D.A. Green, E. Payen, J. Tomkinson, S.F. Parker, Phys. Chem. Chem. Phys. 1 (1999) 3357–3363.
[31] S.J. Tauster, T.A. Pecoraro, R.R. Chianelli, J. Catal. 63 (1980) 515–519.
[32] H. Topsøe, R. Candia, N.-Y. Topsøe, B.S. Clausen, Bull. Soc. Chim. Belg. 93 (1984) 783–806.
[33] M. Salmeron, G.A. Somorjai, A. Wold, R. Chianelli, K.S. Liang, Chem. Phys. Lett. 90 (1982) 105–107.
[34] R.J.H. Voorhoev, J. Catal. 23 (1971) 236.
[35] R.J.H. Voorhoev, J.C.M. Stuiver, J. Catal. 23 (1971) 243.
[36] N.-Y. Topsøe, H. Topsøe, J. Catal. 139 (1993) 641–651.
[37] B. Scheffer, N.J.J. Dekker, P.J. Mangnus, J.A. Moulijn, J. Catal. 121 (1990) 31–46.
[38] D.G. Kalthod, S.W. Weller, J. Catal. 98 (1986) 572–576.
[39] J.K. Nørskov, B.S. Clausen, H. Topsøe, Catal. Lett. 13 (1992) 1–8.
[40] P. Zeuthen, P. Stolze, U.B. Pedersen, Bull. Soc. Chim. Belg. 96 (1987) 985–995.
[41] F. Bataille, J.L. Lemberton, P. Michaud, G. Perot, M. Vrinat, M. Lemaire, E. Schulz, M. Breysse, S. Kaztelan, J. Catal. 191 (2000) 409–422.
[42] F. van Looij, P. van de Laan, W.H.J. Stork, D.J. DiCamillo, J. Swain, Appl. Catal. A Gen. 170 (1998) 1–12.
[43] M. Nagai, T. Kabe, J. Catal. 81 (1983) 440–449.
[44] M. Nagai, T. Sato, A. Aiba, J. Catal. 97 (1986) 52–58.
[45] V. LaVopa, C.N. Satterfield, J. Catal. 110 (1988) 375–387.
[46] P. Zeuthen, K.G. Knudsen, D.D. Whitehurst, Catal. Today 65 (2001) 307–314.
[47] P. Wiwel, K. Knudsen, P. Zeuthen, D. Whitehurst, Ind. Eng. Chem. Res. 39 (2000) 533–540.
[48] M. Egorova, R. Prins, J. Catal. 221 (2004) 11–19.
[49] M. Egorova, R. Prins, J. Catal. 224 (2004) 278–287.
[50] T.C. Ho, J. Catal. 219 (2003) 442–451.
[51] U.T. Turaga, X. Ma, C. Song, Catal. Today 86 (2003) 265–275.
[52] E. Furimsky, F.E. Massoth, Catal. Today 52 (1999) 381–495.
[53] C. Song, X. Ma, Appl. Catal. B Environ. 41 (2003) 207–238.
[54] H. Schweiger, P. Raybaud, H. Toulhoat, J. Catal. 212 (2002) 33–38.
[55] L.S. Byskov, J.K. Nørskov, B.S. Clausen, H. Topsøe, J. Catal. 187 (1999) 109–122.
[56] M.V. Bollinger, K.W. Jacobsen, J.K. Nørskov, Phys. Rev. B 67 (2003) 085410.
[57] J.V. Lauritsen, M.V. Bollinger, E. Lægsgaard, K.W. Jacobsen, J.K. Nørskov, B.S. Clausen, H. Topsøe, F. Besenbacher, J. Catal. 221 (2004) 510–522.
[58] Á. Logadóttir, P.G. Moses, B. Hinnemann, N.-Y. Topsøe, K.G. Knudsen, H. Topsøe, J.K. Nørskov, Catal. Today 111 (2006) 44–51.
[59] T. Todorova, R. Prins, T. Weber, J. Catal. 236 (2005) 190.
[60] X. Yao, Y. Li, H. Jiao, J. Mol. Struct. Theochem. 726 (2005) 81.
[61] J.V. Lauritsen, M. Nyberg, J.K. Nørskov, B.S. Clausen, H. Topsøe, E. Lægsgaard, F. Besenbacher, J. Catal. 224 (2004) 94–106.
[62] P. Raybaud, J. Hafner, G. Kresse, H. Toulhoat, Stud. Surf. Sci. Catal. 127 (1999) 309–317.
[63] S. Cristol, J.F. Paul, E. Payen, D. Bougeard, S. Clémendot, F. Hutschka, J. Phys. Chem. B 106 (2002) 5659–5667.
[64] P. Raybaud, J. Hafner, G. Kresse, H. Toulhoat, Phys. Rev. Lett. 80 (1998) 1481–1484.
[65] M. Neurock, R.A. van Santen, J. Am. Chem. Soc. 116 (1994) 4427–4439.
[66] S. Cristol, J.F. Paul, E. Payen, D. Bougeard, F. Hutschka, S. Clémendot, J. Catal. 224 (2004) 138–147.
[67] J.F. Paul, E. Payen, J. Phys. Chem. B 107 (2003) 4057–4064.
[68] L.S. Byskov, M. Bollinger, J.K. Nørskov, B.S. Clausen, H. Topsøe, J. Mol. Catal. A Chem. 163 (2000) 117–122.
[69] S. Cristol, J.F. Paul, E. Payen, D. Bougeard, S. Clémendot, F. Hutschka, J. Phys. Chem. B 104 (2000) 11220–11229.
[70] P. Raybaud, J. Hafner, G. Kresse, S. Kasztelan, H. Toulhoat, J. Catal. 190 (2000) 128–143.
[71] L.S. Byskov, B. Hammer, J.K. Nørskov, B.S. Clausen, H. Topsøe, Catal. Lett. 47 (1997) 177–182.
[72] M. Sun, A.E. Nelson, J. Adjaye, J. Catal. 233 (2005) 411–421.
[73] S. Helveg, J.V. Lauritsen, E. Lægsgaard, I. Stensgaard, J.K. Nørskov, B.S. Clausen, H. Topsøe, F. Besenbacher, Phys. Rev. Lett. 84 (2000) 951–954.
[74] J.V. Lauritsen, S. Helveg, E. Lægsgaard, I. Stensgaard, B.S. Clausen, H. Topsøe, F. Besenbacher, J. Catal. 197 (2001) 1–5.
[75] M.V. Bollinger, J.V. Lauritsen, K.W. Jacobsen, J.K. Nørskov, S. Helveg, F. Besenbacher, Phys. Rev. Lett. 87 (2001) 196801–196803.
[76] A. Carlsson, M. Brorson, H. Topsøe, J. Catal. 227 (2004) 530–536.
[77] B. Hinnemann, P.G. Moses, J. Bonde, K.P. Jørgensen, J.H. Nielsen, S. Horch, I. Chorkendorff, J.K. Nørskov, J. Am. Chem. Soc. 127 (2005) 5308–5309.
[78] B. Hinnemann, J.K. Nørskov, H. Topsøe, J. Phys. Chem. B 109 (2005) 2245–2253.
[79] S.R. Bahn, K.W. Jacobsen, Comput. Sci. Eng. 4 (2002) 56–66.
[80] B. Hammer, L.B. Hansen, J.K. Nørskov, Phys. Rev. B 59 (1999) 7413.
[81] H.J. Monkhorst, J.D. Pack, Phys. Rev. B 13 (1976) 5188–5192.
[82] T. Böker, R. Severin, A. Müller, C. Janowitz, R. Manzke, D. Voss, P. Krüger, A. Mazur, J. Pollmann, Phys. Rev. B 64 (2001) 235305-1–235305-11.
[83] K. Laasonen, A. Pasquarello, R. Car, C. Lee, D. Vanderbilt, Phys. Rev. B 47 (1993) 10142–10153.
[84] N. Troullier, J.L. Martins, Phys. Rev. B 43 (1991) 1993–2006.
[85] D. Vanderbilt, Phys. Rev. B 41 (1990) 7892–7895.
[86] J.P. Perdew, J.A. Chevary, S.H. Vosko, K.A. Jackson, M.R. Pederson, D.J. Singh, C. Fiolhais, Phys. Rev. B 46 (1992) 6671.
[87] H. Jonsson, G. Mills, K.W. Jacobsen, in: B.J. Berne, G. Cicotti, D.F. Coker (Eds.), Classical and Quantum Dynamics in Condensed Phase Systems, Enrico Fermi Summer School, vol. 97, World Scientific, Singapore, 1997.
[88] S.A. Andreev, Y. Brumer, D.R. Reichman, E. Kaxiras, P. Maragakis, J. Chem. Phys. 117 (2002) 4651–4658.
[89] W. Humphrey, A. Dalke, K. Schulten, J. Mol. Graph. 14 (1996) 33–38.
[90] D.L. Sullivan, J.G. Ekerdt, J. Catal. 178 (1998) 226–233.
[91] A. Borgna, E.J.M. Hensen, J.A.R. van Veen, J.W. Niemantsverdriet, J. Catal. 221 (2004) 541–548.
[92] A. Travert, H. Nakamura, R.A. van Santen, J.F. Paul, E. Payen, J. Am. Chem. Soc. 124 (2002) 7084–7095.
[93] P. Mills, S. Korlann, M.E. Bussell, M.A. Reynolds, M.V. Ovchinnikov, R.J. Angelici, C. Stinner, T. Weber, R. Prins, J. Phys. Chem. A 105 (2001) 4418–4429.
[94] R.J. Angelici, Polyhedron 16 (1997) 3073–3088.
[95] S. Cristol, J. Paul, C. Schovsbo, E. Veilly, E. Payen, J. Catal. 239 (2006) 145–153.
[96] D.R. Lide, CRC Handbook of Chemistry and Physics, 83rd ed., CRC Press, Boca Raton, 2002.
[97] M. Daage, R.R. Chianelli, J. Catal. 149 (1994) 414–427.
[98] E.J.M. Hensen, H.J.A. Brans, G.M.H.J. Lardinois, V.H.J. de Beer, J.A.R. van Veen, R.A. van Santen, J. Catal. 192 (2000) 98–107.
[99] M.J. Ledoux, O. Michaux, G. Agostini, P. Panissod, J. Catal. 102 (1986) 275–288.

Paper 4

Scaling Properties of Adsorption Energies for Hydrogen-Containing Molecules on Transition-Metal Surfaces

F. Abild-Pedersen, J. Greeley, F. Studt, J. Rossmeisl, T. R. Munter, P. G. Moses, E. Skúlason, T. Bligaard, and J. K. Nørskov

Center for Atomic-scale Materials Design, Department of Physics, NanoDTU, Technical University of Denmark, DK-2800 Lyngby, Denmark

(Received 13 February 2007; published 6 July 2007)

Density functional theory calculations are presented for CH_x, $x = 0, 1, 2, 3$, NH_x, $x = 0, 1, 2$, OH_x, $x = 0, 1$, and SH_x, $x = 0, 1$ adsorption on a range of close-packed and stepped transition-metal surfaces. We find that the adsorption energy of any of the molecules considered scales approximately with the adsorption energy of the central, C, N, O, or S atom, the scaling constant depending only on x. A model is proposed to understand this behavior. The scaling model is developed into a general framework for estimating the reaction energies for hydrogenation and dehydrogenation reactions.

DOI: 10.1103/PhysRevLett.99.016105 PACS numbers: 82.45.Jn

The formation of a bond between a molecule and a metal surface is an important phenomenon in a number of processes including heterogeneous catalysis [1], contact formation in molecular electronics [2], and anchoring of biomolecules to solids for sensors and other biomedical applications [3]. The adsorption energy is a key quantity describing the strength of the interaction of molecules with the surface. The adsorption energy can be measured by advanced surface science techniques [4–6]. Alternatively, density functional theory (DFT) offers the possibility of calculating adsorption energies with reasonable accuracy [7–11]. While both experiments and DFT calculations are feasible for a limited number of systems, they can hardly be performed in detail for all potentially interesting adsorption systems. There is therefore a need for simple models with the ability to estimate bond energies in a first screening of interesting systems. A successful model will also expose the important factors determining the strength of an adsorbate-surface bond. In the present Letter we will develop such a model for hydrogen-containing molecules. We use DFT calculations to derive a number of correlations between adsorption energies, and we then present a model to explain them. The model shows how the adsorbate valency, together with the properties of the d electrons of the surface, determines the adsorption energy. We further develop the scaling model into a method for estimating hydrogenation or dehydrogenation reaction energies for organic molecules on transition-metal surfaces. The model is tested against full DFT calculations for reactions of hydrocarbons, alcohols, thiols, and amino acids.

First, we present results of extensive DFT calculations of the adsorption energies of CH_x, $x = 0, 1, 2, 3$, NH_x, $x = 0, 1, 2$, OH_x, $x = 0, 1$, and SH_x, $x = 0, 1$ on a range of close-packed and stepped metal surfaces. The study involves the close-packed fcc(111), fcc(100), hcp(0001), and bcc(110) surfaces, and the stepped fcc(211) and bcc(210) surfaces. Each of the surfaces is modeled by a (2×2) or a (1×2) surface unit cell for the close-packed and stepped surfaces, respectively. Each slab has a thickness of three layers in the direction perpendicular to the close-packed surface. These slabs are thick enough to capture the trends in the chemisorption energetics. The adsorbates and the topmost layer are allowed to relax fully in all configurations, and in the case of Fe, Ni, and Co, spin polarization is taken into account. The binding energies of the different species have been taken for the most stable adsorption sites on all surfaces. The RPBE functional [12] in the generalized gradient approximation is used to describe exchange and correlation effects. The calculational method and setup is described in Ref. [13].

Figure 1 summarizes the results of the DFT calculations. We find for all the molecules studied that the adsorption energy of molecule AH_x is linearly correlated with the adsorption energy of atom A:

$$\Delta E^{AH_x} = \gamma \Delta E^{A} + \xi. \quad (1)$$

There is some scatter around the linear relations, but we note that while the adsorption energies vary by several electron volts over the range of metals considered here, the mean absolute error (MAE) is only 0.13 eV. Some of this scatter is related to differences in adsorption sites for adsorbates with different amounts of hydrogen. CH_3, for instance, typically prefers a onefold adsorption site on the close-packed surfaces while C prefers the threefold site. If we were to use the adsorption energy of C in the onefold adsorption site as the reference, the quality of the correlation becomes significantly better (MAE = 0.06 eV); see Fig. 2. We also find that when we use a reference with the same configuration as the molecule of interest, the scaling behavior includes alloys with the same accuracy as for the elemental metals (Fig. 2).

The main observation from Figs. 1 and 2 is that the slope of the linear relationship γ in Eq. (1) is given to a good approximation by the number of H atoms in AH_x as $\gamma(x) = (x_{\max} - x)/x_{\max}$, where $x_{\max}$ is the maximum number of H atoms that can bond to the central atom A ($x_{\max} = 4$ for

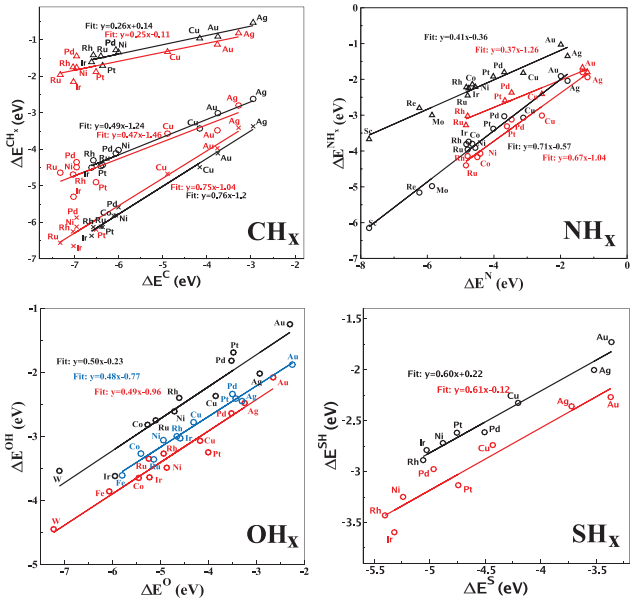

FIG. 1 (color). Adsorption energies of CH_x intermediates (crosses: $x = 1$; circles: $x = 2$; triangles: $x = 3$), NH_x intermediates (circles: $x = 1$; triangles: $x = 2$), OH, and SH intermediates plotted against adsorption energies of C, N, O, and S, respectively. The adsorption energy of molecule A is defined as the total energy of A adsorbed in the lowest energy position outside the surface minus the sum of the total energies of A in vacuum and the clean surface. The data points represent results for close-packed (black) and stepped (red) surfaces on various transition-metal surfaces. In addition, data points for metals in the fcc(100) structure (blue) have been included for OH_x.

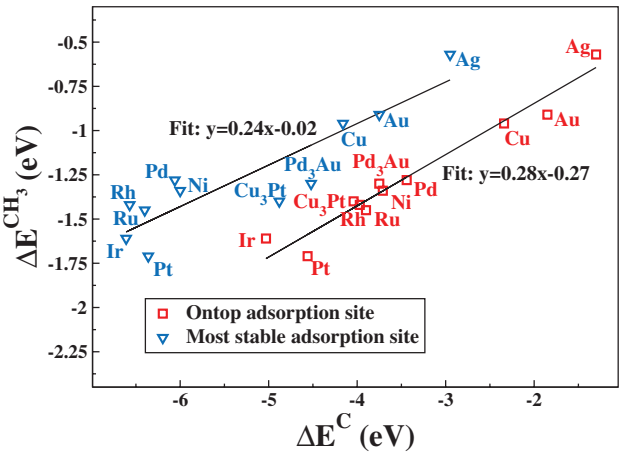

FIG. 2 (color). Binding energies of CH_3 plotted against the binding energies of C for adsorption in the most stable sites (triangles) and in the case where both CH_3 and C have been fixed in the on-top site (squares).

$A = C$, $x_{max} = 3$ for $A = N$, and $x_{max} = 2$ for $A = O, S$). Since $(x_{max} - x)$ is the valency of the AH_x molecule, we conclude that for the four families of molecules considered the slope only depends on the valency of the adsorbate. In the following we will consider a model that allows us to understand the origin of this effect.

For some of the considered systems, simple valency or bond-counting arguments [14] can explain the results: Comparing CH, CH_2, and CH_3 on the close-packed surfaces, we generally find CH (with a valency of 3) to prefer threefold adsorption sites, CH_2 (valency of 2) to prefer twofold adsorption, and CH_3 (valency of 1) to prefer onefold adsorption. The implication of these trends is that unsaturated bonds on the carbon atom form bonds to surface metal atoms; in effect, each unsaturated sp^3 hybrid on the central C atom binds independently to the d states of the nearest neighbor metal atoms, consistent with the slopes in Fig. 1. However, this picture cannot include adsorbed atomic C. Adsorbed C also adsorbs in a threefold site (neglecting long range reconstructions), but it does not have four bonds as would be needed to explain all the C data in Fig. 1. We also note that the overall scaling behavior is independent of the adsorption geometry and hence the details of the bonding; see Fig. 2. The scaling in Figs. 1 and 2 must therefore have a more general explanation that includes the argument above for CH, CH_2, and CH_3 as a special case.

We will base our analysis on the d-band model which has been used quite successfully to understand trends in adsorption energies from one transition metal to the next [8,15–19]. According to the d-band model, it is useful to think of the formation of the adsorbate-surface bond as taking place in two steps. First, we let the adsorbate states interact with the transition metal sp states, and then we include the extra contribution from the coupling to the d states:

$$\Delta E = \Delta E_{sp} + \Delta E_d. \tag{2}$$

The coupling to the metal sp states usually contributes the largest part of the bonding and involves considerable hybridization and charge transfer. In terms of variations from one transition metal to the next it can, however, be considered to be essentially a constant; the sp bands are broad, and all the transition metals have one sp electron per metal atom in the metallic state [20]. According to the d-band model, the main contribution to the *variations* in bond energy from one transition metal to the next comes from the coupling to the metal d states; the d states form narrow bands of states close to the Fermi level, and the width and energy of the d bands vary substantially between transition metals. According to the d-band model, all the variations among the metals observed in Fig. 1 should therefore be given by ΔE_d. That means that the x dependence of $\Delta E^{AH_x}(x)$ must be given by the d coupling alone: Let us assume for the moment that the d coupling for AH_x is proportional to the valency parameter γ defined above:

$$\Delta E_d^{AH_x} = \gamma(x)\Delta E_d^A \tag{3}$$

Using Eq. (1), this will lead to the kind of relationship in Fig. 1. We can write the adsorption energy of molecule AH_x in terms of the adsorption energy of molecule A as

$$\Delta E^{AH_x} = \Delta E_d^{AH_x} + \Delta E_{sp}^{AH_x} = \gamma(x)\Delta E_d^A + \Delta E_{sp}^{AH_x} = \gamma(x)\Delta E^A + \xi, \quad (4)$$

where $\xi = \Delta E_{sp}^{AH_x} - \gamma(x)\Delta E_{sp}^A$ is independent of the metal in question. The parameter γ can be read off Fig. 1 for each AH_x/A combination; see Eq. (1). The parameter ξ can be obtained from calculations on any transition metal. In the following all model data presented are obtained using Pt(111) as the reference system.

The basic question remains, why the coupling to the d states should scale with the valency of the adsorbate as in Eq. (1). We cannot provide a general rigorous proof of the scaling, Eq. (1), and most likely no such proof exists—the scatter in Fig. 1 indicates that the linear relationship is only approximate. What we will do, however, is show that Eq. (1) should hold approximately for the kind of systems investigated in Fig. 1.

The coupling of the adsorbate states to the d band has two contributions [15,16,21], $\Delta E = \Delta E_d^{\text{hyb}} + \Delta E_d^{\text{orth}}$. The first term describes the energy change associated with the formation of bonding and antibonding states. Since the d coupling can often be described in second order perturbation theory [8,15,21], we can write $\Delta E_d^{\text{hyb}} \propto \Delta E_d^{\text{orth}} \propto V_{ad}^2$, where V_{ad} is the Hamiltonian matrix element between the adsorbate and the metal d states [21]. If there is more than one adsorbate state, the total interaction energy will scale with the sum of contributions from the adsorbate states, $V_{ad}^2 = \sum_i V_{a_i d}^2$. We suggest that $V_{ad}^2 \propto \gamma$ for the kind of systems considered in Fig. 1, and this directly gives the relation of Eq. (1). The reason is given in the following.

The coupling strength $V_{ad}^2(\{r_{a-i}\})$ is a function of the number of metal neighbors and their distances to the adsorbate. Since the d coupling is usually a minor perturbation to the bond energy, it is the sp coupling which primarily determines the adsorption bond lengths, r_{a-i}. As H atoms are added to the central C, N, O, or S atom, the adsorption bond lengths increase and the coupling strength decreases. The effective medium theory (EMT) [22] provides a simple way of quantifying this effect. In the EMT the bonding of an atom A to other atoms in the vicinity is approximated by the interaction of A with a homogeneous electron gas (the effective medium) of a density given by a spherical average n of the density provided by the surrounding atoms: $\Delta E = \Delta E_{\text{hom}}(n)$.

Such a local density approximation for the interaction energy gives a good description of general trends in bonding, including bond lengths of atoms in metals, adsorbates on metal surfaces, and of molecules [22–24]. The energy of embedding an atom in a homogeneous electron gas, $\Delta E_{\text{hom}}(n)$, generally has a minimum for a particular electron density, n_0, and the equilibrium geometry of atom A is given by the position where A experiences the optimum electron density, $n = n_0$.

Consider for instance a C atom outside a metal surface. The adsorption bond length is given by the distance outside the surface where the electron density from the surface around the C atom is $n_{\text{surf}} = n_0$. Now add H atoms to the C atom. Each H atom will provide electron density to the C atom, and the electron density needed from the surface to reach $n = n_0$ is smaller. For a fixed adsorption site (one-, two-, or threefold), the bond length between the surface atoms and the C atom must therefore increase. Alternatively, the adsorption site can change as in the case of CH, CH_2, and CH_3 discussed above. In that case we would then expect the C-metal bond length to be independent of x, since the change in metal coordination number corresponds exactly to the increase in the H coordination number for this sequence of systems. This is precisely what we find in the calculations. Returning to the general case, the electron density from the surface n_{surf} needed to obtain $n = n_0$ will continue to decrease as the number x of H atoms increases. When $x = 4$ the H atoms must contribute all the electron density needed for the central C atom, $4n_{\text{H}} = n_0$, since a methane molecule does not bind to the surface at all (neglecting van der Waals interactions). The density contribution from the surface at the equilibrium site for CH_x is therefore

$$n_{\text{surf}} = \frac{(x_{\text{max}} - x)}{x_{\text{max}}} n_0 = \gamma(x) n_0. \quad (5)$$

The linear dependence on x in Eq. (5) is based on the reasonable assumption that the contribution to the electron density is the same for all x H atoms, and that the total density should add up to n_0 [25]. The electron density n can be viewed as a generalized bond order [26,27], and the requirement that $n = n_0$ is then an example of bond order conservation.

Since we are using EMT to model the sp contribution to the bonding, n_{surf} denotes the sp electron density outside the surface. The decay length of n_{surf} outside the surface is given asymptotically by the work function (the energy of the Fermi level relative to vacuum). Since the d states have energies close to the Fermi level as well, their decay length is roughly the same. That means that to a first approximation V_{ad}^2 scales with n_{surf}. We have therefore shown that the following relations hold approximately,

$$\Delta E_d(x) \propto V_{ad}^2(x) \propto n_{\text{surf}}(x) \propto \frac{x_{\text{max}} - x}{x_{\text{max}}} = \gamma(x), \quad (6)$$

which implies Eq. (1).

Given the understanding provided above, we can try to generalize the findings in Fig. 1. For any hydrogenation or dehydrogenation reaction of molecules bonding to a transition-metal surface via C, N, O, or S atoms, we should be able to estimate the reaction energy for all transition metals given the reaction energy for just one metal. For each atom A_i $i = 1, \ldots, N$ bonding to the surface, we determine the change $\Delta\gamma_i$ in the valence parameter during the reaction, and we can then estimate variation in the bond energy for the full system from the variations in the bond energies of the A_i:

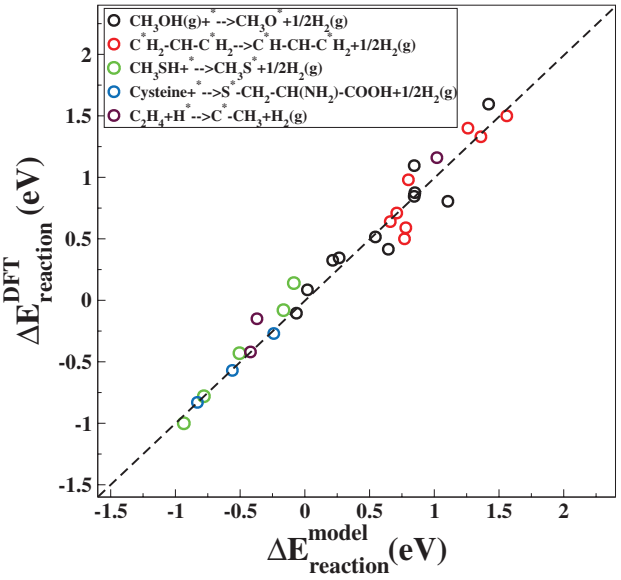

FIG. 3 (color). Calculated reaction energies for a series of dehydrogenation reactions plotted against the model predictions. The model data have been generated using calculated Pt(111) data as reference.

$$\Delta E = \sum_{i=1}^{N} (\Delta\gamma_i \Delta E^{A_i} + \Delta\xi_i) = \sum_{i=1}^{N} (\Delta\gamma_i \Delta E^{A_i}) + \Delta\xi. \quad (7)$$

The change in the ξ parameter for the particular reaction needs to be calculated once and for all by calculating the reaction energy for one single metal. In Fig. 3, we compare the model to complete DFT calculations for hydrogenation or dehydrogenation of a series of hydrocarbons, alcohols, thiols, and amino acids. In each case, we have calculated $\Delta\xi$ from Pt(111) data. The agreement between the model and the full DFT calculations indicates that the model has the power to describe both the absolute magnitude and the trends in reaction energies for hydrogenation or dehydrogenation reactions of a number of organic molecules on transition-metal surfaces. We note that the scaling relations can easily be generalized so that the adsorption energy of any hydrogenated species AH_y is used as the reference instead of A.

By combining the present model with the Brønsted-Evans-Polanyi–type correlations that have been established between activation barriers and reaction energies for surface reactions [8,10,11], it will be possible to estimate the full potential energy diagram for a surface catalyzed reaction for any transition metal on the basis of the C, N, O, and S chemisorption energies and a calculation for a single metal. We suggest that this will be a useful tool in screening for new catalysts. Such estimates can subsequently be followed up by full DFT calculations and experiments for the most interesting systems.

The Center for Atomic-scale Materials Design is sponsored by the Lundbeck Foundation. Additional support from the Danish Research Councils and the Danish Center for Scientific Computing are also acknowledged.

[1] Z. Ma and F. Zaera, Surf. Sci. Rep. **61**, 229 (2006).
[2] C. Joachim and M. Ratner, Proc. Natl. Acad. Sci. U.S.A. **102**, 8801 (2005).
[3] B. Kasemo, Surf. Sci. **500**, 656 (2002).
[4] G. Somorjai, *Introduction to Surface Chemistry and Catalysis* (Wiley, New York, 1994).
[5] W. A. Brown, R. Kose, and D. A. King, Chem. Rev. **98**, 797 (1998).
[6] H. Gross, C. Campbell, and D. A. King, Surf. Sci. **572**, 179 (2004).
[7] J. K. Nørskov, M. Scheffler, and H. Toulhoat, MRS Bull. **31**, 669 (2006).
[8] B. Hammer and J. K. Nørskov, Adv. Catal. **45**, 71 (2000).
[9] J. Greeley and M. Mavrikakis, J. Phys. Chem. B **109**, 3460 (2005).
[10] V. Pallassana and M. Neurock, J. Catal. **191**, 301 (2000).
[11] A. Michaelides *et al.*, J. Am. Chem. Soc. **125**, 3704 (2003).
[12] B. Hammer, L. Hansen, and J. K. Nørskov, Phys. Rev. B **59**, 7413 (1999).
[13] T. Bligaard *et al.*, J. Catal. **224**, 206 (2004).
[14] G. Papoian, J. K. Nørskov, and R. Hoffmann, J. Am. Chem. Soc. **122**, 4129 (2000).
[15] B. Hammer and J. K. Nørskov, Surf. Sci. **343**, 211 (1995).
[16] B. Hammer and J. K. Nørskov, Nature (London) **376**, 238 (1995).
[17] A. Eichler, F. Mittendorfer, and J. Hafner, Phys. Rev. B **62**, 4744 (2000).
[18] J. Greeley and M. Mavrikakis, Nat. Mater. **3**, 810 (2004).
[19] A. Roudgar and A. Gross, Phys. Rev. B **67**, 033409 (2003).
[20] O. K. Andersen, O. Jepsen, and D. Glötzel, *Highlights of Condensed Matter Theory* (North-Holland, New York, 1985).
[21] B. Hammer and J. K. Nørskov, *Theory of Adsorption and Surface Reactions* (Kluwer, Dordrecht, 1997).
[22] J. K. Nørskov and N. D. Lang, Phys. Rev. B **21**, 2131 (1980).
[23] M. Stott and E. Zaremba, Phys. Rev. B **22**, 1564 (1980).
[24] M. Puska, R. Nieminen, and M. Manninen, Phys. Rev. B **24**, 3037 (1981).
[25] NH_3, H_2O, and H_2S do bind weakly to the surface. This bonding by lone pairs cannot be described in the simplest EMT model. The bond lengths to the surface of the fully hydrogenated species are, however, significantly larger than for any of the less hydrogenated species, and the density contribution from the surface is small. This is therefore a small correction to the scaling picture developed here.
[26] E. Shustorovich, Surf. Sci. **176**, L863 (1986).
[27] A. T. Bell and E. Shustorovich, J. Catal. **121**, 1 (1990).

Paper 5

Available online at www.sciencedirect.com
ScienceDirect
Journal of Catalysis 249 (2007) 220–233
JOURNAL OF CATALYSIS
www.elsevier.com/locate/jcat

Location and coordination of promoter atoms in Co- and Ni-promoted MoS_2-based hydrotreating catalysts

Jeppe V. Lauritsen [a,*], Jakob Kibsgaard [a], Georg H. Olesen [a], Poul G. Moses [b], Berit Hinnemann [b,c], Stig Helveg [c], Jens K. Nørskov [b], Bjerne S. Clausen [c], Henrik Topsøe [c], Erik Lægsgaard [a], Flemming Besenbacher [a,*]

[a] *Department of Physics and Astronomy, Interdisciplinary Nanoscience Center (iNANO), University of Aarhus, DK-8000 Aarhus C, Denmark*
[b] *Department of Physics and Center for Atomic-Scale Materials Design (CAMD), NanoDTU, Technical University of Denmark, DK-2800 Lyngby, Denmark*
[c] *Haldor Topsøe A/S, Nymøllevej 55, DK-2800 Lyngby, Denmark*

Received 1 December 2006; revised 16 April 2007; accepted 17 April 2007

Available online 8 June 2007

Abstract

In this study, we used scanning tunneling microscopy (STM) and density functional theory (DFT) to investigate the atomic-scale structure of the active Co- or Ni-promoted MoS_2 nanoclusters in hydrotreating catalysts. Co-promoted MoS_2 nanoclusters (Co–Mo–S) are found to adopt a hexagonal shape, with Co atoms preferentially located at $(\bar{1}010)$ edges with a 50% sulfur coverage. The first atom-resolved STM images of the Ni-promoted MoS_2 nanoclusters (Ni–Mo–S) reveal that the addition of Ni also leads to truncated morphologies, but the degree of truncation and the Ni sites are observed to depend on the nanocluster size. Larger clusters (type A) are structurally similar to Co–Mo–S exposing fully Ni-substituted $(\bar{1}010)$ edges with a 50% S coverage. Smaller clusters (type B) show dodecagonal shapes terminated by three different edges, all of which contain Ni-promoter atoms fully or partially substituting the Mo atoms. The findings may shed more light on the different selectivities observed for the Co- and Ni-promoted hydrotreating catalysts.

Keywords: Hydrotreating; Hydrodesulfurization; Hydrodenitrogenation; HDS; Model catalyst; Scanning tunneling microscopy; STM; Molybdenum disulfide; MoS_2 nanoclusters; Morphology; Promoters; Ni–Mo–S; Co–Mo–S

1. Introduction

The catalytic removal of sulfur and nitrogen impurities from oil compounds by hydrotreating is a key process in modern industrial oil refining that is currently receiving considerable attention due to the increasing demand for clean fuels. To meet present and future requirements for fuels with low impurity levels, more active and selective catalysts are being requested by oil refineries [1–4]. Consequently, intense research efforts are being directed toward improving the MoS_2-based hydrotreating catalyst that have been widely applied in this area for more than half a century [5–7].

The commercial hydrotreating catalysts consist of promoted MoS_2 or WS_2 particles distributed on a high-surface area support, such as alumina. It is well established that the MoS_2 crystallites in typical high-activity catalysts are present as single-layer S–Mo–S slabs with an average size of 2–3 nm under operating conditions [5]. Furthermore, it is well established that Co or Ni added to the MoS_2 increases the reactivity of the catalysts, and because only a small fraction of Co or Ni relative to Mo is needed, they are considered *promoters* rather than catalysts in their own right. For both promoters, the overall hydrotreating activity generally increases by more than an order of magnitude, and the specific selectivities of the sulfided CoMo or NiMo catalysts change with respect to hydrodesulfurization (HDS), hydrodenitrogenation (HDN), and hydrogenation

* Corresponding authors.
E-mail addresses: jvang@inano.dk (J.V. Lauritsen), fbe@inano.dk (F. Besenbacher).

0021-9517/$ – see front matter
doi:10.1016/j.jcat.2007.04.013

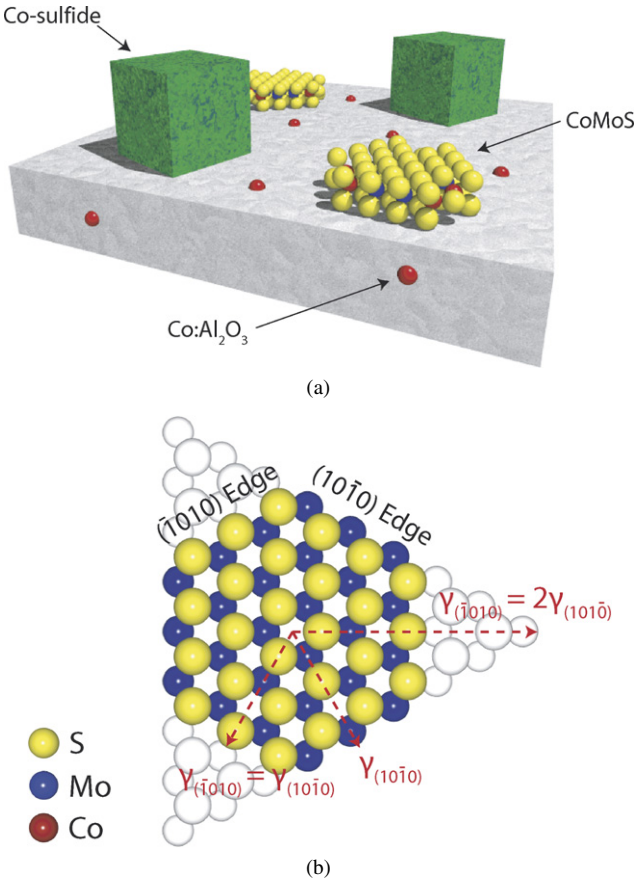

Fig. 1. (a) Illustration of the phases in a sulfided Co–Mo catalyst. (b) Ball model of a bulk-truncated, hypothetical hexagonal MoS_2 nanocluster exposing the (0001) basal plane.

(HYD). Thus, the effect of the two promoters may be quite different [5,8].

Many studies have been carried out to correlate the structure of the active promoted phases in catalysts to the reactivity [5, 9–17], and general consensus has been reached in the literature on the so-called "Co–Mo–S" model [5]. This model originates from the finding that Co atoms may be located at the edge positions of MoS_2 nanostructures [18,19], and the observations that the Co–Mo–S structures are responsible for the promotion of the reactivity [19,20]. Co is present in three different phases in the catalyst (Fig. 1a). The catalytically most interesting Co–Mo–S phase has an MoS_2-like texture, into which Co atoms are incorporated. Co–Mo–S is non-stoichiometric with respect to the Co/Mo ratio, and no unit cell can be defined in the crystallographic sense. For unpromoted MoS_2, it has long been known that only the edges, not the basal plane sites, are active [5,21,22], and thus it has been proposed that the Co atoms located at edge positions create new and more active sites by, for example, providing active sites in the form of sulfur vacancies at or next to the Co sites [18,19,23,24]. But the exact origin of the promoting role of Co remains a matter of intense debate, since most analysis tools provide only indirect evidence of the location of Co in Co–Mo–S structures [12,25–28]. Fewer structural studies have been performed for the Ni-promoted system [29–31]. It is generally believed that a Ni–Mo–S phase exists with a structure similar to Co–Mo–S, but no direct experimental information is available on the location of the Ni promoters on Ni–Mo–S. Theoretical studies based on slab models [32–37] or calculations of cluster structures [38] have been used to investigate the affinities for Co or Ni to replace Mo at the MoS_2 edges, and such studies have also provided information on the sulfur coverage at the edges under experimental and reaction conditions.

Recently, we used high-resolution scanning tunneling microscopy (STM) to investigate the atomic-scale structure of MoS_2 and Co–Mo–S nanoclusters on a gold [39–42] or a graphite model substrate [43]. The main advantage of using STM to study model catalysts is that it provides real-space, atom-resolved microscopy images of the individual nanoclusters, making it possible to resolve some of the above-mentioned important questions related to the detailed structure and morphology of the Co–Mo–S and Ni–Mo–S nanoclusters. In particular, the present study has provided the first experimental microscopy images of single Ni promoter atoms in Ni–Mo–S, along with theoretical support for previous STM studies of Co–Mo–S clusters [39]. Interestingly, we observed significant differences in the morphology and atomic-scale structure of Ni–Mo–S compared with Co–Mo–S; such insights may provide the basis for a better understanding of the differences in activity and selectivity in the two promoted systems. This insight may also shed more light on the observation that direct desulfurization (DDS) and HYD routes in HDS are not always inhibited in the same way in Ni–Mo–S as in MoS_2 or Co–Mo–S in the presence of nitrogen-containing compounds [7, 44,45]. This is explained in terms of competitive adsorption on the sites responsible for sulfur extrusion or HYD. We have previously shown that metallic brim states at the edges of unpromoted MoS_2 nanoclusters are active as HYD sites [42,46], whereas sulfur vacancies formed at the edges are active in direct sulfur extrusion. Interestingly, we observed in this study several metallic edge states in the promoted clusters as well, and, given the potential importance of these in HYD reactions, we have provided a thorough electronic structure characterization of these metallic edge states in both Co–Mo–S and Ni–Mo–S.

2. Methods

2.1. Experimental details

The experiments were performed in an ultra-high vacuum (UHV) chamber equipped with standard surface analysis equipment and equipment for depositing refractory metals by *e*-beam evaporation and for introducing high-purity gases to the chamber. The homebuilt Aarhus scanning tunneling microscope [47] was used for the experiments.

As demonstrated in previous studies for the unpromoted MoS_2 model catalysts [40–42] and the first studies of Co–Mo–S [39], a single crystal Au(111) surface can be used as a suitable model substrate to synthesize highly dispersed ensembles of Co–Mo–S or Ni–Mo–S nanoclusters. Recently, the same surface was used to synthesize other supported sulfide nanostructures [48,49]. STM studies have shown that a graphite

(HOPG) substrate also can be used [43] for the synthesis of MoS_2 nanoparticles and the edge structure of the supported MoS_2 nanoclusters was observed to be identical to MoS_2 supported on gold. But in these studies, the Au(111) substrate was preferred, because it exposes the characteristic herringbone reconstruction [50], providing a regular array of nucleation sites for metal atoms and thereby facilitating a high dispersion of submonolayer amounts of Mo, Ni, or Co into nanoclusters [40,51–53]. The Au(111) single crystal surface was prepared by cycles of Ar^+ sputtering, followed by annealing at 900 K for 10 min. This procedure generated a clean and regular Au(111) surface, as judged by Auger electron spectroscopy (AES) and STM. For the synthesis of Co–Mo–S and Ni–Mo–S nanoclusters, the pure metals were evaporated onto the substrate using an *e*-beam evaporator (Oxford Applied Research, EGCO-4).

Using the approach described in Ref. [39] as the starting point, we investigated a number of synthesis procedures for formation of the mixed phases of both the Ni- and Co-promoted MoS_2 nanoclusters. Using the procedure to form unpromoted MoS_2 nanoclusters as described in Refs. [40,54] and subsequently deposit Co or Ni in a sulfiding atmosphere of 10^{-6} mbar of H_2S, we found that this approach did not lead to the spontaneous formation of bimetallic sulfided structures. Instead, well-separated MoS_2 nanoclusters and cobalt-sulfide or nickel-sulfide patches could be identified in atom-resolved STM images. The bimetallic Co–Mo–S and Ni–Mo–S nanoclusters could be formed when Mo was simultaneously deposited together with Co or Ni, respectively, in the sulfiding atmosphere of 10^{-6} mbar of H_2S. This step was followed by postannealing at temperatures of 673 K while maintaining the sulfiding atmosphere to further crystallize the nanoclusters. The most efficient method involved deposition of Mo onto the Au(111) surface in a sulfiding atmosphere to form sulfided Mo embryos, followed by co-deposition of additional Mo together with Ni or Co to form a capped layer of bimetallic sulfide. The total coverages in all experiments were calibrated before the S exposure and were estimated to be 10 ± 1% of a monolayer (ML) for Mo and 4 ± 1% ML for Ni and Co.

2.2. Computational details

The theoretical calculations were based on DFT using the generalized gradient approximation for the exchange-correlation part of the total energy functional. The edges of single-layer MoS_2 particles were investigated using a model consisting of semi-infinite slabs of MoS_2 repeated in a supercell geometry, as reported in [32,54,55]. The stripes used for the calculations in this work were composed of repeat units containing one or two MoS_2 units. Each supercell exposed the $(\bar{1}010)$ edge at one edge and the $(10\bar{1}0)$ edge at the other. The edges were separated by six unit cells of MoS_2. Promoted structures were obtained by replacing Mo with Co or Ni at the relevant edge positions. In the case of Co, all Mo atoms at the $(\bar{1}010)$ edge were replaced by Co, which is known to be the most energetically favorable location of Co [34,38,56]. In the case of Ni, locations at both edges were considered and either 50 or 100% of the Mo atoms at the edge were replaced by Ni. Hydrogen adsorption was also investigated, but based on the adsorption energies found, the concentration of adsorbed hydrogen was estimated to be negligible under experimental conditions for all Co–Mo–S and Ni–Mo–S edges investigated. The plane wave DFT code DACAPO [57,58] was used for all calculations. The Brillouin zone was sampled by Monkhorst–Pack sampling [59] using 12 k-points in the x-direction and 1 k-points in the y- and z-directions for the 1 × 6 stripe and 6 k-points in the x-direction and 1 k-points in the y- and z-directions for the 2 × 6 unit-cell. A plane wave cutoff of 30 Rydberg and a density cutoff of 60 Rydberg were used for the Co–Mo–S calculations, and a plane wave cutoff of 25 Rydberg and a density cutoff of 50 Rydberg were used for the Ni–Mo–S calculations. This double-grid technique [60] ensured sufficient accuracy of energies and forces. Ultrasoft pseudopotentials were used for all species except sulfur, for which a soft pseudopotential was used when investigating Co–Mo–S [61,62]. Ultrasoft pseudopotentials were used for all species when investigating Ni–Mo–S, allowing for the lower plane wave cutoff. Fermi smearing with an electronic temperature of $k_BT = 0.1$ eV/Å was used for all calculations. The PW91 functional [63] was used as an exchange-correlation functional. Co and Ni are both magnetic materials; thus, all calculations were performed spin-polarized. All structures were relaxed until the remaining total force was below 0.1 eV/Å. We carefully checked that our results were well converged with these parameters.

Relative edge free energies for the promoted edges (γ) were used to evaluate the edge stability at experimental conditions and were calculated using the DFT energies and the thermodynamic model introduced by [38,54,64,65] by considering the chemical potentials of sulfur (μ_S) and hydrogen (μ_H) [41,54]. As described in detail in Refs. [41,54], it was necessary to consider chemical potential parameters for both synthesis conditions (sulfiding: $\mu_S = -0.39$ eV, $\mu_H = -1.08$ eV) and vacuum conditions (imaging: $\mu_S = -0.29$ eV, $\mu_H = -0.49$ eV) due to the quench-and-look approach in the experiments. For the STM analysis in this paper, simulated STM images were calculated using the Tersoff–Hamann model [66]. The STM simulations were performed as reported in [54] by matching the corrugation on the MoS_2 basal plane to the experimentally measured value of 0.2 Å and then plotting calculated contours of constant local density of the electron states. For some simulations, the effect of the Au substrate also was included, but generally this did not change the qualitative appearance of the edges [55].

3. Results and discussion

The synthesis procedure for the promoted hydrotreating model catalyst produces two significantly different types of surface structures: (i) cobalt- or nickel-sulfide islands at the Au(111) step edges, and (ii) well-dispersed Co–Mo–S or Ni–Mo–S nanoclusters on the terraces of the Au(111) substrate. The growth of cobalt or nickel-sulfide islands at the substrate step edges (Figs. 2a and 2b) arises due to the excess amounts of Ni or Co added relative to the available number of substitutional sites on the MoS_2 nanoclusters. The tendency to form

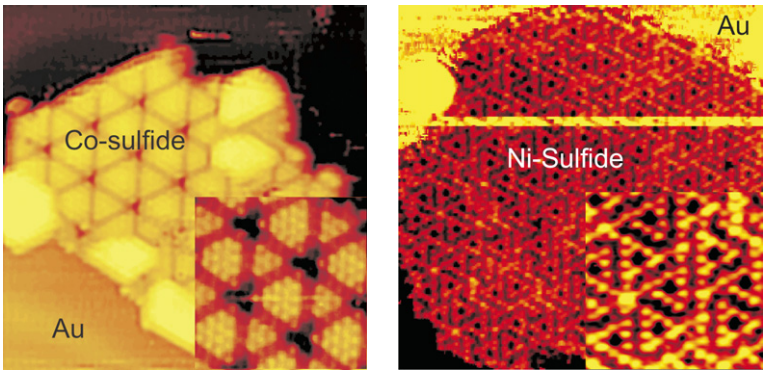

(a) (b)

Fig. 2. (a) Cobalt sulfide formed on Au(111). The insert shows the proposed $Co_3S_4(111)$ facet. Adapted from [39]. (b) Nickel sulfides formed at the step edges of the Au(111) surface. The insert shows the proposed $Ni_3S_2(111)$ facet.

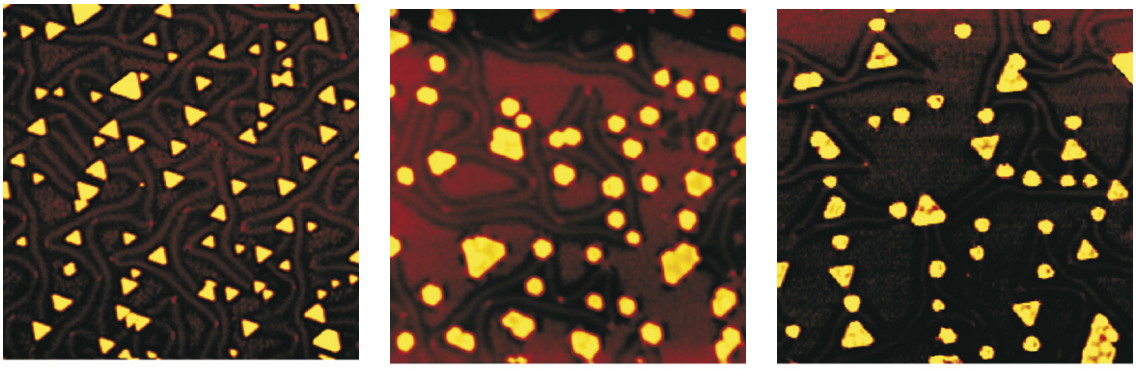

(a) (b) (c)

Fig. 3. (a) Morphology of unpromoted, Co-promoted and Ni-promoted nanoclusters. (a) MoS_2 on Au(111) (700 × 700 $Å^2$). (b) Co–Mo–S on Au(111) and 700 × 700 $Å^2$. (c) Ni–Mo–S on Au(111) 700 × 700 $Å^2$.

these sulfides at the step edges is initiated by a high mobility of Co and Ni on the Au(111) surface in the presence of H_2S. The structures observed with STM match the (111) facets of Co_3S_4 and Ni_3S_2, respectively, but considering the fact that such sulfides do not have an appreciable HDS reactivity [5], the following discussion concentrates on the much more interesting crystalline Co–Mo–S and Ni–Mo–S nanoclusters nucleated on the Au(111) terraces.

The main indicator for the formation of promoted Co–Mo–S and Ni–Mo–S phases is a pronounced change in the equilibrium morphology relative to that of unpromoted MoS_2 nanoclusters. The large-scale STM images in Fig. 3 clearly illustrate this change in morphology. The unpromoted MoS_2 nanoclusters (Fig. 3a) are mainly triangular while the Co–Mo–S (Fig. 3b) and Ni–Mo–S (Fig. 3c) exhibit truncated morphologies. The unpromoted triangular MoS_2 nanoclusters shown in Fig. 3a have previously been characterized in detail [40–42,67], and they are characterized as single-layer MoS_2 nanoclusters oriented with the $MoS_2(0001)$ facet in parallel to the substrate. The changes observed in the morphology of the promoted clusters relative to the triangular MoS_2 nanoclusters formed under the same conditions were invoked only by the presence of promoter atoms (with all other synthesis parameters the same); thus, the observed shift in morphology can be attributed directly to the incorporation of promoters into the MoS_2 structure, that is, the formation of Ni–Mo–S or Co–Mo–S structures.

Atomically resolved STM images of Co–Mo–S and Ni–Mo–S nanoclusters also revealed a flat and perfectly crystalline basal plane consisting of hexagonally arranged protrusions with an interatomic spacing of 3.16 Å (Figs. 4a and 7a). The height profile of the clusters corresponded to the values found for the single-layer MoS_2 nanoclusters in previous studies [40]; thus, the addition of the promoters left the internal structure of the cluster unchanged as MoS_2. Therefore, the truncated morphology of the promoted clusters may be explained by a perturbation of the edge free energy of the two low-index edge terminations of MoS_2 driven by the affinity of Co or Ni to replace Mo at the edges.

3.1. Co–Mo–S morphology

The near-hexagonal shape observed for Co–Mo–S implies that two types of low-indexed edge terminations are exposed in the clusters (see Fig. 4a). The exact shape is according to the Wulff-theorem determined by the competition between two low-index MoS_2 edges, referred to as the $(\bar{1}010)$ edge (S edge) and $(10\bar{1}0)$ edge (Mo edge), as illustrated in Fig. 1b for a hypothetical, single-layer MoS_2 nanocluster [5,40,64,68]. The triangular shape observed previously for unpromoted MoS_2

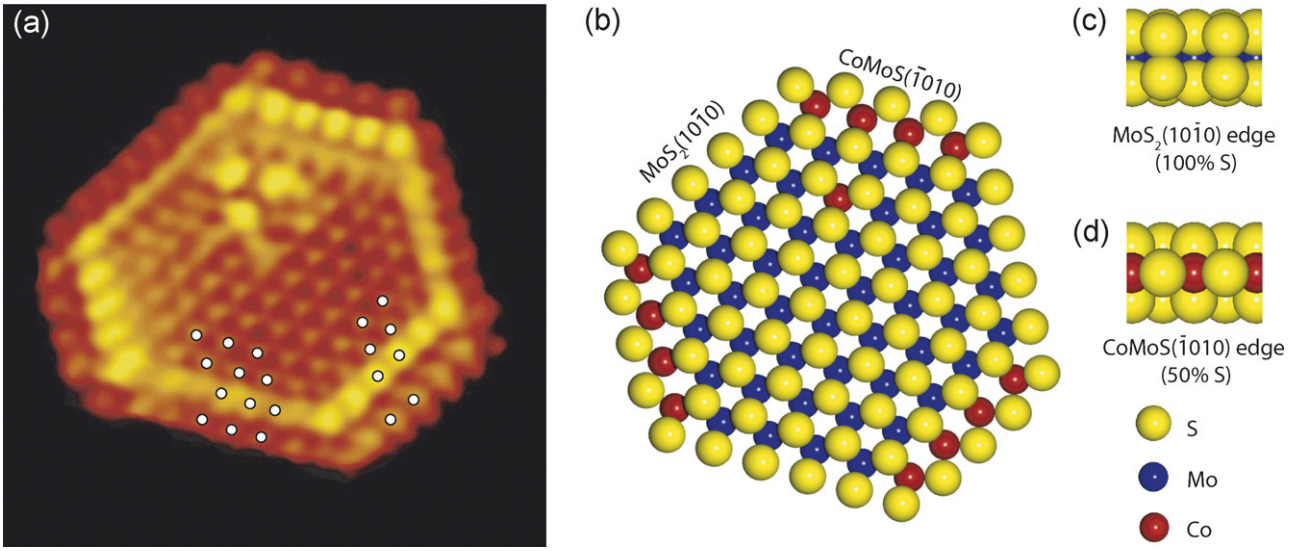

Fig. 4. (a) Atom-resolved STM image of Co–Mo–S (51 × 52 Å^2, V_t = 95.2 mV, I_t = 0.81 nA). (b) Ball model of the Co–Mo–S. (c) Side view of the $MoS_2(10\bar{1}0)$ edge. (d) Side view of Co-substituted Co–Mo–S($\bar{1}010$) edge. S: yellow, Mo: blue, Co: red.

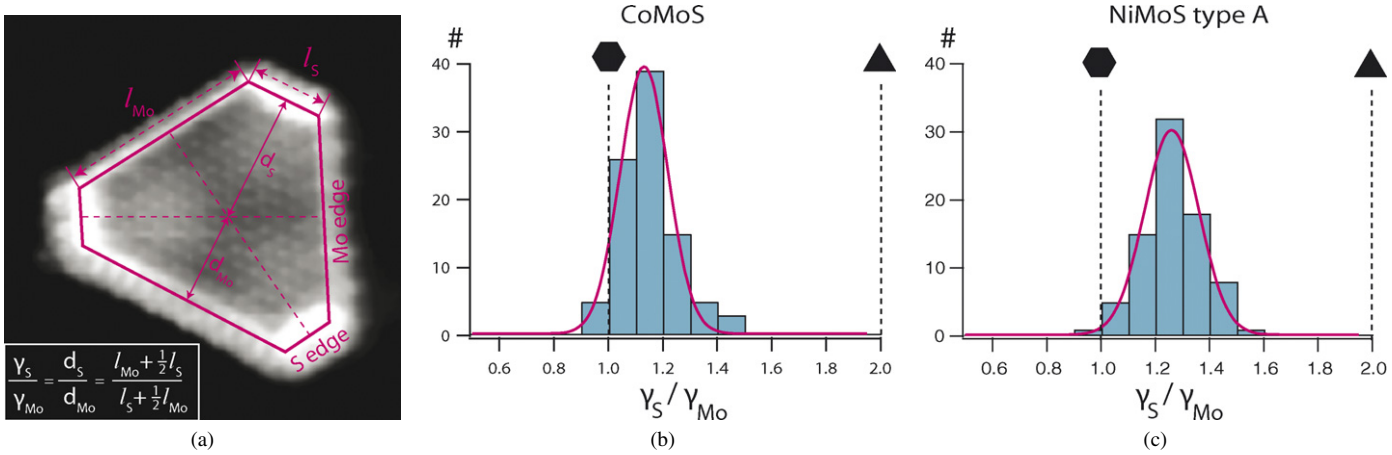

Fig. 5. (a) Ratio of edge free energies ($\gamma_{(\bar{1}010)}/\gamma_{(10\bar{1}0)}$) is connected to the cluster shape. (b) Histogram of relative edge free energies for Co–Mo–S particles, and (c) for Ni–Mo–S.

(Fig. 3a) reflected that the ratio of the edge free energies of these edges was greater than a factor of two ($\gamma_{(\bar{1}010)} > 2\gamma_{(10\bar{1}0)}$); that is, only ($10\bar{1}0$) edges (Mo edges) we exposed. The situation is clearly changed for Co–Mo–S and as was shown in Ref. [39], it is possible in atom-resolved STM images to identify both the ($\bar{1}010$) edge and ($10\bar{1}0$) edge in the Co–Mo–S particles. In the present study, measuring the distribution of both edges for a large number of clusters provides an estimate of the ratio between the edge free energies in Co–Mo–S $\gamma_{(\bar{1}010)}/\gamma_{(10\bar{1}0)}$ to be 1.1 ± 0.2; that is, the ($10\bar{1}0$) edge is only slightly more stable in Co–Mo–S (see Figs. 5a and 5b).

3.2. Co–Mo–S edge structure

On the basis of the detailed atomic-scale information provided by the STM images (Fig. 4), a structural model of the Co–Mo–S nanoclusters was proposed in Ref. [39] in which the Co–Mo–S clusters are terminated by ($10\bar{1}0$) edges with no Mo atoms substituted by Co and ($\bar{1}010$) edges in which all Mo atoms are substituted by Co atoms. The unpromoted ($10\bar{1}0$) edge type in Co–Mo–S, shown in Fig. 4a, is characterized by a row of edge protrusions located with the regular 3.16 Å interatomic distance of MoS_2, but with the edge protrusions clearly located *out* of registry with the lattice of S atoms belonging to the basal plane. This edge also is identified by the presence of a bright brim (0.4 ± 0.1 Å) located adjacent to the outermost edge protrusions. This appearance is in exact qualitative and quantitative agreement with the ($10\bar{1}0$) edge structure observed for unpromoted MoS_2 triangles [40,41,55].

The morphological change observed with STM for the promoted system is thus induced by the tendency for Co to be located *only* at the Co–Mo–S($\bar{1}010$) edges. As depicted in the ball model in Figs. 4b and 4d, the Co–Mo–S($\bar{1}010$) edges are proposed to have a *tetrahedral* coordination of the Co atoms if the outermost sulfurs are bridge-bonded S monomers. The edge stabilities obtained from DFT calculations in Fig. 6a confirm this configuration, as well as a configuration with 75% sul-

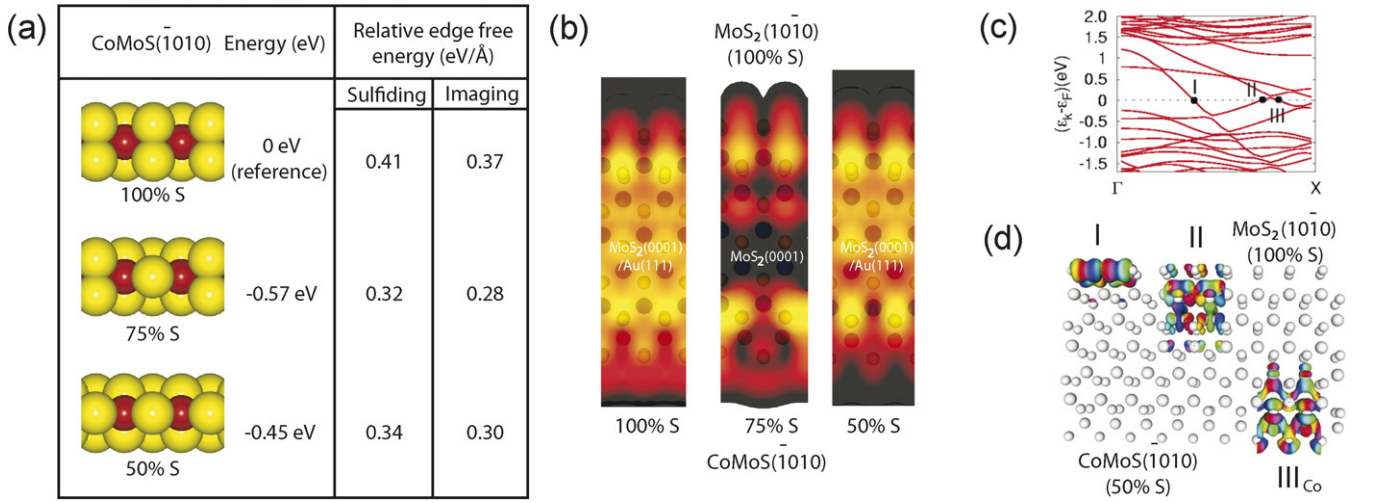

Fig. 6. (a) DFT results for Co–Mo–S($\bar{1}010$) edges (S: yellow, Co: red), (2 × 6 unit cell). (b) STM simulation (1 × 6 unit cell) of the Co–Mo–S($\bar{1}010$) edge with 100, 75, and 50% sulfur. (c) Band structure of the MoS_2 slab exposing the 50% S Co–Mo–S($\bar{1}010$) and $MoS_2(10\bar{1}0)$. (d) Plot of the wavefunction contours associated with the three metallic edge states in Co–Mo–S.

fur as the most stable structures differing by only 0.02 eV/Å in edge free energy. Edge terminations with sulfur coverage <50% are not considered further, because such configurations were found to be very unstable [36,38,56]. The possibility that Co substitutes only a fraction of the Mo atoms at the Co–Mo–S($\bar{1}010$) edges can also be ruled out, because this would not give rise to the observed regular edge pattern in STM images. A detailed comparison of the experimental image with a simulated edge reveals the structure of the observed Co–Mo–S edge. A grid superimposed on the basal plane S atoms near the Co–Mo–S($\bar{1}010$) edges in the experimental image (Fig. 4a) shows edge protrusions located at positions *in* registry with the basal plane S lattice. Compared with the position of the bulk lattice, however, a slight displacement of □0.5 Å perpendicular away from the edge can be seen. The ($\bar{1}010$) edge also exhibits a very bright brim parallel to the edge in the row immediately behind the edge protrusions. The brim structure is significantly brighter than that of the ($10\bar{1}0$) edge, with a height of 0.9 ± 0.2 Å above the basal plane atoms.

Agreement with this appearance in the STM image was obtained only for the simulation of the Co–Mo–S($\bar{1}010$) edge with a 50% S coverage (Fig. 6b). This assignment of the structure of the Co-promoted edge is in good accordance with previous STM simulations by Schweiger et al., who also used a calculation of a cluster structure to directly calculate the relative stability of the two edge types in Co–Mo–S as a function of μ_S [38]. The predicted truncated hexagonal shape was also in agreement with the experiment in Ref. [39].

The STM simulation for the Co–Mo–S($\bar{1}010$) edge shows that protrusions at the edges reflect the position of the monomer S atoms, and that a bright brim is present at the position of the adjacent row of sulfur atoms. These sulfurs are also coordinated to the substituted Co atoms. As in the experimental image, the brim in the simulated image (Fig. 6b) also shows a significant corrugation in cross-sections drawn parallel to the edge. It is important to emphasize that the bright brim in Co–Mo–S does not reflect S atoms located geometrically higher than the basal plane. Our STM simulations and that in Ref. [38] performed without the gold substrate also show that this qualitative appearance is not influenced by the gold substrate. As for the $MoS_2(10\bar{1}0)$ edges [54,55], the brim is related instead to a perturbation of the electronic structure at the edges of the clusters and the existence of metallic, one-dimensional edge states. The edge states in Co–Mo–S are revealed in the electronic band structure of the Co-substituted ($\bar{1}010$) edge in Fig. 6c. The band structure diagram shows three bands (denoted I, II, and III_{Co}) penetrating into the band gap region of MoS_2 and crossing the Fermi level. Edge states I and II pertain to the $MoS_2(10\bar{1}0)$ edge and are the same as those reported previously in [55]. In the plot of the wave-function contours in Fig. 6d, the edge state III_{Co} is located directly at the Co-substituted Co–Mo–S($\bar{1}010$) edge. The edge state is localized on the outermost four rows of atoms counted inward from the edge and is responsible for the very intense bright brim. The resemblance of the brim associated with the metallic edge state III_{Co} pertaining to the promoted edge with that of the unpromoted MoS_2 nanoclusters is very interesting from a catalytic standpoint, because the metallic brim sites on the $MoS_2(10\bar{1}0)$ edges are relatively strong adsorption sites active in HYD and the C–S splitting of thiophene molecules [42,46]. In particular, it is speculated that the close vicinity of the metallic brim sites and edge sites on the Co–Mo–S($\bar{1}010$), which contains intrinsically undercoordinated Co atoms, may provide a favorable environment for reaction.

3.3. Ni–Mo–S morphology

A distinct change of the particle morphology of Ni–Mo–S is also observed relative to that of the unpromoted MoS_2 nanoclusters (Figs. 3a and 3c). However, in contrast to the Co-promoted case, two types of Ni–Mo–S clusters are seen. These clusters are distinguished in terms of the size and shape and may coexist on the same sample. The first type (Fig. 7) is characterized by a truncated triangular shape similar to that of the Co–Mo–S nanoclusters. The second (Fig. 8) shows a more com-

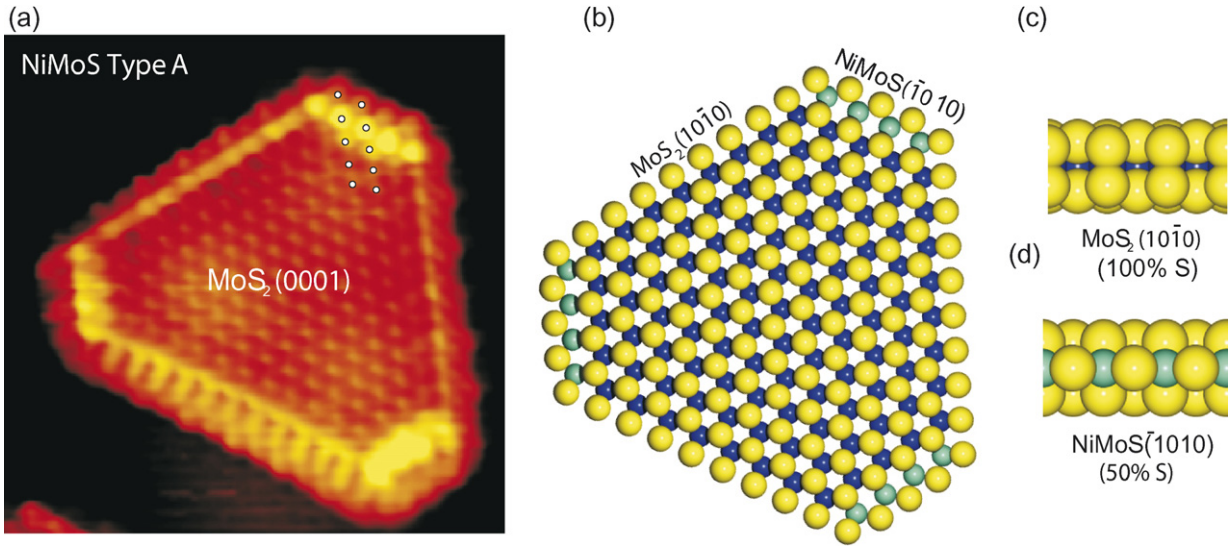

Fig. 7. (a) Atom-resolved STM image of type A Ni–Mo–S (61 × 61 Å^2, V_t = −600 mV, I_t = −0.51 nA). (b) Ball model of type A Ni–Mo–S. (c) Side view of the $MoS_2(10\bar{1}0)$ edge. (d) Side view of the Ni–Mo–S($\bar{1}$010) edge. S: yellow, Mo: blue, Ni: cyan.

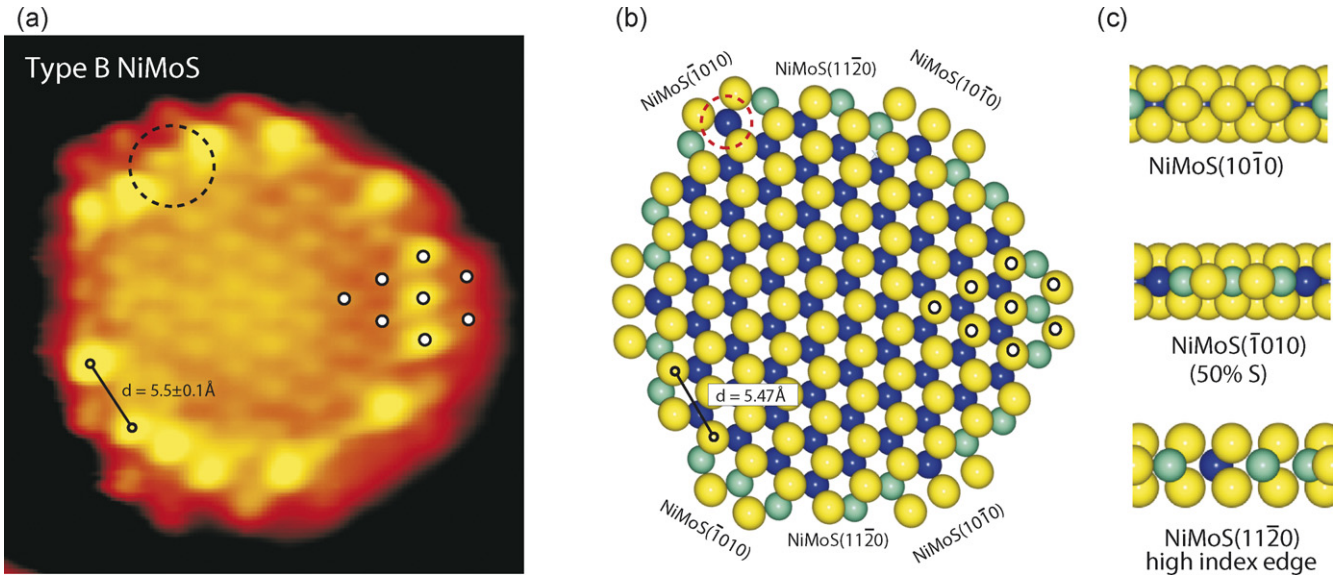

Fig. 8. (a) Atom-resolved STM image of type B Ni–Mo–S (39 × 40 Å^2, V_t = −520 mV, I_t = 0.44 nA). (b) Ball model of type B Ni–Mo–S. (c) Side views of Ni–Mo–S($\bar{1}$010), Ni–Mo–S(10$\bar{1}$0) and Ni–Mo–S(11$\bar{2}$0) edges. S: yellow, Mo: blue, Ni: cyan.

plex morphology that fits a dodecagonal shape. In what follows, the truncated triangular structures are referred to as *type A Ni–Mo–S*, and the dodecagonal-like nanoclusters are termed *type B Ni–Mo–S*.

The distribution of type A and type B Ni–Mo–S nanoclusters is very sensitive to the annealing temperature of the preparation. The particle size distribution shown in Fig. 9 illustrates this effect for three synthesis temperatures in the range 673–773 K. At the normal synthesis temperature of 673 K, the size distribution exhibits a quite typical distribution due to nucleation and growth on a uniform substrate. The average size of the nanoclusters is □800 Å^2, and a small shoulder is found at higher values. As the temperature is increased, the distribution shifts to a clear bimodal distribution, with a peak remaining close to the original size of □800 Å^2 and a much broader peak at higher average size that increases in intensity and shifts to higher values as a function of temperature. The gradual redistribution of the average cluster size is attributed to a higher surface mobility during synthesis at increased temperatures. The correlation between the cluster shape and size indicates that the peak fixed at □800 Å^2 is associated exclusively with the dodecagonally shaped *type B Ni–Mo–S*, whereas the larger clusters exclusively adopt the shape corresponding to the truncated triangular *type A Ni–Mo–S*. After prolonged sulfidation (up to 1 h), the unexpected bimodal distribution remained the same, indicating that the observations are not the result of kinetic limitations during growth. Interestingly, these observations indicate that the equilibrium shape of Ni–Mo–S (i.e. the ratio of edge free energies) depends on the size of the particles. A surprising variation in edge structure and sulfur coverage as a function of nanoclus-

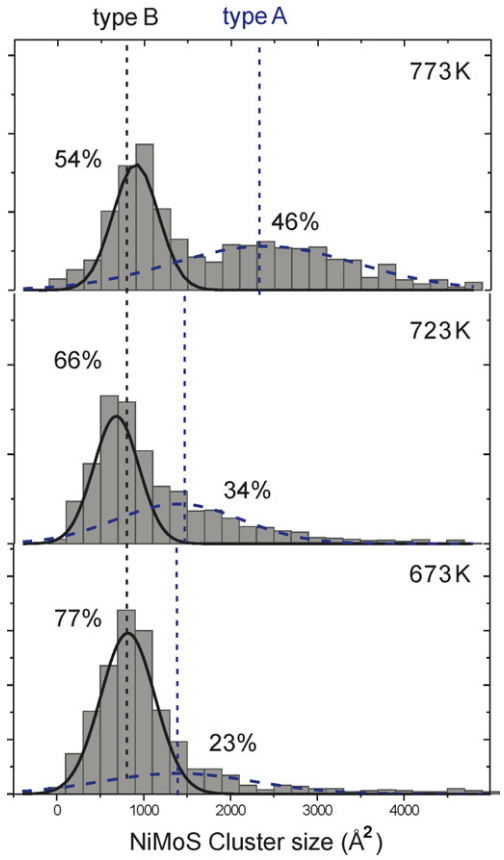

Fig. 9. Particle size distribution for Ni–Mo–S prepared at three temperatures from 673 to 773 K. Bin size is 200 Å^2. For clarity, the distribution is fitted with Gaussians assuming a bimodal distribution.

ter size also was recently observed for the unpromoted MoS_2 triangles formed under similar sulfiding conditions [67].

3.4. Type A Ni–Mo–S edge structure

Fig. 7 shows an atomically resolved STM image of a type A Ni–Mo–S particle. The hexagonal morphology observed with STM directly implies that both low-index edge terminations of MoS_2 are exposed in the nickel promoted clusters, i.e. a $(\bar{1}010)$ edge and a $(10\bar{1}0)$ edge. The longer edges of the Ni–Mo–S nanocluster in Fig. 7 are observed to be identical to the fully sulfided $MoS_2(10\bar{1}0)$ edges (100% S) observed on unpromoted MoS_2 triangles. Thus, for the larger type A Ni–Mo–S, the substitution of Ni promoter atoms appears to be disfavored at the $(10\bar{1}0)$ edges under the conditions of the experiment. As shown in Fig. 5c, the ratio between the edge free energies of the Ni substituted Ni–Mo–S$(\bar{1}010)$ edge and the unsubstituted $(10\bar{1}0)$ edge is found to be $\gamma_{(\bar{1}010)}/\gamma_{(10\bar{1}0)} = 1.3$ for the type A Ni–Mo–S; that is, the relative stability is slightly in favor of the unpromoted $(10\bar{1}0)$ edge.

In Fig. 7, the Ni–Mo–S$(\bar{1}010)$ edges in the Ni–Mo–S nanocluster are again observed to contain a very intense brim in the second row behind the edge. A line scan reveals the height of the brim in Ni–Mo–S to be 0.8 ± 0.1 Å, slightly lower than that of the corresponding Co–Mo–S$(\bar{1}010)$ edges. Furthermore, the edge protrusions themselves are observed to be placed *in* registry with the basal plane atoms, and the outermost protrusions are shifted slightly (□0.8 Å) away from the edge. Edges with alternating Mo and Ni atoms located on the $(\bar{1}010)$ edge have been proposed to be energetically feasible [36], but the present experiments demonstrate no tendency to form edges with a partial Ni-substitution in the type A Ni–Mo–S nanoclusters, which would give rise to patterns in STM linescans with a periodicity larger than the observed single atomic distance. (The situation may be different for type B Ni–Mo–S, as discussed below.) Therefore, we associate the Ni–Mo–S$(\bar{1}010)$ edges in Fig. 7 with a structure in which Ni atoms have completely replaced every Mo atom at the edge positions.

Numerous edge configurations of Ni–Mo–S$(\bar{1}010)$ are possible, and due to the comparatively small differences in energy, we have investigated many of them in detail, simulating the corresponding STM images (Fig. 10b and Supplementary material). The most significantly reduced configurations (0 and 25% sulfur coverage) are found to be energetically unstable and thus not presented here. We also do not see evidence of partially Ni-substituted $(\bar{1}010)$ edges. The three most stable configurations corresponding to 50, 75, and 100% sulfur coverage are shown in Fig. 10a. A fully sulfided Ni–Mo–S$(\bar{1}010)$ edge is the most stable structure in terms of edge free energies, with the 75 and 50% S coverages being about 0.03 eV/Å less stable. Only the simulation of the 50% sulfur coverage is, however, found to match the experimental images of the Ni–Mo–S$(\bar{1}010)$ (Fig. 10b and Supplementary material). This difference may be due to a corner effect that dominates for the rather short cluster edges of an effect of the substrate, which is not accounted for in the DFT calculations. The relative edge free energies for the 50, 75, and 100% S coverage are the same within 0.03 eV/Å, and, given, the short edges (10–20 Å), a small offset in energy due to a corner effect might change the stability. The Ni–Mo–S$(\bar{1}010)$ edge terminations have been investigated by Schweiger et al. [38], who also calculated the equilibrium shape. A similar apparent offset in the energies seems to be present in these studies because the observed 50% S coverage and ratio of edge free energies if Ni–Mo–S type A ($\gamma_{(\bar{1}010)}/\gamma_{(10\bar{1}0)} = 1.3$) is predicted only at a significantly lower chemical potential of sulfur than used in the experiment.

The STM simulation given in Fig. 10b shows the unpromoted $MoS_2(10\bar{1}0)$ edge with dimers (upper part) appearing as in previous studies [40,55]. For the Ni–Mo–S$(\bar{1}010)$ edge, the best match is clearly seen for the 50% S coverage, where the protrusions on the Ni–Mo–S$(\bar{1}010)$ edge (lower part) reflect sulfur monomers, and, as observed in the experiment, a very bright brim is located on the sulfurs in the second row behind the edge. Again, the bright brim of the Ni–Mo–S$(\bar{1}010)$ edge can be related to edge states that render the Ni-substituted edge metallic. In the band structure for this edge configuration (Fig. 10c), four bands are seen to cross the Fermi level. From the plot of the wavefunction contours, edge states I and II are found to belong to the $MoS_2(10\bar{1}0)$ edge, whereas edge states III_{Ni} and IV_{Ni} are located at the Ni-substituted Ni–Mo–S$(\bar{1}010)$ edge. Edge state III_{Ni} is similar to edge state III_{Co} of the Co–Mo–S$(\bar{1}010)$ (Fig. 6d) and is the state giving rise to the bright brim. Nonetheless, it is interesting that the edge state IV_{Ni} has

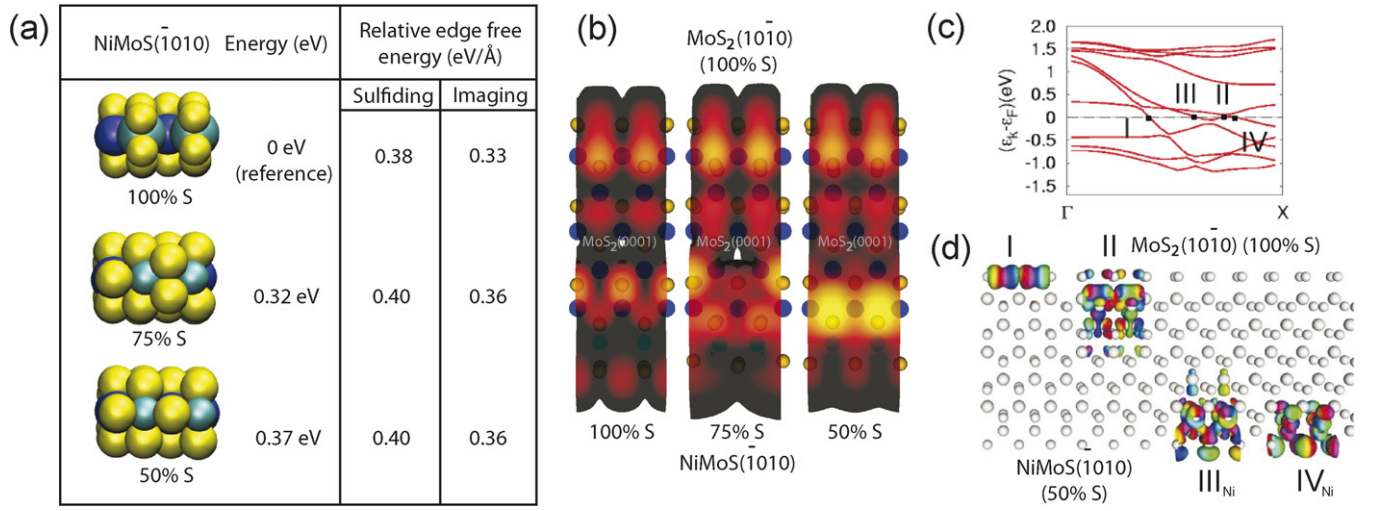

Fig. 10. (a) DFT results for the (100% Ni) Ni–Mo–S($\bar{1}010$) edge (2 × 6 unit cell). (b) STM simulation (1 × 6 unit cell) of the fully Ni-substituted Ni–Mo–S($\bar{1}010$) edge with a 50, 75, and 100% S coverage. (c) Band structure, and (d) plot of wavefunction contours associated with the two metallic edge states in 50% S Ni–Mo–S($\bar{1}010$).

no Co–Mo–S counterpart. This edge state has a p_z-like geometry on the front S atoms. The possibilities that this edge state plays a role in catalysis and that the different activity and selectivity of Ni–Mo–S compared with Co–Mo–S is related to this additional metallic edge state in Ni–Mo–S should be investigated.

In conclusion, it was found that the truncated hexagonal type A Ni–Mo–S clusters are terminated by unpromoted, fully sulfided $MoS_2(10\bar{1}0)$ edges and fully Ni-substituted Ni–Mo–S($\bar{1}010$) edges with 50% coverage of sulfur.

3.5. Type B Ni–Mo–S edge structure

The smaller type B Ni–Mo–S clusters (Fig. 8) are characterized by a markedly different cluster shape than type A Ni–Mo–S (Fig. 7). The shape of type B Ni–Mo–S particles can be described as dodecagonal, that is, particles exposing 12 edges. Thus, the shape of type B Ni–Mo–S particles cannot be described as originating from a simple low-index edge-truncated shape of a triangle as in the Wulff-type model in Fig. 1b. Instead, a model that includes edges with higher Miller indices must be included. As shown in Fig. 8, a model in which a MoS_2 hexagon exposing Ni–Mo–S($10\bar{1}0$)-type edges and Ni–Mo–S($\bar{1}010$)-type edges is truncated at the corners by 6 new edges of the ($11\bar{2}0$)-type matches the experiment closely. Thus, in the smaller type B Ni–Mo–S, the Ni not only seems to affect the S edges, but also appears to stabilize edges of the ($11\bar{2}0$) type.

A ball model of a type B Ni–Mo–S cluster is illustrated in Fig. 8b. Note that the cluster in the experimental image (Fig. 8a) contains only 11 edges; that is, only five of six possible corners have been truncated by Ni to form Ni–Mo–S($11\bar{2}0$) edges. The Ni-substituted Ni–Mo–S($\bar{1}010$) edges are readily identified in the atom-resolved image in Fig. 8 because they are imaged in the same way as the Ni–Mo–S($\bar{1}010$) edges in the larger type A Ni–Mo–S particles (Fig. 7). Also note that one of the Ni–Mo–S ($\bar{1}010$) edges in Fig. 8 exhibits a pattern most likely resulting from partial substitution of Mo with Ni (indicated by a black dashed circle), but this is observed only rarely and thus should be considered more a single defect than a stable structure.

The ($10\bar{1}0$) edges are rotated 60 degrees relative to the ($\bar{1}010$) edges in the dodecagonal type B Ni–Mo–S particles. A zoom-in on a ($10\bar{1}0$) edge of a type B Ni–Mo–S cluster is shown in Fig. 11a. The type B Ni–Mo–S($10\bar{1}0$) edge seems different from the type A Ni–Mo–S($10\bar{1}0$) edges found in the larger particles (Fig. 7). First, the brim in the middle part of the edge is reduced almost to the level of the basal plane, whereas it has a much higher intensity near the corners. We associate this appearance with substitution of some of the Mo atoms by Ni atoms at the two edge positions near the corners between a Ni–Mo–S($\bar{1}010$) edge and a ($11\bar{2}0$) high-index edge. This is shown in detail in the ball model in Fig. 11b. Note that Ni was added in excess amounts, and thus the observed partially substituted Ni–Mo–S($10\bar{1}0$) can be considered an intrinsic and stable feature of the Ni–Mo–S type B particles.

In the STM image in Fig. 11a, the outermost edge region of the type B Ni–Mo–S($10\bar{1}0$) edges has a very low intensity. This observation may indicate that sulfur atoms are missing on the ($10\bar{1}0$) edges compared with the fully sulfided edges observed in type A Ni–Mo–S, Co–Mo–S, and MoS_2. To understand the observed structure for type B Ni–Mo–S, further DFT calculations were performed for the ($10\bar{1}0$) edges. For the theoretical analysis, models of the ($10\bar{1}0$) edges in which Mo edge atoms are either fully substituted by Ni atoms or partially substituted with alternating Ni on every second site are considered. These configurations represent parts of the ($10\bar{1}0$) edges terminated with either Ni–Ni or Ni–Mo sections, respectively. The relative edge free energies in Figs. 11c and 11e are calculated with the same reference and thus are directly comparable. The fully Ni-substituted Ni–Mo–S($10\bar{1}0$) with 0% sulfur is seen to be most stable. But again, the edge free energy differences relative to the most stable partially substituted edges are of the order of 0.04 eV/Å; thus, for short edges (□10 Å), as in type B Ni–Mo–S, partial substitution cannot safely be neglected. The

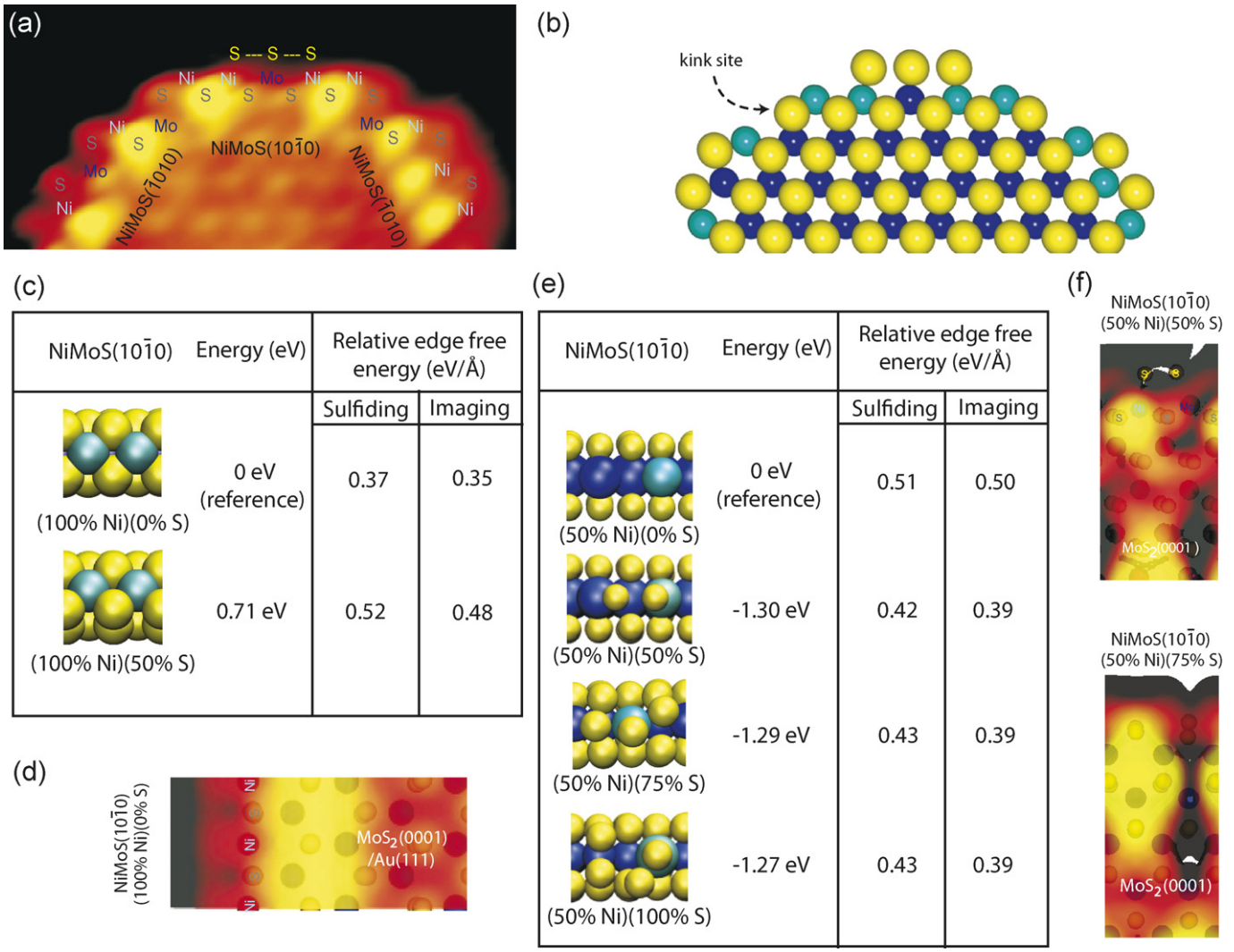

Fig. 11. (a) Zoom-in on a type B Ni–Mo–S nanocluster. (b) A topview ball model. (c) DFT results (2×6 unit cell) for a fully substituted (100% Ni) Ni–Mo–S(10$\bar{1}$0) edge. (d) STM simulation of 100% Ni and 0% S Ni–Mo–S(10$\bar{1}$0) edge. (e) DFT results (2 × 6 unit cell) for a 50% Ni Ni–Mo–S(10$\bar{1}$0) edge. (f) STM simulation of (50% Ni) Ni–Mo–S(10$\bar{1}$0) edge with 50% S and 75% S.

fully Ni-substituted edge with 0% sulfur coverage represents the parts of the ($\bar{1}$010) edge with neighboring Ni–Ni pairs near the corners as shown in (Fig. 11b). The simulation (Fig. 11d) produces a bright region behind the Ni row, as seen in the experiment. These brim regions have a comparable height to the brim on the Ni-substituted ($\bar{1}$010) edge, as also seen in the experiment; moreover, the outermost edge region in which no S atoms are present indeed has a very low intensity. Due to the higher affinity of Mo to sulfur, the situation is likely different in the middle part of the edge, where both Ni and Mo are present at neighboring sites on the edge. Fig. 11e shows the three sulfur coverages in the range 50–100% found to be most likely edge terminations for an edge exposing alternating Ni or Mo atoms (50% Ni substitution). All three investigated sulfur coverages in the range 50–100% are very close in terms of edge free energy (<0.01 eV/Å); however, the STM simulations of the edge with 75% (Fig. 11f, lower part) or 100% sulfur show no clear match with the experimental image. Instead, the 50% S-covered edge (Fig. 11f, upper part) reproduces the experimental STM image, including the bright protrusion behind the Ni site and a depleted intensity behind the Mo site. Furthermore, it is seen that both S atoms adsorbed on Ni or Mo are associated with a very low intensity, as also observed in the experiment. Note that previous DFT studies also found a very small energy difference between an unpromoted and a Ni-substituted (10$\bar{1}$0) edge [38]; a competition between the two promoted and unpromoted edges depending on the experimental conditions was proposed.

Our STM findings clearly reveal that both configurations may coexist on the same edge. This finding implies that the tendency for Ni substitution is linked to the overall cluster size and appears to be predominant only at positions adjacent to a (11$\bar{2}$0) edges of the octahedral Ni–Mo–S type B particles.

The short edges on either side of the Ni–Mo–S(10$\bar{1}$0) edge in Fig. 11a appear to be based on the (11$\bar{2}$0) edge structure. They are identified by their orientation ±30 degrees relative to the (10$\bar{1}$0) and ($\bar{1}$010) edges and also by the two bright protrusions (see Fig. 8a) separated by □5.5 Å, which precisely matches the interatomic periodicity of 5.47 Å in the direction parallel

to the $(11\bar{2}0)$ edges of MoS_2 (Fig. 8b). The observation of these edges in equilibrium structures is highly interesting, because such high-index-edge terminations were once considered too energetically unfavorable. The Ni is structurally similar to the Ni on the Ni–Mo–S$(10\bar{1}0)$ edge but has a lower sulfur coordination, because only S monomers are present on the neighboring Ni–Mo–S$(\bar{1}010)$ edge. The more open structure of the corner site may provide an attractive site for hosting reactive sulfur vacancies during reaction conditions, and clearly an improved understanding of the catalytic relevance of such sites in future DFT and STM investigations is important. Typically the $(11\bar{2}0)$ edges are very short, spanning only a single unit cell, and thus could be considered a corner effect for the finite-size clusters; surprisingly, however, we even observed clusters with $(11\bar{2}0)$ edges two or three unit cells wide. The abundance of these edge terminations suggests that the $(11\bar{2}0)$ cluster termination must have comparable edge free energy to the more closely packed $(10\bar{1}0)$ and $(\bar{1}010)$ edges for this cluster size.

Cluster DFT calculations of Ni–Mo–S particles of different sizes could shed more light on the observed size-dependent affinity for Ni substitution and Ni–Mo–S morphology. They also could help determine whether the $(11\bar{2}0)$ edges should be considered a stable edge termination of Ni–Mo–S or a corner effect that dominates only for the smallest Ni–Mo–S clusters.

4. Comparison of Co–Mo–S and Ni–Mo–S structures with X-ray absorption results

It is interesting to compare the present surface science results with previous X-ray absorption fine-structure (XAFS) studies that have provided information on the average interatomic distances and coordination numbers of Co and Ni promoter atoms for supported Co–Mo–S and Ni–Mo–S particles. To avoid the influence from promoter atoms in structures other than Co(Ni)–Mo–S (in, e.g., the alumina support), the structure surrounding the Co and Ni atoms was typically studied on carbon-supported catalysts. For Co–Mo–S, the structural surroundings of the Co present in carbon-supported Co–Mo sulfide catalysts was studied by X-ray absorption near-edge structure (XANES) spectroscopy at the Co K-edge. Comparing XANES spectra of the catalysts with those of Co_9S_8 and CoS_2 model compounds shows [30,69,70] that the Co atoms in the Co–Mo–S state have a distorted 5- to 6-fold S coordination and that on average, every Co atom is in contact with 2 Mo atoms at a distance of 2.80 Å [30]. Comparing the XANES structure of carbon-supported sulfided Ni–Mo catalysts with well-defined model structures [29,31,71] demonstrates that the Ni atoms have a sulfur coordination number below 6, different from that of an octahedral-like S coordination. The Ni atom in Ni–Mo–S have been suggested to be located in a square pyramid of 5 S atoms at a distance of about 2.21 Å from the S atoms. An EXAFS contribution due to a Mo atom at 2.82 Å from the Ni atom also has been identified [72].

Tables 1 and 2 summarize main XAFS results in the literature for the coordination number and interatomic distances of Co–S, Co–Co, Ni–S, and Ni–Ni obtained from studies of Co–Mo and Ni–Mo sulfided catalysts ([14,69,73–75] and [29,31,71,72]). These tables also present the corresponding interatomic distances and coordination numbers taken from the detailed models of the promoted edges in Co–Mo–S and Ni–Mo–S in the STM experiments and DFT calculations. To allow direct comparison with the XANES values, the STM/DFT values from this study are calculated from the weighted average coordination of all Co or Ni atoms in the Co–Mo–S and type A and B Ni–Mo–S models proposed earlier (Figs. 4, 7, and 8). The average coordination values of the promoters are functions of cluster size and shape (degree of truncation), because corner or edge promoter atoms have a different coordination. This is a particularly important effect for small cluster sizes. There is a general trend toward increasing sulfur coordination when corner sites start to dominate and the promoter-promoter coordination decreases toward 1. The STM experiments typically revealed promoted edges 2 to 6 unit cells wide for both Ni- and Co-promoted edges; therefore, the data range listed in the tables reflects the actual variation in the size and truncation (Fig. 5) of the observed Co–Mo–S and Ni–Mo–S nanoclusters. The interatomic distances in the STM/DFT row are determined from DFT calculations.

Table 1
Coordination numbers and interatomic distances for Co in Co–Mo–S

	$N_{Co–S}$	$d_{Co–S}$ (Å)	$N_{Co–Co}$	$d_{Co–Co}$ (Å)
Co–Mo–S				
STM/DFT	4.5–5.3	2.10	1.3–1.7	3.22
EXAFS	4.9–5.5	2.20–2.26	0.6–1.2	2.6–2.9

Note. XAFS data are compiled from [14,69,73–75]. Typical uncertainties of the XAFS values are around 20% for nearest neighbors. Interatomic distances (STM/DFT) are based on the calculated structures.

Table 2
Coordination numbers and interatomic distances for Ni in Ni–Mo–S

	$N_{Ni–S}$	$d_{Ni–S}$ (Å)	$N_{Ni–Ni}$	$d_{Ni–Ni}$ (Å)
Type A Ni–Mo–S				
STM/DFT	4.5–5.3	2.14	1.3–1.7	3.22
Type B Ni–Mo–S				
STM/DFT	4.0–4.6	2.14	1.0–1.2	3.21
EXAFS	4.7–5.6	2.12–2.24	1.0	3.21

Note. XAFS data are compiled from [29,31]. Typical uncertainties of the XAFS values are around 20% for nearest neighbors. Interatomic distances (STM/DFT) are based on the calculated structures.

The agreement of the Co–Mo–S XANES data with the present findings is good in terms of both coordination number and interatomic distances. The XAFS measurements in general estimate a slightly higher sulfur coordination to Co ($N_{Co–S} \approx 4.9–5.5 \pm 1$) compared with the STM experiments. In this context, however, it is noteworthy that many of the Co–Mo–S clusters have one or more Co atoms substituted at bulk sites (Fig. 4). The Co atoms are six-fold coordinated to sulfur, and the presence of Co bulk inclusions may shift the average Co–S coordination upward. Furthermore, the Co–Co coordination is slightly lower on the fully substituted Co–Mo–S$(\bar{1}010)$ edges ($N_{Co–Co} = 0.6–1.2 \pm 1$) compared with the average coordination (corner and edge sites) in the STM-based model

(N_{Co-Co} = 1.3–1.7). This finding may indicate that Co substitution of Co–Mo–S clusters is incomplete, or that the Co–Mo–S clusters in the industrial alumina-supported catalysts are slightly smaller than those reported in this experiment.

Ni–Mo–S also exhibits good agreement between XANES data and the present STM/DFT results. XANES estimates a Ni coordination number to sulfur of $N_{Ni-S} \approx 4.9–5.5 \pm 1$, which is precisely the value found for the type A Ni–Mo–S particles. In the type B Ni–Mo–S, Ni is substituted at three different type of sites with similar or lower sulfur coordination: the Ni–Mo–S($\bar{1}010$) edges, Ni–Mo–S($10\bar{1}0$) edges, and Ni–Mo–S($11\bar{2}0$) edges. This produces a slightly lower average S coordination number compared with that for type A Ni–Mo–S. In the case of Ni–Mo–S, we never observed inclusions on the basal plane indicating the presence of six-fold coordinated Ni. The values found for the Ni–S coordination could thus indicate that predominantly Ni–Mo–S type A particles are present in the technical Ni–Mo sulfided catalysts. However, these values are very sensitive to actual cluster size, and comparing the Ni–Ni coordination number shows that type B Ni–Mo–S also can match the STM experiment for this particular parameter.

These findings demonstrate that the proposed models for Co–Mo–S and Ni–Mo–S are fully consistent with the XAFS data for technical sulfided Co–Mo and Ni–Mo catalysts. Nonetheless, we emphasize that more than one preferential site of Ni was not considered in previous models, and in general it is unclear whether one or more Ni–Mo–S morphologies were present in the previous studies. The fact that the XAFS data were obtained on samples exposed to HDS relevant conditions (H_2/H_2S mixture), whereas the structures analyzed in the present study were formed in a highly sulfiding atmosphere, also should be taken into account. Regardless, there is nothing to indicate a lower sulfided state of Ni–Mo–S or Co–Mo–S in the XAFS experiments compared with the STM experiments, because the sulfur coordination is estimated to be slightly higher.

5. Conclusion

This study used STM studies and DFT calculations to investigate the atomic-scale structure and morphology of individual Co–Mo–S and Ni–Mo–S nanoclusters synthesized on a gold substrate as model systems for Co- and Ni-promoted MoS_2-based hydrotreating catalysts. In accordance with the widely accepted Co–Mo–S model for the promoted hydrotreating catalyst, we found a distinct tendency for Co and Ni to substitute Mo atoms at edge sites of single-layer MoS_2 nanoclusters, which leads to truncation of the cluster morphology relative to unpromoted MoS_2. An analysis of atom-resolved STM images showed that the substitution occurred only at very specific edge sites in Co–Mo–S and Ni–Mo–S, and, interestingly, that Ni–Mo–S may exist in different structural modifications.

In Co–Mo–S, Co substitution induced an almost hexagonal morphology compared with that triangular morphology of unpromoted MoS_2, and atom-resolved STM images showed that this shift in cluster shape seems to be driven by the tendency for Co to be located only at Co–Mo–S($\bar{1}010$) edge sites. The Co–Mo–S($\bar{1}010$) edges had every edge Mo atom substituted with Co and 50% sulfur coverage. Because in this structure, the sulfur atoms do not occupy the regular MoS_2 lattice positions, the Co atoms have a tetrahedral coordination to sulfur. STM images of the Co-promoted edges revealed a very bright brim structure, indicating a modified electronic structure that were related (through DFT calculations) to the presence of a single metallic edge state pertaining to Co–Mo–S.

For Ni–Mo–S, the morphology and affinity for Ni to substitute Mo were found to depend on cluster size. Larger Ni–Mo–S particles (type A Ni–Mo–S) exhibited a truncated triangular shape similar to that observed for Co–Mo–S nanoclusters, whereas the smaller Ni–Mo–S particles (type B Ni–Mo–S) had a dodecagonal shape. The type A Ni–Mo–S structures are terminated by two types of edges. One of these edges is unpromoted and exhibits the same structure as the $MoS_2(10\bar{1}0)$ edges; the other is a Ni–Mo–S($\bar{1}010$) edge, at which Ni has fully substituted all edge Mo sites and the edge is covered with 50% sulfur.

STM images revealed a significantly modified electronic edge structure, which in terms of DFT calculations were shown to be related to two distinct Ni–Mo–S metallic edge states, one of which was similar to that in Co–Mo–S and the other which had no Co–Mo–S or MoS_2 counterpart. The smaller dodecagonal-shaped type B Ni–Mo–S clusters are terminated by three different types of edges. One of these edge types is exactly the same as the fully Ni-substituted Ni–Mo–S($\bar{1}010$) edge in larger clusters. STM images showed that the other two edges also have Ni atoms substituted at Mo edge sites. One of these is a Ni–Mo–S($10\bar{1}0$) edge type that differs from the Ni–Mo–S($10\bar{1}0$) edge in the larger particles. The type B Ni–Mo–S($10\bar{1}0$) edge underwent partial substitution of Mo by Ni, and sulfur adsorption occurred in only parts of the edge with alternating Mo–Ni sections. The last type of edges in type B Ni–Mo–S is associated with high-index ($11\bar{2}0$) edge. These edge types are normally not considered to be stable edge terminations in the literature, but the STM experiments show that such edges may be exposed under equilibrium conditions in the type B Ni–Mo–S structures.

Previous spectroscopic and activity correlation studies of unpromoted and Co- and Ni-promoted catalysts have provided evidence of the existence of different types of MoS_2, Co–Mo–S, and Ni–Mo–S structures [5]. Differences such as those observed in type I and type II Co–Mo–S structures have been shown to be related to differences in the interaction between the sulfide structure and support. Recent DFT calculations [37,76] and STM experiments [43] have provided a better atomistic understanding of support interactions. However, it should be stressed that the type A Ni–Mo–S and type B structures observed in the present study have different intrinsic properties which are not related to support interactions or stacking effects of the MoS_2 layers. Ni is observed to be located at different types of sites in the two types of structures, and, therefore, they are also expected to have very different chemical and catalytic properties. A key goal of future studies will be to achieve a better understanding of these differences, and

such new insight may lead to a better understanding of HDS, HDN and HDY selectivities as a function of the promoter type.

Acknowledgments

This work was supported by the Danish Ministry of Science, Technology, and Innovation through the iNANO center. J.V.L. acknowledges support from the Carlsberg Foundation. Fruitful discussions with Alfons Molenbroek and Anna Maria Puig Molina are gratefully acknowledged.

Supplementary material

The online version of this article contains additional supplementary material.

Please visit DOI: 10.1016/j.jcat.2007.04.013.

References

[1] K.G. Knudsen, B.H. Cooper, H. Topsøe, Appl. Catal. A 189 (1999) 205.
[2] C. Song, X. Ma, Appl. Catal. B 41 (2003) 207.
[3] I.V. Babich, J.A. Moulijn, Fuel 82 (2003) 607.
[4] D.D. Whitehurst, T. Isoda, I. Mochida, Adv. Catal. 42 (1998) 345.
[5] H. Topsøe, B.S. Clausen, F.E. Massoth, in: J.R. Anderson, M. Boudart (Eds.), Catalysis—Science and Technology, vol. 11, Springer-Verlag, Berlin–Heidelberg, 1996.
[6] T. Kabe, A. Ishihara, W. Qian, Hydrodesulfurization and Hydrogenation—Chemistry and Engineering, Wiley–VCH, Kodansha, 1999.
[7] R. Prins, in: G. Ertl, H. Knözinger, J. Weitkamp (Eds.), Handbook of Heterogeneous Catalysis, vol. 4, VHC, Weinheim, 1997, p. 1908.
[8] R. Prins, Adv. Catal. 46 (2002) 399.
[9] B.S. Clausen, S. Mørup, H. Topsøe, R. Candia, J. Phys. 37 (1976) 249.
[10] R. Prins, V.H.J. de Beer, G. Somorjai, Catal. Rev. Sci. Eng. 31 (1989) 1.
[11] P. Gajardo, P. Grange, B. Delmon, J. Catal. 63 (1980) 201.
[12] T.G. Parham, R.P. Merrill, J. Catal. 85 (1984) 295.
[13] M. Karroua, P. Grange, B. Delmon, Appl. Catal. 50 (1989) L5.
[14] M.W.J. Craje, S.P.A. Louwers, V.H.J. de Beer, R. Prins, A.M. Vanderkraan, J. Phys. Chem. 96 (1992) 5445.
[15] R. Chianelli, M. Daage, M. Ledoux, Adv. Catal. 40 (1994) 177.
[16] R. Leliveld, A. van Dillen, J. Geus, D.C. Koningsberger, J. Catal. 175 (1998) 108.
[17] A.M. de Jong, V.H.J. de Beer, J.A.R. van Veen, J.W. Niemantsverdriet, J. Vac. Sci. Technol. A 15 (1997) 1592.
[18] H. Topsøe, B.S. Clausen, R. Candia, C. Wivel, S. Mørup, J. Catal. 68 (1981) 433.
[19] N.-Y. Topsøe, H. Topsøe, J. Catal. 84 (1983) 386.
[20] C. Wivel, R. Candia, B.S. Clausen, S. Mørup, H. Topsøe, J. Catal. 68 (1981) 453.
[21] M. Salmeron, G. Somorjai, A. Wold, R. Chianelli, K. Liang, Chem. Phys. Lett. 90 (1982) 105.
[22] K. Tanaka, Adv. Catal. 33 (1985) 99.
[23] R.R. Chianelli, A.F. Ruppert, S.K. Behal, B.H. Kear, A. Wold, R. Kershaw, J. Catal. 92 (1985) 56.
[24] H. Topsøe, B.S. Clausen, Catal. Rev. Sci. Eng. 26 (1984) 395.
[25] O. Sørensen, B.S. Clausen, R. Candia, H. Topsøe, Appl. Catal. 13 (1985) 363.
[26] Y. Okamoto, T. Kubota, Catal. Today 86 (2003) 31.
[27] Y. Okamoto, M. Kawano, T. Kawabata, T. Kubota, I. Hiromitsu, J. Phys. Chem. B 109 (2005) 288.
[28] T. Shido, R. Prins, J. Phys. Chem. B 102 (1998) 8426.
[29] W. Niemann, B.S. Clausen, H. Topsøe, Catal. Lett. 4 (1990) 355.
[30] S.M.A.M. Bouwens, J.A.R. van Veen, D.C. Koningsberger, V.H.J. de Beer, R. Prins, J. Phys. Chem. 95 (1991) 123.
[31] S. Louwers, R. Prins, J. Catal. 133 (1992) 94.
[32] L.S. Byskov, J.K. Nørskov, B.S. Clausen, H. Topsøe, J. Catal. 187 (1999) 109.
[33] L.S. Byskov, J.K. Nørskov, B.S. Clausen, H. Topsøe, Catal. Lett. 64 (2000) 95.
[34] P. Raybaud, J. Hafner, G. Kresse, S. Kasztelan, H. Toulhoat, J. Catal. 190 (2000) 128.
[35] A. Travert, H. Nakamura, R. van Santen, S. Cristol, J. Paul, E. Payen, J. Am. Chem. Soc. 124 (2002) 7084.
[36] M.Y. Sun, A.E. Nelson, J. Adjaye, J. Catal. 226 (2004) 32.
[37] B. Hinnemann, J.K. Nørskov, H. Topsøe, J. Phys. Chem. B 109 (2005) 2245.
[38] H. Schweiger, P. Raybaud, H. Toulhoat, J. Catal. 212 (2002) 33.
[39] J.V. Lauritsen, S. Helveg, E. Lægsgaard, I. Stensgaard, B.S. Clausen, H. Topsøe, F. Besenbacher, J. Catal. 197 (2001) 1.
[40] S. Helveg, J.V. Lauritsen, E. Lægsgaard, I. Stensgaard, J.K. Nørskov, B.S. Clausen, H. Topsøe, F. Besenbacher, Phys. Rev. Lett. 84 (2000) 951.
[41] J.V. Lauritsen, M.V. Bollinger, E. Lægsgaard, K.W. Jacobsen, J.K. Nørskov, B.S. Clausen, H. Topsøe, F. Besenbacher, J. Catal. 221 (2004) 510.
[42] J.V. Lauritsen, M. Nyberg, J.K. Nørskov, B.S. Clausen, H. Topsøe, E. Lægsgaard, F. Besenbacher, J. Catal. 224 (2004) 94.
[43] J. Kibsgaard, J.V. Lauritsen, B.S. Clausen, H. Topsøe, F. Besenbacher, J. Am. Chem. Soc. 128 (2006) 13950.
[44] V. LaVopa, C. Satterfield, J. Catal. 110 (1988) 375.
[45] M. Egorova, R. Prins, J. Catal. 241 (2006) 162.
[46] J.V. Lauritsen, M. Nyberg, R.T. Vang, M.V. Bollinger, B.S. Clausen, H. Topsøe, K.W. Jacobsen, F. Besenbacher, E. Lægsgaard, J.K. Nørskov, F. Besenbacher, Nanotechnology 14 (2003) 385.
[47] F. Besenbacher, Rep. Prog. Phys. 59 (1996) 1737.
[48] T.H. Cai, Z. Song, J.A. Rodriguez, J. Hrbek, J. Am. Chem. Soc. 126 (2004) 8886.
[49] M.M. Biener, J. Biener, C.M. Friend, J. Chem. Phys. 122 (2005) 034706.
[50] J.V. Barth, H. Brune, G. Ertl, R. Behm, Phys. Rev. B 42 (1990) 9307.
[51] B. Voigtländer, G. Meyer, N.M. Amer, Phys. Rev. B 44 (1991) 10354.
[52] D.D. Chambliss, R.J. Wilson, S. Chiang, Phys. Rev. Lett. 66 (1991) 1721.
[53] J.A. Meyer, I. Baikie, E. Kopatzki, R.J. Behm, Surf. Sci. 365 (1996) L647.
[54] M.V. Bollinger, K.W. Jacobsen, J.K. Nørskov, Phys. Rev. B 67 (2003) 085410.
[55] M.V. Bollinger, J.V. Lauritsen, K.W. Jacobsen, J.K. Nørskov, S. Helveg, F. Besenbacher, Phys. Rev. Lett. 87 (2001) 196803.
[56] L.S. Byskov, B. Hammer, J.K. Nørskov, B.S. Clausen, H. Topsøe, Catal. Lett. 47 (1997) 177.
[57] S.R. Bahn, K.W. Jacobsen, Comput. Sci. Eng. 4 (2002) 56.
[58] B. Hammer, L.B. Hansen, J.K. Nørskov, Phys. Rev. B 59 (1999) 7413.
[59] H.J. Monkhorst, J.D. Pack, Phys. Rev. B 13 (1976) 5188.
[60] K. Laasonen, A. Pasquarello, R. Car, C. Lee, D. Vanderbilt, Phys. Rev. B 47 (1993) 10142.
[61] D. Vanderbilt, Phys. Rev. B 41 (1990) 7892.
[62] N. Troullier, J.L. Martins, Phys. Rev. B 43 (1991) 1993.
[63] J. Perdew, J. Chevary, S. Vosko, K. Jackson, M. Pederson, D. Singh, C. Fiolhais, Phys. Rev. B 46 (1992) 6671.
[64] H. Schweiger, P. Raybaud, G. Kresse, H. Toulhoat, J. Catal. 207 (2002) 76.
[65] S. Cristol, J.F. Paul, E. Payen, D. Bougeard, S. Clémendot, F. Hutschka, J. Phys. Chem. B 106 (2002) 5659.
[66] J. Tersoff, D.R. Hamann, Phys. Rev. Lett. 50 (1983) 1998.
[67] J.V. Lauritsen, J. Kibsgaard, S. Helveg, H. Topsøe, B.S. Clausen, F. Besenbacher, Nat. Nanotechnol. 2 (2007) 53.
[68] S. Kasztelan, H. Toulhoat, J. Grimblot, J. Bonnelle, Appl. Catal. 13 (1984) 127.
[69] B.S. Clausen, B. Lengeler, R. Candia, J. Als-Nielsen, H. Topsøe, Bull. Soc. Chim. Belg. 90 (1981) 1249.
[70] H. Topsøe, R. Candia, N.-Y. Topsøe, B.S. Clausen, Bull. Soc. Chim. Belg. 93 (1984) 783.

[71] S. Bouwens, D.C. Koningsberger, V.H.J. de Beer, S.P.A. Louwers, R. Prins, Catal. Lett. 5 (1990) 273.
[72] S. Bouwens, N. Barthe-Zahir, V.H.J. de Beer, R. Prins, J. Catal. 131 (1991) 326.
[73] B.S. Clausen, H. Topsøe, Hyperfine Interact. 47–48 (1989) 203.
[74] J.T. Miller, W.J. Reagan, J.A. Kaduk, C.L. Marshall, A.J. Kropf, J. Catal. 193 (2000) 123.
[75] J.T. Miller, C.L. Marshall, A.J. Kropf, J. Catal. 202 (2001) 89.
[76] C. Arrouvel, M. Breysse, H. Toulhoat, P. Raybaud, J. Catal. 232 (2005) 161.

Paper 6

Available online at www.sciencedirect.com
ScienceDirect
Catalysis Today 130 (2008) 86–96
CATALYSIS TODAY
www.elsevier.com/locate/cattod

Recent STM, DFT and HAADF-STEM studies of sulfide-based hydrotreating catalysts: Insight into mechanistic, structural and particle size effects

F. Besenbacher [a], M. Brorson [b], B.S. Clausen [b], S. Helveg [b], B. Hinnemann [b], J. Kibsgaard [a], J.V. Lauritsen [a], P.G. Moses [c], J.K. Nørskov [c], H. Topsøe [b,*]

[a] *Department of Physics and Astronomy, Interdisciplinary Nanoscience Center (iNANO), University of Aarhus, DK-8000 Aarhus C, Denmark*
[b] *Haldor Topsøe A/S, Nymøllevej 55, DK-2800 Lyngby, Denmark*
[c] *Department of Physics and Center for Atomic-scale Materials Design (CAMD), NanoDTU, Technical University of Denmark, DK-2800 Lyngby, Denmark*

Available online 11 September 2007

Abstract

The present article will highlight some recent experimental and theoretical studies of both unpromoted MoS_2 and promoted Co–Mo–S and Ni–Mo–S nanostructures. Particular emphasis will be given to discussion of our scanning tunnelling microscopy (STM), density functional theory (DFT), and high-angle annular dark-field scanning transmission electron microscopy (HAADF-STEM) studies which have provided insight into the detailed atomic structure. In accordance with earlier theoretical studies, the experimental studies show that the Ni–Mo–S structures may in some instances differ from the Co–Mo–S analogues. In fact, the Co–Mo–S and Ni–Mo–S structures may be even more complex than previously anticipated, since completely new high index terminated structures have also been observed. New insight into the HDS mechanism has also been obtained and complete hydrogenation and hydrogenolysis pathways for thiophene hydrodesulfurization (HDS) have been calculated on the type of structures that prevail under reaction conditions. It is seen that important reaction steps may not involve vacancies, and special brim sites are seen to play an important role. Such studies have also provided insight into inhibition and support effects which play an important role in practical HDS. Recent STM studies have shown that MoS_2 clusters below 2–3 nm may exhibit new structural and electronic properties, and a large variety of size-dependent structures have been identified. In view of the large structure sensitivity of hydrotreating reactions this is expected to give rise to large effects on the catalysis.

Keywords: Hydrotreating; Hydrodesulfurization; Hydrodenitrogenation; HDS; Model catalyst; Scanning tunnelling microscopy; STM; Density functional theory; DFT; Molybdenum disulfide; MoS_2; Promoters; Morphology; Ni–Mo–S; Co–Mo–S; Inhibition; Thiophene; Pyridine; HAADF-STEM; Support interaction

1. Introduction

In recent years, new legislation regarding the sulfur content in transport fuels has resulted in the demand for ultra low sulfur diesel (ULSD), and this has introduced new challenges for hydrodesulfurization (HDS) in the refining industry [1–9]. In addition, the demand for diesel fuels is increasing, and as the availability of light petroleum resources decreases, increasingly heavy feedstocks have to be refined. In order to achieve the higher sulfur conversion, very refractory sulfur compounds, like dialkylated dibenzothiophenes (DBT), need to be removed [1,3–6,10]. It has been known for some time that the conversion of the sterically hindered DBTs mainly proceeds via a pre-hydrogenation route (HYD) rather than the direct desulfurization route (DDS), which dominates for molecules like DBT [3]. However, under industrial conditions, the presence of other compounds in the feed often changes the relative role of the HYD and the DDS pathways. In particular, specific basic nitrogen-containing compounds inhibit HDS, and these compounds are observed to mainly inhibit the HYD pathway [11–13]. Furthermore, H_2S is an HDS inhibitor, and interestingly, it mainly inhibits the DDS rather than the HYD pathway [1]. To improve HDS catalysts and gear them to the increasingly heavy feedstocks, detailed understanding of their

* Corresponding author.
E-mail address: het@topsoe.dk (H. Topsøe).

0920-5861/$ – see front matter © 2007 Published by Elsevier B.V.
doi:10.1016/j.cattod.2007.08.009

mechanistic action is necessary so that targeted modifications can be made.

In order to elucidate the HDS reaction and the two different HYD and DDS pathways in detail, it is important to characterize the active nanostructures and in particular to identify the active sites for the two pathways. Until the early 1980s, very little information was available on the structure of active hydrotreating catalysts. A key discovery was the identification of the MoS_2 and Co–Mo–S structures by EXAFS, Mössbauer and infrared techniques, and it was shown that the Co–Mo–S structure was responsible for the promotion of catalytic activity [14–18]. These results revealed that Co–Mo–S (and also Ni–Mo–S) structures are small MoS_2-like nanocrystals, where the promoter atoms are located at the edges of the MoS_2 layers. The results furthermore suggested that Co atoms are located in the same plane as Mo, but that their local coordination is different. In spite of the significant progress, it was for a long-time difficult to address the issue of the detailed edge structure of unpromoted and promoted MoS_2, as no atomic-resolved structures could be obtained. As a consequence, it has also been difficult to understand the nature of HYD and DDS pathways and sites. Recently, we have achieved a large breakthrough in the structural studies of the active nanostructures in HDS using scanning tunnelling microscopy (STM) to image the real-space structure of MoS_2 nanoclusters grown on flat model substrates. With the STM, it was possible for the first time to reveal the equilibrium morphology of the nanoclusters. Furthermore, atomic-resolution STM images made it possible to elucidate the detailed structure of the catalytically important edges, the sulfur coverage and the location of sulfur vacancies, which are normally considered to be active sites [19]. In further studies, we have also managed to synthesize and characterize the atomic-scale structure of Co–Mo–S and Ni–Mo–S and thereby it has been possible to obtain information on the location of the Co and Ni promoter atoms [20,21]. Recently, MoS_2, WS_2 and promoted structures were studied by another new technique, high-angle annular dark-field scanning tunnelling electron microscopy (HAADF-STEM), and additional information on the morphology of MoS_2- and WS_2-based nanostructures could be obtained [22–24]. In most of the STM studies, gold was used as a support of the sulfide nanostructures. Since gold is a weakly interacting support, the studies have provided important insight into the intrinsic properties of the nanostructures. In industrial HDS catalysts, the support usually plays a significant role and the STM studies have recently been extended to carbon-supported systems [25]. Many earlier studies have indicated that hydrotreating reactions are extremely sensitive structure [1]. One may therefore expect that the reactions will depend strongly on the particle size, but not much has been known about such effects. Recently, STM has for the first time provided us with atom resolved images of MoS_2 clusters of different sizes [26]. Many size-dependent structural and electronic changes were observed and such effects must clearly also be taken into account when addressing the catalysis.

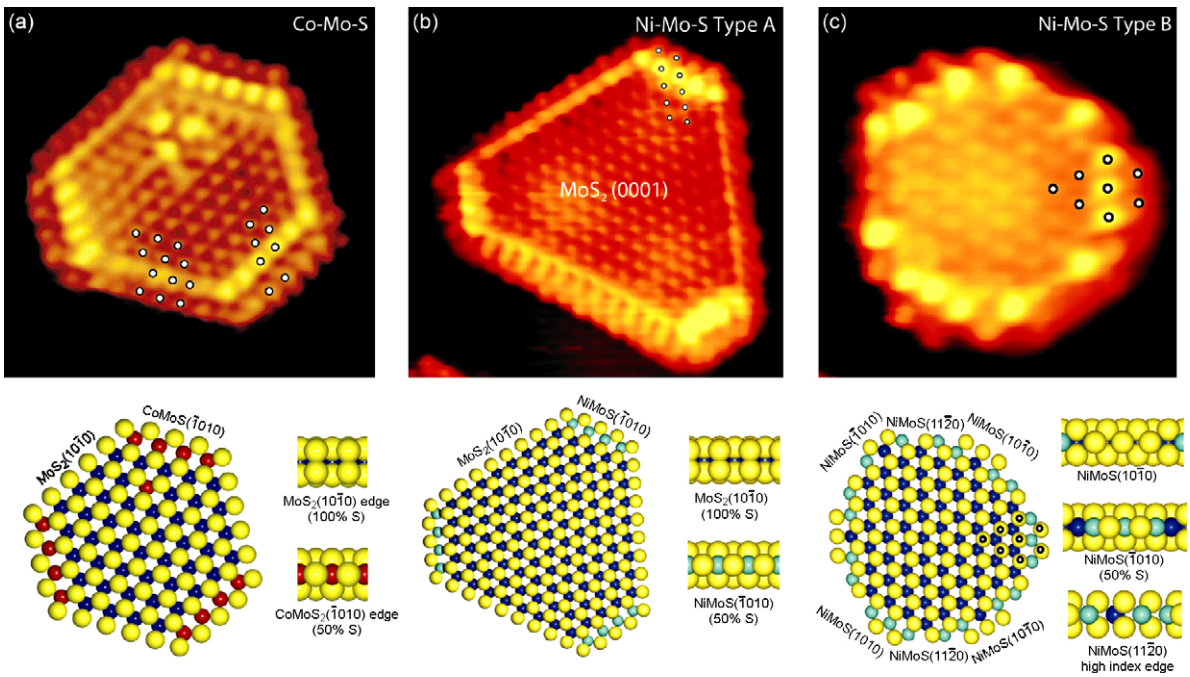

Fig. 1. (a) Top: Atom-resolved STM image (51 Å × 52 Å, I_t = 0.81 nA and V_t = −95.2 mV) of a hexagonally truncated Co–Mo–S nanocluster supported on Au(1 1 1). The superimposed white dots illustrate the registry of protrusions on both types of edges. Bottom: A ball model (top and side views, respectively) of the Co–Mo–S nanocluster based on DFT calculations. (b) Top: Atom-resolved STM image (61 Å × 61 Å, I_t = 0.51 nA and V_t = −600 mV) of a hexagonally truncated type A Ni–Mo–S nanocluster supported on Au(1 1 1). Bottom: A ball model (top and side views, respectively) of the Ni–Mo–S type A nanocluster based on DFT calculations. (c) Top: Atom-resolved STM image (39 Å × 40 Å, I_t = 0.44 nA and V_t = −520 mV) dodecagonally shaped type B Ni–Mo–S nanocluster supported on Au(1 1 1). Bottom: A ball model (top and side views, respectively) of the Ni–Mo–S type B nanocluster based on DFT calculations. (Mo: blue; S: yellow; Co: red; Ni: cyan). Adapted from [21]. (For interpretation of the references to colour in this figure legend, the reader is referred to the web version of the article.)

First principles modelling techniques, like density functional theory (DFT), have over the last decade provided increasing insight into atomic structure and reactivity of the active phases of HDS catalysts. DFT can often provide information that is complementary to the multitude of experimental information, and the synergy of theoretical and experimental approaches can thus give a very detailed picture of catalyst structure and reactivity. After our initial studies of Co–Mo–S [27–29], we have recently used this approach in a series of studies, where STM and DFT were combined to obtain insight into the structure of unpromoted and promoted MoS_2 under different conditions [30–33,21]. The general approach of combining DFT with the chemical potential of the gas phase can be used to connect DFT calculations performed at 0 K and in vacuum to reaction conditions with relevant temperatures and pressures [34–39].

The very powerful combination of STM experiment and DFT calculations has led to several important findings in our studies, and one of the most significant results was the discovery of the so-called brim states and their role in HDS catalysis. It was found that the Mo edge exhibits a special electronic edge state, which can easily be identified in STM images of the nanoclusters as a very bright brim extending along the edges (see e.g. Fig. 1). These brim states arise from a perturbation of the electronic structure near the edges relative to the interior part of the clusters. Detailed analysis using DFT revealed the presence of edge states, which are metallic states that are localized at the cluster edges and give rise to the brim states [30]. Quite surprisingly, it was observed that these states possess reactivity towards the hydrogenation of thiophene, which could be observed using STM [31,32]. Thus, insight into these sites is essential for understanding hydrotreating reactions.

The ever increasing computational power makes it possible to study increasingly complex systems, and in recent years a number of reports on catalyst-support interactions have been published [40–44]. Also, the reaction pathway of thiophene and thiophene derivatives on MoS_2 have been studied by us [45] and several other groups [46–49] and thus, we can begin to understand reaction pathways and find descriptors for catalytic activity.

In this review, we will highlight some of the above-mentioned developments. In Section 2, we discuss the recent STM and DFT studies of promoted CoMoS and NiMoS structures as well as HAADF-STEM studies on unpromoted and promoted MoS_2 and WS_2. In Section 3, we summarize the results concerning support interactions and in Section 4 we discuss recent developments concerning reaction pathways and inhibition. In Section 5, recent STM results regarding size effects are described.

2. Structure of MoS_2, Co–Mo–S and Ni–Mo–S

According to the now well-accepted Co–Mo–S model for the promoted MoS_2 hydrotreating catalysts, the Co and Ni promoter atoms are located at edge positions of MoS_2 nanostructures. Their substitution of Mo at edge sites is believed to enhance vacancy formation and the creation of new and more active sites. Several studies have been carried out to correlate the structure of the active promoted phases to the activity [1,15,17], but the exact location and coordination of the promoter atoms have been debated extensively [1,14,50–54]. Lack of structural insight has hampered the progress. Consequently, the origin of the promoting effect of Co and Ni is still not fully understood, and in particular it has been interesting to resolve the origin of the different specific selectivities with respect to hydrodesulfurization (HDS), hydrodenitrogenation (HDN) and hydrogenation (HYD) for the two types of promoted systems [1,3,4,8,10,55].

Following the initial STM studies of unpromoted MoS_2 nanoclusters [19], we have used STM to reveal the atomic scale structure of both Co–Mo–S [20] and more recently Ni–Mo–S [21]. Fig. 1 shows the STM images of Co–Mo–S and Ni–Mo–S nanoclusters. One can see that the main indicator of the formation of promoted Co–Mo–S and Ni–Mo–S phases is a distinct change in morphology compared to the unpromoted MoS_2 nanoclusters, which under similar synthesis conditions have a very regular triangular shape. This change in morphology is concluded to be mainly driven by the preference for the promoter atoms (Co and Ni) to substitute certain sites. In many instances, there is a preference for the substitution at the $(\bar{1}\,0\,1\,0)$ S edges of MoS_2 rather than at the $(1\,0\,\bar{1}\,0)$ Mo edges which under similar conditions are the only edges exposed in the unpromoted triangular clusters.

The above situation is illustrated for Co–Mo–S in Fig. 1a, which shows that the nanocluster adopts a clear hexagonally truncated shape, indicating that both $(1\,0\,\bar{1}\,0)$ Mo edges and $(\bar{1}\,0\,1\,0)$ S edges are present. One type of edge in the Co–Mo–S structure is found to be identical to that observed for the unpromoted MoS_2 triangles [19], with the outermost row of protrusions out of registry with the basal plane S atoms and a clear bright brim along the edge. This type of edge can therefore be identified as a $(1\,0\,\bar{1}\,0)$ Mo edge. The other edges must according to the symmetry be the $(\bar{1}\,0\,1\,0)$ S edges. This type of edge is seen to exhibit an even brighter brim structure in which individual protrusions can be identified. The periodicity of one lattice distance along the brim indicates that Co atoms have replaced all Mo atoms at the S edge creating a $(\bar{1}\,0\,1\,0)$ Co–Mo–S edge. It is, however, not straightforward to identify the exact edge structure and sulfur termination exclusively from STM images. We have therefore performed DFT calculations to identify the edge termination of the $(\bar{1}\,0\,1\,0)$ Co–Mo–S edges [21], and simulated STM images show that only a 50% sulfur covered edge is consistent with the experimental STM images. Furthermore, this theoretical analysis reveals that a metallic edge state (brim state) is responsible for the very bright brim observed at the promoted edge. This resulting local structure around the Co atoms is in good agreement with previous spectroscopic measurements [51,56,57].

The edge truncation effects observed in the STM studies are more complex for the Ni–Mo–S nanoclusters [21]. In addition, the nature of the truncation for the Ni–Mo–S system was seen to depend on the cluster size. The larger type A clusters are characterized by a hexagonally truncated shape similar to that

of the Co–Mo–S nanoclusters (See Fig. 1b). The smaller type B clusters, on the other hand, have a more complex dodecagonal morphology (See Fig. 1). The Ni–Mo–S type A structures are terminated by two types of edges. As for the Co–Mo–S case, the Ni–Mo–S type A clusters expose both an unpromoted $(1\,0\,\bar{1}\,0)$ Mo edge and a new $(\bar{1}\,0\,1\,0)$ Ni–Mo–S edge structure, in which Ni has fully substituted all edge Mo sites. In order to understand the structure and properties of this edge in detail, we have again used DFT. The DFT-based simulated STM images show that only an edge with 50% sulfur coverage is energetically favourable and consistent with the experimental images. The structure of Ni–Mo–S type A, which is depicted in the ball model in Fig. 1b, is thus similar to that of Co–Mo–S. The DFT calculations of the $(\bar{1}\,0\,1\,0)$ Ni–Mo–S edge show that the bright brim observed with STM is related to two distinct Ni–Mo–S metallic edge states. One of the metallic Ni–Mo–S edge states is similar to the one in Co–Mo–S, but the other one has no MoS_2 or Co–Mo–S counterpart [21,30] and it is possible that this edge state plays a catalytic role and is responsible for differences in catalytic activity and selectivity between Co–Mo–S and Ni–Mo–S. The smaller dodecagonally shaped type B Ni–Mo–S clusters (Fig. 1c) are structurally more complicated and are seen to be terminated by three different types of edges. Two of the edge types can be identified as the same fundamental types as the $(1\,0\,\bar{1}\,0)$ Mo edge and the $(\bar{1}\,0\,10)$ Ni–Mo–S edge also found in the type A Ni–Mo–S clusters. However, the STM images show bright protrusions on the Mo edges indicating that Ni atoms also have substituted at Mo edge sites creating $(1\,0\,\bar{1}\,0)$ Ni–Mo–S edges (Fig. 1c). Comparing the experimental STM images with simulated STM images from DFT, we conclude that type B $(1\,0\,\bar{1}\,0)$ Ni–Mo–S edges have a partial substitution of Mo by Ni, and only the parts of the edge with alternating Mo–Ni sections are seen to have sulfur adsorbed [21]. The last type of edge present in type B Ni–Mo–S is associated with a high-index $(1\,1\,\bar{2}\,0)$ edge. The presence of such edges is quite surprising, since previously, such edges have not been considered as stable edge terminations in Co–Mo–S or Ni–Mo–S structures. The STM experiments and the HAADF-STEM measurements discussed below are the first experimental evidence that such edges may be present under sulfiding conditions.

The presented observations suggest that the promoting role of Co and Ni may be two-fold. The change in the electronic structure as indicated by the modified brim and the lower S coordination on the promoted $(\bar{1}\,0\,1\,0)$ Ni–Mo–S edges may be an attractive situation enabling adsorption of sulfur-containing molecules. Furthermore, the presence of Ni–Mo–S type B clusters clearly demonstrate that there may be major differences in the morphologies of Co–Mo–S and Ni–Mo–S catalysts exposed to similar sulfiding environments, and this may be a key to explain the different selectivities of the two systems in the hydrotreating processes.

Recently, we have employed high-angle annular dark-field scanning transmission electron miscroscopy (HAADF-STEM) to obtain morphological information on unpromoted and promoted WS_2 and MoS_2 structures and to gain more insight into the changes induced by the promoter atoms [22–24]. Traditionally, researchers have been using high-resolution transmission electron microscopy (HRTEM) to obtain morphological insight into HDS catalysts [58–72]. However, it has been difficult to get such insights from HRTEM measurements since single S–Mo–S layers are typically only imaged when they are oriented approximately edge-on relative to the electron beam, i.e. the layers are viewed as lines in the images. In contrast, HAADF-STEM uses electron scattering at high angles to create a *Z*-contrast image with *Z* denoting the atomic number. This situation is especially advantageous for heavy elements and in the first study [22], we investigated WS_2/C catalysts and observed that even single WS_2 layers could be imaged with the beam along the *c*-axis. In this way, the morphology of the layers could be directly imaged. In accordance with the STM results, we observed that the shape of the nanostructures may deviate significantly from the hexagonal morphology observed for bulk crystals. Recently, we have applied this method to MoS_2, Co–Mo–S and Ni–Mo–S structures [24] and some of the resulting HAADF-STEM pictures are shown in Fig. 2. It can be seen that in spite of the high sulfiding temperature (1073 K), many of the single layer clusters still contain irregularities and defects, which distinguish them from the much more regular STM images of MoS_2 on Au(1 1 1). Also in industrial catalysts, the structures may have defects and layers are often curved [1]. It should be remarked that the clusters observed here are larger

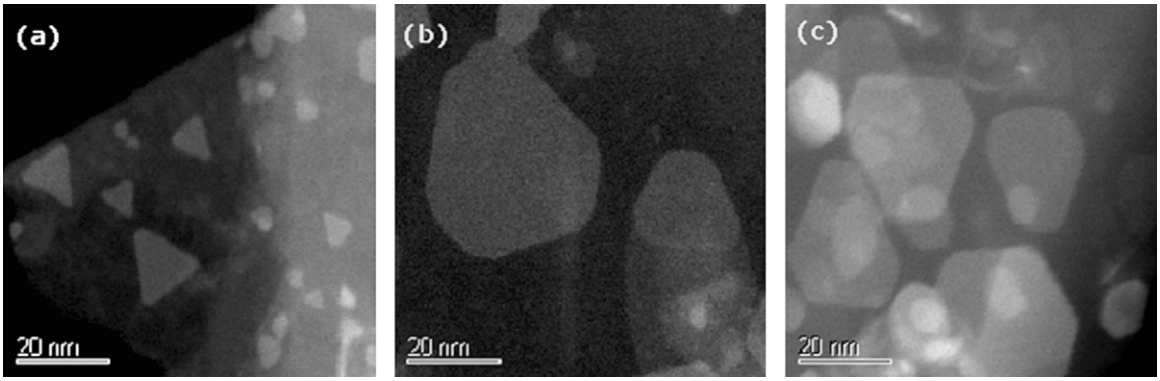

Fig. 2. HAADF-STEM images of (a) MoS_2, (b) Co–Mo–S and (c) Ni–Mo–S clusters supported on a thin graphite sheet oriented approximately perpendicular to the line of observation. The image (c) displays accidental overlap of clusters located along the same line of observation, possibly clusters located at opposite sides of the same graphite sheet. Adapted from Ref. [24].

than the ones in the STM study on Au(1 1 1). We find that most of the imaged clusters are single-layer clusters, as also shown by edge-on images presented in [22]. For the unpromoted MoS_2 structures, we find that the predominant shape is a truncated hexagon. From comparison with the STM images of MoS_2 on Au(1 1 1) [19] and with DFT calculations on edge stability [38], one can assume that predominantly Mo edges are exposed and they therefore correspond to the longer edges observed in the images. The promoted Co–Mo–S and Ni–Mo–S structures were also investigated and they are depicted in Fig. 2b and c, respectively. In accordance with the STM results it is found that promotion changes the morphology of the nanoclusters and that their shape becomes significantly more hexagonal. Furthermore, some of the hexagons appear with rounded corners, which indicate that high-index edge terminations are exposed also in the case of Co–Mo–S. These results differ from the Co–Mo–S and Ni–Mo–S structures on Au(1 1 1) studied by STM [21], where only Ni–Mo–S was observed to expose higher-index edge terminations. This difference may be due to the different supports as well as different preparation and sulfidation methods. The STM samples have been prepared by gas phase metal deposition onto a gold surface, whereas the HAADF-STEM samples have been prepared by impregnation of carbon powder followed by sulfidation. It is not surprising that the choice of such methods may greatly influence the structure of the catalyst [1]. However, considering the different synthesis methods and supports, it should be emphasized that many of the observed structure and the morphology changes induced by Co and Ni in the STM and HAADF-STEM experiments are rather similar. Regarding the possible role of the support, it should be noted that we recently have studied MoS_2 structures on graphite by STM [25], and these results are discussed in the following section.

3. Support interactions

The role of support interactions has been an important topic in catalysis research for many years, since the catalytic properties of MoS_2 are significantly influenced by the support [1]. The most common support is high-surface area alumina, since it allows for the production of small stable nanoclusters of MoS_2. Preparation conditions influence the activity significantly, e.g. it has been observed that an increase in sulfidation temperature resulted in the formation of modified Co–Mo–S structures [73], which had a significantly higher activity than those prepared at lower temperatures. These structures were termed Type II Co–Mo–S as opposed to the Type I Co–Mo–S structures formed at lower temperatures. Extensive characterization studies using EXAFS, FTIR and a multitude of other techniques [74–78] have suggested that Type I Co–Mo–S structures contain Mo–O–Al linkages with the support, whereas no such linkages are present in Type II structures. The Co promoter atoms are not involved in the formation of these linkages, as could be shown by Mössbauer spectroscopy [79,80]. Many studies have shown that catalysts with Type II structures often contain multilayer Co–Mo–S nanoclusters. In this case, only the layers close to the support may be bound to the latter by linkages, whereas the other layers only interact weakly by van der Waals forces and thus exhibit Type II-like activity. One way to avoid the Type I linkages is to increase the sulfidation temperature, but this has a number of unwanted side effects, e.g. sintering and loss of surface area. A different approach is to avoid the formation of linkages altogether and form directly Type II structures, and several studies have shown that this indeed is possible e.g. by the use of chelating ligands or additives [80–82]. It has also been shown that Type II structures may dominate when employing weakly interacting supports as e.g. carbon [1].

Table 1
The investigated structures for the position of oxygen linkages and the corresponding energies (in kJ/mol) for the creation of linkages

Position of OH group	Linkages every row (kJ/mol)	Linkages every sec. row (kJ/mol)
Outer row at Mo edge	0	0
Second row at Mo edge	89	25
Second row at S edge	52	7
Outer row at S edge	−152	−63

Linkages at the outer row of the Mo-edge are taken as the reference energy. Adapted from Ref. [42].

It is of significant interest to understand these support effects in detail, and theoretical modelling with density functional theory has been of great use to investigate these aspects. A few earlier [40,41] and several recent studies [43,44] have investigated support effects by modelling promoted and unpromoted MoS_2-based cluster structures on different facets of γ-Al_2O_3, and in the latter studies different adsorption geometries and configurations were mapped out in great detail. Such investigations are complicated further by the fact that the precise location of non-spinel sites in γ-Al_2O_3 is not completely known and still under discussion [83–87].

In a recent study [42], we have investigated a simplified system, where we modelled the linkages by hydroxyl groups,

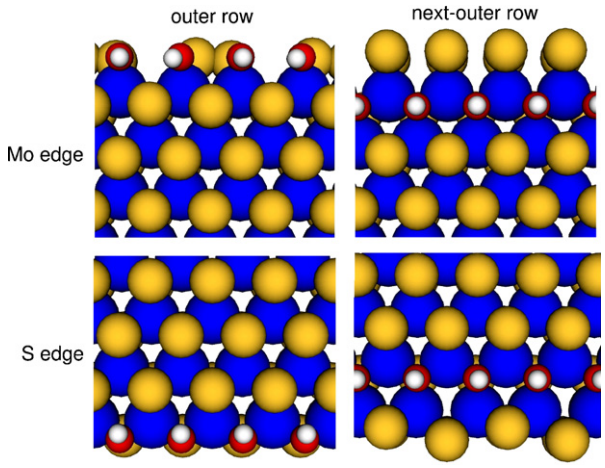

Fig. 3. The investigated structures for the position of oxygen linkages. The corresponding energies are listed in Table 1. Color code of the atoms: sulfur (yellow), molybdenum (blue), oxygen (red), hydrogen (white). Adapted from Ref. [42]. (For interpretation of the references to colour in this figure legend, the reader is referred to the web version of the article.)

concentrating exclusively on the chemical impact of support linkages without considering steric issues. We found that linkages have a thermodynamic preference for the S-edge, as illustrated in Table 1 and Fig. 3. Furthermore, vacancy formation, both at the linkage sites themselves and in the immediate vicinity, is energetically much more expensive and therefore not favoured. We also found that the electronic structure of the linkage sites as well as hydrogen adsorption differs significantly from that of the S-edge without linkages. These findings could explain several experimental observations: In previous high temperature sulfidation studies [16,79] it was found that the temperature at which the support linkages can be broken, i.e., the Type I to Type II transition temperature, depends on the Co loading. For low Co content, the Type I to Type II transition takes place at a higher temperature than for high Co content, and for unpromoted MoS_2, the transition was not observed at all in the employed temperature region. Combining our results with the results that Co primarily is located at the S-edge (see previous section), these results are easy to understand: Linkages and Co are likely not located at the same site, and therefore at high Co content (or higher coverage of the S-edge by Co), there are fewer linkages that have to be broken and thus the transition temperature is lower. In some systems, the transition occurred at the temperature at which edge saturation had occurred. This simplified support interaction model thus allowed us to gain some insight into important phenomena which had remained unexplained for two decades. The results also showed that the linkages may also significantly influence the brim sites which play an important role in the catalysis (see Section 4).

The choice of substrate can be, as discussed above, used as a means of influencing catalyst structure and properties, and in this regard, graphite is highly interesting since Type II structures are formed [88] and indeed, carbon-supported MoS_2-based hydrotreating catalysts exhibit a very high HDS reactivity [88,18,89,90]. This motivation has recently led us to apply STM to investigate the atomic-scale structure and morphology of MoS_2 nanoclusters synthesized on a graphite (HOPG) substrate [25]. Due to a very weak bonding and high mobility of Mo to the graphite it was not possible to synthesize highly dispersed MoS_2 clusters on the clean single crystal HOPG surface. Instead, a HOPG substrate, pretreated by ion bombardment, was used since this created a low density of surface defects capable of stabilizing well-dispersed nanoclusters. Not surprisingly, both the crystallinity, morphology, and stacking of the MoS_2 nanostructures were found to be dependent on the subsequent annealing temperature. Clusters synthesized at 1000 K consist predominantly of a single S–Mo–S layer, whereas the clusters synthesized at 1200 K exclusively grow as stacked multilayer clusters containing typically 2–6 S–Mo–S layers. Atom-resolved STM images of both the single- and multilayer clusters reveal a well ordered MoS_2 basal plane structure in the interior consisting of hexagonally arranged protrusions with an average interatomic spacing of 3.15 Å, in perfect agreement with the interatomic spacing of the S atoms in the (0 0 0 1) basal plane of bulk MoS_2.

The preferential shape of small single-layer MoS_2 nanoclusters is observed to be hexagonal (see Fig. 4). However, the morphology of large single-layer clusters is significantly more complex due to pinning of the cluster edges to defects. Such effects were also observed by HAADF-STEM [22–24]. The interface structure between the S–Mo–S layer and the HOPG is obtained in atomic detail in the STM images of the single-layer clusters. In this way it was possible to pinpoint the anchoring sites of the MoS_2 nanoclusters as surface defects preferentially located directly underneath the nanoclusters edges and not the basal plane.

The multilayer clusters are also predominantly shaped as hexagons (See Fig. 4b). This is not surprising since adjacent layers, in the 2H stacking commonly encountered in bulk MoS_2, are translated and rotated 60° around the *c*-axis. The result is that Mo atoms in one layer are placed on top of S atoms in the next layer and a multilayer cluster will therefore expose Mo edges and S edges in an alternation fashion, and any difference in edge free energy thus tends to cancel out.

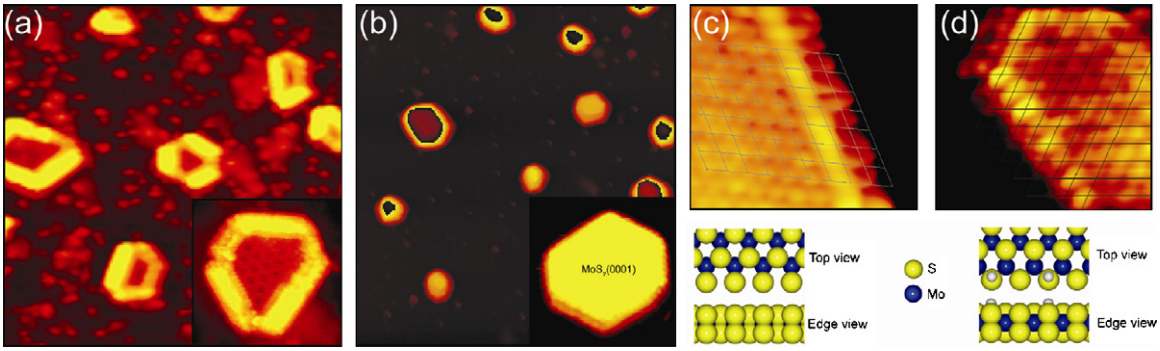

Fig. 4. (a) STM image (430 Å × 430 Å, I_t = 0.23 nA and V_t = −1250 mV) of single-layer MoS_2 nanoclusters on HOPG. The insert shows a zoom-in on a cluster (b) STM image (1000 Å × 1000 Å, I_t = 0.19 nA and V_t = −1250 mV) of multilayer MoS_2 nanoclusters on HOPG. The insert shows a zoom-in on a cluster clearly showing the hexagonal shape. (c) Top: Atom-resolved STM image (36 Å × 35 Å, I_t = 0.23 nA and V_t = −7.9 mV) showing the atomic-scale structure of the $(1\,0\,\bar{1}\,0)$ Mo-edge on a multilayer cluster. The superimposed grid on the basal plane sulfur atoms shows that protrusions at the edge are out of registry. Bottom: A ball model (top and side view, respectively) of the Mo-edge fully saturated with sulfur dimers corresponding to the experiment. (d) Top: Atom-resolved STM image (41 Å × 37 Å, I_t = 0.19 nA and V_t = 0.6 mV) of the $(\bar{1}\,0\,1\,0)$ S-edge. The grid shows that protrusions on the S-edge are imaged in registry. Bottom: A ball model of the fully sulfided S-edge and with a fractional coverage of S–H groups representing the experimental image of the S-edge (Mo: blue; S: yellow; H: gray). Adapted from Ref. [25]. (For interpretation of the references to colour in this figure legend, the reader is referred to the web version of the article.)

The top layer of the multilayer clusters is not perturbed by the defects in the HOPG and can thus be used to obtain interesting atom-resolved information. One of the two edge types has the outermost row of protrusions out of registry with the basal plane S atoms and a clear bright brim along the edge (Fig. 4c). This type of edge is thus completely identical to the edges observed for the unpromoted MoS_2 triangles [19] and this type of edge is therefore identified as a Mo edge fully saturated with sulfur dimers. Importantly, the atom-resolved STM images provide solid evidence for one-dimensional metallic brim sites on the graphite-supported MoS_2, which as discussed further in Section 4 play an important role in the catalytic properties of single-layer MoS_2 [31,32]. Thus the brim sites are not special for the gold supported systems but likely to be an important feature of all MoS_2- and WS_2-based catalysts on different supports.

The other type of edge must according to the symmetry be a S edge (Fig. 4d). This type of edge was not previously observed under the same sulfiding conditions for the Au supported system, since only Mo edges are exposed for the single layer MoS_2 triangles under such conditions [19]. However, the appearance of the edge with the outermost row of protrusions in registry with the basal plane S atom and clearly resolved protrusions along the brim resembles the S edges imaged for hexagonal MoS_2 clusters synthesized in a mixture of H_2 and H_2S [33]. The S edges formed under these conditions are fully sulfided with hydrogen adsorbed in the form of S–H groups [34,38,91,33]. The similarities suggest that the multilayer clusters also expose this kind of S edges and it thus seems plausible that the intensity variation observed along the brim (Fig. 2d) is due to a partial hydrogen adsorption. The observation of hydrogen adsorbates at the clusters edges is highly interesting from a catalytic point of view, since both adsorption of the S-containing molecule and dissociation of H_2 are required to facilitate the HDS reaction, as will be discussed further in the following section.

4. Hydrogenation and direct desulfurization reaction routes

As discussed in Section 2, STM images have clearly revealed that MoS_2, Co–Mo–S, and Ni–Mo–S expose bright brims at the edges [19,20,21]. Using DFT, these brims have been shown to be the result of one or more metallic edge states [30,38]. Combined STM and DFT studies have investigated thiophene HDS over MoS_2 particles at STM conditions, and it was found that fully sulfided MoS_2 particles which have a bright brim are able to hydrogenate thiophene and make 2,5-dihydrothiophene. Furthermore, it is important to note that at these sites one is also able to break one S–C bond and thereby produce *cis*-2-butenethiolate [31,32]. These studies indicate that brims can play a role in hydrogenation reactions and also in S–C scission reactions. Contrary to the general view in the previous literature, the results show that S–C scission may occur without the involvement of vacancies.

In a recent DFT study [45], we have further investigated the HDS reactions of thiophene over MoS_2. In order to make the studies of direct relevance for actual HDS, we have as starting point used the edge configurations corresponding to actual HDS conditions. The study clearly shows that there may be several HYD and DDS pathways on the $(1\,0\,\bar{1}\,0)$ Mo and the $(\bar{1}\,0\,10)$ S edges. The structure of MoS_2 is very dependent on reaction conditions [34–39] and the structure at HDS conditions (seen in Fig. 5) may therefore be quite different from that present at vacuum conditions for STM imaging. However, it was found that the brim sites consisting of metallic edge states are also present at HDS conditions [38].

The reaction scheme obtained from our DFT study is depicted in Fig. 5. In general, we find that the active site at the S edge is most likely a vacancy site whereas the active site at the Mo edge is a brim site and not a coordinatively unsaturated site [45]. It is important to note that the brim sites are present at the equilibrium edge configuration under HDS conditions, while

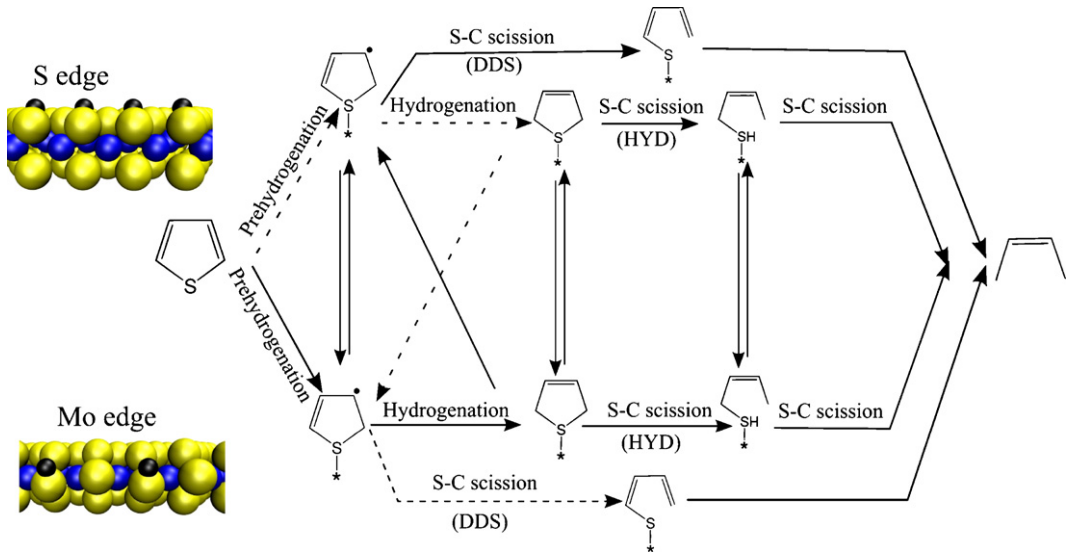

Fig. 5. Schematic overview of HDS of thiophene. Upper part: The equilibrium structure at HDS conditions at the S edge and the possible reactions occurring at the S edge. Lower part: The equilibrium structure at HDS conditions at the Mo edge and the possible reactions occurring at the Mo edge. The dotted lines represent slow reactions. Adapted from Ref. [45].

the S edge vacancy site first needs to be created from the equilibrium structure. For this creation of the vacancy site, it was found that the effective energy barrier for vacancy formation depends on the hydrogen pressure. Investigating the HYD pathway it was found that hydrogenation and H transfer steps have lower barriers at the Mo edge brim site than at the S edge vacancy sites. In contrast, the S–C scission reactions have lower barriers at the S edge. Furthermore, thiophene prefers to be adsorbed at the Mo edge while the intermediates prefer to adsorb at the S edge vacancy site.

The investigated HYD pathway proceeds via thiophene adsorption, followed by hydrogenation to 2-hydrothiophene, and further hydrogenation to 2,5-dihydrothiophene and then subsequent S–C scission. The DDS pathway is initiated by hydrogenation to 2-hydrothiophene which is then immediately followed by S–C scission. The relative importance of the S edge and the Mo edge in HDS of thiophene was found to depend on reaction conditions and the different possible reaction pathways have been summarized in Fig. 5. The HYD pathway may occur at the Mo edge brim site without involving a coordinative unsaturated site as seen in Fig. 5. Therefore, the Mo edge brim site is able to both hydrogenate thiophene and break S–C bonds. The HYD pathway may also proceed via prehydrogenation and hydrogenation at the Mo edge brim site, diffusion to the S edge and then S–C scission at the S edge vacancy site. The S–C scission reactions have lower barriers at the S edge and the intermediates bind more strongly but the number of active sites is much lower since vacancies need to be created prior to reaction. The edge interaction between the Mo edge and the S edge will probably be of importance at high hydrogen pressures or low H_2S pressures where the vacancy coverage at the S edge is significant. The S edge vacancy site was also found to be the primary site for the S–C scission in the DDS pathway. The crucial step is for both the HYD and the DDS pathway proposed to be the active site regeneration. It was therefore proposed that an activity descriptor could be the minimum energy required to either add or remove S from the equilibrium edge structures.

The identification of the Mo edge brim site as the hydrogenation site explains the low inhibiting effect of H_2S on hydrogenation as found in many studies [1,92], since H_2S does not bind to the fully coordinated brim sites. Inhibition of HDS by nitrogen-containing compounds is of central importance in practical HDS of many feedstocks [1,8,93]. In particular, it has been shown that basic heterocyclic compounds as e.g. pyridine primarily inhibit the HYD pathway of the HDS reaction [94,95]. This is especially important, as there is an increasing demand for deep desulfurization, where sterically hindered alkyl substituted molecules like 4,6-DMDBT have to be desulfurized. In these molecules, access to the sulfur is sterically hindered and HDS of the pure component proceeds primarily via the HYD route [3], and thus there is an interest to avoid inhibition of especially this route. Furthermore, understanding of inhibition, by e.g. pyridine, offers the opportunity to gain further insight into where the reactive sites are located. For non-sterically hindered heterocyclic compounds with nitrogen in a six-membered ring, as for instance pyridine, it has been observed that the inhibitor strength and the gas phase proton activities are correlated [12,96]. Aromatic hydrocarbons, e.g. benzene also primarily inhibit the HYD route, but their effect is much weaker than for e.g. pyridine.

In a recent study [97], we investigated the effects of the three different inhibitors pyridine, benzene and H_2S. We found that pyridine itself only adsorbs weakly on the Mo edge, but in the presence of hydrogen under HDS conditions, pyridine becomes protonated. The resulting pyridinium ion adsorbs strongly on the Mo-edge and forms a chemical bond to the surface, as shown in Fig. 6. It should be noted that the pyridinium ion interacts with the special brim sites that, as discussed above, also are involved in the HYD reaction [30]. Interestingly, it was found that protonation of pyridine does not take place at the S edge, as hydrogen itself is too strongly bound to this edge and thus not available. Benzene and H_2S only bind weakly to both edges, which explains why their inhibition effect is much lower than pyridine. These results also point to the Mo edge primarily

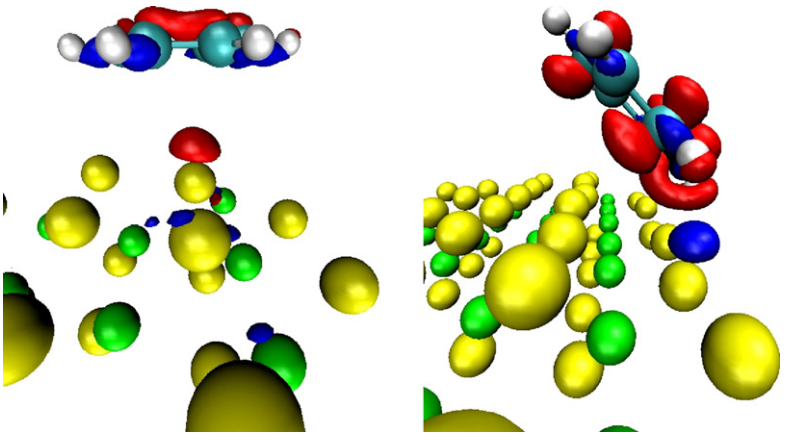

Fig. 6. Electron density difference plot of benzene (left) and pyridinium (right) on the Mo-edge. Note that in the pyridinium (left) plot, a proton has been transferred from the Mo-edge to the pyridine molecule to form a pyridinium ion. Color code: Depletion of electron density (red) plotted at a contour value of −0.03 eV/Å^3 and increase of electron density (blue) plotted at a contour value of +0.03 eV/Å^3. Color code of the atoms: sulfur (yellow), molybdenum (green), nitrogen (black), carbon (blue), hydrogen (white). Adapted from Ref. [97]. (For interpretation of the references to colour in this figure legend, the reader is referred to the web version of the article.)

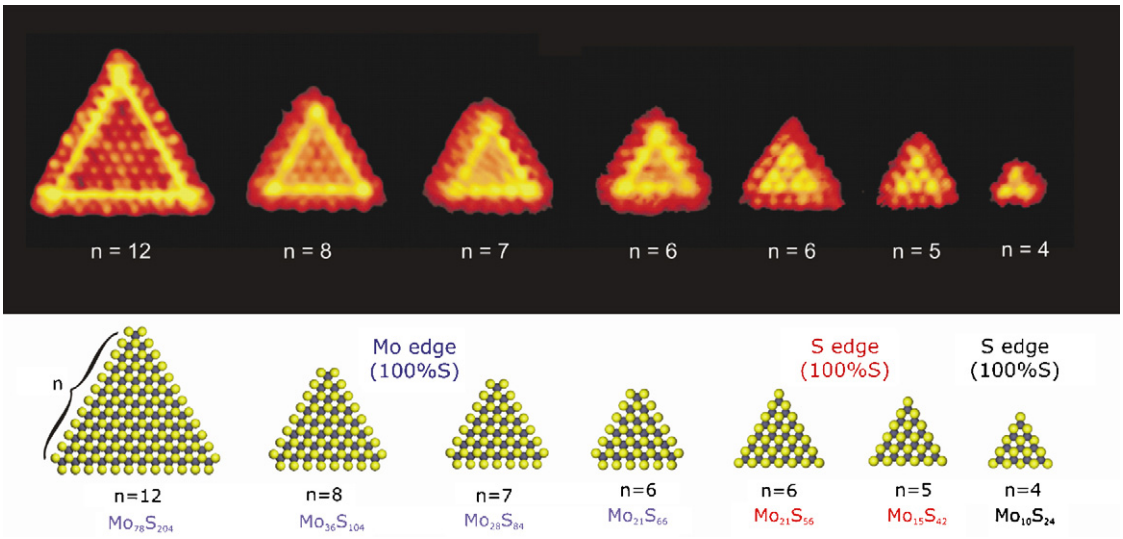

Fig. 7. STM images illustrating the structural progression of single-layer MoS_2 nanocrystals as a function of size. Upper part: STM images of cluster with varying size, where n denotes the number of Mo atoms on the cluster edge. Lower part: Ball models (top view) associated with the MoS_2 triangles observed by STM and the corresponding cluster composition Mo_XS_Y (Mo: blue; S: yellow). Adapted from [26]. (For interpretation of the references to colour in this figure legend, the reader is referred to the web version of the article.)

being the active site for the HYD pathway, and the results support that the brim sites seem to play a special role.

5. Size effects

It is well-known that materials scaled down to particles in the nanometer regime may adopt new and interesting structural and electronic properties that are significantly different from those observed in bulk systems [98]. Numerous studies have shown that this also may lead to unique catalytic properties. For example, catalysts based on gold nanoparticles supported on a metal oxide have indeed been shown to exhibit interesting size-dependent activities for low temperature oxidation reactions [99]. In a ''nanocatalysis'' context this is often highlighted as a prototype system since bulk gold is noble and catalytically inert. We have recently revealed that very strong structure-size effects also exist for MoS_2 nanoclusters catalysts, and such effects are expected to influence the hydrogenation and hydrodesulfurization activities of MoS_2 nanoclusters in this size regime [26]. Fig. 7 shows a series of atom-resolved STM images of seven single-layer MoS_2 nanoclusters with varying size. It should be noted that all clusters with the same size exhibit similar images. The large variation in the images of different size clusters demonstrates that for each cluster size there appears to be a ''unique'' minimum energy structure. The STM images also provide information on how the electronic structure like the brim sites vary with changing cluster size, and the results clearly show that the smallest clusters do not possess extended metallic states. The four largest clusters all adopt the structure described in Section 2 and in the previous studies [19,30], and these clusters are terminated by fully sulfided Mo edges. For the triangular clusters with less than six Mo atoms on the edge ($n \leq 6$), the edge structure appears differently and also the appearance of the interior of the cluster becomes brighter and different from that of normal basal planes. In Ref. [26], the structural changes were suggested to be caused by a rearrangement of the cluster edges in response to an increase of the S:Mo ratio for the smallest nanoclusters. Even in the fairly large nanoclusters ($n = 8$), a large ''excess'' of sulfur exists (S:Mo ≈ 2.89 for $n = 8$). If the edge structure remains constant, smaller clusters would have S:Mo ratios greater than three. In Ref. [26], it was noted that the large excess of sulfur can be avoided by exposing different edges (see ball models in Fig. 7). Thus, it was suggested in Ref. [26] that below a given cluster size a complete inversion of the edge structure may take place. Furthermore, for very small clusters ($n \leq 4$) indications for spontaneous formation of sulfur vacancies were noted [26] and the edge structure may be described as a ~75% S covered S edge. Importantly, this scenario illustrates that the bonding energy of sulfur in the clusters and thus the tendency to form the catalytically important sulfur vacancies on the cluster edges could exhibit a significant variation with cluster size. A detailed analysis of the images and a deconvolution of the structural and electronic effects await a full DFT-STM study. Nevertheless, even without a detailed interpretation, the present results clearly show that small MoS_2 clusters have interesting new structural and electronic properties. In view of the discussion in the previous sections, such clusters will undoubtedly also exhibit novel and very different catalytic properties and it will be an interesting challenge to prepare and investigate systems containing such clusters with well-defined sizes.

6. Conclusions and outlook

Using a combination of novel experimental and theoretical techniques like STM, DFT and HAADF-STEM, we have recently gained further insight into structure, support, size and reactivity effects in hydrotreating catalysis. One picture which emerges from these studies is the important concept of the special ''brim sites'', which we have shown to exhibit catalytic

activity for hydrogenation reactions. This is quite contrary to the common belief that vacancy sites are the key active sites, since the brim sites are not coordinatively unsaturated sites. Nevertheless, the emerging picture is shown to be consistent with many inhibition steric and poisoning effects which have been difficult to interpret using a ''vacancy model''. DFT calculations have helped us gain detailed insight into the HDS of thiophene under industrial conditions, and it is suggested that the hydrogenation reactions take place on the brim sites, whereas the sulfur removal can take place at both edges. Furthermore, the results reveal how the promoters Co and Ni change the morphology of the nanoparticles, and recently several novel forms of the Ni–Mo–S and Co–Mo–S type structures have been observed. Using STM, also unique size dependent structures of MoS_2 have been observed and these changes also result in significant variations in the electronic structure of the clusters. In the future, the new experimental and theoretical tools should be able to provide further insight into the structure sensitivity and size effects and the studies should be able to reveal how structural and morphological changes give rise to changes in the catalytic activity.

References

[1] H. Topsøe, B.S. Clausen, F.E. Massoth, in: J.R. Anderson, M. Boudart (Eds.), Hydrotreating Catalysis—Science and Technology, vol. 11, Springer Verlag, Berlin, 1996.
[2] M.V. Landau, Catal. Today 36 (1997) 393.
[3] B.C. Gates, H. Topsøe, Polyhedron 16 (1997) 3213.
[4] D.D. Whitehurst, T. Isoda, I. Mochida, Adv. Catal. 42 (1998) 345.
[5] K.G. Knudsen, B.C. Cooper, H. Topsøe, Appl. Catal. A 189 (1999) 205.
[6] T. Kabe, A. Ishihara, W. Qian, Hydrodesulfurization and Hydrogenation, Chemistry and Engineering, Wiley-CH, Kodanska, 1999.
[7] S.F. Venner, Hydrocarbon Process. 79 (2000) 51.
[8] C. Song, Catal. Today 86 (2003) 211.
[9] I.V. Babich, J.A. Moulijn, Fuel 82 (2003) 607.
[10] M. Breysse, G. Diega-Mariadassou, S. Pessayre, C. Geantet, M. Vrinat, G. Perot, M. Lemaire, Catal. Today 84 (2003) 129.
[11] M. Nagai, T. Kabe, J. Catal. 81 (1983) 440.
[12] V. LaVopa, C.N. Satterfield, J. Catal. 110 (1988) 375.
[13] P. Zeuthen, K.G. Knudsen, D.D. Whitehurst, Catal. Today 65 (2001) 307.
[14] H. Topsøe, B.S. Clausen, R. Candia, C. Wivel, S. Mørup, J. Catal. 68 (1981) 433.
[15] C. Wivel, R. Candia, B.S. Clausen, S. Mørup, H. Topsøe, J. Catal. 68 (1981) 453.
[16] B.S. Clausen, H. Topsøe, R. Candia, J. Villadsen, B. Lengeler, J. Als-Nielsen, F. Christensen, J. Phys. Chem. 85 (1981) 3868.
[17] N.-Y. Topsøe, H. Topsøe, J. Catal. 84 (1983) 386.
[18] M. Breysse, B.A. Bennett, D. Chadwick, M. Vrinat, Bull. Soc. Chim. Belg. 90 (1981) 1271.
[19] S. Helveg, J.V. Lauritsen, E. Lægsgaard, I. Stensgaard, J.K. Nørskov, B.S. Clausen, H. Topsøe, F. Besenbacher, Phys. Rev. Lett. 84 (2000) 951.
[20] J.V. Lauritsen, S. Helveg, E. Lægsgaard, I. Stensgaard, B.S. Clausen, H. Topsøe, F. Besenbacher, J. Catal. 197 (2001) 1.
[21] J.V. Lauritsen, J. Kibsgaard, G.H. Olesen, P.G. Moses, B. Hinnemann, S. Helveg, J.K. Nørskov, B.S. Clausen, H. Topsøe, E. Lægsgaard, F. Besenbacher, J. Catal. 249 (2007) 220.
[22] A. Carlsson, M. Brorson, H. Topsøe, J. Catal. 227 (2004) 530.
[23] A. Carlsson, M. Brorson, H. Topsøe, J. Microsc. 223 (2006) 179.
[24] M. Brorson, A. Carlsson, H. Topsøe, Catal. Today 123 (2007) 31.
[25] J. Kibsgaard, J.V. Lauritsen, E. Lægsgaard, B.S. Clausen, H. Topsøe, F. Besenbacher, J. Am. Chem. Soc. 128 (2006) 13950.
[26] J.V. Lauritsen, J. Kibsgaard, S. Helveg, H. Topsøe, B.S. Clausen, F. Besenbacher, Nat. Nanotechnology 2 (2007) 53.
[27] L.S. Byskov, B. Hammer, J.K. Nørskov, B.S. Clausen, H. Topsøe, Catal. Lett. 47 (1997) 177.
[28] L.S. Byskov, J.K. Nørskov, B.S. Clausen, H. Topsøe, J. Catal. 187 (1999) 109.
[29] L.S. Byskov, J.K. Nørskov, B.S. Clausen, H. Topsøe, Catal. Lett. 64 (2000) 95.
[30] M.V. Bollinger, J.V. Lauritsen, K.W. Jacobsen, J.K. Nørskov, S. Helveg, F. Besenbacher, Phys. Rev. Lett. 87 (2001) 196803.
[31] J.V. Lauritsen, M. Nyberg, R.T. Vang, M.V. Bollinger, B.S. Clausen, H. Topsøe, K.W. Jacobsen, E. Lægsgaard, J.K. Nørskov, F. Besenbacher, Nanotechnology 14 (2003) 385.
[32] J.V. Lauritsen, M. Nyberg, J.K. Nørskov, B.S. Clausen, H. Topsøe, E. Lægsgaard, F. Besenbacher, J. Catal. 224 (2004) 94.
[33] J.V. Lauritsen, M.V. Bollinger, E. Lægsgaard, K.W. Jacobsen, J.K. Nørskov, B.S. Clausen, H. Topsøe, F. Besenbacher, J. Catal. 221 (2004) 510.
[34] P. Raybaud, J. Hafner, G. Kresse, S. Kasztelan, H. Toulhoat, J. Catal 189 (2000) 129.
[35] P. Raybaud, J. Hafner, G. Kresse, S. Kasztelan, H. Toulhoat, J. Catal. 190 (2000) 128.
[36] H. Schweiger, P. Raybaud, H. Toulhoat, J. Catal. 212 (2002) 33.
[37] S. Cristol, J.-F. Paul, E. Payen, D. Bougeard, S. Clémendot, F. Hutschka, J. Phys. Chem. B 104 (2000) 11220.
[38] M.V. Bollinger, K.W. Jacobsen, J.K. Nørskov, Phys. Rev. B 67 (2003) 085410.
[39] M.Y. Sun, A.E. Nelson, J. Adjaye, J. Catal. 233 (2005) 411.
[40] P. Faye, E. Payen, A. Datta, J. Catal. 179 (1998) 560.
[41] A. Ionescu, A. Allouche, A.-P. Aycard, M. Rajzmann, R. LeGall, J. Phys. Chem. B 107 (2003) 8490.
[42] B. Hinnemann, J.K. Nørskov, H. Topsøe, J. Phys. Chem. B 109 (2005) 2245.
[43] C. Arrouvel, M. Breysse, H. Toulhoat, P. Raybaud, J. Catal. 232 (2005) 161.
[44] D. Costa, C. Arrouvel, M. Breysse, H. Toulhoat, P. Raybaud, J. Catal. 246 (2007) 325.
[45] P.G. Moses, B. Hinnemann, H. Topsøe, J.K. Nørskov, J. Catal. 248 (2007) 188.
[46] P. Raybaud, J. Hafner, G. Kresse, H. Toulhoat, Stud. Surf. Sci. Catal. 127 (1999) 327 (Hydrotreatment and Hydrocracking of Oil Fractions).
[47] S. Cristol, J.-F. Paul, E. Payen, D. Bougeard, J. Hafner, F. Hutschka, Stud. Surf. Sci. Catal. 127 (1999) 327 (Hydrotreatment and Hydrocracking of Oil Fractions).
[48] S. Cristol, J.-F. Paul, E. Payen, D. Bougeard, F. Hutschka, S. Clemendot, J. Catal. 224 (2004) 138.
[49] T. Todorova, R. Prins, T. Weber, J. Catal. 236 (2005) 190.
[50] R.R. Chianelli, M. Daage, M.J. Ledoux, Adv. Catal. 40 (1994) 177.
[51] M.W.J. Craje, S.P.A. Louwers, V.H.J. de Beer, R. Prins, A.M. van der Kraan, J. Phys. Chem. 96 (1992) 5445.
[52] A.M. de Jong, V.H.J. de Beer, J.A.R. van Veen, J.W. Niemantsverdriet, J. Vac. Sci. Tech. A 15 (1997) 1592.
[53] R.G. Leliveld, A.J. van Dillen, J.W. Geus, D.C. Koningsberger, J. Catal. 175 (1998) 108.
[54] R. Prins, V.H.J. de Beer, G.A. Somorjai, Catal. Rev. Sci. Eng. 31 (1989) 1.
[55] R. Prins, Adv. Catal. 46 (2002) 399.
[56] B.S. Clausen, B. Lengeler, R. Candia, J. Als-Nielsen, H. Topsøe, Bull. Soc. Chim. Belg. 90 (1981) 1249.
[57] J.T. Miller, C.L. Marshall, A.J. Kropf, J. Catal. 202 (2001) 89.
[58] J.V. Sanders, Phys. Scr. 14 (1978–1979) 141.
[59] J.M. Thomas, G.R. Millward, L.A. Bursell, Philos. Trans. R. Soc. A 300 (1981) 43.
[60] R. Candia, O. Sørensen, J. Villadsen, N.-Y. Topsøe, B.S. Clausen, H. Topsøe, Bull. Soc. Chem. Belg. 93 (1984) 763.
[61] F. Delannay, Appl. Catal. 16 (1985) 135.
[62] T.F. Hayden, J.A. Dumesic, J. Catal. 103 (1987) 366.
[63] J. Ramirez, S. Fuentes, G. Diaz, M. Vrinat, M. Breysse, M. Lacroix, Appl. Catal. 52 (1989) 6501.

[64] E. Payen, S. Kasztelan, S. Houssenbay, R. Szymanski, J. Grimblot, J. Phys. Chem. 93 (1989) 6501.
[65] S. Srinivasan, A.K. Datye, C.H.F. Peden, J. Catal. 137 (1992) 513.
[66] S. Eijsbouts, J.J.L. Heinerman, H.J.W. Elzerman, Appl. Catal. A 105 (1993) 53.
[67] P.L. Hansen, H. Topsøe, J.O. Halm, in: Proceedings of the 13th International Conference on Electron Microscopy, vol. 2B, Paris, (1994), p. 1077.
[68] R.M. Stockmann, H.W. Zandbergen, A.D. van Langeveld, J.A. Moulijn, J. Mol. Catal. A 102 (1995) 147.
[69] S. Eijsbouts, Appl. Catal. A 158 (1997) 53.
[70] Y. Sakushita, T. Yoneda, J. Catal. 185 (1999) 487.
[71] H.R. Reinhoudt, A.D. van Langeveld, P.J. Kooyman, R.M. Stockmann, R. Prins, H.W. Zandbergen, J.A. Moulijn, J. Catal. 179 (1998) 443.
[72] P.J. Kooyman, E.J.M. Hensen, A.M. de Jong, J.W. Niemantsverdriet, J.A.R. van Veen, Catal. Lett. 74 (2001) 49.
[73] R. Candia, J. Villadsen, N.-Y. Topsøe, B.S. Clausen, H. Topsøe, Bull. Soc. Chim. Belg. 93 (1984) 763.
[74] R.G. Leliveld, A.J. van Dillen, J.W. Geus, D.C. Koningsberger, J. Catal. 165 (1997) 184.
[75] N.-Y. Topsøe, H. Topsøe, J. Catal. 139 (1993) 631.
[76] E.G. Derouane, E. Pedersen, B.S. Clausen, Z. Gabelica, R. Candia, H. Topsøe, J. Catal. 99 (1986) 253.
[77] E.J.M. Hensen, V.H.J. De Beer, J.A.R. van Veen, R.A. van Santen, Catal. Lett. 84 (2002) 59.
[78] E. Diemann, Th. Weber, A. Müller, J. Catal. 148 (1994) 288.
[79] H. Topsøe, R. Candia, N.-Y. Topsøe, B.S. Clausen, Bull. Soc. Chim. Belg. 93 (1984) 783.
[80] J.A.R. van Veen, E. Gerkema, A.M. van der Kraan, A. Knoester, J. Chem. Soc. Chem. Commun. (1987) 1684.
[81] L. Coulier, G. Kishan, J.A.R. van Veen, J.W. Niemantsverdriet, J. Phys. Chem. B 106 (2002) 5897.
[82] M. Sun, D. Nicosia, R. Prins, Catal. Today 86 (2003) 173.
[83] X. Krokidis, P. Raybaud, A.-E. Gobichon, B. Rebours, P. Euzen, H. Toulhoat, J. Phys. Chem. B 105 (2001) 5121.
[84] C. Wolverton, K.C. Hass, Phys. Rev. B 63 (2001) 024102.
[85] G. Paglia, A.L. Rohl, C.E. Buckley, J.D. Gale, Phys. Rev. B 71 (2005) 224115.
[86] M. Digne, P. Sautet, P. Raybaud, P. Euzen, H. Toulhoat, J. Catal. 211 (2002) 1.
[87] M. Digne, P. Sautet, P. Raybaud, P. Euzen, H. Toulhoat, J. Catal. 226 (2004) 54.
[88] H. Topsøe, B.S. Clausen, Catal. Rev. Sci. Eng. 26 (1984) 395.
[89] J.C. Duchet, E.M. van Oers, V.H.J. de Beer, R. Prins, J. Catal. 80 (1983) 386.
[90] J.P.R. Vissers, B. Scheffer, V.H.J. de Beer, J.A. Moulijn, R. Prins, J. Catal. 105 (1987) 277.
[91] S. Cristol, J.F. Paul, E. Payen, D. Bougeard, S. Clémendot, F. Hutschka, J. Phys. Chem. B 106 (2002) 5659.
[92] M. Egorova, R. Prins, J. Catal. 225 (2004) 417.
[93] T.C. Ho, J. Catal. 219 (2003) 442.
[94] M. Egorova, R. Prins, J. Catal. 224 (2003) 278.
[95] N.-Y. Topsøe, H. Topsøe, J. Catal. 139 (1993) 641.
[96] M. Nagai, T. Sato, A. Aiba, J. Catal. 97 (1986) 52.
[97] Á. Logadóttir, P.G. Moses, B. Hinnemann, N.-Y. Topsøe, K.G. Knudsen, H. Topsøe, J.K. Nørskov, Catal. Today 111 (2006) 44.
[98] U. Heiz, U. Landman (Eds.), Nanocatalysis, Springer, Berlin, 2007.
[99] M. Valden, X. Lai, D.W. Goodman, Science 281 (1998) 1647.

Paper 7

IOP PUBLISHING JOURNAL OF PHYSICS: CONDENSED MATTER

J. Phys.: Condens. Matter **20** (2008) 064236 (8pp) doi:10.1088/0953-8984/20/6/064236

Recent density functional studies of hydrodesulfurization catalysts: insight into structure and mechanism

Berit Hinnemann[1], **Poul Georg Moses**[2] **and Jens K Nørskov**[2]

[1] Haldor Topsøe A/S, Nymøllevej 55, DK-2800 Lyngby, Denmark
[2] Department of Physics and Center for Atomic-scale Materials Design (CAMD), NanoDTU, Technical University of Denmark, DK-2800 Lyngby, Denmark

E-mail: behi@topsoe.dk

Received 17 September 2007, in final form 29 November 2007
Published 24 January 2008
Online at stacks.iop.org/JPhysCM/20/064236

Abstract

The present article will highlight some recent density functional theory (DFT) studies of hydrodesulfurization (HDS) catalysts. It will be summarized how DFT in combination with experimental studies can give a detailed picture of the structure of the active phase. Furthermore, we have used DFT to investigate the reaction pathway for thiophene HDS, and we find that the reaction entails a complex interplay of different active sites, depending on reaction conditions. An investigation of pyridine inhibition confirmed some of these results. These fundamental insights constitute a basis for rational improvement of HDS catalysts, as they have provided important structure–activity relationships.

(Some figures in this article are in colour only in the electronic version)

1. Introduction

While the global energy consumption is steadily increasing, fossil energy resources become increasingly limited. This increases the need to upgrade low-quality oil to transport fuels. At the same time, environmental restrictions become stricter. One key environmental requirement is the reduction of sulfur content in the fuel. This necessitates substantial improvements of the hydrodesulfurization (HDS) catalysts, which remove sulfur-containing compounds from crude oil during the refining process [1–9]. In particular, these catalysts must now be able to remove sulfur from compounds where it is both strongly bound within an organic ring compound and possibly also sterically protected, e.g. in methylated dibenzothiophenes (DBTs).

For rational improvements of the HDS catalyst, a detailed understanding of its structure and reactivity is necessary, and this is a formidable challenge given the complexity of the catalyst over several length scales. HDS catalysts commonly consist of Co- and/or Ni-promoted MoS_2 nanostructures as active phase on a high-surface area porous support, typically γ-alumina. A complete description of this complicated system is demanding. Detailed understanding of the active phase structure under reaction conditions is required, and issues like active phase–support interactions and active phase dispersion need to be addressed. A detailed characterization and understanding of catalyst activity and reaction mechanism is complicated by the fact that a typical feedstock contains numerous sulfur-containing compounds, whose reaction mechanisms for HDS may differ. Also, inhibition of HDS by nitrogen-containing compounds, e.g. pyridine, needs to be considered, and often these compounds are first removed from the feedstock by hydrodenitrogenation (HDN).

Even though HDS catalysts have been investigated with different experimental techniques for numerous years [1], not much information about the structure of the active phase under catalytic turnover was available until the 1980s. About that time, a combination of several experimental techniques like Mössbauer spectroscopy, extended x-ray absorption fine structure (EXAFS) and infrared (IR) spectroscopy evidenced a Co–Mo–S active phase, where Co (or Ni) is incorporated into small MoS_2-like nanosized crystals [10–14]. These are present as single or stacked layers on the catalyst support. Since the development of this 'Co–Mo–S' model, numerous experimental studies have refined the structure of the active phase. In particular, scanning tunnelling microscopy (STM) has provided the first atomic-scale resolved information on the structure of unpromoted and promoted MoS_2 nanoparticles [15–17]. Recently, also high angle annular dark field scanning

transmission electron microscopy (HAADF-STEM) has given detailed structural information [18–20].

Despite all available studies, the understanding of HDS structure and reactivity and especially the development of structure–activity relationships remains a challenge. To this end, the advent of density functional theory (DFT) [21, 22] and the development of stable and precise calculational methods and software packages, such as VASP [23, 24], CASTEP [25, 26], DMol^3 [26, 27], Dacapo [28, 29], Abinit [30, 31], Wien2k [32, 33] and numerous other codes [34], provide unprecedented new opportunities for investigating the active phase structure and activity of HDS catalysts in atomic detail. Furthermore, the rapid growth of computational power allows investigation of larger and increasingly realistic model systems. First-principles techniques like DFT allow for investigation of active sites and reaction pathways on an atomic scale, and in this way they have improved our understanding of the HDS process. A particular strength of DFT and related modelling is that it enables probing of specific aspects and questions, which are often not as easily singled out in an experiment.

In this review, we will provide an overview on our DFT activities within HDS catalysis during recent years. We will start by reviewing our work on elucidating both the atomic and the electronic structure of the active phase in detail, where a combination of scanning tunnelling microscopy and density functional theory has proven very successful. We note that a number of groups have contributed significantly to the present theoretical description of the HDS reaction [35–80]. We will also give a short discussion of support effects. Finally, we will summarize our DFT efforts in understanding the HDS of thiophene and its inhibition by pyridine in atomic-scale detail. Our results suggest several activity descriptors that may be useful for designing better HDS catalysts. We will conclude the paper with a discussion on how DFT, most often in combination with experimental techniques, helps us to understand HDS catalysis.

All DFT results which are presented here have been obtained using the DFT code Dacapo [28, 29], which uses plane waves as a basis set and therefore is ideal for the study of periodic systems. The ion–electron interactions are treated by Vanderbilt ultrasoft pseudopotentials [81]. The exchange–correlation energy is included by the generalized gradient approximation (GGA) using the PW91 exchange–correlation functional [82]. From the electronic structure, it is possible to generate simulated STM images, and we have used the Tersoff–Hamann model [83] to do this. The nudged elastic band (NEB) method [84] allows for an efficient calculation of saddle points and reaction pathways.

2. Structure of MoS_2, Co–Mo–S and Ni–Mo–S

A prerequisite for HDS activity studies using theoretical models is detailed structural information about the active phase under reaction conditions. Even though the industrial catalyst consists of Co- or Ni-promoted MoS_2, it is instructive to understand the unpromoted MoS_2 phase first. As shown in figure 1, MoS_2 consists of layered hexagonal sheets as S–Mo–S

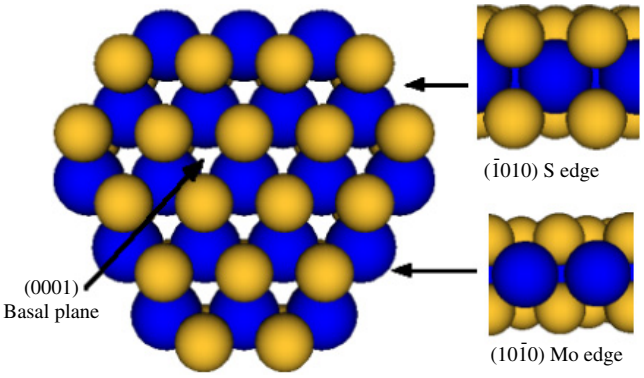

Figure 1. Structure of MoS_2 and the two low-index edge terminations. Colour code: molybdenum, dark (blue online); sulfur, light (yellow online). Note that the edge terminations are shown as truncated from the bulk, not as they are present in a specific gaseous environment.

sandwiches. In the pure compounds the sheets are stacked and held together by van der Waals forces so that MoS_2 in some aspects resembles graphite. A sheet has two low-index edge terminations, the $(10\bar{1}0)$ Mo edge and the $(\bar{1}010)$ S edge. It is well known from numerous experimental studies [1] that the basal plane of MoS_2 is inert and that only the edges exhibit catalytic activity. Thus, it is of fundamental importance to elucidate the detailed edge structure under catalytic conditions, as changing the termination and structure of the exposed edges by e.g. the addition of Co and Ni promoter atoms is one way to enhance catalyst activity.

The shape of the nanoparticle depends on the relative edge free energies according to the Wulff construction, and this determines which edges will be exposed. Furthermore, under reaction conditions, where both H_2 and H_2S are present, the edges may have sulfur, hydrogen or SH groups adsorbed, and this in turn changes the edge free energies. DFT calculations as such provide total energies for structures at $T = 0$ K and in vacuum. To calculate free energies for non-zero temperatures and in the presence of a gas of a certain pressure and composition, a grand canonical formalism including the chemical potential of hydrogen and sulfur, which in turn depend on temperature and H_2 and H_2S partial pressures, has to be employed [43, 47, 57]. This scheme has also been applied to surface thermochemistry under oxidation (see e.g. [85]) and numerous other reactions, and can be regarded as a standard method to account for a finite temperature and the presence of a reactive gas.

An important step in elucidating the structure of unpromoted MoS_2 was the investigation of a model system, where MoS_2 was deposited on Au(111) by STM [15]. The STM images, taken under sulfiding conditions, showed that the MoS_2 was present as single-layer triangular nanoparticles, i.e. only one type of edge was exposed. Subsequently, DFT was used to calculate edge free energies for both the Mo edge and the S edge with a variety of configurations, and it could be concluded that under the STM conditions the $(10\bar{1}0)$ Mo edge with adsorbed sulfur dimers is exposed [49], in line with theoretical studies by other research groups [43, 50, 60, 61, 75].

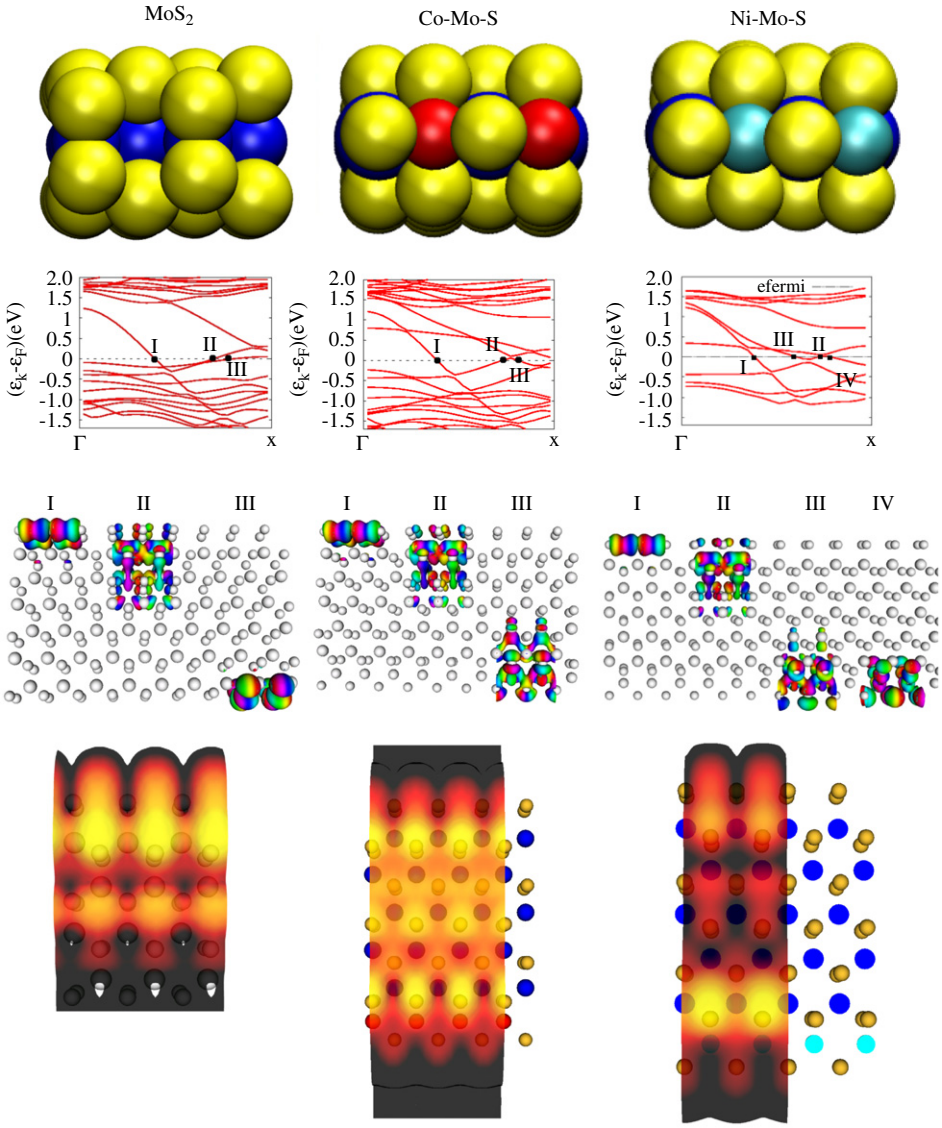

Figure 2. Calculated DFT edge structures, band structures, contour plots for the edge Kohn–Sham wavefunctions and STM simulations for MoS_2, Co–Mo–S and Ni–Mo–S structures. In the case of MoS_2 the Mo edge with sulfur dimers is shown; in the case of Co–Mo–S and Ni–Mo–S the promoted S edges with sulfur monomers are shown. For the STM plots note that for MoS_2 only the simulation for the Mo edge is depicted, whereas for Co–Mo–S and Ni–Mo–S structures the entire slab is shown. Colour code: molybdenum, blue; cobalt, red; nickel, light blue; sulfur, yellow (colours only available in the web version). Adapted from [17, 49, 57].

This edge configuration and the simulated STM image are shown in figure 2, and one can see that the protrusions in the simulated STM image actually are located between the S dimers and form a bright brim along the edge [49]. This bright brim could be understood by a detailed analysis of the electronic state at the Mo edge, and the band-structure diagram and contour plots of the relevant Kohn–Sham wavefunctions are depicted in figure 2. Bulk MoS_2 consisting of infinite sheets of S–Mo–S is semiconducting with a bandgap of about 1.2 eV [86], but the creation of edges, in this case the $(10\bar{1}0)$ Mo edge, creates electronic states around the Fermi level which have metallic character. Visualization of the Kohn–Sham wavefunction corresponding to these metallic states (figure 2) shows that they are one dimensional and localized at the edge. It should be mentioned that DFT calculations on both Au-supported and unsupported MoS_2 structures were performed, and that the metallic edge states were present in both systems and only slightly influenced by the presence of the Au support [49, 57].

It should be emphasized that a change in conditions, i.e. temperature and composition of the gas phase, especially H_2S/H_2 ratio, changes the extent to which the $(10\bar{1}0)$ Mo edge and the $(\bar{1}010)$ S edge are exposed and their respective sulfur and hydrogen coverage. Phase diagrams for edge structures over a range of temperatures and partial pressures of H_2 and H_2S have been constructed by several research groups [43, 50, 56, 57, 60, 61, 75] and it has also been shown using STM that the triangular MoS_2 particles assume hexagonal shape and their edge termination changes upon changing the gaseous atmosphere from sulfiding to reducing conditions [87].

Considering that the active phase of industrial catalysts is Co- and Ni-promoted MoS_2, it is most important to extend the detailed structural understanding to these promoted structures. According to the now well accepted Co–Mo–S model for the promoted MoS_2 hydrotreating catalysts, the Co and Ni promoter atoms are located at edge positions of MoS_2 nanostructures, which are believed to enhance catalytic activity by changing vacancy formation energies and the type and structure of the exposed edges. For the promoted structures, the approach of combining DFT with STM studies again has proven to be very insightful, and the resulting edge terminations, their simulated STM images and their electronic structure are shown in figure 2.

In the case of Co, the Co–Mo–S nanoparticles assume a hexagonal structure and expose both the $(10\bar{1}0)$ Mo edge and a Co-promoted $(\bar{1}010)$ S edge, in which Co substitutes a complete row of Mo atoms [16]. As the Mo edge remained unchanged upon the inclusion of Co, whereas the newly exposed S edge differs in appearance from the unpromoted S edge, it could be concluded that Co exclusively substituted at the S edge [17]. This assignment was in agreement with theoretical studies by other researchers [44, 51, 60, 75]. Thus, the substitution of Mo atoms by Co at the S edge changes the edge free energy such that the Co-promoted S edge is also exposed under sulfiding conditions. From the structure of the Co-promoted $(\bar{1}010)$ S edge (figure 2), one can see that the Co atoms prefer to be tetragonally coordinated to sulfur monomers.

Recently, calculations in the case of Ni-promoted MoS_2 were performed and also compared to STM images [17]. The STM images showed [17] that the case of Ni is much more complicated, as the position of the Ni seems to depend on the particle size. For large particles, Ni seems to change the MoS_2 in a similar way to Co, namely that it substitutes the outermost Mo atoms at the S edge. This results in a Ni-promoted S edge whose structure is shown in figure 2 and in which Ni is tetrahedrally coordinated to sulfur. For smaller Ni–Mo–S particles, however, Ni atoms substitute both at the Mo edge and the S edge, and it was found that higher-index edges are also exposed [17]. In particular, for Ni substitution at the metal edge, the most stable structure has Ni in a square-planar environment without any additional sulfur atoms bound to the edge, as also found previously [51, 60] and as one might expect from inorganic chemistry. In contrast to Co promotion, Ni does not seem to exhibit a clear preference for one edge over the other, and thus it can be located at one or both edges, depending on particle size. In addition, Ni was observed to cause exposure of higher-index edges [17], which is surprising considering that such edges were regarded to be too high in edge energy to be created.

Also the Co–Mo–S and Ni–Mo–S structures exhibit metallic edge states, as can be seen from their band structures and the corresponding Kohn–Sham wavefunctions depicted in figure 2. This is especially interesting in view of the fact that these metallic edge states exhibit catalytic activity for e.g. adsorption and hydrogenation of thiophene, as shown both experimentally and theoretically [88, 89]. A well established view on catalytic HDS activity is that activity mainly depends on the ability of the relevant edge structure to form vacancies, where sulfur-containing structures can adsorb and where sulfur can be removed. However, several recent studies have suggested that the brim sites also have catalytic activity under certain conditions [70, 76, 88, 89]. These aspects will be discussed in detail in section 3.

In conclusion, the combination of DFT with STM investigations and other experimental techniques has proven very powerful to elucidate the atomic-scale structure of both unpromoted and promoted MoS_2. By providing information which is directly comparable to experiments, structural models can be confirmed or disproved, and thus a very detailed understanding of structure and location and influence of the promoter atoms could be obtained.

3. Support effects

One of the central questions in HDS catalysis is how the MoS_2 active phase interacts with the support, and the most widely used and relevant support in industrial catalysis is γ-Al_2O_3. Detailed modelling of the interaction of a MoS_2 nanoparticle with the γ-Al_2O_3 surface is a formidable task, both because of the large number of atoms required in a model and because the precise location of non-spinel sites in γ-Al_2O_3 is not completely known and is still under discussion [90–95]. Several theoretical studies of the support effect of γ-Al_2O_3 have been published [66, 78, 75]. Due to the industrial importance of the Co–Mo–S/γ-Al_2O_3 system, many experimental investigations using different techniques have been carried out, and it was found that the intrinsic activity of the catalyst strongly depends on the sulfidation temperature [1]. For lower sulfidation temperatures, the intrinsic activity is considerably smaller than for higher sulfidation temperatures, and it was suggested that the lower activity was caused by the presence of some Mo–O–Al linkages between the MoS_2 and the alumina support. This Co–Mo–S structure with Mo–O–Al linkages is termed type I Co–Mo–S and the more active Co–Mo–S structure without these linkages is termed type II. Upon increase of the sulfidation temperature, the Mo–O–Al linkages are broken and the more active type II structure is obtained. Interestingly, it was observed that the amount of Co influences the transition temperature, where type II instead of type I Co–Mo–S is formed, and it was found that by increasing the amount of Co in the system the transition temperature decreases [1]. Since these factors have implications for catalyst synthesis and activity optimization, it was of particular interest to understand these trends within an atomistic model.

In a recent study [96], we have taken a very simple approach to study the influence of Mo–O–Al linkages on a MoS_2 catalyst and model the Mo–O–Al linkages by Mo–O–H groups. In this study we were mainly interested in the chemical and electronic consequences of these linkages and did not consider structural effects such as lattice mismatch or rigidity which are not included in this model.

The first question we wanted to answer was at which edge the linkages are formed, and this was investigated by placing the linkages at either the Mo edge, the S edge or at positions

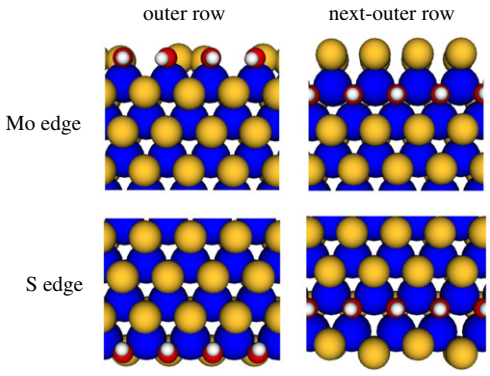

Position of OH group	linkages every row [kJ/mol]	linkages every sec. row [kJ/mol]
outer row at Mo edge	0	0
second row at Mo edge	89	25
second row at S edge	52	7
outer row at S edge	-152	-63

Figure 3. The investigated structures for the position of oxygen linkages and the corresponding energies (in kJ mol^{-1}) for the creation of linkages. Linkages at the outer row of the Mo edge are taken as the reference energy. Colour code: molybdenum, blue; sulfur, yellow; oxygen, red; hydrogen, white (colours only available in the web version). Adapted from [96].

in the next-outer rows, as shown in figure 3. Comparing the energies of the different structures, it could be concluded that the linkages will mostly form at the S edge, as they are energetically much more stable there. This result in itself is quite interesting, as it implies that the linkages are located at the same edge as Co promoter atoms are incorporated. This suggests that the more Co atoms are incorporated at the S edge, the fewer linkages are formed, and this is in accordance with the observation that the type I/type II transition temperature drops with increasing Co content. We also investigated the vacancy formation, as this is one indicator for catalytic activity, and found that it is energetically very expensive to form vacancies both at linkage sites and at the sites next to them. This effect could explain the reduced activity of type I Co–Mo–S structures, where linkages are present.

This very simple model for support linkages allowed us to understand some general trends concerning the reactivity of type I/type II catalyst. Even though the conclusions need validation using a more sophisticated model where the alumina support is included, our model proved useful in providing a framework in which to consider the effect of support linkages.

4. Reactivity and inhibition

A large number of experimental studies have investigated the kinetics of various HDS reactions and have provided insight into areas such as reaction networks, inhibition, and the influence of promoters [1, 8, 97, 98]. They made the general observation that there exist two different reaction pathways in HDS of cyclic sulfur-containing compounds. The first pathway, termed the hydrogenation pathway (HYD), is initiated by hydrogenation followed by S removal. In contrast, in the second pathway, which is termed the direct desulfurization (DDS) pathway, S is removed from the organic compound directly without prior hydrogenation. There is experimental evidence that the two pathways have different active sites [1], but so far it has not been established at which sites they take place.

It would be very relevant to elucidate the structure of the active site for hydrogenation and for desulfurization and to establish at which edges these reactions occur. The answers to these fundamental questions may have implications for catalyst design and synthesis, as it often is desirable to enhance specific properties, e.g. hydrogenation ability, of a catalyst. Knowing the nature of the active sites could provide guidance for optimizing the number of active sites. Furthermore, it would be valuable to know the elementary reaction steps that occur during HDS. Insight into the elementary reactions of HDS catalysis may also guide the development of catalysts with low hydrogen consumption and at the same time high HDS activity.

Density functional theory is well suited for answering questions about reactivity and structure and has done so for less complicated catalytic reactions, e.g. ammonia synthesis [99] or CO oxidation [85]. DFT studies on HDS by us [76, 88, 89] and other groups [36, 41, 59, 65, 75, 79] are also starting to provide detailed information on the elementary steps in the reaction pathway, and in this section some examples of how DFT has improved the insight into the reactivity of HDS catalysts are discussed.

Recently, we have performed a detailed DFT investigation of the HDS of thiophene over an unpromoted MoS_2 catalyst [76]. As a starting point for this study, it was very important to determine and use the edge structures as they are present under HDS conditions, and they differ from e.g. the edge structures under STM conditions, as discussed in the previous section. We used the phase diagrams developed previously [57], which describe the edge structure as a function of temperature and H_2 and H_2S partial pressures. It turned out that the active sites at the two edges are fundamentally different since the active site at the S edge is an undercoordinated vacancy site and the active site at the Mo edge is a so-called brim site (exhibiting a metallic edge state as discussed in the previous section), which is fully coordinated.

We then proceeded to calculate the elementary reaction barriers and intermediates for both the $(10\bar{1}0)$ Mo edge and the $(\bar{1}010)$ *S* edge. The calculations revealed that the hydrogenation steps in the HYD pathway should preferably take place at the Mo edge. However, all S–C bond scission steps, i.e. the final S–C scission step in the HYD pathway and S–C scission in the DDS pathway, seem to be more facile at the S edge, and therefore they probably take place there. The potential energy surface and intermediate structures for the HYD pathway and the DDS pathway on the S edge are shown in figure 4 and illustrate the complexity of this reaction. On a quantitative basis, these reaction pathways allow us to specify the contribution of each edge to the different reaction steps, and such investigations are in process. We emphasize that the discussed activity relations hold for

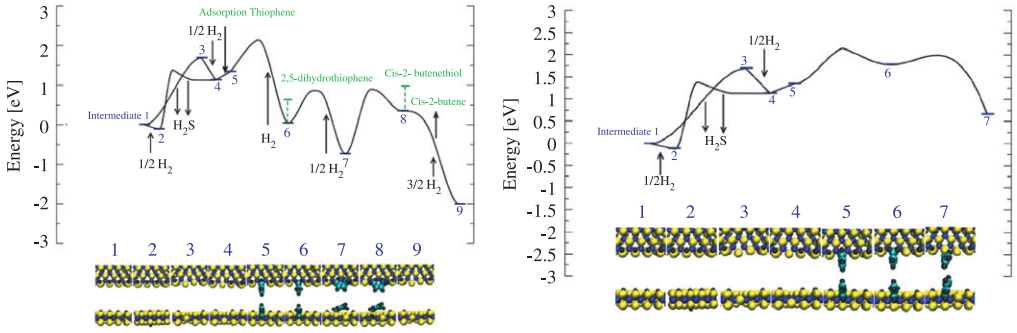

Figure 4. The hydrogenation (HYD) pathway (left) and the direct desulfurization (DDS) pathway (right) at the S edge. Colour code: molybdenum, blue; sulfur, yellow; carbon, turquoise; hydrogen, black (colours only available in the web version). Adapted from [76].

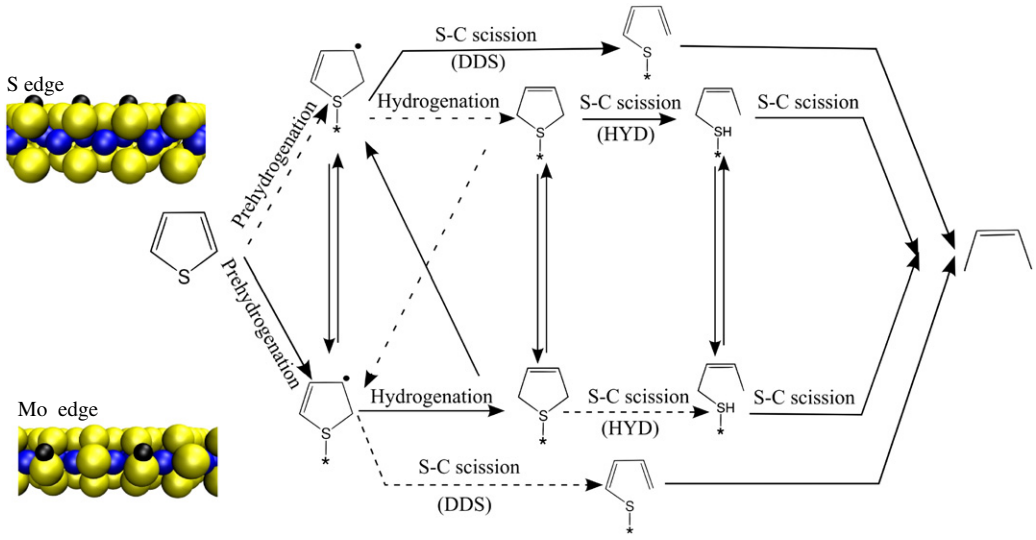

Figure 5. Schematic overview of HDS of thiophene. Upper part: the equilibrium structure at HDS conditions at the S edge and the possible reactions occurring at the S edge. Lower part: the equilibrium structure at HDS conditions at the Mo edge and the possible reactions occurring at the Mo edge. The dotted lines represent slow reactions (colour code is the same as figure 4). Adapted from [76].

unpromoted MoS_2 catalysts, and that promotion by Co and Ni introduces significant changes, as they alter both availability and structure of both edges.

The calculations provided a detailed picture of the reaction network of thiophene HDS on MoS_2, which we summarize in the schematic overview in figure 5. One important result is that the HDS reaction uses different active sites depending on the specific reaction conditions, and that the reaction is a complex interplay between Mo-edge brim sites and S-edge vacancy sites.

Another most important aspect regarding the reactivity of HDS catalyst is the mechanism of inhibition. Today, this is an increasingly important issue for catalyst manufacturers, since heterocyclic compounds inhibit the HYD pathway, which is the primary pathway for desulfurization of the most refractory species like 4,6-dimethyldibenzothiophene, which must be removed in order to fulfil present environmental regulations. The inhibition strength of nitrogen-containing heterocyclic compounds on the HYD pathway has been shown experimentally to follow the proton affinity of the nitrogen-containing compounds [100]. It has also been the subject of theoretical studies [63, 64, 70].

In a recent DFT investigation of inhibition by pyridine [70], we found that pyridine reacts with a proton at the Mo edge and forms a pyridinium ion, which binds much more strongly than pyridine itself. An electron density difference plot of the pyridinium–MoS_2 system (figure 6) shows that the pyridinium ion actually forms a chemical bond to the Mo edge. In contrast, pyridine itself and benzene only physisorb and bind weakly. This provides an explanation as to why basic compounds like pyridine can inhibit hydrogenation, whereas benzene is only a weak inhibitor. Furthermore, the formation of pyridinium ions was found only to be possible at the Mo edge, which interestingly is the edge which was identified as the primary location for hydrogenation of thiophene. This provides further evidence for the Mo edge as being the primary hydrogenation active site.

5. Conclusions and outlook

We have given an overview of our recent DFT studies of hydrodesulfurization catalysts with the aim to understand both active site structure and catalytic activity. These studies

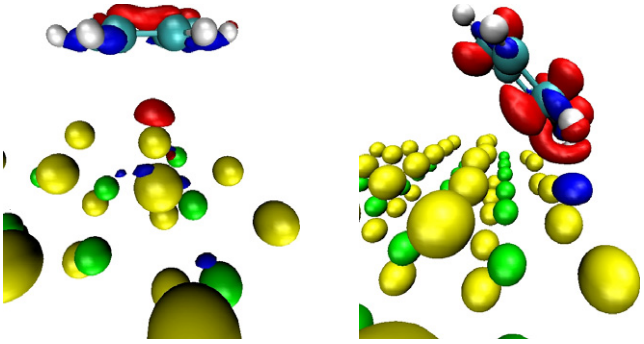

Figure 6. Electron density difference plot of benzene (left) and pyridinium (right) on the Mo edge. Note that in the pyridinium (right) plot, a proton has been transferred from the Mo edge to the pyridine molecule to form a pyridinium ion. For benzene, the depletion of electron density (red) is plotted at a contour value of -0.003 eV Å^{-3} and increase of electron density (blue) plotted at a contour value of $+0.003$ eV Å^{-3}. For pyridinium, the contour values are $+0.03$ eV Å^{-3} for electron density depletion (red) and -0.03 eV Å^{-3} for electron density increase (blue). Colour code of the atoms: sulfur, yellow; molybdenum, green; nitrogen, black; carbon, blue; hydrogen, white (colours only available in the web version). Adapted from [70].

have given us insight as to which edge structures are present under different conditions, and which sites are active for hydrogenation or sulfur extrusion reactions. For instance, by establishing the active sites for hydrogenation, one obtains information on which sites should preferentially be present in a catalyst with a high hydrogenation activity. These fundamental insights provide a basis for rational improvement of HDS catalysts.

References

[1] Topsøe H, Clausen B S and Massoth F E 1996 *Hydrotreating Catalysis—Science and Technology* vol 11, ed J R Anderson and M Boudart (Berlin: Springer)
[2] Landau M V 1997 *Catal. Today* **36** 393
[3] Gates B C and Topsøe H 1997 *Polyhedron* **16** 3213
[4] Whitehurst D D, Isoda T and Mochida I 1998 *Adv. Catal.* **42** 345
[5] Knudsen K G, Cooper B C and Topsøe H 1999 *Appl. Catal.* A **189** 205
[6] Kabe T, Ishihara A and Qian W 1999 *Hydrodesulfurization and Hydrogenation, Chemistry and Engineering* (Kodanska: Wiley–CH)
[7] Venner S F 2000 *Hydrocarb. Process.* **79** 51
[8] Song C 2003 *Catal. Today* **86** 211
[9] Babich I V and Moulijn J A 2003 *Fuel* **82** 607
[10] Topsøe H, Clausen B S, Candia R, Wivel C and Mørup S 1981 *J. Catal.* **68** 433
[11] Wivel C, Candia R, Clausen B S, Mørup S and Topsøe H 1981 *J. Catal.* **68** 453
[12] Clausen B S, Topsøe H, Candia R, Villadsen J, Lengeler B, Als-Nielsen J and Christensen F 1981 *J. Phys. Chem.* **85** 3868
[13] Topsøe N Y and Topsøe H 1983 *J. Catal.* **84** 386
[14] Breysse M, Bennett B A, Chadwick D and Vrinat M 1981 *Bull. Soc. Chim. Belg.* **90** 1271
[15] Helveg S, Lauritsen J V, Lægsgaard E, Stensgaard I, Nørskov J K, Clausen B S, Topsøe H and Besenbacher F 2000 *Phys. Rev. Lett.* **84** 951
[16] Lauritsen J V, Helveg S, Lægsgaard E, Stensgaard I, Clausen B S, Topsøe H and Besenbacher F 2001 *J. Catal.* **197** 1
[17] Lauritsen J V, Kibsgaard J, Olesen G H, Moses P G, Hinnemann B, Helveg S, Nørskov J K, Clausen B S, Topsøe H, Lægsgaard E and Besenbacher F 2007 *J. Catal.* **249** 220
[18] Carlsson A, Brorson M and Topsøe H 2004 *J. Catal.* **227** 530
[19] Carlsson A, Brorson M and Topsøe H 2006 *J. Microsc.* **233** 179
[20] Brorson M, Carlsson A and Topsøe H 2007 *Catal. Today* **123** 31
[21] Hohenberg P and Kohn W 1964 *Phys. Rev.* B **136** 864
[22] Kohn W and Sham L J 1965 *Phys. Rev.* A **140** 1133
[23] Kresse G and Furthmüller J 1996 *Comput. Mater. Sci.* **6** 15
[24] http://cms.mpi.univie.ac.at/vasp
[25] Payne M C, Teter M P, Allan D C, Arias T A and Joannopoulos J D 1992 *Rev. Mod. Phys.* **64** 1045
[26] CASTEP and DMol^3 are commercialized within the materials studio software package by Accelrys http://www.accelrys.com
[27] Delley B 2000 *J. Chem. Phys.* **113** 7756
[28] Hammer B, Hansen L B and Nørskov J K 1999 *Phys. Rev.* B **59** 7413
[29] The Dacapo code is available under the GNU general public license at http://www.camp.dtu.dk/software.aspx
[30] Gonze X, Beuken, Caracas R, Detraux F, Fuchs M, Rignanese G-M, Sindic L, Verstraete M, Zerah G, Jollet F, Torrent M, Roy A, Mikami M, Ghosez Ph, Raty J-Y and Allan D C 2002 *Comput. Mater. Sci.* **25** 478
[31] The Abinit code is available under the GNU general public license at http://www.abinit.org
[32] Schwarz K and Blaha P 2003 *Comput. Mater. Sci.* **28** 259
[33] http://www.wien2k.at
[34] Nørskov J K, Scheffler M and Toulhoat H 2006 *MRS Bull.* **31** 673
[35] Byskov L S, Hammer B, Nørskov J K, Clausen B S and Topsøe H 1997 *Catal. Lett.* **47** 177
[36] Raybaud P, Hafner J, Kresse G and Toulhoat H 1998 *Phys. Rev. Lett.* **80** 1481
[37] Raybaud P, Hafner J, Kresse G and Toulhoat H 1998 *Surf. Sci.* **407** 237
[38] Faye P, Payen E and Bougeard D 1999 *J. Mol. Modell.* **5** 63
[39] Toulhoat H, Raybaud P, Kasztelan S, Kresse G and Hafner J 1999 *Catal. Today* **50** 629
[40] Byskov L S, Nørskov J K, Clausen B S and Topsøe H 1999 *J. Catal.* **187** 109
[41] Cristol S, Paul J-F, Payen E, Bougeard D, Hafner J and Hutschka F 1999 *Stud. Surf. Sci. Catal.* **127** 327
[42] Byskov L S, Nørskov J K, Clausen B S and Topsøe H 2000 *Catal. Lett.* **64** 95
[43] Raybaud P, Hafner J, Kresse G, Kasztelan S and Toulhoat H 2000 *J. Catal.* **189** 129
[44] Raybaud P, Hafner J, Kresse G, Kasztelan S and Toulhoat H 2000 *J. Catal.* **190** 128
[45] Alexiev V, Prins R and Weber Th 2000 *Phys. Chem. Chem. Phys.* **2** 1815
[46] Ma X and Schobert H H 2000 *J. Mol. Catal.* A **160** 409
[47] Cristol S, Paul J-F, Payen E, Bougeard D, Clémendot S and Hutschka F 2000 *J. Phys. Chem.* B **104** 11220
[48] Alexiev V, Prins R and Weber Th 2001 *Phys. Chem. Chem. Phys.* **3** 5326
[49] Bollinger M V, Lauritsen J V, Jacobsen K W, Nørskov J K, Helveg S and Besenbacher F 2001 *Phys. Rev. Lett.* **87** 196803
[50] Schweiger H, Raybaud P, Kresse G and Toulhoat H 2002 *J. Catal.* **207** 76
[51] Schweiger H, Raybaud P and Toulhoat H 2002 *J. Catal.* **212** 33

[52] Travert A, Nakamura H, van Santen R A, Cristol S and Payen J F E 2002 *J. Am. Chem. Soc.* **124** 7084
[53] Cristol S, Paul J-F, Payen E, Bougeard D, Clémendot S and Hutschka F 2002 *J. Phys. Chem.* B **106** 5659
[54] Orita H, Uchida K and Itoh N 2003 *J. Mol. Catal.* A **193** 197
[55] Yang H, Fairbridge C and Ring Z 2003 *Energy Fuels* **17** 387
[56] Paul J F and Payen E 2003 *J. Phys. Chem.* B **107** 4057
[57] Bollinger M V, Jacobsen K W and Nørskov J K 2003 *Phys. Rev.* B **67** 085410
[58] Todorova T, Alexiev V, Prins R and Weber T 2004 *Phys. Chem. Chem. Phys.* **6** 3023
[59] Cristol S, Paul J-F, Payen E, Bougeard D, Hutschka F and Clémendot S 2004 *J. Catal.* **224** 138
[60] Sun M, Nelson A E and Adjaye J 2004 *J. Catal.* **226** 32
[61] Sun M, Nelson A E and Adjaye J 2005 *J. Catal.* **233** 411
[62] Sun M, Nelson A E and Adjaye J 2005 *Catal. Today* **105** 36
[63] Sun M, Nelson A E and Adjaye J 2005 *J. Catal.* **231** 223
[64] Sun M, Nelson A E and Adjaye J 2005 *Catal. Today* **109** 49
[65] Todorova T, Prins R and Weber T 2005 *J. Catal.* **236** 190
[66] Arrouvel C, Breysse M, Toulhoat H and Raybaud P 2005 *J. Catal.* **232** 161
[67] Zeng T, Wen X-D, Li Y-W and Jiao H 2005 *J. Mol. Catal.* A **241** 219
[68] Zeng T, Wen X-D, Wu G-S, Li Y-W and Jiao H 2005 *J. Phys. Chem.* B **109** 2846
[69] Zeng T, Wen X-D, Li Y-W and Jiao H 2005 *J. Phys. Chem.* B **109** 13704
[70] Logadóttir Á, Moses P G, Hinnemann B, Topsøe N-Y, Knudsen K G, Topsøe H and Norskov J K 2006 *Catal. Today* **111** 44
[71] Travert A, Dujardin C, Maugé F, Veilly E, Cristol S, Paul J-F and Payen E 2006 *J. Phys. Chem.* B **110** 1261
[72] Sun M, Nelson A E and Adjaye J 2006 *Catal. Lett.* **109** 133
[73] Wen X-D, Li Y-W, Wang J and Jiao H 2006 *J. Phys. Chem.* B **110** 21060
[74] Cristol S, Paul J F, Schovsbo C, Veilly E and Payen E 2006 *J. Catal.* **239** 145
[75] Raybaud P 2007 *Appl. Catal.* A **322** 76
[76] Moses P G, Hinnemann B, Topsøe H and Nørskov J K 2007 *J. Catal.* **248** 188
[77] Wen X-D, Ren J, Li Y-W, Wang J and Jiao H 2007 *Chem. Phys. Lett.* **436** 209
[78] Costa D, Arrouvel C, Breysse M, Toulhoat H and Raybaud P 2007 *J. Catal.* **246** 325
[79] Todorova T, Prins R and Weber T 2007 *J. Catal.* **246** 109
[80] Aray Y, Rodríguez J, Vidal A B and Coll S 2007 *J. Mol. Catal.* A **271** 105
[81] Vanderbilt D 1990 *Phys. Rev.* B **41** 7892
[82] Perdew J P, Chevary J A, Vosko S H, Jackson K A, Pederson M R, Singh D J and Fiolhais C 1992 *Phys. Rev.* B **46** 6671
[83] Tersoff J and Hamann D R 1983 *Phys. Rev. Lett.* **50** 1998
[84] Jonsson H, Mills G and Jacobsen K W 1997 Nudged elastic band method for finding minimum energy paths of transitions *Classical and Quantum Dynamics in Condensed Phase Systems: Enrico Fermi Summer School 1997* (Singapore: World Scientific)
[85] Reuter K and Scheffler M 2002 *Phys. Rev.* B **65** 035406
[86] Kam K K and Parkinson B A 1982 *J. Phys. Chem.* **86** 463
[87] Lauritsen J V, Bollinger M V, Lægsgaard E, Jacobsen K W, Nørskov J K, Clausen B S, Topsøe H and Besenbacher F 2004 *J. Catal.* **221** 510
[88] Lauritsen J V, Nyberg M, Vang R T, Bollinger M V, Clausen B S, Topsøe H, Jacobsen K W, Lægsgaard E, Nørskov J K and Besenbacher F 2003 *Nanotechnology* **14** 385
[89] Lauritsen J V, Nyberg M, Nørskov J K, Clausen B S, Topsøe H, Lægsgaard E and Besenbacher F 2004 *J. Catal.* **224** 94
[90] Wolverton C and Hass K C 2001 *Phys. Rev.* B **63** 024102
[91] Paglia G, Buckley C E, Rohl A L, Hunter B A, Hart R D, Hanna J V and Byrne L T 2003 *Phys. Rev.* B **68** 144110
[92] Paglia G, Rohl A L, Buckley C E and Gale J D 2005 *Phys. Rev.* B **71** 224115
[93] Krokidis X, Raybaud P, Gobichon A E, Rebours B, Euzen P and Toulhoat H 2001 *J. Phys. Chem.* B **105** 5121
[94] Digne M, Sautet P, Raybaud P, Euzen P and Toulhoat H 2004 *J. Catal.* **226** 54
[95] Sun M Y, Nelson A E and Adjaye J 2006 *J. Phys. Chem.* B **110** 2310
Paglia G, Buckley C E and Rohl A L 2006 *J. Phys. Chem.* B **110** 2072 1 (comment)
Digne M, Raybaud P, Sautet P, Rebours B and Toulhoat H 2006 *J. Phys. Chem.* B **110** 20719 (comment)
Nelson A E, Sun M Y and Adjaye J 2006 *J. Phys. Chem.* B **110** 20724 (reply)
[96] Hinnemann B, Nørskov J K and Topsøe H 2005 *J. Phys. Chem.* B **109** 2245
[97] Cooper B H and Knudsen K G 2006 Ultra deep desulfurization of diesel: how an understanding of the underlying kinetics can redure investment costs *Practical Advances in Petroleum Processing* ed C S Hsu and P R Robinson (New York: Springer) chapter 10, pp 297–316
[98] Egorova M and Prins R 2006 *J. Catal.* **241** 162
[99] Honkala K, Hellman A, Remediakis I N, Logadóttir Á, Carlsson A, Dahl S, Christensen C H and Nørskov J K 2005 *Science* **307** 555
[100] LaVopa V and Satterfield C N 1988 *J. Catal.* **110** 375

Paper 8

Scaling Relations

DOI: 10.1002/anie.200((will be filled in by the editorial staff))

Scaling Relations for Adsorption Energies on Transition Metal Oxide, Sulfide and Nitride surfaces**

*Eva M. Fernández, Poul G. Moses, Anja Toftelund, Heine A. Hansen, José I. Martínez, Frank Abild-Pedersen, Jesper Kleis, Berit Hinnemann, Jan Rossmeisl, Thomas Bligaard, and Jens K. Nørskov**

Density functional theory calculations of the adsorption of O, OH, S, SH, N, NH, and NH_2 on a range of transition metal oxide, sulfide and nitride surfaces are presented. It is shown that the adsorption energies of AH_x molecules, ΔE^{AH_x}, scale with the adsorption energies of the A atoms, ΔE^{A}, as $\Delta E^{AH_x} = \gamma(x)\,\Delta E^{A} + \xi$, where the proportionality constant, $\gamma(x)$, is independent of the metal and only depends on the number of H atoms in the molecule. We discuss the origin of this effect by comparing with similar scaling relations for transition metal surfaces.

There has been substantial progress in the description of adsorption and chemical reactions of simple molecules on transition metal surfaces. Adsorption energies and activation energies have been obtained for a number of systems and complete catalytic reactions have been described in some detail.[1-7] There has also been considerable progress in the theoretical description of the interaction of molecules with transition metal oxides,[8-19] sulfides,[20-25] and nitrides,[26-29] but such systems are considerably more complicated to describe theoretically. Complications arise from dificulties describing the stoichiometry and structure of such surfaces and from possible shortcomings in the use of ordinary generalized gradient approximation (GGA) type density functional theory (DFT).[30]

In the present communication we introduce a method that may facilitate the description of bonding of gas molecules to transition metal oxides, sulfides and nitrides. It was recently found that there are a set of scaling relations between the adsorption energies of different partially hydrogenated intermediates on transition metal surfaces.[31] We will show that there exist similar scaling relations for adsorption on transition metal oxide, sulfide and nitride surfaces. This means that knowing the adsorption energy for one transition metal compound it is possible to quite easily generate data for a number of other compounds and in this way obtain reactivity trends.

[*] E. M. Fernández, P. G. Moses, A. Toftelund, H. A. Hansen, J. I. Martinez, Fran Abild-Pedersen, J. Kleis, J. Rossmeisl, T. Bligaard, J. K. Nørskov
Center for Atomic-scale Materials Design, Department of Physics Department, NanoDTU
Technical University of Denmark
DK-2800 Lyngby (Denmark)
Fax: (+45) 4593-2399
E-mail: norskov@fysik.dtu.dk

B. Hinnemann
Haldor Topsøe A/S
((Institution))
Nymøllevej 55, DK-2800 Lyngby (Denmark)

[**] The Center for Atomic-scale Materials Design is funded by the Lundbeck Foundation. The authors wish to acknowledge additional support from the Danish Research Agency through grant 26-04-0047 and the Danish Center for Scientific Computing through grant HDW-0107-07.

The results presented in this communication are calculated using self-consistent DFT. Exchange and correlation effects are described using the revised Perdew-Burke-Ernzerhof (RPBE)[32] GGA functional. It is known that GGAs give adsorption energies with reasonable accuracy for the transition metals.[32,33] It is not clear, however, that a similar accuracy can be expected for the oxides, sulfides, and nitrides, although there are examples of excellent agreement between DFT calculations and experiments, e.g. RuO_2 surfaces.[9] In the following we will focus entirely on variations in absorption energies from one system to the next, and we expect that such results will be less dependent on the description of exchange and correlation than the absolute adsorption energies.

For the nitrides, the clean surface and the surface with a nitrogen vacancy are studied. For MX_2-type oxides (sulfides) an oxygen (sulfur) covered surface with an oxygen (sulfur) vacancy are studied. The structures of the clean surface considered in the present work and their unit cells are shown in Fig. 1. The adsorption energies given below are for the adsorbed species in the most stable adsorption site on the surface.

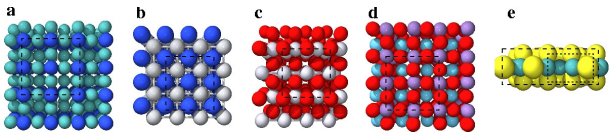

Figure 1. *Structures used to describe surfaces of transition metal nitrides, oxides and sulfides. a) fcc-like structure for the M_2N (100) surface, M = Mo and W. Dark blue and light blue spheres represent metal and nitrogen atoms, respectively. b) fcc-like rock salt structure for the TiN (100) surface. Dark blue and gray spheres represent Ti and N atoms, respectively, c) rutile-like (110) surface for the PtO_2. Red and white spheres represent oxygen and metal atoms, respectively. d) perovskite structure for the $LaMO_3$ (100) surface , with M = Ti, Ni, Mn, Fe, and Co. Red, light blue, and violet spheres represent oxygen, lanthanum and metal atoms, respectively. e) hcp-like (-1010) surfaces for NbS_2, TaS_2, MoS_2, WS_2, Co-Mo-S, Ni-Mo-S and Co-W-S. Yellow and green spheres represent sulfur and metal atoms, respectively. The black dashed boxes indicates the unit cell.*

By performing calculations for a large number of transition metal surfaces of different orientations,[31] it has been found that the adsorption energy of molecules of the type AH_x is linearly correlated with the adsorption energy of atom A (N, O, S):

$$\Delta E^{AH_x} = \gamma(x)\,\Delta E^{A} + \xi \quad , \qquad (1)$$

where the scaling constant is given to a good approximation by

$$\gamma(x) = (x_{max} - x)/x_{max} \, . \qquad (2)$$

Here x_{max} is the maximum number of H atoms that can bond to the central atom A (x_{max}=3 for A=N, and x_{max}=2 for A=O, S), i.e. the number of hydrogen atoms that the central atom, A, would bond to

in order to form neutral gas phase molecules.

We have performed similar calculations for oxygen, sulfur, and nitrogen adsorption on a series of transition metal oxide, sulfide and nitride surfaces, see Fig. 2. We find that scaling relations also exist for these systems, which are considerably more complex than the transition metal surfaces. Such a correlation between adsorption energies of O and OH has earlier been found for the MO_2 oxides.[12] Further more, it can be seen that the scaling constant $\gamma(x)$ is given to a good approximation by the same expression, Eq. (2) as for adsorption on the transition metals. We find that the mean absolute error (MAE) is lower than 0.19 eV for all the species considered here. The nitride surfaces present a poorer correlation than the rest mainly because TiN(100) is a clear outlier.

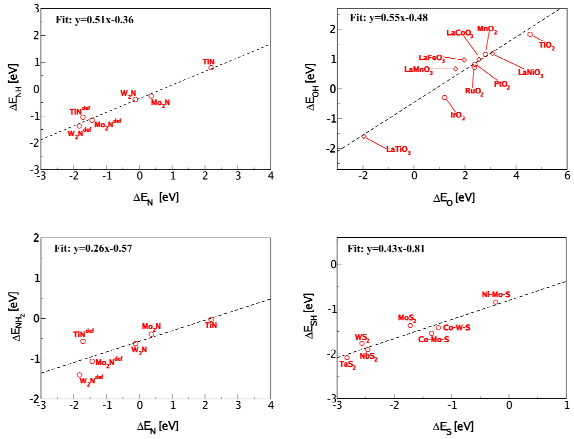

Figure 2. Adsorption energies of NH and NH_2 intermediates over nitrides, OH intermediate over oxides and SH intermediate over sulfides plotted against adsorption energies of N, O and S, respectively. The adsorption energy of AH_x is defined as: $\Delta E_{AH_x} = E(AH_x^*)+(x_{max}-x)/2*E(H_2)-E(^*)-E(AH_{x_{max}})$ where $E(AH_x^*)$ is the total energy of an AH_x molecule adsorbed on the most stable adsorption site, $E(^*)$ is the total energy of the surface without the A atom adsorbed, and $E(H_2)$ and $E(AH_{x_{max}})$ are the total energy of the hydrogen molecule and the $AH_{x_{max}}$ molecule in vacuum, respectively.

It is interesting to compare the results of Fig. 2 with the equivalent results for the transition metals, see Fig. 3. It is found that for the nitrides the linear relationships are essentially the same for the two classes of systems. For the oxides and partially for the sulfides the results for the compounds are shifted from those of the metals. We trace this to a difference in the adsorption sites on the two kinds of systems. On the transition metal surfaces O and OH are generally found to adsorb on highly coordinated sites with more than one metal neighbor. On the other hand, on the oxide surfaces the O atoms are generally coordinated to a single metal atom. If we use adsorption energies for O and OH on the transition metals, where they are forced to adsorb in an on-top position, the results now fall on the same line as for the oxides, see Fig. 3. For the sulfides the S also adsorbs on a different site than on the metal. If the same adsorption site on the metal is considered the data agree, as for the oxides, with the sulfide results.

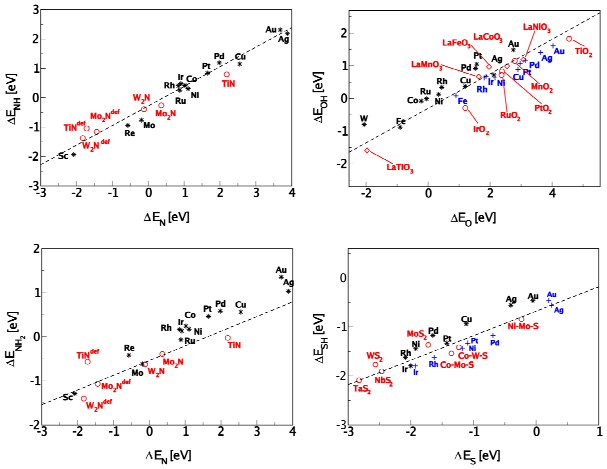

Figure 3. *Adsorption energies of NH and NH_2 intermediates on transition metal nitrides and transition metal surfaces, the OH intermediate on transition metals oxides and transitions metal surfaces, and the SH intermediate on transition metal sulfides and transition metal surfaces plotted against adsorptions energies of N, O, and S, respectively.* Close-packed surfaces for NH_x and OH_x intermediates and the stepped surface for SH_x intermediates are considered. *The adsorption energies for the OH intermediate on top site and S intermediates on bridge site over transition metals are included (blue points). The dash line is the exact slope, $\gamma(x)$, obtained by eq. 2.*

The results of Figs. 2 and 3 are remarkable and indicate that the nature of the adsorption bond is similar for the transition metals and the compounds. For the transition metal surfaces the scaling relations can be understood within the *d*-band model.[34-39] The variation in adsorption energies for a given atom or molecule among the transition metals is mainly given by the variations in the strength of the coupling of the adsorbate valence states with the transition metal *d* states. The variations in the adsorption energy of an atom A from one transition metal surface to the next reflect this. If H atoms are now added to atom A, the ability of A to couple to the metal *d* states decreases either because the A states couple to fewer *d* states or because the bonds become longer.[31] The principle of bond order conservation would indicate that the weakening of the bond strength is proportional to the number of H atoms added, hence Eq. (2).[31] The scaling behaviour observed in Figs. 2 and 3 indicates that similar arguments should hold for adsorption on transition metal oxides, sulfides and nitrides. The key to understand this can be found in recent work by Lundqvist *et al.*[40] where they show that a suitably modified *d*-band model can be used to understand trends in adsorption energies on transition metal carbides and nitrides.

The strength of the scaling relations is shown by the following example. If one has a calculated or an experimental adsorption energy of an adsorbate AH_x, $\Delta E_{M1}^{AH_x}$, for one transition metal or transition metal compound, M1, we can estimate the energy, $\Delta E_{M2}^{AH_x}$, of the same intermediate on another system, M2, from the adsorption energies of atom A on the two systems as:

$$\Delta E_{M2}^{AH_x} = \Delta E_{M1}^{AH_x} + \gamma(x)(\Delta E_{M2}^{A} - \Delta E_{M1}^{A}), \qquad (3)$$

where $\gamma(x)$ is a rational number given by Eq. (2). If we have a database of atomic adsorption energies for a number of systems, we may estimate the adsorption energy of a number of intermediates.

This opens the possibility of obtaining an overview of adsorption energies on oxides, sulfides, and nitride surfaces on the basis of a few calculations.

Methods

The results presented in the present communication are calculated using self-consistent DFT. The ionic cores and their interaction with the valence electrons are described by ultra-soft pseudopotentials (soft pseudopotential for S)[41] and the valence wave functions are expanded in a basis set of plane waves with a kinetic energy cut-off of 350-400 eV. The electron density of the valence states is obtained by a self-consistent iterative diagonalization of the Kohn-Sham Hamiltonian with Pulay mixing of the densities.[42] The occupation of the one-electron states is calculated using an electronic temperature of k_BT=0.1 eV (0.01 eV for the molecules in vacuum); all energies are extrapolated to T=0 K. The ionic degrees of freedom are relaxed using the quasi-Newton minimization scheme, until the maximum force component is found to be smaller than 0.05 eV/Å. Spin magnetic moments for the oxides, Co-Mo-S, Ni-Mo-S, and Co-W-S are taken into account. Exchange and correlation effects are described using the revised Perdew-Burke-Ernzerhof (RPBE)[32] generalized gradient approximation (GGA) functional.
We use the periodic slab approximation and the unit cells considered are modeled by a (2x2) unit cell for the nitrides and perovskite-type oxides, a (2x1) unit cell for PtO_2, a (2x1) unit cell for Co-W-S and MS_2 surfaces with M = Mo, Nb, Ta, and W, and a (4x1) unit cell for M-Mo-S surface with M = Ni and Co. A four layer slab for the nitrides and perovskite-type oxides, a four trilayer slab for PtO_2-type oxides, and a 8 or 12 layer slab for sulfides are employed in the calculations. Neighboring slabs are separated by more than 10 Å of vacuum. The results for the MO_2 surfaces with M = Ir, Mn, Ru, and Ti are taken from Refs.[12,15] The adsorbate together with the two topmost layers for the nitrides and perovskite-type oxides, the two topmost trilayers for MO_2 oxides and all layers for the sulfides, are allowed to fully relax. The Brillouin zone of the systems is sampled with a 4x4x1 Monkhorst-Pack grid for nitride and oxide surfaces and with a 6x1x1 (4x1x1) for the 2x1 (4x1) supercell for the sulfide surfaces.

Received: ((will be filled in by the editorial staff))
Published online on ((will be filled in by the editorial staff))

Keywords: adsorption energy · density-functional calculations · scaling relations · transition metals

[1] A. Alavi, P. Hu, T. Deutsch, P. L. Silvestrelli, J. Hutter, *Phys. Rev. Lett*. **1998,** *80,* 3650.
[2] A. Eichler, J. Hafner, *Phys. Rev*. **1999**, *59*, 5960.
[3] B. Hammer, *J. Catal*. **2001**, *199*, 171.
[4] A. Logadottir, J. K. Nørskov, *J. Catal.* **2003,** *220,* 273.
[5] S. Linic, M. A. Barteau, *J. Am. Chem. Soc.* **2003**, *125*, 4034.
[6] S. Ovesson, B. I. Lundqvist, W. F. Schneider, A. Bogicevic, *Phys. Rev. B* **2005**, *71*, 115406.
[7] S. Kandoi, J. Greeley, M. A. Sanchez-Castillo, S. T. Evans, A. A. Gokhale, J. A. Dumesic, M. Mavrikakis, *Top. Catal.* **2006**, 37, 17.
[8] S. Wendt, R. Schaub, J. Matthiesen, E. K. Vestergaard, E. Wahlström, M. D. Rasmussen, P. Thostrup, L.M. Molina, E. Lægsgaard, I. Stensgaard, B. Hammer, F. Besenbacher, *Surf. Sci.* **2005**, *598*, 226.
[9] K. Reuter K, D. Frenkel, M. Scheffler, *Phys. Rev. Lett.* **2004**, *93*, 116105.
[10] Y. Yanga, M. Sushchikha, G. Mills, H. Metiu, E. McFarland, *Appl. Surf. Sci.* **2004**, *229*, 346.
[11] S. Chrétien, H. Metiu, *Cat. Lett* **2006**, *107*, 143.
[12] J. Rossmeisl, Z.-W. Qu, H. Zhu, G.-J. Kroes, J. K. Nørskov, *J. Electroanal. Chem.* **2007**, *607*, 83.
[13] M. D. Rasmussen, L. M. Molina, B. Hammer, *J. Chem. Phys.* **2004**, *120*, 988.
[14] Z. W. Qu, G. J. Kroes, *J. Pys. Chem. B* **2006**, *110*, 23306.
[15] J. Rossmeisl, K. Dimitrievski, P. Siegbahn, J. K. Nørskov, *J. Phys. Chem. Lett.* **2007**, xxx.
[16] T. Bredow, G. Pacchioni, *Chem. Phys. Lett*. **2002**, *79*, 753.
[17] M. Abu Halja, S. Guimond, Y. Romansyshyn, A. Uhi, H. Kulenbeck, T. K. Todorova, M. V. Ganduglia-Pirovano, J. Döbler, J. Sauer, H.-J. Freund, *Surf. Sci.* **2006**, *600*, 1497.
[18] G. Pacchioni, C. Di Valentini, D. Dominguez-Ariza, F. Illas, T. Bredow, T. Kluner, V. Staemmier, *J. Phys. Cond. Matt.* **2004**, *16*, 2497.
[19] K. M. Neyman, S. Ph. Ruzankin, N. Rösch, *Chem. Phys. Lett.* **1995**, *246,* 546.
[20] M. Neurock, R. A. van Santen, *J. Am. Chem. Soc.* **1994**, *116*, 4427.
[21] S. Cristol, J.-F. Paul, E. Payen, D. Bougeard, S. Clémendot, F. Hutschka, *J. Phys. Chem. B* **2002**, *106*, 5659.
[22] M. Sun, A.-E. Nelson, J. Aadjaye, *J. Catal*. **2004**, *226*, 41.
[23] M. V. Bollinger, K. W. Jacobsen, J. K. Nørskov, *Phys. Rev. B* **2003**, *67*, 084310.
[24] H. Schweiger, P. Raybaud, H. Toulhat, *J. Catal.* **2002**, *212*, 33.
[25] T. Todorova, R. Prins, T. Weber, *J Catal.* **2007**, *246*, 109.
[26] A. Vojvodic, C. Ruberto, B. I. Lundqvist, *Surf. Sci.* **2006**, *600*, 3619.
[27] P. Liu, J. A. Rodriguez, *Cat. Lett.* **2003**, *91*, 247
[28] G. Frapper, M. Pélisser, *J. Phys. Chem. B* **2000**, *104***,** 11972.
[29] J. Ren J, C.-F. Huo, X.-D. Wen, Z. Cao, J. Wang, J.-W. Li, H. Jiao, *J. Phys. Chem. B* **2006**, *110*, 22563.
[30] O. Begone, M. Alouani, P. Blöchl, J. Hugei, *Phys. Rev. B* **2000**, *62*, 16392.
[31] F. Abild-Pedersen, J. Greeley, F. Studt, J. Rossmeisl, T. R. Munter, P. G. Moses, E. Skúlason, T. Bligaard, J. K. Nørskov, *Phys. Rev. Lett.* **2007**, *99*, 016105.
[32] B. Hammer, L. B. Hansen, J. K. Nørskov, *Phys. Rev. B* **1999**, *59,* 7413.
[33] J. Greely, M. Mavrikakis, *J. Phys. Chem. B* **2005**, *109*, 3460.
[34] B. Hammer, J. K. Nørskov, *Surf. Sci.* **1995**, *343*, 211.
[35] B. Hammer, J. K. Nørskov, *Nature (London)* **1995**, *376*, 238 .
[36] B. Hammer, J. K. Nørskov, *Adv. Catal.* **2000**, *45***,** 71.
[37] A. Eichler, F. Mittendorfer, J. Hafner, P*hys. Rev. B* **2000**, *62*, 4744.
[38] J. Greeley, M. Mavrikakis, *Nat. Mater.* **2004**, *3*, 810 .
[39] A. Roudgar, A. Gross, *Phys. Rev. B* **2003**, *67*, 033409 .
[40] C. Ruberto, B. I. Lundqvist *Phys. Rev. B* **2007**, *75*, 235438.
[41] D. Vanderbilt, *Phys. Rev. B* **1990**, *41*, 1510.
[42] G. Kresse, J. Furthmuller *Comput. Matter. Sci.* **1996**, *6*, 15.

Entry for the Table of Contents (Please choose one layout)

Layout 1:

Scaling Relations

Eva M. Fernández, Poul G. Moses, Anja Toftelund, Heine A. Hansen, José I. Martínez, Frank Abild-Pedersen, Jesper Kleis, Berit Hinnemann, Jan Rossmeisl, Thomas Bligaard, and Jens K. Nørskov*

_____ **Page – Page**

Scaling Relations for Adsorption Energies on Transition Metal Oxide, Sulfide and Nitride surfaces

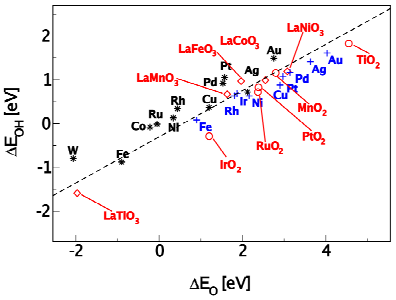

Scaling relations for adsorption energies on transition metals oxide, sulfide and nitride surfaces are studied using DFT calculations. The nature of the adsorption bond is similar for the transition metals and the compounds. This opens the possibility of obtaining an overview of adsorption energies on oxides, sulfides, and nitride surfaces on the basis of a few calculations.

Layout 2:

((Catch Phrase))

((Author(s), Corresponding Author(s)*))

_____ **Page – Page**

((Title Text))

((TOC Graphic))

((Text for Table of Contents, max. 450 characters))

Paper 9

Hydrogen Evolution on Nano-particulate Transition Metal Sulfides

Jacob Bonde[a], Poul G. Moses[b] , Thomas F. Jaramillo[c], Jens K. Nørskov[b], Ib Chorkendorff [*a]

Received (in XXX, XXX) 1st January 2007, Accepted 1st January 2007
First published on the web 1st January 2007
DOI: 10.1039/b000000x

The Hydrogen Evolution Reaction (HER) on carbon supported MoS_2 nanoparticles is investigated and compared to findings with previously published work on Au(111) supported MoS_2. An investigation into MoS_2 oxidation is presented and used to quantify the surface concentration of MoS_2. Other metal sulfides with morphologies similar to MoS_2 such as WS_2, cobalt-promoted WS_2, and cobalt-promoted MoS_2 were also investigated in the search for improved HER activity. Experimental findings are compared to Density Functional Theory (DFT) calculated values for the hydrogen binding energies (ΔG_H) on each system.

Introduction

Research efforts to develop electrocatalysts for energy conversion reactions have increased substantially in recent years. Platinum, the ubiquitous electrocatalyst used in PEM fuel cells, is both expensive and scarce, prompting widespread efforts to discover cost-effective materials to replace Pt. In this work we focus on non-noble metal sulfide catalysts for the Hydrogen Evolution Reaction (HER) under acidic conditions, a reaction catalyzed most effectively by Pt-based materials[1] .

Previously, MoS_2 has been studied as a catalyst in hydrodesulfurisation[2] and in the photo-oxidation of organics[3,4]. In electrocatalysis, it has recently been shown that the edge structure of nanoparticulate MoS_2 is active for the HER, mimicking the active sites/co-factor of the hydrogen evolving enzymes nitrogenase and hydrogenase[5,6]. This work aims to extend the investigation on carbon-supported nanoparticulate MoS_2 for the HER. Unlike the case of Au(111) supported MoS_2 studied by STM in previous work[6], the catalysts probed herein are more commercially relevant, which also implies that they are less homogeneous and more difficult to image on the atomic scale. As knowledge of the concentration of active sites on a catalyst surface is paramount to elucidating structure-composition-activity relationships, the first aim of this work is to utilize electrochemical oxidation to probe MoS_2 surface area, distinguishing between basal plane and edge sites. In developing this methodology to quantify active sites on a macroscopic scale, we then direct our attention to related catalyst systems, namely WS_2, cobalt-promoted WS_2, and cobalt-promoted MoS_2. We end by comparing experimentally determined activity data to predictions made by Density Functional Theory (DFT) models of these systems in order to gain insight into trends in catalyst activity.

It has been found that ΔG_H, the hydrogen binding energy to a given surface, is a good descriptor for identifying electrocatalyst materials with high exchange current densities[1,7,8]. A recent study[5]using DFT showed that the active sites on nitrogenase and hydrogenase bind hydrogen weakly, similar to Pt. It was also found that the overpotential of carbon supported MoS_2 is comparable to the DFT calculated hydrogen binding energy on the edge of the nanoparticles. In another study MoS_2 nanoparticles on Au(111) were synthesized under UHV conditions, characterized by STM and examined for HER activity[6].This study showed direct evidence that the active site of the MoS_2 nanoparticles is indeed the edge. The exchange current density was also found to be in agreement with the volcano relation between the HER exchange current density and the DFT calculated values for ΔG_H proposed by Nørskov et al[7]. By having identified the active site of MoS_2 particles, the next step is to modify that edge such that its ΔG_H approaches even closer to zero where the HER volcano curve has its maximum, and this is a major aim of the work presented herein.

Bulk MoS_2 consists of stacked S-Mo-S layers, and MoS_2 nanoparticles can be synthesized as single layer hexagonal structures exposing two different kinds of edges, the so-called Mo-edge and the S-edge[9]. It has been shown that the structure of nanoparticulate MoS_2 is a single layered truncated triangle primarily exposing the Mo-edge when supported on Au(111)[6, 9], Highly Ordered Pyrolytic Graphite (HOPG)[10] or graphitic carbon[11]. Brorson et al[11,12]also found truncated triangles by means of HAADF-STEM (High-Angle Annular Dark-Field-Scanning Transmission Electron Microscopy) in their investigation of MoS_2, WS_2 and cobalt-promoted MoS_2.

Estimating the number of active sites on a nanoparticulate catalyst is not trivial. One approach is to measure activity on well defined model systems characterized by STM, for example UHV-deposited nanoparticles[6,13]or physi- or chemisorbed molecular clusters[14]. Another option is to use a well established method to measure electrochemically active surface area such as that used with Pt based on the adsorption-desorption behavior of underpotentially deposited hydrogen,

H_{upd}[15]. We note, however, that this method still relies upon the assumption that the sites active for H_{upd} are the same as those active for the HER. As we are studying metal sulfides where no such method exists, the irreversible oxidation of metal sulfides will be investigated as a measure of their surface area and edge sites.

In the following we will show our investigation of MoS_2, WS_2 and cobalt promoted WS_2 (Co-W-S) and MoS_2 (Co-Mo-S), prepared similarly to the ones imaged by Brorson et al[11] and supported on Toray carbon paper. The electrochemical measurements will be discussed in relation to DFT calculations of ΔG_H for each of the metal sulfates investigated in order to identify structure-composition-activity relationships for these systems.

Results and discussion:

Synthesis and electrochemical characterization of MoS_2.

MoS_2 particles on Toray carbon paper were prepared by dropping 25 µL of an aqueous ammonia heptamolybdate (1mM Mo) solution onto 1 cm^2 of Toray paper. The sample was dried in air at 140 C followed by sulfidation in 10% H_2S in H_2 at 450 C for 4 hours, and subsequently cooled in that same gas stream. This preparation method would typically give the highest current on a per gram basis; higher loadings usually led to lower currents.

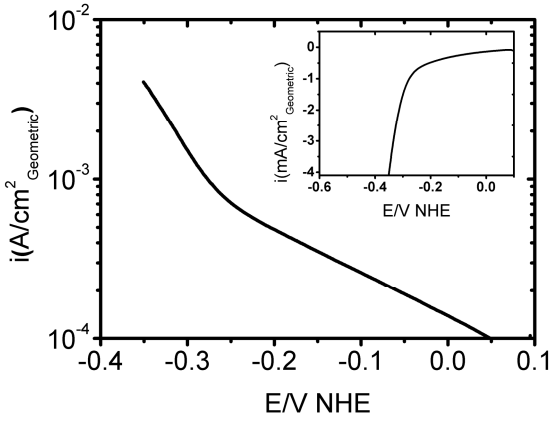

Fig. 1 Tafel plot (main) and polarization curve (inset) in the cathodic potential range of MoS_2 supported on Toray paper. The scan rate is 5 mV/s and the Tafel slope in the HER region is found to be 120 mV/dec.

HER activity was measured (See experimental details) and the results are plotted as Tafel (log i - E) and polarization curves (i-E) in Figure 1. The Tafel plot exhibits a slope of 120 mV/dec and an exchange current density of 4.6 10^{-6} $A/cm^2_{geometric}$. Samples prepared by different methods have often yielded different Tafel slopes, ranging between 110 mV/dec. and several hundred mV/dec. We attribute this to transport limitations through the fibrous, porous network characteristic of Toray carbon paper. Although sample/substrate preparation could potentially be optimized further, the consistent results achieved using the preparation method described above allows for accurate cross-comparisons among different catalyst materials. It should be noted that hydrogen evolution is taking off at around -0.2 V vs. NHE just as we have previously seen on MoS_2[5,6].

The current measured from approx. +0.1 V vs. NHE to -0.15 V is most likely not due to the HER but rather oxygen reduction at the interface between the electrolyte and the electrode. Finally it should be noted that sweeps between -0.35 and +0.1 V vs. NHE showed negligible change over time, apart from the effects of bubble formation on the electrode.

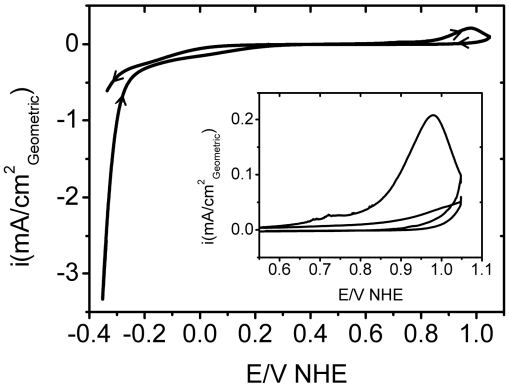

Fig. 2 Cyclic voltammogram of the oxidation and subsequent deactivation of the MoS_2 sample. Scanrate 2mV/s. Main: The deactivation of the sample showing one sweep from -0.35 V vs. NHE to 1.05 V vs NHE and back to -0.35 V vs. NHE. On the 1st anodic sweep an irreversible oxidation peak occurs at 0.6 V vs. NHE and is followed by a subsequent decrease in current at cathodic potentials (-0.35 V vs. NHE), indicating a deactivation of the active sites. Inset: The first and second sweep at anodic potentials showing a significant decrease in the oxidation peak.

Figure 2 shows a cyclic voltammogram of MoS_2/C where the potential is cycled between -0.3 and +1.05 V vs. NHE. At approx. +0.6 V vs. NHE an irreversible oxidation begins to occur with a maximum at +0.98 V vs. NHE. On the subsequent cathodic sweep a significant drop in HER activity is noticed. On the ensuing anodic sweep seen in the inset of Figure 2, the oxidation peak is no longer present. Thus, the loss of HER activity is attributed to irreversible MoS_2 oxidization. In subsequent studies, fresh samples were subjected to CVs in which an initially narrow potential window was widened gradually to more positive (anodic) potentials. It was found that the HER activity of MoS_2/C remained stable with every sweep as long as the anodic potential was limited to $\leq$ +0.6 V vs. NHE.

MoS_2 electro-oxidation

To our knowledge, the electrochemical oxidation of nanoparticulate MoS_2 is not covered in the literature, which instead focuses on the corrosion of bulk MoS_2. Kautek[16] found that the bulk system preferentially oxidized at the $(10\bar{1}1)$ face and that it did not corrode at the (0001) basal plane. On the nanoparticles this would correspond to corrosion of the particle edges. Closer examination of the insert of Figure 2 reveals two distinct oxidation peaks. The major peak has its maximum at approx. +0.98 V vs. NHE whereas the minor peak has its maximum at approx. +0.7 V vs. NHE. As the edges of MoS_2 nanoparticles are expected to be more readily oxidized than the basal plane[16], we interpret the two distinct oxidation peaks to correspond to the edges (minor peak, +0.7 V vs. NHE) and the basal planes (major peak, +0.98 V vs. NHE) of the particles. While only one cycle to +1.05 V vs. NHE will completely deactivate the sample for the HER, it takes several cycles to +0.7 V vs. NHE to achieve the same effect. This implies that not all edge sites are oxidized with a single sweep to +0.7 V vs. NHE. Had the sample been deactivated for the HER after a single sweep to +0.7 V vs. NHE, we could definitely have used this peak as a measure of the concentration of edge sites. But as this is not the case we will use the major peak at +0.98 V vs. NHE to determine the total surface area of MoS_2/C. We have however attempted to use the weak feature at +0.7 V vs. NHE to get an estimate of our particle size. At low sweep rates (2 mV/s) the feature is typically not dominated by the major feature at +0.98 V vs. NHE. The area of the edge feature is approx. 8 % of the major peak. If the particles are triangular this corresponds to an edge length of around 25 nm, consistent with the particle sizes observed by Brorson et al[11].

XPS was also employed in this investigation to study the MoS_2/C at three stages of its life: freshly prepared, after HER in H_2SO_4 and after oxidation in H_2SO_4 at high anodic potentials (see experimental details). To obtain a reasonable signal to noise ratio for the XPS studies the Toray paper was dip coated in a 0.14 M Mo solution instead of dropping a known amount of solution on the surface, resulting in a higher loading of Mo than previously described (a factor of 5-10 according to the charge of the oxidation peak). The survey spectra of the different samples showed no contaminants on the freshly prepared samples. On the samples that had been submerged in H_2SO_4 peaks corresponding to sulfate were seen and a peak corresponding to N *1s* was also seen. The N *1s* peak is most likely caused by trace amounts of NH_3 present in air absorbed by H_2SO_4 as $(NH_4)_2SO_4$ with a N *1s* binding energy of 401.3 eV[17].

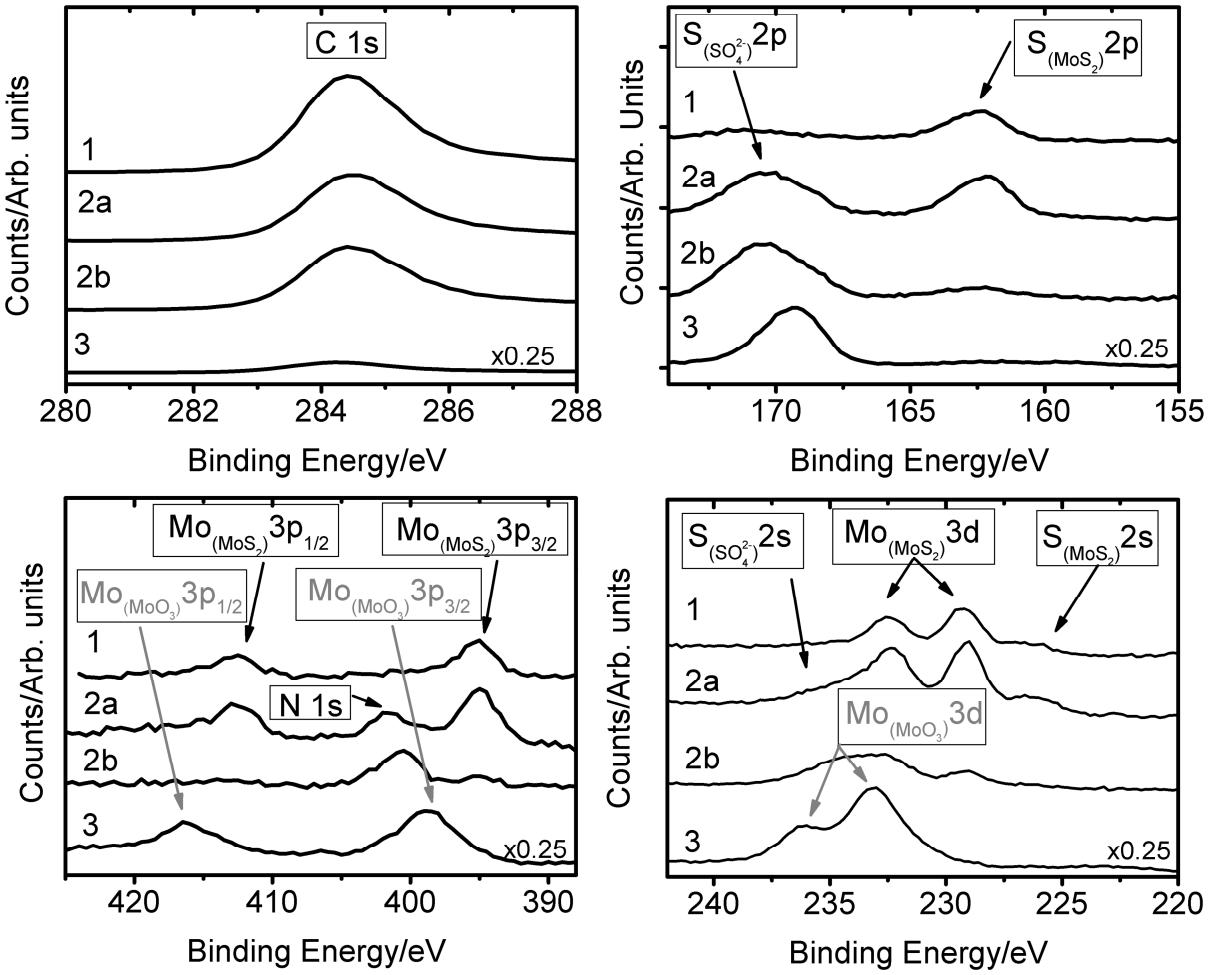

Fig. 3 XPS spectra of MoS_2 on Toray paper recorded at different stages of its life. 1): As prepared after sulfidation. 2a): After initial activity measurements of the HER(CVs between +0.1 and -0.4 V vs. NHE). 2b): Sample 2a after measurements of the HER and subsequent oxidation/deactivation (CVs between +1.4 and -0.4 V vs. NHE) and removal from the electrolyte at -0.32 V vs. NHE. 3): After measurements of the HER and subsequent oxidation/deactivation (CVs between +1.4 and -0.4 V vs. NHE) and removal from the electrolyte at 0.4 V vs. NHE.

The XPS data, see Figure 3. reveals that the freshly prepared sample (no. 1) of MoS_2 is similar to previously reported spectra[18-20]. The XPS data from a similarly prepared sample that was tested for the HER (sample no. 2a) by sweeping the potential between +0.1 V and -0.45 V vs. NHE, showed an increase in the SO_4^{2-} peak which is to be expected as the sample had been submerged in H_2SO_4. Apart from the increase in the SO_4^{2-} peak no significant changes were found compared to the freshly prepared sample, indicating that MoS_2/C does not change significantly during the HER. After XPS analysis of sample no. 2a was examined for the HER again, then cycled between -0.4 V vs. NHE and +1.4. V vs. NHE and removed from the solution at -0.32 V vs. NHE (sample no. 2b in the XPS spectra). A significant decrease of the Mo *3d*, Mo *3p*, S *2s* and S *2p* peaks was observed and there was no XPS signal corresponding to MoO_3. Thus, although the amount of surface Mo decreased significantly it still maintained its Mo^{4+} character(as in MoS_2). There are several possible explanations for the lack of Mo on the surface: (1) The MoS_2 desorbs from the surface at high anodic potentials, (2) The oxidation product of MoS_2, MoO_3, dissolves[21], (3) That MoO_3 is reduced to Mo^{3+} at -0.32 V vs. NHE and subsequently dissolves[21]. To answer this question, sample no. 3 was subjected to the same oxidation treatment as sample no. 2b but in this case the sample was pulled out of solution at a higher potential (+0.4 V vs. NHE) where MoO_3 is thermodynamically stable according to the Pourbaix diagrams[21]. XPS reveals a shift of the Mo *3d* and Mo *3p* towards higher binding energies just as expected for MoO_3. Thus it is unlikely that MoS_2 dissolves at anodic potentials.

We note that the Mo peaks of the MoO_3 were significantly greater than the Mo peaks observed on the other samples and at the same time the C *1s* peak was significantly smaller. The increase in intensity could be due to a higher loading on this specific sample but we only found a factor of 2 larger oxidation peak on sample 3 than on sample 2a/b. This leads us

to believe that there could be surface enrichment of Mo species on the outermost exposed surface the Toray paper after repeated dissolution-redeposition cycles during each potential sweep.

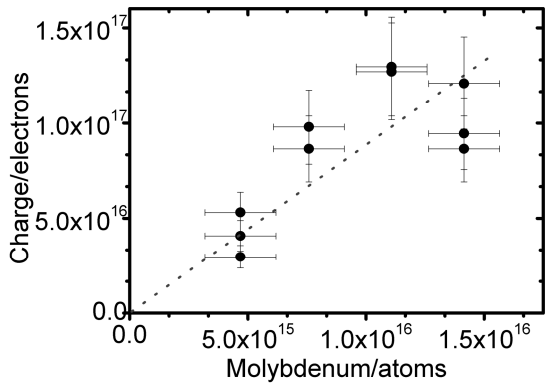

Fig. 4 The charge of the irreversible oxidation peak as a function of the amount of Mo used during the synthesis of MoS_2.

Having established that the MoS_2 is in fact being oxidized at high anodic potentials we will now elaborate on possible reaction mechanisms. The reaction mechanism will enable us to use the irreversible oxidation peaks to determine the amount of MoS_2 present on the surface. A plot of the correlation between the amount of Mo used during synthesis and the charge of the irreversible oxidation peak is shown on figure 4. In a corrosion study by Jaegermann[18], bulk MoS_2 was electrochemically oxidized in KNO_3 and examined by XPS. A shift toward higher binding energies was observed for the S *2p* and Mo *3d* peaks and a broadening was observed in the S *2p* line. This was interpreted as MoS_2 degradation to SO_4^{2-}, S_2^{2-} and MoO_3. We can with this knowledge consider how many electrons we expect to use to oxidize one Mo atom. If we consider one extreme where the carbon supported MoS_2 is decomposed into MoO_3 and SO_4^{2-} the following reactions would take place, where 18 electrons are transferred per Mo atom

$$MoS_2 + 11\ H_2O \rightarrow MoO_3 + 2\ SO_4^{2-} + 22\ H^+ + 18e^- \qquad (1)$$

The other extreme would be that MoS_2 is decomposed into MoO_3 and S_2^{2-} where 4 electrons are needed

$$MoS_2 + 3\ H_2O \rightarrow MoO_3 + S_2^{2-} + 6\ H^+ + 4e^- \qquad (2)$$

According to figure 4 the correlation between the oxidation peak and the deposited amount of Mo yields 8.9 (r^2 =0.55) electrons per Mo atom used in the deposition. This number is in between the two extremes mentioned above. Revisiting the XPS data we can not see whether we have produced excess SO_4^{2-} due to the background of H_2SO_4. We are however also not seeing any significant amounts S_2^{2-} after cyclic voltammetry. While the samples have been subject to a high anodic (1.4 vs. NHE) potential where S_2^{2-} can be oxidized to SO_4^{2-} the subsequent high cathodic (-0.4 vs. NHE) potential can reduce the S_2^{2-} to H_2S[21]. We can not conclusively determine the exact nature of the oxidation reaction. But our measurements indicate that the sulfur in the MoS_2 is only partially oxidized during anodic sweeps, resulting in the following proposed reaction mechanism:

$$MoS_2 + 7\ H_2O \rightarrow MoO_3 + SO_4^{2-} + \tfrac{1}{2}\ S_2^{2-} + 14\ H^+ + 10\ e^- \qquad (3)$$

HER activity of MoS_2/C

In order to determine the activity of the MoS_2/C system per active site, we start with the irreversible oxidation to estimate the total surface area of MoS_2 on the Toray paper. The irreversible oxidation peak of the sample shown in Figure 1 and Figure 2 has a charge of 0.014 C. If we assume that 10 electrons are involved in the oxidation of MoS_2, as presented in the previous section, the surface area will be 4.2 cm^2 of single layered MoS_2 giving an exchange current density(i_0) of $1.1*10^{-6}$ A/cm^2 (and a Tafel slope of 120mV/dec). We have previously shown that the active sites of Au(111) supported MoS_2 nanoparticles are situated on the edge[6](i_0 =$7.9*10^{-6}$ A/cm^2).

The exchange current density on a per active site basis will clearly be higher than the exchange current densities reported above since few of the MoS_2 sites are on the edge. Thus the values above constitute a lower bound for activity. If we incorporate the fact that the MoS_2 nanoparticles are triangular with an edge length of 25 nm approx. 8 % of the atoms will be situated at the edge of the particle. This would lead to a 12-fold increase in exchange current density per active site.

Electrochemical characterization of WS_2

WS_2 exhibits a layered structure similar to MoS_2[11,12], forming the same triangular shape as MoS_2 when prepared under similar conditions. WS_2 supported on SiO_2 has previously been proposed as a catalyst for the hydrogen evolution reaction[22].

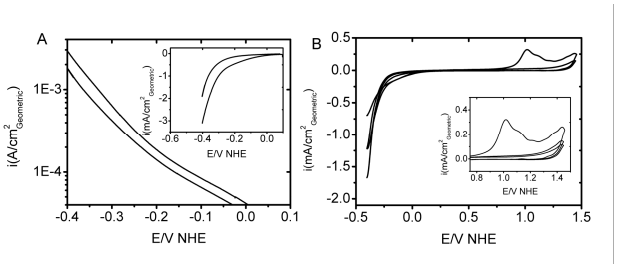

Fig. 5 A:Tafel and polarization curve(inset) of WS_2/C, scanrate 5 mV/s both the initial and the final stable scan is shown. B: CV of WS_2/C showing the deactivation of WS_2.

The WS_2 was studied on Toray paper and the preparation method was similar to that of the MoS_2 samples (See experimental details). In Figure 5 the results of the electrochemical measurements are shown. Figure 5 A) shows a Tafel plot (log i - E) and a polarization curve (i - E) in the region where we have previously observed hydrogen evolution on MoS_2 samples. On the polarization curve (inset of Figure 5 A)) the cathodic current increases at potentials more negative than -0.2 V vs. NHE ascribed to HER activity. The Tafel slope on this sample is found to be 135mV/dec. indicating that the current could be transport limited. Figure 5 b) shows the deactivation of the sample at positive potentials. As with the MoS_2/C sample, an oxidation feature is observed with a peak at approx. 1 V vs. NHE, and on consecutive sweeps the peak disappears concurrent with a drop in the HER current. This is the same behavior as we have seen on the MoS_2/C sample except that the WS_2 sample required two sweeps towards highly anodic potentials before the HER current was affected. This behavior was also observed with high loadings of MoS_2/C samples that surely had formed multilayer's. In this case, the outer layer could be passivated by a sulfur/oxide layer, thus requiring several oxidation/reduction steps to completely dissolve the metal sulfide. Apart from the potential formation of multilayer's the oxidation of the WS_2 is similar to that of MoS_2/C and it is assumed that the oxidation process is similar to that of MoS_2/C.

Cobalt promoted MoS_2 and WS_2

Cobalt is often used to promote WS_2 and MoS_2 in catalyzing the hydrodesulfurization reaction. Both the structural and the catalytic effect of adding cobalt has been extensively studied[2]. It is widely accepted that the cobalt is located at the edge of MoS_2, more specifically the so called S-edge(-1010). Cobalt promotion of MoS_2 has also been shown to change the morphology significantly[11]. Cobalt promoted MoS_2 is usually found as truncated triangles exposing the S-edge $(\bar{1}010)$ predominantly, unlike the unpromoted MoS_2, in which the triangles are less truncated and primarily expose their Mo-edge(10-10)[23]. In the following we will show data for sulfided Co and Co promoted WS_2 and MoS_2.

Electrochemical characterization of cobalt sulfide CoS_x)

The first step in testing the promotion by cobalt is the test of sulfided cobalt itself. We have used Co(acetate) as the Co precursor as described in[11]. The precursor was sulfided under the same conditions as the MoS_2 and the WS_2 samples (see experimental details). The Co is expected to be in the form of Co_8S_9 immediately after sulfidation, but as this form is not stable in air[24] our Co sulfide is most likely partially sulfided (CoS_x).

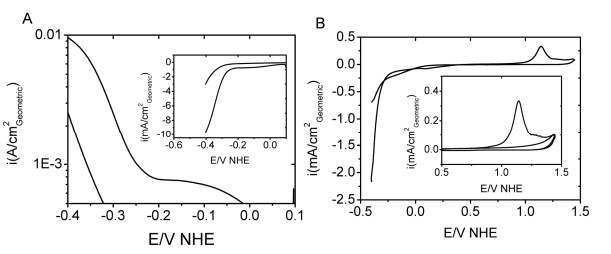

Fig. 6 A:Tafel and polarization curve(inset) of CoS_x/C, both the initial and the final stable scan is shown. B: CV of CoS_x/C showing the oxidation/deactivation of CoS_x

Figure 6 A) shows the initial and the stable Tafel (log i - E) and polarization curves (i - E) within a narrow potential window (maximum +0.1 V vs. NHE). Initially the activity is high, but unlike MoS_2 and WS_2, subsequent sweeps within this potential window show a significant decrease in activity. The decrease is most likely due to the CoS_x instability in sulfuric acid, introducing ambiguity into the interpretation of the current at cathodic potentials as the HER competes with cathodic desorption or dissolution of CoS_x. In Figure 6 B) a wide sweep is exhibited. The CoS_x exhibits similar oxidation features as we have seen on the MoS_2 and WS_2, but in this case the oxidation peak is shifted towards a higher potential(1.14 V vs. NHE). After oxidation the HER activity drops just as with MoS_2 and WS_2, again indicating oxidation of the material.

Cobalt promoted MoS_2(Co-Mo-S) and WS_2(Co-W-S)

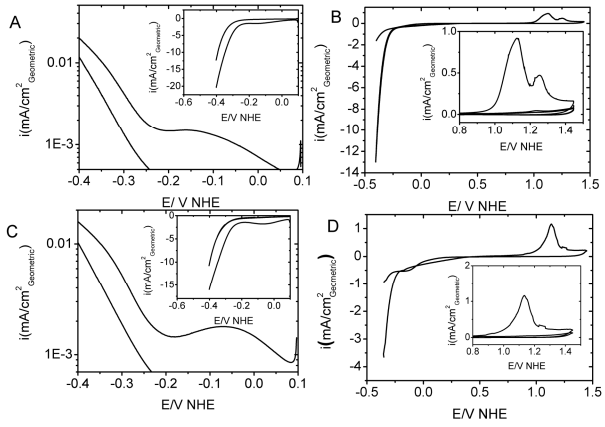

Fig. 7 A,C:Tafel and polarization curve(inset) of Co-Mo-S(A) and Co-WS(C), the scan rate is 5 mV/S both the initial and the final stable scan is shown. B,D: CV of Co-Mo-S(B) and Co-W-S(D) showing the deactivation of Co-Mo-S and Co-W-S.

The Co promoted WS_2 and MoS_2 was prepared by co impregnation of the Mo/W and the Co precursor (see experimental details). Figure 7 A) and C) shows the Tafel (log i - E) and the polarization (inset) curve (i - E) within a narrow potential window (maximum +0.1 V vs. NHE). The

HER current diminishes just as on the pure CoS_x sample: it is initially high and after subsequent sweeps the current decreases noticeably, but unlike the case of pure CoS_x, remains stable at a fairly high level. This indicates that some of the Co promoter is in the state of CoS_x, but as the current stabilizes at a higher level than pure CoS_x, MoS_2 or WS_2 the remaining Co must have a promotion effect. The Tafel slopes are also in the expected region (Co-W-S 132 mV/dec., Co-Mo-S 101 mV/dec.). In Figure 7 B) and D) the CVs within a wide potential window are shown and just as on the other metal sulfides we observe an irreversible oxidation peak followed by a significant decrease in HER activity. The peak maximum, however, seems to be shifted to a more anodic potential (approx. 1.1 V vs. NHE) than those corresponding to the unpromoted MoS_2 and WS_2.

DFT calculations on WS_2, MoS_2, Co-Mo-S and Co-W-S

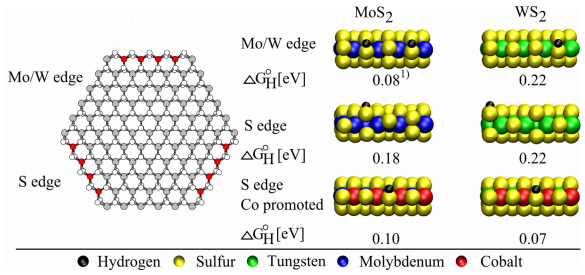

Fig. 8 Left: Ball model of a Mo/WS_2 particle exposing both S edge and Mo/W edge. Right: Differential free energies of hydrogen adsorption. 1) from reference[5].

We have calculated ΔG_H at the S edge $(\bar{1}010)$ and the Mo/W edge $(10\bar{1}0)$ of WS_2 and MoS_2 and on the Co promoted S edge $(\bar{1}010)$ edge of WS_2 and MoS_2 over a wide range of S coverage and H coverage. The choice of the relevant edge configurations have been based on the chemical potential of hydrogen and sulfur at the experimental sulfiding conditions using a thermodynamic model similar to the one presented in[25] . The structure and the differential free energies of H adsorption for these structures can be seen in Figure 8. The results indicate that non promoted WS_2 and MoS_2 nanoparticles should be reasonably good hydrogen evolution catalysts since both edges on both systems have free energies of adsorption close to zero. Hydrogen evolution on MoS_2 is expected to take place predominantly at the Mo edge (ΔG_H = 0.08 eV) rather than the S edge (ΔG_H = 0.18 eV), while for WS_2 both edges are equally good (ΔG_H = 0.22 eV). Given these values for ΔG_H, non-promoted MoS_2 is predicted to be a better hydrogen evolution catalyst than WS_2.

The incorporation of cobalt into the edge structures of both WS_2 and MoS_2 is expected to have a promotion effect. The cobalt only incorporates itself into the S edge of both cases, so ΔG_H values at the Mo/W edge remain unaffected. At the S edge, however, ΔG_H is reduced to 0.10 eV and 0.07 eV for MoS_2 and WS_2, respectively (down from 0.18 eV and 0.22 eV). We note that the free energy of hydrogen adsorption at the cobalt-promoted S edge of MoS_2 is very similar to the free energy of hydrogen adsorption on the Mo edge of MoS_2. Therefore, for MoS_2 the effect of promotion is the increase in the number of sites with high activity. On WS_2 the effect of cobalt promotion is the creation of new sites with higher activity than that prior to promotion.

In comparing all catalyst systems, DFT calculations suggest that cobalt-promoted MoS_2 (Co-Mo-S) should be a better catalyst than Co promoted WS_2 (Co-W-S) because it would have active sites on both edges and therefore a higher total number of active sites.

Linking catalyst structure and composition to HER activity

Calculated DFT values are best compared to experimental data where the activity has been normalized with respect to the number of active sites on the catalyst, in this case the number and type of edge sites on the different metal sulfides. We accomplish this normalization by using the irreversible oxidation features of each sulfide.

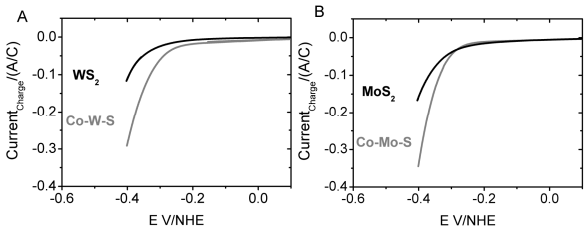

Fig. 9 Polarization curves where the currents of the different metal sulfides have been normalized with respect to the charge of the irreversible oxidation peak. A: Polarization curve of the HER on WS_2 and cobalt promoted WS_2(Co-W-S).B: Polarization curve of the HER on MoS_2 and cobalt promoted MoS_2(Co-Mo-S).

Figure 9 exhibits normalized polarization curves (E- i) pertaining to each of the different samples. There is an apparent promotion effect of Co on both the MoS_2 and the WS_2 samples. The promotion effect on the WS_2 sample can be explained by the DFT calculations predicting that the Co promotion should decrease the free energy of hydrogen adsorption from 0.22 eV to 0.07 eV on the S-edge and thus effectively increase the activity of the active site. MoS_2 is a slightly different case. It has previously been found that MoS_2's Mo-edge, which has a ΔG_H of 0.08 eV, is the major edge exposed, and that this edge does not adsorb cobalt[23, 26, 27]. However, the inhomogenous nature of these nanoparticulate catalysts suggests that both the Mo-edge and the S-edge will be present in significant fractions. Thus, the cobalt on MoS_2's S-edge promotes the HER as its free energy of hydrogen adsorption is decreased from 0.18 eV to 0.10 eV. In other words, the number of active sites is increased since the normally less active S-edges becomes more active in the

presence of cobalt.

Experimental/Calculation details

Toray carbon paper was used as support material because it is inert, of high purity, has high conductivity and because it has adsorption sites/defects that will anchor the metal sulfide particles. The Toray paper was cut into strips that were 1 cm wide and 5 cm long. The Toray paper was loaded with catalyst by wetness impregnation with an aqueous solution of $(NH_4)_6Mo_7O_{24}\cdot 4H_2O$ in the case of MoS_2 and an aqueous solution of $H_{24}N_6O_{39}W_{12}\cdot xH_2O$ in the case of WS_2. In the case of the sulfided Co, $C_4H_4CoO_4\cdot 4H_2O$ in an aqueous solution was used. The promoted WS_2 and MoS_2 were made by co-impregnation of Co and Mo/W. The impregnation of the pure sulfides was done by dropping a 25 µL aliquot (0.3-1 mM for Mo, 0.8 mM for W, 4mM for Co). The co-impregnation of the promoted sulfides was done by adding a 25 µL aliquot of Mo(0.7mM) or W(0.8 mM) solution followed by a 25 µL aliquot of Co(4mM) solution. A different sample preparation was used for the MoS_2 sample for XPS analysis where a the Toray paper was dip coated in the Mo solution(0.14 M) to obtain a more uniform impregnation.

The samples were dried at 140 ˚C and afterwards sulfided in a tube furnace under 10% H_2S in H_2 at 450 ˚C for 4 hours. The samples were cooled down in the same gas stream.

The electrochemical measurements where performed in N_2 purged 0.5 M H_2SO_4 (pH 0.4). To avoid contamination from the SCE reference electrode a salt bridge was used. A Pt mesh was used as the counter electrode.

The XPS data was recorded using a Perkin-Elmer surface analysis system (Physical Electronics Industries Inc., USA) with a chamber base pressure of 10^{-10} Torr.

Al-Kα radiation (1486.6 eV) was used for excitation. The XPS scans on Figure 4 were measured with a pass energy of 100 eV, a step size of 1 eV, and 250 ms/step.

DFT calculations

An infinite stripe model, which has previously been proven successful to investigate MoS_2 based systems [5, 28-30] ,is used to investigate the edges of MoS_2. The infinite stripe exposes both the $(10\bar{1}0)$Mo edge and the $(\bar{1}010)$ S edge. The supercell has 4 Mo atoms in the x-direction and 4 Mo atoms in the y-direction, in order to allow for important reconstructions with a period of 2 in the x direction and to allow decoupling of the Mo edge and the S edge in the y-direction. The stripes are separated by 14.8Å in the z-direction and 9Å in the y-direction.

The plane wave density functional theory code *DACAPO* [31, 32] is used to perform the DFT calculations. The Brillouin zone is sampled using a Monkhorst-Pack k-point set[33] containing 4 k-points in the x-direction and 1 k-point in the y- and z-direction. The calculated equilibrium lattice constant is 3.235Å and 3.214Å for MoS_2 and WS_2 respectively. A plane-wave cutoff of 30 Rydberg and a density wave cutoff of 45 Rydberg are employed using the double-grid technique[34]. Ultrasoft pseudopotentials are used except for sulfur, where a soft pseudopotential is employed[35, 36]. A Fermi temperature of k_BT=0.1eV is used for all calculations and energies are extrapolated to zero electronic temperature. The exchange correlation functional RPBE is used. The convergence criterion for the atomic relaxation is that the norm of the total force should be smaller than 0.15eV/Å, which corresponds approximately to a max force on one atom below 0.05eV/Å . Figures of atomic structures have been made using VMD[37].

The differential free energies are calculated as described in [5] where 0.29eV is added to the pure DFT energy of adsorption in order to take zero point energy and entropy into account.

Conclusions

We have studied the hydrogen evolution on Co promoted and unpromoted nanoparticulate MoS_2 and WS_2 structures. Cyclic voltammetry revealed that they are irreversibly oxidized at high anodic potentials. We have used the irreversible oxidation features to determine the surface area of MoS_2 and proposed a possible oxidation mechanism of MoS_2. XPS analysis showed no change in the oxidation state of MoS_2 after HER measurements, but after oxidation at potentials above 0.6 V vs. NHE MoS_2 was oxidized. We found that the activity of the carbon supported MoS_2 is comparable to that of our previously published results on Au(111) supported MoS_2. WS_2 has a similar structure and was also investigated in this study. It was found to irreversibly oxidize at high anodic potentials, just like MoS_2 and was found to be almost as active. Tests of Cobalt promoted MoS_2 and WS_2 samples were also performed and Co is indeed promoting the HER in both cases. The findings are corroborated by DFT calculations showing that the activity of the different samples should be WS_2<MoS_2=Co-Mo-S<Co-W-S.

Acknowlegdements

J.B. acknowledges support from the Danish Strategic Research Council. T.F.J. acknowledge H.C. Ørsted Postdoctoral Fellowships from the Technical University of Denmark The Center for Atomic-scale Materials Design is supported by the Lundbeck Foundation. We thank the Danish Center for Scientific Computing for computer time. The Center for Individual Nanoparticle Functionality is supported by the Danish National Research Foundation.

Notes and references

[a] *Center for Individual Nanoparticle Functionality (CINF), Department of Physics, Technical University of Denmark, DK-2800 Lyngby, Denmark*
[b] *Center for Atomic-scale Materials Design (CAMd), Department of Physics, Technical University of Denmark, DK-2800 Lyngby, Denmark*

[c] *Department of Chemical Engineering, Stanford University, 381 North-South Mall, Stauffer III, Stanford, CA 94305-5025, USA*
**corresponding author: ibchork@fysik.dtu.dk*

1 J. Greeley, T. F. Jaramillo, J. Bonde, I. B. Chorkendorff and J. K. Nørskov, *Nature Materials,* 2006, **5**, 909-913.

2 H. Topsøe, B. S. Clausen and F. E. Massoth, *Hydrotreating Catalysis*, Springer-Verlag, Berlin, 1996.

3 H. Tributsch, *Zeitschrift Fur Naturforschung Section A-a Journal of Physical Sciences,* 1977, **32**, 972-985.

4 J. P. Wilcoxon, *J Phys Chem B,* 2000, **104**, 7334-7343.

5 B. Hinnemann, P. G. Moses, J. Bonde, K. P. Jorgensen, J. H. Nielsen, S. Horch, I. Chorkendorff and J. K. Nørskov, *J Am Chem Soc,* 2005, **127**, 5308-5309.

6 T. F. Jaramillo, K. P. Jørgensen, J. Bonde, J. H. Nielsen, S. Horch and I. Chorkendorff, *Science : International Edition - AAAS,* 2007, **316**, 100-101.

7 J. K. Nørskov, T. Bligaard, A. Logadottir, J. R. Kitchin, J. G. Chen, S. Pandelov and U. Stimming, *J. Electrochem. Soc.,* 2005, **152**, J23.

8 J. Greeley, J. K. Nørskov, L. A. Kibler, A. M. El-Aziz and D. M. Kolb, *Chemphyschem,* 2006, **7**, 1032-1035.

9 S. Helveg, J. V. Lauritsen, E. Lægsgaard, I. Stensgaard, J. K. Nørskov, B. S. Clausen, H. Topsøe and F. Besenbacher, *Phys. Rev. Lett.,* 2000, **84**, 951-954.

10 J. Kibsgaard, J. V. Lauritsen, E. Laegsgaard, B. S. Clausen, H. Topsoe and F. Besenbacher, *J. Am. Chem. Soc.,* 2006, **128**, 13950-13958.

11 M. Brorson, A. Carlsson and H. Topsøe, *Catalysis Today,* 2007, **123**, 31-36.

12 A. Carlsson, M. Brorson and H. Topsøe, *J. Catal.,* 2004, **227**, 530-536.

13 J. Meier, K. A. Friedrich and U. Stimming, *Faraday Discuss.,* 2002, **121**, 365-372.

14 T. F. Jaramillo, J. Zhang, B. L. Ooi, J. Bonde, K. Andersson, J. Ulstrup, J. K. Nørskov and I. Chorkendorff, In preparation 2008,.

15 N. M. Markovic and P. N. Ross, *Surface Science Reports,* 2002, **45**, 121-229.

16 W. Kautek and H. Gerischer, *Surface Science,* 1982, **119**, 46-60.

17 C.D. Wagner, A. V. Naumkin, A. Kraut-Vass, J. W. Allison, C. J. Powerll and J. R. Rumble Jr., *NIST X-Ray Photoelectron Spectroscopy Database, Standard Reference Database 20, Version 3.4 (2008) http://srdata.nist.gov/xps.*

18 W. Jaegermann and D. Schmeisser, *Surface Science,* 1986, **165**, 143-160.

19 T. Weber, J. C. Muijsers, H. J. M. C. van Wolput, C. P. J. Verhagen and J. W. Niemantsverdriet, *J. Phys. Chem.,* 1996, **100**, 14144-14150.

20 J. H. Nielsen, K. P. Jørgensen, J. Bonde, K. Nielsen, L. Bech, Y. Tison, S. Horch, T. F. Jaramillo and I. Chorkendorff, In preparation 2008,.

21 M. Pourbaix, *ATLAS OF ELECTROCHEMICAL EQUILIBRIA...*, 1966.

22 A. Sobczynski, A. Yildiz, A. J. Bard, A. Campion, M. A. Fox, T. Mallouk, S. E. Webber and J. M. White, *J. Phys. Chem.,* 1988, **92**, 2311-2315.

23 J. V. Lauritsen, J. Kibsgaard, G. H. Olesen, P. G. Moses, B. Hinnemann, S. Helveg, J. K. Nørskov, B. S. Clausen, H. Topsøe, E. Lægsgaard and F. Besenbacher, *Journal of Catalysis,* 2007, **249**, 220-233.

24 I. Alstrup, I. Chorkendorff, R. Candia, B. S. Clausen and H. Topsøe, *Journal of Catalysis,* 1982, **77**, 397-409.

25 M. V. Bollinger, K. W. Jacobsen and J. K. Nørskov, *Phys Rev B,* 2003, **67**, 085410.

26 P. Raybaud, J. Hafner, G. Kresse, S. Kasztelan and H. Toulhoat, *J Catal,* 2000, **190**, 128-143.

27 H. Schweiger, P. Raybaud and H. Toulhoat, *Journal of Catalysis,* 2002, **212**, 33-38.

28 B. Hinnemann, J. K. Nørskov and H. Topsøe, *J Phys Chem B,* 2005, **109**, 2245-2253.

29 J. V. Lauritsen, M. Nyberg, R. T. Vang, M. V. Bollinger, B. S. Clausen, H. Topsøe, K. W. Jacobsen, E. Lægsgaard, J. K. Nørskov and F. Besenbacher, *Nanotechnology,* 2003, **14**, 385-389.

30 L. S. Byskov, J. K. Nørskov, B. S. Clausen and H. Topsøe, *J Catal,* 1999, **187**, 109-122.

31 S. R. Bahn and K. W. Jacobsen, *Comput Sci Eng,* 2002, **4**, 56-66.

32 B. Hammer, L. B. Hansen and J. K. Nørskov, *Physical Review B,* 1999, **59**, 7413-7421.

33 H. J. Monkhorst and J. D. Pack, *Phys Rev B,* 1976, **13**, 5188-5192.

34 K. Laasonen, A. Pasquarello, R. Car, C. Lee and D. Vanderblit, *Phys Rev B,* 1993, **47**, 10142-10153.

35 N. Troullier and J. L. Martins, *Phys Rev B,* 1991, **43**, 1993-2006.

36 D. Vanderbilt, *Phys. Rev. B,* 1990, **41**, 7892-7895.

37 W. Humphrey, A. Dalke and K. Schulten, *J. Mol. Graph.,* 1996, **14**, 33

Paper 10

Adsorption and van der Waals binding of thiophene, butadiene, and benzene on the basal plane of MoS_2 -A density functional study.

Poul Georg Moses[a], Bengt Lundqvist[a,b], and Jens K. Nørskov[a,*]

[a]*Center for Atomic-scale Materials Design (CAMD), Department of Physics, Building 307, Nano DTU, Technical University of Denmark, DK-2800 Kgs. Lyngby, Denmark.*

[b]*Department of Applied Physics, Chalmers University of Technology, SE – 412 96 Göteborg, Sweden*

[*]Corresponding author: Jens K. Nørskov: norskov@fysik.dtu.dk

Accurate calculations of adsorption energies of cyclic molecules are of key importance in investigations of e.g. hydrodesulfurization catalysis. The present density functional theory (DFT) study demonstrates that van der Waals interactions are of importance for binding energies on MoS_2 surfaces and that DFT with a recently developed vdW-DF exchange-correlation functional accurately calculates the van der Waals energy. We have calculated values for the adsorption energy of thiophene, butadiene and benzene on the basal plane of MoS_2. These molecules are important reactants and products in HDS catalysis. We find that the adsorption is mainly due to van der Waals interactions, which gives quite significant contributions to the binding of thiophene, butadiene, and benzene.

1 Introduction

The strict legislations on sulphur contents in diesel fuel require that the most refractory sulphur containing compounds are removed from the crude oil. This has increased the interest in the reaction mechanisms in hydrodesulfurization (HDS) catalysis in order to improve present day catalysts. The key to understand the reaction mechanisms is detailed knowledge of the reaction energy landscape. This requires methods to accurately calculate or measure adsorption energies of reactants, products, and inhibitors and barriers of the reactions.

Several density functional theory (DFT) studies have successfully investigated HDS catalysis and have provided valuable insight into the structure, adsorption properties and reactivity of HDS catalyst e.g. [1-13]. The success of DFT is due to a well-proven record in calculating accurate chemisorption energies of molecules on surfaces [14]. However, calculating the physisorption energy is much more of a challenge due to the absence of van der Waals (vdW) forces in the most widely used implementations of DFT. The lack of vdW forces could be problematic in studies of HDS since most of the molecules of interest in HDS are aromatic. Such molecules are believed to have considerable binding due to vdW forces. However, recent developments in exchange-correlation functionals [15] have shown promising results for adsorption and binding of systems dominated by vdW interactions [15-22].

The adsorption of thiophene, butadiene, and benzene on the basal plane of MoS_2 is investigated by use of the novel exchange correlation functional, vdW-DF [15]. Thereby, the importance of vdW forces on adsorption energies on MoS_2 is elucidation. It is found that the adsorption energies of thiophene, butadiene, and benzene are dominated by vdW interactions, and the theoretical predictions agree with results from well defined ultra high vacuum surface science experiments [23]. The present results

indicate that the vdW interaction for adsorption on MoS_2 based system is well described by the vdW-DF functional.

2 Calculational details

A slab model is used to investigate the basal plane (0001) of MoS_2. The supercell has 4 MoS_2 units in the x- and y-direction. The slabs are separated by 21.82Å in the z-direction. This model represents the basal plane of MoS_2 single crystal where the effect of the second layer of MoS_2 is assumed to be small, which has been shown to be a reasonable approximation for graphite [17]. The plane wave density functional theory code *DACAPO* [14, 24] is used to perform the DFT calculations. The Brillouin zone is sampled using a Monkhorst-Pack k-point set [25] containing 4 k-points in the x- and y-direction and 1 k-point in z-direction. The calculated equilibrium lattice constant of a=3.235 Å compares well to the experimental lattice constant of 3.16Å [26]. A plane-wave cutoff of 30 Rydberg and a density wave cutoff of 60 Rydberg (45 Rydberg for benzene) are employed using the double-grid technique [27]. Ultrasoft pseudopotentials are used except for sulfur, where a soft pseudopotential is employed [28, 29]. A Fermi temperature of k_BT=0.1eV(0.001eV) is used for slab (molecules) and energies are extrapolated to zero electronic temperature. Figures of atomic structures have been made using VMD [30]. The convergence criterion for the atomic relaxation is that the maximum force on one atom should be smaller than 0.01eV/Å.

The exchange correlation functional RPBE[14] (revPBE [31]) is used for structure optimization of thiophene and pyridine (for benzene). The binding curves have been constructed using the vdW-DF functional [15] which has recently been implemented in the grid based real space projected augmented wave code GPAW [32]. The $E_{vdW\text{-}DF}$ energy of thiophene and butadiene (benzene) is calculated as a

perturbation to the RPBE (revPBE) density and calculated using the self consistent RPBE (revPBE) density. The vdW-DF exchange correlation energy given in equation 1

Equation 1 $E_{xc} = E_{LDA,c} + E_{GGA,x} + E_c^{nl.}$

Where $E_{GGA,x}$ is the RPBE (revPBE) exchange for thiophene and butadiene (revPBE) and $E_{LDA,C}$ is the LDA correlation. E_c^{nl} is calculated as seen in equation 2,

Equation 2 $$E_c^{nl} = \frac{1}{2}\int\int n(r)\phi(r,r')n(r')drdr'$$

Where the interaction kernel $\phi(r,r')$ is calculated as described in [15]. The integral is calculated for densities above $0.0001/a_0^3$ an a density grid with 0.10Å (0.11Å) for thiophene and butadiene (benzene). The periodic boundary conditions are included using the minimum image convention [33]. The binding site and orientation of the molecule have been identified by constrained minimization fixing the slab and the z coordinate of the molecule and/or free minimization of the molecule fixing the slab. The binding curves are calculated by moving the molecule in the z direction and not allowing for possible reconstructions of the molecule and the slab.

3 Results and discussion

We have investigated the adsorption of thiophene, butadiene, and benzene on the basal (0001) plane of MoS_2. The adsorption of thiophene and butadiene have previously been investigated in a well defined surface science experiment [23], which found that the binding on the basal plane is weak, with thiophene and butadiene adsorption energy values measured as -0.42eV and -0.37eV respectively.

3.1 Thiophene

For thiophene, there are two adsorption configurations (a,b in Fig 1.) that have very similar binding energies and the binding curves are also similar. There is little or no chemical bonding and the entire

bond is given by vdW interaction. The calculated adsorption energy is -0.47eV which compares well with the experimental adsorption energy of -0.42eV.

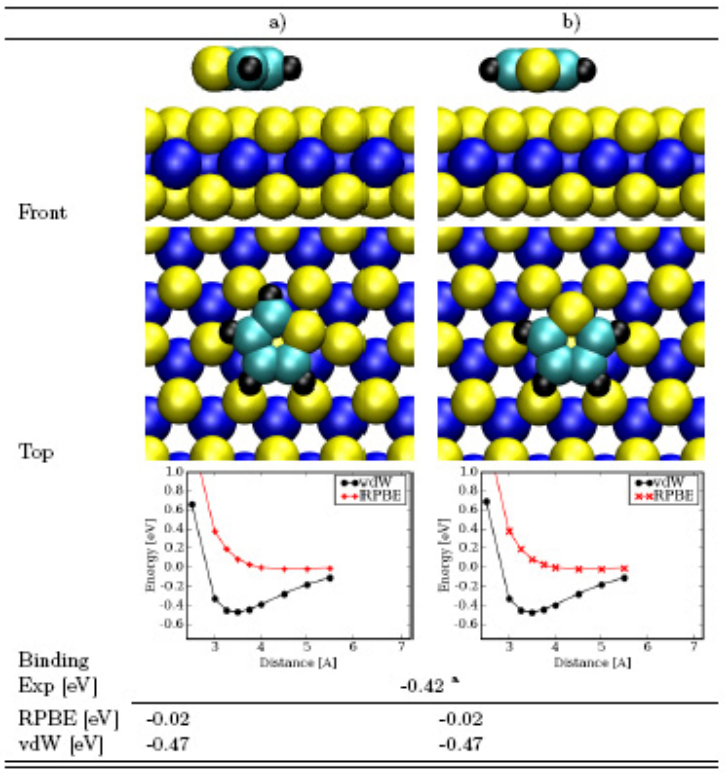

Figure 1 Thiophene adsorption. potential-energy curve calculated with RPBE and vdW-DF exchange-correlation functionals, respectively, in two confurations (a) and b)). Experimental value (a) is from [23]

3.2 Butadiene

Three different butadiene adsorption configurations (seen in Fig. 2) have been investigated and the binding curves can be seen in Fig 2. The binding energies for the different adsorption configurations are very similar and the maximum binding energy is -0.4eV. Like for thiophene the binding energies are dominated by vdW interactions. The agreement between the experimental and the calculated adsorption-energy values is high.

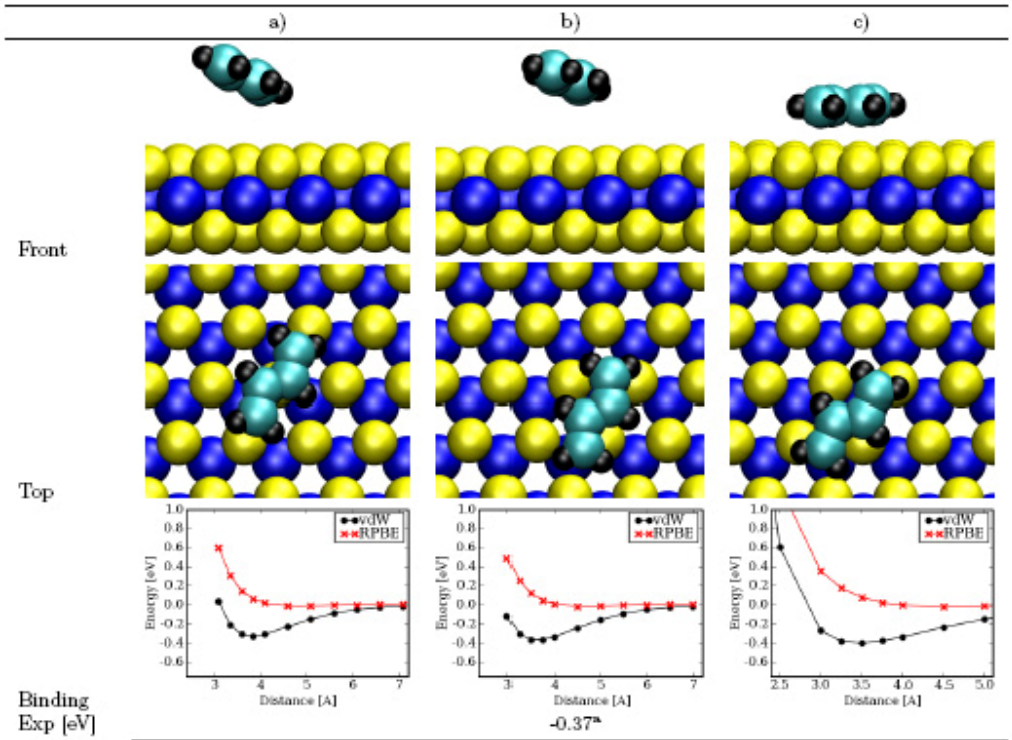

Figure 2 Butadiene adsorption on the basal plane of MoS_2 in three different configurations (a), b), and c)). The abscissa in the binding curves is the distance from the center of mass of butadiene to the z position of the top sulfur layer. Experimental value from [23]

3.3 Benzene

A single adsorption configuration have been investigated for benzene (see Fig. 3.). The binding energy is -0.47eV. Like for thiophene and butadiene the binding energy is dominated by vdW interactions.

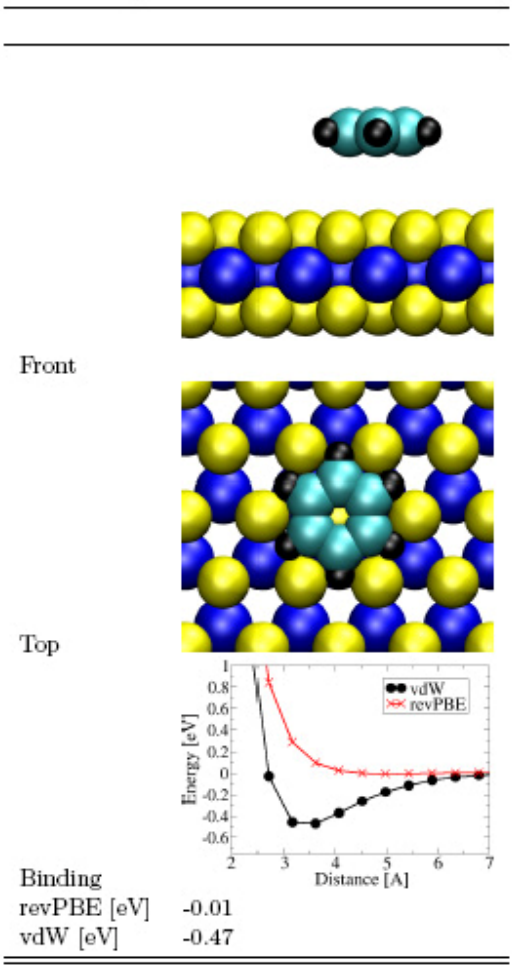

Figure 3 Benzene adsorption on the basal plane of MoS_2. The abscissa in the binding curve is the distance from the center of mass of benzene to the z position of the top sulfur layer.

The overall picture is that vdW forces dominate the bonds between benzene, thiophene, and butadiene and the basal plane of MoS_2. The adsorption energy values of the three molecules lie rather close, slightly below 0.5eV. It is largest for thiophene followed by butadiene and benzene.

There is good agreement between experimental and theoretical values.

The binding energy varies very little between different adsorption geometries

The relatively strong vdW binding energy of thiophene, butadiene and benzene could be due to the fact that these molecules have delocalised electrons in the aromatic structure of thiophene and benzene and the conjugated double bonds in butadiene.

The present results indicate that including vdW binding will significantly affect the adsorption energy and thereby the coverage of aromatic compounds on MoS_2 based catalysts. Increasing the adsorption energies by 0.5eV and possibly more for larger molecules will be of significant importance since molecules like thiophene and dibenzoethiophene have been found to make weak chemical bonds with the equilibrium edge structures and single vacancies on the equilibrium edges [3, 5, 7, 12, 13].

4 Conclusion

We have calculated the adsorption properties of thiophene, butadiene and benzene on the basal plane of MoS_2 using the recently developed exchange correlation functional vdW-DF [15] . For adsorption energy values, a high degree of agreement is found between experiment and theory. For all three molecules the bond is found to be due to vdW interactions. The present results for the vdW binding of thiophene, butadiene, and benzene (-0.47eV, -0.40eV , and -0.47 respectively) show a magnitude that will influence the coverage of these species considerably. Obvious, the van der Waals forces cannot be neglected when calculating adsorption energies of aromatic compounds and conjugated compounds on inert surfaces, like the basal plane of MoS_2. The high degree of agreement between theory and experiment shows that the vdW-DF functional is promising for accurately calculating adsorption energies.

Needless to say, there are several aspects of the vdW-DF and its application in a context like this that need to be scrutinzed, including optimization of the account of exchange, understanding of how seeminly different surfaces, like graphite and the basal plane of MoS_2, can give so similar physisorption

values, and experience of the coexistence of vdW forces with other forces of a similar magnitude, like electrostatic ones in, *e.g.*, H_2S adsorption and expected covalent ones at, *e.g.*, the edge of nanosized MoS_2 trippellayers.

Acknowledgements: Fruitful discussions with Jens Jørgen Mortensen. The Lundbeck foundation and the Danish center for scientific computing grant number x.xxx.

References

[1] M.V. Bollinger, K.W. Jacobsen, J.K. Nørskov, Phys Rev B 67 (2003) 085410.

[2] H. Schweiger, P. Raybaud, H. Toulhoat, Journal of Catalysis, 212 (2002) 33.

[3] J. Paul, S. Cristol, E. Payen, Catalysis Today, 130 (2008) 139.

[4] S. Cristol, J. Paul, C. Schovsbo, E. Veilly, E. Payen, J Catal 239 (2006) 145.

[5] S. Cristol, J.F. Paul, E. Payen, D. Bougeard, F. Hutschka, S. Clémendot, J Catal 224 (2004) 138.

[6] A. Travert, H. Nakamura, R.A.C. van Santen S., J.F. Paul, E. Payen, J Am Chem Soc 124 (2002) 7084.

[7] P.G. Moses, B. Hinnemann, H. Topsoe, J.K. Norskov, Journal of Catalysis 248 (2007) 188.

[8] A. Logadottir, P.G. Moses, B. Hinnemann, N.Y. Topsøe, K.G. Knudsen, H. Topsøe, J.K. Nørskov, Catal Today 111 (2006) 44.

[9] T. Weber, J.A. Rob van Veen, Catalysis Today, 130 (2008) 170.

[10] B. Hinnemann, P.G. Moses, J.K. Norskov, Journal of Physics-Condensed Matter 20 (2008) 064236.

[11] L.S. Byskov, M. Bollinger, J.K. Nørskov, B.S. Clausen, H. Topsøe, J Mol Catal A-Chem Chemical 163 (2000) 117.

[12] R. Koide, E.J.M. Hensen, J.F. Paul, S. Cristol, E. Payen, H. Nakamura, R.A. van Santen, Catalysis Today 130 (2008) 178.

[13] R. Koide, E.J.M. Hensen, J.F. Paul, S. Cristol, E. Payen, H. Nakamura, R.A. van Santen, Topics in Catalysis 45 (2007) 175.

[14] B. Hammer, L.B. Hansen, J.K. Norskov, Physical Review B 59 (1999) 7413.

[15] M. Dion, H. Rydberg, E. Schroder, D.C. Langreth, B.I. Lundqvist, Phys. Rev. Lett. 92 (2004) 246401.

[16] S.D. Chakarova-Kack, O. Borck, E. Schroder, B.I. Lundqvist, Physical Review B 74 (2006) 155402.

[17] S.D. Chakarova-Kack, E. Schroder, B.I. Lundqvist, D.C. Langreth, Phys. Rev. Lett. 96 (2006) 146107.

[18] J. Kleis, B.I. Lundqvist, D.C. Langreth, E. Schoder, Physical Review B 76 (2007) 100201.

[19] A. Puzder, M. Dion, D.C. Langreth, J. Chem. Phys. 124 (2006) .

[20] T. Thonhauser, A. Puzder, D.C. Langreth, J. Chem. Phys. 124 (2006) .

[21] K. Johnston, J. Kleis, B.I. Lundqvist, R.M. Nieminen, Physical Review B 77 (2008) .

[22] V.R. Cooper, T. Thonhauser, A. Puzder, E. Schroder, B.I. Lundqvist, D.C. Langreth, J. Am. Chem. Soc. 130 (2008) 1304.

[23] M. Salmeron, G.A. Somorjai, A. Wold, R. Chianelli, K.S. Liang, Chemical Physics Letters 90 (1982) 105.

[24] S.R. Bahn, K.W. Jacobsen, Comput Sci Eng 4 (2002) 56.

[25] H.J. Monkhorst, J.D. Pack, Phys Rev B 13 (1976) 5188.

[26] T. Böker, R. Severin, A. Müller, C. Janowitz, R. Manzke, D. Voss, P. Krüger, A. Mazur, J. Pollmann, Phys Rev B 64 (2001) 235305.

[27] K. Laasonen, A. Pasquarello, R. Car, C. Lee, D. Vanderblit, Phys Rev B 47 (1993) 10142.

[28] N. Troullier, J.L. Martins, Phys Rev B 43 (1991) 1993.

[29] D. Vanderbilt, Phys. Rev. B 41 (1990) 7892.

[30] W. Humphrey, A. Dalke, K. Schulten, J. Mol. Graph. 14 (1996) 33.

[31] Y.K. Zhang, W.T. Yang, Phys. Rev. Lett. 80 (1998) 890.

[32] J.J. Mortensen, L.B. Hansen, K.W. Jacobsen, Physical Review B 71 (2005) 035109.

[33] W.W. Wood, F.R. Parker, J. Chem. Phys. 27 (1957) 720.